Vol. 64 ▪ No. 6 ▪ June 2023

JNM

The Journal of Nuclear Medicine

FEATURED ARTICLE

Radiolabeled GPVI-Fc for PET Imaging of Multiple Extracellular Matrix Fibers: A New Look into Pulmonary Fibrosis Progression. Simon Isser et al. See page 940.

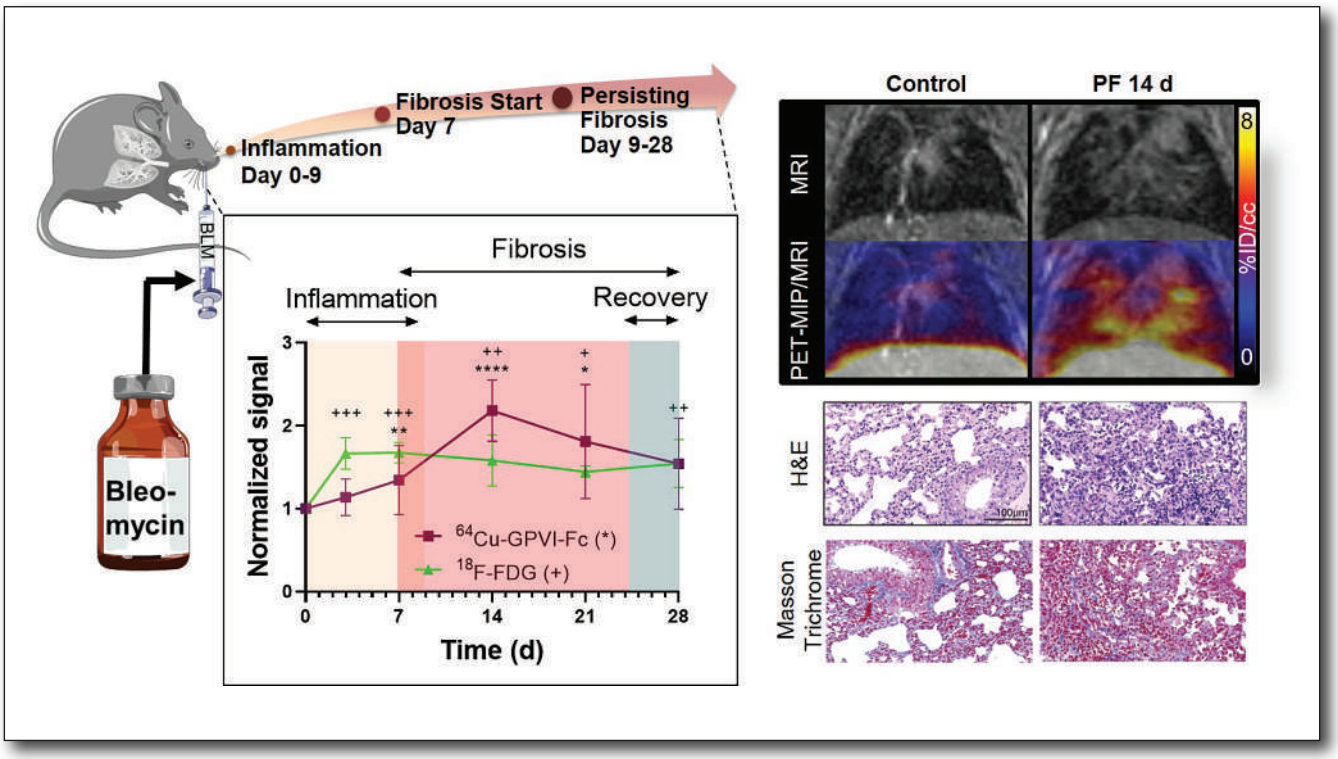

Prostate cancer PROs: Incorporating patient-reported outcomes in radionuclide therapy monitoring. Lisa Gudenkauf et al. See page 869.

SNMMI SOCIETY OF NUCLEAR MEDICINE & MOLECULAR IMAGING

Come see us at Booth #2065

Together let's make this moment count

Visit Booth #2065 at the SNMMI Annual Meeting and we'll donate $10 to Alex's Lemonade Stand on your behalf!*

Help us with our fundraiser for Alex's Lemonade Stand Foundation (ALSF) to support the fight against childhood cancer!

Please stop by our booth (at the 2023 SNMMI in Chicago) to get your badge scanned and make your visit count for ALSF!

* Jubilant Radiopharma will donate $10 USD per visitor, for a maximum of $5,000 USD for the duration of the SNMMI 2023 meeting.

Alex's Lemonade Stand FOUNDATION FOR CHILDHOOD CANCER ™

Or visit our Lemonade Stand to join us in the fight against childhood cancer
https://www.alexslemonade.org/mypage/3253774

Alex's Lemonade Stand Foundation (ALSF), a registered 501(c)3 charity, has raised millions of dollars toward fulfilling Alex's dream of finding a cure, funding hundreds of pediatric cancer research projects nationally. In addition, ALSF provides support to families affected by childhood cancer through programs such as Travel For Care and SuperSibs.

Jubilant DraxImage Inc. dba Jubilant Radiopharma,
16751 Trans-Canada Highway, Kirkland, Quebec, Canada H9H 4J4
Phone: 1.888.633.5343 / 514.630.7080

www.JubilantRadiopharma.com

JUBILANT RADIOPHARMA

Improving Lives Through Nuclear Medicine™

JNM

Volume 64 • Number 6 • June 2023

Cardiolite®

Kit for the Preparation of
Technetium Tc99m Sestamibi for Injection

Myocardial Perfusion Function and Risk Stratification[1,2]

- **First technetium-labeled myocardial perfusion imaging agent providing physicians prognostic information for patient management decisions related to coronary artery disease[1,3]**
- **Used in over 10 million patients since 1991[3]**

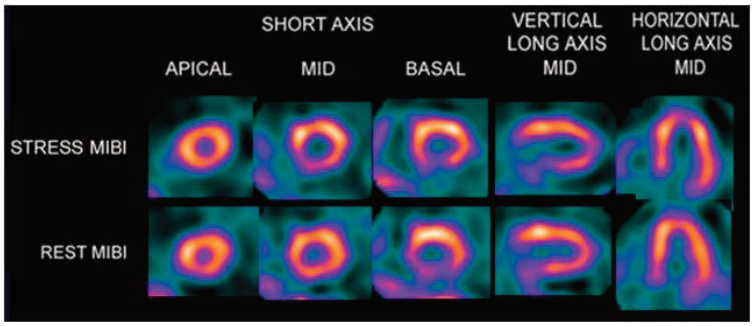

INDICATIONS AND USAGE FOR CARDIOLITE®

Myocardial Imaging: Cardiolite® (Kit for the Preparation of Technetium Tc99m Sestamibi for Injection), is a myocardial perfusion agent that is indicated for detecting coronary artery disease by localizing myocardial ischemia (reversible defects) and infarction (non-reversible defects), in evaluating myocardial function and developing information for use in patient management decisions. Cardiolite® evaluation of myocardial ischemia can be accomplished with rest and cardiovascular stress techniques (e.g. exercise or pharmacologic stress in accordance with the pharmacologic stress agent's labeling).

CONTRAINDICATIONS:

None known.

IMPORTANT SAFETY INFORMATION:

Cardiolite® has been rarely associated with acute severe allergic and anaphylactic events of angioedema and generalized urticaria. In some patients the allergic symptoms developed on the second injection during Cardiolite® imaging. The most frequently reported adverse events include headache, chest pain/angina, ST segment changes on ECG, nausea, and abnormal taste and smell.

Infrequently, death has occurred 4 to 24 hours after Tc99m Sestamibi use and is usually associated with exercise stress testing (See Section 5.2). Pharmacologic induction of cardiovascular stress may be associated with serious adverse events such as myocardial infarction, arrhythmia, hypotension, bronchoconstriction and cerebrovascular events.

WARNINGS AND PRECAUTIONS:

In studying patients in whom cardiac disease is known or suspected, care should be taken to assure continuous monitoring and treatment in accordance with safe, accepted clinical procedure.

Caution should be exercised and emergency equipment should be available when administering Cardiolite®.

Before administering Cardiolite® patients should be asked about the possibility of allergic reactions to either Cardiolite® or Miraluma®. Miraluma® is an identical compound used in breast imaging.

The contents of the vial are intended only for use in the preparation of Technetium Tc99m Sestamibi and are not to be administered directly to the patient without first undergoing the preparative procedure.

Please see Brief Prescribing Summary on the following page.

Please see Full Prescribing information at www.cardiolite.com

References:
1. Cardiolite® [package insert]. N. Billerica, MA: Lantheus Medical Imaging.
2. Hachamovitch R, Berman DS, Shaw LJ, et al. Incremental prognostic value of myocardial perfusion single photon emission computed tomography for the prediction of cardiac death: differential stratification for risk of cardiac death and myocardial infarction. *Circulation. 1998;97:535-543.*
3. Data on file. Lantheus Medical Imaging, Inc.

LANTHEUS™

Cardiolite®
Kit for the Preparation of
Technetium Tc99m Sestamibi for Injection

FOR DIAGNOSTIC USE

BRIEF SUMMARY

Please see Full Prescribing Information available at https://www.lantheus.com/assets/Cardiolite-US-PI-513121-0619mktg.pdf for complete information.

INDICATION AND USAGE

Myocardial Imaging: CARDIOLITE®, Kit for the Preparation of Technetium Tc99m Sestamibi for Injection, is a myocardial perfusion agent that is indicated for detecting coronary artery disease by localizing myocardial ischemia (reversible defects) and infarction (non-reversible defects), in evaluating myocardial function and developing information for use in patient management decisions. CARDIOLITE® evaluation of myocardial ischemia can be accomplished with rest and cardiovascular stress techniques (e.g., exercise or pharmacologic stress in accordance with the pharmacologic stress agent's labeling).

It is usually not possible to determine the age of a myocardial infarction or to differentiate a recent myocardial infarction from ischemia.

Breast Imaging: MIRALUMA®, Kit for the Preparation of Technetium Tc99m Sestamibi for Injection, is indicated for planar imaging as a second line diagnostic drug after mammography to assist in the evaluation of breast lesions in patients with an abnormal mammogram or a palpable breast mass.

MIRALUMA® is not indicated for breast cancer screening, to confirm the presence or absence of malignancy, and it is not an alternative to biopsy.

CONTRAINDICATIONS

None known

WARNINGS AND PRECAUTIONS

Warnings

In studying patients in whom cardiac disease is known or suspected, care should be taken to assure continuous monitoring and treatment in accordance with safe, accepted clinical procedure. Infrequently, death has occurred 4 to 24 hours after Tc99m Sestamibi use and is usually associated with exercise stress testing.

Pharmacologic induction of cardiovascular stress may be associated with serious adverse events such as myocardial infarction, arrhythmia, hypotension, bronchoconstriction and cerebrovascular events. Caution should be used when pharmacologic stress is selected as an alternative to exercise; it should be used when indicated and in accordance with the pharmacologic stress agent's labeling.

Technetium Tc99m Sestamibi has been rarely associated with acute severe allergic and anaphylactic events of angioedema and generalized urticaria. In some patients the allergic symptoms developed on the second injection during CARDIOLITE® imaging. Patients who receive CARDIOLITE® or MIRALUMA® imaging are receiving the same drug. Caution should be exercised and emergency equipment should be available when administering Technetium Tc99m Sestamibi. Also, before administering either CARDIOLITE® or MIRALUMA®, patients should be asked about the possibility of allergic reactions to either drug.

General Precautions

The contents of the vial are intended only for use in the preparation of Technetium Tc99m Sestamibi and are not to be administered directly to the patient without first undergoing the preparative procedure.

Radioactive drugs must be handled with care and appropriate safety measures should be used to minimize radiation exposure to clinical personnel. Also, care should be taken to minimize radiation exposure to the patients consistent with proper patient management.

Contents of the kit before preparation are not radioactive. However, after the Sodium Pertechnetate Tc99m Injection is added, adequate shielding of the final preparation must be maintained. The components of the kit are sterile and non-pyrogenic. It is essential to follow directions carefully and to adhere to strict aseptic procedures during preparation.

Technetium Tc99m labeling reactions depend on maintaining the stannous ion in the reduced state. Hence, Sodium Pertechnetate Tc99m Injection containing oxidants should not be used.

Technetium Tc99m Sestamibi should not be used more than six hours after preparation.

Radiopharmaceuticals should be used only by physicians who are qualified by training and experience in the safe use and handling of radionuclides and whose experience and training have been approved by the appropriate government agency authorized to license the use of radionuclides.

Stress testing should be performed only under the supervision of a qualified physician and in a laboratory equipped with appropriate resuscitation and support apparatus.

The most frequent exercise stress test endpoints sufficient to stop the test reported during controlled studies (two-thirds were cardiac patients) were:

Fatigue	35%
Dyspnea	17%
Chest Pain	16%
ST-depression	7%
Arrhythmia	1%

ADVERSE REACTIONS

Adverse events were evaluated in 3741 adults who were evaluated in clinical studies. Of these patients, 3068 (77% men, 22% women, and 0.7% of the patient's genders were not recorded) were in cardiac clinical trials and 673 (100% women) in breast imaging trials. Cases of angina, chest pain, and death have occurred. Adverse events reported at a rate of 0.5% or greater after receiving Technetium Tc99m Sestamibi administration are shown in the following table:

Table 2.0
Selected Adverse Events Reported in > 0.5% of Patients Who Received Technetium Tc99m Sestamibi in Either Breast or Cardiac Clinical Studies*

Body System	Breast Studies	Cardiac Studies		
	Women n = 673	Women n = 685	Men n = 2361	Total n = 3046
Body as a Whole	21 (3.1%)	6 (0.9%)	17 (0.7%)	23 (0.8%)
Headache	11 (1.6%)	2 (0.3%)	4 (0.2%)	6 (0.2%)
Cardiovascular	9 (1.3%)	24 (3.5%)	75 (3.2%)	99 (3.3%)
Chest Pain/Angina	0 (0%)	18 (2.6%)	46 (1.9%)	64 (2.1%)
ST segment changes	0 (0%)	11 (1.6%)	29 (1.2%)	40 (1.3%)
Digestive System	8 (1.2%)	4 (0.6%)	9 (0.4%)	13 (0.4%)
Nausea	4 (0.6%)	1 (0.1%)	2 (0.1%)	3 (0.1%)
Special Senses	132 (19.6%)	62 (9.1%)	160 (6.8%)	222 (7.3%)
Taste Perversion	129 (19.2%)	60 (8.8%)	157 (6.6%)	217 (7.1%)
Parosmia	8 (1.2%)	6 (0.9%)	10 (0.4%)	16 (0.5%)

*Excludes the 22 patients whose gender was not recorded.

In the clinical studies for breast imaging, breast pain was reported in 12 (1.7%) of the patients. In 11 of these patients the pain appears to be associated with biopsy/surgical procedures.

The following adverse reactions have been reported in ≤ 0.5% of patients: signs and symptoms consistent with seizure occurring shortly after administration of the agent; transient arthritis, angioedema, arrythmia, dizziness, syncope, abdominal pain, vomiting, and severe hypersensitivity characterized by dyspnea, hypotension, bradycardia, asthenia, and vomiting within two hours after a second injection of Technetium Tc99m Sestamibi. A few cases of flushing, edema, injection site inflammation, dry mouth, fever, pruritis, rash, urticaria and fatigue have also been attributed to administration of the agent.

DRUG INTERACTIONS

Specific drug-drug interactions have not been studied.

OVERDOSAGE

The clinical consequences of overdosing with CARDIOLITE® are not known.

PATIENT COUNSELING INFORMATION

CARDIOLITE® and MIRALUMA® are different names for the same drug. Patients should be advised to inform their health care provider if they had an allergic reaction to either drug or if they had an imaging study with either drug.

Lactation: Interruption of breastfeeding after exposure to Technetium Tc99m Sestamibi is not necessary, however, a lactating woman should be advised to consider restricting close contact with her breast fed infant to a maximum of 5 hours in the 24 hour period after Technetium Tc99m Sestamibi administration in order to minimize radiation exposure.

To report SUSPECTED ADVERSE REACTIONS, contact Lantheus Medical Imaging, Inc. at 1-800-362-2668 or FDA at 1-800-FDA-1088 or www.fda.gov/medwatch.

Distributed by:
Lantheus Medical Imaging®
331 Treble Cove Road, N. Billerica, Massachusetts 01862 USA
For Ordering Tel: Toll Free: 800-299-3431
All Other Business: 800-362-2668
(For Massachusetts and International call 978-667-9531)

LANTHEUS™

PM-US-CA-0022 513121-0619

JNM The Journal of NUCLEAR MEDICINE

The Official Publication of **SNMMI**

MISSION STATEMENT: *The Journal of Nuclear Medicine* advances the knowledge and practice of molecular imaging and therapy and nuclear medicine to improve patient care through publication of original basic science and clinical research.

JNM (ISSN 0161-5505 [print]; ISSN 2159-662X [online]) is published monthly by SNMMI, 1850 Samuel Morse Drive, Reston, VA 20190-5316. Periodicals postage is paid at Herndon, VA, and additional mailing offices. Postmaster, send address changes to *The Journal of Nuclear Medicine,* 1850 Samuel Morse Drive, Reston, VA 20190-5316. The costs of publication of all nonsolicited articles in *JNM* were defrayed in part by the payment of page charges. Therefore, and solely to indicate this fact, these articles are hereby designated "advertisements" in accordance with 18 USC section 1734.

DISCLOSURE OF COMMERCIAL INTEREST: Johannes Czernin, MD, editor-in-chief of *The Journal of Nuclear Medicine,* has indicated that he is a founder of Sofie Biosciences and holds equity in the company and in intellectual property invented by him, patented by the University of California, and licensed to Sofie Biosciences. He is also a founder and board member of Trethera Therapeutics and holds equity in the company and in intellectual property invented by him, patented by the University of California, and licensed to Triangle. He also serves on the medical advisory board of Actinium Pharmaceuticals and on the scientific advisory boards of POINT Biopharma, RayzeBio, and Jubilant Pharma and is a consultant for Amgen. No other potential conflicts of interest were reported. Manuscripts submitted to *JNM* with potential conflicts are handled by a guest editor.

EDITORIAL COMMUNICATIONS should be sent to: Editor-in-Chief, Johannes Czernin, MD, *JNM* Office, SNMMI, 1850 Samuel Morse Drive, Reston, VA 20190-5316. Phone: (703) 326-1185; Fax: (703) 708-9018. To submit a manuscript, go to https://submit-jnm.snmjournals.org.

BUSINESS COMMUNICATIONS concerning permission requests should be sent to the publisher, SNMMI, 1850 Samuel Morse Drive, Reston, VA 20190-5316; (703) 708-9000; home page address: jnm.snmjournals.org. Subscription requests and address changes should be sent to Membership Department, SNMMI at the address above. Notify the Society of change of address and telephone number at least 30 days before date of issue by sending both the old and new addresses. Claims for copies lost in the mail are allowed within 90 days of the date of issue. Claims are not allowed for issues lost as a result of insufficient notice of change of address. For information on advertising, contact Team SNMMI (Kevin Dunn, Rich Devanna, and Charlie Meitner; (201) 767-4170; fax: (201) 767-8065; TeamSNMMI@cunnasso.com). Advertisements are subject to editorial approval and are restricted to products or services pertinent to nuclear medicine. Closing date is the first of the month preceding the date of issue.

INDIVIDUAL SUBSCRIPTION RATES for the 2023 calendar year are $633 within the United States and Canada; $680 elsewhere. Make checks payable to the SNMMI. CPC IPM Sales Agreement No. 1415158. Sales of individual back copies from 1999 through the current issue are available for $60 at http://www.snmmi.org/subscribe (subscriptions@snmmi.org; fax: (703) 667-5134). Individual articles are available for sale online at http://jnm.snmjournals.org.

ALZHEIMER'S® ASSOCIATION | AAIC®23

ADVANCE DEMENTIA RESEARCH AND ACCELERATE YOUR CAREER.

Register today to share, network and collaborate.

Join researchers, clinicians and dementia professionals from all career stages in Amsterdam, Netherlands, and online, at the Alzheimer's Association International Conference® 2023 (AAIC®). Share your work and accelerate your career at the largest and most influential international conference on dementia science.

AAIC 2023: JULY 16-20, AMSTERDAM, NETHERLANDS, AND ONLINE

Educational Workshops and Preconferences: July 14-15

Exhibits: July 16-19

Register at alz.org/AAIC-JNM.

SPECTRUM
DYNAMICS MEDICAL

SPECTRUM DYNAMICS MEDICAL AT

SNMMI 2023 Annual Meeting

Meet us in Chicago, IL USA

Booth 4023 | June 24-27, 2023

Join our SNMMI 2023
Satellite Lunch Symposium:

Reaching Higher Peaks in Digital SPECT Imaging

Tuesday, June 27, 2023 | 12:00pm-1:00pm CST
East/Lakeside Building – Room E450b

www.spectrum-dynamics.com

Discussions with leaders: Kostakoglu talks with Vincent Rajkumar, MD, from the Mayo clinic, about collaborative and pioneering work in establishing influential guidelines in the treatment of myeloma.. . . . . ***Page 831***

^{18}F-labeled SSTR tracers: Leupe and colleagues provide an update of currently available clinical data regarding ^{18}F-labeled somatostatin analog tracers and justification for clinical applications. . . . . ***Page 835***

PET/CT and osteosarcoma management: Oh and colleagues offer an educational overview of clinical aspects of osteosarcoma management and assess the role of ^{18}F-FDG PET/CT, with special focus on pediatric and young adult patients. . . . . ***Page 842***

^{18}F-Fluciclovine PET in glioblastoma: Nabavizadeh and colleagues report on a study assessing the value of ^{18}F-fluciclovine PET for differentiating pseudoprogression from tumor progression in patients with suspected radiographic recurrence of glioblastoma.. . . . . ***Page 852***

^{68}Ga-DOTA-MGS5 PET/CT in MTC: von Guggenberg and colleagues describe imaging results with this ^{68}Ga-labeled minigastrin analog to evaluate cholecystokinin-2 receptor expression status and local recurrence/metastases in patients with advanced medullary thyroid cancer. . . . . ***Page 859***

Imaging tumor status in prostate cancer: al Jalali and colleagues explore the use of [^{68}Ga]PSMA and [^{18}F]FDHT in PET imaging as a potential substitute for analysis of prostate cancer tumors, particularly in evaluating androgen receptor expression. . . . . ***Page 863***

Patient-reported outcomes for PC: Gudenkauf and colleagues detail development of a patient-reported outcome measure for radionuclide therapy in prostate cancer, with utility as a standardized tool to monitor relevant symptoms and toxicities. . . . . ***Page 869***

Signaling network response to TAT: Qin and colleagues investigate cellular responses to targeted α-particle therapy and demonstrate the radiosensitizing potential of histone deacetylase inhibitors for ^{225}Ac-PP-F11N in cholecystokinin B receptor–positive tumors. . . . . ***Page 873***

PRRT in high liver tumor burden: Gococo-Benore and colleagues assess the risk of hepatotoxicity for patients with gastroenteropancreatic neuroendocrine tumors and very high liver tumor burden undergoing peptide-receptor radionuclide therapy. . . . . ***Page 880***

^{124}I-MIBG dosimetry-guided ^{131}I-MIBG therapy: Maric and colleagues report on the efficacy and safety of ^{124}I-MIBG dosimetry-guided high-activity ^{131}I-MIBG therapy in patients with advanced pheochromocytoma or neuroblastoma. . . . . ***Page 885***

PSMA dosimetry in HGG: Graef and colleagues investigate [^{177}Lu]Lu-PSMA therapy in high-grade glioma, with a focus on intratherapeutic dosimetry. . . . . ***Page 892***

PSMA PET/CT criteria and prognosis: Lunger and colleagues explore the prognostic utility of conventional biochemical/imaging response criteria and ^{68}Ga-PSMA11 PET-based criteria for overall survival in metastatic hormone-sensitive and castration-resistant prostate cancer treated with taxane-based chemotherapy.. . . . . ***Page 896***

^{68}Ga-PSMA PET for PB recurrence SRT: Sonni and colleagues use ^{68}Ga-PSMA-11 PET/CT to evaluate patterns of prostate bed recurrence and guide salvage radiotherapy in prostate-specific antigen persistence or biochemical recurrence after radical prostatectomy.. . . . . ***Page 902***

PSMA expression in CRPC: Calderoni and colleagues examine PSMA expression in patients with castration-resistant prostate cancer and compare PET/CT response with prostate-specific antigen variation as a prognostic factor for progression-free and overall survival. . . . . ***Page 910***

PSMA-positive LNs and ENRT templates: Trapp and colleagues analyze PSMA PET/CT–positive lymph nodes and compare results with those from several templates proposed for salvage elective nodal radiotherapy, emphasizing the role of imaging in individualization of treatment. . . . . ***Page 918***

[^{225}Ac]Ac-ofatumumab and lymphoma: Longtine et and colleagues describe preparation of ^{225}Ac-labeled anti-CD20 ofatumumab and evaluate its in vitro characteristics and therapeutic efficacy in a murine model of disseminated human lymphoma. . . . . ***Page 924***

Strain analysis from ECG-gated PET MPI: Huang and colleagues detail development of a measure of longitudinal, radial, and circumferential myocardial strain at rest and during pharmacologic stress using ^{82}Rb PET electrocardiography-gated myocardial perfusion imaging. . . . . ***Page 932***

PET and pulmonary fibrosis: Isser and colleagues use a ^{64}Cu-labeled platelet glycoprotein VI fusion protein targeting extracellular matrix fibers as a PET tracer to observe longitudinal remodeling in a bleomycin-induced pulmonary fibrosis mouse model. . . . . ***Page 940***

Pretreatment ^{131}I-omburtamab imaging and dosimetry: Pandit-Taskar and colleagues perform ^{131}I-omburtamab imaging and dosimetric analysis for estimation of absorbed dose to the cerebrospinal fluid compartment before ^{131}I-omburtamab therapy for leptomeningeal disease. . . . . ***Page 946***

AI-denoised low-dose ^{64}Cu-DOTATATE PET: Loft and colleagues ask whether artificial intelligence approaches can be used to restore visual quality and lesion detection in PET images acquired with $<$50 MBq of ^{64}Cu-DOTATATE in patients with neuroendocrine neoplasms.. . . . . ***Page 951***

Total-body ^{68}Ga-FAPI parametric imaging: Chen and colleagues explore the pharmacokinetics of ^{68}Ga-FAPI-04 PET/CT in pancreatic and gastric cancer and conduct parametric imaging of dynamic total-body data compared with SUV-based imaging. . . . . ***Page 960***

Perfusion index with [^{18}F]MK6240: Guehl and colleagues research the potential utility of the early phase of imaging with [^{18}F]MK6240, with high affinity and selectivity for hyperphosphorylated tau, as a surrogate index of cerebral perfusion. . . . . ***Page 968***

Explainable AI: Bradshaw and colleagues summarize key arguments for and against the use of "explainable artificial intelligence" from the perspectives of data science, clinical practice, and bioethics. . . . . ***Page 976***

Ultrahigh-resolution small-animal PET: Kang and colleagues report on an ultrahigh-resolution small-animal PET scanner that can provide a resolution approaching 0.6 mm to visualize mouse brain function and serve as a promising molecular imaging tool for neuroscience research. . . . . ***Page 978***

Theranostic radiopharmaceuticals: Urbain and colleagues review currently available education and accreditation offerings and policies for theranostics around the world and discuss educational and proficiency challenges.. . . . . ***Page 986***

^{68}Ga-FAPI-46 urachal remnant: Maliha and colleagues present an example of potentially confounding incidental uptake in a urachal remnant on preoperative ^{68}Ga-FAPI-46 PET/CT. . . . . ***Page 992***

Incidental bronchial findings on ^{18}F-PSMA PET/CT: Orciuolo and colleagues describe a case of large-airway PSMA localization in a patient with chronic airway inflammation, highlighting the potential for false-positive findings. . . . . ***Page 993***

Memorial Sloan Kettering Cancer Center

Nuclear Medicine Faculty Position – Molecular Imaging and Therapy Service (MITS)

Memorial Sloan Kettering Cancer Center (MSK) is one of the world's premier cancer centers, committed to exceptional patient care, leading-edge research, and superb educational programs. The blending of research with patient care is at the heart of everything we do. The institution is a comprehensive cancer center whose purposes are the treatment and control of cancer, the advancement of biomedical knowledge through laboratory and clinical research, and the training of scientists, physicians and other health care workers.

The Molecular Imaging and Therapy Service (MITS) is part of the Department of Radiology at MSK. Our team of physicians, technologists, nurses, physicists, pharmacists and radiochemists provides a comprehensive clinical service, conducts translational and clinical research, and provides institutional research support for a large number of diagnostic and therapeutic clinical trials. We are looking for additional faculty members at the junior or mid-career level to join our service, starting in the fall of 2023 or in 2024.

Interested candidates should have:

Excellent clinical skills covering the entire spectrum of nuclear medicine with particular interest in oncologic imaging

- Board certification in nuclear medicine (ABNM)
- Eligibility for New York State license
- Willingness to participate in clinical and translational research
- Interpersonal skills to collaborate productively within our service and across the institution

For inquiries and applications (including a cover letter outlining your interest, your CV, and the names of three references), please contact:

Heiko Schöder, MD
Chief, Molecular Imaging and Therapy Service
Memorial Sloan Kettering Cancer Center

c/o Dorisela Martinez
Faculty Appointment Coordinator
martind5@mskcc.org

Salary: $350,000-$440,000

Physician compensation is based on multiple variables. This range represents annual salary only and does not include supplemental performance-based pay or any one-time payments that eligible candidates may be offered at the time of hire.

SNMMI would like to thank our Value Initiative Industry Alliance member companies for their support. Together we have made incredible progress advancing patient care and precision medicine.

Leadership Circle

BLUE EARTH DIAGNOSTICS
A Bracco Company

SIEMENS Healthineers

Biogen

CardinalHealth
Essential to care™

CURIUM™
LIFE FORWARD

Eisai

GE HealthCare

itm
PASSION FOR PRECISION

JUBILANT RADIOPHARMA

LANTHEUS

Lilly

NOVARTIS

UNITED IMAGING

Visionary Member

IONETIX

mim SOFTWARE

Principal Member

BAYER

Boston Scientific
Advancing science for life™

BRACCO
LIFE FROM INSIDE

cyclomedica

DAXOR
THE BLOOD VOLUME COMPANY

Digirad

isotopia
Nuclear Medicine

MEDTRACE

MIRION TECHNOLOGIES

monrol

NorthStar
MEDICAL RADIOISOTOPES, LLC

PharmaLogic
Take The Lead

POINT BIOPHARMA

SHINE

SPECTRUM
DYNAMICS MEDICAL

Telix

VIEWPOINT
molecular targeting

Voximetry

Corporate Member

CLOVIS ONCOLOGY

HERMES MEDICAL SOLUTIONS

MiE medical imaging electronics

SNMMI SOCIETY OF NUCLEAR MEDICINE & MOLECULAR IMAGING
VALUE INITIATIVE

Learn more about becoming a Value Initiative Member Company:
valueinitiative.snmmi.org

Transforming the Science and Practice of Nuclear Medicine

Munir Ghesani

Division of Nuclear Medicine, Icahn School of Medicine at Mount Sinai, New York, New York

The nuclear medicine and molecular imaging field has made significant progress in the past year, and the Society of Nuclear Medicine and Molecular Imaging (SNMMI) is making every effort to support that growth. In October 2022, the society established a new strategic plan focusing on 8 key areas: research and discovery, advocacy, outreach, education, quality of practice, workforce pipeline, membership, and organizational strength and sustainability. Work in all of these areas is currently in progress, and I am pleased to share what has been achieved so far.

Encouraging research and innovation has led to scientific advances that will continue to push our field forward. At last year's annual meeting, the SNMMI launched the Mars Shot Research Fund, an ambitious initiative aimed at raising $100 million to support research in nuclear medicine, molecular imaging, and therapy. Within the first year, over $3 million has been raised to fund innovative research in prostate, breast, and neuroendocrine cancers as well as other best-in-class ideas. Recently, the SNMMI collaborated with the Lobular Breast Cancer Alliance to establish a $100,000 joint fellowship for invasive lobular carcinoma imaging research—the first award from the new fund. With continued support from donors, the SNMMI aims to accelerate the development of new and effective treatments, ultimately improving patient outcomes.

The Journal of Nuclear Medicine is the SNMMI's flagship publication, and it continues to publish groundbreaking research, from concept through clinical trials. Perspectives on current issues promote discussion in the field and foster collaboration and innovation, advancing research and improving patient outcomes. *The Journal of Nuclear Medicine* remains the top journal in the nuclear medicine field and ranks fourth in terms of impact factor among all medical imaging journals.

To support the growth of radiopharmaceutical therapy, the society developed a Radiopharmaceutical Therapy Central website (https://therapy.snmmi.org/) that houses tools, resources, education, and additional information, including a list of Radiopharmaceutical Therapy Centers of Excellence. Since its creation in 2022, this program has designated 32 comprehensive sites, 16 clinical centers, and 3 basic centers. With more than 60 companies currently developing radiopharmaceutical therapies and many clinical trials under way, it is exceptionally important to ensure that nuclear medicine facilities have comprehensive quality control measures in place, that physicians practicing nuclear medicine have up-to-date training, and that technologists practicing nuclear medicine are appropriately trained and certified.

The SNMMI is also partnering with the Intersocietal Accreditation Commission to establish a new accreditation program for facilities that offer radiopharmaceutical therapy procedures. This accreditation will demonstrate that a facility adheres to specific standards for training and education, performance, and documentation, confirming its dedication to maintaining high levels of quality and patient safety. The program is expected to launch later this year.

Munir Ghesani, MD

To increase patient access to nuclear medicine, the SNMMI is leading the charge on the Facilitating Innovative Nuclear Diagnostics Act of 2023 (House of Representatives bill 1199), working in partnership with more than 80 stakeholder organizations, including the Medical Imaging and Technology Alliance and the Council on Radionuclides and Radiopharmaceuticals. By modifying the reimbursement process for diagnostic nuclear medicine radiopharmaceuticals—appropriately recognizing them as radiopharmaceutical drugs rather than supplies—the act will improve the availability of nuclear medicine procedures, ultimately improving patient outcomes. The bill was introduced to the House of Representatives in February and has already garnered more than 25 cosponsors; it was introduced in the Senate in May. For more information or to support, visit www.snmmi.org/FINDAct.

The SNMMI played a key role in removing the national coverage determination for infection and inflammation, working closely with the Centers for Medicare and Medicaid Services. This has allowed local Medicare administrative contractors to make determinations without coding restrictions, improving patient access to nuclear medicine procedures.

Elevating the visibility of nuclear medicine and molecular imaging has been a significant priority for the SNMMI. In the fall of 2021, the society launched a new consumer media program designed to enhance public awareness of nuclear medicine, emphasizing its precision and effectiveness, safety, and ability to deliver exceptional outcomes. Stories have been carried by major consumer media in markets across the nation. The program has yielded remarkable results, having already reached well over 1 billion consumers.

The SNMMI has also conducted targeted outreach to engage specific groups. One initiative is a new theranostics leadership and operational group that brings together nuclear medicine section chiefs and targeted radiopharmaceutical therapy leaders of academic institutions as well as community and private practices. This initiative creates networking opportunities for sharing best practices and for providing solutions to any individual institution's specific needs, as well as reiterating and reinforcing the importance of nuclear medicine as an integral part of the health-care team.

In another initiative, the SNMMI is working with a growing number of patient and physician groups to provide key information, educate and support patients, and advocate on shared concerns. International outreach also remains a priority for the SNMMI, as the society partners with the U.S. Department of Energy to expand access to nuclear medicine in sub-Saharan Africa and undertakes global initiatives to standardize terminology for radiopharmaceutical therapy and establish a neuroblastoma registry.

The SNMMI has consistently offered top-notch educational opportunities that are a cornerstone of society activities. In 2022, as the pandemic surge receded, the society hosted 2 successful therapeutics conferences educating attendees on the latest innovations and clinical applications in radiopharmaceutical therapy; another conference is scheduled in the fall of 2023. The mid-winter meeting in San Francisco, with a special focus on brain imaging, was also highly successful.

This year's annual meeting in Chicago, with the theme of "eye on the patient," will feature some significant updates: a revamped science pavilion will replace the poster hall, and new "Best of" scientific sessions will showcase important science presented at other significant meetings that intersect with nuclear medicine. The Knowledge Bowl will be expanded and enhanced, arena sessions will encourage engagement, and "Eye on U" stage talks will focus on personal growth. Following this year's meeting theme, Patient Education Day will provide a unique opportunity for patients and caregivers to learn about nuclear medicine, radiation safety, and clinical trials, with in-depth sessions on specific types of cancer as well as a tour of the exhibit hall. All these changes promise to offer a unique and enriching experience for attendees looking to stay current with the latest advances in nuclear medicine and molecular imaging.

Dosimetry is an integral part of precision nuclear medicine. The SNMMI recently released the *MIRD Primer 2022*—a comprehensive, state-of-the-art guide to radiopharmaceutical dosimetry that reflects the dramatic evolution of the field of nuclear medicine, including molecular imaging and radiopharmaceutical therapy. The popular hands-on dosimetry open-house sessions will continue at this year's annual meeting. In addition, the SNMMI is developing a new dosimetry certificate program in response to the growing demand for qualified personnel to perform personalized dosimetry calculations for radiopharmaceutical therapy.

The SNMMI is committed to standardizing and optimizing nuclear medicine through quality initiatives. Since the beginning of 2022, the society has developed 12 guidelines and appropriate-use criteria, many of them in collaboration with other nuclear medicine organizations. The society is working to develop its radiopharmaceutical registry (RaPTR) and RaPTR+PLUS databases, which focus on prostate cancer therapy clinical data; the first 2 pilot sites have received institutional review board approval for data entry into RaPTR+PLUS, which will begin shortly. Additionally, the SNMMI has launched a new therapy clinical trials network to support and facilitate research trials for radiopharmaceutical therapy.

SNMMI recognizes the critical importance of building a strong workforce pipeline for the field of nuclear medicine. To this end, the society has collaborated with IMV Inc., a recognized leader in medical market research, on a comprehensive study to assess current and future trends in the nuclear medicine workforce. A new docuseries titled "Jobs of Tomorrow" will be released to showcase the exciting opportunities that lie ahead for up-and-coming professionals in the field. The annual meeting will feature a nuclear medicine career fair and a student leadership academy, providing valuable opportunities for career growth and networking. Keep an eye out for more exciting developments in this area.

The SNMMI is working hard to advance the field of nuclear medicine and molecular imaging. As my term as president comes to a close, I will be passing the torch to the capable hands of Helen Nadel, and I look forward to an even stronger year ahead under her helm. I would like to extend my heartfelt gratitude to the SNMMI leadership, Value Initiative members, volunteers, and staff who have all contributed to the progress of our field. The future of nuclear medicine and molecular imaging looks promising, and it is a more exciting time than ever to be a part of this profession.

Defining Myeloma and Advancing Treatment Options

A Conversation Between S. Vincent Rajkumar and Lale Kostakoglu

S. Vincent Rajkumar[1] and Lale Kostakoglu[2]

[1]*Division of Hematology, Mayo Clinic, Rochester, Minnesota; and* [2]*University of Virginia Health System, Charlottesville, Virginia*

Lale Kostakoglu, MD, MPH, a professor of radiology and medical imaging at the University of Virginia School of Medicine (Charlottesville), talked with Vincent Rajkumar, MD, the Edward W. and Betty Knight Scripps Professor of Medicine at the Mayo Clinic (Rochester, MN) about his collaborative work in publishing findings that have established influential guidelines in the treatment of myeloma. Dr. Rajkumar is the cochair of the International Myeloma Working Group (IMWG) and chair of the Eastern Cooperative Oncology Group (ECOG) myeloma committee. He is the editor in chief of the *Blood Cancer Journal* and serves as an associate editor for *Mayo Clinic Proceedings, Leukemia,* and the *European Journal of Haematology*. Dr. Rajkumar has received several international awards, including the Robert A. Kyle Lifetime Achievement Award from the International Myeloma Foundation (2016), the Giants of Cancer Care Award (2019) from OncLive, and the Jan Waldenstrom Award (2021) from the International Myeloma Society. He was named as a Mayo Clinic Distinguished Investigator in 2018. He has led numerous phase I, II, and III clinical trials investigating new agents in myeloma, including pivotal trials that led to the approval of thalidomide for myeloma in the United States. He was named as a Mayo Clinic Distinguished Investigator in 2018. He has published more than 400 peer-reviewed articles and more than 200 reviews and book chapters, primarily on myeloma and related plasma cell disorders.

Dr. Kostakoglu: *Vincent, thank you so much for setting aside time to talk to us today. Could you tell us a little about your amazing journey from Madras to Minnesota and the defining moments of your career choices?*

Dr. Rajkumar: I was born in Madras, India, now called Chennai. Getting into medical school in India is very difficult. I was unable to secure a spot in any of the medical schools in my first 2 attempts, but in 1984 I finally achieved acceptance to Christian Medical College (Vellore), one of the leading medical schools in the country. The difficulty getting into medical school probably made me more mature, focused, and keen on excelling. During medical school, I became interested in hematology, because I had a very strong role model, Mammen G. Chandy, MD. However, India had no real formal training program for hematology at that time, so I wanted to move to the United States for training. It took me 2 years to get into a residency program after medical school. In those 2 years, I had an obligation to work in mission hospitals in India, which were mainly focused on delivering care for the underprivileged. I worked in a rural mission hospital that focused on the treatment of leprosy. It was really interesting, because as part of my work there I used the myeloma drug thalidomide.

S. Vincent Rajkumar, MD

Dr. Kostakoglu: *This is one of the most impressive stories I have heard. Seeing medicine at all layers of society has probably made you a more critical thinker.*

Dr. Rajkumar: I had a mentor from Australia, Alan Gijsbers, MBBS, who introduced me to clinical epidemiology and critical review of the literature. As a medical student I read all of the works of David Sackett, MD, MSc, and Robert Fletcher, MD, MPH, on evidence-based clinical epidemiology and became good at critical appraisal. This helped me differentiate opinion-driven from evidence-driven decisions.

Dr. Kostakoglu: *Your background also made you one of the most impactful leaders in myeloma, transforming it from a highly fatal to a manageable chronic disease. How did you select myeloma as your primary area of interest?*

Dr. Rajkumar: I went straight from 110° in Madras, India, to subzero temperatures in Fargo, ND, for residency. My program director there, Anthony Gustafson, MD, was a remarkable person who became aware of my interest in critical appraisal of clinical research as well as hematology. He propelled my career and helped me get into the Mayo Clinic for my fellowship. I was fortunate to train at Mayo with legends such as Robert Kyle, MD, Philip Greipp, MD, and Morie Gertz, MD, who were all very important in my choice of career path.

Dr. Kostakoglu: *If you had to name the 3 most remarkable advances in the field supporting progress in myeloma, what would they be?*

Dr. Rajkumar: I think the first major advance was a better understanding of the disease biology and recognition of the different cytogenetic subtypes of myeloma. The second would be the discovery of multiple new effective drugs. I have been a small part of these discoveries, starting with thalidomide and continuing with bortezomib, lenalidomide, pomalidomide, and carfilzomib. More recently, immunotherapy has dramatically improved the life-span of myeloma patients. The third advance would be discoveries that have led to a better understanding of how the disease evolves from the premalignant stage of monoclonal gammopathy of undetermined significance (MGUS) to the smoldering myeloma entity and then to full-blown myeloma.

Dr. Kostakoglu: *That's a great summary. Let's expand on the initial diagnosis of myeloma a bit. If we start with biomarkers,*

Received Apr. 14, 2023; revision accepted Apr. 14, 2023.

DOI: 10.2967/jnumed.123.265877

what are the most important current prognostic and predictive biomarkers of myeloma?

Dr. Rajkumar: When I started in the field, myeloma was unique among cancers in that it was defined using clinical endpoints such as hypercalcemia and bone lesions. Waiting for the development of end-organ damage delayed therapy in so many patents. I was fortunate to lead the effort to redefine myeloma in 2014. As the IMWG, we published that work in *Lancet Oncology* (2014;15:e538–e548); this article has now become the most-cited myeloma paper ever. These IMWG revised diagnostic criteria incorporated biomarkers to further define the disease. The biomarkers included more than 60% clonal plasma cells in the marrow, a very high free-light-chain ratio, and 2 or more focal lesions on whole-body MRI. After diagnosis, the main prognostic determinants are certain high-risk cytogenetic abnormalities: translocations t(4;14), t(14;16), t(14;20), deletion 17p, p53 mutation, and chromosome 1 abnormalities.

Dr. Kostakoglu: *In the context of predictive biomarkers, there has been a lot of pressure, especially from drug companies, to approve cancer drugs based merely on surrogate endpoints. Is it really a good concept in myeloma to use surrogate endpoints?*

Dr. Rajkumar: I am very much in favor of traditional surrogate endpoints for many settings in myeloma, because many of the ones that we use are quite reliable and well validated. If we had waited for the hard endpoint of overall survival for new drug approval, the availability of many life-saving drugs we currently have in myeloma would have been delayed by 2–3 years. Thalidomide, bortezomib, carfilzomib, and pomalidomide were all initially approved using surrogate endpoints. With the exception of a few rare occasions, drugs that prolonged progression-free survival (PFS) in myeloma have eventually shown survival improvement. I strongly feel that the initial call that was made early on to use response rate and PFS as surrogate endpoints for refractory myeloma drug approvals was the right call.

Dr. Kostakoglu: *A surrogate endpoint for PFS is one thing, but using a molecular or even an imaging biomarker as a surrogate endpoint is another. Will these latter approaches be established one day?*

Dr. Rajkumar: What we really need are new biomarkers that show that the drug is clinically active and has a high likelihood of providing clinical benefit to patients who are confronting a serious, life-threatening cancer. Drugs granted accelerated approval using surrogate endpoints or single-arm trials must show clear proof of clinical benefit in subsequent well-designed randomized trials. Thankfully, this is the process we have followed in the myeloma field so far.

Dr. Kostakoglu: *The other big topic in myeloma is racial disparities. You were involved in an important metaanalysis of genome-wide association (*Cancer Epidemiol Biomarkers Prev. *2016;25: 1609–1618). Could you briefly tell us about the results of that study?*

Dr. Rajkumar: The incidence of MGUS and myeloma is 2–3 times more common in Black than White people. We have done genomic studies and found that a lot of the disparity in MGUS is driven by an excess of t(11;14) translocation in people with African ancestry genes. I think we should screen for monoclonal gammopathy in African Americans who have one affected relative with myeloma. We need to enroll a diverse patient population in our clinical trials. Finally, we need to determine whether responses to current myeloma drugs vary by race or ethnicity. Our studies suggest that the reason for lower survival seen in African Americans may be more related to access and affordability than to biologic reasons such as a more aggressive form of myeloma.

Dr. Kostakoglu: *That is an ongoing and fascinating research field; hopefully it will lead to easier access to effective treatments. Let's move on to another important topic: big data. Are there any ongoing landmark studies that will provide unprecedented big data on myeloma genomics to further personalize treatments?*

Dr. Rajkumar: I think a lot of groups are undertaking efforts in this direction. There's really a lot of opportunity to pull these resources in and get impactful data out. We need to open these resources to all interested parties who want to use them for scientific advancement.

Dr. Kostakoglu: *What are the barriers to accessing these data?*

Dr. Rajkumar: I've been disappointed at how difficult it has been to obtain data on cooperative group studies that we have conducted. I think bureaucratic barriers should be reduced so that we can help advance the field. We have a complicated system with many strict rules and procedures to access samples and data. We can keep talking about big data, but by the time we produce any information it may be outdated because of existing barriers.

Dr. Kostakoglu: *It certainly sounds frustrating. We will probably rely on you as the leader to push this forward. We should touch more on the kaleidoscopic landscape of myeloma treatment. In the past decade, the U.S. Food and Drug Administration (FDA) approved numerous new agents that have significantly transformed the myeloma treatment paradigm. Could you tell us why myeloma is so challenging to treat?*

`We need to be clear about whether a treatment is curative or primarily for disease control. … True cure means you do not need continuous suppressive treatment. That's the goal.´

Dr. Rajkumar: In the last 20 years, we have probably had more than 16 drugs approved for myeloma treatment. The overall survival rates for patients of all ages have more than doubled. It is true that it has become a little more complicated, because we have so many drugs and regimens from which to choose. But by and large it is easier to control myeloma now than before. At Mayo we publish our guidelines on mSMART.org, where we outline precisely our recommendations on the regimen we use at each stage of the disease.

Dr. Kostakoglu: *You have led and participated in many pivotal trials in myeloma. In fact, you led the ECOG trial using thalidomide and then a second-generation lenalidomide study. Could you describe the major breakthroughs in the treatment of myeloma?*

Dr. Rajkumar: I think the most important breakthrough would be the discovery that thalidomide works in multiple myeloma in relapsed refractory disease. The credit goes to Bart Barlogie, MD. I was fortunate to lead the first confirmatory study at the Mayo Clinic (*Mayo Clin Proc.* 2000;75:897–901) and the subsequent ECOG randomized trial of thalidomide plus dexamethasone versus dexamethasone for newly diagnosed myeloma (*J Clin Oncol.* 2008;26:2171–2177).

The second big breakthrough would be the discovery of the effectiveness of proteasome inhibitors in myeloma treatment. Many people worked on this, including Robert Orlowski, MD,

PhD, and Kenneth Anderson, MD, and associated researchers. Dr. Orlowski's father, Marian Orlowski, MD, was a pioneering scientist in proteasome inhibition decades earlier.

The third breakthrough would be the finding that lenalidomide plus low-dose dexamethasone (Rd regimen) is a great backbone for myeloma therapy. The credit there goes to Michael Katz, MBA, patient advocate at ECOG, who challenged us to find a tolerable myeloma regimen. The Rd regimen was developed through the ECOG E4A03 trial, which I was fortunate again to lead. We found that low-dose dexamethasone was not only more tolerable with fewer side effects but also associated with better overall survival. That led to the Rd backbone, which subsequently became the frontline regimen in the Frontline Investigation of Revlimid and Dexamethasone versus Standard Thalidomide (FIRST) trial and then became the backbone of almost all major myeloma regimens we use right now.

The fourth advance would be the concept of maintenance therapy after transplantation as something that prolongs overall survival, which allows us to do a transplantation and then get a prolonged duration of remission.

And then, finally, the immunotherapy revolution: first with the introduction of monoclonal antibodies (daratumumab, isatuximab, and elotuzumab) and then subsequently now with CAR T cells and bispecific antibodies.

Dr. Kostakoglu: *If I hear correctly, the most recent revolution in myeloma treatment is in immune-based therapies. In that sense, how do CAR T cells work in myeloma?*

Dr. Rajkumar: CAR T cells have been found to be effective in diffuse large B-cell lymphoma and acute lymphoblastic leukemia. In myeloma, we have 2 CAR T-cell products approved, and both target B-cell maturation antigen (BCMA), with a high response rate of 80%–100%. Unlike in leukemia and lymphoma, they don't appear to be curative, but they do give a PFS of about 1–2 years.

Dr. Kostakoglu: *What about the newly approved bispecific antibody teclistamab? Are you excited about that? Bispecific antibodies and CAR T cells are both immune therapies, but which one would you favor?*

Dr. Rajkumar: Teclistamab is a bispecific that targets T cells through CD3 and plasma cells by binding to the BCMA. It has a single-agent response rate of about 60% in relapsed refractory disease, which is amazing considering that prior myeloma drugs, such as thalidomide, lenalidomide, and even carfilzomib, had a single-agent response rates of only 30%. Several other BCMA-targeted bispecifics are in the pipeline in addition to teclistamab. CAR-T availability is very limited, so a lot of patients are going to get bispecific antibodies because these are more easily available. We also have new bispecific antibodies that target other antigens besides BCMA.

Dr. Kostakoglu: *Can we briefly talk about response assessment in imaging? The latest IMWG response criteria have been amended to include molecular minimal residual disease (MRD) as well as PET imaging. What is MRD negativity, and does it really translate to longer survival?*

Dr. Rajkumar: MRD negativity is defined as complete response by immunofixation plus a bone marrow assessment that shows no evidence of residual plasma cells by either a highly sensitive flow cytometry approach or a next-generation sequencing approach. Determining MRD negativity requires PET negativity in addition to paraprotein and bone marrow MRD criteria. We know that MRD status is a major prognostic factor. What we are struggling with now is whether we can use MRD status to adjust treatment. Here we need data from randomized controlled trials, and these are ongoing.

Dr. Kostakoglu: *The PET-based response criteria were proposed by the Italian and French groups in a 2020 JCR article* (Zamagni E, Nanni C, Dozza L, et al. Standardization of ^{18}F-FDG-PET/CT According to Deauville Criteria for Metabolic Complete Response Definition in Newly Diagnosed Multiple Myeloma. J Clin Oncol. 2021;39(2):116-125.). *So what are your thoughts about the use of these criteria?*

Dr. Rajkumar: We use PET scan and imaging responses very much in the clinic. When we publish the response criteria, however, these are not formally included in the definition of partial or complete response, because when we change the established response criteria or the definition of progression, we change metrics by which the FDA has been adjudicating drugs for approval. Having said that, PET response assessment in day-to-day clinical practice is invaluable. The response criteria as written in articles are mostly for drug approval and for clinical trials. We use additional measures of response assessment in practice, including imaging.

Dr. Kostakoglu: *You were recognized as an outstanding researcher and leader in the field of myeloma and have been the recipient of many prestigious awards, including the Giants of Cancer Care recognition in 2019 and Waldenström Award in 2021 from the International Myeloma Society. What do you believe to be the most important achievement that contributed to your recognition?*

Dr. Rajkumar: I think in terms of sheer clinical impact and lives saved, the ECOG trial of lenalidomide plus high-dose dexamethasone versus lenalidomide plus low-dose dexamethasone has saved a significant number of lives, as well as spared people an enormous amount of toxicity. The initial reviews suggested that it was a boring trial, because we just wanted to compare high- and low-dose dexamethasone. But I really thought it was a very important question and saw it through.

Dr. Kostakoglu: *You have a leadership role in the IMWG producing consensus guidelines. In that capacity, you work closely with European colleagues. Have you observed differences between European and U.S. physician scientists in their approach to clinical trials?*

Dr. Rajkumar: That's a great question. Our myeloma community is very close-knit and works well together. The unifying factor is that all of us are very much interested in how to improve outcomes for myeloma patients. But in terms of approach to clinical trial design and implementation, the main difference is that the United States has a lot more bureaucracy, making it difficult for myeloma experts to do the trials we want to do. European colleagues are able to put together proposals that are quickly approved, because the process recognizes that these are the best minds designing these trials for the best outcomes. The second difference is that in the United States we are more reluctant to put patients on clinical trials and more willing to put people on experimental therapy outside of trials. In Europe, they put more patients on clinical trials and treat them on study with much faster recruitment rates. They are better at working across countries than we are at working across institutions.

Dr. Kostakoglu: *We all know that oncologists mostly focus on treatment choices to increase survival. With increasing survival times, quality-of-life issues are as important to patients as longer survival. Could we allow incorporation of quality-of-life endpoints in clinical trial designs?*

Dr. Rajkumar: Certainly. I think for certain stages of the disease, such as maintenance, it's better to show that PFS is prolonged and quality of life is also improved rather than simply showing that PFS is prolonged. We have tried to include quality of life as at least a secondary endpoint in all our ECOG trials.

Dr. Kostakoglu: *Is it easy to use patient-reported outcomes in myeloma trials?*

Dr. Rajkumar: It is a little bit harder in myeloma to evaluate patient-reported outcomes that truly reflect improvement in disease status. On the other hand, if a treatment prolongs PFS and we can show that it also improves quality of life, that's definitely better than just showing improvement in PFS. A finding that quality of life was also improved is a very strong indication of clinical benefit.

Dr. Kostakoglu: *The last topic is health economics—a big ugly bag. You're well known for your advocacy of disease control versus cure. But controlling disease with maintenance therapies increases cumulative treatment costs. What's the solution for cost containment?*

Dr. Rajkumar: Great question. We need to be clear about whether a treatment is curative or primarily for disease control. I am all for a cure, because a cure is by far the most economical, most desirable endpoint for myeloma as well as other cancers. Achieving a cure means that treatment is given for a finite period of time and that in a certain number of people the disease will not recur, as we've seen with acute leukemia or Hodgkin disease. True cure means you do not need continuous suppressive treatment. That's the goal.

On the health economic side, cure is clearly associated with a better approach than trying to control a disease with very expensive drugs for a protracted period of time. I've been very vocal on drug costs. The U.S. prescription drug system is broken. It allows new drugs to be highly priced regardless of the value they provide. We need to make major changes to drug prescription and pricing policies so that our public has access to affordable drugs. This includes Medicare's being able to negotiate from the launch of the drug and strict policies that prevent drug companies from increasing prices when they feel like it. It includes reforming the patent system, easier entry of generics and biosimilars, and pharmacy benefit manager reforms. Physicians should also be aware of and advocate for access and affordability.

Dr. Kostakoglu: *I don't see a quick cure for this problem, which is unsustainable, with new targeted treatments costing $300,000–$400,000 per year.*

Dr. Rajkumar: If insulin can cost 10 times more in the United States than in other countries, it is no wonder that cancer drugs are so expensive. I want to make a plug for a film that recently premiered called *Pay or Die,* which highlights the insulin price crisis.

Dr. Kostakoglu: *I will certainly watch that film. Let's conclude with an aside about your personal unknowns. What is your most unexpected or unusual hobby?*

Dr. Rajkumar: I have a strong passion for music. I sing, play the guitar a little, learned a little bit of the piano, and can record and edit music.

Dr. Kostakoglu: *So diversified! A final question: which 3 famous people would you invite to a dinner party?*

Dr. Rajkumar: One would be Michael Jordan, who has been an incredible role model. He strived for perfection every day on the court. It would be amazing to talk to him. The second would be President Obama. He is another great role model. The third person I would love to have dinner with is a composer from India, Ilaiyaraaja. He is among the most prolific composers in the world and can compose a song in 30 min using only pencil and paper. He composed 2 songs a day for decades. So he's someone I would love to talk to about how he does it.

Dr. Kostakoglu: *Thank you, Vincent. It has been a great pleasure talking to you on many interesting topics. Thanks for your generosity of time and willingness to share your valuable perspectives.*

Dr. Rajkumar: It is an honor to be interviewed. Thank you so much.

^{18}F-Labeled Somatostatin Analogs as PET Tracers for the Somatostatin Receptor: Ready for Clinical Use

Hannes Leupe[1], Stephen Ahenkorah[2], Jeroen Dekervel[3], Marcus Unterrainer[4,5], Eric Van Cutsem[3], Chris Verslype[3], Frederik Cleeren[2], and Christophe M. Deroose[1]

[1]*Nuclear Medicine, University Hospitals Leuven, and Nuclear Medicine and Molecular Imaging, Department of Imaging and Pathology, University of Leuven, Leuven, Belgium;* [2]*Radiopharmaceutical Research, Department of Pharmacy and Pharmacology, University of Leuven, Leuven, Belgium;* [3]*Digestive Oncology, University Hospitals Leuven, Leuven, Belgium;* [4]*Department of Radiology, University Hospital, LMU Munich, Munich, Germany; and* [5]*Department of Nuclear Medicine, University Hospital, LMU Munich, Munich, Germany*

Molecular imaging of the somatostatin receptor plays a key role in the clinical management of neuroendocrine tumors. PET imaging with somatostatin analogs (SSAs) labeled with ^{68}Ga or ^{64}Cu is currently the gold standard in clinical practice. However, widespread implementation of ^{68}Ga imaging is often hampered by practical and economic issues related to ^{68}Ge/^{68}Ga generators. ^{18}F offers several advantages to tackle these issues. Recent developments in radiochemistry have allowed a shift from ^{68}Ga toward ^{18}F labeling, leading to promising clinical translations of ^{18}F-labeled SSAs, such as Gluc-Lys-[^{18}F]FP-TOCA, [^{18}F]F-FET-βAG-TOCA, [^{18}F]AlF-NOTA-octreotide, [^{18}F]SiTATE, and [^{18}F]AlF-NOTA-JR11. This review gives an update of currently available clinical data regarding ^{18}F-labeled SSA tracers and provides justification for the clinical application of this class of tracers.

Key Words: neuroendocrine; radiopharmaceuticals; fluorine-18-labeled PET tracer; neuroendocrine tumor; somatostatin analogue; somatostatin receptor

J Nucl Med 2023; 64:835–841
DOI: 10.2967/jnumed.123.265622

Neuroendocrine tumors (NETs) are a heterogeneous group of tumors derived from cells of the diffuse neuroendocrine system. They are most commonly found in the gastrointestinal tract or respiratory system and can secrete various hormones, giving rise to a wide range of clinical symptoms. Although typically described as rare, the incidence of NETs has increased steadily over the past 40 y, with a currently estimated incidence of 5 per 100,000 persons per year (*1*).

Most differentiated NETs are characterized by an overexpression of the somatostatin receptor (SSTR), a G-protein–coupled membrane receptor (*2*). Five different human SSTR subtypes have been identified: 1, 2A/2B, 3, 4, and 5. For subtype 5, truncated splice variants have been described in NETs (*3*). SSTRs are expressed by a wide variety of normal human tissues, each exhibiting a characteristic expression pattern of the different SSTR subtypes (*4*). SSTRs have also been identified in several human tumor types, with NETs representing one of the groups with the highest incidence of SSTR expression (*5*). For example, SSTRs are present in 80%–100% of gastroenteropancreatic NETs, and most gastroenteropancreatic NETs have moderate-to-high overexpression of SSTRs, especially subtype 2A (*6*). SSTR overexpression is also seen in other NETs, such as pheochromocytomas, paragangliomas, small-cell lung cancers, lung carcinoids, pituitary adenomas, Merkel cell carcinomas, neuroblastomas, and medullary thyroid carcinomas (*7*). However, SSTR expression in tumors is not limited to NETs and can also be found in a large variety of other solid and hematologic malignancies (*8*).

The overexpression of SSTRs on NETs is the foundation on which treatment with somatostatin analogs (SSAs) is based. Moreover, SSAs can be labeled with radionuclides, allowing for imaging or therapy (*2*). These peptide-based radiopharmaceuticals typically consist of the biologically active synthetic peptide (the vector molecule), linked to the radionuclide by means of a chelator (*9*). SSTR imaging was first performed in 1989 using ^{123}I-Tyr^3-octreotide scintigraphy (*10*). ^{123}I was quickly replaced by ^{111}In because of several practical disadvantages such as limited availability, high cost, and suboptimal image quality due to pronounced intestinal accumulation (*11*). [^{111}In]In-DTPA-octreotide (or [^{111}In]In-pentetreotide) SPECT imaging with or without CT has been successfully used for over 2 decades for staging and therapy selection for NETs (*12*). However, the use of ^{111}In was also hampered by several disadvantages, such as unfavorable nuclear physical characteristics resulting in suboptimal image quality and a relatively high radiation burden, limited availability, and high costs (*13*). In the early 2000 s, successful developments were made to label SSAs with ^{99m}Tc (e.g., ^{99m}Tc-EDDA/HYNICTOC), showing higher target-to-background ratios and higher tumor uptake values, which improved image quality (*14*).

A major advancement was the development of SSAs labeled with the positron-emitting radionuclide ^{68}Ga, allowing for PET imaging of SSTR. This was made possible by the chelation of ^{68}Ga by DOTA, which can be coupled to SSAs. Since the introduction of [^{68}Ga]Ga-DOTA SSAs, their superiority over conventional SPECT imaging has been well established, making them the current gold standard for evaluation of SSTR in NETs (*15*). ^{68}Ga-based tracers currently used in clinical practice are [^{68}Ga]Ga-DOTATOC, [^{68}Ga]Ga-DOTATATE, and [^{68}Ga]Ga-DOTANOC. Despite the excellent results achieved with [^{68}Ga]Ga-DOTA SSAs, their use in routine clinical practice is often hampered by practical and economic issues related to ^{68}Ge/^{68}Ga-generators. Disadvantages include high costs, limited

Received Feb. 20, 2023; revision accepted Mar. 24, 2023.
For correspondence or reprints, contact Christophe M. Deroose (christophe.deroose@uzleuven.be).
Published online May 11, 2023.

TABLE 1
Direct Comparison of Pharmacokinetic and Practical Properties of ^{68}Ga, ^{18}F, and ^{64}Cu (*45*)

Property	^{68}Ga	^{18}F	^{64}Cu
Half-life	67.6 min	109.8 min	12.7 h
Production yield/batch	2–4 patients	>10 patients, up to 50	>10 patients, up to 50
Positron energy (E_{max})	1,899 keV	634 keV	653 keV
Average positron range in H_2O	3.5 mm	0.6 mm	0.7 mm
Branching ratio	89.1%	96.9%	17.5%
Source	^{68}Ge/^{68}Ga-generator/cyclotron (solid target)	Cyclotron (liquid target)	Cyclotron (solid target)
Central production	No, if generator-based	Yes	Yes

availability, short tracer half-life (68 min), low production yield (2–4 patients per batch), regulatory or reimbursement barriers, and a relatively high average positron energy (0.83 MeV) with a resulting long average positron range (3.5 mm), possibly compromising spatial resolution (Table 1) (*16*).

Another frequently used radionuclide for SSTR PET imaging is ^{64}Cu. Its half-life (12.7 h) allows for centralized production and a more flexible scanning window. Moreover, its low average positron energy (0.28 MeV) with a corresponding short average positron range (0.8 mm) makes high-spatial-resolution PET imaging possible (*16*). Disadvantages are the low branching ratio—only 17.5%—for positron emission decay and a higher radiation exposure.

^{18}F, by far the most widely used PET radionuclide, offers several advantages including a high production yield (50 patients or more per batch) and a more favorable half-life (109.8 min). These properties allow for centralized production and distribution to distant PET centers without an on-site cyclotron. Furthermore, the shorter positron range (0.6 mm) of ^{18}F than of ^{68}Ga and ^{64}Cu could improve the spatial resolution of the acquired PET data. The branching ratio for positrons, 96.9%, is nearly optimal (*16*).

In recent years, several new ^{18}F-based tracers were designed to target SSTR (Fig. 1; Table 2). This article provides an overview of the currently available clinical data regarding SSTR imaging and more specifically of ^{18}F-based tracers targeting SSTR.

^{18}F-LABELED SSA TRACERS

Gluc-Lys-[^{18}F]FP-TOCA

In 2006, Meisetschläger et al. evaluated the clinical use of Gluc-Lys-[^{18}F]FP-TOCA in 25 patients with SSTR-positive tumors seen on conventional ^{111}In-DTPA-octreotide scans (*17*). In a head-to-head comparison of both imaging modalities in 16 of these patients, Gluc-Lys-[^{18}F]FP-TOCA imaging revealed a significantly higher number of lesions (factor of 2.4), indicating diagnostic superiority. Biokinetic evaluation of Gluc-Lys-[^{18}F]FP-TOCA showed a fast and intense tumor accumulation without intracellular trapping, as well as a rapid clearance from blood serum, predominantly through the kidneys but also by hepatobiliary transport. The tumor-to-background ratio was higher for Gluc-Lys-[^{18}F]FP-TOCA than for [^{111}In]In-DTPA-octreotide, which allowed for clear delineation of the liver lesions. Nevertheless, a major obstacle to clinical implementation of Gluc-Lys-[^{18}F]FP-TOCA was its extensive multistep synthesis with limited radiochemical yield (20%–30%) (*17*). Subsequently, only a few clinical studies have been published using Gluc-Lys-[^{18}F]FP-TOCA (*18–20*), and in these trials only a small number of patients were included. Until now, no direct comparison between Gluc-Lys-[^{18}F]FP-TOCA and another SSTR PET tracer has been made. To our knowledge, no further large clinical trials have been performed.

NOTEWORTHY

- ^{18}F-labeled SSAs as PET tracers for SSTR are ready for routine clinical practice.
- ^{18}F-labeled SSA tracers demonstrate higher in vivo stability, higher tumor-to-background ratios, better lesion detection, more beneficial physical properties, a higher production yield, or a more favorable biodistribution than conventional [^{68}Ga]Ga-DOTA SSA PET/CT imaging, indicating suitability for clinical use.
- ^{18}F-labeled SSTR agonist tracers are valid alternatives to SSTR PET. They should be implemented in guidelines and appropriate-use criteria for SSTR PET imaging.

[^{18}F]F-FET-βAG-TOCA

Another ^{18}F tracer targeting SSTR is [^{18}F]F-FET-βAG-TOCA. Dubash et al. assessed the biodistribution and dosimetry of [^{18}F]F-FET-βAG-TOCA in a first in-humans study with 9 NET patients (*21*). [^{18}F]F-FET-βAG-TOCA showed high tumoral uptake and a high tumor-to-background ratio in all organs including the liver, comparable to values reported for [^{68}Ga]Ga-DOTA SSA tracers. Physiologic uptake was observed in the pituitary, salivary glands, and thyroid tissue. Rapid clearance from most organs was found, with both renal and hepatobiliary excretion. As such, the highest absorbed dose was seen in the gallbladder, followed by the spleen, stomach wall, liver, kidneys, and bladder (*21*). In a larger study cohort, Dubash et al. compared [^{18}F]F-FET-βAG-TOCA directly with [^{68}Ga]Ga-DOTATATE in 32 patients (*22*). [^{18}F]F-FET-βAG-TOCA detected more lesions (209/223) than [^{68}Ga]Ga-DOTATATE (197/223), showing a statistically nonsignificant higher overall sensitivity (92.8% vs. 87.5%) in the detection of NET lesions. Moreover, [^{18}F]F-FET-βAG-TOCA detected additional bone and lymph node lesions in 3 of the patients (9.4%). As [^{18}F]F-FET-βAG-TOCA had promising results for lesion detection in NET patients, further developments could lead to the clinical validation of this promising tracer as a potential alternative to [^{68}Ga]Ga-DOTA SSA tracers.

In a recently published proof-of-concept study, the feasibility of SSTR2 imaging as a novel inflammation-specific molecular imaging target was evaluated with [^{18}F]F-FET-βAG-TOCA and

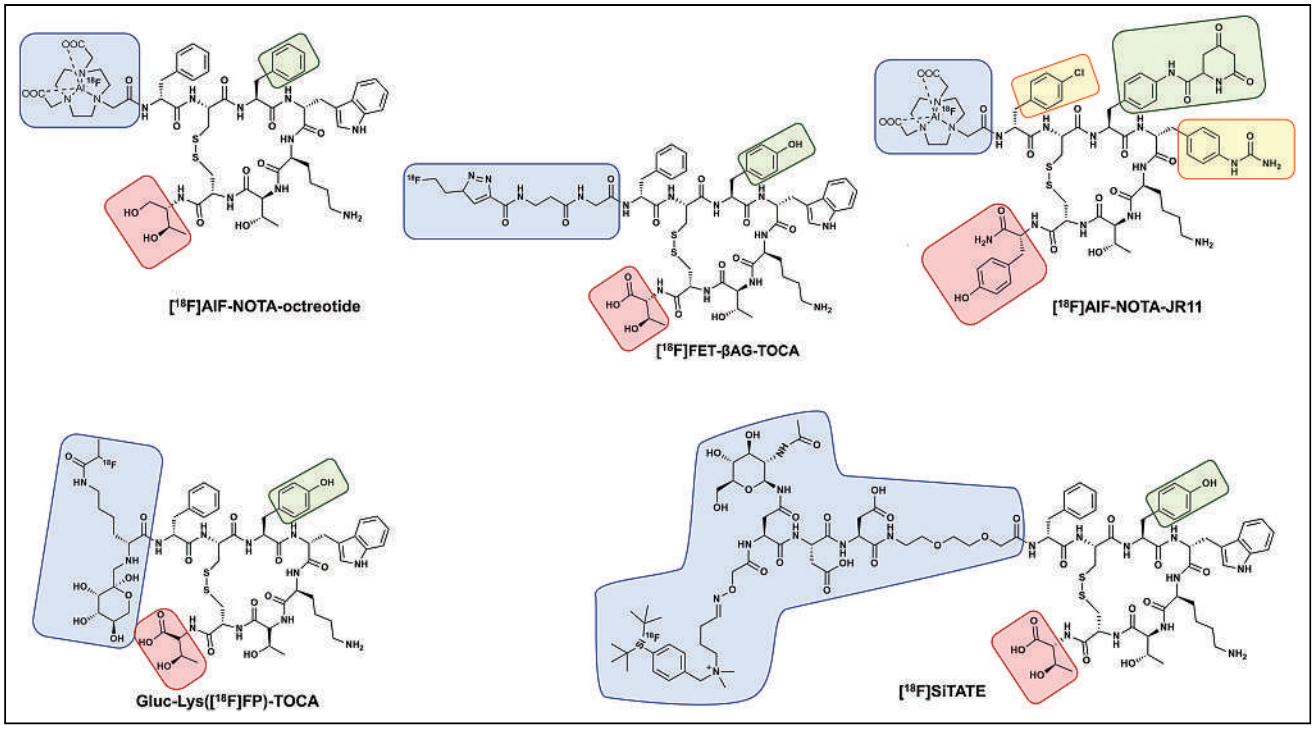

FIGURE 1. Molecular structures of ^{18}F-based SSTR tracers that have been applied in clinical studies.

[^{68}Ga]Ga-DOTATE PET/MR in patients with large-vessel vasculitis. SSTR2 PET/MRI showed major promise for diagnosis and therapeutic monitoring and was generally comparable to [^{18}F]FDG PET/CT, but with a very low background signal in the brain and heart. This allows for better assessment of nearby vascular involvement (*23*).

[^{18}F]AlF-NOTA-Octreotide

Recently, an Al^{18}F-labeled SSTR agonist, [^{18}F]AlF-NOTA-octreotide, was synthesized using a good-manufacturing-practice–compliant, chelator-based, automated radiolabeling method (*24*). In a first in-humans trial by Long et al. on 22 patients with proven NETs, [^{18}F]AlF-NOTA-octreotide PET/CT was directly compared with [^{18}F]FDG PET/CT (*25*). High physiologic uptake was seen in the spleen, kidneys, and bladder, whereas the pituitary, thyroid, adrenal glands, uncinate process of the pancreas, stomach, and intestine also showed mild to moderate physiologic uptake. Brain, lung, muscle, and bone showed a low background activity. The [^{18}F]AlF-NOTA-octreotide PET/CT images showed optimal contrast, with a significantly high tumor-to background ratio. SUV_{max} was higher in well-differentiated NETs than in poorly differentiated tumors. Moreover, lower Ki-67 values were observed in lesions with high [^{18}F]AlF-NOTA-octreotide uptake, and higher [^{18}F]FDG uptake was associated with higher Ki-67 values (*25*). This finding is attributed to a higher metabolic turnover and loss of SSTR expression in high-grade NETs (*6,25*). Hou et al. (*26*) extended the sample size of their previous study (*25*) and evaluated the biodistribution of [^{18}F]AlF-NOTA-octreotide in 128 patients with proven or suspected NETs (*26*). Their analysis confirmed the favorable biodistribution and higher tracer uptake for [^{18}F]AlF-NOTA-octreotide in well-differentiated tumors (G1 or G2) in comparison with G3 lesions, consistent with data from ^{68}Ga-labeled SSTR tracers and in line with lower SSTR expression levels in more aggressive tumors. High tumor-to-background ratios enabled the detection of very small lesions, such as those that are only a few millimeters in size, especially in the lymph nodes and bone. Interestingly, some benign lesions such as thyroid adenoma showed obvious [^{18}F]AlF-NOTA-octreotide uptake, whereas mild to moderate uptake was found in benign lesions such as inflammatory lesions, meningiomas, or fractures, again compatible with uptake patterns observed with ^{68}Ga-labeled SSAs (*26,27*).

After publishing promising results of a direct comparison between [^{18}F]AlF-NOTA-octreotide PET/CT and [^{68}Ga]Ga-DOTATATE in a NET patient (*28*), Pauwels et al. compared both tracers in 6 healthy volunteers and 6 NET patients (*29*). They concluded that [^{18}F]AlF-NOTA-octreotide is safe and well tolerated. The highest dose was received by the spleen, followed by the urinary bladder wall and the kidneys, in accordance with the expected SSTR-specific uptake in the spleen and renal excretion of the tracer. The effective dose was 22.4 ± 4.4 μSv/MBq (*29*).

Generally, both tracers showed a similar physiologic uptake pattern. In comparison with [^{68}Ga]Ga-DOTATATE, most organs, including bone, showed lower uptake for [^{18}F]AlF-NOTA-octreotide PET/CT. Also, liver background uptake was lower for [^{18}F]AlF-NOTA-octreotide, allowing for better liver lesion detection. Moreover, the SUV_{max} for all lesions was significantly lower with [^{18}F]AlF-NOTA-octreotide than with [^{68}Ga]Ga-DOTATATE. However, despite the lower background activity in the bone, [^{18}F]AlF-NOTA-octreotide missed more bone lesions—driven mainly by the results for a single patient (*29*).

In a larger prospective study, Hou et al. compared both tracers in 20 patients with a combined total of 179 lesions and found similar results (*30*). In their analysis, [^{18}F]AlF-NOTA-octreotide showed a 1.5 times lower liver uptake and a 5 times lower uptake in the salivary glands. Both tracers were highly sensitive in lesion detection, with no significant difference in overall diagnostic efficacy.

TABLE 2
Currently Available Clinical Studies on NET or Meningioma Patients Using ^{18}F-Labeled Tracers

Study	Year	*N*	P	^{18}F tracer	Comparator	Outcomes	N_{tot}	N_{tracer} (%)	N_{com} (%)	Main findings
Meisetschläger (*17*)	2006	25	NET	Gluc-Lys-[^{18}F]FP-TOCA	[^{111}In]In-pentetreotide	BD, D, QNA, QLA	—	288	133	ED = 13 μSv/MBq
Seemann (*18*)	2007	31	NET	Gluc-Lys-[^{18}F]FP-TOCA	Triple-phase CT	QLA	1,618	1,519 (93.9)	990 (61.2)	DDR = 32.7%
Wieder (*19*)	2008	10	NET	Gluc-Lys-[^{18}F]FP-TOCA	Triple-phase CT	QNA, QLA	144	139 (96.6)	114 (79.2)	DDR = 17.4%
Astner (*20*)	2009	9	GT	Gluc-Lys-[^{18}F]FP-TOCA	MRI	TD	11	—	—	Improves TD
Dubash (*21*)	2016	9	NET	[^{18}F]F-FET-βAG-TOCA	—	BD, D	—	—	—	ED = 29 μSv/MBq
Dubash (*22*)	2018	32	NET	[^{18}F]F-FET-βAG-TOCA	[^{68}Ga]Ga-DOTATATE	BD, QLA	223	209 (93.7)	197 (88.3)	DDR = 5.4%
Long (*25*)	2019	22	NET	[^{18}F]AlF-NOTA-OC	[^{18}F]FDG	BD, QNA, QLA, D	729	624 (85.6)	390 (53.5)	DDR = 32.1%; ED = 23 μSv/MBq
Hou (*26*)	2021	162	NET	[^{18}F]AlF-NOTA-OC	—	BD, QNA	517	—	—	Similar BD
Pauwels (*28*)	2019	1	NET	[^{18}F]AlF-NOTA-OC	[^{68}Ga]Ga-DOTATATE	QNA	—	—	—	Higher TBR
Pauwels (*29*)	2020	12	NET	[^{18}F]AlF-NOTA-OC	[^{68}Ga]Ga-DOTATATE	BD, D, QLA, QNA	242	218 (90.1)	208 (86.0)	DDR = 4.1%; ED = 22.4 μSv/MBq
Hou (*30*)	2021	20	NET	[^{18}F]AlF-NOTA-OC	[^{68}Ga]Ga-DOTATATE	BD, QLA, QNA	180	177 (98.3)	152 (84.4)	DDR = 13.9%
Pauwels (*31*)	2022	75	NET	[^{18}F]AlF-NOTA-OC	^{68}Ga-labeled SSAs	BD, QLA, QNA	4,709	4,278 (91.1)	3,454 (75.3)	DDR = 15.8%
Haeger (*32*)	2023	20	NET	[^{18}F]AlF-NOTA-OC	[^{68}Ga]Ga-DOTATATE	BD, QLA, QNA	752	747 (99.3)	751 (99.9)	DDR = 0.6%
Ilhan (*36*)	2019	1	NET	[^{18}F]SiTATE	[^{68}Ga]Ga-DOTATOC	BD, QNA	—	—	—	Similar BD and TU
Ilhan (*37*)	2020	13	NET	[^{18}F]SiTATE	[^{68}Ga]Ga-DOTATOC	BD, QNA	109	—	—	Similar BD, higher TU
Beyer (*38*)	2021	8	NET	[^{18}F]SiTATE	[^{68}Ga]Ga-DOTATOC	D, QNA	68	—	—	ED = 15 μSv/MBq
Unterrainer (*40*)	2022	86	M	[^{18}F]SiTATE	CT/MRI	QNA	177	—	—	High TBR
Unterrainer (*41*)	2021	1	M	[^{18}F]SiTATE	[^{68}Ga]Ga-DOTATOC	QNA	1	—	—	Comparable TU
Xie (*43*)	2021	10	NET	[^{18}F]AlF-NOTA-JR11	[^{68}Ga]Ga-DOTATATE	BD, QNA, QLA	227	226 (99.6)	160 (70.5)	DDR = 29.1%

BD = biodistribution; D = dosimetry; DDR = difference in detection rate between tracer and comparator; ED = effective dose studied tracer; GT = skull base glomus tumors; M = meningiomas; N = number of patients; N_{total} = total number of lesions; N_{tracer} = number of lesions detected with ^{18}F tracer; N_{com} = number of lesions detected with comparator tracer; P = study population; QLA = qualitative analysis; QNA = quantitative analysis; TBR = tumor-to-background ratio; TD = target lesion volume delineation); TU = tumor uptake.

However, [^{18}F]AlF-NOTA-octreotide detected more lesions (177 vs. 152; $P = 0.54$), especially lesions in the liver (116 vs. 93; $P < 0.01$), presumably because of the higher tumor-to-background ratio. In contrast to the findings of Pauwels et al. (*29*), the SUV_{max} of [^{18}F]AlF-NOTA-octreotide was higher than that of [^{68}Ga]Ga-DOTATATE, but the difference was not statistically relevant. Interestingly, some patients exhibited higher [^{68}Ga]Ga-DOTATATE uptake in lesions whereas others had higher [^{18}F]AlF-NOTA-octreotide uptake. Moreover, some lesions had higher [^{68}Ga]Ga-DOTATATE uptake whereas others within the same patient had higher [^{18}F]AlF-NOTA-octreotide uptake (*30*).

In a recent prospective, multicenter study, Pauwels et al. compared the diagnostic performance of [^{18}F]AlF-NOTA-octreotide with [^{68}Ga]Ga-DOTATATE or [^{68}Ga]Ga-DOTANOC in 75 patients with histologically confirmed NETs (*31*). With [^{18}F]AlF-NOTA-octreotide, patients underwent whole-body PET 2 h after intravenous injection, whereas conventional PET SSTR imaging is typically done 45–60 min after [^{68}Ga]Ga-DOTA SSA injection. [^{18}F]AlF-NOTA-octreotide detected significantly more lesions (4,278/4,709), with a higher detection rate (91.1%) than [^{68}Ga]Ga-DOTATATE (3,454/4,709; 75.3%), illustrating diagnostic superiority. The detection rate was significantly higher for [^{18}F]AlF-NOTA-octreotide in most organs except for bone lesions, where the difference in detection rate was 2.8%. Although the mean tumor-to-background ratio was significantly higher with [^{18}F]AlF-NOTA-octreotide, no significant differences in mean SUV_{max} were observed. In particular, the lower background uptake with [^{18}F]AlF-NOTA-octreotide resulted in better detection of liver metastases (60.3% vs. 93.3%) (Fig. 2). In accordance with the findings of Hou et al. (*30*), considerable variability in lesion uptake was seen both between and within patients. This can most likely be attributed to tumor heterogeneity and differences in SSTR affinity (*31*). In a recently published prospective trial with 20 NET patients, noninferiority of [^{18}F]AlF-NOTA-octreotide in comparison with [^{68}Ga]Ga-DOTATATE was confirmed (*32*). Differences in lesion detection rate and tumor-to-background ratios were nonsignificant, but [^{18}F]AlF-NOTA-octreotide images showed lower liver and spleen background, providing excellent image quality (*32*).

Besides diagnostic information, [^{18}F]AlF-NOTA-octreotide PET can offer prognostic value in combination with [^{18}F]FDG PET imaging. This was evaluated by Hou et al. in a study of 66 patients with NETs who underwent both imaging modalities (*33*). In this analysis, a visual evaluation method summarizing information from both [^{18}F]FDG and SSTR images (NETPET grading) was further investigated using [^{18}F]AlF-NOTA-octreotide for SSTR imaging. In multivariate analysis, both NETPET grade and SSTR expression (tumor volume multiplied by SUV_{mean}) were independent predictors of progression-free survival (*33*).

[^{18}F]SiTATE

Another promising SSA radiotracer labeled with ^{18}F is [^{18}F]SiTATE, which has shown high selectivity for SSTR2 and can be synthesized in conformation with good manufacturing practices (Fig. 3) (*34,35*). In 2019, the first in-humans [^{18}F]SiTATE PET/CT scan was performed on a patient with metastatic NET and showed cardiac and bone metastasis uptake comparable to that on [^{68}Ga]Ga-DOTATATE PET/CT (*36*). The biodistribution, tumor uptake, and image quality of [^{18}F]SiTATE and [^{68}Ga]Ga-DOTATOC were directly compared in a retrospective study by Ilhan et al. including 13 patients with grade 1 or 2 neuroendocrine neoplasia (*37*). For [^{18}F]SiTATE, physiologic tracer uptake was significantly higher in the kidneys and nonsignificantly higher in the liver, adrenal glands, and spleen. For [^{18}F]SiTATE, a significantly higher tumor uptake was described in almost all tumor lesions in common metastatic sites of NET, including the liver, lymph nodes, and bone, but not in lung lesions. This led to tumor-to-background ratios similar to those for [^{68}Ga]Ga-DOTATOC. One limitation of this study was the relatively large range in time interval between

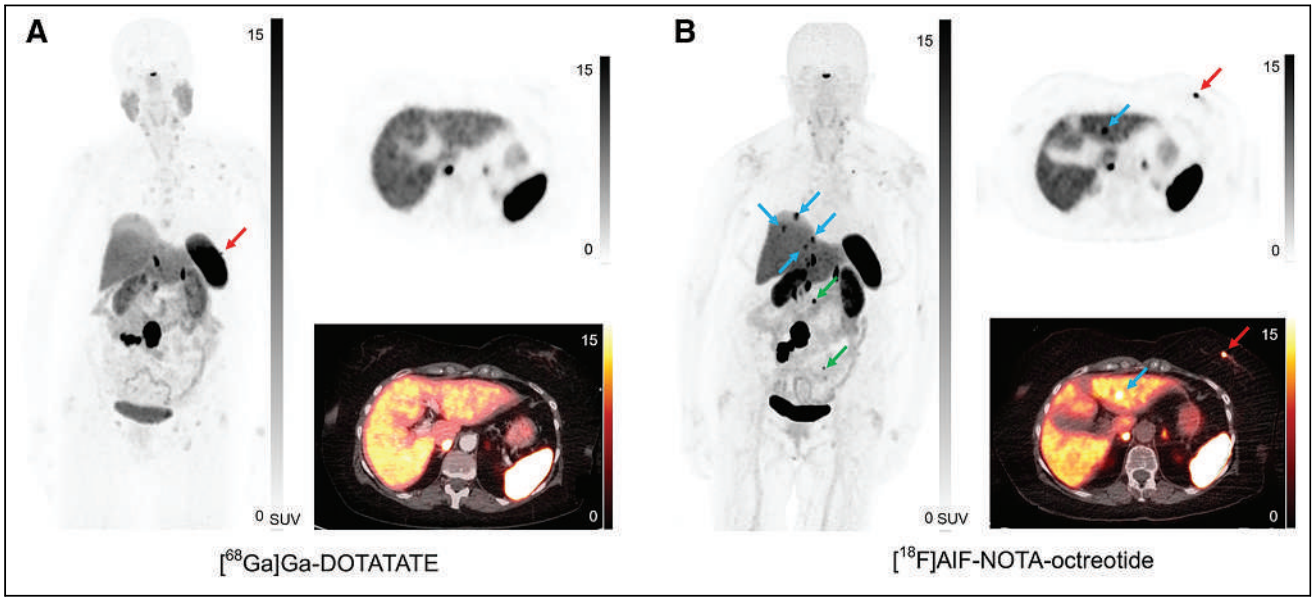

FIGURE 2. [^{68}Ga]Ga-DOTATATE (A) and [^{18}F]AlF-NOTA-octreotide (B) maximum-intensity-projection, PET, and PET/CT images of 69-y-old woman with intestinal NET, multiple liver and lymph node metastases, and 1 breast metastasis. [^{18}F]AlF-NOTA-octreotide PET/CT showed multiple liver lesions (blue arrows), whereas previous [^{68}Ga]Ga-DOTATATE PET/CT (7 d before) showed no liver disease. Furthermore, 2 new lymph node metastases were detected with [^{18}F]AlF-NOTA-octreotide (green arrows). Breast metastasis (red arrow) was also seen on [^{68}Ga]Ga-DOTATATE images but is not depicted on slice shown.

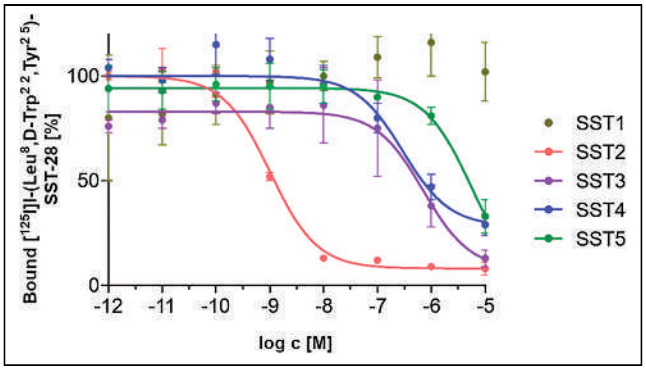

FIGURE 3. In vitro competition experiment using membranes of SSTR subtype–expressing cells. Image shows bound fraction of [^{125}I]I-(Leu^{8}, D-Trp^{22}, Tyr^{25})-SST-28 with increasing concentrations of [^{18}F]SiTATE. [^{18}F]SiTATE shows excellent selectivity for SSTR subtype 2, with only minor affinity to SSTR subtypes 3 and 4. (Reprinted from (*35*).)

the 2 scans (4–26 mo), including heterogeneous therapy options that were applied in between (*37*). Beyer et al. evaluated the biodistribution, optimal scan time, and dosimetry for both tracers in 8 patients and found similar results (*38*). When imaging took place 60 min after injection, tumor-to-background ratios did not significantly differ between [^{68}Ga]Ga-DOTATATE and [^{18}F]SiTATE for most lesions. However, [^{18}F]SiTATE uptake further increased for almost all types of metastases after 60 min, leading to higher tumor-to-background ratios at later scan times. Biodistribution was comparable to [^{68}Ga]Ga-DOTATATE, with bladder and spleen showing the highest radiotracer uptake, followed by kidneys and adrenal glands (*38*). In a recently published study, Eschbach et al. investigated the influence of long-acting SSA medication before [^{18}F]SiTATE on tumor uptake and physiologic uptake (*39*). Similar to ^{68}Ga-labeled SSAs, a significantly lower [^{18}F]SiTATE uptake in normal liver and spleen tissue was observed in patients receiving treatment with long-acting SSAs. However, there was no significant reduction in tumor-to-background ratios, supporting the clinical approach not to discontinue any SSA medication before a PET/CT examination (*39*).

[^{18}F]SiTATE can also be applied for PET imaging of meningiomas. Unterrainer et al. evaluated the feasibility of [^{18}F]SiTATE PET/CT in 86 patients with known or suspected meningioma (*40*). Tracer uptake was very high in meningiomas compared with healthy tissue and nonmeningioma lesions, leading to a high detection of osseous involvement and previously unknown meningioma sites (*40,41*).

[^{18}F]AlF-NOTA-JR11

Noninternalizing SSTR antagonists have the potential to improve SSTR PET/CT imaging because they bind to a greater number of binding sites than agonists, leading to higher tumor accumulation and possibly higher imaging sensitivity. [^{68}Ga]Ga-NODAGA-JR11 has a high affinity for SSTR and is one of the lead molecules for this novel route of SSTR imaging (*42*). In a recent pilot study, Xie et al. compared [^{18}F]AlF-NOTA-JR11, an Al^{18}F-labeled SSTR antagonist, with [^{68}Ga]Ga-DOTATATE in 10 patients with neuroendocrine neoplasia and evaluated biodistribution and tumor detectability (*43*). The physiologic uptake of [^{18}F]AlF-NOTA-JR11 was significantly lower than that of [^{68}Ga]Ga-DOTATATE in the liver, spleen, adrenal gland, intestine, and pancreas but was higher in the blood and lungs. Furthermore, [^{18}F]AlF-NOTA-JR11 showed a significantly higher SUV_{max} in the liver lesions than did [^{68}Ga]Ga-DOTATATE, whereas no significant difference was found among the other groups. More primary and secondary lesions were detected with [^{18}F]AlF-NOTA-JR11 (226/227 lesions) than with [^{68}Ga]Ga-DOTATATE (160/227 lesions) because of the lower physiologic uptake by the digestive system. These findings indicate that [^{18}F]AlF-NOTA-JR11 could be a promising alternative to [^{68}Ga]Ga-DOTATATE, especially in lesions of the digestive system (*43*). However, novel high-affinity Al^{18}F-labeled SSTR2 antagonists might be warranted to further increase NET imaging sensitivity and to fully exploit the advantages of SSTR antagonists combined with the logistic advantages of ^{18}F.

FUTURE PERSPECTIVES

^{18}F-labeled SSA tracers are a promising alternative to ^{68}Ga-labeled SSAs. However, multiple questions about their use in clinical practice still remain unanswered. First, to our knowledge, no currently available clinical studies evaluated the interobserver agreement rate. Differences in interobserver concordance rates have already been described for ^{18}F-labeled prostate-specific membrane antigen tracers in comparison with their ^{68}Ga-labeled counterparts. Therefore, interobserver variability should also be assessed for ^{18}F-labeled SSA PET tracers. Second, several attempts have been made to evaluate the relationship between [^{68}Ga]Ga-DOTA SSA PET–derived quantitative parameters and treatment response after PRRT. Nevertheless, given the heterogeneous results of these studies, the predictive value of currently used ^{68}Ga-labeled SSA tracers is suboptimal in identifying patients who would benefit from PRRT (*44*). This limitation could possibly be overcome by the higher diagnostic accuracy of ^{18}F-labeled SSA tracers. Third, the impact on clinical management when using ^{18}F-labeled SSAs remains unclear and should be assessed in a multidisciplinary setting. Fourth, a more widespread use of ^{18}F-labeled SSAs may have a beneficial impact on patient outcomes. Improved lesion detection (e.g., by the higher spatial resolution and tumor-to-background ratio) could lead to a more accurate evaluation of disease extent, aiding physicians in making the right therapy choice. Finally, clinical data regarding the use of ^{18}F-labeled SSAs in other SSTR-expressing tumor subtypes (e.g., medullary thyroid cancer and small cell lung cancer) are currently lacking, and these entities need to be assessed in future studies.

CONCLUSION

In recent years, clinical studies have provided data that support the promising role of new ^{18}F-labeled SSA tracers. The beneficial physical properties of ^{18}F in combination with its higher production yield make these tracers an attractive alternative to ^{68}Ga-labeled tracers. Currently available clinical data on ^{18}F-labeled SSA tracers generally demonstrate higher in vivo stability, higher tumor-to-background ratios, better lesion detection, or a more favorable biodistribution than conventional [^{68}Ga]Ga-DOTA SSA tracers, indicating suitability for clinical use. Highly promising data for clinical use have been obtained for [^{18}F]SiTATE and [^{18}F]F-FET-βAG-TOCA. [^{18}F]AlF-NOTA-octreotide has been prospectively validated in a multicenter setting, with a favorable head-to-head comparison to [^{68}Ga]Ga-DOTA SSA tracers. ^{18}F-labeled SSTR agonist tracers should be implemented in guidelines and appropriate-use criteria for SSTR PET imaging, and future studies should focus on interobserver variability, impact on patient management, selection for peptide receptor radionuclide therapy, and therapy monitoring.

DISCLOSURE

Christophe Deroose is a senior clinical investigator from the Research Foundation–Flanders (FWO) and has been a consultant for Terumo, Ipsen, Sirtex, Bayer, and PSI CRO. Frederik Cleeren has been awarded an ERF nuclear medicine pilot research grant by the Neuroendocrine Tumor Research Foundation (NETRF). No other potential conflict of interest relevant to this article was reported.

REFERENCES

1. Hallet J, Law CHL, Cukier M, Saskin R, Liu N, Singh S. Exploring the rising incidence of neuroendocrine tumors: a population-based analysis of epidemiology, metastatic presentation, and outcomes. *Cancer.* 2015;121:589–597.
2. Bozkurt MF, Virgolini I, Balogova S, et al. Guideline for PET/CT imaging of neuroendocrine neoplasms with ^{68}Ga-DOTA-conjugated somatostatin receptor targeting peptides and ^{18}F-DOPA. *Eur J Nucl Med Mol Imaging.* 2017;44:1588–1601.
3. Sampedro-Núñez M, Luque RM, Ramos-Levi AM, et al. Presence of sst5TMD4, a truncated splice variant of the somatostatin receptor subtype 5, is associated to features of increased aggressiveness in pancreatic neuroendocrine tumors. *Oncotarget.* 2016;7:6593–6608.
4. Günther T, Tulipano G, Dournaud P, et al. International union of basic and clinical pharmacology. CV. Somatostatin receptors: structure, function, ligands, and new nomenclature. *Pharmacol Rev.* 2018;70:763–835.
5. Reubi JC, Laissue J, Krenning E, Lamberts SWJ. Somatostatin receptors in human cancer: incidence, characteristics, functional correlates and clinical implications. *J Steroid Biochem Mol Biol.* 1992;43:27–35.
6. Deroose CM, Hindié E, Kebebew E, et al. Molecular imaging of gastroenteropancreatic neuroendocrine tumors: current status and future directions. *J Nucl Med.* 2016;57:1949–1956.
7. Volante M, Rosas R, Allìa E, et al. Somatostatin, cortistatin and their receptors in tumours. *Mol Cell Endocrinol.* 2008;286:219–229.
8. Reubi JC. Somatostatin and other peptide receptors as tools for tumor diagnosis and treatment. *Neuroendocrinology.* 2004;80:51–56.
9. Nedrow JR, White AG, Modi J, Nguyen K, Chang AJ, Anderson CJ. Positron emission tomographic imaging of copper 64- and gallium 68-labeled chelator conjugates of the somatostatin agonist Tyr 3-octreotate. *Mol Imaging.* 2014;13:1–13.
10. Krenning EP, Breeman WAP, Kooij PPM, et al. Localisation of endocrine-related tumours with radioiodinated analogue of somatostatin. *Lancet.* 1989;1:242–244.
11. Krenning EP, Bakker WH, Kooij PPM, et al. Somatostatin receptor scintigraphy with indium-111-DTPA-D-Phe-1-octreotide in man: metabolism, dosimetry and comparison with iodine-123-Tyr-3-octreotide. *J Nucl Med.* 1992;33:652–658.
12. Smit Duijzentkunst DAS, Kwekkeboom DJ, Bodei L. Somatostatin receptor 2-targeting compounds. *J Nucl Med.* 2017;58(suppl 2):54S–60S.
13. Ambrosini V, Fani M, Fanti S, Forrer F, Maecke HR. Radiopeptide imaging and therapy in Europe. *J Nucl Med.* 2011;52(suppl 2):42S–55S.
14. Gabriel M, Decristoforo C, Donnemiller E, et al. An intrapatient comparison of ^{99m}Tc-EDDA/HYNIC-TOC with ^{111}In-DTPA-octreotide for diagnosis of somatostatin receptor-expressing tumors. *J Nucl Med.* 2003;44:708–716.
15. Poletto G, Cecchin D, Sperti S, Filippi L, Realdon N, Evangelista L. Head-to-head comparison between peptide-based radiopharmaceutical for PET and SPECT in the evaluation of neuroendocrine tumors: a systematic review. *Curr Issues Mol Biol.* 2022;44:5516–5530.
16. Pauwels E, Cleeren F, Bormans G, Deroose C. Somatostatin receptor PET ligands the next generation for clinical practice. *Am J Nucl Med Mol Imaging.* 2018;8:311–331.
17. Meisetschläger G, Poethko T, Stahl A, et al. Gluc-Lys([^{18}F]FP)-TOCA PET in patients with SSTR-positive tumors: biodistribution and diagnostic evaluation compared with [^{111}In]DTPA-octreotide. *J Nucl Med.* 2006;47:566–573.
18. Seemann MD. Detection of metastases from gastrointestinal neuroendocrine tumors: prospective comparison of ^{18}F-TOCA PET, triple-phase CT, and PET/CT. *Technol Cancer Res Treat.* 2007;6:213–220.
19. Wieder H, Beer AJ, Poethko T, et al. PET/CT with Gluc-Lys-([^{18}F]FP)-TOCA: correlation between uptake, size and arterial perfusion in somatostatin receptor positive lesions. *Eur J Nucl Med Mol Imaging.* 2008;35:264–271.
20. Astner ST, Bundschuh RA, Beer AJ, et al. Assessment of tumor volumes in skull base glomus tumors using Gluc-Lys[^{18}F]-TOCA positron emission tomography. *Int J Radiat Oncol Biol Phys.* 2009;73:1135–1140.
21. Dubash SR, Nicholas K, Mapelli P, et al. Clinical translation of a click-labeled ^{18}F-octreotate radioligand for imaging neuroendocrine tumors. *J Nucl Med.* 2016;57:1207–1213.
22. Dubash SR, Barwick T, Mauri FA, et al. [^{18}F]FET-βAG-TOCA versus [^{68}Ga]DOTATATE PET/CT in functional imaging of neuroendocrine tumours [abstract]. *J Clin Oncol.* 2018;36(suppl):e24193.
23. Ćorović A, Wall C, Nus M, et al. Somatostatin receptor PET/MR imaging of inflammation in patients with large vessel vasculitis and atherosclerosis. *J Am Coll Cardiol.* 2023;81:336–354.
24. Tshibangu T, Cawthorne C, Serdons K, et al. Automated GMP compliant production of [^{18}F]AlF-NOTA-octreotide. *EJNMMI Radiopharm Chem.* 2020;5:4.
25. Long T, Yang N, Zhou M, et al. Clinical application of ^{18}F-AlF-NOTA-octreotide PET/CT in combination with ^{18}F-FDG PET/CT for imaging neuroendocrine neoplasms. *Clin Nucl Med.* 2019;44:452–458.
26. Hou J, Long T, Yang N, et al. Biodistribution of ^{18}F-AlF-NOTA-octreotide in different organs and characterization of uptake in neuroendocrine neoplasms. *Mol Imaging Biol.* 2021;23:827–835.
27. Hofman MS, Eddie Lau WF, Hicks RJ. Somatostatin receptor imaging with ^{68}Ga-DOTATATE PET/CT: clinical utility, normal patterns, pearls, and pitfalls in interpretation. *Radiographics.* 2015;35:500–516.
28. Pauwels E, Cleeren F, Tshibangu T, et al. Al^{18}F-NOTA-octreotide: first comparison with ^{68}Ga-DOTATATE in a neuroendocrine tumour patient. *Eur J Nucl Med Mol Imaging.* 2019;46:2398–2399.
29. Pauwels E, Cleeren F, Tshibangu T, et al. [^{18}F]AlF-NOTA-octreotide PET imaging: biodistribution, dosimetry and first comparison with [^{68}Ga]Ga-DOTATATE in neuroendocrine tumour patients. *Eur J Nucl Med Mol Imaging.* 2020;47:3033–3046.
30. Hou J, Long T, He Z, et al. Evaluation of ^{18}F-AlF-fetNOTA-octreotide for imaging neuroendocrine neoplasms: comparison with ^{68}Ga-DOTATATE PET/CT. *EJNMMI Res.* 2021;11:55.
31. Pauwels E, Cleeren F, Tshibangu T, et al. 18F-AlF-NOTA-octreotide outperforms 68Ga-DOTATATE/NOC PET in neuroendocrine tumor patients: results from a prospective, multicenter study. *J Nucl Med.* 2023;64:632–638.
32. Haeger A, Soza-Ried C, Kramer V, et al. Al[^{18}F]F-NOTA-octreotide is comparable to [^{68}Ga]Ga-DOTA-TATE for PET/CT imaging of neuroendocrine tumours in the Latin-American population. *Cancers (Basel).* 2023;15:439–450.
33. Hou J, Long T, Yang Y, Chen D, Hu S. The potential prognostic value of dual-imaging PET parameters based on ^{18}F-FDG and ^{18}F-OC for neuroendocrine neoplasms. *Mol Imaging.* 2022;2022:6511179.
34. Lindner S, Simmet M, Gildehaus FJ, et al. Automated production of [^{18}F]SiTATE on a Scintomics GRP^{TM} platform for PET/CT imaging of neuroendocrine tumors. *Nucl Med Biol.* 2020;88–89:86–95.
35. Wängler C, Beyer L, Bartenstein P, Wängler B, Schirrmacher R, Lindner S. Favorable SSTR subtype selectivity of SiTATE: new momentum for clinical [^{18}F]SiTATE PET. *EJNMMI Radiopharm Chem.* 2022;7:22.
36. Ilhan H, Todica A, Lindner S, et al. First-in-human ^{18}F-SiFAlin-TATE PET/CT for NET imaging and theranostics. *Eur J Nucl Med Mol Imaging.* 2019;46:2400–2401.
37. Ilhan H, Lindner S, Todica A, et al. Biodistribution and first clinical results of ^{18}F-SiFAlin-TATE PET: a novel ^{18}F-labeled somatostatin analog for imaging of neuroendocrine tumors. *Eur J Nucl Med Mol Imaging.* 2020;47:870–880.
38. Beyer L, Gosewisch A, Lindner S, et al. Dosimetry and optimal scan time of [^{18}F]SiTATE-PET/CT in patients with neuroendocrine tumours. *Eur J Nucl Med Mol Imaging.* 2021;48:3571–3581.
39. Eschbach RS, Hofmann M, Späth L, et al. Comparison of somatostatin receptor expression in patients with neuroendocrine tumours with and without somatostatin analogue treatment imaged with [^{18}F]SiTATE. *Front Oncol.* 2023;13:992316.
40. Unterrainer M, Unterrainer L, Kunte SC, et al. Next generation PET/CT imaging in meningioma: first clinical experiences using the novel SSTR-targeting peptide ^{18}F-SiTATE [abstract]. *J Nucl Med.* 2022;63(suppl 2):2289.
41. Unterrainer M, Lindner S, Beyer L, et al. PET imaging of meningioma using the novel SSTR-targeting peptide ^{18}F-SiTATE. *Clin Nucl Med.* 2021;46:667–668.
42. Nicolas GP, Schreiter N, Kaul F, et al. Sensitivity comparison of ^{68}Ga-OPS202 and ^{68}Ga-DOTATOC PET/CT in patients with gastroenteropancreatic neuroendocrine tumors: a prospective phase II imaging study. *J Nucl Med.* 2018;59:915–921.
43. Xie Q, Liu T, Ding J, et al. Synthesis, preclinical evaluation, and a pilot clinical imaging study of [^{18}F]AlF-NOTA-JR11 for neuroendocrine neoplasms compared with [^{68}Ga]Ga-DOTA-TATE. *Eur J Nucl Med Mol Imaging.* 2021;48:3129–3140.
44. Ahmadi Bidakhvidi A, Goffin K, Dekervel J, et al. Peptide receptor radionuclide therapy targeting the somatostatin receptor: basic principles, clinical applications and optimization strategies. *Cancers (Basel).* 2021;14:129.
45. Vermeulen K, Vandamme M, Bormans G, Cleeren F. Design and challenges of radiopharmaceuticals. *Semin Nucl Med.* 2019;49:339–356.

^{18}F-FDG PET/CT in the Management of Osteosarcoma

Chiwoo Oh[1], Michael W. Bishop[2], Steve Y. Cho[3], Hyung-Jun Im[1,4,5], and Barry L. Shulkin[6]

[1]Department of Applied Bioengineering, Graduate School of Convergence Science and Technology, Seoul National University, Seoul, Republic of Korea; [2]Department of Oncology, St. Jude Children's Research Hospital, Memphis, Tennessee; [3]Nuclear Medicine and Molecular Imaging Section, Department of Radiology, University of Wisconsin School of Medicine and Public Health, Madison, Wisconsin; [4]Department of Molecular Medicine and Biopharmaceutical Sciences, Graduate School of Convergence Science and Technology, Seoul National University, Seoul, Republic of Korea; [5]Cancer Research Institute, Seoul National University, Seoul, Republic of Korea; and [6]Department of Diagnostic Imaging, St. Jude Children's Research Hospital, Memphis, Tennessee

Learning Objectives: On successful completion of this activity, participants should be able to describe (1) the diagnosis and treatment strategy and response criteria of osteosarcoma; (2) the roles of ^{18}F-FDG PET in staging, prediction of clinical outcome and detection of recurrent disease; and (3) the useful timepoint of ^{18}F-FDG PET in prediction of clinical outcome.

Financial Disclosure: Drs. Chiwoo Oh and Hyung-Jun Im were supported by National Research Foundation of Korea (NRF) (NRF-2021M2E8A1039564, 2020R1C1C1009000, and 2019M2D2A1A01058210), Korea Evaluation Institute of Industrial Technology (KEIT) grant funded by the Korea government (MOTIE) (no. 20018522), and Korea Drug Development Fund funded by Ministry of Science and ICT, Ministry of Trade, Industry, and Energy, and Ministry of Health and Welfare (HN22C0632). Dr. Shulkin was supported by the American Lebanese Syrian Associated Charities (ALSAC). Dr. Im is the cofounder and the Chief Scientific Officer of Portrai. The authors of this article have indicated no other relevant relationships that could be perceived as a real or apparent conflict of interest.

CME Credit: SNMMI is accredited by the Accreditation Council for Continuing Medical Education (ACCME) to sponsor continuing education for physicians. SNMMI designates each *JNM* continuing education article for a maximum of 2.0 AMA PRA Category 1 Credits. Physicians should claim only credit commensurate with the extent of their participation in the activity. For CE credit, SAM, and other credit types, participants can access this activity through the SNMMI website (http://www.snmmilearningcenter.org) throsugh June 2026.

Osteosarcoma is the most common type of primary malignant bone tumor. ^{18}F-FDG PET/CT is useful for staging, detecting recurrence, monitoring response to neoadjuvant chemotherapy, and predicting prognosis. Here, we review the clinical aspects of osteosarcoma management and assess the role of ^{18}F-FDG PET/CT, in particular with regard to pediatric and young adult patients.

Key Words: osteosarcoma; ^{18}F-FDG PET; clinical outcome; prediction; staging

J Nucl Med 2023; 64:842–851
DOI: 10.2967/jnumed.123.265592

Osteosarcoma is the most common type of primary malignant bone tumor. ^{18}F-FDG PET/CT is useful for staging, detecting recurrence, monitoring response to neoadjuvant chemotherapy (NCT), and predicting prognosis. Here, we review the clinical aspects of osteosarcoma management and assess the role of ^{18}F-FDG PET/CT, in particular with regard to pediatric and young adult patients.

DEMOGRAPHICS

Osteosarcoma is the most common type of malignant primary bone tumor, with a peak incidence in 10- to 14-y-olds (*1*) and a second peak incidence in those older than 50 y. Approximately 4.4 cases per million are diagnosed annually in people aged 0–24 y (*2*). Primary osteosarcomas commonly arise within the metaphyses of long bones, with 80% presenting within an extremity. Patients typically present with pain that progresses over weeks to months, with localized swelling and a diminished range of motion or function in the affected limb (*3*). At the time of diagnosis, approximately 10%–20% of patients have evidence of macroscopic metastasis, most commonly in the lung (81%), bone (34%), and, rarely, lymph nodes (2%) (*4*). Five-year event-free survival rates are approximately 70% (*5*). ^{18}F-FDG PET/CT has multiple roles in the evaluation of osteosarcoma for staging, clinical and histologic response to therapy during and at the conclusion of treatment, and determining prognosis after completion of therapy (Fig. 1).

STAGING

^{18}F-FDG PET/CT is useful for staging, detecting recurrence, and predicting histologic response and prognosis in the investigation of osteosarcoma. Conventional imaging modalities other than ^{18}F-FDG PET/CT for staging osteosarcoma are summarized in Supplemental Figure 1 (supplemental materials are available at http://jnm.snmjournals.org). During staging, PET/CT is useful for differential diagnosis of primary bone neoplasms and detecting metastatic lesions (Figs. 2 and 3; images are scaled to SUV units as on the color and intensity bars). Combining PET imaging with CT or MRI provides more accurate information on the staging of osteosarcoma than is possible with PET imaging alone (*6,7*). Also, whole-body imaging with PET/CT can be helpful in staging because osteosarcoma favors the extremities and can be widely metastatic (*8*). London et al. retrospectively compared the sensitivity and specificity of PET/CT and plain radiography for detecting malignant lesions, including primary and metastatic disease, in patients with pediatric primary bone tumors. PET/CT was more sensitive than plain radiography (98% vs. 83%) and more specific (97% vs. 78%) (*9*). Strobel et al. compared the diagnostic accuracy of plain radiography, PET, and PET/CT. They found that PET/CT showed 95% sensitivity and 77% specificity, which were the highest rates

Received Feb. 15, 2023; revision accepted Apr. 26, 2023.
For correspondence or reprints, contact Hyung-Jun Im (iiihjjj@gmail.com) or Barry L. Shulkin (barry.shulkin@stjude.org).
Published online May 18, 2023.

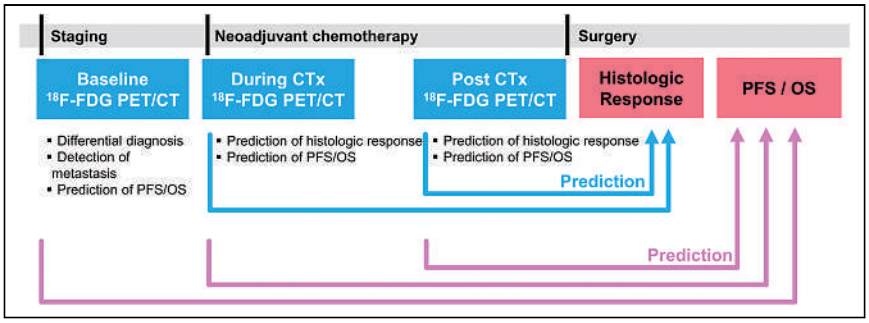

FIGURE 1. Role of ^{18}F-FDG PET/CT in staging and outcome prediction in osteosarcoma. CTx = chemotherapy; PFS = progression-free survival.

among the imaging modalities (*10*). Quartuccio et al. reported that PET/CT has higher accuracy for detecting bone metastasis than CT or dedicated MRI and detects lung metastasis as well as CT does (*11*). Franzius et al. found that PET performed better than bone scanning for detecting bone metastasis (*12*), with Hurley et al. finding that PET/CT was more sensitive but bone scanning was more specific (*13*). Used together in a lesion-based analysis (*14*), the sensitivity of PET/CT plus bone scanning was 100%, which is higher than that of PET/CT or bone scanning alone, supporting the use of both modalities together to detect bone metastasis (Table 1). This is because some osteoblastic metastases may not show elevated uptake of ^{18}F-FDG, thus yielding false-negative results on PET/CT but positive results on bone scanning (*14*). In our experience, false-negative cases are rare, and careful review of the CT bone window in a PET/CT scan could reduce them. Thus, we do not routinely perform bone scans on patients with osteosarcoma.

In a recent metaanalysis, the value of PET/CT in diagnosis and staging was summarized (*15*). This metaanalysis evaluated 26 studies, including the above-mentioned studies. For detecting primary lesions, PET/CT showed 100% sensitivity in 14 studies. Pooled sensitivity and specificity for detecting lung metastases in 8 studies were 81% (95% CI of 72%–88%) and 94% (95% CI of 89%–97%), respectively. For bone metastases, 6 studies showed a pooled sensitivity of 93% (95% CI of 87%–97%) and a pooled specificity of 97% (95% CI of 96%–98%) (Supplemental Fig. 2). Thus, PET/CT is useful for differential diagnosis of the suspected primary bone lesions and for staging.

TREATMENT OVERVIEW

The therapeutic standard of care involves NCT with 3 or more agents with single-agent activity for approximately 8–10 wk, followed by surgical resection of all detectable disease (including metastases) and postoperative adjuvant chemotherapy for 12–29 wk (*16*). Limb-salvage surgery is the surgical treatment in 85%–90% of patients with osteosarcoma, providing better functional and cosmetic results than amputation without compromising survival (*17*).

PREDICTION OF RESPONSE TO NCT

Histologic Response

In 1994, a critical appraisal of osteosarcoma prognostic factors concluded that the histologic response of primary tumors after NCT is the most significant factor in predicting disease-free survival (*3,18*). Although histologic response is prognostic for outcomes, dose-intensifying NCT to increase rates of tumor necrosis have not yielded superior survival curves (*19*). Similarly, adding chemotherapeutic agents for patients experiencing a poor response has not improved their event-free survival or overall survival (OS) (*19*). Several grading systems for assessing the effect of NCT on the primary tumor indicate that having at least 90% tumor necrosis after NCT is a favorable response (Table 2) (*20–22*).

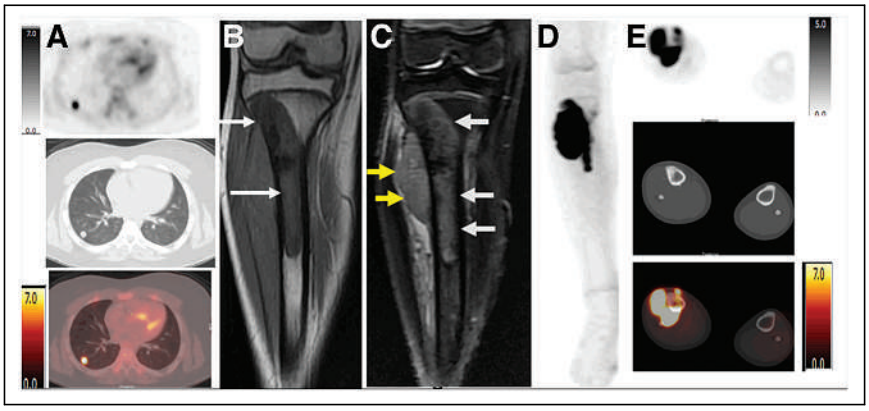

FIGURE 2. A 13-y-old boy with right leg pain. (A) ^{18}F-FDG PET CT shows 1-cm nodule with markedly elevated uptake in right lower lobe (SUV_{max}, 6.7) (^{18}F-FDG PET emission image [top], CT transmission image [middle], and PET/CT image [bottom]). (B) Hypointense signal on coronal T1 MR image shows tumor extending from tibial metaphysis through proximal third of right tibia (arrows). (C) Coronal T2 short-tau inversion recovery MR image shows intermediate signal within intramedullary component of tumor (white arrows), corresponding to hypointense T1 signal, and hyperintensity in soft-tissue component lateral to tibia (yellow arrows). (D) ^{18}F-FDG PET/CT anterior maximum-intensity-projection view shows intense uptake in the proximal aspect of the right distal lower extremity. (E) ^{18}F-FDG PET axial emission image (top), transmission CT bone window (middle), and PET/CT image (bottom) show intense though irregularly increased uptake of ^{18}F-FDG in both bone and soft-tissue components of tumor (SUV_{max}, 15.^{TM}).

Role of ^{18}F-FDG PET/CT

In osteosarcoma, the ability of PET or PET/CT to predict histologic response during or after NCT has been reported. In 1996, Jones et al. first reported using PET to assess response to NCT in 3 patients with osteosarcoma (*23*), finding that SUV declined after NCT, which reflected the histologic response. In the following studies, tumor-to-background ratio or SUV_{max} after NCT, as well as tumor-to-background ratio or SUV_{max} ratio between PET at baseline and after NCT, were found to predict histologic response (*23–32*). Meanwhile, some studies reported that PET/CT was not predictive of histologic response (Table 3; Supplemental Table 1) (*33,34*). These studies agree on the following optimal cutoffs of PET parameters: an SUV_{max} of 2–3 after NCT and a tumor-to-background ratio or SUV_{max} ratio of 0.4–0.6 (*24–29,31–33,35–38*). In a metaanalysis, an SUV_{max} after NCT of less than 2.5 and an SUV_{max} ratio of less than 0.5

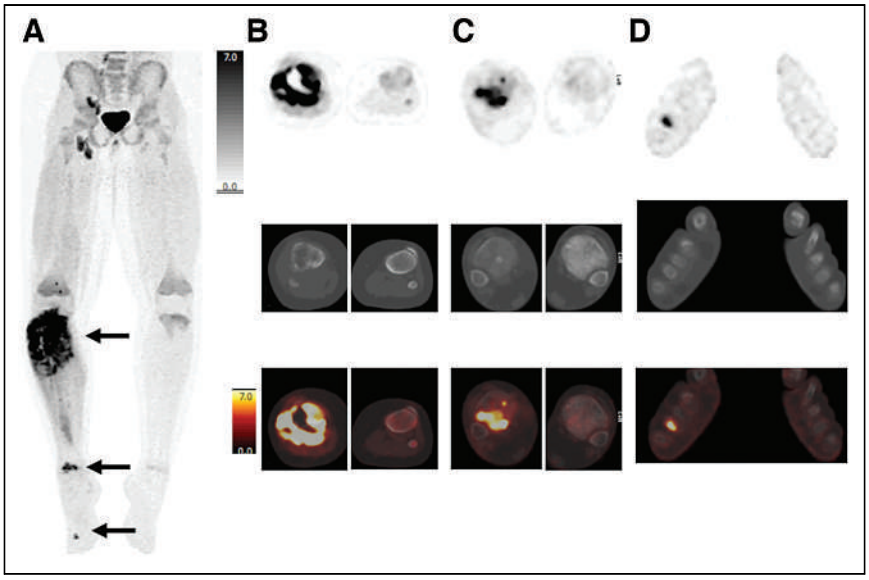

FIGURE 3. A 10-y-old girl with pain in right lower extremity. (A) Anterior maximum-intensity-projection PET image shows primary tumor in proximal right tibia and soft tissue (top arrow; SUV_{max}, 24.4), unsuspected site of metastatic disease in distal right tibia (middle arrow; SUV_{max}, 12.9), and unsuspected site of metastatic disease in fourth right metatarsal (bottom arrow; SUV_{max}, 8.2). (B–D) PET (top), CT (middle), and PET/CT fusion (bottom) images showing the sites indicated in A by top arrow (B), middle arrow (C), and bottom arrow (D). Uptake in ipsilateral popliteal, inguinal femoral, and iliac lymph nodes was considered reactive.

between baseline and after NCT were suggested as optimal cutoffs (*39*). Because of the ability of PET/CT to predict the histologic response, Harrison et al. have proposed further evaluating PET/CT as an imaging biomarker to screen the potential of targeted agents in osteosarcoma (*40*).

Predicting the histologic response of tumor during NCT may be a better option than doing so after completion of NCT in the clinic because the latter is too late to modify the NCT regimen. In 2012, Im et al. found that SUV_{max} after 1 cycle of NCT can also predict the histologic response with an accuracy of 92.9% using a cutoff of 3.2 (*37*). This result was reproduced by Byun et al. in 2014 (*41*) and Davis et al. in 2018 (*38*). Metabolic–volumetric parameters of PET, such as metabolic tumor volume (MTV) and total lesion glycolysis (TLG, the product of tumor segmented SUV_{mean} and MTV), during and after the NCT also showed predictive value for histologic response (*36,37,41*). Byun et al. reported that SUV_{max}, MTV, and TLG after 1 cycle of NCT could predict histologic response, but tumor volume assessed by MRI could not (*41*). Among PET parameters, SUV_{max} could be a better choice than metabolic–volumetric parameters because MTV and TLG measurements depend on the PET tumor segmentation methods, which are not standardized (*42*). Also, SUV_{max} during NCT performed similarly to MTV and TLG in predicting the histologic response (area under the curve, 0.956 for all parameters) (*37*). Because the level of water molecule diffusion can be changed according to the cellularity of the primary lesion, diffusion-weighted MRI can be used to predict the histologic response of osteosarcoma; thus, combining PET and diffusion-weighted MRI may be an effective method to predict the histologic response (*35*).

Furthermore, predicting tumor histologic response using the baseline PET/CT has been attempted. Byun et al. used dual-phase (i.e., dual-time point) baseline PET/CT obtained at 60 and 120 min after ^{18}F-FDG injection (*43*), finding that the mean retention index at baseline PET/CT was predictive of histologic response, with a moderate accuracy of 71% (Supplemental Fig. 3). However, Im et al. reported that although conventional parameters of baseline PET/CT could not predict histologic response, kurtosis and skewness among histogram-based parameters could, with areas under the curve of 0.718 and 0.714, respectively. The predictive value could be enhanced using a machine learning algorithm (area under the curve, 0.821), but the predictive values of texture features depended on the type of segmentation method and machine learning algorithm (*44*). Altogether, more evidence is needed to prove that baseline PET/CT is predictive of histologic response after NCT.

PREDICTION OF OUTCOMES

Prognostic Factors

Tumor site, size, primary metastases, response to chemotherapy, and surgical remission are the reported independent prognostic factors in osteosarcoma (*3*). Osteosarcoma arising in pelvic or axial bones has a worse prognosis than that of disease in extremity bones, with pelvic osteosarcoma having reported 5-y OS rates of 27%–47% (*45*). Osteosarcoma arising in the spine has an even worse prognosis, with a median survival time of 10–23 mo (*46*). Tumor stage is also prognostic. In the Musculoskeletal Tumor Society's Enneking system, stage IA showed an almost 100% 5-y survival rate, yet IIB showed a 5-y survival rate of only 40% (*47*). Among patients with metastases, those with only lung metastases have a more favorable prognosis than do those with extrapulmonary lesions (5-y OS rate, 38% vs. 10.9%) (*3*). The presence of skip metastasis is associated with a poor prognosis (*48*). Being younger than 40 y is a good prognostic factor (5-y survival rate, 65.1% vs. 55.0%) (*3*). In the literature, the most reliable cutoff differentiating favorable from unfavorable response to chemotherapy is 90% necrosis, with greater than 90% necrosis considered favorable (*31*). Prognostic factors can be applied differently according to age. Response to chemotherapy is applied as a prognostic factor in pediatric patients but not in adult patients (*49*). Meanwhile, pathologic fracture was associated with poor prognosis in adult patients but not in pediatric patients (*50*).

Role of ^{18}F-FDG PET/CT

Evaluations of the prognostic value of PET/CT parameters are summarized in Table 4. In 2009, Costelloe et al. was the first to report that SUV_{max} and TLG, both at baseline and after NCT, could predict progression-free survival and OS (*51*). Hawkins et al. reported that an SUV_{max} of over 2.5 after NCT is associated with worse progression-free survival (*33*). Byun et al. also reported that baseline MTV and TLG could predict metastasis-free survival (*52*). However, Bailly et al.'s tests of multiple baseline PET/CT parameters for predicting prognosis indicated that only the elongation feature, a type of shape feature, was significantly associated with progression-free survival and OS (*53*). The elongation feature is the ratio of the longer and shorter edges of the smallest rectangle that encloses the measured region. An elongation factor of 1 indicates maximum symmetry. Most PET/CT parameters were not

TABLE 1
Staging and Diagnosis using ^{18}F-FDG PET/CT vs. Other Imaging Modalities

Objective	Study design	Patients (*n*)	Age (y) Median	Age (y) Mean	Procedure	Category	Sensitivity	Specificity	Accuracy	Reference
Differential diagnosis of primary lesion	Prospective	50	NR	36.9	Conventional radiograph		85%	65%	78%	(*10*)
					PET		85%	35%	68%	
					PET/CT		91%	77%	86%	
Detection of lung metastasis	Retrospective	20	NR	13.1	PET/CT		84%	79%	95%	(*11*)
					CT		94%	71%	67%	
Detection of bone metastases	Retrospective	70	14	NR	PET	Patient	90%	96%	95%	(*12*)
						Lesion	72%	NR	NR	
					BS	Patient	71%	92%	88%	
						Lesion	72%	NR	NR	
Detection of bone metastases	Retrospective	206	15	NR	PET/CT	Patient	94.5%	98.1%	98%	(*14*)
						Lesion	92.1%	NR	NR	
					BS	Patient	76.3%	97.0%	97%	
						Lesion	74.2%	NR	NR	
					PET/CT + BS	Patient	100%	96.3%	97%	
						Lesion	100%	NR	NR	
Detection of bone metastases	Retrospective	39	12	NR	PET/CT		95%	98%	98%	(*13*)
					BS		76%	97%	96%	
					PET/CT + BS		100%	96%	97%	

NR = not reported; PET = ^{18}F-FDG PET; BS = bone scan.

TABLE 2
Histologic Response Grading Systems

System	Grade	Description
Rosen et al. (*20*)		
	IV	No viable tumor cells
	III	>90% tumor necrosis
	II	50% ≤ 90% tumor necrosis
	I	0% < 50% tumor necrosis
Picci et al. (*21*)		
	Total response	No viable tumor
	Good response	90%∼99% necrosis
	Fair response	60%∼89% necrosis
	Poor response	<60% necrosis
Salzer-Kuntschik et al. (*22*)		
	I	No viable tumor cell
	II	Single tumor cell or 1 vital cell cluster < 0.5 cm
	III	Vital tumor < 10%
	IV	Vital tumor 10%–50%
	V	Vital tumor > 50%
	VI	No effect of chemotherapy

TABLE 3
Predicting Histologic Response Using ^{18}F-FDG PET/CT

Study design	Patients (*n*)	Median age (y)	PET parameter	Time point	Histologic assessment	Histologic responder criteria	Cutoff for histologic responder	Histologic response predicted?	Reference
Prospective	15	17	SUV_{max}, SUV_{max} ratio, TBR, TBR ratio	Baseline, after NCT	Salzer-Kuntschik	Grade I–III (>90% necrosis)	TBR ratio > 0.46	Yes	(*32*)
Prospective	70	14	SUV_{max}, SUV_{max} ratio	Baseline, after NCT	Rosen	Grade III–IV (>90% necrosis)	SUV_{max} (after NCT) ≤ 2, SUV_{max} ratio ≥ 0.6	Yes	(*25*)
Retrospective	40	15.1	SUV_{max}, SUV_{max} ratio	Baseline, after NCT	Salzer-Kuntschik	Grade I–III (>90% necrosis)	SUV_{max} (after NCT) < 2.5, SUV_{max} ratio < 0.5	No	(*33*)
Retrospective	19	24.1	SUV_{max}, SUV_{max} ratio, SUV_{mean}, SUV_{mean} ratio, MTV, MTV ratio	During NCT, after NCT	% necrosis	>90% necrosis	SUV_{max} (after NCT) < 2.5, MTV ratio < 0.5	Yes	(*36*)
Prospective	9	23	SUV_{peak}, SUV_{mean}	Baseline, during NCT, after NCT	% necrosis	NR	NR	Yes	(*23*)
Prospective	27	17	TBR, TBR ratio	Baseline, after NCT	Salzer-Kuntschik	Grade I–III (>90% necrosis)	TBR ratio > 0.6	Yes	(*31*)
Retrospective	16	NR	Visual assessment, TBR, TBR % change	Baseline, after NCT	% necrosis	>90% necrosis	TBR (after NCT) < 1.4	Yes	(*30*)
Prospective	10	18	SUV_{mean}, SUV_{mean} % change	Baseline, after NCT	Salzer-Kuntschik	Grade I–III (>90% necrosis)	NR	No	(*34*)
Retrospective	11	17	SUV_{max}, SUV_{max} ratio	Baseline, after NCT	European Osteosarcoma Intergroup trials	>90% necrosis	SUV_{max} (after NCT) < 2.5, SUV_{max} ratio > 0.5	Yes	(*27*)
Prospective	20	15	SUV_{max}, SUV_{max} ratio, MTV, MTV ratio, TLG, TLG ratio	Baseline, during NCT, after NCT	Salzer-Kuntschik	Grade I–III (>90% necrosis)	SUV_{max} (after NCT) < 3, SUV_{max} (during NCT) < 3.2, SUV_{max} ratio (baseline/during) < 0.49, SUV_{max} ratio (baseline/after) < 0.56	Yes	(*37*)
Prospective	27	15	SUV_{max}, MRV, apparent diffusion coefficient	Baseline, after NCT	Rosen	Grade III–IV (>90% necrosis)	SUV_{max} % change ≥ 52%, apparent diffusion coefficient % change > 13%	Yes	(*35*)
Prospective	31	15	RI_{max}, RI_{mean}	Baseline, after NCT	Rosen	Grade III–IV (>90% necrosis)	RI_{mean} (before NCT) < 10%	Yes	(*43*)

TBR = tumor to background ratio; NR = not reported; RI_{max} = maximum retention index; RI_{mean} = mean retention index.

TABLE 4
Predicting Prognosis Via ^{18}F-FDG PET/CT

Study design	Patients (*n*)	Median age (y)	Time points	Parameters	Clinical outcome	Cutoff for worse prognosis	Hazard ratio	95% CI	*P*	Reference
Retrospective study	31	27.5	Baseline, after NCT	SUV_{max}, TLG	PFS	SUV_{max} (baseline) > 15	4.514	1.335–15.26	0.015	(*51*)
						SUV_{max} (after NCT) > 5	4.527	1.548–13.24	0.006	
						TLG % change (10%)	1.096	1.017–1.181	0.016	
					OS	SUV_{max} (after NCT) > 3.3	NR		0.043	
						TLG (baseline, per unit)	1.003	1.000–1.005	0.021	
Retrospective review	40	15.1	Baseline, after NCT	SUV_{max}	PFS	SUV_{max} (after NCT) > 2.5	NR		0.021	(*33*)
Retrospective study	83	16	Baseline, after NCT	SUV_{max}, MRV, MTV, TLG	Metastasis-free survival	Baseline MTV (2.0) > 105	3.8	1.5–9.59	0.002	(*52*)
						Baseline TLG (45%) > 187	2.47	1.056–5.79	0.037	
Retrospective study	31	13.9	Baseline, after NCT	SUV_{max}, SUV_{peak}, SUV_{mean}, MTV, TLG, textural features, shape features	PFS	Elongation (baseline) (cutoff NR)	5.583	NR	0.019	(*53*)
					OS	Elongation (baseline) (cutoff NR)	7.113	NR	0.0062	
Retrospective review	34	12.2	Baseline, during NCT, after NCT	SUV_{max}, SUV_{peak}, MTV, TLG	Event-free survival	MTV (2.5) (baseline) > 238.06	5.024*	1.51–16.77	0.01*	(*54*)
						TLG (2.5) (baseline) > 981.97	5.740*	1.34–24.51	0.006*	
						MTV (2.5) (during NCT) > 35.8	8.155*	1.52–43.69	0.046*	
					OS	MTV (2.5) (baseline) > 238.06	29.447*	2.21–392.27	0.033*	
						TLG (2.5) (baseline) > 1,022.3	29.447*	2.21–392.27	0.033*	
						TLG (2.5) (during NCT) > 120.4	34.789*	2.50–483.84	0.033*	

Retrospective review = retrospective review of prospective study; PFS = progression-free survival; NR = not reported.

*Adjusted for histologic response.

Numbers in parentheses indicate segmentation methods to measure MTV and TLG, with (2.0) indicating fixed absolute threshold of SUV 2.0, (2.5) indicating fixed absolute threshold of SUV 2.5, and (45%) indicating fixed relative threshold of 45% of SUV_{max}.

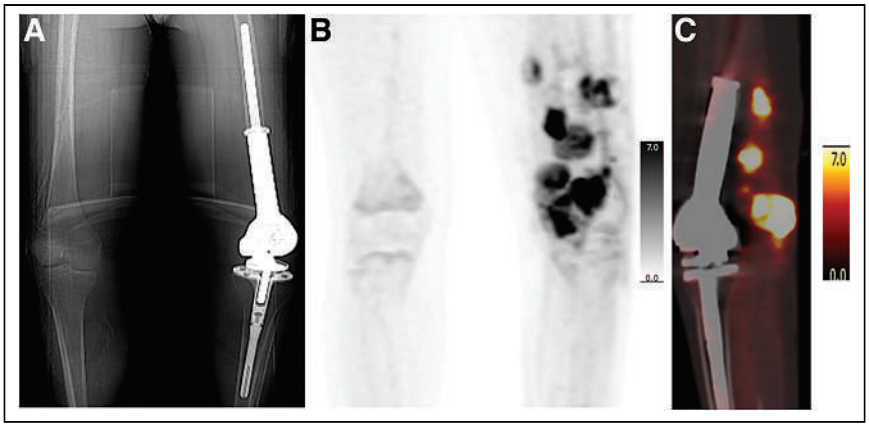

FIGURE 4. A 15-y-old boy with history of osteosarcoma in left femur and limb-sparing procedure on left lower extremity. (A) Topogram from attenuation-correction CT shows rotating-hinge modular prosthesis in left distal femur and left knee. (B) Anterior maximum-intensity projections shows multiple areas of markedly elevated uptake in left lower extremity. (C) PET/CT sagittal view of left leg shows numerous soft-tissue nodules with intense uptake posterior to prosthesis (SUV_{max}, 20.3).

prognostic in the study, and the parameters were used as continuous variables only. However, the previous studies found that the dichotomized PET/CT parameters are prognostic (*53*). We reported that most of the dichotomized PET/CT parameters, including SUV_{max}, SUV_{peak}, MTV, and TLG at baseline, during, and after NCT, are predictive of event-free survival and OS (Supplemental Fig. 4). Furthermore, we found that the parameters were predictive of event-free survival and OS even after adjustment for the histologic response and initial staging (*54*).

The studies showed similar results via diverse methods. For example, the segmentation methods of MTV and TLG vary widely. Costelloe et al. set a relative SUV threshold of 45% (*51*), but Byun et al. used fixed SUV thresholds of 2%, 2.5%, and 45% (*52*). Im et al. used the fixed SUV thresholds of 2% and 2.5%, relative SUV thresholds of 40% and 60%, and liver-based thresholds, reporting that fixed thresholds or liver-based thresholds were more robust than relative thresholds in predicting prognosis. The MTV and TLG based on relative thresholds were not prognostic during or after NCT because the tumor volumes tend to be overestimated (*54*). Also, the cutoffs of parameters for predicting prognosis differed: Hawkins et al. used the an SUV_{max} cutoff of 2.5 (*33*); the other studies used the optimized cutoffs (*51,52,54*). All studies were retrospective in some way, necessitating larger, prospective studies to confirm these results and to define the optimal cutoff for predicting prognosis in osteosarcoma.

RECURRENT DISEASE

PET/CT can detect osteosarcoma recurrence after completion of treatment (Fig. 4; Supplemental Fig. 5). A metaanalysis of the detection of recurrent disease in 7 studies revealed excellent diagnostic performance, with pooled sensitivity and specificity rates of 91% (95% CI, 81% to 96%) and 93% (95% CI, 87% to 97%), respectively (*15*). Angelini et al. assessed the diagnostic accuracy of PET/CT for detecting recurrence in 37 patients who were treated with adequate surgical resection, were suspected to have relapsed disease, and had histologic validation of disease relapse after PET/CT. Altogether, 33 patients (89.2%) had PET/CT-detected recurrence. The sensitivity, specificity, and accuracy were 91%, 75%, and 89%, respectively (*55*). Likewise, Sharp et al. reported that PET/CT was positive in 10 local recurrences, observing either a solid or a peripheral/nodular pattern with a wide range of SUV_{max} (3.0–15.7) (*56*). Osteosarcoma has the potential to metastasize to various organs; examples of such metastases include cerebral (Fig. 5), pulmonary pleural caking (Supplemental Fig. 6), epimyocardial (Supplemental Fig. 7), renal (Fig. 6), pancreatic (Supplemental Fig. 8), and tumor thrombosis (Supplemental Fig. 9).

PET/MRI

Generally, PET/MRI has advantages over PET/CT for its excellent soft-tissue contrast and lower radiation exposure, which is a clear benefit for pediatric patients (*57,58*). Schäfer reported that PET/MRI showed a 73% reduction in radiation exposure compared with PET/CT and demonstrated an identical rate of detecting lesions (*59*). Platzek et al. reported that TNM staging of PET/MRI was almost identical to that of conventional modalities (CT plus MRI) in 29 patients with sarcoma (*60*). Also, Eiber et al. compared the ability of PET/MRI and PET/CT to detect bone metastasis in patients with various primary malignancies. They reported that PET with T1-weighted turbo spin echo MRI did not provide a significant difference in detection of malignant bone lesions but was superior to PET/CT in the anatomic delineation of ^{18}F-FDG-positive lesions (*61*). Buchbender et al. suggested in their continuing education paper that PET/MRI could provide similar diagnostic accuracy for T staging with MRI alone and similar performance for N staging with PET/CT. (*62*). Orsatti et al. found that in 13 pediatric sarcoma patients, there was a significant negative correlation between apparent diffusion coefficients and SUV in primary lesions as measured using PET/MRI (*63*). In response monitoring, whole-body diffusion-weighted MRI during induction chemotherapy could predict

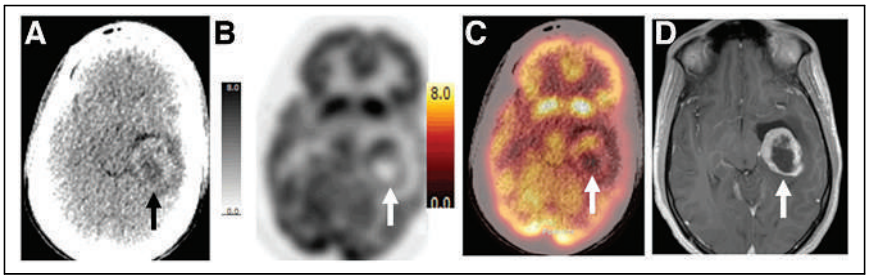

FIGURE 5. A 23-y-old man with progressive metastatic osteosarcoma: attenuation-correction CT image (A), PET emission image (B), PET/CT image (C), and axial T1 MR image (D). ^{18}F-FDG PET/CT shows previously unknown left temporal lobe metastasis (arrows) (SUV_{max}, 6.4). There is uptake at periphery of lesion, with reduced uptake centrally, consistent with necrosis. Contrast-enhanced T1 MR image obtained following day shows irregularly rimmed ring enhancing lesion in left temporal lobe, consistent with metastatic disease.

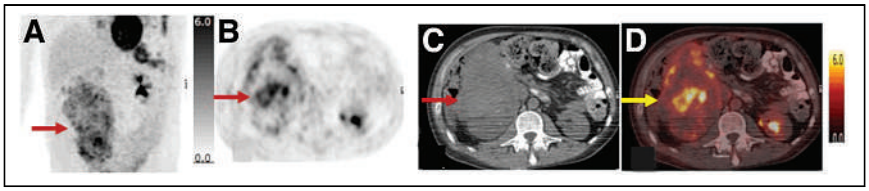

FIGURE 6. A 25-y-old man with multiple recurrent osteosarcoma and large right renal metastasis (arrows; SUV_{max}, 7.1): anterior maximum-intensity-projection view (A); ^{18}F-FDG PET axial emission image (B), corresponding axial CT image from attenuation correction lesion localization CT (C), and PET/CT image (D).

clinical response well (area under the curve, 0.98) and exhibited significant agreement with PET/MRI in 56 patients with sarcoma or lymphoma. The biologic and clinical significance of discordant response assessment between diffusion-weighted MRI and PET/MRI in 8 of the 56 patients has not been assessed (*64*). Therefore, it is warranted to evaluate the additive value by combination of PET/MRI with diffusion-weighted MRI in response monitoring. In addition, Baratto et al. described that PET/MRI can improve monitoring of response to immunotherapy and potentially be used for identification of nonresponders by tumor-associated macrophage imaging using iron oxide nanoparticles (*65*).

NEW TRACERS

^{18}F-NaF is an excellent bone-seeking agent; therefore, NaF PET has been used for skeletal imaging for many decades (*66*). Pathologic bone changes and soft-tissue metastasis with dystrophic calcification can be detected by NaF PET (*67*). Cai et al. reported that NaF PET images could detect hepatic metastasis in patients with osteosarcoma. ^{18}F-NaF activity was more prominent in the calcified lateral portion (*68*). Chou et al. reported that ^{18}F-NaF could detect cardiac osteosarcoma metastasis, which is a rare metastatic site in patients with osteosarcoma (*67*). Also, Verma et al. reported that NaF PET could detect a tumor thrombus arising from osteosarcoma (*69*). Recently, Kairemo et al. proposed NaF PET-based response criteria: NaF PET response criteria for solid tumors (NAFCIST). In the study, the treatment response of 17 patients with metastatic osteosarcoma who were treated with $^{223}RaCl_2$ was assessed using conventional PERCIST based on ^{18}F-FDG PET/CT and NAFCIST based on NaF PET. NAFCIST could predict the OS but PERCIST could not (*70*). Altogether, NaF PET is excellent for finding specific tumor regions, including rare metastasis, and could be a good prognostic biomarker.

Radiolabeled fibroblast activation protein inhibitors (FAPIs) have attracted increasing attention as new theranostic agents that specifically target cancer-associated fibroblast (*71–73*). Kratochwil et al. retrospectively evaluated ^{68}Ga-FAPI PET uptake in 80 patients with 28 different types of malignancies, including 8 patients with sarcoma. The SUV_{mean} of the sarcoma group was the second highest among 28 types of malignancies (*71*). Koerber et al. retrospectively evaluated the diagnostic ability of ^{68}Ga-FAPI PET in 15 patients with sarcoma, including 1 with osteosarcoma. ^{68}Ga-FAPI PET showed high potential as a probe for diagnosis in sarcoma because it showed high uptake in the primary tumor (median, 7.16; range, 4.64–9.79) (*72*). Kessler et al. compared the accuracy of ^{68}Ga-FAPI PET with that of ^{18}F-FDG PET in 47 patients with sarcoma, including 8 patients with osteosarcoma. They found a significant association between FAP expression and ^{68}Ga-FAPI PET uptake through histopathologic verification (Spearman r = 0.43, P = 0.03). In per-patient basis analysis, the detection rate of ^{68}Ga-FAPI and ^{18}F-FDG PET were 76.6% and 81.4%, respectively. However, ^{68}Ga-FAPI PET could detect more metastatic lesions, resulting in an upstaging compared with ^{18}F-FDG PET in 8 (18.6%) patients (*73*). On the basis of the promising results in these early imaging studies of FAPI PET in patients with sarcoma, further studies are warranted to compare the performance of FAPI PET in various clinical situations, such as staging, treatment monitoring, and recurrence, with that of current standard imaging modalities, including ^{18}F-FDG PET. Furthermore, a theranostic approach using FAPI could open new avenues for osteosarcoma management (*74*).

The membrane glycolipid GD2 is overexpressed in osteosarcoma; however, anti-GD2 immunotherapy for recurrent osteosarcoma has been limited because of the intertumoral heterogeneity of GD2 expression in osteosarcoma. Therefore, immuno-PET agents to assess GD2 expression have been developed and have shown promising results in a preclinical PET/CT study (*75*) and a PET/MRI case report of an osteosarcoma patient with lung metastasis (*76*).

CONCLUSION

In osteosarcoma, ^{18}F-FDG PET/CT is useful for staging, monitoring response to therapy, predicting prognosis, and characterizing recurrent disease. It has been extensively validated in studies involving pediatric patients, and similar findings have also been observed in research that includes adult patients, highlighting its effectiveness across different age groups. ^{18}F-FDG PET/CT could ease the drug development process for newer osteosarcoma therapies by facilitating patient selection based on prognosis and serving as early determinants of disease response.

ACKNOWLEDGMENTS

We thank Cherise Guess, PhD, ELS, senior scientific editor, St. Jude Children's Hospital, for expert review and advice, and Amanda Meek for expert administrative support.

REFERENCES

1. Kansara M, Teng MW, Smyth MJ, Thomas DM. Translational biology of osteosarcoma. *Nat Rev Cancer.* 2014;14:722–735.
2. Mirabello L, Troisi RJ, Savage SA. Osteosarcoma incidence and survival rates from 1973 to 2004: data from the Surveillance, Epidemiology, and End Results Program. *Cancer.* 2009;115:1531–1543.
3. Bielack SS, Kempf-Bielack B, Delling G, et al. Prognostic factors in high-grade osteosarcoma of the extremities or trunk: an analysis of 1,702 patients treated on neoadjuvant cooperative osteosarcoma study group protocols. *J Clin Oncol.* 2002; 20:776–790.
4. Kager L, Zoubek A, Pötschger U, et al. Primary metastatic osteosarcoma: presentation and outcome of patients treated on neoadjuvant cooperative osteosarcoma study group protocols. *J Clin Oncol.* 2003;21:2011–2018.
5. Meyers PA, Schwartz CL, Krailo M, et al. Osteosarcoma: a randomized, prospective trial of the addition of ifosfamide and/or muramyl tripeptide to cisplatin, doxorubicin, and high-dose methotrexate. *J Clin Oncol.* 2005;23:2004–2011.
6. Partovi S, Kohan AA, Zipp L, et al. Hybrid PET/MR imaging in two sarcoma patients: clinical benefits and implications for future trials. *Int J Clin Exp Med.* 2014;7:640–648.
7. Behzadi AH, Raza SI, Carrino JA, et al. Applications of PET/CT and PET/MR imaging in primary bone malignancies. *PET Clin.* 2018;13:623–634.

8. Webb HR, Latifi HR, Griffeth LK. Utility of whole-body (head-to-toe) PET/CT in the evaluation of melanoma and sarcoma patients. *Nucl Med Commun.* 2018;39: 68–73.
9. London K, Stege C, Cross S, et al. ^{18}F-FDG PET/CT compared to conventional imaging modalities in pediatric primary bone tumors. *Pediatr Radiol.* 2012;42: 418–430.
10. Strobel K, Exner UE, Stumpe KD, et al. The additional value of CT images interpretation in the differential diagnosis of benign vs. malignant primary bone lesions with ^{18}F-FDG-PET/CT. *Eur J Nucl Med Mol Imaging.* 2008;35:2000–2008.
11. Quartuccio N, Fox J, Kuk D, et al. Pediatric bone sarcoma: diagnostic performance of ^{18}F-FDG PET/CT versus conventional imaging for initial staging and follow-up. *AJR.* 2015;204:153–160.
12. Franzius C, Sciuk J, Daldrup-Link HE, Jurgens H, Schober O. FDG-PET for detection of osseous metastases from malignant primary bone tumours: comparison with bone scintigraphy. *Eur J Nucl Med.* 2000;27:1305–1311.
13. Hurley C, McCarville MB, Shulkin BL, et al. Comparison of ^{18}F-FDG-PET-CT and bone scintigraphy for evaluation of osseous metastases in newly diagnosed and recurrent osteosarcoma. *Pediatr Blood Cancer.* 2016;63:1381–1386.
14. Byun BH, Kong CB, Lim I, et al. Comparison of ^{18}F-FDG PET/CT and ^{99m}Tc-MDP bone scintigraphy for detection of bone metastasis in osteosarcoma. *Skeletal Radiol.* 2013;42:1673–1681.
15. Liu F, Zhang Q, Zhou D, Dong J. Effectiveness of ^{18}F-FDG PET/CT in the diagnosis and staging of osteosarcoma: a meta-analysis of 26 studies. *BMC Cancer.* 2019; 19:323.
16. Carrle D, Bielack SS. Current strategies of chemotherapy in osteosarcoma. *Int Orthop.* 2006;30:445–451.
17. Geller DS, Gorlick R. Osteosarcoma: a review of diagnosis, management, and treatment strategies. *Clin Adv Hematol Oncol.* 2010;8:705–718.
18. Davis AM, Bell RS, Goodwin PJ. Prognostic factors in osteosarcoma: a critical review. *J Clin Oncol.* 1994;12:423–431.
19. Bishop MW, Chang Y-C, Krailo MD, et al. Assessing the prognostic significance of histologic response in osteosarcoma: a comparison of outcomes on CCG-782 and INT0133—a report from the Children's Oncology Group Bone Tumor Committee. *Pediatr Blood Cancer.* 2016;63:1737–1743.
20. Rosen G, Caparros B, Huvos AG, et al. Preoperative chemotherapy for osteogenic sarcoma: selection of postoperative adjuvant chemotherapy based on the response of the primary tumor to preoperative chemotherapy. *Cancer.* 1982;49:1221–1230.
21. Picci P, Bacci G, Campanacci M, et al. Histologic evaluation of necrosis in osteosarcoma induced by chemotherapy: regional mapping of viable and nonviable tumor. *Cancer.* 1985;56:1515–1521.
22. Salzer-Kuntschik M, Delling G, Beron G, Sigmund R. Morphological grades of regression in osteosarcoma after polychemotherapy: study COSS 80. *J Cancer Res Clin Oncol.* 1983;106:21–24.
23. Jones DN, McCowage GB, Sostman HD, et al. Monitoring of neoadjuvant therapy response of soft-tissue and musculoskeletal sarcoma using fluorine-18-FDG PET. *J Nucl Med.* 1996;37:1438–1444.
24. Benz MR, Czernin J, Tap WD, et al. FDG-PET/CT imaging predicts histopathologic treatment responses after neoadjuvant therapy in adult primary bone sarcomas. *Sarcoma.* 2010;2010:143540.
25. Cheon GJ, Kim MS, Lee JA, et al. Prediction model of chemotherapy response in osteosarcoma by ^{18}F-FDG PET and MRI. *J Nucl Med.* 2009;50:1435–1440.
26. Denecke T, Hundsdorfer P, Misch D, et al. Assessment of histological response of paediatric bone sarcomas using FDG PET in comparison to morphological volume measurement and standardized MRI parameters. *Eur J Nucl Med Mol Imaging.* 2010;37:1842–1853.
27. Hamada K, Tomita Y, Inoue A, et al. Evaluation of chemotherapy response in osteosarcoma with FDG-PET. *Ann Nucl Med.* 2009;23:89–95.
28. Kim DH, Kim SY, Lee HJ, et al. Assessment of chemotherapy response using FDG-PET in pediatric bone tumors: a single institution experience. *Cancer Res Treat.* 2011;43:170–175.
29. Kong CB, Byun BH, Lim I, et al. ^{18}F-FDG PET SUVmax as an indicator of histopathologic response after neoadjuvant chemotherapy in extremity osteosarcoma. *Eur J Nucl Med Mol Imaging.* 2013;40:728–736.
30. Nair N, Ali A, Green AA, et al. Response of osteosarcoma to chemotherapy: evaluation with F-18 FDG-PET scans. *Clin Positron Imaging.* 2000;3:79–83.
31. Schulte M, Brecht-Krauss D, Werner M, et al. Evaluation of neoadjuvant therapy response of osteogenic sarcoma using FDG PET. *J Nucl Med.* 1999;40: 1637–1643.
32. Ye Z, Zhu J, Tian M, et al. Response of osteogenic sarcoma to neoadjuvant therapy: evaluated by ^{18}F-FDG-PET. *Ann Nucl Med.* 2008;22:475–480.
33. Hawkins DS, Conrad EU III, Butrynski JE, Schuetze SM, Eary JF. [F-18]-fluorodeoxy-D-glucose-positron emission tomography response is associated with outcome for extremity osteosarcoma in children and young adults. *Cancer.* 2009;115: 3519–3525.
34. Huang TL, Liu RS, Chen TH, Chen WY, Hsu HC, Hsu YC. Comparison between F-18-FDG positron emission tomography and histology for the assessment of tumor necrosis rates in primary osteosarcoma. *J Chin Med Assoc.* 2006;69:372–376.
35. Byun BH, Kong CB, Lim I, et al. Combination of ^{18}F-FDG PET/CT and diffusion-weighted MR imaging as a predictor of histologic response to neoadjuvant chemotherapy: preliminary results in osteosarcoma. *J Nucl Med.* 2013;54:1053–1059.
36. Gaston LL, Di Bella C, Slavin J, Hicks RJ, Choong PF. ^{18}F-FDG PET response to neoadjuvant chemotherapy for Ewing sarcoma and osteosarcoma are different. *Skeletal Radiol.* 2011;40:1007–1015.
37. Im HJ, Kim TS, Park SY, et al. Prediction of tumour necrosis fractions using metabolic and volumetric ^{18}F-FDG PET/CT indices, after one course and at the completion of neoadjuvant chemotherapy, in children and young adults with osteosarcoma. *Eur J Nucl Med Mol Imaging.* 2012;39:39–49.
38. Davis JC, Daw NC, Navid F, et al. ^{18}F-FDG uptake during early adjuvant chemotherapy predicts histologic response in pediatric and young adult patients with osteosarcoma. *J Nucl Med.* 2018;59:25–30.
39. Hongtao L, Hui Z, Bingshun W, et al. ^{18}F-FDG positron emission tomography for the assessment of histological response to neoadjuvant chemotherapy in osteosarcomas: a meta-analysis. *Surg Oncol.* 2012;21:e165–e170.
40. Harrison DJ, Parisi MT, Khalatbari H, Shulkin BL. PET with ^{18}F-fluorodeoxyglucose/computed tomography in the management of pediatric sarcoma. *PET Clin.* 2020;15:333–347.
41. Byun BH, Kong CB, Lim I, et al. Early response monitoring to neoadjuvant chemotherapy in osteosarcoma using sequential ^{18}F-FDG PET/CT and MRI. *Eur J Nucl Med Mol Imaging.* 2014;41:1553–1562.
42. Im H-J, Bradshaw T, Solaiyappan M, Cho SY. Current methods to define metabolic tumor volume in positron emission tomography: which one is better? *Nucl Med Mol Imaging.* 2018;52:5–15.
43. Byun BH, Kim SH, Lim SM, et al. Prediction of response to neoadjuvant chemotherapy in osteosarcoma using dual-phase ^{18}F-FDG PET/CT. *Eur Radiol.* 2015;25: 2015–2024.
44. Im H-J, McIlwain S, Ong I, et al. Prediction of response to neoadjuvant chemotherapy using machine learning algorithm trained by baseline FDG-PET textural parameters in osteosarcoma [abstract]. *J Nucl Med.* 2017;58(suppl 1):44.
45. Kawai A, Healey JH, Boland PJ, Lin PP, Huvos AG, Meyers PA. Prognostic factors for patients with sarcomas of the pelvic bones. *Cancer.* 1998;82:851–859.
46. Ozaki T, Flege S, Liljenqvist U, et al. Osteosarcoma of the spine: experience of the Cooperative Osteosarcoma Study Group. *Cancer.* 2002;94:1069–1077.
47. Cates JMM. Simple staging system for osteosarcoma performs equivalently to the AJCC and MSTS systems. *J Orthop Res.* 2018;36:2802–2808.
48. Enneking WF, Kagan A. "Skip" metastases in osteosarcoma. *Cancer.* 1975;36: 2192–2205.
49. Testa S, Hu BD, Saadeh NL, et al. A retrospective comparative analysis of outcomes and prognostic factors in adult and pediatric patients with osteosarcoma. *Curr Oncol.* 2021;28:5304–5317.
50. Kelley LM, Schlegel M, Hecker-Nolting S, et al. Pathological fracture and prognosis of high-grade osteosarcoma of the extremities: an analysis of 2,847 consecutive cooperative osteosarcoma study group (COSS) patients. *J Clin Oncol.* 2020;38: 823–833.
51. Costelloe CM, Macapinlac HA, Madewell JE, et al. ^{18}F-FDG PET/CT as an indicator of progression-free and overall survival in osteosarcoma. *J Nucl Med.* 2009;50: 340–347.
52. Byun BH, Kong CB, Park J, et al. Initial metabolic tumor volume measured by ^{18}F-FDG PET/CT can predict the outcome of osteosarcoma of the extremities. *J Nucl Med.* 2013;54:1725–1732.
53. Bailly C, Leforestier R, Campion L, et al. Prognostic value of FDG-PET indices for the assessment of histological response to neoadjuvant chemotherapy and outcome in pediatric patients with Ewing sarcoma and osteosarcoma. *PLoS One.* 2017;12:e0183841.
54. Im HJ, Zhang Y, Wu H, et al. Prognostic value of metabolic and volumetric parameters of FDG PET in pediatric osteosarcoma: a hypothesis-generating study. *Radiology.* 2018;287:303–312.
55. Angelini A, Ceci F, Castellucci P, et al. The role of ^{18}F-FDG PET/CT in the detection of osteosarcoma recurrence. *Eur J Nucl Med Mol Imaging.* 2017;44: 1712–1720.
56. Sharp SE, Shulkin BL, Gelfand MJ, McCarville MB. FDG PET/CT appearance of local osteosarcoma recurrences in pediatric patients. *Pediatr Radiol.* 2017;47: 1800–1808.
57. Purz S, Sabri O, Viehweger A, et al. Potential pediatric applications of PET/MR. *J Nucl Med.* 2014;55(suppl 2):32S–39S.
58. Manhas NS, Salehi S, Joyce P, Guermazi A, Ahmadzadehfar H, Gholamrezanezhad A. PET/computed tomography scans and PET/MR imaging in the diagnosis and management of musculoskeletal diseases. *PET Clin.* 2020;15:535–545.

59. Schäfer JF, Gatidis S, Schmidt H, et al. Simultaneous whole-body PET/MR imaging in comparison to PET/CT in pediatric oncology: initial results. *Radiology.* 2014;273:220–231.
60. Platzek I, Beuthien-Baumann B, Schramm G, et al. FDG PET/MR in initial staging of sarcoma: initial experience and comparison with conventional imaging. *Clin Imaging.* 2017;42:126–132.
61. Eiber M, Takei T, Souvatzoglou M, et al. Performance of whole-body integrated ^{18}F-FDG PET/MR in comparison to PET/CT for evaluation of malignant bone lesions. *J Nucl Med.* 2014;55:191–197.
62. Buchbender C, Heusner TA, Lauenstein TC, Bockisch A, Antoch G. Oncologic PET/MRI, part 2: bone tumors, soft-tissue tumors, melanoma, and lymphoma. *J Nucl Med.* 2012;53:1244–1252.
63. Orsatti G, Zucchetta P, Varotto A, et al. Volumetric histograms-based analysis of apparent diffusion coefficients and standard uptake values for the assessment of pediatric sarcoma at staging: preliminary results of a PET/MRI study. *Radiol Med (Torino).* 2021;126:878–885.
64. Theruvath AJ, Siedek F, Muehe AM, et al. Therapy response assessment of pediatric tumors with whole-body diffusion-weighted MRI and FDG PET/MRI. *Radiology.* 2020;296:143–151.
65. Baratto L, Hawk KE, States L, et al. PET/MRI improves management of children with cancer. *J Nucl Med.* 2021;62:1334–1340.
66. Bastawrous S, Bhargava P, Behnia F, Djang DS, Haseley DR. Newer PET application with an old tracer: role of ^{18}F-NaF skeletal PET/CT in oncologic practice. *Radiographics.* 2014;34:1295–1316.
67. Chou YH, Ko KY, Cheng MF, Chen WW, Yen RF. ^{18}F-NaF PET/CT images of cardiac metastasis from osteosarcoma. *Clin Nucl Med.* 2016;41:708–709.
68. Cai L, Chen Y, Huang Z, Wu J. Incidental detection of solitary hepatic metastasis by ^{99m}Tc-MDP and ^{18}F-NaF PET/CT in a patient with osteosarcoma of the tibia. *Clin Nucl Med.* 2015;40:759–761.
69. Verma P, Purandare N, Agrawal A, Shah S, Rangarajan V. Unusual finding of a tumor thrombus arising from osteosarcoma detected on ^{18}F-NaF PET/CT. *Clin Nucl Med.* 2016;41:e304–e306.
70. Kairemo K, Rohren EM, Anderson PM, et al. Development of sodium fluoride PET response criteria for solid tumours (NAFCIST) in a clinical trial of radium-223 in osteosarcoma: from RECIST to PERCIST to NAFCIST. *ESMO Open.* 2019;4:e000439.
71. Kratochwil C, Flechsig P, Lindner T, et al. ^{68}Ga-FAPI PET/CT: tracer uptake in 28 different kinds of cancer. *J Nucl Med.* 2019;60:801–805.
72. Koerber SA, Finck R, Dendl K, et al. Novel FAP ligands enable improved imaging contrast in sarcoma patients due to FAPI-PET/CT. *Eur J Nucl Med Mol Imaging.* 2021;48:3918–3924.
73. Kessler L, Ferdinandus J, Hirmas N, et al. ^{68}Ga-FAPI as a diagnostic tool in sarcoma: data from the ^{68}Ga-FAPI PET prospective observational trial. *J Nucl Med.* 2022;63:89–95.
74. Zhao L, Chen J, Pang Y, et al. Fibroblast activation protein-based theranostics in cancer research: a state-of-the-art review. *Theranostics.* 2022;12:1557–1569.
75. Butch ER, Mead PE, Amador Diaz V, et al. Positron emission tomography detects in vivo expression of disialoganglioside GD2 in mouse models of primary and metastatic osteosarcoma. *Cancer Res.* 2019;79:3112–3124.
76. Trautwein NF, Reischl G, Seitz C, et al. First-in-humans PET/MRI of in vivo GD2 expression in osteosarcoma. *J Nucl Med.* 2023;64:337–338.

Distinguishing Progression from Pseudoprogression in Glioblastoma Using ^{18}F-Fluciclovine PET

Ali Nabavizadeh[1], Stephen J. Bagley[2], Robert K. Doot[1], Jeffrey B. Ware[1], Anthony J. Young[1], Satyam Ghodasara[1], Chao Zhao[3], Hannah Anderson[1], Erin Schubert[1], Erica L. Carpenter[2], Jacob Till[2], Fraser Henderson Jr.[4], Austin R. Pantel[1], H. Isaac Chen[5], John Y.K. Lee[5], Nduka M. Amankulor[2,5], Donald M. O'Rourke[2,5], Arati Desai[2], MacLean P. Nasrallah[6], and Steven Brem[2,5]

[1]*Department of Radiology, Hospital of University of Pennsylvania, Perelman School of Medicine of the University of Pennsylvania, Philadelphia, Pennsylvania;* [2]*Abramson Cancer Center, University of Pennsylvania, Philadelphia, Pennsylvania;* [3]*Department of Surgery, Children's Hospital of Philadelphia, Philadelphia, Pennsylvania;* [4]*Department of Neurosurgery, Loma Linda University Medical Center, Loma Linda, California;* [5]*Department of Neurosurgery, Hospital of University of Pennsylvania, Perelman School of Medicine of the University of Pennsylvania, Philadelphia, Pennsylvania; and* [6]*Division of Neuropathology, Department of Pathology and Laboratory Medicine, Perelman School of Medicine, University of Pennsylvania, Philadelphia, Pennsylvania*

Accurate differentiation between tumor progression (TP) and pseudoprogression remains a critical unmet need in neurooncology. ^{18}F-fluciclovine is a widely available synthetic amino acid PET radiotracer. In this study, we aimed to assess the value of ^{18}F-fluciclovine PET for differentiating pseudoprogression from TP in a prospective cohort of patients with suspected radiographic recurrence of glioblastoma. **Methods:** We enrolled 30 glioblastoma patients with radiographic progression after first-line chemoradiotherapy for whom surgical resection was planned. The patients underwent preoperative ^{18}F-fluciclovine PET and MRI. The relative percentages of viable tumor and therapy-related changes observed in histopathology were quantified and categorized as TP (≥50% viable tumor), mixed TP (<50% and >10% viable tumor), or pseudoprogression (≤10% viable tumor). **Results:** Eighteen patients had TP, 4 had mixed TP, and 8 had pseudoprogression. Patients with TP/mixed TP had a significantly higher 40- to 50-min SUV_{max} (6.64 + 1.88 vs. 4.11 ± 1.52, $P = 0.009$) than patients with pseudoprogression. A 40- to 50-min SUV_{max} cutoff of 4.66 provided 90% sensitivity and 83% specificity for differentiation of TP/mixed TP from pseudoprogression (area under the curve [AUC], 0.86). A maximum relative cerebral blood volume cutoff of 3.672 provided 90% sensitivity and 71% specificity for differentiation of TP/mixed TP from pseudoprogression (AUC, 0.779). Combining a 40- to 50-min SUV_{max} cutoff of 4.66 and a maximum relative cerebral blood volume of 3.67 on MRI provided 100% sensitivity and 80% specificity for differentiating TP/mixed TP from pseudoprogression (AUC, 0.95). **Conclusion:** ^{18}F-fluciclovine PET uptake can accurately differentiate pseudoprogression from TP in glioblastoma, with even greater accuracy when combined with multiparametric MRI. Given the wide availability of ^{18}F-fluciclovine, larger, multicenter studies are warranted to determine whether amino acid PET with ^{18}F-fluciclovine should be used in the routine posttreatment assessment of glioblastoma.

Key Words: MRI; PET; ^{18}F-fluciclovine; glioblastoma; pseudoprogression; tumor progression

J Nucl Med 2023; 64:852–858
DOI: 10.2967/jnumed.122.264812

Received Aug. 21, 2022; revision accepted Dec. 21, 2022.
For correspondence or reprints, contact Ali Nabavizadeh (ali.nabavizadeh@pennmedicine.upenn.edu).
Published online Dec. 22, 2022.

Glioblastoma is the most common malignant primary brain tumor in adults and remains incurable after standard temozolomide-based chemoradiotherapy (*1*). Accurate assessment of tumor response and progression after treatment remains a significant clinical challenge in neurooncology, complicating both routine care and the conduct of clinical trials (*2*). Contrast-enhanced MRI, the current standard for tumor monitoring, lacks specificity for detecting neoplastic progression in the brain. This is largely because an increase in contrast enhancement can be due to any cause of blood–brain barrier breakdown and resultant contrast extravasation, including secondary to effective chemoradiotherapy (*3*). This phenomenon, referred to as pseudoprogression (*4*), has been reported in up to 30% of patients after chemoradiotherapy as defined by the Response Assessment in Neuro-Oncology Working Group (i.e., within 12 wk after completion of radiotherapy) (*5*); however, late pseudoprogression may also occur beyond 12 wk (*6*). Radiographic changes that occur 6 mo to several years after treatment, namely radiation necrosis (*7*), also share common pathophysiologic features with pseudoprogression (*7*).

In posttreatment glioblastoma, accurate differentiation of pseudoprogression from true tumor progression (TP) represents a significant unmet clinical need, as erroneous interpretation can lead to premature discontinuation of an effective treatment or overestimation of the efficacy of subsequent salvage therapies (*8*). In addition, early recognition of TP offers the possibility for earlier therapeutic interventions, such as reresection or recruitment to experimental clinical trials, at a time in the disease course when patients are healthier overall and with relatively preserved performance status. Although advanced MRI techniques such as dynamic susceptibility contrast (DSC), dynamic contrast-enhanced (DCE), and diffusion-weighted imaging have improved the ability to differentiate pseudoprogression from TP, the application of these techniques in both routine practice and clinical trials has been hampered by considerable variability in acquisition and analysis approaches between institutions (*9*). In addition, these techniques have imperfect accuracy and are frequently affected by imaging artifacts, especially in the posttreatment setting (*10*).

Metabolic imaging can provide additional valuable information about tumor status. In particular, PET with amino acid tracers,

including ^{11}C-methionine (*11*), ^{18}F-fluorodopa (*12*), and *O*-(2-^{18}F-fluoroethyl)-L-tyrosine (^{18}F-FET) (*13,14*), have shown value in differentiating pseudoprogression from TP, as amino acid uptake is increased in tumor tissue but low in areas of treatment-related change. Recent expert reviews by the Response Assessment in Neuro-Oncology Working Group found amino acid tracers (^{11}C-methionine, ^{18}F-FET, and ^{18}F-fluorodopa) to have higher diagnostic accuracy than conventional and advanced MRI in the differentiation of glioma recurrence (*15,16*).

^{18}F-fluciclovine is a synthetic amino acid PET tracer approved by the U.S. Food and Drug Administration in the setting of biochemical recurrence of prostate cancer and has an excellent safety profile (*17*). ^{18}F-fluciclovine is an isoleucine analog that is transported into glial cells by both L-amino acid transporters (especially subtype 1) and alanine–serine–cysteine transporters (especially subtype 2), which are upregulated in glioma cells and demonstrate low expression in the normal brain parenchyma (*18*). ^{18}F-fluciclovine has also demonstrated utility for discrimination between low-grade and high-grade glioma (*19–22*). In comparison with ^{11}C-methionine in both treatment-naïve and recurrent glioma, ^{18}F-fluciclovine demonstrated similar detection accuracy but better contrast between tumor and background uptake (*19*). In contrast to ^{11}C-methionine, which has a short half-life (20 min) and is limited to PET centers with a cyclotron (*19*), ^{18}F-fluciclovine has the same longer half-life (109.8 min) as ^{18}F-FET and ^{18}F-fluorodopa, which allows time for it to be shipped from the manufacturer to the imaging centers. In addition, unlike ^{18}F-FET and ^{18}F-fluorodopa, ^{18}F-fluciclovine is widely available in the United States, given its use in the setting of prostate cancer (*23*). Our group previously demonstrated the feasibility of ^{18}F-fluciclovine PET/MRI–guided biopsy in posttreatment glioblastoma to distinguish areas of highest tumor recurrence from areas of treatment-related changes in a small case series (*24*). The aim of this study was to assess the independent and additive value of ^{18}F-fluciclovine PET and multiparametric MRI for differentiating pseudoprogression from TP. Importantly, we used a study cohort in which all patients had available resected tumor tissue to serve as ground truth for TP versus pseudoprogression.

MATERIALS AND METHODS

Study Design and Patient Population

We conducted a prospective cohort study (NCT03990285) of 30 adults with a previously confirmed diagnosis of glioblastoma (defined according to the World Health Organization 2021 classification) (*25*) who were previously treated with standard-of-care radiation and temozolomide and scheduled to have surgery based on radiographic progression (i.e., new contrast-enhancing lesions or lesions showing a ≥25% increase in the sum of the products of the perpendicular diameters on MRI) according to the criteria of the Response Assessment in Neuro-Oncology Working Group (*26*). The patients underwent preoperative multiparametric MRI and 60 min of dynamic brain PET/CT after intravenous administration of ^{18}F-fluciclovine and subsequently underwent maximal safe resection of the enhancing lesion. The percentages of viable tumor and therapy-related changes comprising the specimen were quantified on histopathology by a board-certified neuropathologist. All patients provided written informed consent. This study was approved by the Institutional Review Board of the University of Pennsylvania.

Image Acquisition

PET. ^{18}F-fluciclovine (Axumin; Blue Earth Diagnostics) was produced by PETNET Solutions facilities under U.S. Pharmacopeia–compliant procedures and was administered under an investigational-new-drug application exemption. All PET studies were performed on an Ingenuity TF PET/CT device (Philips Healthcare) using a previously described method of image reconstruction (*27*). Patients underwent 60 min of dynamic PET imaging after injection of 191 ± 21 MBq of ^{18}F-fluciclovine. In 2 patients, PET acquisition was performed for 40 and 45 min instead of 60 min. Patients fasted for 4 h before administration of ^{18}F-fluciclovine. The patients were monitored for adverse events for 24 h after each injection of the ^{18}F-fluciclovine radiotracer, and none were observed.

MRI. Brain MRI was performed using the brain tumor imaging protocol of the University of Pennsylvania on a 3-T magnet (Trio; Siemens), which included an axial T1-weighted 3-dimensional magnetization-prepared rapid gradient echo sequence before and after contrast administration, a postcontrast axial fluid-attenuated inversion recovery sequence, a diffusion tensor imaging sequence ($n = 30$), a DCE perfusion sequence ($n = 29$), and a DSC perfusion sequence ($n = 27$ after excluding 2 patients with degraded source data due to susceptibility effects). Representative imaging parameters are presented in Supplemental Table 1 (supplemental materials are available at http://jnm.snmjournals.org). Two contrast boluses (gadoterate meglumine; Guerbet) with a dose of 0.1 mmol/kg were sequentially administered for DCE followed by DSC imaging, with the dose administered for DCE serving as a preload dose for DSC to reduce the effect of contrast agent leakage on relative cerebral blood volume (rCBV) measurements.

Image Analysis

PET. PET measurements were performed in MIM (the versions were updated throughout the study from 6.9 to 7.1). Volumes of interest were defined in the resected tumor using PET images and coregistered to T1 postcontrast MR images and fluid-attenuated inversion recovery images, with placement confirmed by a board-certified neuroradiologist and a nuclear radiologist. Measurements were taken of tumor SUV_{max}, 1 cm^3 SUV_{peak}, and 50% threshold SUV_{mean} defined on summed images at 20–30, 30–40, 40–50, 50–60, 40–60, and 30–60 min after injection (g/mL units). Normal-tissue volumes of interest and SUV_{mean} measurements were made in the contralateral normal brain, pituitary gland, and superior sagittal sinus. The volumes of interest in the contralateral normal brain were 20 mm in diameter, whereas those in the pituitary and superior sagittal sinus were 15 mm in diameter. Tumor SUVs and SUV ratios normalized to each normal-tissue SUV_{mean} were calculated.

Time–activity curves of ^{18}F-fluciclovine SUV_{peak} uptake in the tumor were generated by application, to the entire dynamic dataset, of a spheric volume of interest with a volume of 1 cm^3 centered on maximal tumor uptake. Time–activity curves for each lesion were visually assessed by an experienced board-certified nuclear radiologist as previously described (*28*) and assigned to one of the following curve patterns: constantly increasing without identifiable peak uptake (pattern I), peaking at a midpoint followed by a plateau or a small descent (pattern II), and peaking early followed by a constant descent (pattern III) (*28*). In addition, time to peak (TTP) with a lower threshold time of at least 10 min was measured and compared among groups.

MRI. Regions of abnormal contrast enhancement, necrosis, and nonenhancing fluid-attenuated inversion recovery signal intensity were segmented using a semiautomated segmentation tool (ITK-SNAP) (*29*) followed by manual editing by 2 board-certified neuroradiologists. Diffusion tensor imaging was processed with FSL (*30*) and included removal of nonbrain tissue as well as correction for motion and eddy currents. Diffusion data were then fit to the tensor model, and maps of whole-brain apparent diffusion coefficients were used in subsequent analysis.

DCE images were corrected for motion, and nonbrain tissue was removed using image processing tools available in FSL. DCE data were then analyzed using the extended Toft model, as implemented by

the ROCKETSHIP software package (*31*) in the MATLAB programming environment (2014a; MathWorks), to derive voxelwise maps of the volume transfer constant Ktrans, plasma volume fraction Vp, extravascular extracellular volume fraction Ve, and washout rate constant of contrast agent from the EES to the intravascular space Kep defined as Kep = Ktrans/Ve. Because of the inconsistent availability of T1 mapping among subjects, a fixed prebolus T1 value (1,000 ms) was used to transform signal intensity curves to contrast concentration curves in DCE analysis. DSC data were used to generate leakage-corrected rCBV maps using the γ-variate function as implemented in NordicICE software (NordicNeuroLab). For each functional modality (diffusion tensor imaging, DCE, and DSC), a reference image derived from source data was used to compute a linear transformation from the functional space to the subject's T1 postcontrast magnetization-prepared rapid gradient echo sequence using the Advanced Normalization Tools registration tool (*32*). These transformations were then used to coregister all parameter maps to the anatomic space. DCE and DSC imaging metrics were normalized to the median value of a region of interest placed in normal-appearing white matter by a board-certified neuroradiologist at the same slice levels as the abnormality. Subsequent statistical analysis was based on the mean rCBV and maximum rCBV ($rCBV_{max}$) and DCE metric values as well as the mean and minimum apparent diffusion coefficients extracted from the intersection of the segmented contrast-enhanced and PET ROI.

Histopathologic Evaluation and Analysis of Molecular Markers

After resection, the surgically extracted tissue specimens were entirely fixed in 10% buffered formalin, routinely processed, and embedded in paraffin. Five-micrometer-thick sections of each specimen were cut onto glass slides, stained with hematoxylin and eosin, and assessed by a board-certified neuropathologist (who was unaware of the preoperative MRI and PET imaging data). The presence or absence of pseudopalisading necrosis and microvascular proliferation (features of recurrent glioblastoma), the presence or absence of dystrophic calcification and vascular hyalinization, and the percentage of geographic necrosis (representative of treatment-related changes) were quantified. Proliferative activity was determined by quantification of the number of mitotic figures in 10 high-power fields and semiquantitative assessment of the Ki-67 proliferative index by immunostaining (mouse monoclonal, MIB-1, IR62661; Dako). On the basis of the combined assessment of these features, the entire resected specimen was assigned a tumor percentage of 0%–100%. Patients were considered TP if viable tumor represented at least 50% of the resected specimen, mixed TP if less than 50% and more than 10%, and pseudoprogression if no more than 10%.

Statistical Methods

Given that the number of PET variables (6 summed images and normalized to normal contralateral brain, pituitary, and superior sagittal sinus) and MRI variables was higher than the number of subjects, the least absolute shrinkage and selection operator (LASSO) was used to determine the variables most predictive of viable tumor percentage on histopathology. In addition to imaging variables, the clinical variables of age, sex, *O*-6-methylguanine methyltransferase (*MGMT*) promoter methylation status, and duration from the end of first-line radiotherapy to recurrent surgery were included in the LASSO analysis. The strengths of correlations between primary outcome and selected variables were assessed by Pearson correlation or point-biserial correlation (rpb). A receiver-operating-characteristic curve was used to illustrate the diagnostic ability of a binary classifier system as its discrimination threshold was varied. The criteria for determination of the most appropriate cutoff was based on the point on the curve at a minimum distance from the left upper corner of the unit square. Furthermore, the leave-one-out cross-validation procedure was used to estimate the performance of the LASSO regression model by making predictions on test data. The differences in PET uptake between different groups (TP/mixed TP vs. pseudoprogression and TP vs. pseudoprogression) were compared using the Wilcoxon rank-sum exact test. The Kruskal–Wallis test was used to compare time to peak (TTP) between different groups. The χ^2 test was performed to compare MGMT methylation status in patients with TP compared with pseudoprogression. An α value of 0.05 was used as the cutoff for significance. All the statistical analyses were computed using code written in R, version 4.1.0 (R Foundation).

RESULTS

The baseline characteristics of the study cohort are summarized in Table 1. Histopathologic analysis revealed 18 patients with TP, 4 with mixed TP, and 8 with pseudoprogression. Tumor percentage ranged from 0% to 100% (median, 57.50%; SD, 31.66), and Ki-67 ranged from 1% to 70% (median, 10%; SD, 13.38). Of patients with TP, 8 of 18 (44%) had MGMT methylated tumors. Of patients with pseudoprogression, 1 of 8 (13%) had MGMT methylated tumor. A χ^2 test revealed no statistically significant difference in the rate of MGMT methylation between patients with TP and those with pseudoprogression ($P = 0.29$). All patients in this study (100%) had isocitrate dehydrogenase wild-type tumors. A detailed description of demographics, clinical symptoms at the time of radiographic progression, MGMT and isocitrate dehydrogenase status, and tumor percentage on histopathology is provided in Supplemental Table 2).

Correlation of ^{18}F-Fluciclovine PET and MRI Parameters with Histopathologic and Clinical Variables

A 50- to 60-min 50% threshold SUV_{mean} ($r = 0.54$, $P = 0.004$), 50- to 60-min 50% threshold SUV_{mean}/superior sagittal sinus

TABLE 1
Demographics and Baseline Clinical Characteristics of Patients (n = 30)

Characteristic	Data
Sex	
Male	10 (33.3)
Female	20 (66.7)
Age (y)	62 (31–81)
MGMT status	
Positive (methylated)	10 (33.3)
Negative (unmethylated)	19 (63.3)
Unknown	1 (3.3)
Dose of first-line radiotherapy received (Gy)	
40	6 (20)
60	22 (73.3)
75	2 (6.7)
Interval between completion of radiotherapy and surgery for recurrent glioblastoma (wk)	31.7 (5–283)
Interval between PET scan and surgery for recurrent glioblastoma (d)	4 (1–13)

Qualitative data are number and percentage; continuous data are median and range.

TABLE 2
Analysis of PET and MRI Parameters for Differentiation of TP/Mixed TP from Pseudoprogression

Variable	OR	rpb	*P*
40- to 50-min SUV_{max}	1.14	0.49	0.011
40- to 50-min SUV_{max}/pituitary	1.43	0.56	0.003
$rCBV_{max}$	1.13	0.47	0.016

($r = 0.55$, $P = 0.003$), and a 40- to 50-min SUV_{max}/pituitary ($r = 0.51$, $P = 0.008$) correlated positively with viable tumor percentage on histopathology. Among the MRI parameters, only $rCBV_{max}$ was selected by the LASSO analysis and had a positive correlation with tumor percentage ($r = 0.49$; $P = 0.011$). The 40- to 50-min SUV_{peak} correlated positively with Ki-67 ($r = 0.38$), with a trend toward significance ($P = 0.056$). There was no correlation between tumor percentage and age, sex, *MGMT* promoter methylation status, time elapsed between end of radiation and the patient's reoperation, or prior radiotherapy dose.

Differentiation of TP/Mixed TP from Pseudoprogression

Analysis of 25 subjects who had all the PET and MRI parameters (Table 2) demonstrated that patients with histopathologically proven TP/mixed TP had a higher 40- to 50-min SUV_{max} (odds ratio [OR], 1.14; rpb, 0.49; $P = 0.011$) and 40- to 50-min SUV_{max}/pituitary (OR, 1.43; rpb, 0.56; $P = 0.003$). None of the PET variables normalized to normal brain were selected by the LASSO analysis. Among the MRI parameters, $rCBV_{max}$ (OR, 1.13; rpb, 0.47, $P = 0.016$) was higher in the TP/mixed TP groups than in the pseudoprogression group. Other MRI parameters were not selected by the LASSO analysis.

Analysis of 28 subjects with an available 0- to 60-min dynamic acquisition demonstrated that the 50- to 60-min 50% threshold SUV_{mean} (OR, 1.31; rpb, 0.52, $P = 0.004$), 40- to 50-min SUV_{max} (OR, 1.20; rpb, 0.50, $P = 0.005$), 40- to 50-min SUV_{max}/pituitary (OR, 1.01; rpb, 0.47, $P = 0.010$), and 20- to 30-min SUV_{max} (OR, 1.12; rpb, 0.49, $P = 0.007$) were higher in the TP/mixed TP group than in the pseudoprogression group.

Patients who demonstrated TP/mixed TP had a significantly higher 40- to 50-min SUV_{max} (6.64 ± 1.88 vs. 4.11 ± 1.52, $P = 0.009$) and 20- to 30-min SUV_{max} (6.59 ± 2.15 vs. 3.89 ± 1.30, $P = 0.002$) than did patients with histologic pseudoprogression (Fig. 1). An illustrative case in which ^{18}F-fluciclovine PET uptake correctly predicted TP, whereas rCBV on DSC perfusion MRI did not, is displayed in Figure 2.

Although the main purpose of this work was to differentiate patients with TP/mixed TP from those with pseudoprogression, an exploratory analysis was also performed to differentiate TP from pseudoprogression (Supplemental Results; Supplemental Fig. 1; Supplemental Table 3).

Receiver-Operating-Characteristic Curve Analyses

A 20- to 30-min SUV_{max} cutoff of 4.457 provided 95% sensitivity and 83% specificity for differentiation of TP/mixed TP from pseudoprogression (area under the curve [AUC], 0.902). A 40- to 50-min SUV_{max} cutoff of 4.662 provided 90% sensitivity and 83% specificity for differentiation of TP/mixed TP from pseudoprogression (AUC, 0.856). An $rCBV_{max}$ cutoff of 3.672 provided 90% sensitivity and 71% specificity for differentiation of TP/mixed TP from pseudoprogression (AUC, 0.779). Combining a 40- to 50-min SUV_{max} cutoff of 4.662 and an $rCBV_{max}$ cutoff of 3.672 provided 100% sensitivity and 80% specificity for differentiating TP/mixed TP from pseudoprogression (AUC, 0.95; Fig. 3). A similar AUC of 0.95 was obtained after combining a 20- to 30-min SUV_{max} cutoff of 4.457 and an $rCBV_{max}$ cutoff of 3.672. Combining a 40- to 50-min SUV_{max} cutoff of 4.662 and an $rCBV_{max}$ cutoff of 3.672

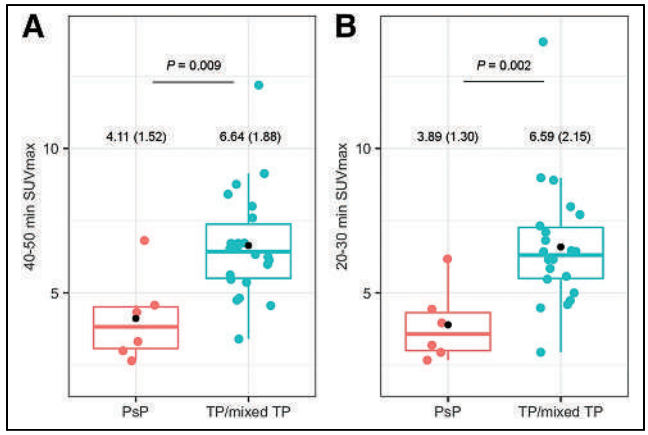

FIGURE 1. Comparison of PET parameters in patients with TP/mixed TP vs. pseudoprogression. PsP = pseudoprogression.

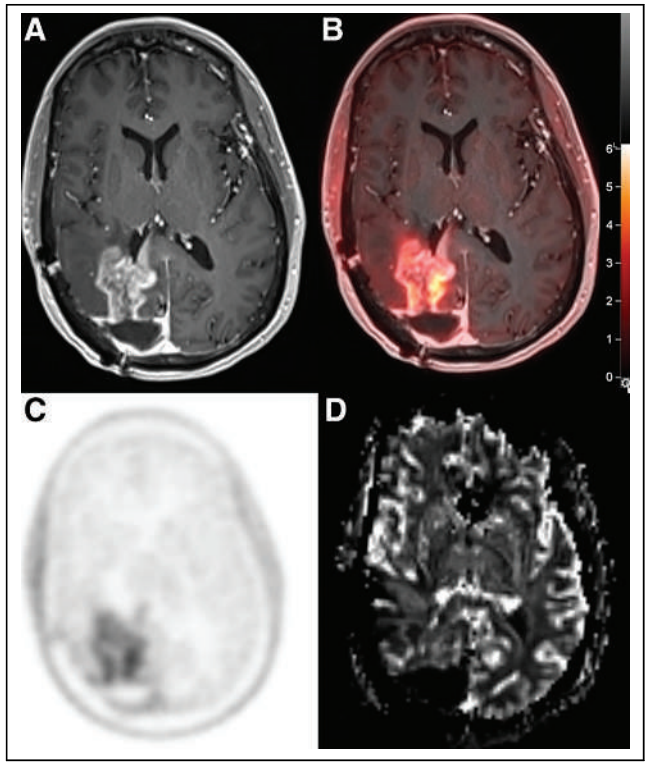

FIGURE 2. Example of false-negative MRI results. In postcontrast T1 (A) and fused PET/MRI (B), a 65-y-old man with history of right occipital glioblastoma showed progressive enhancement adjacent to resection cavity. (C and D) ^{18}F-fluciclovine PET imaging (C) demonstrated marked increased uptake (SUV_{max}, 5.46) compared with only mild increase (rCBV, 2.43) in $rCBV_{map}$ on DSC perfusion MRI (D). Patient underwent resection, and pathology showed that 60% of specimen consisted of viable tumor and 40% consisted of therapy-related changes. The intensity scale bar represents SUV.

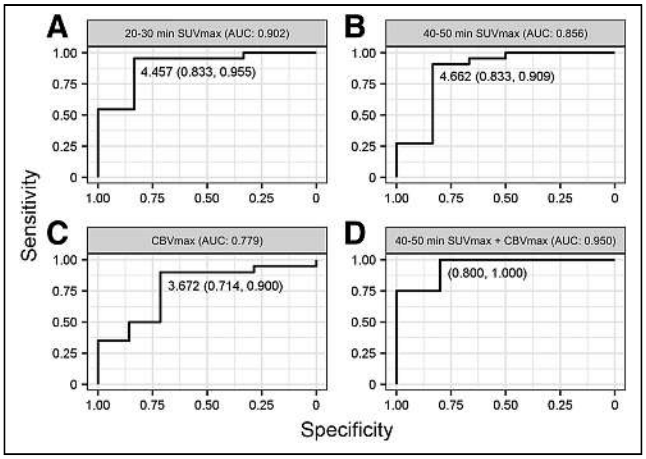

FIGURE 3. Receiver-operating-characteristic curve analysis of 20- to 30-min SUV_{max} (A), 40- to 50-min SUV_{max} (B), $rCBV_{max}$ (C), and combined 40- to 50-min SUV_{max}–$rCBV_{max}$ (D) to differentiate TP/mixed TP from pseudoprogression.

applying leave-one-out cross-validation provided 100% sensitivity and 80% specificity for differentiation of TP/mixed TP from pseudoprogression (AUC, 0.800; Supplemental Fig. 2).

PET Tracer Kinetics

The time–activity curve demonstrated accumulation at the tumor bed that reached a steady state after 20 min (Fig. 4A). All patients except two demonstrated a type II (plateau) pattern (Fig. 4B). One patient with TP and extracranial extension of tumor to the overlying scalp demonstrated a type III pattern. One patient with TP demonstrated a type I pattern. The TTP did not differ ($P = 0.830$) between groups (Fig. 4C). Representative patients from the TP, TP/mixed TP, and pseudoprogression groups are demonstrated in Figure 5.

DISCUSSION

In this study, we demonstrated that ^{18}F-fluciclovine PET can accurately differentiate pseudoprogression from TP/mixed TP in glioblastoma patients after chemoradiotherapy. The accuracy of ^{18}F-fluciclovine PET in our study is in the higher range of prior studies using ^{18}F-FET and ^{18}F-fluorodopa and higher than with ^{11}C-methionine PET (*13,14,16,28,33–41*). In addition, we demonstrated that ^{18}F-fluciclovine PET has higher accuracy than advanced MRI sequences and that combining ^{18}F-fluciclovine PET with DSC perfusion MRI resulted in even better performance for differentiation between TP/mixed TP and pseudoprogression. A recent study of 21 patients with suspected recurrent high-grade glioma who received ^{18}F-fluciclovine PET imaging (*42*) demonstrated a high median lesion-to-background ratio (*42*); however, no patients with confirmed pseudoprogression were included. To the best of our knowledge, our study is the first report that demonstrates the ability of ^{18}F-fluciclovine PET to discriminate between TP and pseudoprogression. We also found a positive correlation between Ki-67 and PET parameters, which is consistent with a previous ^{18}F-fluciclovine study on biopsy-proven low- and high-grade gliomas (*20*) and a report of ^{18}F-fluciclovine PET/MRI–guided biopsy in a patient with treatment-naïve oligodendroglioma (*21*).

Although multiparametric MRI including postcontrast imaging is widely used for posttreatment surveillance of glioblastoma, differentiation of pseudoprogression from TP using MRI is challenging because both of these entities may disrupt the blood–brain barrier and lead to contrast extravasation and enhancement (*43*). Amino acid PET imaging enables analysis of the tumor environment beyond disruption of the blood–brain barrier because it is based on upregulation of amino acid transporters in the tumor cells (independent of blood–brain barrier disruption) (*44–46*). In addition, chronic blood products in the surgical bed cause susceptibility artifacts and interfere with advanced MRI techniques such as DSC perfusion imaging, frequently confounding studies in posttreatment glioblastoma patients. In our study, DSC perfusion images were nondiagnostic in 2 patients and had to be excluded. Multiple studies compared the diagnostic accuracy of ^{18}F-FET PET and DSC perfusion MRI, and the results ranged from superior performance for PET to equal performance for both modalities (*34,47–49*). PET and DSC perfusion imaging were found to have added value in some studies (*34,48,49*), but these consisted of heterogeneous cohorts with grades 2–4 glioma, and the final diagnosis was based on histology in only a subset of patients. Our results showed that the accuracy of DSC MRI was comparable to that observed in prior studies, and multiparametric analysis of PET and MRI provided improved accuracy in our study, consistent with prior ^{18}F-FET studies (*34,47,49*).

Unlike other amino acid PET agents, we found that absolute SUV measurements are more accurate for differentiating pseudoprogression from TP than are normalized tumor-to-brain ratios, secondary to very low normal-brain uptake and variability of normal-brain uptake between patients. Conversely, normalization of SUV_{max} to the pituitary gland showed similar accuracy to SUV_{max} in differentiation of TP/mixed TP from pseudoprogression. Previous studies with ^{18}F-FET demonstrated the usefulness of a time–activity curve with curve pattern II or III and a TTP of less than 45 min for differentiating TP from treatment-related changes (*34,35,50*). In our study, we did not find TTP and time–activity curve patterns to be useful because almost all patients demonstrated a type II (plateau) pattern, consistent with a prior study on pretreatment glioma (*17*). One patient with extracranial extension of tumor to the overlying scalp demonstrated a type III pattern (uptake peaking early followed by a constant descent), similar to the described literature on prostate cancer (*51*).

Our study had limitations, including its single-institution nature, which warrants future multicenter prospective studies to

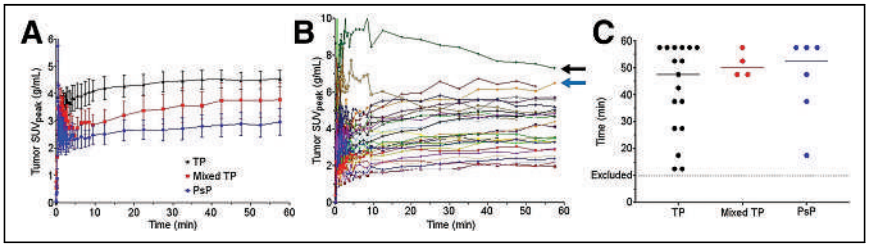

FIGURE 4. (A) Comparison of mean time–activity curves in patients with TP, mixed TP, and pseudoprogression demonstrated accumulation at tumor bed that reached steady state after 20 min. (B) Time–activity curves in individual patients. All patients except two demonstrated type II (plateau) pattern. One patient with TP and extracranial extension of tumor (black arrow) to overlying scalp demonstrated type III pattern, and 1 patient with TP demonstrated type I pattern (blue arrow). (C) Comparison of mean TTP in patients with TP, mixed TP, and pseudoprogression. PsP = pseudoprogression.

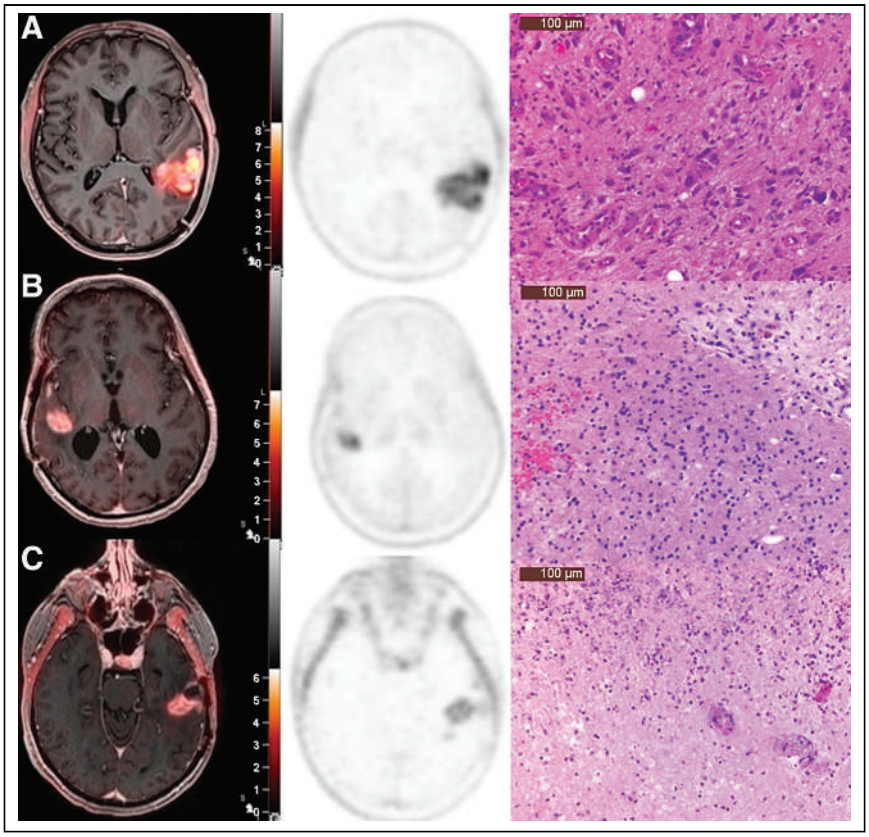

FIGURE 5. Imaging and histopathologic findings in 3 patients with true progression (A), mixed true progression–pseudoprogression (B), and pseudoprogression (C). (A) A 69-y-old woman with history of left temporoparietal glioblastoma with progressive enhancement in resection bed. ^{18}F-fluciclovine PET imaging demonstrated marked increased uptake (SUV_{max}, 6.73). Patient underwent resection, and histopathology showed that most resected tissue comprised atypical glial cells, with enlarged, irregular, hyperchromatic nuclei consistent with recurrent glioma (overall, 80% tumor). (B) A 64-y-old woman with history of right temporal glioblastoma with progressive enhancement in resection bed. ^{18}F-fluciclovine PET imaging demonstrated moderate increased uptake (SUV_{max}, 4.75). Histopathology demonstrated treatment-related changes and 40% infiltrating glioma throughout specimen. (C) A 65-y-old man with history of left temporal glioblastoma with progressive enhancement in resection bed. ^{18}F-fluciclovine PET imaging demonstrated only mild uptake (SUV_{max}, 2.65). Histopathology demonstrated abundant treatment-related changes with no tumor in specimen. The intensity scale bar represents SUV.

validate the generalizability of our findings. However, the prospective design, availability of histopathologic confirmation for all patients, and short interval between ^{18}F-fluciclovine PET and surgery are unique strengths compared with most prior studies of amino acid PET tracers, which have been largely retrospective and have relied on clinical follow-up to distinguish TP from pseudoprogression in most patients. In this study, all patients underwent dynamic PET imaging over 60 min. Given the 20-min plateau in uptake and the high accuracy of both 20- to 30-min and 40- to 50-min SUV_{max}, static imaging with both these imaging windows can be used in clinical practice, depending on the preference of the center. Given the significant uptake when compared with normal brain parenchyma in all patients (Fig. 5), quantitative criteria and not visual analysis alone is needed to differentiate between TP and pseudoprogression. Overall, our results suggest that ^{18}F-fluciclovine PET imaging can accurately differentiate pseudoprogression from TP in glioblastoma patients. Given the wide availability of ^{18}F-fluciclovine, studies that are larger and multicenter are warranted to determine whether amino acid PET imaging with ^{18}F-fluciclovine should be used in the routine posttreatment assessment of glioblastoma.

CONCLUSION

^{18}F-fluciclovine PET uptake can accurately differentiate pseudoprogression from TP in glioblastoma, with even greater accuracy when combined with multiparametric MRI. Given the wide availability of ^{18}F-fluciclovine, larger, multicenter studies are warranted to determine whether amino acid PET with ^{18}F-fluciclovine should be used in the routine posttreatment assessment of glioblastoma.

DISCLOSURE

Ali Nabavizadeh received research funding (paid to the institution) from Blue Earth Diagnostics and compensation of travel expenses to present the results of this study. No other potential conflict of interest relevant to this article was reported.

KEY POINTS

QUESTION: Can ^{18}F-fluciclovine PET distinguish progression from pseudoprogression in glioblastoma?

PERTINENT FINDINGS: Our prospective study demonstrated that ^{18}F-fluciclovine PET uptake correlated with tumor percentage on histology and can distinguish progression from pseudoprogression in glioblastoma.

IMPLICATIONS FOR PATIENT CARE: Given the wide availability of ^{18}F-fluciclovine in the United States as a Food and Drug Administration–approved radiotracer, this study has immediate translational relevance.

REFERENCES

1. Stupp R, Mason WP, van den Bent MJ, et al. Radiotherapy plus concomitant and adjuvant temozolomide for glioblastoma. *N Engl J Med.* 2005;352:987–996.
2. Ellingson BM, Wen PY, Cloughesy TF. Modified criteria for radiographic response assessment in glioblastoma clinical trials. *Neurotherapeutics.* 2017;14:307–320.
3. Hygino da Cruz LC Jr, Rodriguez I, Domingues RC, Gasparetto EL, Sorensen AG. Pseudoprogression and pseudoresponse: imaging challenges in the assessment of posttreatment glioma. *AJNR.* 2011;32:1978–1985.
4. Langen KJ, Galldiks N, Hattingen E, Shah NJ. Advances in neuro-oncology imaging. *Nat Rev Neurol.* 2017;13:279–289.
5. Wen PY, Chang SM, Van den Bent MJ, Vogelbaum MA, Macdonald DR, Lee EQ. Response assessment in neuro-oncology clinical trials. *J Clin Oncol.* 2017;35:2439–2449.
6. Kebir S, Fimmers R, Galldiks N, et al. Late pseudoprogression in glioblastoma: diagnostic value of dynamic O-(2-[^{18}F]fluoroethyl)-L-tyrosine PET. *Clin Cancer Res.* 2016;22:2190–2196.
7. Ellingson BM, Chung C, Pope WB, Boxerman JL, Kaufmann TJ. Pseudoprogression, radionecrosis, inflammation or true tumor progression? Challenges associated with glioblastoma response assessment in an evolving therapeutic landscape. *J Neurooncol.* 2017;134:495–504.
8. Reardon DA, Weller M. Pseudoprogression: fact or wishful thinking in neuro-oncology? *Lancet Oncol.* 2018;19:1561–1563.

9. Patel P, Baradaran H, Delgado D, et al. MR perfusion-weighted imaging in the evaluation of high-grade gliomas after treatment: a systematic review and meta-analysis. *Neuro-oncol.* 2017;19:118–127.
10. van Dijken BRJ, van Laar PJ, Smits M, Dankbaar JW, Enting RH, van der Hoorn A. Perfusion MRI in treatment evaluation of glioblastomas: clinical relevance of current and future techniques. *J Magn Reson Imaging.* 2019;49:11–22.
11. Terakawa Y, Tsuyuguchi N, Iwai Y, et al. Diagnostic accuracy of ^{11}C-methionine PET for differentiation of recurrent brain tumors from radiation necrosis after radiotherapy. *J Nucl Med.* 2008;49:694–699.
12. Chen W, Silverman DH, Delaloye S, et al. ^{18}F-FDOPA PET imaging of brain tumors: comparison study with ^{18}F-FDG PET and evaluation of diagnostic accuracy. *J Nucl Med.* 2006;47:904–911.
13. Pöpperl G, Götz C, Rachinger W, Gildehaus FJ, Tonn JC, Tatsch K. Value of O-(2-[^{18}F]fluoroethyl)-L-tyrosine PET for the diagnosis of recurrent glioma. *Eur J Nucl Med Mol Imaging.* 2004;31:1464–1470.
14. Rachinger W, Goetz C, Pöpperl G, et al. Positron emission tomography with O-(2-[^{18}F]fluoroethyl)-L-tyrosine versus magnetic resonance imaging in the diagnosis of recurrent gliomas. *Neurosurgery.* 2005;57:505–511.
15. Albert NL, Weller M, Suchorska B, et al. Response Assessment in Neuro-Oncology Working Group and European Association for Neuro-Oncology recommendations for the clinical use of PET imaging in gliomas. *Neuro Oncol.* 2016;18:1199–1208.
16. Galldiks N, Niyazi M, Grosu AL, et al. Contribution of PET imaging to radiotherapy planning and monitoring in glioma patients: a report of the PET/RANO group. *Neuro Oncol.* 2021;23:881–893.
17. Kondo A, Ishii H, Aoki S, et al. Phase IIA clinical study of [^{18}F]fluciclovine: efficacy and safety of a new PET tracer for brain tumors. *Ann Nucl Med.* 2016;30:608–618.
18. Shoup TM, Olson J, Hoffman JM, et al. Synthesis and evaluation of [^{18}F]1-amino-3-fluorocyclobutane-1-carboxylic acid to image brain tumors. *J Nucl Med.* 1999;40:331–338.
19. Michaud L, Beattie BJ, Akhurst T, et al. ^{18}F-fluciclovine (^{18}F-FACBC) PET imaging of recurrent brain tumors. *Eur J Nucl Med Mol Imaging.* 2020;47:1353–1367.
20. Parent EE, Benayoun M, Ibeanu I, et al. [^{18}F]fluciclovine PET discrimination between high- and low-grade gliomas. *EJNMMI Res.* 2018;8:67.
21. Karlberg A, Berntsen EM, Johansen H, et al. Multimodal ^{18}F-fluciclovine PET/MRI and ultrasound-guided neurosurgery of an anaplastic oligodendroglioma. *World Neurosurg.* 2017;108:989.e1–989.e8.
22. Wakabayashi T, Iuchi T, Tsuyuguchi N, et al. Diagnostic performance and safety of positron emission tomography using ^{18}F-fluciclovine in patients with clinically suspected high- or low-grade gliomas: a multicenter phase IIB trial. *Asia Ocean J Nucl Med Biol.* 2017;5:10–21.
23. Songmen S, Nepal P, Olsavsky T, Sapire J. Axumin positron emission tomography: novel agent for prostate cancer biochemical recurrence. *J Clin Imaging Sci.* 2019;9:49.
24. Henderson F Jr, Brem S, O'Rourke DM, et al. ^{18}F-fluciclovine PET to distinguish treatment-related effects from disease progression in recurrent glioblastoma: PET fusion with MRI guides neurosurgical sampling. *Neurooncol Pract.* 2020;7:152–157.
25. Louis DN, Perry A, Wesseling P, et al. The 2021 WHO classification of tumors of the central nervous system: a summary. *Neuro Oncol.* 2021;23:1231–1251.
26. Wen PY, Macdonald DR, Reardon DA, et al. Updated response assessment criteria for high-grade gliomas: Response Assessment in Neuro-Oncology Working Group. *J Clin Oncol.* 2010;28:1963–1972.
27. Kolthammer JA, Su KH, Grover A, Narayanan M, Jordan DW, Muzic RF. Performance evaluation of the ingenuity TF PET/CT scanner with a focus on high count-rate conditions. *Phys Med Biol.* 2014;59:3843–3859.
28. Galldiks N, Dunkl V, Stoffels G, et al. Diagnosis of pseudoprogression in patients with glioblastoma using O-(2-[^{18}F]fluoroethyl)-L-tyrosine PET. *Eur J Nucl Med Mol Imaging.* 2015;42:685–695.
29. Yushkevich PA, Piven J, Hazlett HC, et al. User-guided 3D active contour segmentation of anatomical structures: significantly improved efficiency and reliability. *Neuroimage.* 2006;31:1116–1128.
30. Smith SM, Jenkinson M, Woolrich MW, et al. Advances in functional and structural MR image analysis and implementation as FSL. *Neuroimage.* 2004;23(suppl 1):S208–S219.
31. Barnes SR, Ng TS, Santa-Maria N, Montagne A, Zlokovic BV, Jacobs RE. Rocketship: a flexible and modular software tool for the planning, processing and analysis of dynamic MRI studies. *BMC Med Imaging.* 2015;15:19.
32. Avants BB, Epstein CL, Grossman M, Gee JC. Symmetric diffeomorphic image registration with cross-correlation: evaluating automated labeling of elderly and neurodegenerative brain. *Med Image Anal.* 2008;12:26–41.
33. Mihovilovic MI, Kertels O, Hänscheid H, et al. O-(2-(^{18}F)fluoroethyl)-L-tyrosine pet for the differentiation of tumour recurrence from late pseudoprogression in glioblastoma. *J Neurol Neurosurg Psychiatry.* 2019;90:238–239.
34. Pyka T, Hiob D, Preibisch C, et al. Diagnosis of glioma recurrence using multiparametric dynamic ^{18}F-fluoroethyl-tyrosine PET-MRI. *Eur J Radiol.* 2018;103:32–37.
35. Galldiks N, Stoffels G, Filss C, et al. The use of dynamic O-(2-^{18}F-fluoroethyl)-L-tyrosine PET in the diagnosis of patients with progressive and recurrent glioma. *Neuro Oncol.* 2015;17:1293–1300.
36. Karunanithi S, Sharma P, Kumar A, et al. ^{18}F-FDOPA PET/CT for detection of recurrence in patients with glioma: prospective comparison with ^{18}F-FDG PET/CT. *Eur J Nucl Med Mol Imaging.* 2013;40:1025–1035.
37. Minamimoto R, Saginoya T, Kondo C, et al. Differentiation of brain tumor recurrence from post-radiotherapy necrosis with ^{11}C-methionine PET: visual assessment versus quantitative assessment. *PLoS One.* 2015;10:e0132515.
38. Nihashi T, Dahabreh IJ, Terasawa T. Diagnostic accuracy of PET for recurrent glioma diagnosis: a meta-analysis. *AJNR.* 2013;34:944–950.
39. Karunanithi S, Sharma P, Kumar A, et al. Comparative diagnostic accuracy of contrast-enhanced MRI and ^{18}F-FDOPA PET-CT in recurrent glioma. *Eur Radiol.* 2013;23:2628–2635.
40. Werner JM, Weller J, Ceccon G, et al. Diagnosis of pseudoprogression following lomustine-temozolomide chemoradiation in newly diagnosed glioblastoma patients using FET-PET. *Clin Cancer Res.* 2021;27:3704–3713.
41. Salber D, Stoffels G, Pauleit D, et al. Differential uptake of O-(2-^{18}F-fluoroethyl)-L-tyrosine, L-3H-methionine, and 3H-deoxyglucose in brain abscesses. *J Nucl Med.* 2007;48:2056–2062.
42. Bogsrud TV, Londalen A, Brandal P, et al. ^{18}F-fluciclovine PET/CT in suspected residual or recurrent high-grade glioma. *Clin Nucl Med.* 2019;44:605–611.
43. Bagley SJ, Schwab RD, Nelson E, et al. Histopathologic quantification of viable tumor versus treatment effect in surgically resected recurrent glioblastoma. *J Neurooncol.* 2019;141:421–429.
44. Ono M, Oka S, Okudaira H, et al. Comparative evaluation of transport mechanisms of trans-1-amino-3-[^{18}F]fluorocyclobutanecarboxylic acid and l-[methyl-^{11}C]-methionine in human glioma cell lines. *Brain Res.* 2013;1535:24–37.
45. Oka S, Okudaira H, Ono M, et al. Differences in transport mechanisms of trans-1-amino-3-[^{18}F]fluorocyclobutanecarboxylic acid in inflammation, prostate cancer, and glioma cells: comparison with l-[methyl-^{11}C]methionine and 2-deoxy-2-[^{18}F]fluoro-D-glucose. *Mol Imaging Biol.* 2014;16:322–329.
46. Scarpelli ML, Healey DR, Mehta S, Quarles CC. Imaging glioblastoma with ^{18}F-fluciclovine amino acid positron emission tomography. *Front Oncol.* 2022;12:829050.
47. Verger A, Filss CP, Lohmann P, et al. Comparison of O-(2-^{18}F-fluoroethyl)-L-tyrosine positron emission tomography and perfusion-weighted magnetic resonance imaging in the diagnosis of patients with progressive and recurrent glioma: a hybrid positron emission tomography/magnetic resonance study. *World Neurosurg.* 2018;113:e727–e737.
48. Jena A, Taneja S, Gambhir A, et al. Glioma recurrence versus radiation necrosis: single-session multiparametric approach using simultaneous O-(2-^{18}F-fluoroethyl)-L-tyrosine PET/MRI. *Clin Nucl Med.* 2016;41:e228–e236.
49. Steidl E, Langen KJ, Hmeidan SA, et al. Sequential implementation of DSC-MR perfusion and dynamic [^{18}F]FET PET allows efficient differentiation of glioma progression from treatment-related changes. *Eur J Nucl Med Mol Imaging.* 2021;48:1956–1965.
50. Werner JM, Stoffels G, Lichtenstein T, et al. Differentiation of treatment-related changes from tumour progression: a direct comparison between dynamic FET PET and ADC values obtained from DWI MRI. *Eur J Nucl Med Mol Imaging.* 2019;46:1889–1901.
51. Turkbey B, Mena E, Shih J, et al. Localized prostate cancer detection with ^{18}F FACBC PET/CT: comparison with MR imaging and histopathologic analysis. *Radiology.* 2014;270:849–856.

Preliminary Clinical Experience with Cholecystokinin-2 Receptor PET/CT Using the ^{68}Ga-Labeled Minigastrin Analog DOTA-MGS5 in Patients with Medullary Thyroid Cancer

Elisabeth von Guggenberg*, Christian Uprimny*, Maximilian Klinger, Boris Warwitz, Anna Sviridenko, Steffen Bayerschmidt, Gianpaolo di Santo, and Irene J. Virgolini

Department of Nuclear Medicine, Medical University of Innsbruck, Innsbruck, Austria

PET/CT with the new ^{68}Ga-labeled minigastrin analog DOTA-DGlu-Ala-Tyr-Gly-Trp-(*N*-Me)Nle-Asp-1-Nal-NH_2 (^{68}Ga-DOTA-MGS5) was performed on patients with advanced medullary thyroid cancer (MTC) to evaluate cholecystokinin-2 receptor expression status. **Methods:** Six patients with advanced MTC underwent PET/CT with ^{68}Ga-DOTA-MGS5. From the images acquired 1 and 2 h after injection, preliminary data on the biodistribution and tumor-targeting properties were evaluated in a retrospective analysis. **Results:** In total, 87 lesions with increased radiotracer uptake considered malignant were detected (2 local recurrences, 8 lymph node lesions, 27 liver lesions, and 50 bone lesions). In general, radiotracer accumulation in lesions was higher at 2 h than at 1 h after injection (mean SUV_{max}, 7.2 vs. 6.0, respectively; mean SUV_{mean}, 4.4 vs. 3.6, respectively). **Conclusion:** The preliminary results clearly demonstrate the potential of ^{68}Ga-DOTA-MGS5 PET/CT in detecting local recurrence and metastases in patients with advanced MTC.

Key Words: cholecystokin-2 receptor; minigastrin; ^{68}Ga; PET; medullary thyroid cancer

J Nucl Med 2023; 64:859–862
DOI: 10.2967/jnumed.122.264977

Medullary thyroid cancer (MTC) is a rare disease arising from the parafollicular C cells of the thyroid and accounts for 1%–2% of thyroid cancers. Calcitonin is routinely used as a tumor marker for MTC. After primary treatment, additional imaging procedures are recommended when calcitonin levels rise above 150 pg/mL (*1*). Besides conventional radiologic imaging procedures (ultrasound, CT, MRI), PET with different radiotracers is performed to detect and localize persistent or recurrent disease. In patients with suspected MTC recurrence, ^{18}F-FDG PET/CT has a reported detection rate of 59%–69%, whereas 6-[^{18}F]fluoro-L-3,4-dihydroxyphenylalanine (^{18}F-DOPA) PET/CT shows a detection rate of 66%–72%, which increases to 86% in patients with a calcitonin doubling time of less than 24 mo. PET/CT using ^{68}Ga-labeled somatostatin analogs has demonstrated variable sensitivity, with an overall detection rate of 63.5%, and allows selection of patients for peptide receptor radionuclide therapy (*2*).

Received Sep. 29, 2022; revision accepted Jan. 9, 2023.
For correspondence or reprints, contact Irene J. Virgolini (irene.virgolini@i-med.ac.at) or Elisabeth von Guggenberg (elisabeth.von-guggenberg@i-med.ac.at).
*Contributed equally to this work.
Published online Jan. 19, 2023.

Cholecystokinin-2 receptors (CCK2Rs) are overexpressed in more than 90% of MTC cases (*3*). We recently reported development of the new minigastrin analog DOTA-DGlu-Ala-Tyr-Gly-Trp-(*N*-Me)Nle-Asp-1-Nal-NH_2 (DOTA-MGS5) with improved stability in vivo and enhanced tumor targeting (*4*). CCK2R targeting with DOTA-MGS5, therefore, offers a promising new diagnostic and therapeutic approach for patients with advanced MTC.

We here report our initial clinical experience with ^{68}Ga-labeled DOTA-MGS5 for PET/CT, with a primary goal of evaluating the potential of the new radiotracer to detect tumor lesions in patients with proven recurrent or residual metastatic disease.

MATERIALS AND METHODS

Six patients with histologically proven MTC and confirmed metastatic disease from previously performed diagnostic contrast-enhanced CT (ceCT) and PET with ^{18}F-DOPA or ^{68}Ga-labeled DOTATOC underwent PET/CT with ^{68}Ga-labeled DOTA-MGS5. The patient characteristics are in Supplemental Table 1 (supplemental materials are available at http://jnm.snmjournals.org). The patients had not undergone tumor-specific treatment at the time of imaging and were selected individually to evaluate whether radionuclide therapy targeting CCK2R is a potential option. The examination was performed on a named-patient basis, and written informed consent was obtained from all patients as part of the standard practice before any nuclear medicine examination. All procedures were in accordance with the principles of the 1964 Declaration of Helsinki and its subsequent amendments. The retrospective analysis of the data was approved by the Ethics Committee of the Medical University of Innsbruck (approval 1162/2022).

Radiopharmaceutical

^{68}Ga-labeled DOTA-MGS5 was prepared according to the Austrian Medicines Act (Arzneimittelgesetz §8 and §62) as described elsewhere (*5*) and was administered as a slow intravenous injection (~2 min) with a mean administered mass of 16 ± 6 μg (range, 12–28 μg) and a mean administered activity of 177 ± 16 MBq (range, 163–208 MBq).

Imaging Protocol

Scans were obtained on a dedicated PET/CT system in time-of-flight mode (Discovery; GE Healthcare). A whole-body PET scan (skull vertex to upper thighs) in 3-dimensional mode was acquired 1 and 2 h after tracer injection (emission time, 2 min per bed position, with an axial field of view of 20 cm). Five patients underwent diagnostic ceCT 1 h after injection. A CT scan of the thorax, abdomen, and pelvis (shallow breathing) was acquired 40–70 s after injection of contrast agent (60–120 mL of iomeprol, 400 mg J/mL [Iomeron; Bracco], depending on patient body weight), followed by a CT scan of the thorax in deep inhalation. In 1 patient, with ceCT available from another PET/CT

TABLE 1
^{68}Ga-DOTA-MGS5 SUV_{max} in Lesions Considered Malignant

Lesion type	1 h after injection			2 h after injection		
	Mean	Median	Range	Mean	Median	Range
Local recurrence (n = 2)	6.2	6.2	4.6–7.8	6.2	6.2	3.9–8.5
Lymph node (n = 8)	4.3	3.8	2.1–7.1	4.5	3.9	2.2–8.1
Liver (n = 27)	9.6	5.0	2.4–53.2	11.5	5.3	4.0–62.6
Bone (n = 50)	4.3	4.0	1.9–8.0	5.3	4.6	1.9–12.4

examination, only low-dose CT was performed 1 h after injection. All patients underwent low-dose CT 2 h after injection. Low-dose CT was used for attenuation correction of the PET emission data. Images were corrected for random events, scatter, and decay. Reconstruction was performed on a GE Healthcare Advantage Workstation with the iterative reconstruction method VUE Point FX (GE Healthcare), no z-axis filter, and the software package Q.Clear (β = 1,000; GE Healthcare), a fully convergent iterative reconstruction method with noise control.

Image Analysis

All PET/CT images were analyzed with dedicated commercially available software (Advantage Workstation Server, version 3.2-2.0; GE Healthcare), which allowed the review of PET, CT, and fused imaging data in axial, coronal, and sagittal slices. The intensity of tracer accumulation in organs and tissues with physiologic tracer uptake was measured using SUV_{mean} and SUV_{max}. For SUV calculations, volumes of interest were generated automatically with the default isocontour threshold of 42% centered on organs and tissues of interest. SUV calculations 1 and 2 h after injection were performed in the blood pool (aortic arch), gluteal muscle, brain, bone (thoracic vertebra), lung, liver, gallbladder, pancreas, stomach, adrenal gland, spleen, small bowel, large bowel, kidney, renal pelvis, and urinary bladder. For bowel activity, the area with the highest uptake was selected. In addition, PET images were analyzed visually, and lesions with increased radiotracer uptake judged as pathologic were counted with respect to their localization. The SUVs of these lesions were measured on images 1 and 2 h after injection. Furthermore, the tumor-to-background (T/B) ratio was determined, dividing the SUV_{max} of tumor lesions by the SUV_{mean} of the surrounding tissue (SUV_{mean} of blood pool for local recurrence and lymph nodes; SUV_{mean} of normal tissue for liver and bone lesions).

RESULTS

The administration of ^{68}Ga-DOTA-MGS5 was well tolerated, with no adverse effects. In all 6 patients with metastatic MTC confirmed by diagnostic ceCT and PET imaging with ^{18}F-DOPA or ^{68}Ga-labeled DOTA-TOC (Supplemental Table 1), metastatic spread was also shown with ^{68}Ga-DOTA-MGS5. CCK2R-positive local recurrence was detected in 2 patients. Eight CCK2R-positive lymph nodes with pathologic uptake were found in 5 patients, 27 liver lesions with increased uptake suggestive of metastases were found in 3 patients, and 50 tracer-avid bone lesions were found in 2 patients. Semiquantitative assessment of tumor lesions showed a slight increase in radiotracer accumulation between 1 and 2 h after

TABLE 2
^{68}Ga-DOTA-MGS5 SUV_{max} in Organs and Tissues with Physiologic Tracer Uptake

Organ or tissue	1 h after injection			2 h after injection		
	Mean	Median	Range	Mean	Median	Range
Blood pool	3.3	3.3	2.4–4.0	2.9	2.7	2.2–4.0
Gluteal muscle	1.0	1.0	0.8–1.3	0.9	1.0	0.7–1.1
Bone	1.3	1.4	0.9–1.6	1.3	1.3	1.0–1.4
Adrenal gland	2.4	2.3	2.0–2.9	1.8	1.7	1.2–2.4
Brain	0.7	0.6	0.3–1.1	0.7	0.7	0.4–0.8
Lung	1.1	1.2	0.8–1.4	1.0	1.1	0.6–1.2
Spleen	2.0	1.7	1.3–3.7	1.6	1.3	1.1–2.9
Liver	2.4	2.5	2.2–2.6	2.2	2.1	1.3–3.1
Gallbladder	6.7	5.8	4.3–10.7	6.2	6.5	4.7–7.1
Urinary bladder	89.5	101.9	30.1–123.8	132.2	118.6	70.1–213.1
Kidney	6.3	5.9	4.0–11.2	5.1	4.9	3.8–6.8
Renal pelvis	28.8	27.3	8.8–48.0	50.6	35.3	12.9–150.3
Small bowel	3.1	2.5	1.9–6.1	4.1	3.4	1.4–10.0
Large bowel	1.9	1.9	1.6–2.6	2.7	2.0	1.6–5.9
Stomach	21.5	20.4	10.4–38.9	23.6	26.2	11.5–31.3
Pancreas	2.9	3.0	2.2–3.2	2.8	2.8	2.1–3.4

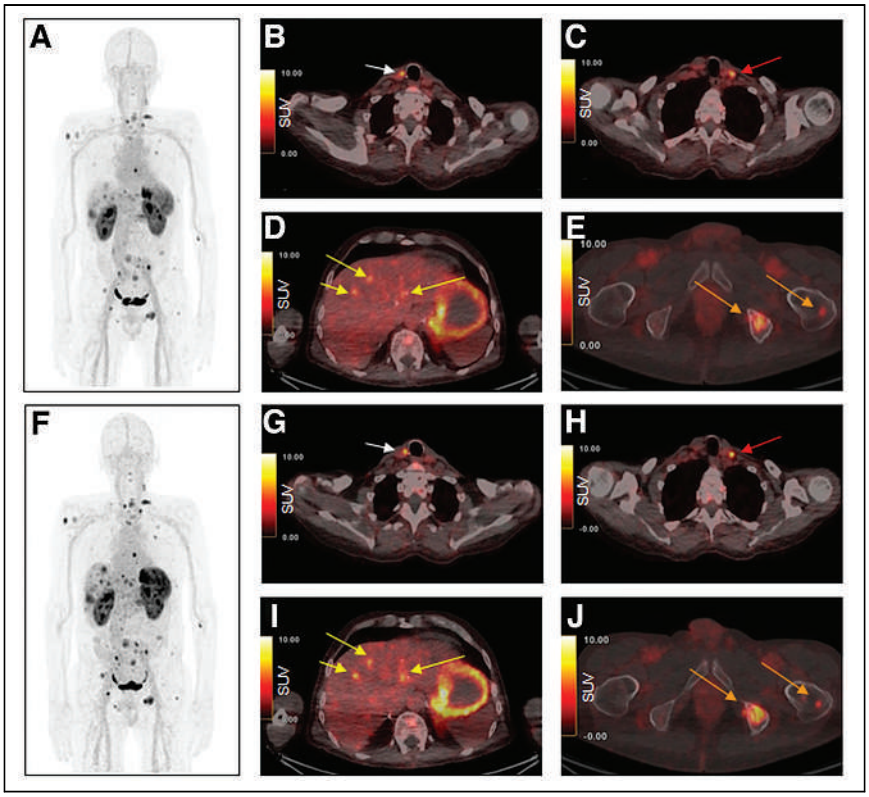

FIGURE 1. Maximum-intensity projection and axial PET/CT images 1 h (A–E) and 2 h (F–J) after injection of ^{68}Ga-DOTA-MGS5 into metastatic MTC patient (calcitonin, >2,000 ng/L). Images show local recurrence in right paratracheal region, with SUV_{max} of 7.8 and 8.5 at 1 and 2 h, respectively (B and G; arrows). A cervical lymph node metastasis is seen in left cervical region, with SUV_{max} of 7.1 and 8.1, respectively (C and H; arrows). Three liver metastases are seen, with SUV_{max} of 5.5, 6.3, and 5.3 vs. 6.7, 7.1, and 6.7, respectively (D and I; arrows). Bone metastases are also seen, in left iliac bone (SUV_{max} of 7.6 and 9.7, respectively) and left femur (SUV_{max} of 3.6 and 5.1, respectively) (E and J; arrows).

injection in lymph nodes and in liver and bone metastases, remaining stable in local recurrences. An overview of the SUVs and T/B ratios of lesions judged as malignant is given in Table 1 and Supplemental Tables 2 and 3.

With regard to the physiologic biodistribution of ^{68}Ga-DOTA-MGS5, physiologic tracer uptake and detailed information on SUVs in normal tissue and organs is presented in Table 2, Supplemental Table 4, and Supplemental Figure 1. An increase in median SUV_{max} 2 h after injection compared with 1 h after injection was observed in the brain, gallbladder, urinary bladder, renal pelvis, small bowel, large bowel, and stomach. In contrast, a decrease in median SUV_{max} between 1 and 2 h after injection was detected in the blood pool, bone, adrenal gland, lung, spleen, liver, kidney and pancreas, whereas the median SUV_{max} of background activity (gluteal muscle) remained stable. Apart from 1 bone lesion, T/B ratio was higher 2 h after injection than 1 h after injection in all lesions, irrespective of tumor site. When the T/B ratios of the different tumor sites were compared, mean T/B ratios of 3.3 at 1 h after injection and 4.1 at 2 h after injection were found for local recurrence, whereas for lymph nodes values of 2.4 and 3.3 were found, respectively. In comparison, higher mean T/B ratios were observed in liver lesions, with values of 5.1 and 7.1 at 1 and 2 h after injection, respectively, as well as in bone lesions, with values of 5.4 and 7.6 at 1 and 2 h after injection, respectively (Supplemental Table 3). Example images of a patient with different sites of metastasis are shown in Figure 1.

DISCUSSION

The potential of CCK2R-targeting peptide analogs for imaging and therapy had already been highlighted by the late 1990s. However, the first ^{111}In-labeled minigastrin analogs suffered from low diagnostic performance, and PET/CT with ^{68}Ga-labeled minigastrin analogs has been reported in only 2 patients so far (*6*). New clinical trials have been initiated evaluating the diagnostic performance and dosimetry of alternative peptide derivatives by scintigraphic imaging (*7,8*). Because DOTA-MGS5 showed increased in vivo stability and enhanced tumor targeting in preclinical investigations, we have performed PET/CT with ^{68}Ga-DOTA-MGS5. All 6 patients revealed at least 1 CCK2R-positive lesion consistent with malignancy. Lesions rated as positive for local recurrence, as well as local and distant metastases (lymph nodes, liver, and bone), could be visualized, as demonstrated in Figure 1. In most lesions (87.4%), a trend was found toward a higher SUV_{max} at 2 h than 1 h after injection. Higher T/B ratios were present 2 h after injection in 98.9% of the lesions. The low radiotracer uptake in normal tissue resulted in high contrast, especially in hepatic and skeletal lesions.

However, the preliminary data have to be interpreted with caution because of the small number of patients and the selection bias, as all patients presented with tumor lesions known from previously performed imaging. In addition, the data do not provide information on the diagnostic accuracy of the new radiotracer, because we did not perform a systematic direct comparison with standard imaging procedures such as ^{18}F-DOPA PET, ^{68}Ga-SSTR PET, and ceCT. Therefore, further studies are needed to confirm the preliminary results in more patients.

CONCLUSION

The preliminary results of this small series of patients clearly demonstrate that ^{68}Ga-DOTA-MGS5 PET/CT has the potential to detect local recurrence and metastases in advanced MTC. ^{68}Ga-DOTA-MGS5 PET/CT further allows evaluation of the feasibility of peptide receptor radionuclide therapy targeting CCK2R. To provide data on the diagnostic performance of ^{68}Ga-DOTA-MGS5 PET/CT in patients with locally advanced or metastatic MTC, we have recently initiated a prospective study (EudraCT number 2020-003932-26; approval 1336/2020) at our center, comparing ^{68}Ga-DOTA-MGS5 PET/CT with ^{18}F-DOPA PET, ^{68}Ga-SSTR PET, and ceCT as reference standard.

DISCLOSURE

Elisabeth von Guggenberg and Maximilian Klingler were named in a patent application (EP3412303) for peptide analogs with improved pharmacokinetics and CCK2R targeting for diagnosis and therapy. No other potential conflict of interest relevant to this article was reported.

ACKNOWLEDGMENTS

We thank all staff members for their help in performing the PET imaging studies.

KEY POINTS

QUESTION: In the diagnostic follow-up of patients with advanced MTC, is there a potential role for ^{68}Ga-DOTA-MGS5 PET/CT targeting the expression of the CCK2R?

PERTINENT FINDINGS: In 6 patients with advanced MTC, ^{68}Ga-DOTA-MGS5 PET/CT visualized local recurrence, as well as metastasis of the lymph nodes, liver, and bone. The low physiologic liver uptake of the radiotracer allowed for high contrast of hepatic lesions.

IMPLICATIONS FOR PATIENT CARE: ^{68}Ga-DOTA-MGS5 PET/CT is an interesting new tool in the diagnostic follow-up of patients with advanced MTC. In addition to localizing tumor lesions, ^{68}Ga-DOTA-MGS5 PET/CT can evaluate the feasibility of peptide receptor radionuclide therapy targeting CCK2R.

REFERENCES

1. Wells SA Jr, Asa SL, Dralle H, et al. Revised American Thyroid Association guidelines for the management of medullary thyroid carcinoma. *Thyroid.* 2015;25:567–610.
2. Giovanella L, Treglia G, Iakovou I, Mihailovic J, Verburg FA, Luster M. EANM practice guideline for PET/CT imaging in medullary thyroid carcinoma. *Eur J Nucl Med Mol Imaging.* 2020;47:61–77.
3. Reubi JC, Schaer JC, Waser B. Cholecystokinin(CCK)-A and CCK-B/gastrin receptors in human tumors. *Cancer Res.* 1997;57:1377–1386.
4. Klingler M, Summer D, Rangger C, et al. DOTA-MGS5, a new cholecystokinin-2 receptor-targeting peptide analog with an optimized targeting profile for theranostic use. *J Nucl Med.* 2019;60:1010–1016.
5. Hörmann AA, Klingler M, Rangger C, et al. Radiopharmaceutical formulation and preclinical testing of ^{68}Ga-labeled DOTA-MGS5 for the regulatory approval of a first exploratory clinical trial. *Pharmaceuticals (Basel).* 2021;14:575.
6. von Guggenberg E, Kolenc P, Rottenburger C, Mikołajczak R, Hubalewska-Dydejczyk A. Update on preclinical development and clinical translation of cholecystokinin-2 receptor targeting radiopharmaceuticals. *Cancers (Basel).* 2021;13:5776.
7. Lezaic L, Erba PA, Decristoforo C, et al. [^{111}In]In-CP04 as a novel cholecystokinin-2 receptor ligand with theranostic potential in patients with progressive or metastatic medullary thyroid cancer: final results of a GRAN-T-MTC phase I clinical trial. *Eur J Nucl Med Mol Imaging.* 2023;50:892–907.
8. Rottenburger C, Nicolas GP, McDougall L, et al. Cholecystokinin 2 receptor agonist ^{177}Lu-PP-F11N for radionuclide therapy of medullary thyroid carcinoma: results of the Lumed phase 0a study. *J Nucl Med.* 2020;61:520–526.

Consecutive Prostate-Specific Membrane Antigen (PSMA) and Antigen Receptor (AR) PET Imaging Shows Positive Correlation with AR and PSMA Protein Expression in Primary Hormone-Naïve Prostate Cancer

Valentin al Jalali[1,2], Gabriel Wasinger[3], Sazan Rasul[4], Bernhard Grubmüller[5], Beatrix Wulkersdorfer[1,2], Theresa Balber[1,4], Markus Mitterhauser[1,4,6], Judit Simon[1,7], Marcus Hacker[4], Shahrokh Shariat[8], Gerda Egger[1,3,9], and Markus Zeitlinger[1,2]

[1]Ludwig Boltzmann Institute Applied Diagnostics, Vienna, Austria; [2]Department of Clinical Pharmacology, Medical University of Vienna, Vienna, Austria; [3]Department of Pathology, Medical University of Vienna, Vienna, Austria; [4]Division of Nuclear Medicine, Department of Biomedical Imaging and Image Guided Therapy, Medical University of Vienna, Vienna, Austria; [5]Department of Urology and Andrology, University Hospital Krems, Karl Landsteiner University of Health Sciences, Krems, Austria; [6]Institute of Inorganic Chemistry, Faculty of Chemistry, University of Vienna, Vienna, Austria; [7]Department of Health Economics, Center for Public Health, Medical University of Vienna, Vienna, Austria; [8]Department of Urology, Medical University of Vienna, Vienna, Austria; and [9]Comprehensive Cancer Center, Medical University of Vienna, Vienna, Austria

The present study was carried out to investigate whether PET imaging can be used as a potential substitute for immunohistochemical analysis of tumor samples in prostate cancer (PC) patients. Correlation between imaging signals of 2 PET tracers and the corresponding target structures was assessed. The first tracer was [^{68}Ga]Ga-PSMA (prostate-specific membrane antigen)-HBED-CC (*N*,*N*′-bis [2-hydroxy-5-(carboxyethyl)benzyl]ethylenediamine-*N*,*N*′-diacetic acid) [^{68}Ga]Ga-PSMA$^{HBED-CC}$ ([^{68}Ga]PSMA), which is already implemented in clinical routines. The second tracer was 16β-[^{18}F]fluoro-5α-dihydrotestosterone (16β-[^{18}F]FDHT), which binds to the androgen receptor (AR). The AR is particularly interesting in PC, because AR expression status and its shift during therapy might directly influence patient care. **Methods:** This prospective, explorative clinical study included 10 newly diagnosed PC patients. Each patient underwent [^{68}Ga]PSMA PET/MRI and [^{18}F]FDHT PET/MRI scans before prostatectomy. Cancer SUVs were determined and related to background SUVs. After prostatectomy, tumor tissue was sampled, and AR and prostate-specific membrane antigen (PSMA) expression was determined. AR and PSMA expression was evaluated quantitatively with the open-source bioimage analysis software QuPath and with a 4-tier rating system. Correlation between imaging signals and marker expression was statistically assessed. **Results:** For [^{18}F]FDHT, the $SUV_{max}/SUV_{background}$ ratio showed a significant, strong correlation ($r = 0.72$; $P = 0.019$) with the AR optical density of the correlating tissue sample. The correlation between PSMA optical density and the [^{68}Ga]PSMA $SUV_{max}/SUV_{background}$ ratio was not significant ($P = 0.061$), yet a positive correlation trend could be observed ($r = 0.61$). $SUV_{max}/SUV_{background}$ ratios were higher for [^{68}Ga]PSMA (mean ± SD, 34.9 ± 24.8) than for [^{18}F]FDHT (4.8 ± 1.2). In line with these findings, the tumor detection rates were 90% for the [^{68}Ga]PSMA PET scan but only 40% for the [^{18}F]FDHT PET scan. The 4-tier rating of PSMA staining intensity yielded very homogeneous results, with values of 3+ for most subjects (90%). AR staining was rated as 1+ in 2 patients (20%), 2+ in 4 patients (40%), and 3+ in 4 patients (40%). **Conclusion:** [^{18}F]FDHT PET may be useful for monitoring AR expression and alterations in AR expression during treatment of PC patients. This approach may facilitate early detection of treatment resistance and allows for adaptation of therapy to prevent cancer progression. [^{18}F]FDHT PET is inferior to [^{68}Ga]PSMA PET for primary PC diagnosis, but the correlation between [^{68}Ga]PSMA SUVs and PSMA expression is weaker than that between [^{18}F]FDHT and the AR.

Key Words: [^{68}Ga]PSMA PET; [^{18}F]FDHT PET; AR protein expression; PSMA protein expression; primary hormone-naïve prostate cancer

J Nucl Med 2023; 64:863–868
DOI: 10.2967/jnumed.122.264981

Prostate cancer (PC) is causing significant mortality and morbidity worldwide and accounts for approximately 3.8% of deaths caused by cancer in men (*1*). Although novel diagnostic and therapeutic options led to a decrease in PC related mortality, the incidence of PC is increasing (*2*).

The androgen receptor (AR) plays a central role in PC development and progression (*3,4*). Multiple therapies for PC target the hormonal axis connected to the AR (*5*). Therefore, information on AR expression status and its shift during therapy and along the treatment course would possibly allow prediction of treatment response and imminent resistance to therapy (*6*).

16β-[^{18}F]fluoro-5α-dihydrotestosterone (16β-[^{18}F]FDHT) binds to the AR and has been discussed as being particularly useful in deciphering the role of the AR in resistant and progressive metastatic PCs (*7*). Fox et al. performed [^{18}F]FDHT and [^{18}F]FDG PET scans on 133 metastatic castration-resistant PC patients in a prospective clinical study. The authors were able to demonstrate that PET-based assessment of AR expression with [^{18}F]FDHT and glycolytic activity with [^{18}F]FDG can detect tumor heterogeneity affecting survival (*7*). Data on [^{18}F]FDHT kinetics are limited to castration-resistant PC patients; its use as an imaging agent is still restricted to clinical studies, and it has not been applied in clinical routines (*8,9*).

In contrast, the clinical utility of [^{68}Ga]Ga-PSMA (prostate-specific membrane antigen)-HBED-CC (*N*,*N*′-bis [2-hydroxy-5-(carboxyethyl) benzyl]ethylenediamine-*N*,*N*′-diacetic acid) [^{68}Ga]Ga-PSMA$^{HBED-CC}$ ([^{68}Ga]PSMA) PET has been widely accepted, and it is regularly

Received Oct. 10, 2022; revision accepted Jan. 12, 2023.
For correspondence or reprints, contact Markus Zeitlinger (markus.zeitlinger@meduniwien.ac.at).
Published online Jan. 19, 2023.

used in routine clinical practice for primary detection of PC and in recurrent disease (*10,11*).

Few clinical studies are available linking histopathologic patterns in tumor tissue to imaging signals (*7,12,13*). To date, there are no studies published that have quantitatively analyzed whether PET-based assessment of AR and prostate-specific membrane antigen (PSMA) expression in PC correlates with histopathologic expression of these markers. However, this knowledge is essential to reliably assess tumor heterogeneity and monitor alterations of AR and PSMA during therapy using noninvasive PET scans as a potential substitute for histopathologic analysis via repeated biopsies.

The aim of the present study was to investigate whether PET imaging can be used as a substitute for immunohistochemical (IHC) analysis of tumor samples in patients with newly diagnosed PC. For this purpose, [^{68}Ga]PSMA and [^{18}F]FDHT PET images were correlated with AR and PSMA IHC expression in PC tissue.

MATERIALS AND METHODS

Ethics

This study was conducted at the Medical University of Vienna (Vienna, Austria) and the Ludwig Boltzmann Institute Applied Diagnostics (Vienna, Austria) in accordance with the Declaration of Helsinki and the Good Clinical Practice Guidelines of the International Conference on Harmonization. The study was approved by the Ethics Committee of the Medical University of Vienna. Before inclusion, all study subjects gave oral and written informed consent to study participation.

Trial Design and Study Population

The present study was designed as a prospective, explorative clinical study. A total of 10 patients with newly diagnosed PC were included. Main inclusion criteria were age of greater than or equal to 18 y, histologically or cytologically confirmed prostate adenocarcinoma, and planned radical prostatectomy. Main exclusion criteria were any contraindication for performing a PET/MRI scan and a patient's ineligibility for the size of the PET/MRI gantry.

Each patient underwent PET/MRI scans with [^{68}Ga]Ga-PSMA$^{HBED\text{-}CC}$ and [^{18}F]FDHT before surgery. Scans were scheduled on 2 separate study days, allowing a scan-free interval of at least 24 h between the 2 scans. A blood sample was taken before the [^{18}F]FDHT PET scan to determine serum testosterone and prostate-specific antigen levels.

Up to 6 wk after the first scan, subjects were admitted to the clinical ward at the Department of Urology and a radical prostatectomy was performed by a urologist in accordance with standardized procedures. The timing and indication of surgery were not influenced by study participation. Tumor tissue obtained during surgery was used for IHC analysis of AR and PSMA expression in addition to the routine pathologic workup at the Department of Pathology (Medical University of Vienna).

PET/MRI

Radiosyntheses. All radiotracers for the study were produced in-house at the Radiopharmacy Unit, Vienna General Hospital, Vienna, Austria, by applying standard procedures in accordance with the state of the art for radiopharmaceutical preparations. Quality control was performed according to the European Pharmacopoeia. For details of the radiosynthesis, see the supplemental material (supplemental materials are available at http://jnm.snmjournals.org).

Imaging Protocols. All PET/MRI examination were conducted on a Biograph mMR (Siemens), consisting of a PET detector integrated with a 3.0-T whole-body MRI scanner. Two different imaging protocols were used. At our hospital, every newly diagnosed PC patient receives a diagnostic [^{68}Ga]PSMA PET/MRI examination using a multiparametric MRI protocol with contrast enhancement to accurately evaluate the primary tumor and the prostate region (*12*). However, because [^{18}F]FDHT PET is not yet established for routine clinical use at our institution and there are no previous studies using [^{18}F]FDHT and PET/MRI scanners, the protocols described in previous studies regarding this tracer in metastatic castration-resistant PC patients were followed. For the clinical evaluation, the most relevant MRI sequences of the pelvic region were acquired (*7,14,15*). The PET images were reviewed by *2* trained nuclear medicine physicians.

[^{18}F]FDHT PET/MRI Protocols. The [^{18}F]FDHT PET/MRI examinations were performed 60 min after intravenous injection of [^{18}F]FDHT at 3 MBq/kg of body weight. A static 10-min sinogram mode for the pelvis and 16-min partial-body PET (skull base to knees) were performed with 4 bed positions, each with a 4-min sinogram mode. For details of the sequence parameters, see the supplemental material.

Reconstruction parameters for PET were 3 iterations/21 subsets and summation of the 10-min pelvic acquisition for visual and semiquantitative analysis. MRI-based attenuation correction was applied using DIXON-VIBE sequences comprising in- and opposed-phase as well as fat- and water-saturated images.

[^{68}Ga]PSMA PET/MRI Protocols. For [^{68}Ga]PSMA PET/MRI studies, a 45-min dynamic list mode PET acquisition of the pelvis started immediately after the intravenous injection of [^{68}Ga]Ga-PSMA$^{HBED\text{-}CC}$ at 2 MBq/kg of body weight. This scan was followed by partial-body PET (skull base to midthigh) performed with 4 bed positions, 4-min sinogram mode each. Reconstruction parameters for PET were 3 iterations/21 subsets and summation of the last 10-min pelvic acquisition for visual and semiquantitative analysis. MRI-based attenuation correction was applied using DIXON-VIBE sequences comprising in- and opposed-phase as well as fat- and water-saturated images. For details of the sequence parameters, see the supplemental material.

To improve image quality, especially of pelvic and abdominal images, forced diuresis with 20 mg of furosemide and 20 mg of hyoscine butylbromide (Buscopan; Boehringer Ingelheim) applied intravenously was done before the [^{68}Ga]PSMA application, and all patients received a bladder catheter.

PET Data Analysis. PET data were analyzed using HybridViewer 3D (Hermes Medical Solutions) software. Anatomically exact regions of interest based on MRI data were defined. Semiautomated threshold-based volumes of interest were generated in areas with focally increased [^{68}Ga]PSMA or [^{18}F]FDHT uptake and evaluated with respect to the following semiquantitative data: SUV_{max}, SUV_{mean}, and SUV_{peak}. A threshold of 90% of the SUV_{max} corrected for local background was applied for semiautomated PET imaging of both [^{68}Ga]PSMA and [^{18}F]FDHT. Background SUV_{mean} was measured in the gluteus muscle for each subject separately ($SUV_{background}$). Ratios of tumor SUV to $SUV_{background}$ were calculated for SUV_{max}, SUV_{mean}, and SUV_{peak}.

IHC Analysis and Handling of Samples

IHC analysis was performed on tumor tissue at the Department of Pathology (Medical University of Vienna) using the automatic staining system VENTANA BenchMark ULTRA (Roche Tissue Diagnostics). For details of IHC analysis, see the supplemental material. Interpretation of marker expression was performed by the same qualified uropathologist. Membranous PSMA and nuclear AR quantification for each sample was semiquantitatively determined by a qualified uropathologist masked with regard to clinical data using a 4-tier system (0, 1+, 2+, and 3+). All regions present on the histologic slide were evaluated. On the basis of the overall expression of said markers, the rating "0" indicates no expression and the rating "3+" indicates the strongest expression. If heterogeneous AR or PSMA expression was present, then the regions were separated into 2 regions with low versus high protein expression. Membranous and cytoplasmic PSMA expression and nuclear expression for AR were also quantitatively determined using the open-source bioimage analysis software QuPath (v.0.3.0). The area chosen for analysis was spatially matched with the area of SUV_{max} detection in [^{18}F]FDHT PET

TABLE 1
Patient Characteristics and Pathologic Tumor Characteristics

Characteristic	Value
No. of subjects	10
Age (y)*	60 (54–67)
Body mass index (m^2/kg)*	25.9 (25–27)
Prostate-specific antigen (μg/L)†	8.8 ± 4.1
Testosterone (ng/mL)†	3.4 ± 1.2
Gleason score*	8 (7–8)
Pathologic stage‡	
pT2	3 (30)
pT3a	3 (30)
pT3b	4 (40)

*Reported as median, with interquartile range in parentheses.
†Reported as mean ± SD.
‡Reported as number of subjects, with percentage in parentheses.

imaging. For AR, the "positive cell detection" function was used to automatically detect positive stained cells in an area of 4 mm^2 on the basis of the average 3,3′-diaminobenzidine staining intensity within the nucleus and given as diaminobenzidine optical density (OD) mean, ranging from 0 to 1, with a cutoff value of 0.05 to detect positive cells. To also account for the cell density in the marked area, the sum of all diaminobenzidine OD mean values (OD mean sum) was chosen for further analysis. For PSMA, a pixel classifier was trained after annotation of sample positive and negative areas. This pixel classifier was used to detect the positive staining area within the mentioned 4-mm^2 area. In the next step, the average diaminobenzidine staining intensity in this positive staining area was calculated and multiplied with the surface area to account for cell density.

Trial Endpoints and Statistical Analysis

The main outcome parameter was the correlation between tracer radiation dose normalized to injected dose, expressed as SUV and PSMA and AR protein expression levels in tissue samples assessed by IHC. Quantitative protein expression levels and the 4-tier ratings were correlated with SUV_{max}, SUV_{mean}, and SUV_{peak} and the respective SUV to $SUV_{background}$ ratios. In case of heterogeneous protein expression, the areas with stronger staining intensity spatially matched the areas of SUV detection and were therefore chosen for the correlation analysis. Linear correlation was investigated using the Pearson correlation coefficient and reported with the 95% CI.

Statistical analysis was performed using a commercially available computer program (GraphPad Prism 9.3.1 for macOS; GraphPad Software). All data collected were expressed as mean ± SD or median with interquartile range.

RESULTS

Demographics and Clinical Characteristics of Subjects

Between February 2020 and March 2021, 10 patients with newly diagnosed PC were included in the study and completed all study procedures (Table 1). None of the patients had received any hormonal cancer therapy. None of the patients had a testosterone level below the castration threshold of 0.5 ng/mL. Pathologic workup of the tumor tissue revealed a median Gleason score of 8 (7–8).

PET Scans

The tumor detection rate of the [^{68}Ga]PSMA PET scan was 90% and 40% for the [^{18}F]FDHT PET scan. Representative [^{68}Ga]PSMA and [^{18}F]FDHT PET scans are shown in Figure 1.

Measured SUVs in PC lesions for [^{68}Ga]PSMA and [^{18}F]FDHT are shown in Figure 2. The SUV_{max} of [^{68}Ga]PSMA PET was 17.0 ± 15.0 (mean ± SD), and that of [^{18}F]FDHT PET was 3.4 ± 0.5. Mean background SUV_{mean} measured in the gluteus muscle was 0.5 ± 0.1 and 0.7 ± 0.1 for [^{68}Ga]PSMA PET and [^{18}F]FDHT PET, respectively. Ratios of tumor SUV to background SUV are shown in Table 2. These were considerably higher for [^{68}Ga]PSMA than for [^{18}F]FDHT. The highest ratios were achieved for SUV_{max} with values of 34.9 ± 24.8 and 4.8 ± 1.2 for [^{68}Ga]PSMA and [^{18}F]FDHT, respectively.

Immunohistochemistry

The quantification results of the IHC staining of PSMA and AR in the tumor tissue are shown in Table 3 and sample pictures of the staining are shown in Figure 1. The semiquantitative evaluation of the membranous staining intensity of PSMA yielded very homogeneous results with values of 3+ for most subjects (90%). In contrast to this, the AR staining was rated with 1+ in 2 patients (20%), with 2+ in 4 patients (40%) and with

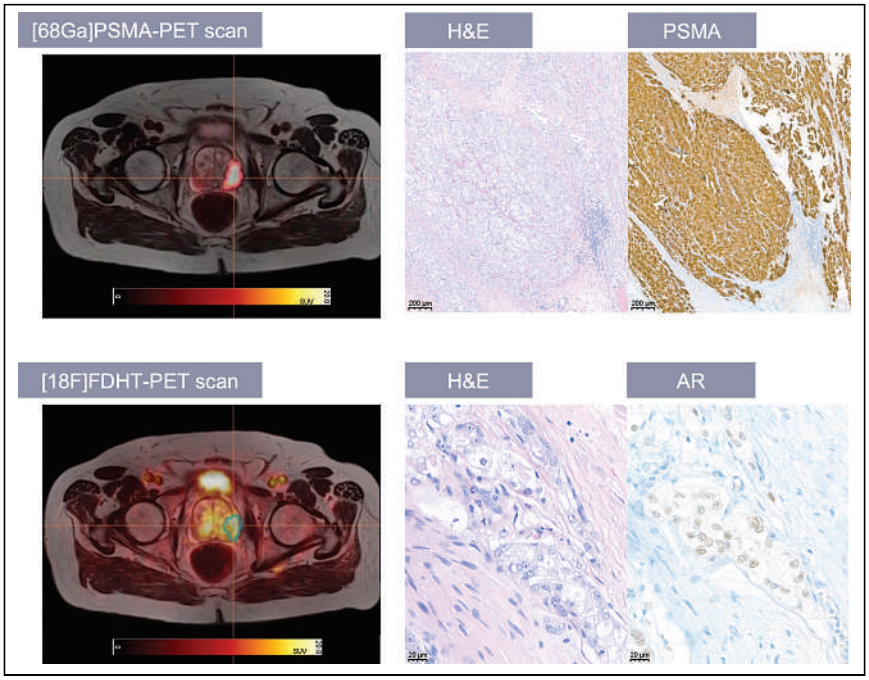

FIGURE 1. PET images and IHC stains for 1 study patient. IHC images of PSMA staining and AR staining are magnified 5-fold and 40-fold, respectively. $SUV_{max}/SUV_{background}$ ratios were 14.3 for [^{68}Ga]PSMA PET scan and 5.0 for [^{18}F]FDHT PET scan. Staining of tissue samples showed strong PSMA expression but weak AR expression. H&E = hematoxylin and eosin stain.

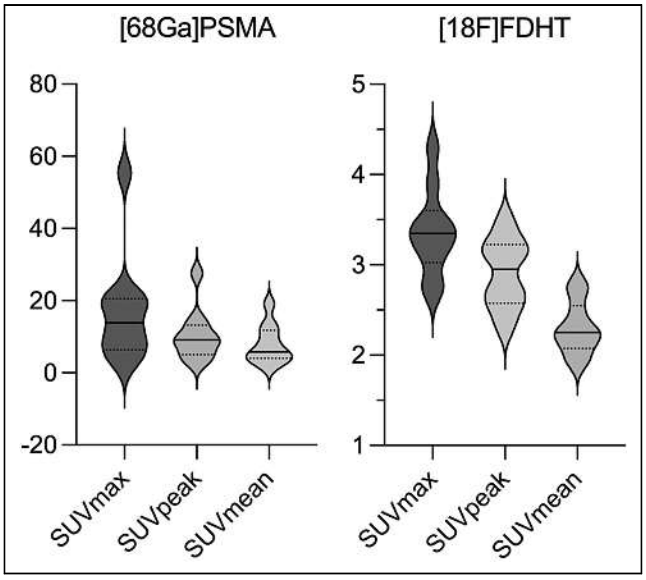

FIGURE 2. SUV_{max}, SUV_{peak}, and SUV_{mean} of PET scans in PC tissue for [^{68}Ga]PSMA and [^{18}F]FDHT.

3+ in 4 patients (40%). Three patients (1, 5 and 6) demonstrated highly heterogeneous AR expression with areas showing negative and positive nuclear AR expression. For subject 5, areas with high AR expression showed considerably lower PSMA expression (Supplemental Fig. 1). In this subject the missing AR staining was found especially in low differentiated, cribriform glands. However, this could not be observed in the other subjects. In contrast, in subject 6 AR staining was only visible in low differentiated, cribriform glands. The Gleason patterns within the different areas of the subjects did not show significant differences [subject 1: 7 (3 + 4); subject 5: 7 (3 + 4), subject 6: 8 (4 + 4)].

The PSMA diaminobenzidine OD measured with QuPath was 2,257,912 ± 1,297,251 (mean ± SD). The nuclear AR diaminobenzidine OD measured with QuPath was 3,857 ± 2,991 (mean ± SD).

Correlations

An overview of the different correlations is given in Table 4. Correlation of imaging signals with the 4-tier rating was not investigated for PSMA since protein expression was high (rated with "3+") in all patients. For all investigated correlations, the SUV_{max}/$SUV_{background}$ ratio consistently yielded the strongest correlation with staining intensity.

A strong significant correlation between the AR expression and the [^{18}F]FDHT SUV_{max}/$SUV_{background}$ ratio with correlation coefficients of $r = 0.72$ (95% CI, 0.17 to 0.93) for the OD (Fig. 3) and $r = 0.80$ (95% CI, 0.34 to 0.95) for the 4-tier rating could be demonstrated.

In contrast, correlation between the PSMA OD and the Ga-PSMA SUV_{max}/$SUV_{background}$ ratio was not significant ($P = 0.061$) with a correlation coefficient of $r = 0.61$ (95% CI, −0.03 to 0.90) (Fig. 3).

TABLE 2
Ratios of Tumor SUV to Background SUV* for [^{68}Ga]PSMA and [^{18}F]FDHT PET Scans

Ratio	[^{68}Ga]PSMA†	[^{18}F]FDHT†
SUV_{max}/background SUV	34.9 ± 24.8	4.8 ± 1.2
SUV_{peak}/background SUV	22.3 ± 14.6	4.1 ± 0.8
SUV_{mean}/background SUV	18.1 ± 17.1	3.3 ± 0.8

*SUV_{mean} measured in gluteus muscle.
†Reported as mean ± SD.

TABLE 3
Intensity of IHC Staining of PSMA and AR Determined in Two Ways*

	Uropathologist (4-tier rating)		QuPath (OD)	
Subject	PSMA	AR	PSMA (10^6)	AR (10^3)
1	3+	0, 1+	1.398	1.203
2	3+	3+	1.557	3.804
3	3+	3+	3.487	5.815
4	3+	3+	1.272	4.660
5	3+, 2+	0, 3+	1.820	10.968
6	3+	0, 2+	3.625	1.291
7	3+	2+	1.487	2.967
8	3+	1+	3.345	3.737
9	3+	2+	4.449	3.575
10	3+	2+	0.141	0.552

*By qualified uropathologist (4-tier rating) and by QuPath software (3,3′-diaminobenzidine OD). PSMA OD was calculated as PSMA diaminobenzidine OD mean × surface area, and AR OD was calculated as AR diaminobenzidine OD mean sum.

DISCUSSION

A significant positive correlation between [^{18}F]FDHT uptake in the PET scans and AR expression in cancer tissue could be demonstrated. For PSMA the PET/IHC correlation showed a positive trend but was not significant.

To our knowledge the present study is the first study that aimed to quantitatively assess whether [^{18}F]FDHT and [^{68}Ga]PSMA uptake in PET scans correlates with histopathologic AR and PSMA expression.

The [^{18}F]FDHT SUV_{max}/$SUV_{background}$ ratio showed a strong significant correlation ($r = 0.72$; $P = 0.019$) with AR OD of the correlating tissue sample. Compared with previous studies in humans, lower [^{18}F]FDHT SUVs were observed in the present study (*8,9*). Larson et al. performed [^{18}F]FDHT PET scans in 7 patients with PC and observed an average SUV_{max} of 5.28 ± 2.57 (*8*). An even higher SUV_{max} of 7.46 ± 3.37 was reported by Vargas et al. in 27 patients with PC (*9*). These values are 1.6- to 2.2-fold higher than the average SUV_{max} (3.4 ± 0.5) observed in the present study. Presumably, the underlying reason for this is that for the present study patients were enrolled who did not receive any hormonal pretherapy and therefore had physiologic testosterone blood levels. It can be assumed that [^{18}F]FDHT binding to ARs was competitively inhibited by endogenous dihydrotestosterone (DHT) leading to comparatively low [^{18}F]FDHT uptake. In contrast, previous studies with [^{18}F]FDHT only included patients with testosterone concentrations below the castration threshold (<50 ng/dL) (*7,8,14*). A finding that supports our theory was described by Larson et al. (*8*). The authors performed a [^{18}F]FDHT PET scan in castrated PC patients and rescanned 2 of the study subjects after

TABLE 4
Pearson Correlation Coefficient and *P* Value for Correlation of OD and 4-Tier Rating with Different Imaging Parameters*

	PSMA OD		AR			
			OD		4-tier rating	
Imaging parameter	Pearson $r^{\dagger}$	*P*	Pearson $r^{\dagger}$	*P*	Pearson $r^{\dagger}$	*P*
SUV_{max}	0.60 (−0.05 to 0.89)	0.068	0.64 (0.02 to 0.91)	0.045	0.73 (0.19 to 0.93)	0.016
SUV_{mean}	0.37 (−0.34 to 0.81)	0.298	0.17 (−0.52 to 0.72)	0.644	0.10 (−0.57 to 0.68)	0.790
SUV_{peak}	0.56 (−0.11 to 0.88)	0.096	0.34 (−0.37 to 0.80)	0.343	0.28 (−0.42 to 0.77)	0.427
$SUV_{max}/SUV_{background}$	0.61 (−0.03 to 0.90)	0.061	0.72 (0.17 to 0.93)	0.019	0.80 (0.34 to 0.95)	0.005
$SUV_{mean}/SUV_{background}$	0.09 (−0.57 to 0.68)	0.814	0.45 (−0.25 to 0.84)	0.193	0.47 (−0.23 to 0.85)	0.176
$SUV_{peak}/SUV_{background}$	0.38 (−0.33 to 0.81)	0.285	0.64 (0.02 to 0.91)	0.047	0.66 (0.05 to 0.91)	0.038

*Correlation with 4-tier rating was not investigated for PSMA because protein expression was rated same in all patients.
†Values in parentheses are 95% CIs.

administration of exogenous testosterone. In 1 of the 2 patients, the plasma DHT concentration was considerably higher before the second [^{18}F]FDHT scan and tracer uptake also decreased substantially. In the other patient, tracer uptake was unchanged compared with the initial scan, probably because plasma DHT initially increased, but then decreased again before the [^{18}F]FDHT scan.

Currently, there are 2 studies published, which investigated the correlation between [^{68}Ga]PSMA uptake in PET and IHC PSMA expression. In the prospective study by Rüschoff et al., IHC staining intensity was only determined semiquantitatively, according to the 4-tier rating system. A positive trend was described for membranous and cytoplasmic PSMA expression, which did not reach significance (*15*). Similar to the study by Rüschoff et al., in the retrospective study by Woythal et al. a 4-tier rating system was used for PSMA staining intensity (*16*). Woythal et al. did not discriminate between membranous and cytoplasmic PSMA expression and they were able to demonstrate a significant correlation between SUV_{max} and the immunoreactivity score which incorporates staining intensity and percentage of positive cells ($P < 0.001$). Unfortunately, the authors do not report the correlation between SUV_{max} and staining intensity. The patient characteristics of the study by Woythal et al. were comparable to the present study with a mean Gleason score of 7.9, but the sample size was larger (31 primary PC patients). In the present study SUV_{max} and staining intensity were positively correlated, but without statistical significance ($r = 0.6$; $P = 0.068$). Compared with the studies mentioned earlier, we used a more refined, granular and objective method for staining intensity assessment. Unfortunately, membranous and cytoplasmic PSMA expression could also not be discriminated in our study due to artifacts generated by the high cytoplasmic background PSMA staining in the automatic cell detection using QuPath. Therefore, the software was not able to reliably differentiate between membranous and cytoplasmic expression. Interestingly, the correlation between PSMA OD and the [^{68}Ga]PSMA $SUV_{max}/SUV_{background}$ ratio was not significant, yet a positive correlation trend could be observed (Fig. 3). The small sample size may account for this lack of significance. However, the present study was designed as an exploratory pilot study and therefore only 10 patients were included.

The tumor detection rate was 40% in the [^{18}F]FDHT PET scans and 90% in the [^{68}Ga]PSMA PET scans. In line with this finding, the SUV_{max} for [^{68}Ga]PSMA was about 7-fold higher than that for [^{18}F]FDHT (34.9 ± 24.8 vs. 4.8 ± 1.2, respectively). Despite the low detection rate, ratios of [^{18}F]FDHT cancer SUV to background SUV were always above 1, indicating increased binding of [^{18}F]FDHT in cancer tissue (Table 2). However, the SUV ratios were not high enough to be identified as tumor-positive areas. This explains that a significant correlation between [^{18}F]FDHT $SUV_{max}/SUV_{background}$ ratio and AR OD could be observed, despite the low tumor detection rate.

In future studies the correlation between [^{18}F]FDHT SUVs and AR expression in patients with low testosterone levels should be examined to investigate the hypothesis that endogenous androgens antagonize [^{18}F]FDHT. In these patients the correlation of [^{18}F]FDHT with AR expression might be more pronounced and is of particular clinical importance, since PC is usually progressed in these patients.

Another interesting finding of our study was the highly heterogeneous AR expression in 3 subjects. Magi-Galluzzi et al. performed a retrospective analysis of 40 PC samples and observed decreasing AR staining with increasing Gleason grade (*17*). To investigate whether the different regions in our subjects indicate different foci of aggressiveness, we determined the Gleason patterns for the

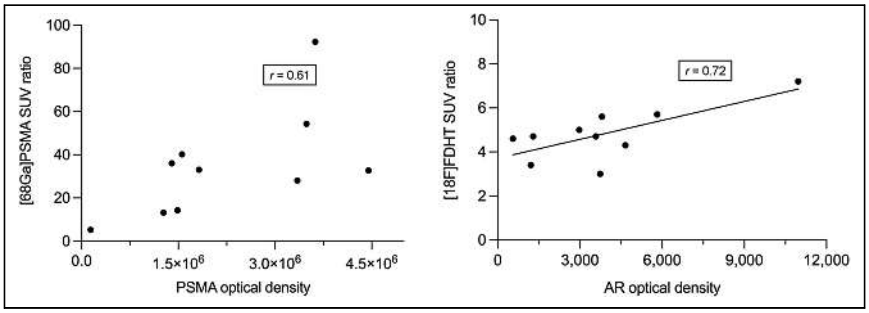

FIGURE 3. Correlation between $SUV_{max}/SUV_{background}$ ratio (SUV ratio) and PSMA diaminobenzidine OD and AR diaminobenzidine OD. Straight line represents linear regression line. PSMA OD was calculated as PSMA diaminobenzidine OD mean × surface area, and AR OD was calculate as AR diaminobenzidine OD mean sum.

different regions of AR expression. However, no significant differences could be observed. Others have observed that AR positive cells were also PSMA positive (*18*). We did not observe this trend. On the contrary, in 1 subject areas with higher AR expression showed lower PSMA expression. In consequence, no correlation between morphology and expression pattern can be derived from these findings and the influence of fixation artifacts in preanalytics cannot be excluded.

As mentioned earlier, a limitation of the present study was the small sample size. For a more robust statistical analysis a higher sample size would have been preferable, but due to the exploratory character of the study only 10 patients were included. In addition, the effects of hormonal therapy on [^{18}F]FDHT uptake and the correlation of [^{18}F]FDHT uptake with therapeutic response remain to be investigated in future longitudinal studies.

CONCLUSION

The findings of our study suggest that [^{18}F]FDHT PET scans may be useful for monitoring AR expression and alterations of AR expression during PC treatment. Knowledge of changes in AR expression during disease progression could help clinicians recognize imminent resistance to therapy and improve patient outcomes.

DISCLOSURE

No potential conflict of interest relevant to this article was reported.

ACKNOWLEDGMENT

We thank Neydher Berroterán-Infante for his help in establishing the [^{18}F]FDHT synthesis.

KEY POINTS

QUESTION: Can PET imaging be used as a substitute for IHC analysis of tumor samples in patients with newly diagnosed PC?

PERTINENT FINDINGS: In this prospective, explorative clinical study in 10 patients with newly diagnosed PC, we investigated the correlation between imaging signals of [^{68}Ga]PSMA and [^{18}F]FDHT and the protein expression of their corresponding target structures (PSMA and AR). The results suggested that [^{18}F]FDHT PET scans may be useful for monitoring AR expression and alterations in AR expression during PC treatment.

IMPLICATIONS FOR PATIENT CARE: Monitoring AR expression during disease progression could help clinicians recognize imminent resistance to therapy and thereby improve patient outcomes.

REFERENCES

1. Bray F, Ferlay J, Soerjomataram I, Siegel RL, Torre LA, Jemal A. Global cancer statistics 2018: GLOBOCAN estimates of incidence and mortality worldwide for 36 cancers in 185 countries. *CA Cancer J Clin.* 2018;68:394–424.
2. Zhai Z, Zheng Y, Li N, et al. Incidence and disease burden of prostate cancer from 1990 to 2017: results from the Global Burden of Disease Study 2017. *Cancer.* 2020;126:1969–1978.
3. Craft N, Sawyers CL. Mechanistic concepts in androgen-dependence of prostate cancer. *Cancer Metastasis Rev.* 1998–1999;17:421–427.
4. Visakorpi T, Hyytinen E, Koivisto P, et al. In vivo amplification of the androgen receptor gene and progression of human prostate cancer. *Nat Genet.* 1995;9:401–406.
5. Wang L, Paller CJ, Hong H, De Felice A, Alexander GC, Brawley O. Comparison of systemic treatments for metastatic castration-sensitive prostate cancer: a systematic review and network meta-analysis. *JAMA Oncol.* 2021;7:412–420.
6. Koivisto P, Kononen J, Palmberg C, et al. Androgen receptor gene amplification: a possible molecular mechanism for androgen deprivation therapy failure in prostate cancer. *Cancer Res.* 1997;57:314–319.
7. Fox JJ, Gavane SC, Blanc-Autran E, et al. Positron emission tomography/computed tomography-based assessments of androgen receptor expression and glycolytic activity as a prognostic biomarker for metastatic castration-resistant prostate cancer. *JAMA Oncol.* 2018;4:217–224.
8. Larson SM, Morris M, Gunther I, et al. Tumor localization of 16ß-^{18}F-fluoro-5α-dihydrotestosterone versus ^{18}F-FDG in patients with progressive, metastatic prostate cancer. *J Nucl Med.* 2004;45:366–373.
9. Vargas HA, Kramer GM, Scott AM, et al. Reproducibility and repeatability of semiquantitative ^{18}F-fluorodihydrotestosterone uptake metrics in castration-resistant prostate cancer metastases: a prospective multicenter study. *J Nucl Med.* 2018;59:1516–1523.
10. Perera M, Papa N, Roberts M, et al. Gallium-68 prostate-specific membrane antigen positron emission tomography in advanced prostate cancer: updated diagnostic utility, sensitivity, specificity, and distribution of prostate-specific membrane antigen-avid lesions—a systematic review and meta-analysis. *Eur Urol.* 2020;77:403–417.
11. Hofman MS, Lawrentschuk N, Francis RJ, et al. Prostate-specific membrane antigen PET-CT in patients with high-risk prostate cancer before curative-intent surgery or radiotherapy (proPSMA): a prospective, randomised, multicentre study. *Lancet.* 2020;395:1208–1216.
12. Grubmüller B, Baltzer P, Hartenbach S, et al. PSMA ligand PET/MRI for primary prostate cancer: staging performance and clinical impact. *Clin Cancer Res.* 2018;24:6300–6307.
13. Orevi M, Shamni O, Zalcman N, et al. [^{18}F]-FDHT PET/CT as a tool for imaging androgen receptor expression in high-grade glioma. *Neurooncol Adv.* 2021;3:vdab019.
14. Rathkopf DE, Morris MJ, Fox JJ, et al. Phase I study of ARN-509, a novel antiandrogen, in the treatment of castration-resistant prostate cancer. *J Clin Oncol.* 2013;31:3525–3530.
15. Rüschoff JH, Ferraro DA, Muehlematter UJ, et al. What's behind ^{68}Ga-PSMA-11 uptake in primary prostate cancer PET? Investigation of histopathological parameters and immunohistochemical PSMA expression patterns. *Eur J Nucl Med Mol Imaging.* 2021;48:4042–4053.
16. Woythal N, Arsenic R, Kempkensteffen C, et al. Immunohistochemical validation of PSMA expression measured by ^{68}Ga-PSMA PET/CT in primary prostate cancer. *J Nucl Med.* 2018;59:238–243.
17. Magi-Galluzzi C, Xu X, Hlatky L, et al. Heterogeneity of androgen receptor content in advanced prostate cancer. *Mod Pathol.* 1997;10:839–845.
18. Batra JS, Pienta KJ, Pomper MG, Gorin MA, Rowe SP. Can the interplay between androgen signaling and PSMA expression be leveraged for theranostic applications? *Transl Androl Urol.* 2019;8(suppl):S263–S264.

Developing a Patient-Reported Outcome Measure for Radionuclide Therapy for Prostate Cancer

Lisa M. Gudenkauf[1], Melody N. Chavez[2], Melinda Leigh Maconi[2], Carley Geiss[2], Ameen Seyedroudbari[3], Pan Thin[3], Aasha I. Hoogland[1], Kathleen Nguyen[3], Vishnu Murthy[3], Wesley R. Armstrong[3], Khaled Komrokji[1], Laura B. Oswald[1], Heather S.L. Jim[1], Ghassan El-Haddad[4], Wolfgang P. Fendler[5], Ken Herrmann[5], David Cella[6], Johannes Czernin[3], Michael S. Hofman[7], Adam P. Dicker[8], Jeremie Calais[3], Scott T. Tagawa[9], and Brian D. Gonzalez[1]

[1]Department of Health Outcomes and Behavior, Moffitt Cancer Center, Tampa, Florida; [2]Participant Research, Interventions, and Measurements Core, Moffitt Cancer Center, Tampa, Florida; [3]Department of Molecular and Medical Pharmacology, UCLA, Los Angeles, California; [4]Department of Diagnostic Imaging and Interventional Radiology, Moffitt Cancer Center, Tampa, Florida; [5]Department of Nuclear Medicine, University of Duisburg–Essen, and German Cancer Consortium–University Hospital Essen, Essen, Germany; [6]Departments of Medical Social Sciences and Psychiatry and Behavioral Sciences, and Lurie Comprehensive Cancer Center, Northwestern University Feinberg School of Medicine, Chicago, Illinois; [7]Prostate Cancer Theranostics and Imaging Centre of Excellence, Cancer Imaging, Peter MacCallum Centre, Melbourne, Victoria, Australia, and MacCallum Department of Oncology, University of Melbourne, Melbourne, Victoria, Australia; [8]Department of Pharmacology and Experimental Therapeutics, Sidney Kimmel Cancer, Thomas Jefferson University, Woodbury, New Jersey; and [9]Department of Urology, Weill Cornell Medical College, New York, New York

The field of radionuclide therapy (RNT) for prostate cancer (PC) is growing rapidly, with recent Food and Drug Administration approval of the first ^{177}Lu-PSMA ligand. We aimed to develop the first patient-reported outcome (PRO) measure for PC patients receiving RNT. **Methods:** We identified relevant symptoms and toxicities by reviewing published trials and interviews with PC patients receiving RNT ($n = 29$), caregivers ($n = 14$), and clinicians ($n = 11$). Second, we selected items for measure inclusion. Third, we refined the item list with input from experts in RNTs and PROs. Fourth, we finalized the Functional Assessment of Cancer Therapy–Radionuclide Therapy (FACT-RNT) with patient input. **Results:** This multistep process yielded a brief 15-item measure deemed by key stakeholders to be relevant and useful in the context of RNT for PC. **Conclusion:** The FACT-RNT is a new standardized tool to monitor relevant symptoms and toxicities among PC patients in RNT trials and real-world settings.

Key Words: genitourinary oncology; radionuclide therapy; radiopharmaceuticals; patient-reported outcomes; prostate cancer; radionuclide therapy

J Nucl Med 2023; 64:869–872
DOI: 10.2967/jnumed.122.264946

Radionuclide therapy (RNT) is a rapidly emerging class of oncology agents for metastatic castration-resistant prostate cancer (PC), spurred by Food and Drug Administration approval of ^{223}Ra-dichloride and ^{177}Lu-PSMA-617. RNTs, such as ^{177}Lu-PSMA-617, improve radiographic progression-free survival and overall survival versus standard care (*1*), with a higher biochemical response rate, fewer grade 3 or 4 adverse events than cabazitaxel (*2*), and improved or preserved health-related quality of life (*3,4*).

The Food and Drug Administration encourages patient-reported outcomes (PROs) as a trial primary endpoint (*5*) or as a complement to clinical and physiologic endpoints (*6*). Because clinicians may underestimate patient-reported toxicities (*7*), PROs are crucial to assessing treatment tolerability. Health-related quality of life among RNT recipients was better than among placebo recipients (e.g., ALSYMPCA trial (*8*)) and similar to that among cabazitaxel recipients (e.g., TheraP trial (*2*)).

PROs are associated with clinical outcomes, such as improved health-related quality of life among patients with better ^{177}Lu-PSMA-617 biochemical response (*9*). Phase 1 trials ($n = 79$) of ^{177}Lu-PSMA-617 or ^{225}Ac-J591 showed that RNT response was associated with PRO changes (*10*). PRO importance is underscored by recent evidence that PRO monitoring improved post-chemotherapy survival and other important outcomes over usual care (*11,12*).

Commonly used PRO measures (e.g., EORTC QLQ-C30 (*13*) and FACT-P (*14*)) are lengthy and were designed to assess the impacts of conventional therapies (e.g., chemotherapy and radiation). Brief PRO measures designed for RNT are needed to optimize measurement, prognostic value, and cross-trial comparison. This study aimed to develop a brief, targeted PRO measure for PC patients receiving RNT. We hypothesized that a multistep approach to identifying relevant symptoms and toxicities and iterative refinement would yield a brief measure relevant to RNT recipients and experts in the fields of RNT and PROs.

MATERIALS AND METHODS

Figure 1 shows the study flow for Functional Assessment of Cancer Therapy–Radionuclide Therapy (FACT-RNT) development from 2021 to 2022, following an approach similar to that of other studies developing PRO instruments for cancer patients (*15*). The protocol was deemed

Received Oct. 11, 2022; revision accepted Dec. 20, 2022.
For correspondence or reprints, contact Lisa M. Gudenkauf (lisa.gudenkauf@moffitt.org).
Published online Jan. 12, 2023.

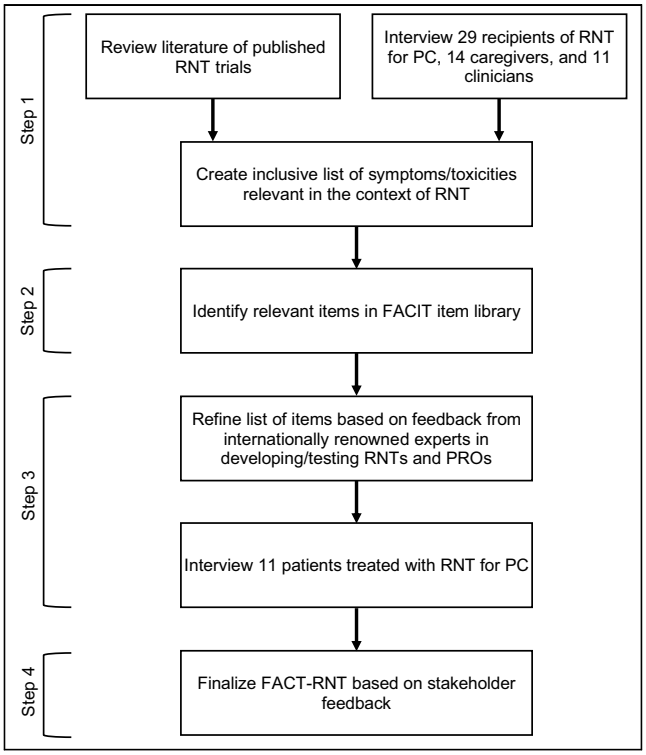

FIGURE 1. Developing PRO measure for RNT for PC.

exempt from institutional review board review, and participants provided informed consent verbally. We recruited English- or Spanish-speaking adults, including PC patients who received RNT, informal caregivers (e.g., a spouse or relative) of RNT recipients with PC, and RNT-experienced clinicians at UCLA or Moffitt Cancer Center. Following qualitative research guidelines (*16,17*), we aimed to interview at least 10 participants per group until reaching saturation.

This study was conducted in 4 steps. In step 1, we identified an intentionally broad, comprehensive list of RNT symptoms and toxicities (e.g., hematotoxicity and nephrotoxicity) experienced by PC patients during or after RNT. This list was compiled by reviewing published trials and by performing semi-structured interviews with patients, caregivers, and clinicians to elicit common, distressing, and/or clinically meaningful symptoms and toxicities. Each participant was compensated $25. The interviews were audio-recorded, transcribed verbatim, and analyzed with NVivo software, version 12, using the immersion/crystallization method by 2 qualitative research staff with strong inter-rater reliability ($\kappa \geq 0.80$) until no new qualitative themes were identified within each group (*17,18*).

In step 2, we searched for RNT symptoms and toxicities identified in step 1 within the Functional Assessment of Chronic Illness Therapy (FACIT) item library (*19*), a rigorously developed catalog of more than 700 items and 100 validated measures of chronic illness management.

In step 3, we interviewed internationally renowned experts in the fields of RNT and PROs to seek consensus on RNT-relevant symptoms and toxicities and corresponding FACIT items. We iteratively refined the item list based on recommended item additions/deletions and drafted the FACT-RNT.

TABLE 1
Characteristics of Interviewed RNT Recipients, Informal Caregivers, and Clinicians

	Step 1			Step 4
Characteristic	RNT recipients (n = 29)	Caregivers (n = 14)	Clinicians (n = 11)	RNT recipients (n = 11)
Age (y)	72 (8)	64 (11)	56 (8)	71 (9)
Male	29 (100%)	0 (0%)	7 (64%)	11 (100%)
Ethnicity				
Hispanic	0 (0%)	0 (0%)	0 (0%)	0 (0%)
Non-Hispanic	26 (90%)	13 (93%)	8 (73%)	9 (82%)
Unknown/not reported	3 (10%)	1 (7%)	3 (27%)	2 (18%)
Race				
White	24 (83%)	11 (79%)	6 (55%)	8 (73%)
Black/African American	0 (0%)	0 (0%)	0 (0%)	0 (0%)
Asian	1 (3%)	2 (14%)	2 (18%)	0 (0%)
Native American/Alaska Native	0 (0%)	0 (0%)	0 (0%)	0 (0%)
Hawaiian/Pacific Islander	0 (0%)	0 (0%)	0 (0%)	0 (0%)
Unknown/not reported	4 (14%)	1 (7%)	3 (27%)	3 (27%)
Years since diagnosis	11.72 (7.02)			11.84 (7.74)
RNT injections received	4.00 (1.65)			4.45 (1.44)

Categorical data are represented by frequencies and percentages; continuous data are represented by means and standard deviations.

TABLE 2
FACT-RNT Items

Item code	Symptom or toxicity
HN2	My mouth is dry
ST16	My eyes are dry
P7	I have difficulty urinating
GP2	I have nausea
O2	I have been vomiting
C5	I have diarrhea (diarrhoea)
Pal5	I am constipated
Ga1	I have a loss of appetite
BP1	I have bone pain
HI7	I feel fatigued
AA1	My fatigue keeps me from doing the things I want to do
GP4	I have pain
P3	My pain keeps me from doing things I want to do
GP5	I am bothered by side effects of treatment
Leu7	I feel isolated from others because of my illness or treatment

FACT-RNT is available at FACIT.org/measures/FACT-RNT. Response options range from 1 (not at all) to 5 (very much).

In step 4, patients from step 1 reviewed the draft FACT-RNT and participated in semi-structured interviews assessing measure acceptability, comprehensibility, RNT relevance, and self-efficacy for completing the measure. The FACT-RNT was subsequently finalized.

RESULTS

Literature review and interviews with 29 PC RNT recipients, 14 caregivers of RNT recipients, and 11 clinicians identified RNT-relevant symptoms and toxicities (e.g., fatigue, bone pain, xerostomia). Table 1 provides participant characteristics.

Patients interviewed received ^{177}Lu-PSMA-617 and/or ^{225}Ac-J591; comprehensive literature review also identified symptoms and toxicities of other RNTs (e.g., ^{223}Ra). Notably, interviews identified social isolation as an unexpected and distressing concern due to recommendations to briefly avoid close social contact and public venues post-infusion.

We selected FACIT items corresponding to each symptom and toxicity and to assess functional impacts (e.g., "I am bothered by side-effects of treatment"). In some instances, multiple FACIT items could be used (e.g., "I have a lack of energy" vs. "I feel fatigued").

Nine RNT and PRO experts from 5 institutions across 3 continents reviewed the draft FACT-RNT and advised on item selection, addition of RNT-relevant symptoms and toxicities (e.g., dry eyes) and removal of less relevant symptoms and toxicities (e.g., neuropathy).

Lastly, 10 RNT recipients from step 1 reported in interviews that FACT-RNT instructions were clear, items were comprehensible and relevant to RNT, response options (e.g., "not at all" vs. "a little bit") were conceptually distinct, and baseline administration is important to assess changes. Experts and patients recommended adding a bone pain severity item to distinguish among different pain types. Table 2 provides the final FACT-RNT.

DISCUSSION

This article describes development of the FACT-RNT, the first (to our knowledge) PRO measure designed for PC patients receiving RNT and developed with multistep feedback from patients, caregivers, clinicians, and experts in RNTs and PROs. FACT-RNT capitalizes on the FACIT item library's strong validity and reliability, multilanguage translation and validation, and utility as self-administered PROs or via interview.

The FACT-RNT for PC addresses the current gap in measuring RNT-specific symptoms and toxicities and responds to Food and Drug Administration guidance on implementing PROs in therapeutic trials (*5*) and real-world settings to identify PC patients at risk for deterioration (i.e., worsening symptoms/toxicities). The FACT-RNT was designed for use and future adaptation with a broad variety of RNT agents with different molecular targeting mechanisms and radioisotopes.

The sample was primarily non-Hispanic White; future studies should validate the FACT-RNT in large, diverse prostate cancer samples. Interviews with leading RNT experts helped ensure consideration of symptoms and toxicities relevant to newer-generation RNT agents and ensure the long-term relevance of FACT-RNT items.

CONCLUSION

We present the FACT-RNT for PC, a new measure developed through multistep collaboration with patients, caregivers, clinicians, and international experts. Next steps include assessment of internal consistency, validity, and reliability and use in RNT clinical trials and real-world settings.

DISCLOSURE

This work was supported by a grant from the U.S. Department of Defense (W81XWH2010351; principal investigator, Brian Gonzalez) and the Moffitt Cancer Center Participant Research, Interventions, and Measurements (PRISM) Core (P30 CA076292; principal investigator, John Cleveland). Heather Jim reports fees unrelated to this work from consultation for RedHill BioPharma, Janssen Scientific Affairs, and Merck. Ghassan El-Haddad reports consulting fees unrelated to this work from Bayer, Boston Scientific, Canon Medical Systems, Curium Pharma, Novartis, and Terumo. Wolfgang Fendler reports fees unrelated to this work from SOFIE Bioscience, Janssen, Calyx, Bayer, Parexel, and AAA. Ken Herrmann reports personal fees unrelated to this work from Bayer, Sofie Biosciences, SIRTEX, Adacap, Curium, Endocyte, IPSEN, Siemens Healthineers, GE Healthcare, Amgen, Novartis, ymabs, Bain Capital, and Aktis Oncology; grants and personal fees unrelated to this work from BTG; and nonfinancial support unrelated to this work from ABX. David Cella reports that he is president of FACIT.org. Michael Hofman reports grants and fees unrelated to this work from PCF, Peter MacCallum Foundation, Medical Research Future Fund, NHMRC, Movember, and PCFA. Adam Dicker reports advisory activities unrelated to this work with Janssen, Oncohost, Oranomed, CVS, IBA, Aptar (Voluntis), Onconova Therapeutics, and SBRBio. Jeremie Calais reports honoraria unrelated to this work from Astellas, Blue Earth Diagnostics, Curium Pharma, DS Pharma, GE Healthcare, Isoray, IBA RadioPharma, Janssen Pharmaceuticals,

Lightpoint Medical, Lantheus, Monrol, Novartis, POINT Biopharma, Radiomedix, Sanofi, and Telix Pharmaceuticals. Brian Gonzalez reports fees unrelated to this work from Sure Med Compliance and Elly Health. No other potential conflict of interest relevant to this article was reported.

KEY POINTS

QUESTION: Can a brief, targeted PRO measure be developed for patients receiving RNT for PC?

PERTINENT FINDINGS: The FACT-RNT was developed through a multistep, iterative process with input from patients, caregivers, clinicians, and experts in RNT and PROs.

IMPLICATIONS FOR PATIENT CARE: The FACT-RNT can assess PROs in PC patients receiving RNT.

REFERENCES

1. Sartor O, De Bono J, Chi KN, et al. Lutetium-177–PSMA-617 for metastatic castration-resistant prostate cancer. *N Engl J Med.* 2021;385:1091–1103.
2. Hofman MS, Emmett L, Sandhu S, et al. [^{177}Lu] Lu-PSMA-617 versus cabazitaxel in patients with metastatic castration-resistant prostate cancer (TheraP): a randomised, open-label, phase 2 trial. *Lancet.* 2021;397:797–804.
3. Calais J, Gafita A, Eiber M, et al. Prospective phase 2 trial of PSMA-targeted molecular RadiothErapy with ^{177}Lu-PSMA-617 for metastatic Castration-reSISTant Prostate Cancer (RESIST-PC): efficacy results of the UCLA cohort. *J Nucl Med.* 2021; 62:1440–1446.
4. Fizazi K, Herrmann K, Krause BJ, et al. Health-related quality of life (HRQoL), pain and safety outcomes in the phase III VISION study of Lu-177-PSMA-617 in patients with metastatic castration-resistant prostate cancer. *Ann Oncol.* 2021; 32(suppl 5):S627–S628.
5. *Guidance for Industry: Patient-Reported Outcome Measures: Use in Medical Product Development to Support Labeling Claims.* Food and Drug Administration; 2009.
6. *Value and Use of Patient-Reported Outcomes (PROs) in Assessing Effects of Medical Devices.* Food and Drug Administration; 2022.
7. Basch E, Iasonos A, McDonough T, et al. Patient versus clinician symptom reporting using the National Cancer Institute Common Terminology Criteria for Adverse Events: results of a questionnaire-based study. *Lancet Oncol.* 2006;7: 903–909.
8. Parker C, Nilsson S, Heinrich D, et al. Alpha emitter radium-223 and survival in metastatic prostate cancer. *N Engl J Med.* 2013;369:213–223.
9. Fendler WP, Reinhardt S, Ilhan H, et al. Preliminary experience with dosimetry, response and patient reported outcome after ^{177}Lu-PSMA-617 therapy for metastatic castration-resistant prostate cancer. *Oncotarget.* 2017; 8:3581–3590.
10. Gonzalez B, Sun M, Thomas C, et al. Patient-reported outcomes in prostate cancer patients receiving PSMA-targeted radionuclide therapy [abstract]. *Ann Oncol.* 2021;32(suppl 5):S663–S664.
11. Basch E, Deal AM, Dueck AC, et al. Overall survival results of a trial assessing patient-reported outcomes for symptom monitoring during routine cancer treatment. *JAMA.* 2017;318:197–198.
12. Basch E, Deal AM, Kris MG, et al. Symptom monitoring with patient-reported outcomes during routine cancer treatment: a randomized controlled trial. *J Clin Oncol.* 2016;34:557–565.
13. Aaronson NK, Ahmedzai S, Bergman B, et al. The European Organization for Research and Treatment of Cancer QLQ-C30: a quality-of-life instrument for use in international clinical trials in oncology. *J Natl Cancer Inst.* 1993;85: 365–376.
14. Esper P, Mo F, Chodak G, Sinner M, Cella D, Pienta KJ. Measuring quality of life in men with prostate cancer using the functional assessment of cancer therapy-prostate instrument. *Urology.* 1997;50:920–928.
15. Hansen AR, Ala-Leppilampi K, McKillop C, et al. Development of the Functional Assessment of Cancer Therapy-Immune Checkpoint Modulator (FACT-ICM): a toxicity subscale to measure quality of life in patients with cancer who are treated with ICMs. *Cancer.* 2020;126:1550–1558.
16. Guest G, Bunce A, Johnson L. How many interviews are enough? An experiment with data saturation and variability. *Field Methods.* 2006;18:59–82.
17. Bowen GA. Naturalistic inquiry and the saturation concept: a research note. *Qual Res.* 2008;8:137–152.
18. Borkan J. Immersion/crystallization. In: Crabtree BM, Miller WL, eds. *Doing Qualitative Research.* Vol 2. Sage Publications; 1999:179–194.
19. Webster K, Cella D, Yost K. The Functional Assessment of Chronic Illness Therapy (FACIT) Measurement System: properties, applications, and interpretation. *Health Qual Life Outcomes.* 2003;1:79.

Signaling Network Response to α-Particle–Targeted Therapy with the ^{225}Ac-Labeled Minigastrin Analog ^{225}Ac-PP-F11N Reveals the Radiosensitizing Potential of Histone Deacetylase Inhibitors

Yun Qin[1,2], Stefan Imobersteg[1], Stephan Frank[3], Alain Blanc[1], Tanja Chiorazzo[1], Philipp Berger[4], Roger Schibli[1,2], Martin P. Béhé[1], and Michal Grzmil[1]

[1]*Center for Radiopharmaceutical Sciences, Paul Scherrer Institute, Villigen, Switzerland;* [2]*Department of Chemistry and Applied Biosciences, ETH Zurich, Zurich, Switzerland;* [3]*Division of Neuropathology, Institute of Pathology, University of Basel, Basel, Switzerland; and* [4]*Laboratory of Nanoscale Biology, Paul Scherrer Institute, Villigen, Switzerland*

α-particle emitters have recently been explored as valuable therapeutic radionuclides. Yet, toxicity to healthy organs and cancer radioresistance limit the efficacy of targeted α-particle therapy (TAT). Identification of the radiation-activated mechanisms that drive cancer cell survival provides opportunities to develop new points for therapeutic interference to improve the efficacy and safety of TAT. **Methods:** Quantitative phosphoproteomics and matching proteomics followed by the bioinformatics analysis were used to identify alterations in the signaling networks in response to TAT with the ^{225}Ac-labeled minigastrin analog ^{225}Ac-PP-F11N (DOTA-(DGlu)$_6$-Ala-Tyr-Gly-Trp-Nle-Asp-Phe) in A431 cells, which overexpress cholecystokinin B receptor (CCKBR). Western blot analysis and microscopy verified the activation of the selected signaling pathways. Small-molecule inhibitors were used to validate the potential of the radiosensitizing combinatory treatments both in vitro and in A431/CCKBR tumor–bearing nude mice. **Results:** TAT-induced alterations were involved in DNA damage response, cell cycle regulation, and signal transduction, as well as RNA transcription and processing, cell morphology, and transport. Western blot analysis and microscopy confirmed increased phosphorylations of the key proteins involved in DNA damage response and carcinogenesis, including p53, p53 binding protein 1 (p53BP1), histone deacetylases (HDACs), and H2AX. Inhibition of HDAC class II, ataxia-telangiectasia mutated (ATM), and p38 kinases by TMP269, AZD1390, and SB202190, respectively, sensitized A431/CCKBR cells to ^{225}Ac-PP-F11N. As compared with the control and monotherapies, the combination of ^{225}Ac-PP-F11N with the HDAC inhibitor vorinostat (suberoylanilide hydroxamic acid, SAHA) significantly reduced the viability and increased the DNA damage of A431/CCKBR cells, led to the most pronounced tumor growth inhibition, and extended the mean survival of A431/CCKBR xenografted nude mice. **Conclusion:** Our study revealed the cellular responses to TAT and demonstrated the radiosensitizing potential of HDAC inhibitors to ^{225}Ac-PP-F11N in CCKBR-positive tumors. This proof-of-concept study recommends development of novel radiosensitizing strategies by targeting TAT-activated and survival-promoting signaling pathways.

Key Words: ^{225}Ac; phosphoproteomics; minigastrin; CCKBR; radioresistance

J Nucl Med 2023; 64:873–879
DOI: 10.2967/jnumed.122.264597

Targeted radionuclide therapy delivers cytotoxic radionuclides to cancer lesions and shows promise for the treatment of patients with unresectable metastatic cancers (*1*). In 2018, the Food and Drug Administration approved Lutathera (^{177}Lu-labeled dotatate peptide; Advanced Accelerator Applications) as a first-in-class peptide receptor radionuclide therapy for somatostatin receptor–positive gastroenteropancreatic and neuroendocrine tumors. More recently, the ^{177}Lu-labeled prostate-specific membrane antigen (PSMA) ligand ^{177}Lu-PSMA-617 (Pluvicto; Advanced Accelerator Applications) has been approved for the treatment of PSMA-positive metastatic castration-resistant prostate cancer patients (*2,3*).

To improve therapeutic efficacy, previous studies used α-emitters such as ^{225}Ac, with high linear energy transfer and a low tissue-penetrating range (40−100 μm) (*4*). Despite promising therapeutic outcomes, the effectiveness of targeted α-particle therapy (TAT) requires further optimization due to the impaired life quality of treated patients (*5*). Understanding the responses of cancer cells to TAT would allow the development of radiosensitization strategies with improved therapeutic efficacy at lower activities and reduced side effects.

We have recently developed the ^{225}Ac-labeled minigastrin analog ^{225}Ac-PP-F11N, which targets overexpressed cholecystokinin B receptor (CCKBR) in various human cancers including medullary thyroid, ovarian, and small-cell lung cancer, as well as gliomas (*6*). In a pilot and a phase I study (NCT02088645), ^{177}Lu-PP-F11N demonstrated medullary thyroid cancer–specific accumulation and low retention in kidney and bone marrow, whereas the median tumor-to-stomach dose ratio of 3.34 indicated stomach as a potential dose-limiting organ (*7*). To understand cellular responses to ionizing irradiation caused by α-particle–emitting radiolabeled minigastrin, and to further develop concomitant radiosensitizing strategies, we analyzed signaling networks in response to ^{225}Ac-PP-F11N in A431/CCKBR cells by quantitative phosphoproteomics and corresponding proteomics analysis.

Received Jul. 5, 2022; revision accepted Dec. 27, 2022.
For correspondence or reprints, contact Martin P. Béhé (martin.behe@psi.ch) or Michal Grzmil (michal.grzmil@psi.ch).
Published online Feb. 2, 2023.

The current study translates acquired basic radiobiology knowledge into novel treatment opportunities and provides proof of concept for the development of radiosensitizing strategies for targeted radionuclide therapies.

MATERIALS AND METHODS

Reagents and Radiolabeling

The selective inhibitors 7-fluoro-1-isopropyl-3-methyl-8-(6-(3-(piperidin-1-yl)propoxy)pyridin-3-yl)-1H-imidazo[4,5-c]quinolin-2(3H)-one (AZD1390) (ataxia-telangiectasia mutated [ATM]), *N*-[[tetrahydro-4-(4-phenyl-2-thiazolyl)-2H-pyran-4-yl]methyl]-3-[5-(trifluoromethyl)-1,2,4-oxadiazol-3-yl]-benzamide (TMP269) (class IIa histone deacetylase [HDAC]), 4-(4-fluorophenyl)-2-(4-hydroxyphenyl)-5-(4-pyridyl)-1H-imidazole (SB202190) (p38α and p38β2), and suberoylanilide hydroxamic acid (SAHA) (class II, III, and IV HDAC) were obtained from Lucerna-Chem. ^{225}Ac (in 0.1 M HCl) was purchased from ITG GmbH, whereas the N-terminal DOTA-conjugated gastrin analog PP-F11N (DOTA-(DGlu)$_6$-Ala-Tyr-Gly-Trp-Nle-Asp-Phe) was from PSL GmbH. Radiolabeling and separation of ^{225}Ac-PP-F11N are described in the supplemental materials (available at http://jnm.snmjournals.org) (*6*).

Cell Culture and Proliferation Assay

Human squamous carcinoma A431 cells, which overexpress CCKBR, were kindly provided by Dr. Luigi Aloj (*8*) and cultured under standard conditions, and the cell proliferation was analyzed using the CellTiter 96 AQueous Non-Radioactive Cell Proliferation Kit (Promega) according to the manufacturer's instruction as described in the supplemental materials.

Proteomics, Phosphoproteomics, and Bioinformatics

The supplemental materials describe preparation of tryptic peptides, phosphopeptide enrichment, liquid chromatography–mass spectrometry analysis, protein and phosphopeptide identification, label-free quantification, and bioinformatics (*9*).

Western Blot and Immunocytochemistry

For the analysis of protein level and phosphorylation, cells were subjected to Western blot analysis and immunocytochemistry as described in the supplemental materials.

In Vivo Therapy Study

All experiments involving mice complied with Swiss animal protection laws and were approved by the Cantonal Committee of Animal Experimentation (license 75699, 2017). Immunocompromised CD-1 female nude mice (Charles Rivers) were implanted with 5 million A431/CCKBR cells via subcutaneous injection. Seven days after inoculation, the mice carrying A431/CCKBR tumors were randomly grouped (the average tumor volume per group was 0.13 cm^3; range, 0.11–0.14 cm^3) and received 10 daily 50 mg/kg doses of SAHA (dissolved in dimethylsulfoxide/polyethylene glycol 400/polysorbate80/saline [10:40:5:45]) or vehicle control via intraperitoneal injection. The SAHA dose was based on the previous animal studies, which showed antitumor activity without detectable toxicity (*10*).

On the second day of treatment, a 30-kBq dose of ^{225}Ac-PP-F11N dissolved in 100 μL of phosphate-buffered saline, or phosphate-buffered saline alone as a vehicle control, was injected intravenously. Tumor diameter, animal weight, and animal well-being were recorded at least 3 times a week, and the tumor volume was calculated as (width^2 × length)/2. The mice were killed when the tumor reached the endpoint volume (>1.5 cm^3). Mice with ulcerated tumors, found randomly in all groups, were killed prematurely and were excluded from the study.

For the histopathologic assessment, postmortem-dissected stomach and kidney were formalin-fixed, dehydrated, and paraffin-embedded for preparation of hematoxylin- and eosin-stained tissue sections as described previously (*11*). Image analysis and documentation were performed using a slide scanner (Nikon Instruments Europe).

Statistics

Nonparametric Mann–Whitney unpaired testing and the Bliss independence model were used for in vitro treatments and calculations of combination index. In vivo, 1-way ANOVA followed by Tukey multiple-comparison testing were performed for 3 or more groups using GraphPad Prism, version 7.00, for Microsoft Windows, version 10. For survival analysis, Gehan–Breslow–Wilcoxon testing was performed. Values of P less than 0.05 were considered statistically significant.

RESULTS

Signaling Network Changes in Response to TAT with ^{225}Ac-PP-F11N

We performed quantitative phosphoproteomics and proteomics analysis of the protein lysates derived from the control and ^{225}Ac-PP-F11N–treated A431/CCKBR cells to identify molecular changes in response to the ^{225}Ac-labeled minigastrin analog. Phosphoproteomics quantified the abundance of 8952 phosphopeptides, whereas matching proteomics quantified 4250 protein groups (Fig. 1A). The phosphoproteomics and proteomics analysis identified 342 phosphopeptides (Supplemental Tables 1 and 2) and 3 proteins (Supplemental Table 3), respectively, with significantly altered abundance in the ^{225}Ac-PP-F11N–treated cells as compared with control cells. Bioinformatics analysis using the STRING platform identified the interaction networks among the proteins with altered levels of phosphorylation in the ^{225}Ac-PP-F11N–treated cells (Fig. 1B). The increased phosphorylation of HDAC9, HDAC4, and HDAC5 at S246, S259, and S220, respectively; p53 binding protein 1 (p53BP1) at S1778; and p53 at S15 was validated by Western blot analysis using phospho-specific antibodies (Fig. 1C). The total protein level of p53BP1 and housekeeping protein GAPDH showed no significant difference. Further bioinformatics analysis using the DAVID web-based platform identified fold enrichment for the biologic processes, including DNA damage response (DDR), cell cycle regulation, and signal transduction pathways (Table 1), as well as RNA transcription and processing, cell morphology and adhesion, and protein modifications and transport (Supplemental Table 4).

Targeting TAT-Induced Pathways Sensitizes Cancer Cells to ^{225}Ac-PP-F11N

We investigated inhibition of ^{225}Ac-PP-F11N–activated signaling pathways to explore novel strategies for radiosensitization of TAT, previously reported to be associated with radioresistance or survival. We selected 3 druggable pathways—HDAC class II, ATM, and p38—which can be targeted by the commercially available selective small-molecule inhibitors TMP269, AZD1390, and SB202190, respectively. For the combinatory treatments, the optimal inhibitor concentration was determined in A431/CCKBR cells, whereby 5 μM of TMP269, 5 μM of AZD1390, and 2 μM of SB202190 reduced cell proliferation to 69%–89% of control (Supplemental Fig. 1). Concomitant treatment of A431/CCKBR cells with different doses of ^{225}Ac-PP-F11N and TMP269, AZD1390, or SB202190 reduced cell proliferation from 63% to 23%, from 14% to 8%, or from 32% to 23% of control, respectively, and was significantly lower ($P < 0.05$) than with the monotherapy with ^{225}Ac-PP-F11N or inhibitor alone (Figs. 2A–2C). The combination of ^{225}Ac-PP-F11N with TMP269 showed a synergistic effect (CI, 0.62–0.85), whereas moderate synergistic and additive effects were obtained for SB202190 and AZD1390, with a combination index of 0.81–0.99 and 0.96–0.98, respectively. The inhibitions of

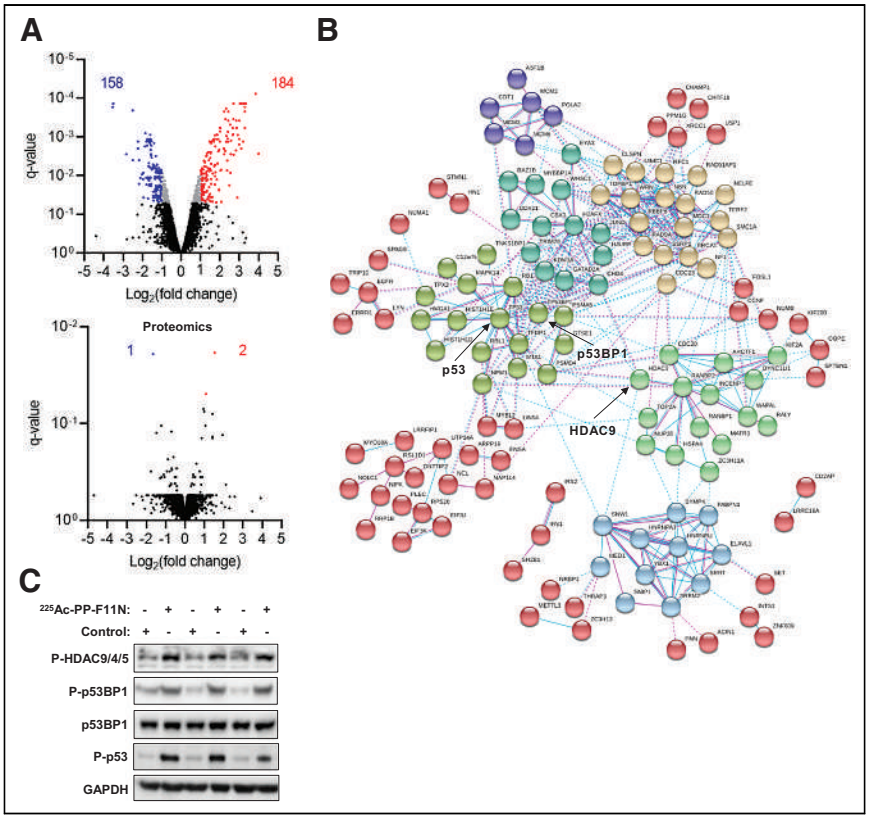

FIGURE 1. Cellular responses to TAT with ^{225}Ac-PP-F11N. (A) A431/CCKBR cells were treated with ^{255}Ac-PP-F11N, and the generated tryptic peptides and phosphopeptide-enriched samples were subjected to proteomics and phosphoproteomics analysis, respectively. Volcano plots display phosphopeptide (phosphoproteomics) and protein (proteomics) abundance shown as log2-transformed fold change. Red and blue dots indicate significantly altered abundance of phosphopeptides or proteins. Q-value < 0.05. (B) Interaction networks of proteins with altered phosphorylation or expression in response to ^{225}Ac-PP-F11N treatment. (C) Western blot analysis for phosphorylation of HDAC9, HDAC4, and HDAC5 at S246, S259, and S220, respectively; p53BP1 at S1778; p53 at S15; and total p53BP1 and GAPDH in protein lysates isolated from ^{225}Ac-PP-F11N–treated and untreated (control) cells.

HDAC9, HDAC4, and HDAC5 phosphorylation at S246, S259, S220, respectively; of p53 at S15; and of p53BP1 at S1778 in response to TMP269 and AZD1390 treatment were determined by Western blot analysis in ^{225}Ac-PP-F11N–treated cells (Fig. 2D).

HDAC Inhibitor SAHA Improves Therapeutic Efficacy of ^{225}Ac-PP-F11N

In a search for novel radiosensitizing approaches for ^{225}Ac-PP-F11N, we selected the Food and Drug Administration–approved HDAC inhibitor SAHA, which inhibited cell proliferation to 74% of control at 2 μM (Supplemental Fig. 1). We analyzed the DNA double-strand break marker γH2AX (H2AX phosphorylation at S139) to investigate effects on the DNA damage, which expression correlated with the response to targeted radionuclide therapy (*12*). The combination of ^{225}Ac-PP-F11N and SAHA showed a significantly increased speckle number and intensity of γH2AX in the nucleus (Figs. 3A–3C) and reduced A431/CCKBR cell viability (Supplemental Fig. 2) as compared with the monotherapies and control. A431/CCKBR tumor–bearing nude mice were analyzed after administration of a daily 50 mg/kg dose of SAHA for 10 d, alone or in combination with a single 30-kBq dose of ^{225}Ac-PP-F11N. All treatments delayed tumor growth (Fig. 4A). The first mouse reached the endpoint in the control group on day 13 after ^{225}Ac-PP-F11N application, and the average tumor volumes in the ^{225}Ac-PP-F11N and combinatorial treatment groups were significantly reduced to 0.46 cm^3 (P = 0.04) and 0.36 cm^3 (P = 0.02), respectively, as compared with control (0.90 cm^3). Treatment with SAHA reduced the average tumor volume to 0.55 cm^3 (P = 0.12). The mean survival of mice treated with SAHA and ^{225}Ac-PP-F11N was significantly extended (33 d, P = 0.04) as compared with the control (22 d) (Figs. 4B and 4C). In contrast, monotherapies with ^{225}Ac-PP-F11N or SAHA extended mean survival to 28 and 25 d, respectively, but these results did not reach statistical significance. To investigate potential toxicity to healthy organs, we analyzed the kidney, involved in circulating radiopeptide excretion, and the stomach, accumulating ^{225}Ac-PP-F11N because of endogenous CCKBR expression (*6*). Histopathologic assessment of kidney and stomach tissue sections from mice treated with SAHA and ^{255}Ac-PP-F11N did not show any differences from controls (3 mice per group) (Fig. 5). Furthermore, during therapy, no body weight loss was observed in any treatment group (Supplemental Fig. 3).

DISCUSSION

Despite new advances in TAT, cancer radioresistance remains a challenge that worsens therapeutic outcomes in the clinic (*13,14*). To identify radiosensitizing molecular targets and to develop combinatory treatments, we characterized changes in the cancer signaling network in response to peptide receptor radionuclide therapy with the ^{225}Ac-labeled minigastrin analog ^{225}Ac-PP-F11N. Understanding cancer cell responses can result in the coherent design of radiosensitization strategies to improve the therapeutic window, reduce applied activity, and, thus, minimize adverse effects. This rational approach can be also applied to other radioconjugates to develop safer and more efficacious cancer treatments.

Our phosphoproteomic analysis identified phosphorylation changes in proteins involved in DDR, repair, and nucleus structure, as well as in cell cycle regulation, RNA processing, and signal transduction. Consistently, ionizing radiation leads to the formation of DNA damage foci and activation of DDR pathways via activation of ATM/checkpoint kinase 2 and ATM- and Rad3-related/checkpoint kinase 1, which regulate proteins involved in DNA repair, cell cycle progression, and chromatin regulation and gene expression (*1*). Although mass spectrometry–based quantitative characterization of proteome and posttranslational modifications was previously used in the prediction of drug responses (*15*), the identification of cancer biomarkers, and the identification of sensitization targets for external-beam radiation therapy (*16,17*), little is known about cancer responses to targeted radionuclide therapy.

Recently, mass spectrometry–based phosphoproteomics analyzed altered signaling networks in response to targeted radioligand

TABLE 1
Significantly Enriched ($P < 0.01$) Biologic Processes and Signal Transduction Pathways in Response to ^{225}Ac-PP-F11N Treatment

^{225}Ac-PP-F11N	Fold enrichment	*P*
DDR, repair and nucleus structure		
DNA replication (BRCA1, POLA2, RAD50, RAD9A, RBBP8, SET, TICRR, WRN, CDT1, CHTF18, CLSPN, MCM2, MCM3AP, MCM3, MCM6, NBN, RFC1, SSRP1, TOPBP1) GOTERM_BP	9.1	3.1E−12
DNA repair (BRCA1, RAD50, RAD51AP1, RAD9A, RBBP8, TICRR, WRN, BOD1L1, CLSPN, NBN, NPM1, SMC1A, SSRP1, TOPBP1, TRIM28) GOTERM_BP	4.7	3.8E−6
Double-strand break repair via nonhomologous end joining (BRCA1, H2AFX, RAD50, WHSC1, MDC1, NBN, TP53BP1, UIMC1) GOTERM_BP	9.4	2.1E−5
Double-strand break repair via homologous recombination (BRCA1, H2AFX, RAD50, RAD51AP1, RBBP8, XRCC1, NBN, NUCKS1) GOTERM_BP	8.0	6.1E−5
Strand displacement (BRCA1, RAD50, RAD51AP1, RBBP8, WRN, NBN) GOTERM_BP	17.1	2.2E−5
DNA damage checkpoint (H2AFX, RAD9A, CLSPN, MAPK14, NBN, TP53BP1) GOTERM_BP	14.8	4.6E−5
DNA synthesis involved in DNA repair (BRCA1, RAD50, RAD51AP1, RBBP8, WRN, NBN) GOTERM_BP	12.7	9.9E−5
DNA unwinding involved in DNA replication (HMGA1, MCM2, MCM6, TOP2A) GOTERM_BP	29.6	2.7E−4
DNA double-strand break processing (BRCA1, RAD50, RBBP8, NBN) GOTERM_BP	19.7	9.7E−4
DNA duplex unwinding (RAD50, WRN, CHD4, MCM3, NBN) GOTERM_BP	8.4	2.8E−3
Nucleosome assembly (H2AFX, SET, ASF1B, HIST1H1D, HIST1H1E, MCM2, NPM1, NAP1L4) GOTERM_BP	5.0	1.1E−3
Telomere maintenance via telomerase (RAD50, RFC1, TNKS1BP1, TERF2) GOTERM_BP	16.4	1.7E−3
Covalent chromatin modification (RB1, RBL1, ASF1B, CBX3, C17orf49, TRIM28, ZMYND11) GOTERM_BP	4.6	4.3E−3
Telomere maintenance via recombination (POLA2, RAD50, WRN, RFC1) GOTERM_BP	9.2	9.0E−3
Cell cycle regulation		
Cell division (CD2AP, RBBP8, RB1, TPX2, TRIOBP, WAPL, ARPP19, CDC20, CDC23, CDCA2, CCNF, DYNC1LI1, ENSA, HELLS, KIF20B, KIF2A, MAP4, MISP, NUMA1, PSRC1, PKN2, SMC1A, ZC3HC1) GOTERM_BP	4.9	2.2E−9
Mitotic nuclear division (CD2AP, RBBP8, TPX2, TRIOBP, ARPP19, CDC20, CDC23, CDCA2, CCNF, DYNC1LI1, ENSA, HELLS, INCENP, KIF20B) GOTERM_BP	5.4	4.5E−8
Meiotic cell cycle (H2AFX, RBBP8, RBM7, NBN, NUMA1, ZNF318) GOTERM_BP	13.1	8.6E−5
Cell cycle (BRCA1, HJURP, RBL1, CDC20, CHTF18, LIN54, MCM2, NOLC1, PKN2, TERF2, TP53, ZMYND11) GOTERM_BP	4.1	1.8E−4
G1/S transition of mitotic cell cycle (POLA2, RANBP1, RBBPB8, RB1, CDT1, MCM2, MCM3, MCM6) GOTERM_BP	5.8	4.6E−4
Regulation of cell cycle (JUND, MYBL2, RB1, RBL1, CCNF, FIGNL1, LIN54, MED1) GOTERM_BP	4.8	1.4E−3
G2 DNA damage checkpoint (BRCA1, RBBP8, CLSPN, UIMC1) GOTERM_BP	14.8	2.3E−3
Cell cycle checkpoint (RBBP8, RB1, TICRR) GOTERM_BP	24.7	6.1E−3
Mitotic cell cycle checkpoint (RB1, TTK, NBN, SMC1A) GOTERM_BP	9.2	9.0E−3
Mitotic spindle organization (TTK, KIF2A, MAP4, STMN1, SMC1A) GOTERM_BP	12.3	6.7E−4
Chromosome segregation (BRCA1, HJURP, CDCA2, INCENP, PPP1R7, TOP2A) GOTERM_BP	6.5	2.2E−3
Sister chromatid cohesion (AHCTF1, RANBP2, WAPL, CDC20, INCENP, KIF2A, SMC1A) GOTERM_BP	5.0	2.7E−3
Signal transduction and cellular response		
Regulation of signal transduction by p53 class mediator (BRCA1, RAD50, RAD9A, RBBP8, TPX2, WRN, CHD4, MAPK14, NBN, SSRP1, TOPBP1, TP53) GOTERM_BP	7.2	9.2E−7
Cellular response to DNA damage stimulus (BRCA1, H2AFX, LYN, RAD50, RAD9A, TIGAR, WRN, BOD1L1, BAZ1B, TOP2A, TOPBP1, TP53BP1, TP53) GOTERM_BP	4.6	2.6E−5
Response to ionizing radiation (BRCA1, EYA3, H2AFX, TICRR, MTA1, TOPBP1, UIMC1) GOTERM_BP	10.6	4.8E−5
Cellular response to ionizing radiation (RAD51AP1, RAD9A, FIGNL1, MAPK14, TP53) GOTERM_BP	11.9	7.6E−4
Cellular response to epidermal growth factor stimulus (ERRFI1, ZFP36L2, ZFP36, EGFR, MED1) GOTERM_BP	11.2	9.6E−4
Cellular response to dexamethasone stimulus (ERRFI1, CBX3, EGFR, HNRNPU) GOTERM_BP	10.2	6.8E−3
DDR, signal transduction by p53 class mediator resulting in cell cycle arrest (GTSE1, NPM1, TNKS1BP1, TFDP1, TP53) GOTERM_BP	6.0	9.7E−3
ATM signaling pathway (BRCA1, RAD50, RBBP8, NBN, TP53) BIOCARTA	8.6	2.0E−3
Role of BRCA1, BRCA2, and ATM- and Rad3-related in cancer susceptibility (BRCA1, RAD50, RAD9A, NBN, TP53) BIOCARTA	8.2	2.4E−3

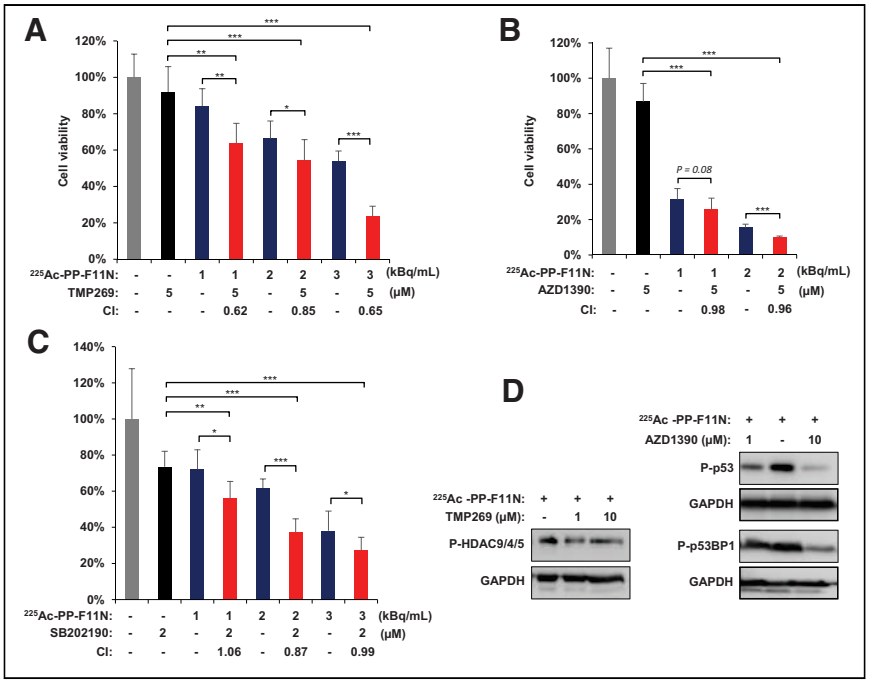

FIGURE 2. Treatment with HDAC, p38, and ATM inhibitors sensitizes A431/CCKBR cells to ^{225}Ac-PP-F11N. Cell viability 48 h after treatment with ^{225}Ac-PP-F11N alone or in combination with HDAC inhibitor TMP269 (A), ATMi AZD1390 (B), and p38i SB202190 (C). Bars represent mean ± SD. Corresponding combination index values between 0.9 and 1.1 indicate additive effects, and below 0.9 indicates synergism. (D) Western blot analysis for phosphorylation of HDAC9, HDAC4, and HDAC5 at S246, S259, and S220, respectively; p53 at S15; and p53BP1 at S1778 in protein lysates isolated from treated and control cells. Western blots were reprobed with antibody against GAPDH. $^{*}P < 0.05$. $^{**}P < 0.01$. $^{***}P < 0.001$.

therapy with ^{177}Lu- and ^{255}Ac-labeled PSMA in a prostate cancer mouse model (*18*). Similarly, the study identified alterations in DNA damage and replication stress response as well as in p53 pathways and suggests that the identified pathways may mediate radioresistance, yet the validation and development of radiosensitizing strategies await further investigation. Despite similarities in the response to targeted radionuclide therapy, the genetic heterogeneity of various cancers influences activation of the signaling pathways, and thus, effective radiosensitization might require development of cancer-type–specific strategies. Among identified alterations, our validation study confirmed increased phosphorylation of HDAC9, HDAC4, and HDAC5 at S246, S259, and S220, respectively, as well as p53BP1 at S1778 and p53 at S15 in response to ^{225}Ac-PP-F11N. HDACs play a role in the chromatin remodeling and regulation of posttranscriptional gene expression, which are essential processes in DDR (*19*).

The phosphorylation of HDAC regulates nucleocytoplasmic shuttling, complex formation, and catalytic activity (*20,21*). Notably, Biade et al. reported chromatin conformation changes after cotreatment with the HDAC inhibitor trichostatin A and external-beam radiation therapy, which led to enhanced radiation sensitivity in intrinsically radioresistant colon carcinoma cells (*22*). Consistently in our study, the combination of HDAC inhibitor with TAT resulted in a synergistic effect on cell viability inhibition, which could be explained by the enhanced number of DNA double-strand breaks. In addition, the chromatin modulators, including demethylating agents and HDAC inhibitors, were reported to upregulate SSTR2 expression and thus increased tumor uptake of the radiolabeled octreotide in neuroendocrine and prostate cancer cells (*23*). An assessment of whether these findings also apply to other targeted receptors, including CCKBR, requires further investigation.

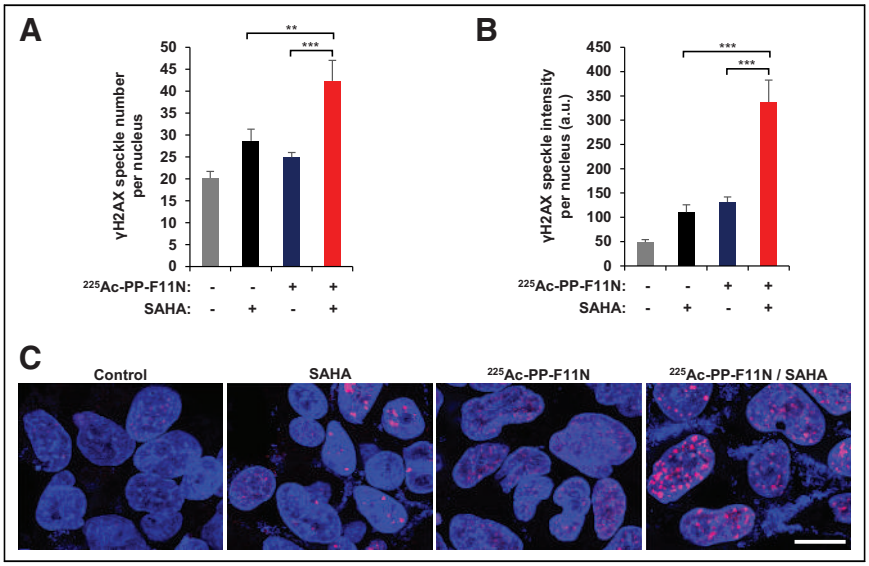

FIGURE 3. HDAC inhibition by SAHA increased level of γH2AX in ^{225}Ac-PP-F11N–treated cells. A431/CCKBR cells were treated with 3 kBq/mL dose of ^{225}Ac-PP-F11N or 2 μM SAHA alone or in combination for 24 h. (A and B) Bars represent mean ± SEM of numbers and intensities of γH2AX-positive speckles per nucleus. (C) Typical images of treated and control cells. Red = γH2AX; blue = Hoechst 33258; scale bar = 20 μm; a.u. = arbitrary units. $^{**}P < 0.01$. $^{***}P < 0.001$.

The ATM-phosphorylated p53BP1 acts as a sensor protein of DNA damage and is involved in recruiting repair proteins to the damaged chromatin (*24*). Interaction of p53BP1 with the telomere-associated protein RIF1 potentiated cell survival after multifractionated radiotherapy, and this survival benefit can be revoked by p53BP1 inhibition (*25*). Furthermore, the elevated phosphorylation level of the tumor suppressor p53 on serine-15 after ionizing radiation has been reported to mediate cell growth arrest, which provides time to facilitate DNA repair (*26,27*). Our phosphoproteomics identified increased phosphorylation of MAPK14 (p38 isoform α), which regulates various biologic responses including proliferation, differentiation, migration, and inflammation, as well as stress responses and survival (*28–30*). Notably, Rac1-mediated p38 activation in

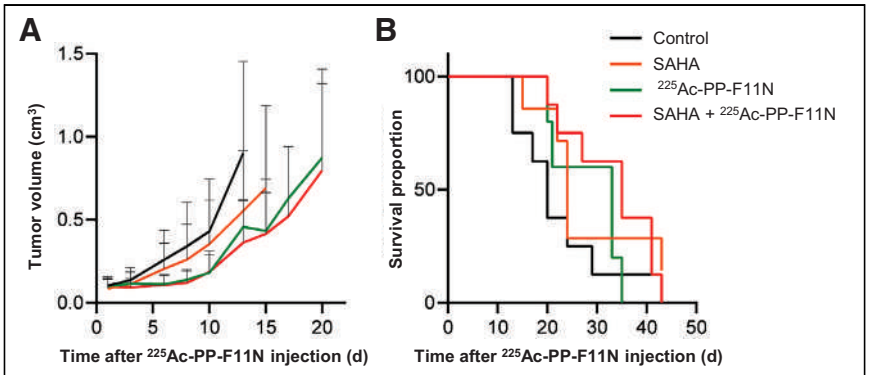

C

Treatments	Tumor volume (cm^3)	Survival (d)
Control	0.90 ± 0.55	22
^{225}Ac-PP-F11N	0.46 ± 0.16*	28
SAHA	0.55 ± 0.36	25
SAHA + ^{225}Ac-PP-F11N	0.36 ± 0.25*	33*

FIGURE 4. Tumor growth inhibition and prolonged survival in SAHA and ^{225}Ac-PP-F11N–treated mice. (A) Tumor growth curves in A431/CCKBR xenografted mice after administration of ^{225}Ac-PP-F11N or phosphate-buffered saline (control) alone or in combination with SAHA. Values represent mean ± SD. (B) Survival proportion presented as Kaplan–Meier curves of control and different treatment groups. (C) Mean tumor volume ± SD on day 13 and survival in control and different treatment groups. *$P < 0.05$.

response to γ-rays supported cervical carcinoma cell survival, and the inhibition of Rac1 activity abrogated the radioresistance conferred by Rac1/p38 activation and significantly enhanced apoptosis (*31*). Thus, the important roles of the HDACs, ATM/p53, and p38 pathways in DDR and survival, previously reported and identified by our study, increased phosphorylations in response to TAT, pointing them to potential radiosensitizing targets.

Indeed, in the present study, inhibition of the HDAC class II, ATM, and p38 pathways by small-molecule inhibitors significantly enhanced the cytotoxic effect of ^{225}Ac-PP-F11N in CCKBR-positive cells. As expected, interference with DDR pathways by ATMi AZD1390 sensitized cancer cells to ionizing radiation, whereas p38i showed a weaker radiosensitizing effect than HDAC inhibitor, which showed the synergistic effect with ^{225}Ac-PP-F11N. Thus, in a search for the most efficient radiosensitizing strategy for clinical applications, we selected for in vivo validation the HDAC inhibitor SAHA (vorinostat), which is approved by the Food and Drug Administration for the treatment of cutaneous T-cell lymphoma patients (*32*). In addition, SAHA showed better anticancer activity than the other HDAC inhibitor, TMP269, and significantly enhanced the DNA damage and cytotoxicity of ^{225}Ac-PP-F11N in our in vitro assays. As compared with the monotreatment and control groups, SAHA in combination with ^{225}Ac-PP-F11N produced the most effective therapeutic response in vivo.

This first proof-of-concept study confirms the radiosensitizing potential of HDAC inhibitors, yet to maximize therapeutic response this study requires further optimization. In agreement with our results, the radiosensitization effects of the HDAC inhibitor were previously reported in various cancer models (*19*), and more recently, cotreatment with vorinostat improved the response to the radiolabeled peptide ligand ^{212}Pb-DOTA-MC1L in mice bearing human melanoma xenografts (*33*). Furthermore, in CD1 nude mice human xenografted with RT112 bladder cancer, radiotherapy in combination with the HDAC inhibitor panobinostat delayed cancer growth without significantly increasing acute and short-term normal-tissue radiation toxicity (*34*). Similarly, in our study, neither acute radiation toxicity to the kidney or stomach nor significant body weight losses were identified in mice that received combinatory treatment, indicating that the applied doses of ^{225}Ac-PP-F11N and SAHA were relatively safe and well tolerated. Moreover, the combination of vorinostat with external radiotherapy has recently entered clinical trials with non–small cell lung cancer (NCT00821951) and glioblastoma (NCT03426891) patients to assess safety, tolerability, and efficacy, thus suggesting that HDAC inhibitor treatment is a clinically feasible radiosensitizing strategy for TAT in cancer patients.

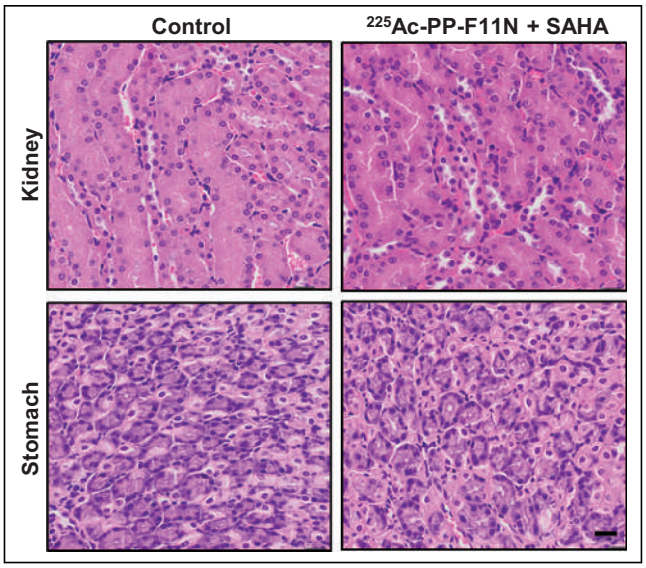

FIGURE 5. Histology of kidney and stomach. Representative images of tissue sections stained with hematoxylin and eosin of kidney and stomach isolated from control and ^{225}Ac-PP-F11N and SAHA-treated mice 35–43 d after injection of activity. Scale bar = 20 μm.

CONCLUSION

Our phosphoproteomic analysis followed by a validation study revealed alterations in the signaling networks and identified radiosensitizing molecular targets, including HDAC, ATM, and p38, in response to TAT with a ^{225}Ac-labeled minigastrin analog in CCKBR-positive cancer cells. In this study, the explored radiobiology was used to verify new radiosensitizing strategies based on the targeting radiation-activated and survival-supporting pathways. The combination of ^{225}Ac-PP-F11N with the HDAC inhibitor vorinostat enhanced DNA damage and cancer cell cytotoxicity and improved therapeutic efficacy in A431/CCKBR tumor–bearing nude mice. Our proof-of-concept study indicates that HDAC inhibitor treatment is an effective radiosensitization strategy for

^{225}Ac-PP-F11N and further recommends phosphoproteomics for the identification of novel radiosensitizing targets.

DISCLOSURE

This research was supported by funds from the Swiss Cancer League (KFS-3960-08-2016-R) to Michal Grzmil, Martin Béhé, and Roger Schibli. Martin Béhé and Roger Schibli are listed as inventors on patent WO2015/067473: "Mini-Gastrin Analog, in Particular for Use in CCK2 Receptor Positive Tumor, Diagnosis or Treatment." No other potential conflict of interest relevant to this article was reported.

ACKNOWLEDGMENT

We thank the Functional Genomic Center Zürich for proteomics and phosphoproteomics service and support.

KEY POINTS

QUESTION: How do cancer cells respond to TAT, and which survival-supporting pathways are potential molecular targets for the rational development of radiosensitizing strategies?

PERTINENT FINDINGS: TAT with ^{255}Ac-PP-F11N induced DDR, cell cycle regulation, RNA transcription and processing, as well as signal transduction pathways in treated cancer cells. Targeting of identified HDAC, ATM, and p38 pathways shows radiosensitizing potential in cancer cells, and the clinically approved HDAC inhibitor vorinostat (SAHA) significantly improves the efficacy of TAT in vivo.

IMPLICATIONS FOR PATIENT CARE: Patients with CCKBR-positive tumors might benefit from combinatory treatment with HDAC inhibitor and a radioactive minigastrin analog because of the enhanced radiosensitivity and anticancer activity of the HDAC inhibitor.

REFERENCES

1. Grzmil M, Meisel A, Behé M, Schibli R. An overview of targeted radiotherapy. In: Lewis JS, Windhorst AD, Zeglis BM, eds. *Radiopharmaceutical Chemistry.* Springer International Publishing; 2019:85–100.
2. Hennrich U, Kopka K. Lutathera®: the first FDA- and EMA-approved radiopharmaceutical for peptide receptor radionuclide therapy. *Pharmaceuticals (Basel).* 2019;12:114.
3. FDA approves Pluvicto/Locametz for metastatic castration-resistant prostate cancer. *J Nucl Med.* 2022;63(5):13N.
4. Poty S, Francesconi LC, McDevitt MR, Morris MJ, Lewis JS. α-emitters for radiotherapy: from basic radiochemistry to clinical studies—part 1. *J Nucl Med.* 2018; 59:878–884.
5. Kratochwil C, Bruchertseifer F, Giesel FL, et al. ^{225}Ac-PSMA-617 for PSMA-targeted α-radiation therapy of metastatic castration-resistant prostate cancer. *J Nucl Med.* 2016;57:1941–1944.
6. Qin Y, Imobersteg S, Blanc A, et al. Evaluation of actinium-225 labeled minigastrin analogue [^{225}Ac]Ac-DOTA-PP-F11N for targeted alpha particle therapy. *Pharmaceutics.* 2020;12:1088.
7. Rottenburger C, Nicolas GP, McDougall L, et al. Cholecystokinin 2 receptor agonist ^{177}Lu-PP-F11N for radionuclide therapy of medullary thyroid carcinoma: results of the Lumed phase 0a study. *J Nucl Med.* 2020;61:520–526.
8. Aloj L, Caraco C, Panico M, et al. In vitro and in vivo evaluation of ^{111}In-DTPAGlu-G-CCK8 for cholecystokinin-B receptor imaging. *J Nucl Med.* 2004;45:485–494.
9. Deutsch EW, Bandeira N, Sharma V, et al. The ProteomeXchange consortium in 2020: enabling 'big data' approaches in proteomics. *Nucleic Acids Res.* 2020;48: D1145–D1152.
10. Butler LM, Agus DB, Scher HI, et al. Suberoylanilide hydroxamic acid, an inhibitor of histone deacetylase, suppresses the growth of prostate cancer cells in vitro and in vivo. *Cancer Res.* 2000;60:5165–5170.
11. Grzmil M, Qin Y, Schleuniger C, et al. Pharmacological inhibition of mTORC1 increases CCKBR-specific tumor uptake of radiolabeled minigastrin analogue [^{177}Lu]Lu-PP-F11N. *Theranostics.* 2020;10:10861–10873.
12. Graf F, Fahrer J, Maus S, et al. DNA double strand breaks as predictor of efficacy of the alpha-particle emitter Ac-225 and the electron emitter Lu-177 for somatostatin receptor targeted radiotherapy. *PLoS One.* 2014;9:e88239.
13. Sgouros G, Bodei L, McDevitt MR, Nedrow JR. Radiopharmaceutical therapy in cancer: clinical advances and challenges. *Nat Rev Drug Discov.* 2020;19:589–608.
14. Gill MR, Falzone N, Du Y, Vallis KA. Targeted radionuclide therapy in combined-modality regimens. *Lancet Oncol.* 2017;18:e414–e423.
15. Frejno M, Meng C, Ruprecht B, et al. Proteome activity landscapes of tumor cell lines determine drug responses. *Nat Commun.* 2020;11:3639.
16. Nader JS, Boissard A, Henry C, et al. Cross-species proteomics identifies CAPG and SBP1 as crucial invasiveness biomarkers in rat and human malignant mesothelioma. *Cancers (Basel).* 2020;12:2430.
17. Wiechmann S, Saupp E, Schilling D, et al. Radiosensitization by kinase inhibition revealed by phosphoproteomic analysis of pancreatic cancer cells. *Mol Cell Proteomics.* 2020;19:1649–1663.
18. Stuparu AD, Capri JR, Meyer CAL, et al. Mechanisms of resistance to prostate-specific membrane antigen-targeted radioligand therapy in a mouse model of prostate cancer. *J Nucl Med.* 2021;62:989–995.
19. Karagiannis TC, El-Osta A. Modulation of cellular radiation responses by histone deacetylase inhibitors. *Oncogene.* 2006;25:3885–3893.
20. Parra M. Class IIa HDACs: new insights into their functions in physiology and pathology. *FEBS J.* 2015;282:1736–1744.
21. Hanigan TW, Aboukhatwa SM, Taha TY, Frasor J, Petukhov PA. Divergent JNK phosphorylation of HDAC3 in triple-negative breast cancer cells determines HDAC inhibitor binding and selectivity. *Cell Chem Biol.* 2017;24:1356–1367.e8.
22. Biade S, Stobbe CC, Boyd JT, Chapman JD. Chemical agents that promote chromatin compaction radiosensitize tumour cells. *Int J Radiat Biol.* 2001;77:1033–1042.
23. Adant S, Shah GM, Beauregard JM. Combination treatments to enhance peptide receptor radionuclide therapy of neuroendocrine tumours. *Eur J Nucl Med Mol Imaging.* 2020;47:907–921.
24. Panier S, Boulton SJ. Double-strand break repair: 53BP1 comes into focus. *Nat Rev Mol Cell Biol.* 2014;15:7–18.
25. Eke I, Zong D, Aryankalayil MJ, et al. 53BP1/RIF1 signaling promotes cell survival after multifractionated radiotherapy. *Nucleic Acids Res.* 2020;48:1314–1326.
26. Canman CE, Lim DS, Cimprich KA, et al. Activation of the ATM kinase by ionizing radiation and phosphorylation of p53. *Science.* 1998;281:1677–1679.
27. Fei P, El-Deiry WS. P53 and radiation responses. *Oncogene.* 2003;22:5774–5783.
28. Igea A, Nebreda AR. The stress kinase p38alpha as a target for cancer therapy. *Cancer Res.* 2015;75:3997–4002.
29. Deak M, Clifton AD, Lucocq LM, Alessi DR. Mitogen- and stress-activated protein kinase-1 (MSK1) is directly activated by MAPK and SAPK2/p38, and may mediate activation of CREB. *EMBO J.* 1998;17:4426–4441.
30. Wagner EF, Nebreda AR. Signal integration by JNK and p38 MAPK pathways in cancer development. *Nat Rev Cancer.* 2009;9:537–549.
31. Kim MJ, Byun JY, Yun CH, Park IC, Lee KH, Lee SJ. c-Src-p38 mitogen-activated protein kinase signaling is required for Akt activation in response to ionizing radiation. *Mol Cancer Res.* 2008;6:1872–1880.
32. Marks PA, Breslow R. Dimethyl sulfoxide to vorinostat: development of this histone deacetylase inhibitor as an anticancer drug. *Nat Biotechnol.* 2007;25: 84–90.
33. Li M, Liu D, Lee D, et al. Enhancing the efficacy of melanocortin 1 receptor-targeted radiotherapy by pharmacologically upregulating the receptor in metastatic melanoma. *Mol Pharm.* 2019;16:3904–3915.
34. Groselj B, Ruan JL, Scott H, et al. Radiosensitization in vivo by histone deacetylase inhibition with no increase in early normal tissue radiation toxicity. *Mol Cancer Ther.* 2018;17:381–392.

Evaluation of Hepatotoxicity from Peptide Receptor Radionuclide Therapy in Patients with Gastroenteropancreatic Neuroendocrine Tumors and a Very High Liver Tumor Burden

Denise A. Gococo-Benore*[1], Justin Kuhlman*[1], Ephraim E. Parent[2], Akash Sharma[2], Joseph Accurso[2], Ming Yang[3], Ayse Tuba Kendi[4], Geoff Johnson[4], Mohamad Bassam Sonbol[5], Timothy Hobday[6], Thorvardur R. Halfdanarson[6], and Jason Starr[7]

[1]*Department of Internal Medicine, Mayo Clinic, Jacksonville, Florida;* [2]*Department of Radiology, Mayo Clinic, Jacksonville, Florida;* [3]*Department of Radiology, Mayo Clinic, Scottsdale, Arizona;* [4]*Department of Radiology, Mayo Clinic, Rochester, Minnesota;* [5]*Division of Hematology Oncology, Mayo Clinic, Phoenix, Arizona;* [6]*Division of Medical Oncology, Mayo Clinic, Rochester, Minnesota; and* [7]*Division of Hematology Oncology, Mayo Clinic, Jacksonville, Florida*

The aim of the current study was to describe the risk of hepatotoxicity for patients with gastroenteropancreatic neuroendocrine tumors undergoing peptide receptor radionuclide therapy (PRRT) with a very high liver tumor burden, defined as tumor involving more than 75% of the liver. **Methods:** We conducted a retrospective analysis of 371 patients who received at least 1 cycle of ^{177}Lu-DOTATATE at Mayo Clinic for advanced gastroenteropancreatic neuroendocrine tumors. We identified 15 total patients with more than 75% liver involvement on ^{68}Ga-DOTATATE PET/CT and with either a contrast-enhanced abdominal MRI or dual-phase abdominal CT examination. **Results:** Of the 15 patients with more than 75% liver involvement, 1 experienced hepatotoxicity (i.e., worsening liver enzymes or bilirubin) as defined by the Common Terminology Criteria for Adverse Events, version 5.0. No patients had grade 3–5 hepatotoxicity (i.e., clinical signs of liver failure). **Conclusion:** When considering the risk of liver injury from PRRT due to burden of disease, our data suggest that PRRT may be a safe option in patients with more than 75% liver involvement. Future efforts should be made to determine the safety profile of PRRT in patients with varying degrees of liver involvement.

Key Words: gastrointestinal; neuroendocrine; peptides; hepatic; neuroendocrine tumor; peptide receptor radionuclide therapy

J Nucl Med 2023; 64:880–884
DOI: 10.2967/jnumed.122.264533

Neuroendocrine tumors (NETs) constitute a heterogeneous group of tumors arising from neuroendocrine cells. They can originate in any organ that has neuroendocrine cells but most commonly are in the pulmonary system and the gastrointestinal tract. The liver is the most common distant site of metastasis in patients with gastroenteropancreatic NETs and is also the main site of organ involvement leading to morbidity and mortality (*1*). Liver tumor burden is also a consideration when determining patient candidacy for peptide receptor radionuclide therapy (PRRT). Although there is concern about an increased risk of radiation-induced hepatitis with increasing liver involvement, PRRT with ^{177}Lu-DOTATATE has been shown to be both safe and effective in patients with more than 50% liver involvement, with no difference in progression-free survival (*2*). However, it is unclear whether PRRT is safe in patients with a very high liver tumor involvement, namely, in those for whom the liver appears to be mostly replaced by metastatic tumor.

PPRT is a paradigm-shifting treatment for gastroenteropancreatic NETs, especially since the publication of the NETTER-1 trial on patients with small-bowel NETs (*2*). Although no randomized trials of PRRT in patients with pancreatic NETs have yet been reported, there is an abundance of evidence suggesting efficacy in that patient cohort, which comprises the second largest subgroup of patients with gastroenteropancreatic NETs (*3*). ^{177}Lu-DOTATATE has been rapidly adopted as a treatment modality in the United States since its approval by the Food and Drug Administration in January 2018. PRRT works by binding to the somatostatin receptor, most commonly somatostatin receptor 2, on the surface of the NET cell. This allows for the discriminative delivery of a payload (i.e., radionuclide). ^{177}Lu-DOTATATE emits β- and γ-radiation causing single-stranded DNA breaks within the cell (*4,5*). The more common toxicities that have been discovered in relation to PRRT include nephrotoxicity, myelosuppression, and hepatotoxicity (*6–11*). Although there is a hypothetical concern about an increased risk of radiation-induced hepatitis in patients with increasing liver involvement, PRRT with ^{177}Lu-DOTATATE has been shown to be both safe and effective in those with less than 25%, 25%–50%, and more than 50% liver involvement, with no significant differences in progression-free survival or rates of hepatotoxicity despite varying rates of tumor burden (*7*). It is worth questioning whether the gradient of liver involvement, for example more than 75% involvement, would still have similar outcomes to more than 50%. Thus, it remains unknown whether PRRT is safe in patients with a very high liver tumor involvement, namely, in those for whom the liver appears to be mostly replaced by metastatic tumor. The aim of this study was to assess and describe the risk of hepatotoxicity from PRRT in NET patients with more than 75% liver involvement.

MATERIALS AND METHODS

The institutional review board approved this retrospective study, and the requirement to obtain informed consent was waived. We then conducted a retrospective analysis of 371 patients who received at least 1 cycle of PRRT at 1 of the 3 Mayo Clinic sites (Minnesota, Florida,

Received Jun. 16, 2022; revision accepted Feb. 7, 2023.
For correspondence or reprints, contact Jason Starr (starr.jason@mayo.edu).
*Contributed equally to this work.
Published online Apr. 20, 2023.

or Arizona). As a screening tool, we performed a refined search for "innumerable liver metastasis" within either the ^{68}Ga-DOTATATE PET/CT or contrast-enhanced abdominal MRI or CT imaging report. We used this search term to identify potential candidates with permeative or extensive hepatic metastatic disease that compromised most of the physiologic liver parenchyma. Although we did not specifically try to identify patients with bulky oligometastatic hepatic disease that could in theory replace large portions of the liver parenchyma, this presentation is much less common (*12*). We identified 22 potential patients with more than 75% liver metastatic involvement based on clinical reports, and subsequently, 3 independent reviewers confirmed a total of 15 patients with more than 75% liver involvement as identified on ^{68}Ga-DOTATATE PET/CT and either diagnostic contrast-enhanced MRI or CT. Baseline laboratory values were obtained within 1 mo before the initiation of PRRT. Post-PRRT laboratory values were determined as the highest recorded values anywhere from the start of PRRT to 3 mo after the completion of therapy. Ascites as a complication of PRRT was defined as any reading of ascites on imaging after at least 1 cycle of PRRT in a patient who did not previously show ascites on any formal imaging. Hepatotoxicity was defined as any change in alanine aminotransferase, aspartate aminotransferase, alkaline phosphatase, or total bilirubin that was grade 2 or higher according to the Common Terminology Criteria for Adverse Events, version 5.0. The time to follow-up was calculated from the start of PRRT to the date of each patient's last follow-up appointment.

Selection of Regions of Interest

To determine that more than 75% of liver had been replaced by hepatic metastatic disease, ^{68}Ga-DOTATATE PET images were coregistered to either T1-weighted contrast-enhanced sequences of the corresponding MRI of the liver (8/15) or contrast-enhanced CT (7/15) if MRI was not available. A board-certified radiologist using the Absolute Threshold Contouring Tool (MIM Software) drew regions of interest over the enhancing tumors and entire liver to calculate a preliminary percentage of tumor involvement of the liver. Metabolically active somatostatin-expressing hepatic metastatic disease was then confirmed in the enhancing lesions when the ^{68}Ga-DOTATATE SUV_{max} of the enhancing tumor was more than 2.0 times that of the normal hepatic parenchyma. This ^{68}Ga-DOTATATE PET analysis was done to confirm that the enhancing lesions were also somatostatin-avid and thus likely to incorporate ^{177}Lu-DOTATATE at a rate greater than physiologic liver parenchyma. The SUV_{max} of normal hepatic parenchyma was identified by placing up to a 30-mm spheric region of interest over nonenhancing normal hepatic liver parenchyma, depending on the area of the uninvolved liver.

RESULTS

Demographics

In total, 15 patients were identified as having more than 75% liver involvement before initiation of PRRT. Patient demographics are described in Table 1. The median time to follow-up was 19.4 mo (range, 3.9–45.6 mo). The median age of the included patients was 62 y (range, 36–77 y), and most patients were male (11/15; 73%). The median Eastern Cooperative Oncology Group performance status for all patients was 1 (range, 0–2) before PRRT. The primary site of disease was the small bowel (9/15; 60%), and most patients had World Health Organization grade 2 tumors (9/15; 60%) (*13*). Before the initiation of PRRT, 6 of 15 (40%) patients had grade 1 elevation in alkaline phosphatase levels at baseline. One of these 6 patients had a concomitant grade 1 elevation in aspartate transaminase and alanine transaminase levels (Table 2). Additionally, 3 of 15 (20%) patients had a grade 3 elevation in alkaline phosphatase. Ascites was present on abdominal imaging in 5 of 15 (33%) patients: 3 patients had grade 1 ascites, and 2 patients had grade 2 ascites. In 1 of 15 patients, hepatic miliary disease was noted on ^{68}Ga DOTATATE PET/CT and MRI (Figs. 1A–1D). Regarding concomitant medication use, 9 of 15 patients were deemed as taking potentially hepatotoxic medications: 6 were taking acetaminophen as needed for pain, 2 were taking moderate-intensity statin medications, and 1 was taking allopurinol.

TABLE 1
Patient Demographics

Demographic	Data
Total patients	15
Mean age (y)	62
Sex	
Male	11 (73%)
Female	4 (27%)
Primary site of disease	
Small bowel	9
Pancreas	5
Unknown	1
World Health Organization tumor grade	
1	4
2	9
3	1
Unknown	1

Data are *n,* except for age.

Hepatotoxicity

After PRRT, in 1 of 15 (6%) patients we identified hepatotoxicity, which we defined as any change in alanine aminotransferase, aspartate aminotransferase, alkaline phosphatase, or total bilirubin of grade 2 or higher according to the Common Terminology Criteria for Adverse Events, version 5.0 (Table 2). This patient experienced grade 2 hyperbilirubinemia. Grade 1 hepatoxicity was also discovered in 5 of 15 (53%) patients, with 4 of these patients having a grade 1 elevation in alkaline phosphatase levels alone and 1 of these patients also having a concomitant grade 1 elevation in aspartate aminotransferase. No patients in our review experienced grade 3–5 hepatotoxicity. Grade 1 ascites was noted in 3 of 15 (33%) patients and was not present before therapy, but none of these cases of ascites occurred in the setting of fulminant hepatic failure. All 3 cases of ascites appeared to be secondary to disease progression rather than a complication of PRRT. Albumin and international normalized ratios were also monitored during and after therapy, and no patients experienced adverse events in relation to these 2 indices. Interestingly, the patient who had miliary spread of hepatic disease did not experience significant hepatotoxicity as a complication of therapy.

Hematologic Toxicity, Nephrotoxicity, and Other Adverse Effects

Cytopenia (defined as grade 2 or above in the Common Terminology Criteria for Adverse Events, version 5.0) developed in 4 of 12 (33%) patients who did not have cytopenia present before treatment. Only 2 of these patients had grade 3 toxicity. One of these 4 patients had a gastrointestinal bleed in the setting of PRRT-induced cytopenia.

TABLE 2
Pre-PRRT and Post-PRRT Laboratory Values

Treatments before PRRT	Pre-PRRT laboratory values					No. of PRRT cycles	Post-PRRT laboratory values				
	AST	ALT	ALP	TBIL	Ascites		AST	ALT	ALP	TBIL	Ascites
Somatostatin analog	17	9	128	0.7	Y*	4	17	15	162*	0.3	Y
Somatostatin analog, everolimus	23	27	98	0.9	N	4	25	29	94	0.5	N
Somatostatin analog	24	23	81	0.4	N	4	34	44	138*	0.3	N
Somatostatin analog	27	24	84	0.4	N	3	46	18	114*	0.9	N
Somatostatin analog, everolimus	24	14	164	0.3	Y*	1	47	41	177	0.5	N
Somatostatin analog	16	12	134	0.3	N	4	25	13	111	0.5	Y*
Somatostatin analog	81	60	206	0.2	N	4	73	73	283	0.4	N
Somatostatin analog, everolimus	43	23	934	0.7	Y*	2	45	40	575	0.6	N
Somatostatin analog, everolimus	48	11	105	0.7	N	2	68*	19	151*	1.6†	Y*
Somatostatin analog, hepatic embolization	42	42	164	0.6	Y†	4	23	15	121	0.5	Y
None	95	114	723	1.2	N	4	107	124	685	1	N
Somatostatin analog, capecitabine	42	59	610	1.2	N	4	44	90	320	1.0	N
Somatostatin analog	27	25	170	0.3	N	4	27	24	224	0.6	Y*
Somatostatin analog, capecitabine	22	12	172	1	Y†	4	23	10	150	1.1	N
Somatostatin analog, everolimus	25	22	103	0.4	N	4	35	34	198*	0.3	N

*Grade 1 adverse event.
†Grade 2 adverse event.
AST = aspartate aminotransferase; ALT = alanine aminotransferase; ALP = alkaline phosphatase; TBIL = total bilirubin.

Additionally, 2 of 15 patients (13%) developed grade 2 renal failure after PRRT. Symptomatically, 6 of 15 (40%) patients complained of fatigue and 1 of 15 (6%) complained of nausea or vomiting after PRRT therapy. One patient developed a small-bowel obstruction after initiation of PRRT. Another patient with metastatic carcinoid heart disease developed acute pericarditis after initiation of PRRT, but after treatment with nonsteroidal antiinflammatory drugs, the patient was safely able to continue additional PRRT. Eastern Cooperative Oncology Group performance status declined in only 1 patient (6%), whereas the performance status of the rest of the patients remained the same or improved after treatment.

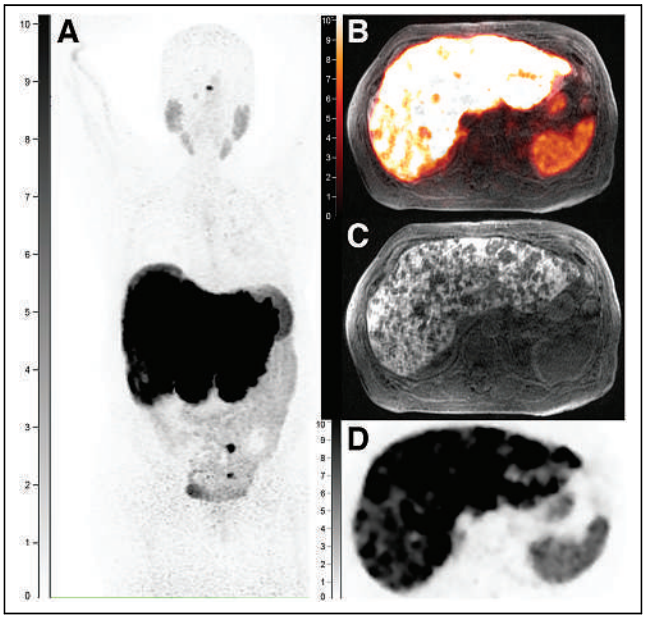

FIGURE 1. Miliary disease demonstrated on ^{68}Ga-DOTATATE PET/CT highlighting diffuse uptake in liver (PET maximum-intensity projection [MIP] [A], fused MRI/PET [B], and nonfused PET [D]) alongside T2 diffusion-weighted MRI of liver highlighting diffuse cancer involvement (MRI T2 diffusion-weighted image [C]). Scale = SUV.

Treatment Response and Survival

Overall, 4 of 15 patients completed fewer than 4 cycles of PRRT because of complications unrelated to hepatotoxicity: 1 experienced progressive disease, 1 developed severe renal failure, 1 developed cytopenia with infectious complications, and the last was still receiving PRRT at the time of analysis. Of those who had completed 4 cycles of PRRT (11/15; 73%) at the time of analysis, radiographic tumor response after therapy revealed improvement in 2 patients (18%), no change in 5 patients (45%), and progressive disease in 4 patients (36%). One patient had completed 3 cycles of PRRT and developed progressive disease. Two other patients had undergone only 2 cycles, and both experienced no change in radiographic tumor response. One patient has undergone just 1 cycle and has already demonstrated improvement. No patients died within 100 d of receiving PRRT. Five patients had died by the time of analysis. Among the 5 patients who died, the median time to death from the date of the last treatment with PRRT was 400 d (range, 100–619 d). Three patients died of progressive disease, 1 died of infection, and 1 died of renal failure.

DISCUSSION

Our retrospective review describes the largest analysis, to our knowledge, of patients with metastatic NETs who possessed a very high liver tumor burden (i.e., >75% involvement). Our results

suggest that PRRT may not pose a significant risk for hepatotoxicity in those with more than 75% liver involvement. Only 1 of 15 (6%) patients experienced a grade 2 or higher elevation in bilirubin level after PRRT with ^{177}Lu-DOTATATE. It remains indeterminate whether this patient experienced hepatoxicity in response to PRRT or disease progression. Previously, it has been shown that those with less than 25%, 25%–50%, and more than 50% hepatic involvement did not experience significant hepatotoxicity as a result of PRRT (*7*). A recent study suggested that pretreatment abnormalities of liver chemistries were associated with increased risk of PRRT cancellation, but that study did not address the liver tumor burden and safety of PRRT in patients with extensive liver metastases (*14*). Several studies have evaluated the estimated absorbed doses of organs and metastatic lesions of patients treated with ^{177}Lu-DOTATATE (*15–17*) and showed wide variation in the mean absorbed dose to tumor lesions, with sample reported average doses of 4.79 ± 4.23 Gy/GBq (*15*) and 3.85 ± 1.74 Gy/GBq (*18*). Our own unpublished data (August 2019) on a separate cohort of patients undergoing ^{177}Lu-DOTATATE, and who underwent same-day SPECT/CT to document uptake of ^{177}Lu-DOTATATE in the known metastatic disease, demonstrated a wide range of incorporation depending on the cycle of ^{177}Lu-DOTATATE treatment. Thus, because we did not perform prospective dosimetry on these patients, we did not attempt to retrospectively calculate an estimated radiation dose to the lesions and liver. Nonetheless, our laboratory and clinical findings support the notion that baseline liver tumor burden does not necessarily correlate with an increased risk for radiation-induced liver injury, even in patients with more than 75% liver involvement.

Although an increased rate of clinically overt hepatotoxicity (i.e., hepatic encephalopathy, ascites requiring intervention, and death from acute liver failure) has been previously reported in those receiving PRRT when compared with those receiving traditional NET therapy, details on hepatic tumor burden were lacking. For example, a retrospective analysis of 102 patients with pancreatic NETs treated with ^{177}Lu-DOTATATE found that a liver tumor burden of more than 50%, more than 1 line of chemotherapy, and an elevated level of alkaline phosphatase were independent risk factors for both progression and death, but only 1.0% of patients developed radiation hepatotoxicity from ^{177}Lu-DOTATATE (*19*). Several other retrospective studies of patients with NETs and documented metastatic liver disease treated with ^{177}Lu-DOTATATE found no cases of radiation-induced hepatotoxicity but also did not clearly document the degree of hepatic involvement (*20–22*). In our review, 3 patients developed new-onset ascites that was not present on formal abdominal imaging before PRRT, but each case reflected only grade 1 ascites and was likely attributable more to disease progression than to a complication of therapy. Moreover, no patients developed hepatic encephalopathy or acute liver failure or died within 100 d of treatment. Although 4 patients died from various causes, none died from treatment-associated liver failure. Although only 1 patient safely underwent radioembolization before PRRT, there may be an added hepatotoxic risk toward those who undergo previous radioembolization before PRRT (*7*).

Despite the availability of various radiopharmaceutical options for those with advanced gastroenteropancreatic NETs, all patients received ^{177}Lu-DOTATATE. This provides the highest affinity for somatostatin receptor 2–positive cells and undergoes renal clearance at an accelerated rate compared with other radiotherapies, such as ^{90}Y-DOTATOC, thereby decreasing the risks of bone marrow irradiation and nephrotoxicity (*23–26*). Although 42% of patients developed new cytopenias after PRRT, this rate represents no significant difference from the rate of cytopenias seen in traditional treatment modalities for metastatic NETs with liver involvement as reported elsewhere (*6,7*). Only 2 patients seemed to experience acute complications related to cytopenia: 1 patient experienced a gastrointestinal bleed, and another died of infectious complications. Although clinically significant nephrotoxicity after ^{177}Lu-DOTATATE PRRT is considered rare, 2 patients (13%) experienced renal failure after PRRT, consistent with previous reports (*6,7*). However, both were promptly seen and evaluated by nephrology specialists, and in neither case was the kidney injury attributed to the PRRT. One was thought to be secondary to dehydration compounded by renal oxalosis due to enteric hyperoxaluria after small-bowel resection for NETs. The second case demonstrated a resolution in estimated glomerular filtration rate seemingly overnight and was attributed to dehydration and the use of medications, including pseudoephedrine. Patients with progressive hepatic disease have reported a significantly improved quality of life in response to PRRT with ^{177}Lu-DOTATATE (*27*). In our own review, the Eastern Cooperative Oncology Group performance status remained the same or improved after PRRT in all but a single patient.

There are several limitations to the current review. In addition to the retrospective nature of the study, the primary limitation is the small sample size. Future directions should include validation of our results on a larger population with consideration of collaboration across multiple institutions. Future reproducibility incorporating the current methodology may also be limited given the subjective criteria for patients with more than 75% liver involvement as determined by 3 independent radiologists. Moreover, our study lacks information on the lesion and whole-liver dosimetry, which is an important factor to properly assess tumor burden.

CONCLUSION

When considering the risk of liver injury from PRRT due to burden of disease, our data suggest that PRRT may be a safe option even in patients with more than 75% liver involvement. Future studies should focus on stratifying patients according to the degree of liver involvement and volume of distribution (i.e., dosimetry). Moreover, efforts should be made to determine the safety profile on patients with an extremely high liver tumor burden.

DISCLOSURE

Jason Starr has received honoraria for consulting and serving on advertising boards for Ipsen, Advanced Accelerated Applications, Pfizer, Taiho, Tersera, Natera, Tempus, Cancer Expert Now, and Helsinn Therapeutics. No other potential conflict of interest relevant to this article was reported.

KEY POINTS

QUESTION: Is the risk of life-threatening hepatotoxicity from PRRT too great in NET patients with a liver tumor burden greater than 75%?

PERTINENT FINDINGS: Our retrospective cohort study of 15 patients showed that PRRT does not increase the risk of hepatotoxicity in this population.

IMPLICATIONS FOR PATIENT CARE: PRRT is likely a safe option even in patients with a very high liver tumor burden.

REFERENCES

1. Cai W, Tan Y, Ge W, Ding K, Hu H. Pattern and risk factors for distant metastases in gastrointestinal neuroendocrine neoplasms: a population-based study. *Cancer Med.* 2018;7:2699–2709.
2. Strosberg J, El-Haddad G, Wolin E, et al. Phase 3 trial of ^{177}Lu-Dotatate for midgut neuroendocrine tumors. *N Engl J Med.* 2017;376:125–135.
3. Starr JS, Sonbol MB, Hobday TJ, Sharma A, Kendi AT, Halfdanarson TR. Peptide receptor radionuclide therapy for the treatment of pancreatic neuroendocrine tumors: recent insights. *Onco Targets Ther.* 2020;13:3545–3555.
4. Kunz PL, Reidy-Lagunes D, Anthony LB, et al. Consensus guidelines for the management and treatment of neuroendocrine tumors. *Pancreas.* 2013;42:557–577.
5. Bergsma H, van Vliet EI, Teunissen JJ, et al. Peptide receptor radionuclide therapy (PRRT) for GEP-NETs. *Best Pract Res Clin Gastroenterol.* 2012;26:867–881.
6. Cives M, Strosberg J. Radionuclide therapy for neuroendocrine tumors. *Curr Oncol Rep.* 2017;19:9.
7. Katona BW, Roccaro GA, Soulen MC, et al. Efficacy of peptide receptor radionuclide therapy in a United States based cohort of metastatic neuroendocrine tumor patients: single-institution retrospective analysis. *Pancreas.* 2017;46:1121–1126.
8. Riff BP, Yang Y-X, Soulen MC, et al. Peptide receptor radionuclide therapy–induced hepatotoxicity in patients with metastatic neuroendocrine tumors. *Clin Nucl Med.* 2015;40:845–850.
9. Bodei L, Cremonesi M, Ferrari M, et al. Long-term evaluation of renal toxicity after peptide receptor radionuclide therapy with ^{90}Y-DOTATOC and ^{177}Lu-DOTATATE: the role of associated risk factors. *Eur J Nucl Med Mol Imaging.* 2008;35:1847–1856.
10. Kwekkeboom DJ, Teunissen JJ, Bakker WH, et al. Radiolabeled somatostatin analog [^{177}Lu-DOTA0, Tyr3] octreotate in patients with endocrine gastroenteropancreatic tumors. *J Clin Oncol.* 2005;23:2754–2762.
11. Sabet A, Ezziddin K, Pape U-F, et al. Long-term hematotoxicity after peptide receptor radionuclide therapy with ^{177}Lu-octreotate. *J Nucl Med.* 2013;54:1857–1861.
12. Eshmuminov D, Studer DJ, Lopez Lopez V, et al. Controversy over liver transplantation or resection for neuroendocrine liver metastasis: tumor biology cuts the deal. *Ann Surg.* August 17, 2022 [Epub ahead of print].
13. Strosberg J, Kunz PL, Hendifar A, et al. Impact of liver tumour burden, alkaline phosphatase elevation, and target lesion size on treatment outcomes with ^{177}Lu-Dotatate: an analysis of the NETTER-1 study. *Eur J Nucl Med Mol Imaging.* 2020; 47:2372–2382.
14. Heckert JM, Kipnis ST, Kumar S, et al. Abnormal pretreatment liver function tests are associated with discontinuation of peptide receptor radionuclide therapy in a US-based neuroendocrine tumor cohort. *Oncologist.* 2020;25:572–578.
15. Kamaldeep, Das T, Basu S, Banerjee S. Estimation of absorbed doses of indigenously produced "direct-route" lutetium-177-[^{177}Lu]Lu-DOTA-TATE PRRT in normal organs and tumor lesions in patients of metastatic neuroendocrine tumors: comparison with no-carrier-added [^{177}Lu]Lu-DOTA-TATE and the trend with multiple cycles. *Cancer Biother Radiopharm.* 2022;37:214–225.
16. Thakral P, Sen I, Das SS, Manda D, Cb V, Malik D. Dosimetric analyses of intra-arterial versus standard intravenous administration of ^{177}Lu-DOTATATE in patients of well differentiated neuroendocrine tumor with liver-dominant metastatic disease. *Br J Radiol.* 2021;94:20210403.
17. Löser A, Schwarzenbock SM, Heuschkel M, Willenberg HS, Krause BJ, Kurth J. Peptide receptor radionuclide therapy with ^{177}Lu-DOTA-octreotate: dosimetry, nephrotoxicity, and the effect of hematological toxicity on survival. *Nucl Med Commun.* 2018;39:236–246.
18. Thakral P, Sen I, Pant V, et al. Dosimetric analysis of patients with gastro entero pancreatic neuroendocrine tumors (NETs) treated with PRCRT (peptide receptor chemo radionuclide therapy) using Lu-177 DOTATATE and capecitabine/temozolomide (CAP/TEM). *Br J Radiol.* 2018;91:20170172.
19. Fröss-Baron K, Garske-Roman U, Welin S, et al. ^{177}Lu-DOTATATE therapy of advanced pancreatic neuroendocrine tumors heavily pretreated with chemotherapy: analysis of outcome, safety, and their determinants. *Neuroendocrinology.* 2021; 111:330–343.
20. Ezziddin S, Khalaf F, Vanezi M, et al. Outcome of peptide receptor radionuclide therapy with ^{177}Lu-octreotate in advanced grade 1/2 pancreatic neuroendocrine tumours. *Eur J Nucl Med Mol Imaging.* 2014;41:925–933.
21. Demirci E, Kabasakal L, Toklu T, et al. ^{177}Lu-DOTATATE therapy in patients with neuroendocrine tumours including high-grade (WHO G3) neuroendocrine tumours: response to treatment and long-term survival update. *Nucl Med Commun.* 2018;39:789–796.
22. Sansovini M, Severi S, Ianniello A, et al. Long-term follow-up and role of FDG PET in advanced pancreatic neuroendocrine patients treated with ^{177}Lu-DOTATATE. *Eur J Nucl Med Mol Imaging.* 2017;44:490–499.
23. Rindi G, Klimstra DS, Abedi-Ardekani B, et al. A common classification framework for neuroendocrine neoplasms: an International Agency for Research on Cancer (IARC) and World Health Organization (WHO) expert consensus proposal. *Mod Pathol.* 2018;31:1770–1786.
24. De Jong M, Valkema R, Jamar F, et al. Somatostatin receptor-targeted radionuclide therapy of tumors: preclinical and clinical findings. *Semin Nucl Med.* 2002;32:133–140.
25. Druce MR, Lewington V, Grossman AB. Targeted radionuclide therapy for neuroendocrine tumours: principles and application. *Neuroendocrinology.* 2010;91:1–15.
26. Reubi JC, Mäcke HR, Krenning EP. Candidates for peptide receptor radiotherapy today and in the future. *J Nucl Med.* 2005;46(suppl 1):67S–75S.
27. Marinova M, Mücke M, Fischer F, et al. Quality of life in patients with midgut NET following peptide receptor radionuclide therapy. *Eur J Nucl Med Mol Imaging.* 2019;46:2252–2259.

Efficacy and Safety of ^{124}I-MIBG Dosimetry-Guided High-Activity ^{131}I-MIBG Therapy of Advanced Pheochromocytoma or Neuroblastoma

Ines Maric[1,2], Manuel Weber[1,2], Andre Prochnow[1], Jochen Schmitz[1,2], Nicole Unger[2,3], Benedikt M. Schaarschmidt[2,4], Thorsten D. Poeppel[5], Christoph Rischpler[1,2], Andreas Bockisch[1,2], Ken Herrmann[1,2], Walter Jentzen[1,2], and Wolfgang P. Fendler[1,2]

[1]Department of Nuclear Medicine, University Hospital Essen, University Duisburg-Essen, Essen, Germany; [2]German Cancer Consortium (DKTK), partner site, Essen, Germany; [3]Department of Endocrinology, Diabetes and Metabolism, University Hospital Essen, University Duisburg-Essen, Essen, Germany; [4]Institute of Diagnostic and Interventional Radiology and Neuroradiology, University Hospital Essen, University Duisburg-Essen, Essen, Germany; and [5]Nuklearmedizin, MVZ CDT Strahleninstitut, Cologne, Germany

We aim to evaluate the efficacy and safety of ^{124}I-metaiodobenzylguanidine (MIBG) dosimetry-guided high-activity ^{131}I-MIBG therapy of advanced pheochromocytoma or neuroblastoma. **Methods:** Fourteen patients with advanced pheochromocytoma or neuroblastoma, age 9–69 y, underwent ^{124}I-MIBG PET scans and whole-body retention measurements to assess the whole-body dose as a surrogate of bone marrow toxicity and tumor (absorbed) dose per unit of administered activity. Dosimetry results together with individual patient characteristics were combined to guide a single therapeutic activity to achieve a high tumor dose without exceeding toxicity threshold. Toxicity was assessed for hematologic, hepatic, and renal function. Response was evaluated by RECIST, International Society of Pediatric Oncology Europe Neuroblastoma–like score, change in PET uptake, and quantitative PET parameters (SUV_{max}, SUV_{peak}, metabolic tumor volume, total lesion glycolysis), as well as visual decrease in number or in visual intensity of lesions on baseline to follow-up ^{124}I-MIBG PET/CT. **Results:** The average therapeutic activity was 14 GBq. Eleven of 14 patients (79%) received each more than 10 GBq. One male patient was treated with a single activity of 50 GBq. Three patients were treated with lower activities between 3.5 and 7.0 GBq. Median overall survival was 85 mo (95% CI), and median progression-free survival was 25 mo (95% CI). Four (29%) and 5 (36%) patients demonstrated response (complete response or partial response) by RECIST and functional imaging, respectively. One patient exceeded whole-body dose of 2 Gy and demonstrated grade 3 hematologic toxicity, which resolved spontaneously within 12 mo after the therapy without the need for further treatment. Three patients (21%) demonstrated transient grade 1 renal toxicity. **Conclusion:** ^{124}I-MIBG dosimetry-guided high-activity ^{131}I-MIBG therapy in patients with advanced pheochromocytoma or neuroblastoma resulted in durable responses with a low rate of manageable adverse events. Efficacy of ^{124}I-MIBG–guided activity escalation should further be assessed in a prospective setting.

Key Words: MIBG; therapy; dosimetry; theranostics

J Nucl Med 2023; 64:885–891
DOI: 10.2967/jnumed.122.264775

Received Aug. 15, 2022; revision accepted Jan. 30, 2023.
For correspondence or reprints, contact Ines Maric (ines.maric@uk-essen.de).
Published online Feb. 2, 2023.

Metaiodobenzylguanidine (MIBG), a guanethidine derivative, is a substrate for norepinephrine reuptake transporters, which are highly expressed on the cell surface of neuroendocrine tumors, such as pheochromocytoma or neuroblastoma (*1*). $^{123/131}$I-MIBG imaging is one of the most sensitive lesion detection modalities for pheochromocytoma and neuroblastoma. Although ^{123}I-MIBG allows for quantification, ^{124}I-MIBG offers the benefit of quantification at higher PET spatial resolution (*2,3*). Similar biodistribution compared with ^{123}I-MIBG allows for translation of established systems of image interpretation and therapy monitoring (e.g., International Society of Pediatric Oncology Europe Neuroblastoma score [SIOPEN] or Curie score) (*3–5*). ^{124}I-MIBG imaging and dosimetry is a companion tool for planning of high-activity ^{131}I-MIBG therapy (*6*).

Patients with malignant unresectable, metastatic, or recurring pheochromocytoma have a poor prognosis with an average 5-y survival rate of 12%–20% (*7,8*), whereas in refractory or relapsing neuroblastoma, the 10-y survival probability is less than 15% (*9*). Efficacy of ^{131}I-MIBG for the treatment of unresectable, locally advanced, and metastatic pheochromocytoma and paraganglioma using empiric activities led to recent US Food and Drug Administration approval (*10*). In the prospective trial, objective tumor response occurred in 15 patients (22%; 95% CI, 14%–33%). However, most patients did not demonstrate notable tumor shrinkage despite focal ^{131}I-MIBG uptake in tumor lesions. Nonresponder patients under empiric activities might benefit from high-activity regimens. Pretherapeutic ^{124}I-MIBG PET/CT-based dosimetry of the tumor and organs at risk enables planning of patient-specific activity escalation (*11,12*). However, feasibility, toxicity, and efficacy have, to the authors' knowledge, not yet been assessed.

The aim of this study was to evaluate the efficacy and safety of ^{124}I-MIBG dosimetry-guided high-activity ^{131}I-MIBG therapy in patients with long follow-up after treatment of advanced pheochromocytoma or neuroblastoma.

MATERIALS AND METHODS

Study Design

This is a retrospective, single center study of the efficacy and safety of ^{124}I-MIBG dosimetry-guided, activity-escalated ^{131}I-MIBG therapy of unresectable neural crest tumors. The goal was to achieve a high

tumor (absorbed) dose without exceeding the toxicity threshold. This retrospective analysis was approved by the ethics committee of the University Hospital Essen (reference no. 20–9656-BO). Long-term follow-up included survival, imaging, clinical information, and laboratory data. Primary endpoints in these patients were overall survival (OS) and progression-free survival (PFS) after ^{131}I-MIBG therapy. Secondary endpoints included late hematologic/liver/renal toxicity in relation to the estimated whole-body dose evaluated up to 12 mo after therapy and the efficacy of ^{124}I-MIBG-guided ^{131}1-MIBG therapy as determined by response rate (partial response [PR] and complete response [CR]) within 12 mo after therapy in relation to achieved lesion tumor doses.

Patient Cohort

Patients who underwent ^{124}I-MIBG PET/CT with subsequent ^{131}I-MIBG therapy between August 2006 and July 2016 were included. Thirty patients with histologically proven unresectable neural crest tumors were considered for evaluation. Pretherapeutic imaging revealed no detectable tumor lesions by means of ^{124}I-PET/CT in 16 patients. In total, 14 patients with at least 1 tumor lesion with measurable volume and uptake underwent tumor and whole-body dosimetry. All therapy patients demonstrated progressive disease at baseline, defined either by an endocrinologist/oncologist by worsening clinical symptoms or by radiology/nuclear medicine specialists, defined by RECIST, or both. All patients received a potassium iodide–saturated solution to prevent thyroid accumulation of free radioactive iodine starting 48 h before administration and continuing for 15 d after therapy according to European Association of Nuclear Medicine Practice Guidelines (*13*). The patients provided written informed consent before dosimetry and therapy and were admitted to our ward in accordance with radiation protection requirements. Both ^{124}I- and ^{131}I-MIBG were applied intravenously. Labeling and preparation of the carrier-added ^{124}I-MIBG are described elsewhere (*3*).

Tumor and Whole-Body Dosimetry

Our ^{124}I-MIBG dosimetry protocol involves determination of the estimated tumor dose per unit of administered ^{131}I-MIBG activity for selected tumor deposits by serial PET and PET/CT examinations (*14*) and of determination of the maximum tolerable whole-body ^{131}I-MIBG activity via whole-body retention measurements (*11*). The approach is similar to the pretherapy dosimetry protocol used in thyroid cancer patients (*15–17*). Both the tumor dose and maximum tolerable whole-body ^{131}I-MIBG activity serve as primary input for the choice of the actual recommended therapeutic activity and other interventions, supplemented by clinical judgment based on patient and disease characteristics (age, previous myelotoxic therapies, current general and nutritional condition, comorbidities, notes from [pediatric] oncologists, availability of autologous stem cells) and biochemistry results (bone marrow and kidney and liver function).

For tumor dosimetry, serial PET data were acquired 4, 24, 48, and 96–120 h after ^{124}I-MIBG administration (average activity of 46 MBq

TABLE 1
Patient Characteristics

Characteristic (n = 14)	Patient			
	n	%	Median	Range
Diagnosis				
Pheochromocytoma	10	(71)		
Neuroblastoma	4	(29)		
Sex				
Male	8	(57)		
Female	6	(43)		
Age at entry (y)			36	9–69
Time from diagnosis to entry (mo)			66	1–189
Prior treatments				
Surgery	13	(93)		
Radiotherapy	6	(43)		
Chemotherapy	7	(50)		
No. of ^{131}I-MIBG therapies				
1	14	(100)		
2	8	(57)		
3	2	(14)		
4	1	(7)		
5	1	(7)		
^{131}I-MIBG activity at entry (GBq)			10.5	3.5–50
^{131}I-MIBG activity, all treatments (GBq)			38	4.8–50
TNM				
N1	9	(64)		
M1 bone	8	(57)		
M1 visceral	9	(64)		

^{124}I-MIBG). The PET scans were performed on 2 PET systems: a dedicated ECAT EXACT HR+ PET scanner (Siemens) and a PET/CT Biograph Emotion Duo scanner (Siemens Medical Solutions). The interscanner variability was examined elsewhere (*18*), demonstrating good agreement between the 2 systems with individual deviations of less than 10%. PET and PET/CT emission data were acquired through whole-body scans performed from head to thigh using 5–8 bed positions (5 min each). PET image reconstruction was performed using an iterative attenuation-weighted ordered-subset expectation maximation algorithm (2 iterations and 8 subsets, 5-mm postreconstruction gaussian filter) (*17*). For the dedicated PET and PET/CT scanning, the rod source transmission data and CT data were used for PET attenuation correction, respectively. Recovery correction was performed as described by Jentzen et al. (*14*). The metastatic lesion volumes for recovery correction were estimated using anatomic information obtained by the CT component of PET/CT. If no lesion volume could be derived from anatomic information, a PET volumetric segmentation method was used (*19,20*). The predicted cumulative activity per unit of administered ^{131}I-MIBG activity (tumor residence time) was obtained using the time–activity curves of the serial PET scans corrected with the measured recovery coefficient and corrected for the difference in the physical half-lives of ^{124}I and ^{131}I (*14,21*). Both the tumor volume (mass) and the respective residence time were used to predict the tumor dose using the sphere model of OLINDA/EXM.

For whole-body dosimetry, multiple whole-body retention measurements (2, 4, 24, 48, 72, and 96 h after ^{124}I-MIBG administration) were performed placing the patient approximately 3 m in front of an uncollimated γ-camera (E.CAM Signature Series; Siemens). Anterior and posterior counts for calculation of a geometric mean were measured considering dead time effects. After correcting for the difference in the physical half-lives of ^{124}I and ^{131}I, the whole-body residence time was calculated using the whole-body retention curves. The predicted whole-body dose per unit administered activity was calculated using the whole-body-to-whole-body S values corrected for patient mass (*11*). The resulting whole-body dose per administered activity was used to calculate the maximum tolerable whole-body ^{131}I-MIBG activity, a value that represents the maximum therapeutic activity that can be safely administered without exceeding the 2-Gy whole-body absorbed dose threshold (as a surrogate to estimate the myelotoxicity).

Analysis

At least 1 and up to 4 tumor lesions with measurable volume and uptake were taken into consideration per patient. Toxicity was graded with Common Terminology Criteria for Adverse Events version 3.0. Response was evaluated by baseline to follow-up changes in ^{124}I-MIBG-PET/CT, defined by RECIST criteria (*10*), and by visual and quantitative (SUV_{max}, SUV_{peak}, metabolic tumor volume, total lesion glycolysis) PET analysis. For tumors in which exact size measurements were not available, such as osteoblastic bone metastases, a visual impression of nuclear medicine physicians was used. Visual ^{124}I-MIBG PET evaluation was categorized as follows: CR was described as the disappearance of all lesions; PR was a decrease in the number or visual intensity of lesions; stable disease was no discernible change; and progressive disease was the appearance of new lesions (*11*). Furthermore, we defined a SIOPEN-like score for baseline to follow-up response assessment (not including the assessment of soft-tissue areas of tumor) as follows: the scan area was segmented into 8 body regions, excluding the 4 lower limb areas, which are not included in the usual PET/CT scan field of view performed in the clinical routine in our institution. Each region was assigned with 1–6 points, corresponding to established SIOPEN scoring (*4*), and then summarized. The baseline to follow-up change in this sum was then used as an additional mean to assess the response in accordance with the SIOPEN score.

Statistics and Software

Statistical analysis was performed using IBM SPSS Statistics, version 26 (IBM Corp.). Patient characteristics, toxicity, and response are presented as descriptive statistics. Assessment of statistically significant differences between groups was performed using a *t* test. Predictors for PFS and OS were assessed by univariate Cox regression analysis and log-rank test and plotted using Kaplan–Meier curves. PMOD 3.1 (PMOD Technologies Ltd.) was used to coregister and determine the volumes and activities shown. The absorbed tumor dose was calculated using OLINDA/EXM 1.1 software (Vanderbilt University).

RESULTS

Patient Characteristics

Patient characteristics are summarized in Table 1. The mean patient age (range) was 36 (9–69) y. Six of 14 (43%) patients were female, and 8 of 14 (57%) were male. Among the 14 patients, 4 (29%) had histologically confirmed neuroblastoma and 10 (71%) had malignant pheochromocytoma. An average time period of 1.2 ± 1.6 (SD) mo from pretherapeutic ^{124}I-MIBG dosimetry to therapy and an average of 4.6 ± 2.4 (SD) mo for the interval between therapy and posttherapeutic follow-up PET/CT were documented. A single therapy activity ranged from 3.5 to 50 GBq

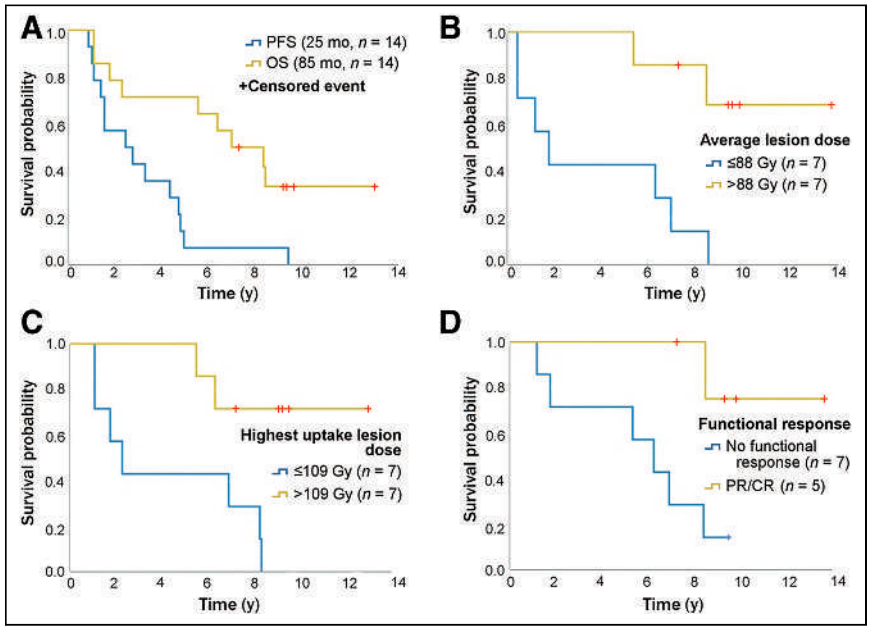

FIGURE 1. Kaplan–Meier survival. (A) OS and PFS of patients who underwent ^{124}I-MIBG PET-based dosimetry followed by ^{131}I-MIBG therapy; OS was significantly associated with several factors, including (B) average tumor lesion dose higher than median (88 Gy; $P < 0.004$); (C) highest uptake tumor lesion dose higher than median (109 Gy; $P < 0.009$); and (D) functional response as assessed by ^{124}I-MIBG PET/CT ($P < 0.001$). Predictors for PFS and OS were assessed by univariate Cox regression analysis and log-rank test and plotted using Kaplan–Meier curves.

TABLE 2
Dosimetry Data of Patients Who Underwent ^{124}I-MIBG PET-Based Dosimetry Followed by Targeted ^{131}I-MIBG Therapy

Characteristic (n = 14)	Patient
Whole-body dose (Gy)	
Median	1.45
Range	0.48–6

(average, 13.7 GBq; ±11.3 SD). The average time from diagnosis to dosimetry-based ^{131}I-MIBG therapy was 75 ± 55.8 (SD) mo (range, 1–189 mo). All eligible patients had received previous therapies, including surgery (93%), radiotherapy (43%), or chemotherapy (50%).

Survival

Figure 1 shows OS and PFS along with predictors of survival.

Median OS after therapy was 85 mo (hazard ratio 6.9; 95% CI [3.2–10.5]), and median PFS was 25 mo (hazard ratio 1.9; 95% CI [0.0–4.3]). Minimum follow-up time was 5 mo, and the average follow-up time (range) for the cohort was 76 ± 48.7 (SD) mo (range, 5–164 mo). Five of 14 (36%) patients died during the observation period. By log-rank analysis, significant predictors of OS and functional response were achieved with average tumor lesion dose higher than median (88 Gy; $P < 0.004$), the highest uptake lesion dose higher than median (109 Gy; $P < 0.009$), and the functional response by means of ^{124}I-MIBG PET/CT defined as CR/PR, respectively ($P < 0.001$). Changes in SIOPEN-like score translated from conventional ^{123}I-MIBG imaging did not show a significant correlation with OS ($P < 0.205$) or response ($P < 0.059$ for morphologic response and $P < 0.017$ for functional response).

Dosimetry and Toxicity

The dosimetry and toxicity data are shown in Tables 2 and 3. One patient received a single therapy activity of 50 GBq ^{131}I-MIBG (in a curative intention and close cooperation with the pediatric oncologists, after autologous stem cells have been collected and cryopreserved), exceeded the estimated whole-body dose of 2 Gy (median in all patients, 1.4 Gy; range, 0.4–6 Gy), and demonstrated transient grade 3 hematologic toxicity (leukocytopenia and thrombocytopenia), which resolved spontaneously within 12 mo after therapy without the need for stem cell rescue. Additionally, 2 patients demonstrated grade 1 hematologic toxicity. Transitional grade 1 kidney function deterioration was noted in 3 patients (21%). One patient with pheochromocytoma showed a transitional grade 1 kidney function deterioration after receiving a cumulative activity of 21.6 GBq and was diagnosed with operable urothelial carcinoma (pTa, R0) 4 y after ^{131}I-MIBG therapy.

TABLE 3
Toxicity Data of Patients (n = 14) Who Underwent ^{124}I-MIBG PET-Based Dosimetry Followed by Targeted ^{131}I-MIBG Therapy

	Any grade		Grades 3–4	
Category	n	%	n	%
Hematologic	3	21	1	7
Renal	3	21	0	0
Possible secondary malignancy	1	7	Urothelial carcinoma	

Treatment Response

Treatment response is summarized in Table 4. Of the 14 evaluable patients, 4 (29%) and 5 (36%) demonstrated CR/PR by RECIST and functional imaging, respectively. Disease control, defined by CR, PR, or stable disease, was achieved in 71% of the patients according to morphologic imaging and in 79% by functional imaging. All 4 patients (3 with neuroblastoma and 1 with metastatic pheochromocytoma) demonstrating progressive disease by means of morphologic imaging were extensively pretreated during the long disease history.

The median tumor dose of the lesions with highest uptake was 109 Gy, ranging from 10.5 to 495 Gy. An overview of individual patient characteristics combined with individual tumor dose along with response is given in Table 5. Figure 2 shows an example of a patient with metastatic pheochromocytoma. Figure 3 shows an example of a patient with metastatic neuroblastoma.

DISCUSSION

^{131}I-MIBG is an efficacious therapy for MIBG-positive unresectable, locally advanced/metastatic neural crest tumors. Prospective phase 2 data (*10*) recently led to the US Food and Drug Administration approval of ^{131}I-MIBG for the treatment of unresectable, locally advanced, and metastatic pheochromocytoma and paraganglioma using empiric activities. High-activity ^{131}I-MIBG therapy has been reported previously; however, the feasibility of the $^{124/131}$I-MIBG theranostic pair for dose escalation has not yet been assessed systematically. Here we demonstrate feasibility of dosimetry guided $^{124/131}$I-MIBG theranostic therapy, which resulted in durable responses in 57% and 50% of patients at 12 and 24 mo, respectively. Median OS after therapy was 85 mo, and median PFS was 25 mo, which compares favorably to previously published data (*10,22,23*). For instance, overall response (CR/PR) rate was 22%, and 8% of patients maintained stable disease for greater than 12 mo in the cohort described by Gonias et al. (*22*). In comparison, the median OS was 36.7 mo in a study by Pryma et al. (*10*). In the long-term follow-up, 1 grade 3 event was noted for 1 patient, and possible secondary malignancy

TABLE 4
Morphologic (CT/MRI) and Functional (PET) Response After ^{131}I-MIBG Therapy (n = 14)

	(RECIST) CT/MRI		^{124}I-MIBG PET	
Response	n	%	n	%
CR	0	0	0	0
PR	4	29	5	36
Stable disease	6	43	6	43
PD	4	29	1	7
No follow-up	0	0	2	14
Disease control (CR, PR, stable disease)	10	71	11	79
Any response (CR, PR)	4	29	5	36

TABLE 5
Individual Patient Characteristics Combined with Tumor Dose and Response

Patient characteristic (n=14)	Patient													
	1	2	3	4	5	6	7	8	9	10	11	12	13	14
Sex	M	F	F	M	M	F	M	M	F	M	M	M	F	F
Age at entry, y	17	24	68	69	57	23	54	65	68	38	34	9	21	16
Diagnosis	PCC	PCC	PCC	PCC	PCC	PCC	PCC	PCC	PCC	PCC	NB	NB	NB	NB
N1	Yes	No	Yes	No	Yes	Yes	No	Yes	No	Yes	Yes	No	Yes	Yes
M1	Yes	Yes	Yes	Yes	Yes	No	Yes	Yes	Yes	Yes	Yes	Yes	Yes	Yes
Time from diagnosis to entry, mo	7	1	122	3	101	50	144	51	79	79	189	53	123	53
^{131}I-MIBG activity, GBq	50.0	15.0	10.0	7.0	10.0	20.0	15.0	3.5	10.0	11.0	10.0	4.8	11.0	15.0
Number of MIBG therapies	1	1	5	2	2	2	1	2	2	1	2	1	3	1
Activity (all) MIBG therapies, GBq	50.0	15.0	38.0	21.6	21.1	27.4	15.0	10.5	20.0	11.0	16.0	4.8	26.2	15.0
Whole-body dose after therapy, Gy	6.0	1.8	1.4	0.5	1.3	2.0	1.7	1.1	1.7	1.5	0.9	0.5	1.0	1.5
Median absorbed tumor dose, Gy	356.5	93.0	78.0	93.1	208.5	107.0	40.5	10.5	179.0	41.8	142.8	9.0	30.8	82.5
Number of prior therapy lines	1	1	2	2	3	1	3	2	1	1	5	3	4	3
Chemotherapy/radiation	Yes	No	No	No	Yes	No	Yes	No	No	No	Yes	Yes	Yes	Yes
Surgery	No	Yes	Yes	Yes	Yes	Yes	Yes	Yes	Yes	Yes	Yes	Yes	Yes	Yes
Time from dosimetry to therapy, mo	0	0	1	1	0	2	2	1	1	0	0	6	3	0
Time from therapy to dosimetry follow-up, mo	3	6	7	11	6	3	4	3	3	5	4	1	5	4
OS, mo	164	112	75	101	118	114	14	21	87	83	64	5	102	5
PFS, mo	115	48	27	11	53	54	11	9	34	5	23	2	56	4
Morphologic response	Stable disease	PR	PD	PR	Stable disease	Stable disease	Stable disease	PD	Stable disease	Stable disease	PD	PD	PD	PR
Functional response	PR	PR	PR	PR	Stable disease	Stable disease	Stable disease	PD	Stable disease	Stable disease	NA	Stable disease	NA	PR
SIOPEN-like score (baseline)	11	5	17	8	5	16	4	6	6	39	39	6	20	9
SIOPEN-like score (follow up)	11	4	7	7	4	11	4	6	6	32	NA	6	NA	7

Morphologic response was determined by RECIST (PR, lesion diameter decreasing in 30%; PD, lesions diameter increasing in 20% or appearance of new lesions; stable disease, none of the aforementioned criteria are met); functional response was assessed as change in baseline to follow-up ^{124}I-MIBG imaging (PR, decrease in lesion number/uptake intensity; stable disease, no significant change; PD, new lesions). The change in SIOPEN-like score was consistent with outcome; however, it was not statistically significant.

PCC = pheochromocytoma; NB = neuroblastoma. NA = not available.

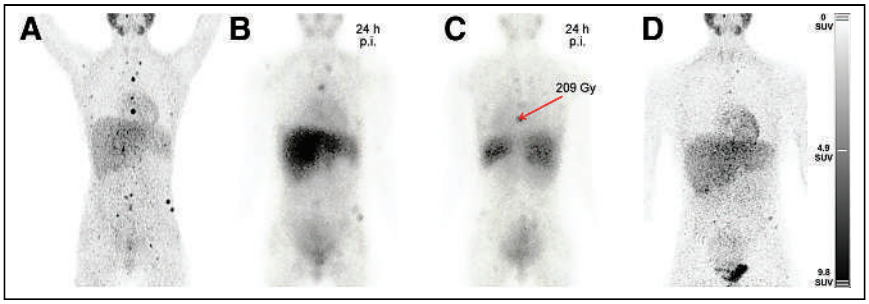

FIGURE 2. Patient 2 (female, 24 y) with metastatic pheochromocytoma before (A) and 6 mo after (D) single ^{124}I-MIBG dosimetry-guided high-activity ^{131}I-MIBG therapy with 15 GBq (B and C: post-therapeutic scintigraphy 24 h after injection, anterior and posterior views). PR in morphologic and functional imaging was noted 6 mo after treatment (OS was 112 mo and PFS was 48 mo; maximum lesion dose [marked with arrow] achieved was 209 Gy). p.i. = after injection.

was noted in 1 patient in our cohort. The much lower toxicity rates compared with previous data, reporting grade 3/4 neutropenia in 85%, low platelet count in 83%, and anemia in 8% of patients (*22*), additionally strengthen ^{124}I-MIBG dosimetry to mitigate toxicity.

This study demonstrates the advantages of calculated treatment planning and targeted therapy in a heterogenous group of patients with neural crest tumors. Here we provide evidence for the feasibility of using the theranostic pair ^{124}I/^{131}I-MIBG to achieve a high tumor dose without exceeding toxicity thresholds, especially for the bone marrow (*10,22*). The superior diagnostic performance and improved possibilities of quantification of ^{124}I-MIBG PET/CT over scintigraphy with ^{123}I- or ^{131}I-MIBG have been discussed and confirmed in the current literature (*2,3,24*). Previous studies conducted in a preclinical environment have shown similar potential (*6,25*). Furthermore, the use of the ^{124}I/^{131}I pair is well established for imaging and therapy of differentiated thyroid carcinoma (*15,26–29*).

A low adverse events rate in comparison with other activity-escalated concepts (*22,23,30,31*) additionally confirms the central role of ^{124}I-MIBG PET/CT dosimetry in targeted therapy planning. Improved quantification possibilities using ^{124}I-MIBG PET/CT and the knowledge of tumor doses can further help to assess the individual response probability and establish the threshold doses needed to achieve partial or complete response (absorbed doses in relation to associated response rates), similar to data published for differentiated thyroid carcinoma (*26,32–34*). Significant predictors of OS and functional response in our cohort were an achieved tumor dose in the highest uptake lesion higher than 109 Gy and the average achieved dose higher than 88 Gy, as well as the functional response defined as CR/PR. Disease control, defined by either CR, PR, or stable disease, was achieved in 71% of the patients by morphologic imaging and in 79% by functional imaging lesion count, respectively. Changes in SIOPEN-like score did not show a significant correlation with OS or response. An association between lesions dose and response/survival is noted. Therefore, dosimetry-guided high-activity therapy could be critical for favorable outcomes. In addition, through ^{124}I-MIBG prescreening/dosimetry, patients most likely to benefit from ^{131}I-MIBG therapy can be selected, and long-term outcomes can be predicted to guide subsequent management.

Strengths of our study include dosimetry guidance and long-term follow-up with mature survival data. Limitations of this study include a small sample size, the retrospective study design, and the heterogenous patient cohort concerning tumor entity and age. Prospective studies are needed to compare efficacy and safety of ^{124}I-MIBG dosimetry-guided ^{131}I-MIBG therapy versus conventional ^{131}I-MIBG therapy using standard activities in larger patient cohorts.

CONCLUSION

^{124}I-MIBG dosimetry-guided high-activity ^{131}I-MIBG therapy is feasible and results in durable responses, long survival, and a low rate of manageable adverse events. ^{124}I-MIBG PET-derived tumor dose and response assessment predict survival after ^{131}I-MIBG therapy.

^{124}/^{131}I-MIBG theranostics offer individual treatment planning with a promising efficacy/safety tradeoff: ^{124}I-MIBG–guided ^{131}I-MIBG activity escalation should further be assessed in prospective trials.

DISCLOSURE

This work is a part of the doctoral thesis of Ines Maric. Andre Prochnow, Jochen Schmitz, Nicole Unger, Thorsten Poeppel, Christoph Rischpler and Andreas Bockisch have nothing to declare. Walter Jentzen received research funding from Siemens Healthineers. Manuel Weber reports fees from Boston Scientific, Terumo, Advanced Accelerator Applications, and Lilly, outside of the submitted work. Benedikt M. Schaarschmidt is supported by a research grant from PharmaCept, outside the submitted work. Ken Herrmann reports personal fees from Bayer SIRTEX, Adacap, Curium, Endocyte, IPSEN, Siemens Healthineers, GE Healthcare, Amgen, Novartis, and ymabs; personal fees and other from Sofie Biosciences; nonfinancial support from ABX; and grants and personal fees from BTG, outside the submitted work. Wolfgang Fendler reports fees from SOFIE Bioscience (research funding), Janssen (consultant, speaker), Calyx (consultant), Bayer (consultant, speaker, research

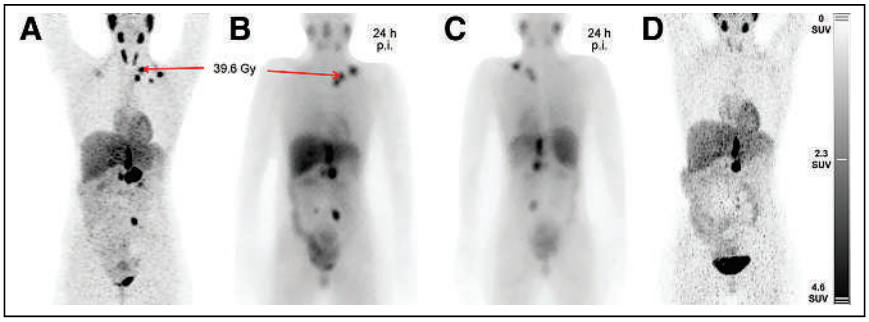

FIGURE 3. Patient 13 (female, 21 y) with metastatic neuroblastoma before (A) and 5 mo after (D) single ^{124}I-MIBG dosimetry-guided high-activity ^{131}I-MIBG therapy with 11 GBq (B and C: posttherapeutic scintigraphy 24 h after injection, anterior and posterior views, respectively). Maximum lesion dose achieved was 39.6 Gy (arrows). PR in morphologic and functional imaging was noted 5 mo after treatment (OS was 102 mo and PFS was 56 mo). p.i. = after injection.

funding), Parexel (image review), Novartis (speaker), and Telix (speaker), outside of the submitted work. No other potential conflict of interest relevant to this article was reported.

KEY POINTS

QUESTION: Is ^{124}I-MIBG dosimetry-guided high-activity ^{131}I-MIBG therapy of advanced pheochromocytoma or neuroblastoma effective and safe?

PERTINENT FINDINGS: ^{124}I-MIBG dosimetry-guided high-activity ^{131}I-MIBG therapy is feasible and results in durable responses, long survival, and a low rate of manageable adverse events. ^{124}I-MIBG PET tumor uptake and tumor response assessment can further predict outcome after ^{131}I-MIBG therapy.

IMPLICATIONS FOR PATIENT CARE: ^{124}/^{131}I-MIBG theranostics offer individual treatment planning with a promising efficacy/safety tradeoff: ^{124}I-MIBG-guided ^{131}I-MIBG activity escalation should further be assessed in prospective trials.

REFERENCES

1. Vallabhajosula S, Nikolopoulou A. Radioiodinated metaiodobenzylguanidine (MIBG): radiochemistry, biology, and pharmacology. *Semin Nucl Med.* 2011;41: 324–333.
2. Aboian MS, Huang SY, Hernandez-Pampaloni M, et al. ^{124}I-MIBG PET/CT to monitor metastatic disease in children with relapsed neuroblastoma. *J Nucl Med.* 2021;62:43–47.
3. Weber M, Schmitz J, Maric I, et al. Diagnostic performance of [124 I]m-iodobenzylguanidine PET/CT in patients with pheochromocytoma. *J Nucl Med.* 2022;63: 869–874.
4. Lewington V, Lambert B, Poetschger U, et al. ^{123}I-mIBG scintigraphy in neuroblastoma: development of a SIOPEN semi-quantitative reporting, method by an international panel. *Eur J Nucl Med Mol Imaging.* 2017;44:234–241.
5. Ady N, Zucker J, Asselain B, et al. A new ^{123}I-MIBG whole body scan scoring method–application to the prediction of the response of metastases to induction chemotherapy in stage IV neuroblastoma. *Eur J Cancer.* 1995;31A:256–261.
6. Marsh IR, Grudzinski J, Baiu DC, et al. Preclinical pharmacokinetics and dosimetry studies of ^{124}I/^{131}I-CLR1404 for treatment of pediatric solid tumors in murine xenograft models. *J Nucl Med.* 2019;60:1414–1420.
7. John H, Ziegler WH, Hauri D, Jaeger P. Pheochromocytomas: can malignant potential be predicted? *Urology.* 1999;53:679–683.
8. Park J, Song C, Park M, et al. Predictive characteristics of malignant pheochromocytoma. *Korean J Urol.* 2011;52:241–246.
9. Garaventa A, Parodi S, De Bernardi B, et al. Outcome of children with neuroblastoma after progression or relapse. A retrospective study of the Italian neuroblastoma registry. *Eur J Cancer.* 2009;45:2835–2842.
10. Pryma DA, Chin BB, Noto RB, et al. Efficacy and safety of high-specific-activity ^{131}I-MIBG therapy in patients with advanced pheochromocytoma or paraganglioma. *J Nucl Med.* 2019;60:623–630.
11. Buckley SE, Chittenden SJ, Saran FH, Meller ST, Flux GD. Whole-body dosimetry for individualized treatment planning of ^{131}I-MIBG radionuclide therapy for neuroblastoma. *J Nucl Med.* 2009;50:1518–1524.
12. Buckley SE, Saran FH, Gaze MN, et al. Dosimetry for fractionated ^{131}I-mIBG therapies in patients with primary resistant high-risk neuroblastoma: Preliminary results. *Cancer Biother Radiopharm.* 2007;22:105–112.
13. Giammarile F, Chiti A, Lassmann M, Brans B, Flux G. EANM procedure guidelines for ^{131}I-meta-iodobenzylguanidine (^{131}I-mIBG) therapy. *Eur J Nucl Med Mol Imaging.* 2008;35:1039–1047.
14. Jentzen W, Freudenberg L, Bockisch A. Quantitative imaging of (124)I with PET/CT in pretherapy lesion dosimetry. Effects impairing image quantification and their corrections. *Q J Nucl Med Mol Imaging.* 2011;55:21–43.
15. Jentzen W, Bockisch A, Ruhlmann M. Assessment of simplified blood dose protocols for the estimation of the maximum tolerable activity in thyroid cancer patients undergoing radioiodine therapy using ^{124}I. *J Nucl Med.* 2015;56: 832–838.
16. Jentzen W, Hoppenbrouwers J, Van Leeuwen P, et al. Assessment of lesion response in the initial radioiodine treatment of differentiated thyroid cancer using ^{124}I PET imaging. *J Nucl Med.* 2014;55:1759–1765.
17. Freudenberg LS, Jentzen W, Görges R, et al. ^{124}I-PET dosimetry in advanced differentiated thyroid cancer: therapeutic impact. *Nucl Med (Stuttg).* 2007;46: 121–128.
18. Jentzen W, Weise R, Kupferschläger J, et al. Iodine-124 PET dosimetry in differentiated thyroid cancer: recovery coefficient in 2D and 3D modes for PET(/CT) systems. *Eur J Nucl Med Mol Imaging.* 2008;35:611–623.
19. Jentzen W, Freudenberg L, Eising EG, Heinze M, Brandau W, Bockisch A. Segmentation of PET volumes by iterative image thresholding. *J Nucl Med.* 2007;48: 108–114.
20. Jentzen W. An improved iterative thresholding method to delineate PET volumes using the delineation-averaged signal instead of the enclosed maximum signal. *J Nucl Med Technol.* 2015;43:28–35.
21. Jentzen W, Hobbs RF, Stahl A, Knust J, Sgouros G, Bockisch A. Pre-therapeutic ^{124}I PET(/CT) dosimetry confirms low average absorbed doses per administered ^{131}I activity to the salivary glands in radioiodine therapy of differentiated thyroid cancer. *Eur J Nucl Med Mol Imaging.* 2010;37:884–895.
22. Gonias S, Goldsby R, Matthay KK, et al. Phase II study of high-dose [131i]metaiodobenzylguanidine therapy for patients with metastatic pheochromocytoma and paraganglioma. *J Clin Oncol.* 2009;27:4162–4168.
23. Wakabayashi H, Kayano D, Inaki A, et al. High-dose ^{131}I-mIBG as consolidation therapy in pediatric patients with relapsed neuroblastoma and ganglioneuroblastoma: the Japanese experience. *Ann Nucl Med.* 2020;34:840–846.
24. Shapiro B, Copp JE, Sisson JC, Eyre PL, Wallis J, Beierwaltes WH. Iodine-131 metaiodobenzylguanidine for the locating of suspected pheochromocytoma: experience in 400 cases. *J Nucl Med.* 1985;26:576–585.
25. Lee CL, Wahnishe H, Sayre GA, et al. Radiation dose estimation using preclinical imaging with i 124 -metaiodobenzylguanidine (MIBG) PET. *Med Phys.* 2010;37: 4861–4867.
26. Jentzen W, Freudenberg L, Eising EG, Sonnenschein W, Knust J, Bockisch A. Optimized ^{124}I PET dosimetry protocol for radioiodine therapy of differentiated thyroid cancer. *J Nucl Med.* 2008;49:1017–1023.
27. Kolbert KS, Pentlow KS, Pearson JR, et al. Prediction of absorbed dose to normal organs in thyroid cancer patients treated with ^{131}I by use of ^{124}I PET and 3-dimensional internal dosimetry software. *J Nucl Med.* 2007;48:143–149.
28. Ruhlmann M, Sonnenschein W, Nagarajah J, Binse I, Herrmann K, Jentzen W. Pretherapeutic 124 i dosimetry reliably predicts intratherapeutic blood kinetics of 131 i in patients with differentiated thyroid carcinoma receiving high therapeutic activities. *Nucl Med Commun.* 2018;39:457–464.
29. Ballinger JR. Theranostic radiopharmaceuticals: established agents in current use. *Br J Radiol.* 2018;91:20170969.
30. Rubio PM, Galán V, Rodado S, Plaza D, Martínez L. MIBG therapy for neuroblastoma: precision achieved with dosimetry, and concern for false responders. *Front Med (Lausanne).* 2020;7:173.
31. Weiss B, Vora A, Huberty J, Hawkins RA, Matthay KK. Secondary myelodysplastic syndrome and leukemia following ^{131}I-metaiodobenzylguanidine therapy for relapsed neuroblastoma. *J Pediatr Hematol Oncol.* 2003;25:543–547.
32. Maxon HR, Englaro EE, Thomas SR, et al. Radioiodine-131 therapy for well-differentiated thyroid cancer—a quantitative radiation dosimetric approach: outcome and validation in 85 patients. *J Nucl Med.* 1992;33:1132–1136.
33. Jentzen W, Verschure F, Van Zon A, et al. ^{124}I PET assessment of response of bone metastases to initial radioiodine treatment of differentiated thyroid cancer. *J Nucl Med.* 2016;57:1499–1504.
34. Wierts R, Brans B, Havekes B, et al. Dose-response relationship in differentiated thyroid cancer patients undergoing radioiodine treatment assessed by means of ^{124}I PET/CT. *J Nucl Med.* 2016;57:1027–1032.

[^{177}Lu]Lu-PSMA Therapy as an Individual Treatment Approach for Patients with High-Grade Glioma: Dosimetry Results and Critical Statement

Josefine Graef[1], Stephanie Bluemel[1], Winfried Brenner[1,2], Holger Amthauer[1], Peter Truckenmueller[3], David Kaul[2,4], Peter Vajkoczy[3], Julia S. Onken[2,3,5], and Christian Furth[1]

[1]*Department of Nuclear Medicine, Charité–Universitätsmedizin Berlin, Berlin, Germany;* [2]*German Cancer Consortium, Partner Site Berlin, German Cancer Research Center, Heidelberg, Germany;* [3]*Department of Neurosurgery, Charité–Universitätsmedizin Berlin, Berlin, Germany;* [4]*Department of Radiation Oncology, Charité–Universitätsmedizin Berlin, Berlin, Germany; and* [5]*Berlin Institute of Health at Charité–Universitätsmedizin Berlin, Berlin, Germany*

The theranostic use of prostate-specific membrane antigen (PSMA) appears to be promising in patients with high-grade glioma. This study investigated [^{177}Lu]Lu-PSMA therapy as an individual treatment approach with a focus on intratherapeutic dosimetry. **Methods:** Three patients were treated with a median of 6.03 GBq (interquartile range [IQR], 5.74–6.10) of [^{177}Lu]Lu-PSMA. Intratherapeutic dosimetry was performed using a hybrid scenario with planar whole-body scintigraphy at 2, 24, and 48 h after treatment injection and SPECT/CT at 48 h after injection. Additive whole-body scintigraphy at 8 d after injection was performed on 1 patient. **Results:** The median doses were 0.56 Gy (IQR, 0.36–1.25 Gy) to tumor, 0.27 Gy (IQR, 0.16–0.57 Gy) to risk organs, 2.13 Gy (IQR, 1.55–2.89 Gy) to kidneys, and 0.76 Gy (IQR, 0.70–1.20 Gy) to salivary glands. Whole-body exposure was 0.11 Gy (IQR, 0.06–0.18 Gy). **Conclusion:** Because the intratherapeutic tumor dose is lower than that used in external radiation oncology, the effectiveness of treatment is questionable.

Key Words: [^{68}Ga]Ga-PSMA; [^{177}Lu]Lu-PSMA; glioma; PET/MRI; theranostics

J Nucl Med 2023; 64:892–895
DOI: 10.2967/jnumed.122.264850

The overall prognosis for high-grade glioma (HGG) patients is dismal, and treatment options are limited (*1*). In patients with prostate cancer, the use of prostate-specific membrane antigen (PSMA)–based isotopes has already been established as a theranostic approach (*2*). Although PSMA shows high expression levels in prostate cancer cells, it has also been found in other tumors, such as in HGG (*3–5*). Compared with low-grade gliomas, HGGs have presented generally higher PSMA uptake on PET (*6,7*). The expression was present in de novo HGG as well as in recurrent disease, and worsened survival has been reported for patients with high PSMA levels in recurrence and for patients with increasing vascular PSMA expression during the course of the disease (*8*).

To date, only a few case reports have been published analyzing the possible use of radiolabeled PSMA as a theranostic approach for HGG. Two case reports have been published presenting promising results for [^{177}Lu]Lu-PSMA in the treatment of HGG (*9,10*). On the basis of these results, we investigated [^{177}Lu]Lu-PSMA therapy as an individual treatment approach in 3 patients with HGG. A special focus was placed on intratherapeutic dosimetry.

MATERIALS AND METHODS

A detailed version of the methods can be found in the supplemental materials (available at http://jnmt.snmjournals.org).

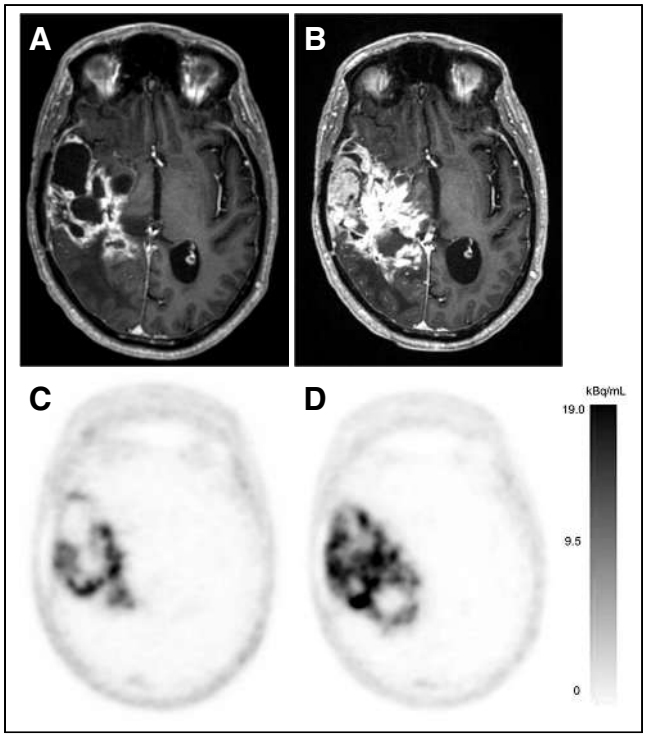

FIGURE 1. [^{68}Ga]Ga-PSMA PET/MRI of patient before first treatment cycle (A and C) and after second treatment cycle (B and D) of [^{177}Lu]Lu-PSMA. Spatial spread of contrast-enhanced tumor areas on MRI grew (A and B), and lesion avidity to tracer (i.e., SUV_{max}) increased from 4.4 (C) to 6.6. (D).

Received Sep. 2, 2022; revision accepted Jan. 6, 2023.
For correspondence or reprints, contact Josefine Graef (josefine.graef@charite.de).
Published online Apr. 28, 2023.

TABLE 1
Intratherapeutic Dosimetry Results Using Hybrid Scenario with Whole-Body Scintigraphy at 2, 24, and 48 Hours After Treatment Injection and SPECT/CT at 48 Hours After Injection

Patient	Treatment cycle	Activity (GBq)	Tumor (Gy)	Liver (Gy)	Kidneys (Gy)	Salivary glands (Gy)	Whole body (Gy)
1	1	6.023	1.06	0.33	2.64	0.83	0.16
	2	5.052	0.36*	0.16*	1.55*	0.62*	0.06*
2	1	6.09	0.35	0.42	1.91	0.73	0.14
	2	5.969	1.83	1.0	3.65	2.31	0.23
3	1	6.045	0.59	0.16	2.34	0.72	0.06
	2	6.148	0.53	0.21	1.53	0.79	0.07

*Whole-body scintigraphy was usable only 24 and 48 h after injection.
MPRAGE = magnetization-prepared rapid gradient echo.

According to the European Association of Nuclear Medicine guideline on selecting eligible patients with metastatic castration-resistant prostate cancer (*11*) for treatment with [^{177}Lu]Lu-PSMA, only 3 of 20 patients with HGG who underwent [^{68}Ga]Ga-PSMA PET/MRI at our institution were suitable for treatment. Following the recommendation of the interdisciplinary tumor board and in accordance with the European Association of Nuclear Medicine guideline (*11,12*), they were scheduled for 2 cycles of [^{177}Lu]Lu-PSMA therapy with a median treatment activity of 6.03 GBq (interquartile range [IQR], 5.74–6.10 GBq).

Intratherapeutic imaging was performed, including planar whole-body scintigrams at 2, 24, and 48 h after injection and SPECT/low-dose CT of the head, thorax, abdomen, and pelvis at 48 h after injection. In accordance with Kunikowska et al. (*9*), 1 patient received a prolonged protocol for the second treatment cycle, including an additional whole-body scintigram at 8 d after injection. The dosimetry data were analyzed using a hybrid scenario applying both the whole-body scintigraphy data and the SPECT/CT data (*13–15*).

RESULTS

Treatment with [^{177}Lu]Lu-PSMA

Although all 20 patients showed increased tracer uptake in tumors on [^{68}Ga]Ga-PSMA PET/MRI (supplemental results), only 3 of 20 patients were eligible for the treatment (*12*). No early treatment-related toxicities were detected.

Because 1 patient with underlying myelodysplastic syndrome presented chronic thrombocytopenia between the first and second treatment cycles (Common Terminology Criteria for Adverse Events, version 5.0, definition II) (*12*), we reduced the dose to 5 GBq for his second treatment cycle.

Because of an increasing deterioration in the health status of 2 of 3 patients, only 1 patient underwent early follow-up PET/MRI at 6 wk after the second treatment cycle; the results showed spatial tumor growth and an increasing tumor SUV_{max} (Fig. 1).

The short follow-up period, with only 1 patient undergoing follow-up PET/MRI, makes it difficult to draw conclusions about the possible risk of late-term side effects.

TABLE 2
Comparative Intratherapeutic Dosimetry of Patient 3 During His Second Treatment with 6.148 GBq of [^{177}Lu]Lu-PSMA Using Hybrid Scenario with Whole-Body Scintigraphy at 2, 24, and 48 Hours After Treatment Injection and SPECT/CT at 48 Hours After Injection as Standard Protocol and Prolonged Protocol with Additive Whole-Body Scintigraphy at 8 Days After Injection

Protocol	Tumor (Gy)	Liver (Gy)	Kidneys (Gy)	Salivary glands (Gy)	Whole body (Gy)
Standard	0.53	0.21	1.53	0.79	0.07
Prolonged	0.84	0.25	2.05	0.91	0.09

Dosimetry

The median tumor dose was 0.56 Gy (IQR, 0.36–1.25 Gy). The median doses were 0.27 Gy (IQR, 0.16–0.57 Gy) to the liver, 2.13 Gy (IQR, 1.55–2.89 Gy) to the kidneys, 0.76 Gy (IQR, 0.70–1.20 Gy) to the salivary glands, and 0.11 Gy (IQR, 0.06–0.18 Gy) to the whole body. The results are detailed in Table 1. The prolonged protocol, applied to 1 patient, resulted in an increased tumor dose (Table 2; Fig. 2). For this patient, the intratumoral dose distribution is presented in Supplemental Figure 1.

DISCUSSION

In this study, we demonstrated that only a minority of patients with HGG were eligible for treatment with [^{177}Lu]Lu-PSMA (*12*) and that the achieved tumor dose was lower than in a previous case report (*9*) and too low for a sufficient therapeutic effect. The number of patients in our study was small, but because the tumor target doses in all patients were consistently too low, an early interpretation of the study results seems necessary.

The intratherapeutic tumor dose of 0.56 Gy in our study was only 1/25th of the first encouraging results of Kunikowska et al. (*9*). The standard cumulative tumor dose for external-beam radiation is 60 Gy (*16*) and, thus, much higher than the achieved tumor doses both in our patients and in the case report by Kunikowska et al. (*9*). Although overall survival is significantly prolonged after radiochemotherapy, the outcome remains poor (*17*). The dose recommendation of the European Association of Nuclear Medicine guideline for radionuclide therapy (*11*) is based on observational studies. An increase in tumor dose by increasing the applied dose per cycle would be conceivable in principle but only in an experimental approach. There is no clear upper limit at which it can be ensured that the harm to the patient outweighs any possible benefit. Overall, it is debatable whether the achieved doses of internal radionuclide therapy can be sufficient for a relevant treatment effect.

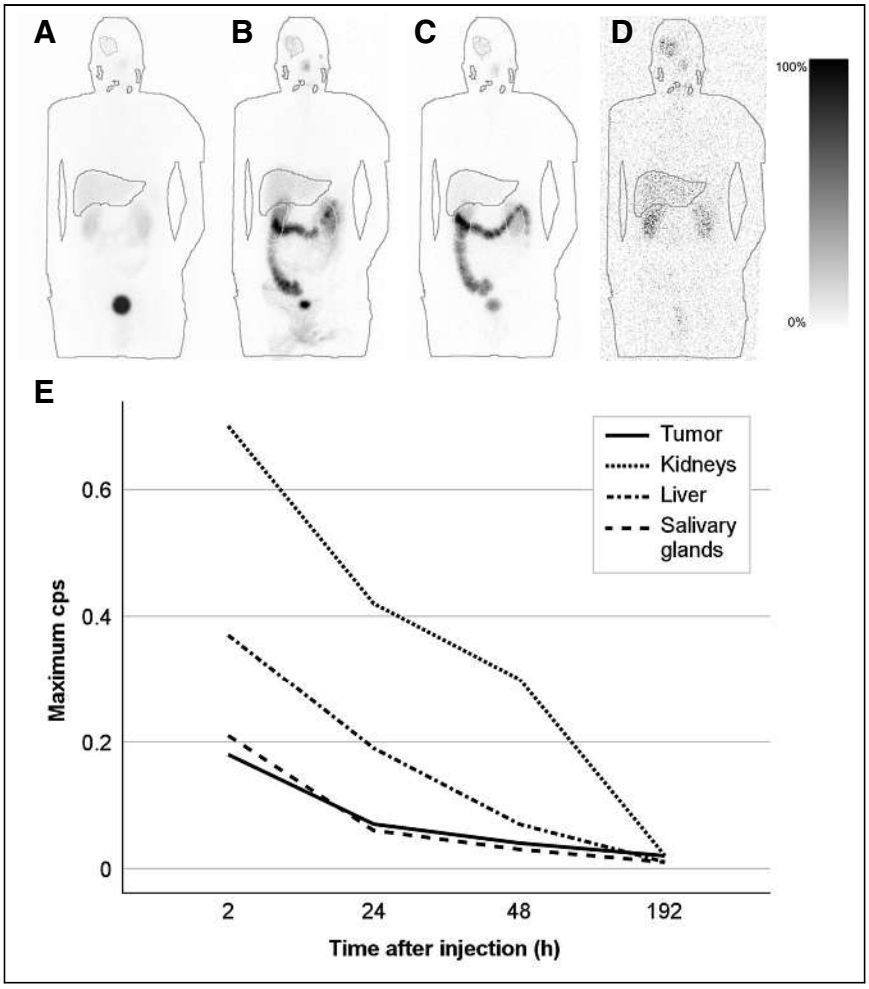

FIGURE 2. Regions of interest for dosimetry of tumor, salivary glands, liver, and kidneys in anterior whole-body scintigrams (A–D) in 1 patient at 2 h (A), 24 h (B), 48 h (C), and 192 h (D) after injection of 6.148 GBq of [^{177}Lu]Lu-PSMA and respective time–activity curves for target lesion and organs at risk (E). cps = counts per second.

Because PSMA is expressed mainly in endothelial cells (*18*), it is assumed that PSMA-based tracers are bound mainly in the angiogenetic part of the tumor (*19*). This might lead to an insufficient radiation distribution within the tumor.

In principle, treatment with [^{177}Lu]Lu-PSMA may offer radiotherapeutic treatment when the limits of external radiation are reached. Our study showed that organs of risk did not receive hazardous radiation (*20,21*).

Temozolomide has increased the survival rate by radiosensitization to external radiation (*22*) and may also improve the treatment effect in combination with PSMA-based therapy. In addition to the use of β^--emitter, there have been a few studies on the use of α-emitters in HGG patients (*23–25*). Compared with the β^--component of [^{177}Lu]Lu, the higher energy levels of α-emitters may be more effective (*26*). Nevertheless, the shorter tissue penetration of α-emitters (*26*) may become a limiting factor in the case of endothelial expression of PSMA in HGG (*3,27*). The wider range and crossfire effects of β^--emitters may be an advantage over α-emitters in HGG. As already discussed for other tumor entities, a cocktail of [^{177}Lu]Lu-PSMA and [^{225}Ac]Ac-PSMA may be advantageous.

CONCLUSION

Despite promising initial case reports, the intratherapeutic tumor dose levels in our study fell well below expectations, and the therapeutic efficiency remains questionable.

DISCLOSURE

No other potential conflict of interest relevant to this article was reported.

KEY POINTS

QUESTION: Does [^{177}Lu]Lu-PSMA therapy in HGG reach a sufficient tumor dose?

PERTINENT FINDINGS: This was a cohort study with a limited number of patients with HGG who underwent [^{177}Lu]Lu-PSMA therapy. The study presents an intratherapeutic reached tumor dose well short of expectations, with a median of 0.56 Gy.

IMPLICATIONS FOR PATIENT CARE: The treatment effect is questionable.

REFERENCES

1. Weller M, van den Bent M, Hopkins K, et al. EANO guideline for the diagnosis and treatment of anaplastic gliomas and glioblastoma. *Lancet Oncol.* 2014;15:e395–e403.
2. Cornford P, van den Bergh RCN, Briers E, et al. EAU-EANM-ESTRO-ESUR-SIOG guidelines on prostate cancer. Part II—2020 update: treatment of relapsing and metastatic prostate cancer. *Eur Urol.* 2021;79:263–282.
3. Chang SS, Reuter VE, Heston WDW, et al. Five different anti-prostate-specific membrane antigen (PSMA) antibodies confirm PSMA expression in tumor-associated neovasculature. *Cancer Res.* 1999;59:3192–3198.
4. Kunikowska J, Bartosz K, Leszek K. Glioblastoma multiforme: another potential application for ^{68}Ga-PSMA PET/CT as a guide for targeted therapy. *Eur J Nucl Med Mol Imaging.* 2018;45:886–887.
5. Salas Fragomeni RA, Menke JR, Holdhoff M, et al. Prostate-specific membrane antigen–targeted imaging with [^{18}F]DCFPyL in high-grade gliomas. *Clin Nucl Med.* 2017;42:e433–e435.
6. Verma P, Malhotra G, Goel A, et al. Differential uptake of ^{68}Ga-PSMA-HBED-CC (PSMA-11) in low-grade versus high-grade gliomas in treatment-naive patients. *Clin Nucl Med.* 2019;44:e318–e322.
7. Saffar H, Noohi M, Tavangar SM, et al. Expression of prostate-specific membrane antigen (PSMA) in brain glioma and its correlation with tumor grade. *Iran J Pathol.* 2018;13:45–53.
8. Holzgreve A, Biczok A, Ruf VC, et al. PSMA expression in glioblastoma as a basis for theranostic approaches: a retrospective, correlational panel study including immunohistochemistry, clinical parameters and PET imaging. *Front Oncol.* 2021;11:646387.
9. Kunikowska J, Charzyńska I, Kuliński R, et al. Tumor uptake in glioblastoma multiforme after IV injection of [^{177}Lu]Lu-PSMA-617. *Eur J Nucl Med Mol Imaging.* 2020;47:1605–1606.
10. Kumar A, Ballal S, Yadav MP, et al. ^{177}Lu-/^{68}Ga-PSMA theranostics in recurrent glioblastoma multiforme: proof of concept. *Clin Nucl Med.* 2020;45:e512–e513.
11. Kratochwil C, Fendler WP, Eiber M, et al. EANM procedure guidelines for radionuclide therapy with ^{177}Lu-labelled PSMA-ligands (^{177}Lu-PSMA-RLT). *Eur J Nucl Med Mol Imaging.* 2019;46:2536–2544.

12. Truckenmueller P, Graef J, Scheel M, et al. [^{68}Ga]Ga-PSMA PET/MRI, histological PSMA expression and preliminary experience with [^{177}Lu]Lu-PSMA therapy in relapsing high-grade glioma. *Front Oncol.* 2022;12:1–10.
13. Nelson AS, Horstman BP. Quantitative SPECT/CT reconstruction with SPECTRATM quant. MIM Software website. https://www.mimsoftware.com/resources/publications. Published February 7, 2022. Accessed April 12, 2023.
14. Cole NM, Mirando D, Nelson AS, et al. Hybrid SPECT/Planar dosimetry for targeted molecular radiotherapy. MIM Software website. https://www.mimsoftware.com/resources/publications. Published November 2, 2020. Accessed April 12, 2023.
15. Nelson AS, Mirando D, Kruzer A, et al. Dosimetry for targeted molecular radiotherapy. MIM Software website. https://www.mimsoftware.com/resources/publications. Published October 19, 2020. Accessed April 12, 2023.
16. Sulman EP, Ismaila N, Armstrong TS, et al. Radiation therapy for glioblastoma: American Society of Clinical Oncology clinical practice guideline endorsement of the American Society for Radiation Oncology guideline. *J Clin Oncol.* 2017;35:361–369.
17. Shieh LT, Guo HR, Ho CH, et al. Survival of glioblastoma treated with a moderately escalated radiation dose: results of a retrospective analysis. *PLoS One.* 2020;15:e0233188.
18. Mahzouni P, Shavakhi M. Prostate-specific membrane antigen expression in neovasculature of glioblastoma multiforme. *Adv Biomed Res.* 2019;8:18.
19. Dréan A, Goldwirt L, Verreault M, et al. Blood-brain barrier, cytotoxic chemotherapies and glioblastoma. *Expert Rev Neurother.* 2016;16:1285–1300.
20. Coia L, Emami B, Solin LJ, et al. Tolerance of normal tissue to therapeutic irradiation. *Int J Radiat Oncol Biol Phys.* 1991;1:35–48.
21. Heynickx N, Herrmann K, Vermeulen K, et al. The salivary glands as a dose limiting organ of PSMA-targeted radionuclide therapy: a review of the lessons learnt so far. *Nucl Med Biol.* 2021;98–99:30–39.
22. Harasaki Y, Waziri A. Potential usefulness of radiosensitizers in glioblastoma. *Neurosurg Clin N Am.* 2012;23:429–437.
23. Bailly C, Vidal A, Bonnemaire C, et al. Potential for nuclear medicine therapy for glioblastoma treatment. *Front Pharmacol.* 2019;10:772.
24. Krolicki L, Bruchertseifer F, Kunikowska J, et al. Prolonged survival in secondary glioblastoma following local injection of targeted alpha therapy with ^{213}Bi-substance P analogue. *Eur J Nucl Med Mol Imaging.* 2018;45:1636–1644.
25. Królicki L, Kunikowska J, Bruchertseifer F, et al. ^{225}Ac- and ^{213}Bi-substance P analogues for glioma therapy. *Semin Nucl Med.* 2020;50:141–151.
26. Królicki L, Bruchertseifer F, Kunikowska J, et al. Safety and efficacy of targeted alpha therapy with ^{213}Bi-DOTA-substance P in recurrent glioblastoma. *Eur J Nucl Med Mol Imaging.* 2019;46:614–622.
27. Liu H, Moy P, Kim S, et al. Monoclonal antibodies to the extracellular domain of prostate-specific membrane antigen also react with tumor vascular endothelium. *Cancer Res.* 1997;57:3629–3634.

Prognostic Role of ^{68}Ga-PSMA11 PET–Based Response in Patients with Prostate Cancer Undergoing Taxane-Based Chemotherapy

Lukas Lunger*[,1], Maythinee Chantadisai*[,2,3], Amir Karimzadeh[2], Isabel Rauscher[2], Calogero D'Alessandria[2], Benedikt Feuerecker[2], Thomas Langbein[2], Robert Tauber[1], Stefan Schiele[1], Wolfgang Weber[2], and Matthias Eiber[2]

[1]*Department of Urology, Rechts der Isar Medical Center, Technical University of Munich, Munich, Germany;* [2]*Department of Nuclear Medicine, Rechts der Isar Medical Center, Technical University of Munich, Munich, Germany; and* [3]*Division of Nuclear Medicine, Department of Radiology, Faculty of Medicine, Chulalongkorn University, King Chulalongkorn Memorial Hospital, The Thai Red Cross Society, Bangkok, Thailand*

This study was performed to assess the prognostic utility of conventional biochemical and imaging response criteria and ^{68}Ga-PSMA11 PET–adapted or –specific systems regarding overall survival (OS) in men with metastatic hormone-sensitive and castration-resistant prostate cancer (PC) treated with taxane-based chemotherapy. **Methods:** A total of 103 patients (metastatic hormone-sensitive PC, $n = 57$; castration-resistant PC, $n = 46$) underwent taxane-based chemotherapy. All patients had a minimum of 2 prostate-specific membrane antigen (PSMA) PET scans (at baseline and up to 3 mo after treatment). PSMA PET response was assessed by RECIST 1.1, adapted Prostate Cancer Working Group Criteria 3 (using PSMA PET instead of bone scan), aPERCIST, and PSMA PET progression (PPP) criteria. Response by each criterion was stratified by either progressive disease (PD) or non-PD. For aPERCIST, stratification by PD, stable disease (SD), and partial/complete remission (PR/CR) was performed. Biochemical response was determined by a prostate-specific antigen decrease of at least 50%. Subgroup analyses were performed by castration status. Univariable Cox proportional hazards regression analyses including Harrell's concordance indices were calculated to investigate the association of PD by response criteria and OS. Kaplan–Meier tests including log-rank statistics were calculated for survival analyses. **Results:** Twenty-six (25%) patients had unmeasurable disease by RECIST 1.1. PD by any response criterion was associated with an at least 2.5-fold increased risk of death and was highest for PD versus CR/PR by aPERCIST (hazard ratio, 11.4) on univariable regression. Stratified by castration status, a similar pattern was observed. PD by any criterion as associated with significantly shortened OS across overall and subgroup analyses. PR/CR by aPERCIST identified patients with lower risk of death and longer OS compared with patients with PD or SD. **Conclusion:** PSMA PET–based response criteria (PPP, aPERCIST, adapted Prostate Cancer Working Group Criteria 3) have high prognostic utility in men with metastatic PC undergoing taxane-based chemotherapy. PPP is simple to use, identified most patients with PD, and showed best prognostic utility regarding OS. PR/CR by aPERCIST identifies a subgroup of responders (PR/CR) showing better outcomes than patients with PD or SD. Future studies are warranted to amend the current paradigm relying on mere differentiation of PD versus non-PD in metastatic PC and to identify true treatment responders by imaging criteria.

Key Words: metastatic prostate cancer; taxane-based chemotherapy; ^{68}Ga-PSMA11 PET/CT; treatment monitoring; survival

J Nucl Med 2023; 64:896–901
DOI: 10.2967/jnumed.122.264962

Prostate cancer (PC) is the most common malignant tumor in men and the second most common cause of cancer-associated mortality (*1*). During the initial hormone-sensitive stage, metastatic PC (mHSPC) typically responds well to androgen deprivation. Nevertheless, most patients will eventually progress despite androgen deprivation, and metastatic castration-resistant PC (mCRPC) develops. This final stage of the disease is associated with poor prognosis and a significantly decreased overall survival (OS) (*2,3*).

Despite the development of novel treatment strategies in both mHSPC and mCRPC, taxane-based chemotherapies remain a standard of care in metastatic PC treatment. Conventional assessment of treatment response in metastatic PC traditionally relies on radiographic criteria including CT and bone scans as proposed by the Prostate Cancer Working Group Criteria 3 (PCWG3) guidelines (*4*). The PCWG3 imaging framework only allows the stratification of progressive disease (PD) versus nonprogression (non-PD) and lacks identifying patients as responders by imaging criteria. The introduction of prostate-specific membrane antigen (PSMA) PET improved the detection of PC metastases compared with conventional imaging (*5*). Current guidelines recommend a PSMA PET in patients with rising or persistently elevated prostate-specific antigen (PSA) after radical treatment (*6,7*).

Whole-body PET imaging has evolved as a reliable tool for assessing response in metastatic disease from various tumor entities (*8,9*). Different frameworks exist for various tumor entities that use either cross-sectional imaging (e.g., RECIST 1.1) or have been introduced for FDG PET (e.g., PERCIST). Most recently, Fanti et al. (*10*) proposed the PSMA PET progression (PPP) criteria for potential use in metastatic PC. However, the use of PSMA PET imaging for assessing response in patients with metastatic PC undergoing systemic treatment is less explored (*11–14*). Despite the introduction of novel frameworks for the application of PSMA PET in metastatic PC, data are limited regarding the prognostic utility of such criteria in comparison to traditional frameworks for the monitoring of treatment response.

The aim of this retrospective analysis was to investigate the comparative prognostic utility of traditional treatment response criteria

Received Sep. 26, 2022; revision accepted Dec. 6, 2022.
For correspondence or reprints, contact Lukas Lunger (lukas.lunger@tum.de).
*Contributed equally to this work.
Published online Dec. 29, 2022.

with PSMA PET criteria regarding OS in patients with metastatic PC (mHSPC and mCRPC) undergoing taxane-based chemotherapy. Traditional criteria comprised nonimaging PSA-based response and conventional anatomy–based RECIST 1.1 (*15*). Specifically, PSMA PET criteria included ^{68}Ga-PSMA11 PET–adapted PERCIST (*16*), adapted PCWG3 (*4*), and PPP criteria (*10*). In addition, we aimed to assess whether the definition of response used in PERCIST would further add prognostic information in the group of patients with response.

MATERIALS AND METHODS

Patients

Patients with either mCRPC or mHSPC undergoing taxane-based chemotherapy and ^{68}Ga-PSMA11 PET before and after treatment between January 2014 and December 2018 at the Technical University Munich were included. The term PSMA PET is used throughout the remaining article and refers to the use of ^{68}Ga-PSMA11 PET/CT in the setting of this retrospective analysis.

We included only patients with pairs of PSMA PET that were performed within a maximum interval of 3 mo before initiation of chemotherapy and up to 3 mo after completion of treatment. Patients without follow-up information and survival data were excluded. Patients with mCRPC underwent up to 1 additional interim PSMA PET after 3 mo from initiation of treatment because of the high risk of progression in these patients. Clinical characteristics and serum PSA level were collected both at baseline and at the posttreatment visit.

All reported investigations were conducted in accordance with the Declaration of Helsinki and with national regulations (*17*). The retrospective study was approved by the Ethics Committee of the Technical University Munich (permit 5665/13), and a waiver of consent was granted. The administration of PSMA11 complied with The German Medicinal Products Act (AMG §13 2b) and the responsible regulatory body (Government of Oberbayern).

Response Assessment

Biochemical response was defined as a PSA decrease of at least 50% after chemotherapy. PET-based response was evaluated as follows: all patients underwent PSMA PET from the skull base to the midthigh using a previously described protocol (*11*). In brief, PET scans were acquired in 3D mode, combined with an intravenous and oral contrast-enhanced CT scan. Images were reviewed by an experienced, board-certified nuclear medicine physician using the Prostate Cancer Molecular Imaging Standardized Evaluation criteria for lesion assessment. Any focal uptake higher than that of the surrounding background and not associated with physiologic uptake was considered suspicious for malignancy (*18*). The posttreatment response was subsequently assessed in accordance with RECIST 1.1 (*15*), PPP (*10*), adapted PERCIST (*16*), and adapted PCWG3 (*4*) criteria as described below.

RECIST 1.1. The revised RECIST 1.1 criteria are widely used for response assessment in solid tumors (*19*). The 2 morphologically largest lesions per organ system were selected in CT as target lesions with a maximum of 5 lesions in total. For targeted tumor lesions, the longest diameter with a minimum size of 10 mm by CT scan was measured. For targeted pathologic nodes, the lesions must meet the criterion of short axis greater than 15 mm by CT images. Finally, a sum of the diameters of all target lesions is evaluated, and the results categorize patients into complete response (CR), partial response (PR), stable disease (SD), and progressive disease (PD). Patients who had only nontarget lesions in the prechemotherapy PET scan, without clear progression or disappearance in postchemotherapy PET, were classified as unmeasurable.

PPP criteria. The PPP criteria were recently proposed by Fanti et al. (*10*). Progression using PSMA PET was defined as follows: appearance of 2 or more new PSMA-positive distant lesions, appearance of 1 new PSMA-positive lesion plus consistent clinical or laboratory data, and an increase in size or PSMA uptake of 1 or more existing lesions of at least 30% plus consistent clinical or laboratory data, together with the confirmation by biopsy or correlative imaging within 3 mo. Clinical and laboratory data included changes in Eastern Cooperative Oncology Group score, the record of any improving or worsening of bone pain, or changes in PSA level before and after treatment. For the last criterion, SUV_{max} was used to evaluate changes in PSMA uptake and lesion size was measured according to the RECIST 1.1 protocol.

Adapted PERCIST. PERCIST 1.0 criteria (*16*) were adapted to the use of PSMA PET as follows: 5 organ systems (prostate or prostate bed, lymph nodes, bone, liver, and other visceral metastatic sites) were recorded per patient. For each organ system, up to 2 lesions with the highest PSMA PET uptake identified on maximum intensity projection PET images were selected on the prechemotherapy PET scan (PET1). To measure the SUV_{peak}, a circular 1.2-cm-diameter volume region of interest was placed over the transaxial slice with maximum ^{68}Ga-PSMA11 PSMA uptake. The posttherapeutic PET (PET2) was compared with the prechemotherapy PET scan (PET1) and interpreted as follows: the absence of any PSMA uptake on PET2 in all target lesions seen on PET1 was considered CR; a decrease in the SUV_{peak} sum of at least 30% (minimum decrease in SUV_{peak} of 0.8) was considered PR; the appearance of a new PET positive lesion on PET2 or an increase in SUV_{peak} sum of at least 30% (minimum increase in SUV_{peak} of 0.8) was considered PD; and an intermediate change in summed SUV_{peak} between −30% and +30% without the appearance of new target lesions was considered SD.

Adapted PCWG3 criteria. PCWG3 criteria (*4*) were adapted to the use of PSMA PET as follows: application of RECIST 1.1 for soft-tissue lesions remained unchanged, and information from PSMA PET was used for assessment of bone lesions instead of a bone scan. Patients who exhibited progression according to RECIST 1.1 or had at least 2 new bone lesions on PET2 were classified as PD. Other conditions were defined as non-PD. Given the high specificity of PSMA PET, no additional confirmation of new bone lesions was demanded.

Statistical Analysis

All values are reported as average (SD) or median (interquartile range [IQR]) for continuous variables and as number and percentage for categoric variables. All statistical tests were conducted for the overall collective and after stratification by castration status. Kaplan–Meier tests including log-rank statistics were calculated for survival analyses. OS was defined as the time from initiation of chemotherapy until death from any causes. Patients who were alive or lost to follow-up were censored at the last date they were known to be alive.

The association between biochemical response and PET-based criteria (aPCWG3, aPERCIST, and PPP) with OS was evaluated using univariate Cox regression analyses and reported as hazard ratio (HR) and 95% CI. To evaluate the goodness of fit of performed Cox regression analyses, the Harrell's concordance index (C-index) was calculated. Ties were included in the calculation of the C-index. $P < 0.05$ was considered statistically significant. All statistical analyses were performed using SPSS version 26 (SPSS).

RESULTS

Patients and Disease Characteristics

A total of 103 patients (mHSPC, $n = 57$; mCRPC, $n = 46$) were included. Clinical characteristics are outlined in Table 1. Most patients had bone metastasis (M1b; $n = 80$ of 103, 78%) and extrapelvic lymph node metastasis (M1a; $n = 72$ of 103, 70%).

Median duration from prechemotherapy PSMA PET to initial chemotherapy was 27 d (IQR, 14–49), whereas the median duration from last chemotherapy application to posttreatment PET was 27 d (IQR, 18–39).

TABLE 1
Clinical Characteristics

Characteristic	Data
Median age (y)	71 (range, 43–85)
Median pre-CTX PSA level (ng/mL)	
mHSPC	15 (IQR, 2–39)
mCRPC	45 (IQR, 10–155)
Gleason score (*n*)	
≤7	31 (30%)
≥8	67 (65%)
NA	5 (5%)
ECOG performance status (*n*)	
0	53 (52%)
1	26 (25%)
2	1 (1%)
NA	23 (22%)
Castration status (*n*)	
mHSPC	57 (55%)
mCRPC	46 (45%)
Pre-CTX miTNM staging (*n*)	
No distant metastasis (M0)	6 (6%)
Extrapelvic node metastasis (M1a)	72 (70%)
Bone metastasis (M1b)	80 (78%)
Visceral metastasis (M1c)	16 (16%)
Pattern of metastatic spread (*n*)	
LN only	21 (21%)
Bone only	9 (9%)
Visceral only	1 (1%)
LN and bone	54 (52%)
LN and visceral organs	1 (1%)
LN, bone, and visceral organs	14 (14%)
LN, bone, and others (subcutaneous, skin metastasis)	2 (2%)
Bone and others (penis)	1 (1%)
Local treatment for PC (*n*)	
Prostatectomy ± lymphadenectomy	58 (56%)
Primary EBRT	13 (13%)
Type of chemotherapy (*n*)	
Docetaxel	95 (92%)
Cabazitaxel	7 (7%)
Docetaxel and cabazitaxel	1 (1%)
Reduction in serum PSA ≥ 50% (*n*)	61 (59%)

CTX = chemotherapy; ECOG = Eastern Cooperative Oncology Group; EBRT = external beam radiotherapy; NA = not available; LN = lymph nodes.

Biochemical Response

Overall, 61 patients (59%) had a PSA decrease of at least 50% after taxane-based chemotherapy. Stratified by castration status, 45 (79%) mHSPC patients and 16 (35%) mCRPC patients had a PSA decrease of at least 50%.

For mHSPC, median pre- and postchemotherapy PSA values were 14.9 (IQR, 1.9–39.3) and 0.6 ng/mL (IQR, 0.04–3.5), respectively. For mCRPC, median pre- and postchemotherapy PSA values were 45 (IQR, 9.5–154.5) and 34 ng/mL (IQR 6.7–153.8), respectively.

Imaging-Based Response

By RECIST 1.1 criteria, 26 (25% of all patients) had unmeasurable disease. Of those, 5 patients had isolated bone metastases without soft-tissue component, 6 patients had nontarget lymph nodes with or without nontarget prostatic bed lesions, and 15 patients had coexisting nontarget nodes and bone lesions. Survival and further response analyses for RECIST 1.1 were therefore omitted. An overview of response rates by PET response criteria is given in Table 2.

Overall, by adapted PERCIST criteria, PD was observed in 33 (32%) patients. For mHSPC and mCRPC, PD was observed in 8 (14%) and 25 (54%) patients, respectively. By aPCWG3 criteria, PD was observed in 34 (33%) patients. For mHSPC and mCRPC, PD was observed in 9 (16%) and 25 (54%) patients, respectively. By PPP criteria, PD was observed in 41 (40%) patients. Stratified by castration status, PD was observed in 11 (19%) mHSPC patients and 30 (65%) mCRPC patients.

Survival Analyses by Response Criteria

Median OS of all patients was 50 mo (95% CI, 31–69). Median OS for patients with mCRPC was 18 mo (95% CI, 15–21 mo) and was not reached for patients with mHSPC.

Kaplan–Meier analyses by biochemical response and imaging-based response criteria are shown in Figures 1A–1D. Progression by any investigated criterion was associated with a significantly shorter OS compared with response (median survival ranging from 14 to 17 mo [PD] vs. median survival ranging from 57 mo – not reached. [no-PD]). Additional survival analyses for stratification by castration status are shown as a cumulative illustration in Supplemental Figure 1 (supplemental materials are available at http://jnm.snmjournals.org).

TABLE 2
Overall Response Rates by Imaging Response Criteria

Criteria	Response	*N* (%)
RECIST 1.1	n/m	26 (25)
	PD	20 (19)
	SD	38 (37)
	PR	15 (15)
	CR	4 (4)
aPERCIST	PD	33 (32)
	SD	18 (18)
	PR	45 (44)
	CR	7 (7)
aPCWG3	PD	34 (33)
	No-PD	69 (67)
PPP	PD	41 (40)
	No PD	62 (60)

n/m = unmeasurable disease.

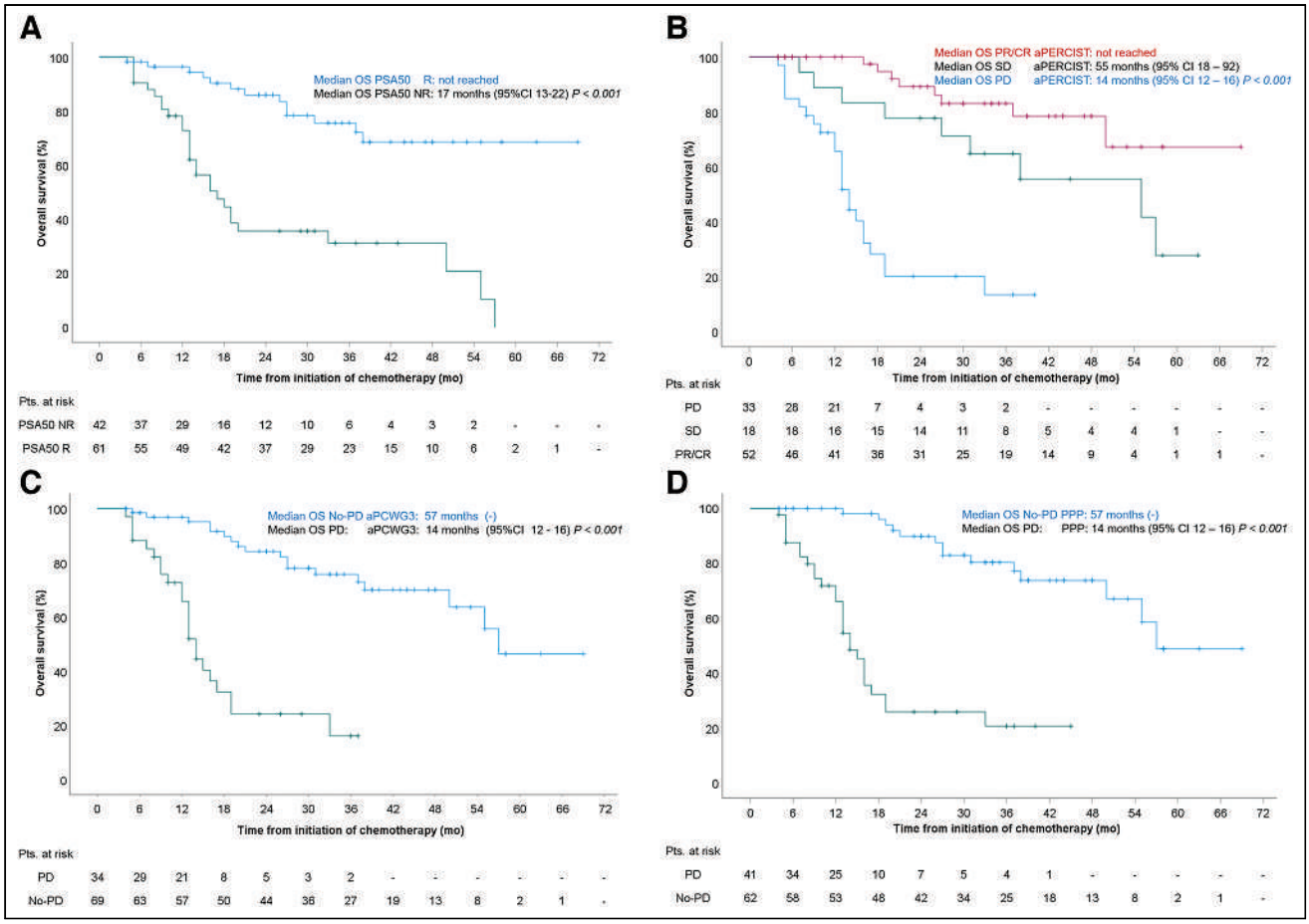

FIGURE 1. Kaplan–Meier estimates of OS by biochemical response (A), adapted PERCIST (B), adapted PCWG3 (C), and PPP (D).

Prognostic Value of Response Criteria

Cox regression analyses investigating the associations of PET-based response criteria and biochemical response with OS are given in Table 3. Of note, on univariable analysis, PD (independent of castration status) as defined by any of the investigated PET criteria in this study was associated with a significantly increased risk of death (HR range, 4.1–8.1; 95% CI, 2.5–16.7). C-index analyses revealed the strongest prognostic values for PPP (HR, 0.77; 95% CI, 0.72–0.81) and aPERCIST (HR, 0.75; 95% CI, 0.69–0.80). Details are presented in Table 3.

Stratified by castration status, for mHSPC, aPCWG3 and PPP criteria showed a strong prognostic value with a C-index > 0.73). For mCRPC status, aPERCIST and PPP criteria C-indices were highest (>0.69; see supplemental Tables 1 and 2 for more detailed results).

DISCUSSION

The objective and reliable evaluation of response to systemic treatment is critical to both clinical research and practice. To date, a variety

TABLE 3
Univariable Cox Regression Analyses for Association of Response Criteria with OS, All Patients (mCRPC and mHSPC) Included

Criteria	Response	*N**	HR	95% CI	*P*	C-index
PSA50	PD vs. no-PD	42 vs. 61	4.8	2.5–9.3	<0.001	0.695 (0.629–0.761)
aPERCIST	PD vs. no-PD	33 vs. 70	8.1	4.1–16.2	<0.001	0.746 (0.690–0.802)
	PD vs. SD	33 vs. 18	4.1	1.7–10.1	<0.001	
	PD vs. PR/CR	33 vs. 52	11.4	4.7–27.1	<0.001	
aPCWG3	PD vs. no-PD	34 vs. 69	7.1	3.5–14.2	<0.001	0.729 (0.670–0.788)
PPP	PD vs. no-PD	41 vs. 62	8.1	4.0–16.7	<0.001	0.765 (0.721–0.808)

n/m = unmeasurable disease; PSA50 = dichotomous, biochemical response with PSA reduction ≥ 50%; *Number of patients.

of frameworks exists to determine response to PC treatment, but data on their prognostic value and use in routine clinical practice are limited. Here, we present a considerably large and evenly balanced cohort including both mCRPC and mHSPC patients to retrospectively compare the prognostic utility of response to taxane-based chemotherapy by serum PSA decrease, RECIST 1.1, aPERCIST, aPCWG3, and PPP criteria regarding OS. Within the used imaging biomarkers, aPERCIST offers the possibility not only to detect PD versus non-PD but also to identify PR/CR.

Overall, PD (independent of castration status) as defined by traditional and PSMA PET frameworks was associated with an at least 2.5-fold increased risk of death by univariable analyses in this study. PD by aPERCIST was associated with the highest risk of death (HR, 11.4; 95% CI, 4.7–27.1) compared with patients with PR/CR ($P < 0.001$). To compare the prognostic utility of reported HRs, C-index analyses were performed. Based on its C-index, PPP was the framework with the highest prognostic value compared with the other investigated criteria; however, it was not statistically different. Overall, Kaplan–Meier curve analyses revealed that PD by any investigated criterion was associated with significantly reduced OS. Of interest, across all criteria, only in patients classified as having PR/CR by aPERCIST was median OS not reached and significantly shorter in patients with PD and SD (14 [95% CI, 12–16] and 55 mo [95% CI, 18–92], respectively; $P < 0.001$). The same pattern was observed after stratification by castration status (Supplemental Figure 1).

A recent review investigated the role of PET-based imaging for response to systemic treatment in metastasized PC (*14*). The results suggest that the volumetric extent of metastatic burden or the total lesion PSMA estimated by PSMA PET may have prognostic value in patients undergoing taxane-based chemotherapy (*14*). However, the evidence backing this conclusion is sparse and relies on a limited number of studies with small sample sizes. Moreover, most studies investigate different endpoints and lack standardized definitions of response and comparable follow-up. Similarly, 2 works by Has Simsek et al. (*12*) and Shagera et al. (*13*) most recently aimed to investigate the prognostic role of total metastatic burden. Of interest, both studies found that PD by PSMA total tumor volume was associated with a significantly shortened OS. Yet, the significance of presented results appears limited by the overall small sample size, the lack of posttreatment PET scans, and the combination of both mCRPC and mHSPC patients in 1 cohort. In contrast, we focused on the use of different diagnostic frameworks for response assessment. Here, we assessed response by comparing a limited number of lesions across 2 different timepoints and assessing the presence of new lesions in follow-up scans. Of note, the investigated methods in our study did not require the determination of the whole-body tumor volume. However, our data clearly indicate that PD, as defined in PPP, PCWG3, and aPERCIST, was associated with shorter OS. Yet, future prospective studies are warranted to validate and determine the prognostic benefit of one framework over the other, including a definition of reliable cutoffs for the measurement of whole-body metastatic tumor volume.

Comparing the investigated frameworks provided insights, and in contrast to previous studies (*11*), our analysis is based on long-term follow-up, allowing a comparison of results from different frameworks with OS as a clinically most meaningful outcome parameter. First, our results showed that PPP and aPERCIST had the highest comparative prognostic value. However, whereas response assessment using PPP is much more feasible in routine practice given its simple application, aPERCIST provides the potential not only to discriminate between PD and non-PD but also to identify responders (CR/PR) within this group with substantially better outcome compared with SD. This finding highlights an important aspect of aPERCIST worth investigation in further prospective studies. To date, the use of software solutions (semi-)automatically detecting, quantifying, and following tumor lesions over time is required to facilitate its adoption. Such tools are currently under development by various vendors but are not yet fully implemented in standard software solutions. Thus, the application of aPERCIST criteria remains currently limited to scientific investigations until automated analyses are routinely available.

Conversely, response by aPCWG3 as a straightforward adoption of PCWG3 for the use with PSMA PET did not outperform aPERCIST or PPP in terms of prognostic utility in this study. In addition, despite the incorporation of similar criteria compared with PPP for bone assessment, the application remains time consuming and is hampered by the manual quantitative measurement of soft-tissue metastases. Similar to previous investigations, response by traditional RECIST 1.1 is not useful for metastasized PC (*20*). In our cohort, 25% of included patients only had unmeasurable disease, confirming a major limitation of this framework for response assessment in metastatic PC. Furthermore, typical for metastasized PC, 78% of patients had bone metastases in this study. However, these lesions cannot be assessed quantitatively within this framework in the absence of extraosseous soft-tissue extension and osteolytic lesions. Progression of sclerotic bone metastases in RECIST 1.1 can only be determined in the case of "unequivocal progression" of nontarget lesions, which is prone to subjective interpretation. These observations led to its combination with bone scintigraphy and their combined use within the PCWG framework (*4*). Taken together, our results suggest that PPP seems most useful for determination of treatment response of metastasized PC in routine clinical practice, given its easy adoption and its comparable prognostic utility to aPCWG3 or aPERCIST.

Here, we also analyzed the utility of traditional response by serum PSA reduction as a prognostic biomarker. Although serum PSA measurement effectively stratified patients in PD and non-PD, its C-index was lower compared with the other imaging-based response criteria. In addition, it is known that its sole use is hampered by the known inter- and intratumor heterogeneity associated especially with mCRPC (*21*), as well as its inability to detect clinically relevant complications (e.g., fractures and embolism) compared with imaging-based response assessment.

Several limitations of this study are noteworthy including the small cohort size and the retrospective study design, associated with selection and misclassification bias. Additionally, the current study reflects a single center experience, and all imaging data sets were reviewed by a single physician. One particularly relevant limitation concerns the study population: here, both patients with mCRPC and mHSPC were included for survival analyses. The inclusion of mHSPC patients might have introduced substantial bias of obtained univariable regression results because of the small study population and the low rate of PD events compared with mCRPC patients alone. Nevertheless, all results followed a similar trend even after stratification by castration status and expand the available knowledge on the prognostic role of PSMA PET–based response criteria regarding OS in a large cohort of patients with metastatic PC.

CONCLUSION

The PSMA PET–based response criteria PPP, aPERCIST, and aPCWG3 are reliable and prognostic tools for the assessment of treatment response after taxane-based chemotherapy in both mHSPC and

mCRPC patients. PPP appears most useful for determination of treatment response of metastasized PC in routine clinical practice. PPP is easy to adopt and implement in clinical routine, and its prognostic utility was similar to aPCWG3 or aPERCIST in this study while lacking the need of (semi)-automated software applications. In contrast, aPERCIST offers the possibility to also identify a subgroup of responders (PR/CR) showing reduced risk of death and associated with a significantly longer OS compared with patients with PD and SD. Its further prospective investigation is warranted to potentially expand the current paradigm assessing only PD versus non-PD to the identification of true response by an imaging biomarker for response in metastasized PC.

DISCLOSURE

Matthias Eiber reports fees from Blue Earth Diagnostics Ltd. (consultant, research funding), Novartis/AAA (consultant), Telix (consultant), Bayer (consultant, research funding), RayzeBio (consultant), Point Biopharma (consultant), Janssen Pharmaceuticals (consultant, speakers bureau), Parexel (image review), and Bioclinica (image review) outside the submitted work and a patent application for rhPSMA. No other potential conflict of interest relevant to this article was reported.

KEY POINTS

QUESTION: What is the comparative prognostic utility of traditional treatment response criteria with PSMA PET criteria for OS in metastatic PC patients undergoing taxane based chemotherapy?

PERTINENT FINDINGS: This retrospective cohort study on (n = 103) metastatic PC patients showed that PD by any response criterion was associated with an at least 2.5-fold increased risk of death and was highest for PD versus CR/PR by aPERCIST. PPP as an easy to determine parameter showed best prognostic utility regarding OS.

IMPLICATIONS FOR PATIENT CARE: PSMA PET–based response criteria have high prognostic utility in men with metastatic PC undergoing taxane-based chemotherapy and may help to identify patients at high risk for reduced OS.

REFERENCES

1. Culp MB, Soerjomataram I, Efstathiou JA, Bray F, Jemal A. recent global patterns in prostate cancer incidence and mortality rates. *Eur Urol.* 2020;77:38–52.
2. Francini E, Gray KP, Shaw GK, et al. Impact of new systemic therapies on overall survival of patients with metastatic castration-resistant prostate cancer in a hospital-based registry. *Prostate Cancer Prostatic Dis.* 2019;22:420–427.
3. Marques RB, Dits NF, Erkens-Schulze S, van Weerden WM, Jenster G. Bypass mechanisms of the androgen receptor pathway in therapy-resistant prostate cancer cell models. *PLoS One.* 2010;5:e13500.
4. Scher HI, Morris MJ, Stadler WM, et al. Trial design and objectives for castration-resistant prostate cancer: updated recommendations from the Prostate Cancer Clinical Trials Working Group 3. *J Clin Oncol.* 2016;34:1402–1418.
5. Hofman MS, Lawrentschuk N, Francis RJ, et al. Prostate-specific membrane antigen PET-CT in patients with high-risk prostate cancer before curative-intent surgery or radiotherapy (proPSMA): a prospective, randomised, multicentre study. *Lancet.* 2020;395:1208–1216.
6. Mottet N, van den Bergh RCN, Briers E, et al. EAU-ESTRO-SIOG guidelines on prostate cancer. Accessed July 27, 2022. https://d56bochluxqnz.cloudfront.net/documents/full-guideline/EAU-EANM-ESTRO-ESUR-ISUP_SIOG-Guidelines-on-Prostate-Cancer-2022_2022-04-25-063938_yfos.pdf
7. Oncology Program Guidelines (German Cancer Society, German Cancer Aid, AWMF): S3 guideline prostate cancer, long version 6.2, 2021, AWMF register number: 043/022OL. Accessed July 27, 2022. http://www.leitlinienprogramm-onkologie.de/leitlinien/prostatakarzinom/
8. Weber WA, Wieder H. Monitoring chemotherapy and radiotherapy of solid tumors. *Eur J Nucl Med Mol Imaging.* 2006;33(suppl 1):27–37.
9. Juweid ME, Cheson BD. Positron-emission tomography and assessment of cancer therapy. *N Engl J Med.* 2006;354:496–507.
10. Fanti S, Hadaschik B, Herrmann K. Proposal for systemic-therapy response-assessment criteria at the time of PSMA PET/CT imaging: the PSMA PET progression criteria. *J Nucl Med.* 2020;61:678–682.
11. Seitz AK, Rauscher I, Haller B, et al. Preliminary results on response assessment using (68)Ga-HBED-CC-PSMA PET/CT in patients with metastatic prostate cancer undergoing docetaxel chemotherapy. *Eur J Nucl Med Mol Imaging.* 2018;45:602–612.
12. Has Simsek D, Kuyumcu S, Karadogan S, et al. Can PSMA-based tumor burden predict response to docetaxel treatment in metastatic castration-resistant prostate cancer? *Ann Nucl Med.* 2021;35:680–690.
13. Shagera QA, Artigas C, Karfis I, et al. (68)Ga-PSMA PET/CT for response assessment and outcome prediction in metastatic prostate cancer patients treated with taxane-based chemotherapy. *J Nucl Med.* 2022;63:1191–1198.
14. Alongi P, Laudicella R, Lanzafame H, et al. PSMA and choline PET for the assessment of response to therapy and survival outcomes in prostate cancer patients: a systematic review from the literature. *Cancers (Basel).* 2022;14:1770.
15. Schwartz LH, Litiere S, de Vries E, et al. RECIST 1.1: update and clarification—from the RECIST committee. *Eur J Cancer.* 2016;62:132–137.
16. Wahl RL, Jacene H, Kasamon Y, Lodge MA. From RECIST to PERCIST: evolving considerations for PET response criteria in solid tumors. *J Nucl Med.* 2009;50(suppl 1):122s–150s.
17. World Medical Association. World Medical Association Declaration of Helsinki. Ethical principles for medical research involving human subjects. *Bull World Health Organ.* 2001;79:373–374.
18. Eiber M, Herrmann K, Calais J, et al. Prostate cancer molecular imaging standardized evaluation (PROMISE): proposed miTNM classification for the interpretation of PSMA-ligand PET/CT. *J Nucl Med.* 2018;59:469–478.
19. Eisenhauer EA, Therasse P, Bogaerts J, et al. New response evaluation criteria in solid tumours: revised RECIST guideline (version 1.1). *Eur J Cancer.* 2009;45:228–247.
20. Gafita A, Rauscher I, Fendler WP, et al. Measuring response in metastatic castration-resistant prostate cancer using PSMA PET/CT: comparison of RECIST 1.1, aPCWG3, aPERCIST, PPP, and RECIP 1.0 criteria. *Eur J Nucl Med Mol Imaging.* 2022;49:4271–4281.
21. Shah RB, Mehra R, Chinnaiyan AM, et al. Androgen-independent prostate cancer is a heterogeneous group of diseases: lessons from a rapid autopsy program. *Cancer Res.* 2004;64:9209–9216.

^{68}Ga-PSMA PET/CT–Based Atlas for Prostate Bed Recurrence After Radical Prostatectomy: Clinical Implications for Salvage Radiation Therapy Contouring Guidelines

Ida Sonni[1–3], Alan Dal Pra[4], Dylan P. O'Connell[5], Zachary Ells[1], Matthias Benz[1,2], Kathleen Nguyen[1], Stephanie M. Yoon[5], Jie Deng[5], Clayton Smith[5], Tristan Grogan[6], Nickolas G. Nickols[5,7], Minsong Cao[5], Amar U. Kishan[5], and Jeremie Calais[1]

[1]*Ahmanson Translational Theranostics Division, Department of Molecular and Medical Pharmacology, David Geffen School of Medicine, University of California Los Angeles, Los Angeles, California;* [2]*Department of Radiology, David Geffen School of Medicine, University of California Los Angeles, Los Angeles, California;* [3]*Nuclear Medicine Unit, Department of Experimental and Clinical Medicine, Magna Graecia University, Catanzaro, Italy;* [4]*Department of Radiation Oncology, Miller School of Medicine, University of Miami, Miami, Florida;* [5]*Department of Radiation Oncology, David Geffen School of Medicine, University of California Los Angeles, Los Angeles, California;* [6]*Department of Medicine Statistics Core, David Geffen School of Medicine, University of California Los Angeles, Los Angeles, California; and* [7]*Department of Radiation Oncology, Veteran Affairs Greater Los Angeles Healthcare System, Los Angeles, California*

The aim of this study was to analyze the patterns of prostate bed (PB) recurrence in prostate cancer patients experiencing prostate-specific antigen (PSA) persistence (BCP) or biochemical recurrence (BCR) after radical prostatectomy using ^{68}Ga-PSMA-11 PET/CT (^{68}Ga-PSMA PET) in relation to the Radiation Therapy Oncology Group (RTOG) clinical target volumes (CTVs). **Methods:** This single-center, retrospective analysis included patients with BCP or BCR after radical prostatectomy and PB recurrence on ^{68}Ga-PSMA PET. The PB recurrences were delineated by nuclear medicine physicians, the CTVs by radiation oncologists contouring guidelines on the ^{68}Ga-PSMA PET, respectively, masked from each other. The coverage of the ^{68}Ga-PSMA PET recurrence was categorized as PSMA recurrence completely covered, partially covered, or not covered by the RTOG-based CTV. Further, we evaluated the differences in PSMA recurrence patterns among patients with different ^{68}Ga-PSMA PET staging (miTNM). Mann–Whitney *U* tests, the chi-square test, and Spearman (ρ) correlation analysis were used to investigate associations between CTV coverage and ^{68}Ga-PSMA PET–based tumor volume, serum PSA levels, miTNM, and rectal/bladder involvement. **Results:** A total of 226 patients were included in the analysis; 127 patients had PSMA recurrence limited to the PB (miTrN0M0), 30 had pelvic nodal disease (miTrN1M0), 32 had extrapelvic disease (miTrN0M1), and 37 had both pelvic nodal disease and extrapelvic disease (miTrN1M1). In the miTrN0M0 cohort, the recurrence involved the rectal and bladder walls in 12 of 127 (9%) and 4 of 127 (3%), respectively. The PSMA-positive PB recurrences were completely covered by the CTV in 68 of 127 patients (53%), partially covered in 43 of 127 (34%), and not covered in 16 of 127 (13%). Full coverage was associated with a smaller tumor volume ($P = 0.043$), a lack of rectal/bladder wall involvement ($P = 0.03$), and lower miTNM staging ($P = 0.035$) but not with lower serum PSA levels ($P = 0.979$). **Conclusion:** Our study suggests that ^{68}Ga-PSMA PET can be a valuable tool for guiding salvage radiation therapy (SRT) planning directed to the PB in the setting of postoperative BCR or BCP. These data should be incorporated into the redefinition of PB contouring guidelines.

Key Words: ^{68}Ga-PSMA PET; RTOG; prostate cancer; prostate bed recurrence; salvage radiation

J Nucl Med 2023; 64:902–909
DOI: 10.2967/jnumed.122.265025

Approximately one-third of patients undergoing radical prostatectomy for prostate cancer will experience disease progression within 10 y (*1–3*). Postoperative radiotherapy to the prostate bed (PB) is a potential curative treatment option either in the presence of high-risk factors for local recurrence (adjuvant radiotherapy) or in patients with biochemical and clinical evidence of local recurrence (*4*).

The definition of the clinical target volume (CTV) for PB radiation has been guided by contouring guidelines mostly based on expert consensus rather than strict anatomic patterns of local recurrence (*5–8*). In the past decade, PET targeting the prostate specific membrane antigen (PSMA PET) has emerged as an accurate and specific imaging tool for the evaluation of patients experiencing biochemical recurrence (BCR) of prostate cancer (*9*). Particularly after the FDA approval of the first PSMA-targeting PET radiopharmaceutical in December 2020 (*10*), ^{68}Ga-PSMA PET has been increasingly implemented in this clinical setting (*11*) and can serve as an anatomic guide for salvage treatments. Therefore, new imaging modalities like ^{68}Ga-PSMA PET could provide important information for a redefinition of the salvage radiation therapy (SRT) contouring guidelines.

Herein we present a detailed analysis of local recurrences detected by ^{68}Ga-PSMA-11 PET/CT (^{68}Ga-PSMA PET) in men with prostate cancer experiencing prostate-specific antigen (PSA) persistence (BCP) or biochemical recurrence (BCR) after radical prostatectomy. In addition, we assessed the location of these lesions in relation to the CTV recommendations by the Radiation Therapy Oncology Group (RTOG) contouring guidelines (*5*).

Received Oct. 21, 2022; revision accepted Jan. 26, 2023.
For correspondence or reprints, contact Ida Sonni (isonni@mednet.ucla.edu).
Published online Feb. 9, 2023.

MATERIALS AND METHODS

Patients

We retrospectively screened all ^{68}Ga-PSMA PET scans acquired in our nuclear medicine clinic at UCLA between November 2016 and November 2020 as part of 2 prospective clinical studies enrolling patients with BCR or BCP (hereafter indicated as BCR) of prostate cancer after radical prostatectomy (NCT02940262, NCT03582774). Men with prostate cancer treated with radical prostatectomy undergoing ^{68}Ga-PSMA PET for BCR were included in our analysis if their clinical report described a recurrence in the PB. BCR was defined as a PSA of 0.2 ng/mL or more measured more than 6 wk after prostatectomy (*9*). The flowchart in Figure 1 shows the patient selection process. Patients' clinical history and clinical data were collected from electronic medical records. This retrospective analysis was approved by the Ethics Committee (UCLA IRB#20–001948), which waived the necessity for study specific consent.

^{68}Ga-PSMA PET

The PSMA-targeting ligand used for ^{68}Ga-PSMA PET was ^{68}Ga-PSMA-11 (Glu-NH-CO-NH-Lys-(Ahx)-[^{68}Ga(HBED-CC)]) (*12*). Images were acquired using a 64-detector PET/CT scanner (2007 Biograph 64 Truepoint or 2010 Biograph mCT 64; Siemens). A diagnostic CT scan (200–240 mAs, 120 kV) was obtained after intravenous or oral contrast administration, unless contraindicated. A whole-body scan was acquired from pelvis to vertex before a dedicated postvoid pelvic scan. The latter was not used for the analysis. All PET images were reconstructed with corrections for attenuation, dead-time, random events, and scatter, using iterative ordered-subsets expectation. The time per bed position was based on patient weight (*13*).

^{68}Ga-PSMA PET Analysis and PB Recurrence Contouring

The clinical ^{68}Ga-PSMA PET reports were used to screen patients who had a suspected PB recurrence after radical prostatectomy. The description of the miTNM staging on the clinical reports was confirmed by 1 investigator (KN) who retrospectively reviewed all ^{68}Ga-PSMA PET scans. After confirming the presence of a PB recurrence on ^{68}Ga-PSMA PET, 2 board certified nuclear medicine physicians (IS and MB) manually delineated the PB lesions according to the ^{68}Ga-PSMA PET procedure guidelines (*14*) using the 2- and 3-dimensional brush tools on MIM v 7.7.5 (MIM Software Inc.). A third nuclear medicine physician (JC) was involved in cases deemed difficult and a consensus was achieved between the 3 readers. ^{68}Ga-PSMA PET–based lesion volumes were recorded.

PSMA PET scans were visualized using a default upper SUV_{max} threshold of 5. Because of the variable intensity of PSMA uptake by different lesions and interference of physiologic urinary bladder uptake, often obscuring visualization of recurrences in its proximity, readers used manual adjustments of the SUV_{max} window thresholds based on each individual case, to help distinguish physiologic from pathologic uptake (*14*). Whenever possible and deemed useful by the readers, the fused CT images were used to facilitate lesion delineation.

The CT component of ^{68}Ga-PSMA PET was used to assess the relation between the PSMA-based recurrence and significant anatomic structures (i.e., the rectal and bladder wall). Any PSMA-avid lesions overlapping the rectal or bladder wall on CT was described as involving the rectal or bladder wall. The association between rectal or bladder wall involvement and the PSMA recurrences was assessed. The ^{68}Ga-PSMA PET readers described each patient's disease spread using the Prostate Cancer Molecular Imaging Standardized Evaluation (PROMISE) criteria and the molecular imaging TNM (miTNM) (*15*). Briefly, the presence of a PB recurrence was described as Tr, pelvic lymph node involvement as N1, extrapelvic nodal or distant organs involvement as M1, pelvic nodal and extrapelvic disease as N1M1. The miTNM was used for a subanalysis investigating the correlation between the CTV coverage and the ^{68}Ga-PSMA PET–based disease stage.

RTOG-Based CTV Contouring

The CTV contours were delineated on the CT component of each ^{68}Ga-PSMA PET scan by 4 radiation oncologists (SMY, JD, CS, and AUK) masked with regard to the PSMA component of the imaging scan, and to the lesions contoured on ^{68}Ga-PSMA PET. The delineation of the PB CTV followed the recommendations of the RTOG contouring guidelines (*5*). In summary, the inferior border of the CTV extended inferiorly 8–12 mm from the vesicourethral anastomosis, and the superior border from the level of the caudal vas deferens remnant. The anterior border of the CTV extended to the posterior border of the pubis up to the top of the pubic symphysis, and the posterior border to the anterior rectal wall. Laterally, at the caudal level, the CTV extended to the levator ani muscle. Above the pubic symphysis, 1–2 cm of the bladder wall was included in the CTV; posteriorly, the CTV extended to the mesorectal fascia, and laterally, to the sacro-recto-genitopubic fascia.

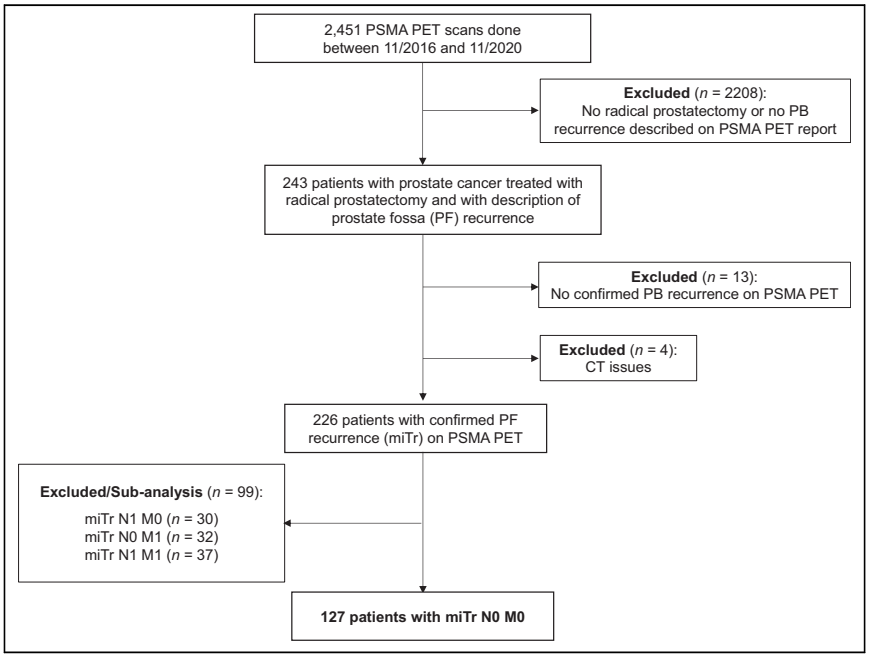

FIGURE 1. Flowchart of screening process.

Coverage Analysis and Heat Map

Two of the investigators, a nuclear medicine physician (IS) and a radiation oncologist (ADP), assessed the CTV coverage of the PB ^{68}Ga-PSMA PET–based recurrence in consensus using 3 prespecified outcomes as follows: ^{68}Ga-PSMA PET recurrence completely covered, partially covered, or not covered by the CTV. The 3 outcomes were further combined into: ^{68}Ga-PSMA PET recurrence completely covered by the CTV and not completely covered by the CTV (including the partially covered and not covered by the CTV outcomes). In case the ^{68}Ga-PSMA PET recurrence was not

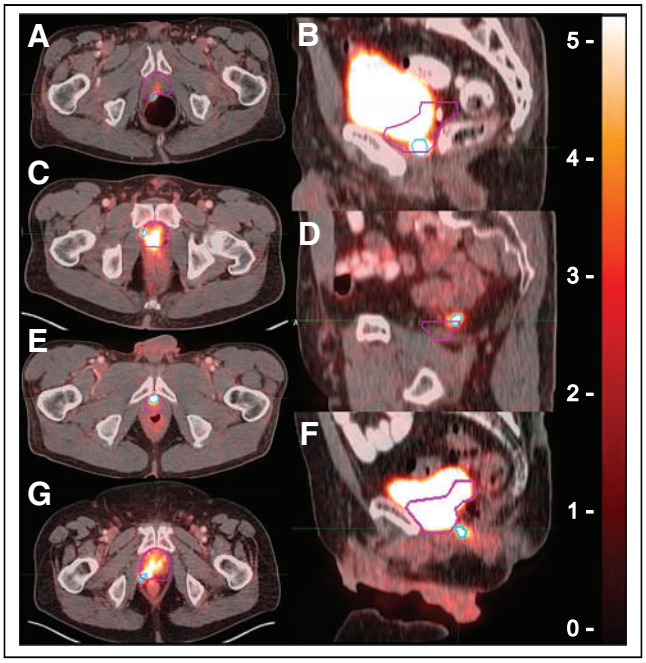

FIGURE 2. Definition of location of ^{68}Ga-PSMA PET lesion exceeding CTV borders. ^{68}Ga-PSMA PET contours are in light blue, and CTV contours are in pink. ^{68}Ga-PSMA PET lesion extended beyond CTV at posterior (A), inferior (B), lateral (C), superior (D), anterior (E), posteroinferior (F), and posterolateral (G) borders.

completely covered by the CTV, the border of PB exceeded by the ^{68}Ga-PSMA PET recurrence was described as anterior, posterior, lateral, inferior, superior, and combinations of them. Individual examples of the image analysis findings are shown in Figure 2.

A 2-dimensional heat map showing the PB recurrence distribution patterns was created by two of the investigators (DPOC and MC) by mapping all ^{68}Ga-PSMA PET contours onto a template patient's CT through manual rigid registration for the whole cohort and for each miTNM staging (Fig. 3). A 3-dimensional representation of all recurrences was generated by one of the investigators (ZE) using 3D Slicer (http://www.slicer.org) (*16*).

As a secondary objective, we conducted a subanalysis evaluating the differences in ^{68}Ga-PSMA PET recurrence patterns among patients with different miTNM staging (i.e., miTrN0M0, miTrN1M0, miTrN0M1, and miTrN1M1).

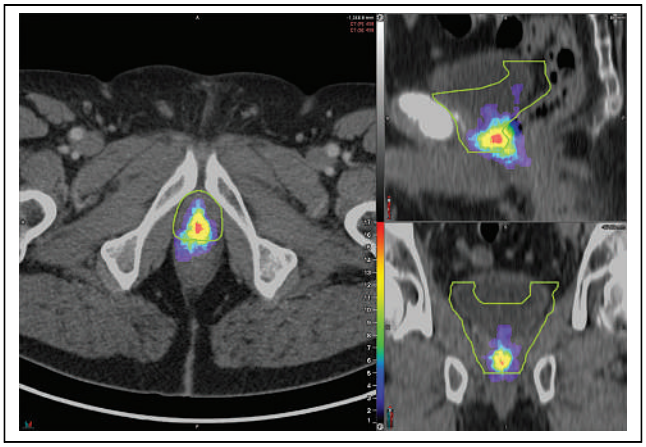

FIGURE 3. Heat map of distribution of prostate bed ^{68}Ga-PSMA PET recurrences in miTrN0Mo cohort (127 patients), mapped on template patient's anatomy (green contour represents CTV).

Statistical Analysis

To assess the association between dichotomized CTV coverage status (fully vs. not fully covered – including the partially covered and not covered outcome) and serum PSA levels we used the Mann–Whitney *U* test because of the distributional properties of PSA levels. Similarly, we compared PSMA-based tumor volume and rectal/bladder involvement to dichotomized CTV coverage status.

To investigate the association between the miTNM stage and the CTV coverage (e.g., fully, partially, and not covered) we used the chi-square test. Descriptive statistics are expressed as median (IQR), unless stated otherwise. All statistical analyses were conducted using Jamovi version 2.2.5 (The jamovi project (2021) retrieved from https://www.jamovi.org) and *P* values of less than 0.05 were considered statistically significant.

RESULTS

Patient Population

A total of 2,451 ^{68}Ga-PSMA PET scans performed between November 2016 and November 2020 were screened for inclusion criteria. Of the 2,451 scans, 226 (9%) were included in this retrospective analysis. The median (IQR) time interval between radical prostatectomy and ^{68}Ga-PSMA PET was 77 mo (28–128). Table 1 shows the clinical characteristics of all patients and the different cohorts included in the subanalysis. Of 226 patients, 127 (56%) had PB limited disease (miTrN0M0), 30 (13%) were classified as miTrN1M0, 32 (14%) as miTrN0M1, and 37 (16%) as miTrN1M1. The main cohort included 127 patients, whereas patients with spread of disease outside the PB were included in a separate a subanalysis.

CTV Coverage of ^{68}Ga-PSMA PET Recurrence

The ^{68}Ga-PSMA PET PB recurrences were fully covered by the CTV in 68 of 127 patients (54%), partially covered in 43 of 127 patients (34%), and not covered in 16 of 127 patients (13%). In the latter 2 groups, the ^{68}Ga-PSMA PET recurrences extended beyond the CTV at the following locations: posteriorly (30/59; 51%), posterolaterally (14/59; 24%), posteroinferiorly (3/59; 5%), anteriorly (1/59; 2%), superiorly (1/59; 2%), and inferiorly (10/59; 17%) (Table 2; Figs. 4 and 5).

Impact of Serum PSA Levels and Tumor Volume on CTV Coverage

The median serum PSA level at time of ^{68}Ga-PSMA PET in the miTrN0M0 cohort was 1.02 ng/mL (IQR, 0.5–2.18; range, 0.10–57.6 ng/mL). In patients with PB recurrences fully covered, partially covered and fully outside the CTV, serum PSA levels were 1.11 ng/mL (0.5–2.2; range, 0.10–28), 1.09 ng/mL (0.46–2.63; range, 0.20–57.63) and 0.84 ng/mL (0.62–1.11; range, 0.23–7.8), respectively.

Thirty-four of 127 patients (27%) had a serum PSA level of less than or equal to 0.5 ng/mL, and 93 of 127 (73%) had a serum PSA level of greater than 0.5 ng/mL. The CTV coverage outcome was not associated with serum PSA levels ($P = 0.98$) or with PSA levels of less than or equal to 0.5 ng/mL ($P = 0.75$). In the 34 patients with PSA levels of less than or equal to 0.5 ng/mL, the ^{68}Ga-PSMA PET PB recurrences were fully covered by the CTV in 19 of 34 patients (56%), partially covered in 12 of 34 patients (35%), and not covered in 3 of 34 patients (9%). In the latter 2 groups, the ^{68}Ga-PSMA PET recurrences extended beyond the CTV at the following locations: posteriorly (8/15; 53%), posterolaterally (3/15; 27%), and inferiorly (4/15; 20%).

TABLE 1
Clinical and Demographic Characteristics of All Patients and All Cohorts*

Characteristic	Full cohort (miTrNxMx)	miTrN0M0 cohort	miTrN1M0 cohort	miTrN0M1 cohort	miTrN1M1 cohort	*P*
No. of patients	226	127	30	32	37	
Median age (y)†	69.5 (64–73)	70 (47–89)	68.5 (63.3–76.3)	65 (61–74.5)	72 (68–76)	0.47‡
Median serum PSA level (ng/mL)†	1.21 (0.3–0.6)	1.02 (0.5–2.18)	1.49 (1–2.25)	1.5 (0.52–4.21)	2.8 (1–9.24)	0.3‡
Median tumor volume (mL)†	0.88 (0.38–1.35)	0.72 (0.04–15)	0.89 (0.44–1.73)	0. 91 (0.39–1.34)	1.55 (0.46–4.6)	0.16‡
NCCN risk group§						<0.001‖
Low risk	9 (5)	8 (6)	0 (0)	1 (3)	0	
Intermediate risk	82 (44)	54 (43)	9 (38)	132 (41)	7 (26)	
High risk	52 (28)	28 (22)	7 (29)	10 (34)	7 (26)	
Very high risk	43 (23)	16 (13)	8 (33)	6 (21)	13 (48)	
Not available	40	21	6	3	10	
Surgical margin involvement§						0.08¶
No	99 (63)	58 (46)	16 (84)	12 (48)	13 (57)	
Yes	57 (37)	31 (24)	3 (16)	13 (52)	10 (43)	
Not available	70	38	11	7	14	
Outcome§						0.35¶
Completely covered by CTV	107 (46)	68 (53)	14 (47)	11 (34)	14 (38)	
Partially covered by CTV	91 (41)	43 (34)	12 (40)	17 (53)	19 (51)	
Not covered by CTV	28 (13)	16 (13)	4 (13)	4 (13)	4 (11)	
Location of recurrence partially or completely exceeding CTV§						Not applicable
Total no.	119 (100)	59 (100)	16 (100)	21 (100)	23 (100)	
Posterior	57 (48)	30 (51)	5 (31)	10 (48)	12 (55)	
Posterolateral	34 (29)	14 (24)	8 (50)	8 (38)	4 (17)	
Posteroinferior	8 (7)	3 (5)	2 (13)	0	3 (13)	
Anterior	1 (1)	1 (2)	0	0	0	
Superior	4 (3)	1 (2)	0	2 (10)	1 (4)	
Inferior	13 (11)	10 (17)	1 (6)	0	2 (9)	
Lateral	2 (2)	0	0	1 (5)	1 (4)	
Lesion extension§						0.23¶
Rectal wall involvement	19 (8)	12 (9)	2 (7)	1 (3)	4 (10)	
Bladder wall involvement	10 (4)	4 (3)	1 (3)	0	5 (13)	

*Location and extension of tumor recurrence on ^{68}Ga-PSMA PET for full cohort and subcohorts. Age and PSA level are at time of PET. Percentages were calculated on basis of total number of patients with data available in selected category.

†Values in parentheses are interquartile ranges.

‡One-way ANOVA.

§Reported as number of patients, with percentages in parentheses. NCCN = National Comprehensive Cancer Network.

‖Spearman (ρ) correlation matrix.

¶χ^2 test.

The median volume of ^{68}Ga-PSMA PET recurrence was 0.72 mL (IQR, 0.04–15; range, 0.04–15). In patients with PB recurrences completely covered, partially covered and not covered by the CTV, tumor volumes were 0.57 mL (0.36–1.13; range, 0.08–11.09), 1.01 mL (0.49–67; range, 0.13–15) and 0.68 mL (0.37–0.96; range, 0.04–4.72), respectively. Complete CTV coverage was significantly associated to smaller tumor volume ($P = 0.04$).

TABLE 2
Clinical Characteristics and Outcome Analysis for miTrN0M0 Cohort*

Characteristic	miTrN0M0 cohort (n = 127)	Completely covered by CTV (n = 68)	Partially covered by CTV (n = 43)	Not covered by CTV (n = 16)	P
No. of patients†	127 (100)	68 (54)	43 (34)	16 (13)	Not applicable
Median age (y)‡	70 (64–73)	69.5 (62–72)	70 (67–75)	68.5 (66.3–75.3)	0.14§
Median serum PSA level (ng/mL)‡	1.02 (0.5–2.18)	1.11 (0.5–2.2)	1.09 (0.46–2.63)	0.84 (0.62–1.11)	0.26§
Median tumor volume (mL)‡	0.72 (0.38–1.35)	0.57 (0.36–1.13)	1.01 (0.49–67)	0.68 (0.37–0.96)	0.12§
NCCN risk group‖					0.38¶
Low risk	8 (8)	7 (10)	0 (0)	1 (6)	
Intermediate risk	54 (51)	26 (38)	19 (44)	8 (50)	
High risk	28 (26)	12 (18)	12 (28)	4 (25)	
Very high risk	16 (15)	9 (13)	5 (12)	2 (13)	
Not available	21	14	7	1	
Surgical margin involvement‖					0.04#
No	58 (65)	21 (45)	20 (69)	12 (92)	
Yes	31 (35)	26 (55)	9 (31)	1 (8)	
Not available	38	21	16	4	
Location of recurrence partially or completely exceeding CTV‖		Not applicable			Not applicable
Total no.	59 (100)		43 (100)	16 (100)	
Posterior	30 (52)		25 (58)	5 (31)	
Posterolateral	14 (24)		10 (23)	4 (25)	
Posteroinferior	3 (5)		1	2 (13)	
Anterior	1 (2)		1 (2)	0	
Superior	1 (2)		1 (2)	0	
Inferior	10 (14)		5 (10)	5 (31)	
Local extension‖					0.002#
Rectal wall involvement	12 (9)	1 (1)	5 (12)	6 (38)	
Bladder wall involvement	4 (3)	4 (6)	0	0	

*Age and PSA level are at time of PET. Percentages were calculated on basis of total number of patients with data available in selected category.
†Values in parentheses are percentages of total number of patients.
‡Values in parentheses are interquartile ranges.
§One-way ANOVA.
‖Reported as number of patients, with percentages in parentheses. NCCN = National Comprehensive Cancer Network.
¶Spearman (ρ) correlation matrix.
#χ^2 test.

Impact of Adverse Pathology Features After Surgery on CTV Coverage

In patients with surgical margin involvement (31/127; 24%) the ^{68}Ga-PSMA PET PB recurrences were fully covered by the CTV in 21 of 31 patient (68%), partially covered in 9 of 31 patients (29%), and not covered in 1 of 31 patients (3%). In patients without surgical margins involvement (58/127; 46%), the ^{68}Ga-PSMA PET PB recurrences were fully covered by the CTV in 26 of 58 patients (45%), partially covered in 20 of 58 patients (34%), and not covered in 12 of 58 patients (21%). For 38 of 127 patients (30%), the information regarding surgical margin involvement was not available.

Impact of Rectal/Bladder Wall Involvement on CTV Coverage

PB lesions involved the rectal wall in 12 of 127 patients (9%) and the bladder wall in 4 of 127 patients (3%). Rectal or bladder wall involvement was significantly associated with lack of full CTV coverage (P = 0.03).

Impact of miTNM Stage on CTV Coverage

Clinical characteristics, location of recurrences and CTV coverage patterns of the full cohort (miTrNxMx) are summarized in Table 1. In the miTrNxMx cohort the ^{68}Ga-PSMA PET PB recurrences were completely covered by the CTV in 107 of 226 patients (46%),

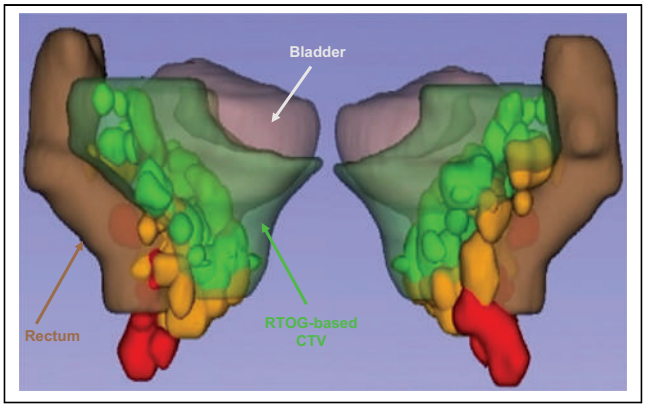

FIGURE 4. Three-dimensional rendering of all PB recurrences in relation to RTOG-based CTV (light green), rectum (brown), and urinary bladder (pink) of template patient. PSMA recurrences are in solid colors: green = completely covered, yellow = partially covered, and red = not covered.

partially covered in 91 of 226 patients (41%), and not covered in 28 of 226 patients (13%). In the latter 2 groups, the ^{68}Ga-PSMA PET recurrences extended beyond the CTV at the following locations: posteriorly (57/119; 48%), posterolaterally (34/119; 29%), posteroinferiorly (8/119; 7%), anteriorly (1/119; 1%), anteroinferiorly (1/119; 1%), superiorly (4/119; 3%), laterally (2/119; 2%), and inferiorly (12/119; 10%) (Table 1; Suppl. Table 1).

The percentage of ^{68}Ga-PSMA PET recurrences completely covered by the CTV was 46%, 35%, and 38% in the miTrN1M0, miTrN0M1, and miTrN1M1 subcohorts, respectively.

The PB recurrences involved the rectal and bladder walls in 19 of 226 patients (8%) and 10 of 226 patients (4%), respectively. Tumor involvement of the rectal or bladder wall was significantly associated with lack of complete CTV coverage in the full cohort ($P = 0.007$).

The median serum PSA levels at time of imaging and ^{68}Ga-PSMA PET–based tumor volume were 1.21 ng/mL (IQR, 2.40) and 0.88 mL (IQR, 1.24), respectively. Complete CTV coverage was significantly associated with smaller tumor volume ($P = 0.009$), and not with lower serum PSA ($P = 0.76$).

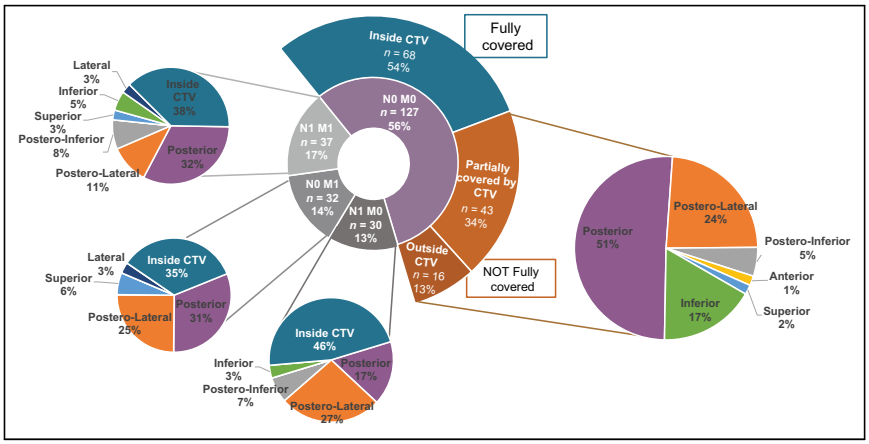

FIGURE 5. Results of coverage analysis and detailed description of location of ^{68}Ga-PSMA PET recurrences exceeding CTV. Two central pie charts show full cohort divided into main cohort (miTrN0M0; purple) and all subcohorts (gray). Full pie charts on sides show location of ^{68}Ga-PSMA PET recurrences exceeding CTV.

DISCUSSION

Our study showed that in a cohort of 127 patients with prostate cancer local recurrence limited to the PB (N0M0), the RTOG-based CTV fully or partially covered the ^{68}Ga-PSMA PET PB recurrences in 87% of the cases, whereas 13% of the recurrences were not covered by the CTV whatsoever. This work provides important information on patterns of PB recurrence based on novel imaging, indicating areas of potential failures that would not be covered by the current RTOG contouring guidelines for SRT directed to the PB.

It is difficult to define standardized target volumes for radiation treatment after radical prostatectomy. The surgical removal of the prostate alters the anatomy of the pelvic organs, which causes significant challenges to radiation oncologists who contour SRT volumes due to significant patient heterogeneity. To date, the target delineation (CTV) for SRT to the PB is guided by consensus guidelines made by experts, but do not account for data from contemporary imaging, such as ^{68}Ga-PSMA PET. Our study used ^{68}Ga-PSMA PET to generate a 3-dimensional heat map of the PB recurrence patterns after radical prostatectomy in relation with the RTOG-based CTVs with the intent to guide the redefinition of these consensus contours.

Although many groups investigated the patterns of failure after prostatectomy for prostate cancer using ^{68}Ga-PSMA PET, our work represents a large dataset that specifically focuses on the detailed description of patterns of local failure in the PB using ^{68}Ga-PSMA PET (*17,18*). In 47% of patients from our cohort, the RTOG-based CTVs did not cover completely the PB recurrences identified on ^{68}Ga-PSMA PET. We observed that in most cases without full coverage, recurrences extended beyond the CTVs posteriorly, specifically at the posterior, posterolateral and posteroinferior borders in 80% of cases, and in 17% of cases at the inferior border. The ^{68}Ga-PSMA PET recurrences rarely overlapped the CTVs anteriorly (2%) or superiorly (2%), indicating an overall adequate coverage on these areas. In fact, we believe that the current RTOG recommendations of extending the coverage anteriorly to the top of the pubic symphysis irradiates a large volume of normal bladder tissue unnecessarily given the low probability of recurrences in that area. Therefore, our work provides important information also for a reduction of the CTVs anterosuperiorly to potentially reduce toxicity rates. Further, they provide a potential explanation for why dose escalation to the prostate fossa has failed to improve BCR outcomes in 2 randomized trials in the postoperative setting while consistently improving BCR outcomes in multiple trials in the intact prostate setting (*19,20*). Although it is true that these trials included patients with serum PSA lower than those of our cohort, a subanalysis of our study specifically looking at CTV coverage in patients with serum PSA levels ≤ 0.5 ng/mL found that the proportions of PB recurrences fully covered and not fully covered were comparable to those of the full cohort. This finding further confirms that PSA levels are not significantly associated with the coverage outcome.

Overall, our results highlight the need for adequate contouring at the posterior border, although RTOG guidelines already recommend extending the posterior treatment volume to the anterior wall of the rectum. This finding can be partly explained by the possible

posterior extension of the recurrences to involve the rectal wall, by possible inaccuracies due spill-over effect, as described earlier, and in part by the lack of strict adherence to the guidelines. In addition, a more extensive coverage at the posterolateral angles on both sides of the rectum may be needed. It is important to mention that recurrences outside the CTV could have been adequately covered by the planning target volumes (PTV) margin expansions. However, the PTV is intended to account for uncertainties in planning or treatment delivery rather than uncertainties in the true anatomic location of disease. A more definitive conclusion on the need for target volumes expansions would require validation on a cohort of patients with local failures after salvage radiotherapy.

Our findings are corroborated by a recent study from Australia (*21*) assessing patterns of failure in relation to the Faculty of Radiation Oncology Genito-Urinary Group and RTOG recommendations. These authors mapped the recurrences relative to vesicourethral anastomosis and showed that the RTOG CTV had better coverage than the Faculty of Radiation Oncology Genito-Urinary Group CTV. They similarly showed the importance of including the posterolateral rectal recesses, and possibly excluding the anterosuperior portion of the CTV.

The results of our subanalysis investigating the patterns of PB recurrences regardless of the N and M status showed that the percentage of ^{68}Ga-PSMA PET recurrences completely covered by the CTV was smaller in patients with wider spread of disease than in those with disease limited to the PB: 46%, 35%, and 38% in the miTrN1M0, miTrN0M1, and miTrN1M1 subcohorts, respectively. The locations of the ^{68}Ga-PSMA PET contours exceeding the CTV were instead similar among the main cohort and the subcohorts, with the vast majority of them extending beyond the posterior, posterolateral, and posteroinferior borders (84%), with a smaller percentage at the inferior border (10%) and a minority at the anterior, superior and lateral borders (6%).

Our study further assessed the correlation of the CTV coverage of PB recurrences with clinical and imaging parameters. The involvement of the rectal or bladder wall, identified in 12 of 127 patients (9%) or 4 of 127 patients (3%), respectively, was found to be significantly associated to worse coverage ($P = 0.03$). The urinary bladder and the rectum are anatomic landmarks used to delineate the PB and represent crucial organs for the definition of the clinical target volumes used for SRT. Increased dose to normal tissues is associated to acute and late GI and GU side effects that significantly decrease patient's quality of life. In fact, a retrospective quality assurance analysis from a randomized trial confirmed that an overlap of the CTV with rectal wall at the time of planning is associated with increased toxicity (*22*).

In our study, PSA and tumor volume were positively correlated with each other, but tumor volume was the only parameter associated with worse coverage. The PSMA-based tumor volumes were significantly associated with PSMA-based recurrence coverage ($P = 0.043$), whereas serum PSA levels at the time of ^{68}Ga-PSMA PET were not ($P = 0.979$).

An important aspect that needs to be taken into consideration when interpreting the results of our study is the intrinsic limitation of tumor contouring using PET due to its finite spatial resolution. Tumor delineation done on ^{68}Ga-PSMA PET images inevitably suffers from partial-volume and spillover effects, which can be described as part of the signal coming from the source (tumor) spilling out and being seen outside the location of the source (*23*). The ultimate result is an over-estimation of the actual tumor volumes, particularly significant for small lesions. In an attempt to overcome this limitation, the nuclear medicine readers used the fused CT images of ^{68}Ga-PSMA PET as an aid for the delineation of the tumor, whenever possible. However, CT does not provide sufficient soft-tissue contrast and its utility is limited (*24*). This is valid also for the definition of rectal or bladder involvement, which is often not possible based on CT images. Therefore, interpretation of the analysis regarding rectal/bladder wall involvement should take into consideration this limitation. The use of information from MRI, and ideally the use of PET/MRI would have been the best approach to minimize this intrinsic limitation and obtain more accurate tumor extent delineation. Other limitations of our study are the lack of follow up information on our cohort and its retrospective nature. The authors are currently monitoring this cohort, and a study investigating the differences in progression free survival in these patients treated with SRT is planned (*25*).

Ideally, using a personalized approach with ^{68}Ga-PSMA PET before SRT would allow us to weigh the potential benefits and harms of extending the RT coverage on an individual basis. A recent study found that the use of SUV_{max} from ^{68}Ga-PSMA PET could identify patients who are at higher risk for progression after SRT and might therefore benefit from a personalized treatment approach (*26*). However, in practice, when ^{68}Ga-PSMA PET is not available, or when ^{68}Ga-PSMA PET is negative at lower PSA levels, data from studies like ours should be used to redefine the PB contouring guidelines with 2 main objectives: improve coverage of PB recurrences and decrease the unnecessary treatment of healthy tissues much less likely to harbor prostate cancer recurrence.

CONCLUSION

Our study showed that in patients experiencing PSA persistence or BCR after radical prostatectomy with disease limited to the PB on ^{68}Ga-PSMA PET (miTrN0M0), the RTOG contouring guidelines for SRT cover the full extent of disease in 54% of the patients, leaving 34% partially covered and 13% fully uncovered. Our study suggests that ^{68}Ga-PSMA PET can be a valuable tool for SRT planning in the setting of BCR for patients with disease limited to the PB and should be incorporated into a redefinition of SRT contouring guidelines.

DISCLOSURE

Amar U. Kishan reports funding support from grant P50CA09213 from the Prostate Cancer National Institutes of Health Specialized Programs of Research Excellence, grant W81XWH-22-1-0044 from the Department of Defense, grant RSD1836 from the Radiologic Society of North America, the STOP Cancer Organization, the Jonsson Comprehensive Cancer Center, and the Prostate Cancer Foundation; personal fees from Varian Medical Systems, Inc., ViewRay Inc., and Intelligent Automation, Inc.; and research support from ViewRay, Inc., the American Society for Radiation Oncology (ASTRO), the Prostate Cancer Foundation, and the Jonsson Comprehensive Cancer Center—all outside of the submitted work. Nicholas G. Nickols reports research support from Lantheus, Janssen, and Bayer, outside of the submitted work, and consulting for PrimeFour, outside of the submitted work. Alan Dal Pra reports research support to institution/sponsor (Veracyte), outside of the submitted work, and advisory board membership (Merck), outside of the submitted work. Jeremie Calais reports prior consulting activities for Advanced Accelerator Applications, Astellas, Blue Earth Diagnostics, Curium Pharma, DS Pharma, EXINI, GE Healthcare, Isoray, IBA RadioPharma, Janssen Pharmaceuticals, Lightpointmedical, Lantheus, Monrol, Novartis, Progenics, POINT biopharma, Radiomedix, Sanofi, and

Telix Pharmaceuticals, outside of the submitted work. No other potential conflict of interest relevant to this article was reported.

KEY POINTS

QUESTION: Are the CTVs used for salvage radiation treatment of the PB covering the full extent of disease on the basis of ^{68}Ga-PSMA PET findings?

PERTINENT FINDINGS: In patients experiencing PSA persistence or biochemical recurrence after radical prostatectomy with disease limited to the PB on ^{68}Ga-PSMA PET, the RTOG-based CTV for salvage radiation therapy left 13% of the recurrences fully uncovered and 34% partially treated. Most of the recurrences not covered by the CTV extended beyond the posterior and inferior aspects of the PB, whereas the anterior and superior borders were rarely involved—highlighting the need for CTV redefinition with ^{68}Ga-PSMA PET.

IMPLICATIONS FOR PATIENT CARE: Using ^{68}Ga-PSMA PET data to redefine current contouring guidelines has 2 advantages: improve coverage of areas of tumor recurrence and reduce unnecessary exposure of healthy tissues to radiation.

REFERENCES

1. Stephenson AJ, Scardino PT, Eastham JA, et al. Preoperative nomogram predicting the 10-year probability of prostate cancer recurrence after radical prostatectomy. *J Natl Cancer Inst.* 2006;98:715–717.
2. Freedland SJ, Humphreys EB, Mangold LA, et al. Risk of prostate cancer-specific mortality following biochemical recurrence after radical prostatectomy. *JAMA.* 2005;294:433–439.
3. Freedland SJ, Rumble RB, Finelli A, et al. Adjuvant and salvage radiotherapy after prostatectomy: American Society of Clinical Oncology clinical practice guideline endorsement. *J Clin Oncol.* 2014;32:3892–3898.
4. Zaorsky NG, Calais J, Fanti S, et al. Salvage therapy for prostate cancer after radical prostatectomy. *Nat Rev Urol.* 2021;18:643–668.
5. Michalski JM, Lawton C, El Naqa I, et al. Development of RTOG consensus guidelines for the definition of the clinical target volume for postoperative conformal radiation therapy for prostate cancer. *Int J Radiat Oncol Biol Phys.* 2010;76:361–368.
6. Poortmans P, Bossi A, Vandeputte K, et al. Guidelines for target volume definition in post-operative radiotherapy for prostate cancer, on behalf of the EORTC Radiation Oncology Group. *Radiother Oncol.* 2007;84:121–127.
7. Sidhom MA, Kneebone AB, Lehman M, et al. Post-prostatectomy radiation therapy: consensus guidelines of the Australian and New Zealand Radiation Oncology Genito-Urinary Group. *Radiother Oncol.* 2008;88:10–19.
8. Wiltshire KL, Brock KK, Haider MA, et al. Anatomic boundaries of the clinical target volume (prostate bed) after radical prostatectomy. *Int J Radiat Oncol Biol Phys.* 2007;69:1090–1099.
9. Cookson MS, Aus G, Burnett AL, et al. Variation in the definition of biochemical recurrence in patients treated for localized prostate cancer: the American Urological Association Prostate Guidelines for Localized Prostate Cancer Update Panel report and recommendations for a standard in the reporting of surgical outcomes. *J Urol.* 2007;177:540–545.
10. FDA approves first PSMA-targeted PET drug. *J Nucl Med.* 2021;62:11N.
11. Valle L, Shabsovich D, de Meerleer G, et al. Use and impact of positron emission tomography/computed tomography prior to salvage radiation therapy in men with biochemical recurrence after radical prostatectomy: a scoping review. *Eur Urol Oncol.* 2021;4:339–355.
12. Eder M, Schäfer M, Bauder-Wüst U, et al. ^{68}Ga-complex lipophilicity and the targeting property of a urea-based PSMA inhibitor for PET imaging. *Bioconjug Chem.* 2012;23:688–697.
13. Halpern BS, Dahlbom M, Quon A, et al. Impact of patient weight and emission scan duration on PET/CT image quality and lesion detectability. *J Nucl Med.* 2004;45:797–801.
14. Fendler WP, Eiber M, Beheshti M, et al. ^{68}Ga-PSMA PET/CT: joint EANM and SNMMI procedure guideline for prostate cancer imaging—version 1.0. *Eur J Nucl Med Mol Imaging.* 2017;44:1014–1024.
15. Eiber M, Herrmann K, Calais J, et al. Prostate cancer molecular imaging standardized evaluation (PROMISE): proposed miTNM classification for the interpretation of PSMA-ligand PET/CT. *J Nucl Med.* 2018;59:469–478.
16. Fedorov A, Beichel R, Kalpathy-Cramer J, et al. 3D Slicer as an image computing platform for the Quantitative Imaging Network. *Magn Reson Imaging.* 2012;30:1323–1341.
17. Rowe LS, Harmon S, Horn A, et al. Pattern of failure in prostate cancer previously treated with radical prostatectomy and post-operative radiotherapy: a secondary analysis of two prospective studies using novel molecular imaging techniques. *Radiat Oncol.* 2021;16:32.
18. Calais J, Czernin J, Cao M, et al. ^{68}Ga-PSMA-11 PET/CT mapping of prostate cancer biochemical recurrence after radical prostatectomy in 270 patients with a PSA level of less than 1.0 ng/mL: impact on salvage radiotherapy planning. *J Nucl Med.* 2018;59:230–237.
19. Ghadjar P, Hayoz S, Bernhard J, et al. Dose-intensified versus conventional-dose salvage radiotherapy for biochemically recurrent prostate cancer after prostatectomy: the SAKK 09/10 randomized phase 3 trial. *Eur Urol.* 2021;80:306–315.
20. Qi X, Li HZ, Gao XS, et al. Toxicity and biochemical outcomes of dose-intensified postoperative radiation therapy for prostate cancer: results of a randomized phase III trial. *Int J Radiat Oncol Biol Phys.* 2020;106:282–290.
21. Horsley PJ, Koo CM, Eade T, et al. Mapping of local recurrences after radical prostatectomy using 68-gallium-prostate-specific membrane antigen positron emission tomography/computed tomography: implications for postprostatectomy radiation therapy clinical target volumes. *Int J Radiat Oncol Biol Phys.* 2023;115:106–117.
22. Beck M, Sassowsky M, Schär S, et al. Adherence to contouring and treatment planning requirements within a multicentric trial: results of the quality assurance of the SAKK 09/10 trial. *Int J Radiat Oncol Biol Phys.* 2022;113:80–91.
23. Soret M, Bacharach SL, Buvat I. Partial-volume effect in PET tumor imaging. *J Nucl Med.* 2007;48:932–945.
24. Daryanani A, Turkbey B. Recent advancements in CT and MR imaging of prostate cancer. *Semin Nucl Med.* 2022;52:365–373.
25. Calais J, Armstrong WR, Kishan AU, et al. Update from PSMA-SRT trial NCT03582774: a randomized phase 3 imaging trial of prostate-specific membrane antigen positron emission tomography for salvage radiation therapy for prostate cancer recurrence powered for clinical outcome. *Eur Urol Focus.* 2021;7:238–240.
26. Spohn SKB, Farolfi A, Schandeler S, et al. The maximum standardized uptake value in patients with recurrent or persistent prostate cancer after radical prostatectomy and PSMA-PET-guided salvage radiotherapy: a multicenter retrospective analysis. *Eur J Nucl Med Mol Imaging.* 2022;50:218–227.

Prostate-Specific Membrane Antigen Expression on PET/CT in Patients with Metastatic Castration-Resistant Prostate Cancer: A Retrospective Observational Study

Letizia Calderoni[1,2], Elisa Maietti[3], Andrea Farolfi[1], Riccardo Mei[1,2], Karly S. Louie[4], Michael Groaning[5], and Stefano Fanti[1,2]

[1]*Nuclear Medicine Division, IRCCS Azienda Ospedaliero-Universitaria di Bologna, Policlinico Di S. Orsola, Bologna, Italy;* [2]*Nuclear Medicine, Alma Mater Studiorum, University of Bologna, Bologna, Italy;* [3]*Department of Biomedical and Neuromotor Sciences, University of Bologna, Bologna, Italy;* [4]*Amgen Ltd., Uxbridge, United Kingdom; and* [5]*Amgen Inc., Thousand Oaks, California*

Monitoring therapy response in patients with metastatic castration-resistant prostate cancer (mCRPC) treated with novel hormonal therapies, taxanes, and newly approved therapies is crucial for optimizing treatment. [^{68}Ga]Ga-prostate-specific membrane antigen (PSMA)-11 positron emission tomography/computed tomography (PSMA PET/CT) is a promising target for managing treatment in patients with prostate cancer. PSMA is overexpressed in patients with mCRPC; understanding how expression might change in patients undergoing treatment could determine its potential for guiding clinical decisions. We examined PSMA expression in patients with CRPC and compared PET/CT response with prostate-specific antigen (PSA) variation as a prognostic factor for progression-free survival and overall survival (PFS and OS, respectively). **Methods:** This was a single-center, retrospective observational cohort study in patients with CRPC enrolled in the PSMA-PROSTATA registry study (EudraCT: 2015-004589-27). A first and second (if applicable) PSMA PET/CT were performed to determine PSMA expression (absence or presence). PET/CT response was assessed as responders (patients with stable disease, partial or complete response) versus nonresponders (patients with progressive disease) by comparing the first with the second PET/CT. PSA variation (increase or decrease from baseline) was assessed across the same time period. PFS was defined as the time between second PET/CT and PSA recurrence or evidence of radiologic progression. **Results:** Overall, 160 patients with CRPC were included in the analysis. At first PET/CT, nearly all ($n = 152$; 95.0%) patients had PSMA expression (classified as mCRPC), irrespective of prior systemic therapy. SUV_{max} was positively associated with baseline PSA levels and velocity (both $P < 0.001$). According to PET/CT response, median SUV_{max} on first PET/CT was numerically lower in nonresponders than in responders (17.5 vs. 20.4; $P = 0.127$). Similarly, patients with a PSA increase had significantly lower median SUV_{max} on first PET/CT (15.8) than did those with a PSA decrease (30.4; $P = 0.018$). PSA change was, on average, 146% in nonresponders and −57% in responders between first and second PET/CT ($P < 0.001$). Agreement between PET/CT and PSA response was 79% ($k = 0.553$, $P < 0.001$). Among the 63 patients included in PFS/OS analyses, 76.2% had a relapse and 36.5% died before 24-mo follow-up; median PFS and OS were 6.1 and 24 mo, respectively. PET/CT response, independent of PSA variation, was a significant prognostic factor for PFS. OS was not significantly different between PET/CT responders and nonresponders. **Conclusion:** PSMA PET/CT may be a useful imaging method predictive of treatment response in patients with mCRPC, regardless of ongoing systemic therapy. Data also suggest that response assessed by PET/CT is a potentially more significant prognostic factor than PSA for PFS. Further studies are needed to understand the potential involvement of PSMA expression on survival.

Key Words: mCRPC; prostate-specific antigen; response to therapy; SUV_{max}; [^{68}Ga]Ga-PSMA-11 PET/CT

J Nucl Med 2023; 64:910–917
DOI: 10.2967/jnumed.122.264964

Prostate cancer (PC) is the most commonly occurring cancer in men in Europe (*1*). Approximately 450,000 new cases were diagnosed in 2018, and the age-standardized mortality rate was 19.4 per 100,000 men. Localized PC may be treated with radiotherapy or surgery; however, many patients develop metastatic disease (*2*). Initial standard treatment for metastatic PC is androgen deprivation therapy (ADT), with or without chemotherapy (*2,3*). Although initially effective, patients gradually become resistant and ultimately progress to metastatic castration-resistant PC (mCRPC), an aggressive disease with a median overall survival (OS) of approximately 2.5 y (*2–4*). Despite multiple available therapies for mCRPC, the optimal treatment sequence or combinations are unknown (*5*) and there remains a high unmet need for treatments with novel mechanisms of action.

Radionuclide therapies provide targeted delivery of therapeutic radiation to metastatic PC sites and allow for selection of patients likely to benefit (*2*). Prostate-specific membrane antigen (PSMA) is overexpressed in most PC cells and levels correlate with disease progression, making it a favorable diagnostic and therapeutic target in mCRPC (*2,6,7*). [^{68}Ga]Ga-PSMA-11 positron emission tomography/computed tomography (PSMA PET/CT) can be used to select patients for [^{177}Lu]Lu-PSMA-617 therapy, a potential treatment option with demonstrated effectiveness in mCRPC (*2,8,9*).

Monitoring therapy responses in patients with mCRPC treated with novel hormonal therapy, taxanes, and radioligand therapy (RLT) enables clinicians to optimize treatment decisions (*5*). In PC, there is increasing evidence to support the superiority of PSMA

Received Sep. 27, 2022; revision accepted Jan. 9, 2023.
For correspondence or reprints, contact Letizia Calderoni (letiziacalderoni@gmail.com).
Published online Jan. 12, 2023.

PET/CT over conventional imaging methods and prostate-specific antigen (PSA) serum levels for predicting early response (*7,10,11*). As such, PSMA is emerging as a promising target for PC imaging (*12*) and might help avoid the administration of costly therapies that are ineffective or not well tolerated.

Currently, data regarding PSMA expression in patients with mCRPC are limited, and it is unclear how treatments may have an impact. The present study aimed to describe PSMA expression in patients with mCRPC and examine whether PET/CT response as compared with PSA variation is a prognostic indicator for progression-free survival (PFS) and OS.

MATERIALS AND METHODS

Study Design, Setting, and Participants

This single-center, retrospective observational cohort study was conducted at the Metropolitan Nuclear Medicine Centre of the S. Orsola-Malpighi University Hospital of Bologna, Italy. The study was based on secondary analysis of patients with mCRPC enrolled in the PSMA-PROSTATA registry study (EudraCT: 2015-004589-27) between March 1, 2016, and October 31, 2020, and who underwent [^{68}Ga]Ga-PSMA-11 PET/CT between January 2016 and October 2019. Inclusion criteria were: age ≥ 18 y; proven diagnosis of PC; a clinical or biochemical diagnosis of CRPC; and being eligible for second- or subsequent-line therapy. Patients with a history of other tumor diagnosis (i.e., not PC) or with a life expectancy of ≤6 mo (as assessed by each clinician) were excluded.

The Institutional Ethics Committee approved this retrospective study. All participants included in the study were appropriately informed of the purpose of this study and provided signed written informed consent.

Data Collection and Imaging

Data were collected from medical records at baseline (time of first PET/CT) and during follow-up. Baseline patient characteristics included age, clinical characteristics (Gleason score, pathologic stage, nodal status, tumor burden), treatment history before enrollment in the PSMA-PROSTATA registry, and PSA values (if available within ≤3 mo before baseline). PSA kinetics were calculated using published methodology (*13*). During follow-up, treatment-related characteristics were collected.

Radiopharmaceutical usage, PET/CT acquisition, and image interpretation were performed as described previously (*14*). PET images were acquired in accordance with the Joint European Association of Nuclear Medicine and Society of Nuclear Medicine and Molecular Imaging procedure guidelines for PC imaging (*15*). First and second (if applicable) PET/CT parameters were collected by an experienced physician evaluating the presence of focal uptake suggestive of prostate disease localization, tumor burden, and SUV_{max} of the most significant lesion or lesions. The maximum-intensity-projection and PET/CT fusion images in axial, coronal, and sagittal slices were assessed at the reporting stage.

Outcomes

The primary outcome was baseline PSMA expression on first PET/CT defined both as SUV_{max} and as the presence of lesions consistent with prostate metastases.

PET/CT response was assessed as responders versus nonresponders by comparing the first with the second PET/CT, as per PSMA PET/CT consensus–based response criteria (*16*): responders were defined as patients with stable disease, partial response, or complete response; nonresponders were defined as patients with progressive disease. PSA variation (*11*) between baseline and second PET/CT was assessed as PSA decrease and PSA increase from baseline.

PFS was defined as time to PSA recurrence or evidence of radiologic progression. PFS and OS were calculated starting from the date of the second PET/CT until the date of last visit, death, or end of the study period (i.e., October 31, 2020), whichever occurred first.

Statistical Analysis

Continuous data were described using median and interquartile range; minimum and maximum values (i.e., range) were also reported in some instances. Categoric data were summarized as absolute and relative frequencies. Statistical significance was considered for a P value of less than 0.05.

The overall proportion of patients with PSMA expression on first PET/CT was calculated and reported with binomial 95% CI. SUV_{max} was compared among response and different treatment-related variable groups using the nonparametric Kruskal–Wallis test (>2 groups) or the Wilcoxon–Mann–Whitney test (2 groups); Benjamini and Hochberg correction was applied for multiple comparisons. The relationship between SUV_{max} and PSA parameters (serum level, doubling time, and velocity) was evaluated using Spearman correlation.

PET/CT response was reported for patients who underwent a second PET/CT. Response groups (responders vs. nonresponders) were compared with respect to treatment-related variables, baseline SUV_{max}, and PSA level variation from baseline to second evaluation using the Wilcoxon–Mann–Whitney test for continuous data and the χ^2 test or the Fisher exact test for categoric variables, as appropriate. Concordance between PSA variation and PET/CT response was assessed with Cohen's κ-coefficient.

In patients who underwent a second PET/CT, PFS and OS analyses were conducted to assess whether PSA variation and PET/CT response were significant predictors. Kaplan–Meier curves were constructed and compared using the log-rank test. A multiple Cox regression model was then estimated to assess whether PSA variation and PET/CT response remained significant after adjustment for age, number of therapy lines, and SUV_{max}/PSA baseline value.

Further details on methodology can be found in the supplemental materials (supplemental materials are available at http://jnm.snmjournals.org) (*11,13,16–19*).

Data Sharing

Qualified researchers may request data from Amgen clinical studies. Complete details are available at: https://www.amgen.com/science/clinical-trials/clinical-data-transparency-practices/clinical-trial-data-sharing-request/.

RESULTS

Baseline Patient Disposition and Clinical Characteristics

A total of 1,012 individuals were enrolled in the PSMA-PROSTATA registry between March 2016 and October 2020. Of these, 160 men with CRPC met the study eligibility criteria and were included in the analysis (Fig. 1). The median age was 72 y (range, 67–77 y), median Gleason score was 8 (range, 7–9), most patients (n = 120/160 [75%]) had undergone radical prostatectomy, and 10% had undergone external beam radiation therapy (Table 1). The median time from primary radical treatment to first PET/CT was 6.1 y (range, 2.9–12.2 y). About half of the patients (49.4%; n = 79/160) had received ≥1 life-prolonging therapy before enrollment. There was no association between time from radical treatment to baseline PET/CT and number of prior systemic life-prolonging therapies. The median PSA level at first PET/CT was 11.7 ng/mL (interquartile range [IQR], 2–68 ng/mL), median PSA doubling time

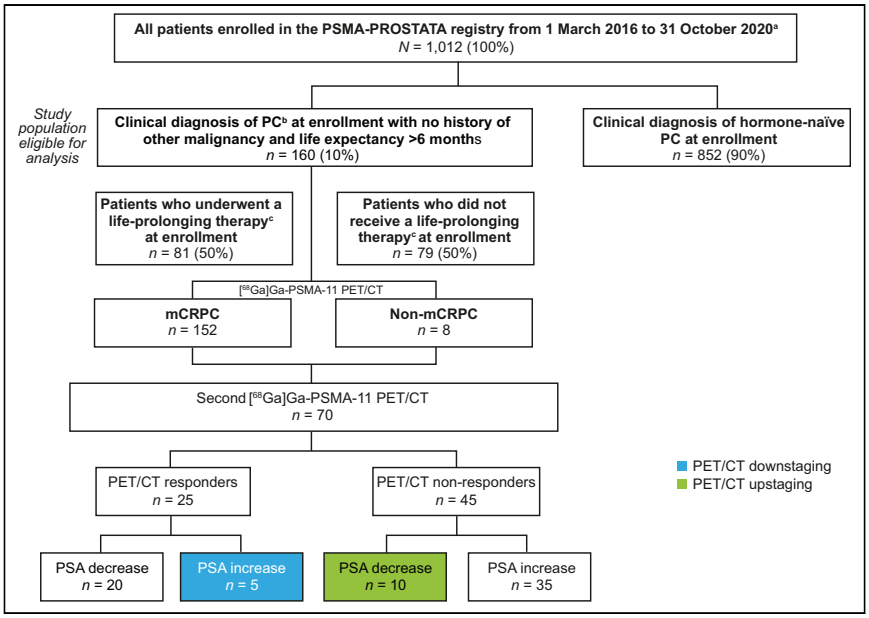

FIGURE 1. Patient disposition. [a]PSMA-PROSTATA registry enrollment criteria: patients enrolled in the trial were men with proven diagnosis of PC, who had received radical prostatectomy or radiotherapy as definitive therapy, who had proven biochemical recurrence (defined as 2 consecutive PSA assays ≥ 0.2 ng/mL), who had PSA levels between 0.2 and 2.0 ng/mL, were aged ≥ 35 y, and who had provided written informed consent. Patients were excluded if they were unable to lie flat, to be still, or to tolerate PET/CT scanning or had a history of treatment for another cancer within 1 y before [^{68}Ga]Ga-PSMA-11 PET/CT. Use of concomitant therapies, including ADT, were allowed. Follow-up data from routine clinical, pathologic, PET/CT imaging, and PSA levels were collected from patient records. [b]Patients eligible for study inclusion had proven diagnosis of CRPC as defined by the European Association of Urology guidelines as: serum testosterone < 50 ng/dL or 1.7 nmol/L plus either biochemical progression (rising serum PSA levels) or radiologic progression (appearance of new lesions). [c]Life-prolonging therapy included novel hormone therapy (abiraterone, enzalutamide), taxanes (docetaxel, cabazitaxel), [^{223}Ra]Ra-NaCl, and PSMA-RLT. CRPC = castration-resistant prostate cancer; mCRPC = metastatic castration-resistant prostate cancer; PC = prostate cancer; PET/CT = positron emission tomography/computed tomography; PSA = prostate-specific antigen; PSMA = prostate-specific membrane antigen; PSMA-RLT = α-/β-emitter prostate-specific membrane antigen-radioligand therapy.

was 5.2 mo (IQR, 2.9–10.6 mo), and median PSA velocity was 6.8 ng/nL/mo (IQR, 2.5–23.6 ng/nL/mo).

Baseline PSMA Expression

PSMA expression at first PET/CT was confirmed in 152 of 160 (95.0%) patients (95% CI, 90.4–97.8); these patients were classified as having mCRPC. The distribution of metastatic sites in patients with mCRPC is shown in Supplemental Table 1. PSMA expression at first PET/CT varied by site of relapse or metastasis (Table 2); SUV_{max} was significantly higher in metastasis involving bone than in relapse or metastasis of other sites (P-adjusted = 0.023 vs. nodes; P-adjusted = 0.003 vs. prostate bed relapse; P-adjusted = 0.047 vs. visceral). SUV_{max} was significantly lower in patients with prostate bed relapse than in those with node lesions (P-adjusted = 0.023).

Of the 79 of 160 patients who received systemic therapy before their first PET/CT, 78 (98.7%) expressed PSMA; among the 81 patients who did not receive prior systemic therapy (excluding ADT), 74 (91.4%) expressed PSMA (between-group difference $P = 0.075$). Baseline SUV_{max} was significantly higher in patients who received systemic treatment before first PET/CT than in those who did not ($P = 0.009$; Table 3). There was no significant difference in SUV_{max} by type of last systemic treatment received before first PET/CT.

Correlation of Baseline PSMA Expression and PSA Parameters

SUV_{max} at first PET/CT was significantly and positively associated with baseline serum PSA levels (Spearman ρ, 0.377; $P < 0.001$) and PSA velocity (Spearman ρ, 0.294, $P < 0.001$), but not with PSA doubling time (Spearman ρ, −0.071; $P = 0.373$). When analyzed according to last systemic treatment received before first PET/CT, positive associations were observed for SUV_{max} at first PET/CT and baseline serum PSA levels in subgroups who received abiraterone/enzalutamide or no systemic treatment ($P = 0.011$ and $P < 0.001$, respectively). There was no association in subgroups who received docetaxel/cabazitaxel or palliative/[^{223}Ra]Ra-NaCl/PSMA-RLT (α-/β-emitter prostate-specific membrane antigen–radioligand therapy).

Baseline PSMA Expression According to PET/CT Response and PSA Variation

Overall, 70 patients underwent a second PET/CT scan: 45 patients (64.3%) were nonresponders and 25 (35.7%) were responders (Supplemental Table 2). There was no significant difference in median time from first to second PET/CT scans between nonresponders and responders (8.5 [IQR, 6.4–12.2] vs. 5.8 [IQR, 5.0–13] mo, respectively; $P = 0.216$).

Nonresponders had numerically lower median SUV_{max} on first PET/CT than responders (17.5 [IQR, 12.0–55.5] vs. 20.4 [IQR, 8.0–35.0], respectively; $P = 0.127$) (Supplemental Table 3). Similarly, nonresponders had numerically lower median SUV_{max} on first PET/CT than responders in those who received the same therapy before and after first PET/CT ($P = 0.064$). In patients who received different therapy before and after first PET/CT, there was no significant difference in median SUV_{max} between nonresponders and responders ($P = 0.568$). Considering the last treatment type before second PET/CT, there were no significant differences in SUV_{max} between nonresponders and responders in any of the treatment subgroups (abiraterone/enzalutamide, docetaxel/cabazitaxel/chemotherapy or palliative/[^{223}Ra]Ra-NaCl/PSMA-RLT).

Patients with a PSA decrease between first and second PET/CT had significantly higher median SUV_{max} on first PET/CT versus patients with a PSA increase (30.4 [IQR, 13.0–55.5] vs. 15.8 [IQR, 7.3–27.6], respectively; $P = 0.018$; Supplemental Table 3). This was particularly evident in patients who received different treatment before and after first PET/CT ($P = 0.039$). Differences were also observed in the subgroup who received docetaxel/cabazitaxel/chemotherapy before second PET/CT ($n = 15$, $P = 0.068$).

There was a significant difference in PSA change between nonresponders and responders at second PET/CT ($P < 0.001$). The median change in PSA between first and second PET/CT was 146% (IQR, 15.6–463) in nonresponders and −56.9% (IQR, −4.6 to −16.6) in responders. Analysis of concordance showed a 78.6% agreement between PET/CT response and PSA variation,

TABLE 1
Patient Characteristics

Characteristic	Overall (N = 160)	mCRPC (n = 152)	nmCRPC (n = 8)
Before PET/CT			
Median age (y)	72 (IQR, 67–77)	72 (IQR, 67–76)	77 (IQR, 73–78)
Gleason score (*n*)			
5	3 (1.9%)	3 (2.0%)	0
6	3 (1.9%)	3 (2.0%)	0
7	58 (36.3%)	56 (36.8%)	2 (25.0%)
8	40 (25.0%)	37 (24.3%)	3 (37.5%)
9	53 (33.1%)	50 (32.9%)	3 (37.5%)
10	3 (1.9%)	3 (2.0%)	0
TNM classification (*n*)			
T2	27 (16.9%)	25 (16.4%)	2 (25.0%)
T3	92 (57.5%)	87 (57.2%)	5 (62.5%)
T4	5 (3.1%)	5 (3.3%)	0
Missing	36 (22.5%)	35 (23.0%)	1 (12.5%)
N1	41 (25.6%)	40 (26.3%)	1 (12.5%)
M1	34 (21.3%)	33 (21.7%)	1 (12.5%)
R1	43 (26.9%)	38 (25.0%)	5 (62.5%)
Primary therapy with radical intent (*n*)			
Radical prostatectomy	120 (75.0%)	114 (75.0%)	6 (75.0%)
Associated with PLND	55 (34.4%)	50 (32.9%)	5 (62.5%)
EBRT	16 (10.0%)	15 (9.9%)	1 (12.5%)
Adjuvant/salvage radiotherapy (*n*)	88 (55.0%)	85 (55.9%)	3 (37.5%)
Median time from primary radical treatment to PET/CT (y)	6.1 (IQR, 2.9–12.2)	6.1 (IQR, 2.8–12.6)	7.5 (IQR, 4.9–10.9)
No. of prior systemic life-prolonging therapies (*n*)*			
No systemic therapy	81 (50.6%)	74 (48.7%)	7 (87.5%)
1 therapy line	38 (23.8%)	37 (24.3%)	1 (12.5%)
2 therapy lines	22 (13.8%)	22 (14.5%)	0
≥3 therapy lines	19 (11.9%)	19 (12.5%)	0
At time of first PET/CT			
Median PSA (ng/mL)	11.7 (IQR, 2–68)	13.1 (IQR, 2.1–77)	1.0 (IQR, 0.5–4.1)
Median PSA doubling time (mo)	5.2 (IQR, 2.9–10.6)	5.0 (IQR, 2.9–10.6)	6.4 (IQR, 5.9–12.3)
>6 mo (*n*)	71 (44.4%)	66 (43.4%)	5 (62.5%)
>10 mo (*n*)	43 (26.9%)	41 (27.0%)	2 (25.0%)
Median PSA velocity (ng/nL/mo)	6.8 (IQR, 2.5–23.6)	7.8 (IQR, 2.7–25.5)	1.5 (IQR, 0.5–4.5)
Ongoing second-line therapy (*n*)	19 (11.9%)	19 (12.5%)	0
Ongoing ADT (*n*)†	106 (66.3%)	101 (66.4%)	5 (62.5%)

*Excluding ADT.
†At time of PSMA ongoing ADT is < 90 d.
ADT = androgen deprivation therapy; EBRT = external beam radiation therapy; IQR = interquartile range; PET/CT = positron emission tomography/computed tomography; PSA = prostate-specific antigen; nm/mCRPC = nonmetastatic/metastatic castration-resistant prostate cancer; PLND = pelvic lymph node dissection; TNM = tumor, node, metastasis.

significantly higher than expected from random chance (Cohen's $k = 0.553$, $P < 0.001$; Supplemental Fig. 1). However, 5 of 70 patients (7.1%) were responders according to second PET/CT but reported an increase in PSA, and 10 of 70 (14.3%) were nonresponders according to second PET/CT but reported a decrease in PSA.

Association of PET/CT Response and PSA Variation with PFS and OS

Sixty-three patients with follow-up after second PET/CT were included in analyses of PFS and OS. Of these, 48 (76.2%) patients had a relapse, 23 (36.5%) died, and 33 (52.4%) were lost before

TABLE 2
PSMA Expression at First PET/CT by Site of Relapse/Metastasis (n = 152)

Site of relapse/metastasis	No. of patients (n)	Median SUV_{max}	Min–max SUV_{max}
Bones	100 (65.8%)	24.0 (IQR, 14.3–37.9)	3.8–127.0
Nodes*	91 (59.9%)	16.7 (IQR, 11.0–28.0)	2.1–138.0
Prostate bed relapse	32 (21.1%)	10.1 (IQR, 7.9–19.9)	3.0–68.0
Visceral	22 (14.5%)	17.5 (IQR, 6.0–27.0)	4.6–45.0

*Pelvic and distant.
IQR = interquartile range; PET/CT = positron emission tomography/computed tomography; PSMA = prostate-specific membrane antigen; SUV_{max} = maximized standardized uptake value.

24-mo follow-up. The median PFS was 6.1 mo, and 24-mo OS was 49%.

PFS was significantly different between PET/CT response groups (log-rank test $P = 0.005$; Fig. 2A). After adjusting for SUV_{max} at first PET/CT, age, and number of therapy lines, PET/CT nonresponders showed an increased risk of progression compared with responders (hazard ratio [HR], 3.0 [95% CI, 1.4–6.7]; $P = 0.006$). PFS was also significantly different between PSA variation groups (i.e., increase vs. decrease from baseline; log-rank test $P = 0.031$; Fig. 2B). After adjusting for PSA at baseline, age, and number of therapy lines, patients with a PSA increase between first and second PET/CT had a higher risk of progression than did those with a decrease (HR, 2.1 [95% CI, 1.0–4.7]; $P = 0.059$).

TABLE 3
PSMA Expression at First PET/CT by Systemic Treatment (n = 160)

Variable	No. of patients (n)	Proportion of patients expressing PSMA* (n)	Median SUV_{max} in lesion with highest value	P
Received systemic treatment before first PET/CT†				0.009
No	81 (50.6%)	74 (91.4%)	16.7 (IQR, 8.0–34.0)	
Yes	79 (49.4%)	78 (98.7%)	29.0 (IQR, 15.0–37.7)	
No. of prior therapy lines if received systemic treatment before first PET/CT				0.087
1	38 (23.8%)	37 (97.4%)	19.9 (IQR, 12.9–37.0)	
2	22 (13.8%)	22 (100%)	32.4 (IQR, 20.4–37.0)	
3	13 (8.1%)	13 (100%)	29.0 (IQR, 20.0–39.0)	
4	6 (3.8%)	6 (100%)	25.9 (IQR, 9.8–38.0)	
Last systemic treatment before first PET/CT				0.698
Abiraterone or enzalutamide	28 (17.5%)	28 (100%)	24.2 (IQR, 13.9–39.0)	
Docetaxel or cabazitaxel	24 (15.0%)	23 (95.8%)	27.5 (IQR, 15.3–37.4)	
Palliative, [^{223}Ra]Ra-NaCl or PSMA-RLT	27 (16.9%)	27 (100%)	30.0 (IQR, 17.0–39.0)	
Ongoing systemic treatment at time of first PET/CT				0.931
No	141 (88.1%)	133 (94.3%)	20.4 (IQR, 12.0–37.0)	
Yes	19 (11.9%)	19 (100%)	19.7 (IQR, 9.9–35.0)	
Second PET/CT				0.277
No	90 (56.3%)	86 (95.6%)	26 (IQR, 14–37)	
Yes	70 (43.8%)	66 (94.3%)	18 (IQR, 9.2–37.7)	

*$SUV_{max} > 2.1$.
†ADT was not considered.
IQR = interquartile range; PET/CT = positron emission tomography/computed tomography; PSMA = prostate-specific membrane antigen; PSMA-RLT = α-/β-emitter prostate-specific membrane antigen-radioligand therapy; SUV_{max} = maximized standardized uptake value.

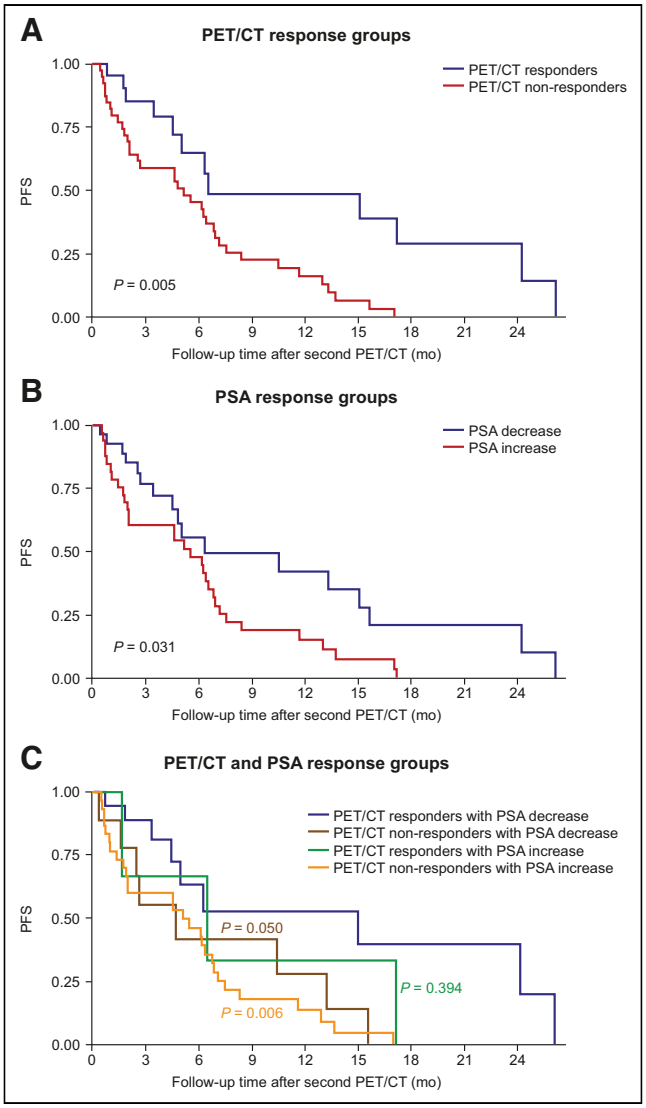

FIGURE 2. Association of PFS after second PET/CT with PET/CT response (A), change from baseline in serum PSA level (B), and combination of PET/CT response and change from baseline in serum PSA level (C) (n = 63). mo = months; PET/CT = positron emission tomography/computed tomography; PFS = progression-free survival; PSA = prostate-specific antigen.

When PET/CT response and PSA variation groups were combined, PET/CT nonresponders with an increase in PSA had a significantly higher risk of disease progression than did PET/CT responders with a decrease in PSA (HR, 3.4 [95% CI, 1.4–8.0]; $P = 0.006$; Fig. 2C). PET/CT nonresponders with a decrease in PSA were also at higher risk of progression than were PET/CT responders with a decrease in PSA (HR, 2.8 [95% CI, 1.0–8.0]; $P = 0.050$). There was no difference in progression risk in PET/CT responders with an increase in PSA compared with PET/CT responders with a decrease in PSA (HR, 1.8 [95% CI, 0.5–7.0]; $P = 0.394$). PET/CT nonresponders appeared to have lower OS than responders (Fig. 3A); however, the difference between the 2 Kaplan–Meier curves was not significant ($P = 0.180$). There was no difference in OS between patients with a decrease in PSA and those with an increase ($P = 0.932$; Figure 3B).

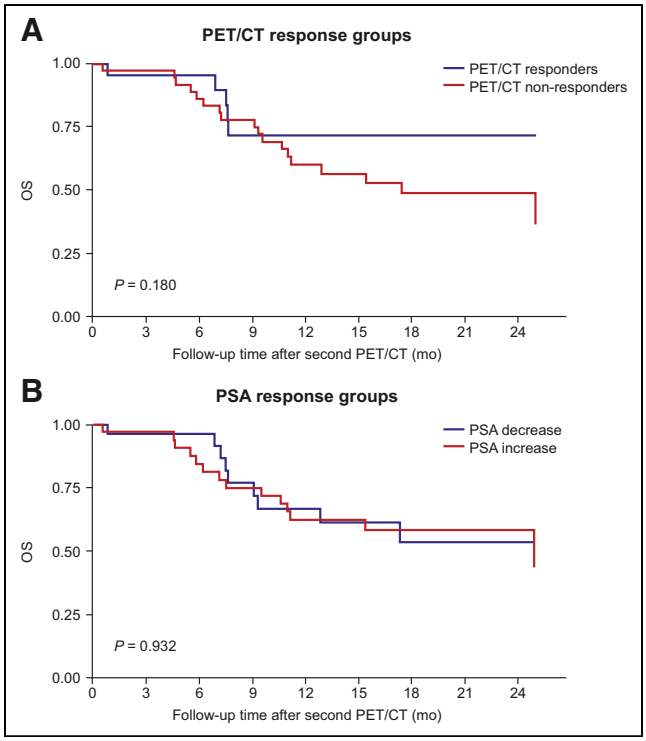

FIGURE 3. Association of OS with PET/CT response (A) and change from baseline in serum PSA level (B) (n = 63). mo = months; OS = overall survival; PET/CT = positron emission tomography/computed tomography; PSA = prostate-specific antigen.

DISCUSSION

The present retrospective analysis of a large, single-center registry examined PSMA expression in patients with CRPC. Monitoring therapy response is important for treatment decisions in patients with mCRPC, and previous evidence suggest that PET/CT may aid in predicting early response to therapy (*7,10,11,20,21*); however, data are limited. Findings in this study suggest that PSMA expression on PET/CT could be more prognostic than PSA parameters for PFS and might be a promising tool for guiding clinical decisions in patients with advanced PC.

Consistent with the literature, most patients (95%) in our analysis had PSMA expression at baseline, as determined by PET/CT imaging (*6*). Interestingly, PSMA expression was higher in patients with prior systemic treatment, although this was irrespective of the number and type of therapy line. Higher PSMA expression in these patients may be due to more advanced and aggressive disease. The type of prior treatment did not influence PSMA expression; of particular note, there was no difference in PSMA expression in the 18% of patients last treated with abiraterone or enzalutamide before first PET/CT compared with patients last treated with other systemic therapies. Studies have shown that enzalutamide may affect the expression of PSMA on the PC cell surface early after treatment initiation (from 14 to 25 d) (*22,23*). Conversely, PSMA variations in patients treated with abiraterone or enzalutamide were not observed when treated over a longer period (87–110 d) (*24*), suggesting that the upregulation of PSMA expression after abiraterone or enzalutamide is transient. These findings are in line with the absent effect of abiraterone or enzalutamide on PSMA expression in our study, although further research is needed given the small number of patients. Variations in PSMA expression were observed according to

the site of relapse or metastasis, and the highest SUV_{max} occurred in metastasis involving the bone. It should be noted that the study included both patients who did and patients who did not undergo radical prostatectomy, which may explain why a relatively high proportion of patients had prostate bed relapse (21%).

As expected, we found that PSMA expression at first PET/CT correlated with PSA levels and velocity, but not doubling time. We also confirmed the general relationship understood to exist between high PSMA expression and advanced stage disease (*6*).

However, higher PSMA expression may also correlate with treatment response; in a retrospective study conducted in patients with mCRPC who had received [^{177}Lu]Lu-PSMA-617, higher PSMA expression was associated with longer OS, longer PFS, and higher PSA variation (*25*). In our analysis, PET/CT nonresponders had numerically lower SUV_{max} on first PET/CT than responders. The lack of statistical significance may relate to the low number of patients who underwent a second PET/CT. There was also no significant difference in SUV_{max} between nonresponders and responders when analyzed by last treatment received before second PET/CT. Patients with an increase in PSA levels had significantly lower SUV_{max} at baseline than patients with a PSA decrease, with good agreement between PET/CT response and PSA variation. These findings are consistent with another retrospective study that demonstrated correlations between SUV_{max} and PSA response in patients with mCRPC (*21*), suggesting that PSMA expression on PET/CT may be a predictive marker of treatment response. This could potentially enable better patient selection for therapies targeting PSMA; patients with lower expression at baseline are less likely to respond to further lines of therapy, possibly due to more aggressive and undifferentiated disease.

Previous studies have demonstrated a higher accuracy of PET/CT in patients with CRPC compared with biochemical response and other conventional methods, supporting its utility as a reliable parameter to predict response to systemic treatment for mCRPC (*7,10,11,20,21*). Although 1 study reported that the performance of PET/CT was not superior to conventional imaging in differentiating progressive disease from response to treatment, this may be due to the small number of patients involved (*20*). Our analysis suggests that PET/CT might be more reliable than PSA for predicting response to therapy; however, our findings were not statistically significant given the small sample size.

Response at first PET/CT and PSA decrease from baseline were both significant prognostic factors for PFS. The combined analysis suggested that PET/CT response may be a more significant prognostic factor than PSA variation. In line with recommendations from the Prostate Cancer Clinical Trials Working Group 3 (*26*), this suggests that therapy should not be discontinued based only on PSA variation. As PSA may not always predict response to therapy, PET/CT may be a more reliable option for early prediction; however, the burden of disease or response to therapy may be underestimated if the timing of PET/CT is not optimal (*27*). Consensus is needed on the appropriate point at which to repeat PET/CT.

In the current analysis, we did not observe any relation between PET/CT response or PSA variation and OS in patients with mCRPC. A retrospective study in patients with mCRPC reported similar results, with no correlations observed between PET parameters and OS (*21*); however, the findings may be explained by the limited number of patients included in these analyses.

As with all retrospective single-centered studies, our findings may not be representative of the general population with mCRPC. The retrospective design and consequent number of patients lost to follow-up also mean that associations between PET/CT response and OS should be interpreted with caution. Further, assessment of response to therapy was not possible in patients without a second PET/CT. A further limitation is the heterogeneity of the cohort of enrolled patients, in terms of therapy management, baseline characteristics, and enrollment. Only those with a suspicion of progression were included, and consequently, a substantial proportion of patients did not undergo PSMA PET/CT during the study period; however, the use of established imaging protocols implemented by experienced operators is a strength of the study.

Finally, in advanced PC, pre- and postdiagnosis management can vary as there are no precise guidelines on the order and duration of second-line therapies, and serious adverse effects may be experienced, particularly by elderly patients and those with comorbidities. This complicates the interpretation of data on the efficacy and usefulness of diagnostic investigations. The ability of PSMA PET/CT to detect recurrence at an earlier stage of disease suggests greater opportunities for life-prolonging treatment; however, given the often indolent clinical course of recurrent PC, the potential benefits of earlier, aggressive therapeutic intervention in patients with limited recurrence will need to be weighed carefully against the risk of associated toxicities and quality of life impairment (*28*).

CONCLUSION

Our findings suggest that PSMA expression on PET/CT may be a predictive marker of treatment response in patients with mCRPC regardless of ongoing systemic therapy at the time of PET/CT. The data also suggest that PET/CT response is a more significant prognostic factor for PFS than PSA variation; however, larger studies are warranted to confirm these findings and to further explore PSMA expression in relation to patient survival.

DISCLOSURE

This study was funded by Amgen Inc. (Thousand Oaks, California, USA), which paid the fee to publish the article's open access and played a role in the study design, data collection and analysis, decision to publish, and preparation of the manuscript. Karly S. Louie was employed by Amgen Ltd. at the time the study was conducted, holds stocks in Amgen, and is an employee of and holds stock options/shares in BioMarin Pharmaceutical Inc. Michael Groaning is an employee of and holds stock in Amgen. Stefano Fanti has consulted for AAA, Amgen, Astellas, AstraZeneca, Bayer, GE, Janssen, Novartis, Sofie, and Telix and has received research funding and travel support from AAA, Amgen, Astellas, AstraZeneca, Bayer, GE, Janssen, Novartis, Sofie, and Telix. Funding for medical writing support for this article was provided by Amgen Ltd (Uxbridge, UK). No other potential conflict of interest relevant to this article was reported.

ACKNOWLEDGMENTS

We thank all patients and investigators involved in the study. Medical writing support, including development of a draft outline and subsequent drafts in consultation with the authors, assembling tables and figures, collating author comments, copyediting, fact checking, and referencing, was provided by Emma McConnell, PhD, CMPP, and Heather Davies, PhD, CMPP, at Aspire Scientific Limited (Bollington, UK).

KEY POINTS

QUESTION: What is the prognostic value (for OS and PFS) of PSMA PET response and how does this compare with PSA response?

PERTINENT FINDINGS: In this retrospective, observational study, nearly all patients with CRPC (95%) had PSMA expression on PET/CT, regardless of prior systemic therapy, and were classified as having mCRPC. PSMA expression was significantly associated with PSA level and velocity; PSA change between first and second PET/CT was 146% in nonresponders and −57% in responders, with a 79% agreement between PET/CT and PSA response; and PET/CT response, despite PSA variation, was a significant prognostic factor for PFS.

IMPLICATIONS FOR PATIENT CARE: Understanding the impact of treatment on PSMA expression could inform utility of [^{68}Ga]Ga-PSMA-11 PET/CT for guiding clinical decisions in patients with mCRPC.

REFERENCES

1. Ferlay J, Colombet M, Soerjomataram I, et al. Cancer incidence and mortality patterns in Europe: estimates for 40 countries and 25 major cancers in 2018. *Eur J Cancer.* 2018;103:356–387.
2. Hofman MS, Emmett L, Violet J, et al. TheraP: a randomized phase 2 trial of (177) Lu-PSMA-617 theranostic treatment vs cabazitaxel in progressive metastatic castration-resistant prostate cancer (Clinical Trial Protocol ANZUP 1603). *BJU Int.* 2019;124(suppl 1):5–13.
3. Galletti G, Leach BI, Lam L, Tagawa ST. Mechanisms of resistance to systemic therapy in metastatic castration-resistant prostate cancer. *Cancer Treat Rev.* 2017; 57:16–27.
4. Claps M, Mennitto A, Guadalupi V, et al. Immune-checkpoint inhibitors and metastatic prostate cancer therapy: learning by making mistakes. *Cancer Treat Rev.* 2020;88:102057.
5. Parker C, Castro E, Fizazi K, et al. Prostate cancer: ESMO clinical practice guidelines for diagnosis, treatment and follow-up. *Ann Oncol.* 2020;31:1119–1134.
6. Ruigrok EAM, van Weerden WM, Nonnekens J, de Jong M. The future of PSMA-targeted radionuclide therapy: an overview of recent preclinical research. *Pharmaceutics.* 2019;11:560.
7. Hofman MS, Lawrentschuk N, Francis RJ, et al. Prostate-specific membrane antigen PET-CT in patients with high-risk prostate cancer before curative-intent surgery or radiotherapy (proPSMA): a prospective, randomised, multicentre study. *Lancet.* 2020;395:1208–1216.
8. Hofman MS, Emmett L, Sandhu S, et al. [^{177}Lu]Lu-PSMA-617 versus cabazitaxel in patients with metastatic castration-resistant prostate cancer (TheraP): a randomised, open-label, phase 2 trial. *Lancet.* 2021;397:797–804.
9. Hofman MS, Violet J, Hicks RJ, et al. [^{177}Lu]-PSMA-617 radionuclide treatment in patients with metastatic castration-resistant prostate cancer (LuPSMA trial): a single-centre, single-arm, phase 2 study. *Lancet Oncol.* 2018;19:825–833.
10. Lawal IO, Mokoala KMG, Mahapane J, et al. A prospective intra-individual comparison of [^{68}Ga]Ga-PSMA-11 PET/CT, [^{68}Ga]Ga-NODAGA(ZOL) PET/CT, and [^{99m}Tc]Tc-MDP bone scintigraphy for radionuclide imaging of prostate cancer skeletal metastases. *Eur J Nucl Med Mol Imaging.* 2021;48:134–142.
11. Grubmüller B, Senn D, Kramer G, et al. Response assessment using ^{68}Ga-PSMA ligand PET in patients undergoing ^{177}Lu-PSMA radioligand therapy for metastatic castration-resistant prostate cancer. *Eur J Nucl Med Mol Imaging.* 2019;46:1063–1072.
12. Farolfi A, Koschel S, Murphy DG, Fanti S. PET imaging in urology: a rapidly growing successful collaboration. *Curr Opin Urol.* 2020;30:623–627.
13. Khan MA, Carter HB, Epstein JI, et al. Can prostate specific antigen derivatives and pathological parameters predict significant change in expectant management criteria for prostate cancer? *J Urol.* 2003;170:2274–2278.
14. Farolfi A, Ceci F, Castellucci P, et al. ^{68}Ga-PSMA-11 PET/CT in prostate cancer patients with biochemical recurrence after radical prostatectomy and PSA <0.5 ng/mL. Efficacy and impact on treatment strategy. *Eur J Nucl Med Mol Imaging.* 2019;46:11–19.
15. Fendler WP, Eiber M, Beheshti M, et al. ^{68}Ga-PSMA PET/CT: Joint EANM and SNMMI procedure guideline for prostate cancer imaging: version 1.0. *Eur J Nucl Med Mol Imaging.* 2017;44:1014–1024.
16. Fanti S, Goffin K, Hadaschik BA, et al. Consensus statements on PSMA PET/CT response assessment criteria in prostate cancer. *Eur J Nucl Med Mol Imaging.* 2021;48:469–476.
17. Eisenhauer EA, Therasse P, Bogaerts J, et al. New response evaluation criteria in solid tumours: revised RECIST guideline (version 1.1). *Eur J Cancer.* 2009;45: 228–247.
18. European Association of Urology. EAU - EANM - ESTRO - ESUR - ISUP - SIOG guidelines on prostate cancer. Uroweb.org website. https://uroweb.org/guideline/prostate-cancer/. Accessed March 7, 2023.
19. Sweat SD, Pacelli A, Murphy GP, Bostwick DG. Prostate-specific membrane antigen expression is greatest in prostate adenocarcinoma and lymph node metastases. *Urology.* 1998;52:637–640.
20. Seitz AK, Rauscher I, Haller B, et al. Preliminary results on response assessment using ^{68}Ga-HBED-CC-PSMA PET/CT in patients with metastatic prostate cancer undergoing docetaxel chemotherapy. *Eur J Nucl Med Mol Imaging.* 2018;45:602–612.
21. Grubmüller B, Rasul S, Baltzer P, et al. Response assessment using [^{68}Ga]Ga-PSMA ligand PET in patients undergoing systemic therapy for metastatic castration-resistant prostate cancer. *Prostate.* 2020;80:74–82.
22. Aggarwal R, Wei X, Kim W, et al. Heterogeneous flare in prostate-specific membrane antigen positron emission tomography tracer uptake with initiation of androgen pathway blockade in metastatic prostate cancer. *Eur Urol Oncol.* 2018;1: 78–82.
23. Rosar F, Dewes S, Ries M, et al. New insights in the paradigm of upregulation of tumoral PSMA expression by androgen receptor blockade: enzalutamide induces PSMA upregulation in castration-resistant prostate cancer even in patients having previously progressed on enzalutamide. *Eur J Nucl Med Mol Imaging.* 2020;47: 687–694.
24. Plouznikoff N, Artigas C, Sideris S, et al. Evaluation of PSMA expression changes on PET/CT before and after initiation of novel antiandrogen drugs (enzalutamide or abiraterone) in metastatic castration-resistant prostate cancer patients. *Ann Nucl Med.* 2019;33:945–954.
25. Gafita A, Calais J, Grogan TR, et al. Nomograms to predict outcomes after ^{177}Lu-PSMA therapy in men with metastatic castration-resistant prostate cancer: an international, multicentre, retrospective study. *Lancet Oncol.* 2021;22:1115–1125.
26. Scher HI, Morris MJ, Stadler WM, et al. Trial design and objectives for castration-resistant prostate cancer: updated recommendations from the Prostate Cancer Clinical Trials Working Group 3. *J Clin Oncol.* 2016;34:1402–1418.
27. Vaz S, Hadaschik B, Gabriel M, Herrmann K, Eiber M, Costa D. Influence of androgen deprivation therapy on PSMA expression and PSMA-ligand PET imaging of prostate cancer patients. *Eur J Nucl Med Mol Imaging.* 2020;47:9–15.
28. Madan RA, Mena E, Lindenberg L, Choyke PL. With new technology comes great responsibility: prostate-specific membrane antigen imaging in recurrent prostate cancer. *J Clin Oncol.* 2022;40:3015–3019.

An Analysis of the Distribution of PSMA PET/CT–Positive Lymph Nodes and Their Coverage by Different Elective Nodal Radiation Volumes in Postoperative Prostate Cancer Patients

Christian Trapp[1], Dmytro Oliinyk[1], Paul Rogowski[1], Rieke von Bestenbostel[1], Ute Ganswindt[2], Minglun Li[1], Chukwuka Eze[1], Peter Bartenstein[3], Leonie Beyer[3], Harun Ilhan[3], Gabriel Sheikh[3], Lena Unterrainer[3], Christian Stief[4], Thilo Westhofen[4], Wolfgang G. Kunz[5], Marcus Unterrainer[5], Claus Belka[1,6], and Nina-Sophie Schmidt-Hegemann[1]

[1]Department of Radiation Oncology, University Hospital, LMU Munich, Munich, Germany; [2]Department of Radiation Oncology, University Hospital, Medical University Innsbruck, Innsbruck, Austria; [3]Department of Nuclear Medicine, University Hospital, LMU Munich, Munich, Germany; [4]Department of Urology, University Hospital, LMU Munich, Munich, Germany; [5]Department of Radiology, University Hospital, LMU Munich, Munich, Germany; and [6]German Cancer Consortium, Munich, Germany

Salvage elective nodal radiotherapy (ENRT) is a treatment option for patients with biochemically persistent or recurrent prostate cancer who have lymph node metastases (LNs) after prostatectomy. Possible ENRT templates were proposed by the Radiation Therapy Oncology Group (RTOG; 2009), the PIVOTAL trialists (2015), and the NRG Oncology Group (2021). The goal of this study was to analyze the distribution of prostate-specific membrane antigen (PSMA) PET/CT–positive LNs and to compare the templates regarding their LN coverage. **Methods:** We analyzed the PSMA PET/CT scans of 105 patients with PET-positive LNs treated with salvage ENRT from 2014 to 2019. All LNs were mapped in an exemplary dataset, classified by region, and assessed with regard to their potential coverage by the 3 ENRT templates. The primary endpoint was the number of missed LNs. The secondary endpoint was the number of patients with full coverage. To compare the templates, a *t* test and McNemar test were used. **Results:** Three hundred thirty-five LNs were contoured (3.19 per patient; 95% CI, 2.43–3.95). Most frequently, LNs were seen in the internal iliac ($n = 94$, 28.1%), external iliac ($n = 60$, 17.9%), periaortic ($n = 58$, 17.3%), common iliac ($n = 55$, 16.4%), perirectal ($n = 26$, 7.8%), and presacral ($n = 19$, 5.7%) regions. The NRG template missed fewer LNs per patient (1.01, 31.7%) than the RTOG (1.28, 40.1%, $P < 0.001$) and PIVOTAL templates (1.19, 37.3%, $P = 0.003$). No difference was observed in the number of patients with full coverage of all LNs: 52 (49.5%) with the NRG template versus 50 (47.6%) with the RTOG ($P = 0.625$) and 49 (46.7%) with the PIVOTAL template ($P = 0.250$). **Conclusion:** The NRG template showed better coverage than the RTOG and PIVOTAL templates. Nevertheless, in this cohort, it would have missed almost one third of all contoured LNs and would have resulted in incomplete coverage in half the patients. This result underlines the importance of advanced imaging, such as PSMA PET/CT scans, before salvage ENRT and shows the need for further individualization of ENRT fields.

Key Words: prostate cancer; nodal recurrence; PSMA PET/CT; elective nodal radiotherapy; ENRT templates

J Nucl Med 2023; 64:918–923
DOI: 10.2967/jnumed.122.265159

Received Nov. 20, 2022; revision accepted Jan. 26, 2023.
For correspondence or reprints, contact Christian Trapp (christian.trapp@med.uni-muenchen.de).
Published online Feb. 2, 2023.

In several clinical situations, elective nodal radiotherapy (ENRT) is part of the treatment of prostate cancer (PC) patients. Possible indications for ENRT can be a high risk for lymph node metastases (LNs) in primary patients or PET-positive or pathologically confirmed LNs in postoperative patients undergoing either adjuvant or salvage radiotherapy. Regarding the benefit of adding ENRT to androgen deprivation therapy in postoperative patients with pathologically confirmed LNs, there is ample retrospective evidence for better PC-specific survival (*1–3*). Likewise, in patients with biochemical recurrence, the addition of ENRT leads to a better outcome than prostate bed radiotherapy with or without short-term androgen deprivation therapy (*4*).

In 2009, the Radiation Therapy Oncology Group (RTOG) reached a consensus for contouring the ENRT volume and published their recommendations (*5*). Another template was suggested by the PIVOTAL trialists in 2015 (*6*). Their intention was to find a compromise between the detailed RTOG recommendations, which are reproducible and easy to delineate, and the complex recommendations for free hand contouring of the Royal Marsden Hospital in London, which were known to be safe at that time. However, some publications raised concerns about incomplete coverage of LNs using the RTOG template (*7–11*). Likewise, an adapted version of the PIVOTAL template demonstrated seemingly insufficient coverage (*12*). In 2021, the NRG oncology group published another contouring guideline (*13*) with the intention to update the RTOG recommendations based on new LN distribution data. To our knowledge, the NRG template has thus far been evaluated only by Filimonova et al. (*14*). Although some of the mentioned studies were performed with conventional imaging (MRI and CT) or with different and nowadays outdated ^{18}F-choline, ^{11}C-acetate, and FDG PET/CT scans (*7,8,15*), other studies already incorporated prostate-specific membrane antigen (PSMA) PET/CT scans (*9–11,14*). Overall, PSMA PET/CT is currently the most sensitive imaging modality for LN detection (*16,17*) and outperforms standard imaging such as bone scanning, CT, and MRI, particularly at low prostate-specific antigen (PSA) levels (*18–20*). Until now, nodal coverage has not been directly compared among the 3 ENRT templates in the postoperative setting. Here, we analyze LN coverage

TABLE 1
Distribution of LNs

Lymphatic drainage*	LNs (*n*)			
	Total	Not covered by RTOG	Not covered by PIVOTAL	Not covered by NRG
Total	335	134 (40%)	125 (37%)	106 (32%)
Internal iliac	94 (28%)	3 (3%)	3 (3%)	4 (4%)
External iliac	60 (18%)	2 (3%)	2 (3%)	2 (3%)
Periaortic	58 (17%)	58 (100%)	58 (100%)	53 (9%)
Common iliac	55 (16%)	14 (26%)	6 (11%)	0 (0%)
Perirectal	26 (8%)	25 (96%)	24 (92%)	22 (85%)
Presacral	19 (6%)	12 (63%)	12 (63%)	5 (26%)
Perivesical	10 (3%)	8 (80%)	9 (90%)	9 (90%)
Inguinal	9 (3%)	9 (100%)	9 (100%)	9 (100%)
Periprostatic/periseminal vesicle	3 (1%)	3 (100%)	2 (67%)	2 (67%)
Mesenteric	1 (0%)	1 (100%)	1 (100%)	1 (100%)

*Modifications: internal iliac includes internal pudendal, and perirectal includes inferior and superior rectal.

applying the various templates in a postoperative PC patient cohort all staged with PSMA PET/CT scans.

MATERIALS AND METHODS

Patient Population

In 2014, PSMA PET/CT scans before radiotherapy were introduced at our institution as the standard diagnostic staging tool routinely used in PC patients. For this analysis, we included a total of 105 consecutive postoperative patients referred for salvage ENRT who had undergone PSMA PET/CT because of PSA persistence or recurrence and who had evidence of PSMA-positive regional and paraaortic LNs. Patients with additional bone metastases were included, whereas patients with additional visceral metastases or supradiaphragmatic LNs were excluded.

This retrospective analysis was performed in compliance with the principles of the Declaration of Helsinki and its subsequent amendments (*21*) and was approved by the local Ethics Committee of the University of Munich (approval 19-361). The requirement to obtain informed consent was waived.

PSMA Ligand and PET/CT Imaging Protocol

Pretreatment imaging was performed with ^{68}Ga- or ^{18}F-labeled PSMA ligand PET/CT scans in 65% (^{68}Ga-PSMA-11) and 35% (^{18}F-PSMA-1007, after 2018) of patients, respectively. Radiolabeling was performed according to good clinical practice as described elsewhere (*22,23*). A Siemens Biograph 64, a Siemens Biograph mCT, or a GE Healthcare Discovery 690 PET/CT scanner was used for PSMA PET/CT imaging. Phantom studies based on the National Electrical Manufacturers Association NU2-2001 standard were conducted to allow for pooling of scanner results. At the time of the PET scan, a contrast-enhanced diagnostic CT scan (120 kV, 100–400 mAs, dose modulation) or a low-dose CT scan (120 kV, 25 mAs) for attenuation correction was performed depending on previous CT scans and contraindications. PSMA PET/CT scans were acquired approximately 60 min after injection of the PSMA ligand. Barring any contraindications, patients were administered 20 mg of furosemide at the time of tracer injection to avoid bladder activity and to reduce radiation exposure.

Image Interpretation

PET/CT scans were interpreted by 1 nuclear medicine physician and 1 radiologist in the sense of a clinical report–based analysis. Both readers had more than 5 y of PET/CT experience. The location of each lesions was determined by a CT scan. PET-positive lesions were visually identified by ^{68}Ga-/^{18}F-PSMA uptake above the background level and not associated with the physiologic uptake (*24*).

Anatomic Mapping

To allow systematic topographic mapping, the cross-sectional nodal atlas published by Martinez-Monge et al. (*25*) with small modifications (Table 1) was used. For each patient, the number and location of the PET-positive LNs were documented. Beyond summarizing these data in a table, we manually contoured each LN in a virtual patient dataset to

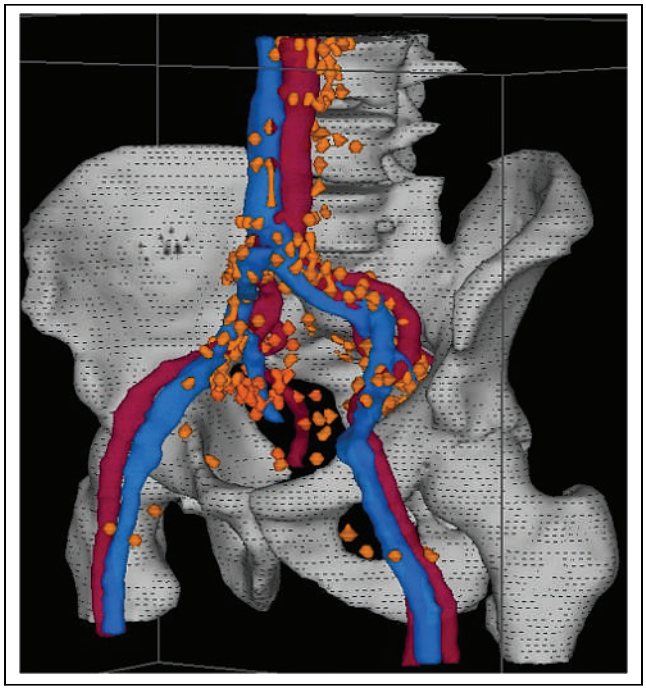

FIGURE 1. CT scan dataset showing veins (blue), arteries (red), bones (gray) and all PSMA-positive LNs of patients with PSA persistence (orange).

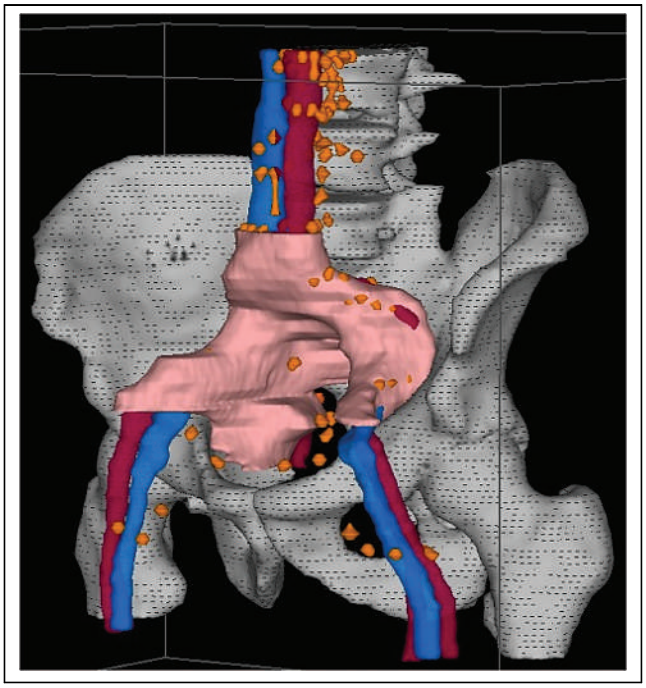

FIGURE 2. CT scan dataset showing veins (blue), arteries (red), bones (gray), NRG ENRT volume (pink) and all PSMA-positive LNs of patients with PSA persistence not covered by NRG volume (orange).

achieve a 3-dimensional visualization of the cumulative LN distribution (Fig. 1). The Oncentra MasterPlan (version 4.5.2; Elekta) planning system was used for contouring and generating 3-dimensional images for the atlas. Moreover, every lymphatic drainage region in each patient was assessed regarding a potential geographic miss by counting LNs that would not have been treated adequately by the 3 templates (Fig. 2). A LN was considered covered if more than the half its volume was covered by the respective clinical target volume (RTOG, PIVOTAL, or NRG). Contouring was performed in accordance with the original publications (*5,6,13*). Main differences between the templates are pointed out in Table 2.

For the assessment of geographic miss, distances to relevant anatomic structures (vessels, bone, muscle, bladder, bowel) were considered, as well as the craniocaudal position in relation to vessel bifurcations or bony landmarks.

Endpoints and Statistical Analysis

The primary endpoint of this study was the potential coverage of LNs by the 3 templates. Because information about coverage was collected for every patient for every lymphatic drainage region, statistical analyses were performed on a per-patient basis. The secondary endpoint was the number of patients with full coverage of all LNs by the 3 templates. Statistical analyses were conducted using IBM-SPSS, version 26.0. To compare the templates regarding the primary endpoint, a paired-samples *t* test was used. Regarding the secondary endpoint, a McNemar test was used. A *P* value of less than 0.05 was considered significant.

RESULTS

Overall, we analyzed the PSMA PET/CT scans of 105 patients who underwent PSMA PET/CT–guided radiotherapy at our institution between 2014 and 2019 due to LN recurrence after radical prostatectomy. Patient characteristics are shown in Table 3. Indications for PSMA PET/CT scans were either biochemical recurrence (29%) or PSA persistence after surgery (71%). Median PSA at time of the PSMA PET/CT scan was 1.65 ng/mL in patients with PSA persistence and 0.65 ng/mL in patients with biochemical recurrence. Additionally, PSMA PET/CT scans revealed bone metastases and local recurrences in the prostate bed in 12% and 31% of cases, respectively.

In total, 335 PSMA PET/CT–positive LNs were detected, which corresponds to 3.19 LNs per patient. The detailed distribution across the lymphatic drainage regions is shown in Table 3. Most frequently, LNs developed in the internal iliac (28%), external iliac (18%), periaortic (17%), and common iliac (16%) regions. In our exemplary CT dataset, the ENRT templates had a volume of 369 cm^2 (RTOG), 375 cm^2 (PIVOTAL), and 432 cm^2 (NRG). In Table 1, the proportion of LNs that would not have been covered by the templates is shown for every lymphatic drainage region.

TABLE 2
Characteristics of and Differences in ENRT Templates

Region	RTOG	PIVOTAL	NRG
Cranial border	L5/S1 interspace	Lower border of L5	Bifurcation of aorta or inferior caval vein (typically L4/L5)
Margin around vessels	7 mm (carving out bone, bowel, bladder)	7 mm (carving out bone, bladder, muscle, rectum, bowel + 3 mm)	5–7 mm (carving out bone, bladder, muscle, bowel), enlarge to 10 mm when indicated
Presacral nodes	S1–S3, 10 mm anterior to sacrum	S1–S3, 12 mm anterior to sacrum	Presacral, prevertebral and posterior perirectal nodes until S3
External iliac nodes	Until top of femoral heads	Until top of femoral heads	Until vessels are more lateral than the most medial aspect of the acetabulum (typically middle of femoral head)
Obturator nodes	Until top of pubic symphysis	Until 1 cm above top of symphysis	Until midportion of prostate bed (in definitive setting until seminal vesicles join the prostate)

TABLE 3
Patient Characteristics (n = 105)

Characteristic	Data
Age (y)	71 (46–82)
Initial tumor stage	
pT2a	1 (1%)
pT2c	16 (15%)
pT3a	29 (28%)
pT3b	55 (52%)
pT4	3 (3%)
Unknown	1 (1%)
Initial nodal stage	
pN0 in patients with PSA…	
Persistence	35 (47%)
Recurrence	22 (73%)
pN1 in patients with PSA…	
Persistence	40 (53%)
Recurrence	5 (17%)
pNx/cN0 in patients with PSA…	
Persistence	0 (0%)
Recurrence	1 (3%)
Unknown	0 (0%)/2 (7%)
Number of removed LNs	12 (2–42)
Positive surgical margins	56 (53%)
International Society of Urological Pathology score	
1	2 (2%)
2	12 (11%)
3	23 (22%)
4	19 (18%)
5	48 (46%)
Unknown	1 (1%)
PSA at diagnosis (ng/mL)	15.1 (1.6–332)
Postoperative PSA (ng/mL)	0.6 (0.0–58.0)
Patients with PSA…	
Persistence	75 (71%)
Recurrence	30 (29%)
PSA at PSMA PET/CT (ng/mL) in patients with PSA…	
Persistence	1.65 (0.10–40.13)
Recurrence	0.75 (0.22–55.65)
Patients with…	
^{68}Ga-PSMA PET/CT	68 (65%)
^{18}F-PSMA PET/CT	37 (35%)
Activity (MBq)	241 (87–367)
Time from injection to PET scan (min)	66 (45–125)
Patients with additional…	
Bone metastases	13 (12%)
Local recurrences	33 (31%)

Qualitative data are number and percentage; continuous data are median and range.

The regions with the greatest differences among the 3 templates were the periaortic, common iliac, perirectal, and presacral.

The RTOG template would have missed 1.28 LNs (mean) per patient (40.1%). Use of the PIVOTAL and NRG templates would have reduced the number of missed LNs per patient to 1.19 (37.3%) and 1.01 (31.7%), respectively (Table 4). This resulted in significantly improved coverage using the NRG template compared with the RTOG ($P < 0.001$) and PIVOTAL templates ($P = 0.003$). However, the PIVOTAL template covered significantly more LNs than the RTOG volume ($P = 0.028$). Regarding the secondary endpoint, the NRG template would not have resulted in a significantly higher proportion of patients with complete coverage of all LNs (52 patients, 49.5%) than would the RTOG (50 patients, 47.6%; $P = 0.625$) or PIVOTAL templates (49 patients, 46.7%; $P = 0.250$ for comparison with NRG, $P = 1.00$ for comparison with RTOG).

DISCUSSION

The present study shows the distribution of PSMA PET/CT–positive LNs in postoperative PC patients. There are several other choline PET/CT– or PSMA PET/CT–based analyses on the location and ENRT coverage of LNs in postoperative PC patients (*9–11,15,26*). The results are mostly similar. Interestingly, the choline PET/CT–derived analyses found comparably fewer internal iliac LNs while describing comparably more common iliac LNs (*15,26*). Moreover, 2 studies with comparably low PSA levels at the time of the PET/CT scans found fewer periaortic and more perirectal LNs (*9,10*).

Furthermore, the present study evaluated how many LNs would have been covered by the respective ENRT templates. Most of the mentioned studies used the RTOG template in this regard (*9–11,26*) and described a slightly better coverage (63%–66%) than our study (60%). First, this better coverage may be associated with lower PSA levels at the time of PET/CT scans (*9,10*), as lower levels are known to correlate with higher coverage because of overall lower LN numbers (*9,11*). Second, the better coverage is most likely because of the staging by the choline PET/CT scan (*26*), which is known to have a lower detection rate than PSMA PET/CT scans (*27*). The study of Schiller et al., which had PSA levels similar to those in the present analysis and used PSMA PET/CT scans, described an even worse coverage (complete and partial) of 48% (*11*). The study of De Bruycker et al. (*15*) using the PIVOTAL template reported a lower miss rate of 27%, which is less than in our study (37%). Admittedly, they modified the template and used a more cranial border (top of L4 instead of bottom of L5), which explains the higher coverage. Regarding the newer NRG template, Filimonova et al. (*14*) found that 35% of patients had LNs outside the template, whereas in our study, 51% had incomplete coverage. This difference is because of the exclusion of paraaortic LNs by Filimonova et al. When excluding patients with paraaortic LNs in the present study, we found that 39% had LNs outside the NRG template (RTOG, 41%; PIVOTAL, 42%), which is similar to Filimonova et al.

To the best of our knowledge, the present study is the first analysis with a direct comparison among the 3 templates. It shows that the PIVOTAL volume, which combines characteristics of the RTOG guideline with the experience of the Royal Marsden Hospital, covers significantly more LNs than the RTOG template and that the NRG volume, which was intended to be an updated and improved version of the RTOG volume, covers significantly more LNs than both other templates. Thus, the changes in the NRG

TABLE 4
Coverage of LNs

Parameter	RTOG	PIVOTAL	NRG
LNs (*n*)			
Median	2		
Mean	3.19 (range, 1–23)		
LNs not covered by ENRT volume (*n*)			
Median	1	1	1
Mean	1.28 (range, 0–13)	1.19 (range, 0–11)	1.01 (range, 0–11)
Patients with all LNs covered by ENRT volume (*n*)	50 (47.6%)	49 (46.7%)	52 (49.5%)

volume improved the former RTOG volume, resulting in an overall better coverage in the present analysis. One of the key differences concerns the superior border, which extends to more cranial regions in the NRG template (aortic or caval bifurcation instead of L5/S1 interspace). Spratt et al. (*7*), who developed another MRI-, CT- and FDG-PET/CT based atlas in PC patients with recurrences after primary radiotherapy, found a coverage of 42% with the RTOG template, which would improve to 93% when extending the volume cranially to the L4/L5 interspace. Nevertheless, there are still lymphatic drainage regions not adequately covered by the NRG template. For example, of 335 LNs in the present analysis, there were 53 periaortic, 22 perirectal, 9 perivesical, and 9 inguinal metastases missed by the NRG template. This finding leads to the question of whether the obvious solution would be to further enlarge the ENRT volumes toward these areas. However, most likely, this solution would be at the expense of increased toxicity. Although some studies have thus far used the RTOG recommendations with a more cranial border (e.g., OLIGOPELVIS (*28*) or the RTOG 0924 trial [results outstanding]), there is no direct comparison evaluating a possible increase in toxicity by extending the template. Concerns about toxicity have also been the reason to exclude perirectal nodes from the NRG template against better knowledge of a potential geographic miss.

Interestingly, despite the better coverage of the NRG template, there was no significant difference among the numbers of patients with full coverage in this study. The reason may be that some patients had several LNs in areas not covered by the templates, which overestimates their statistical impact in the LN-based approach. Thus, the question remains of whether the better coverage of the NRG template really leads to more patients who are adequately treated.

Nevertheless, despite the improvement of the ENRT template by the NRG recommendations, there are still some pending questions. The most important question deals with the indication for ENRT, which is still a subject of intense discussions. Thus far, the results of recent phase 3 studies, for example, the POP-RT trial in the definitive setting (*29*) and—albeit before the PSMA PET/CT scan era—the SPPORT trial in the salvage setting (*4*), have strengthened the role of ENRT. Furthermore, in the clinical setting of PET-positive LNs, there is an ongoing discussion about the best treatment strategy. ENRT with or without a boost to the LNs seems to be associated with fewer recurrences in the adjacent LN regions at the cost of increased toxicity compared with stereotactic body radiotherapy (*30*). In this regard, prospective toxicity data on patients receiving ENRT with the NRG template are pertinent. In our opinion, possible further changes in ENRT fields should always be closely evaluated regarding efficacy and toxicity. Furthermore, clinical and imaging parameters should ideally be defined to allow for further individual adaptation of radiation fields. Until now, the PSA value before PET/CT was the only known parameter associated with a higher risk for LNs outside the template (*9,11*).

Admittedly, there are some limitations of the present analysis. First, it is based on a retrospective cohort incorporating postoperative patients with either biochemical persistence or recurrence and a relatively wide PSA range before PSMA PET/CT scans. Also including patients with high PSA values and bone metastases led to a high number of evaluated LNs but complicates the interpretation of the absolute numbers of the endpoints. In patients with lower-risk profiles, the templates would probably cover considerably more LNs. For example, when restricted to only the subgroup without bone metastases and with a PSA of less than 2.0 ng/mL ($n = 57$ with a mean of 2.68 LNs per patient)—similar to the cohort of the SPPORT trial (*4*)—the templates would have missed 39% (RTOG), 37% (PIVOTAL), and 33% (NRG) of LNs, and 56% (NRG and PIVOTAL) and 58% (RTOG) of the patients would have had full coverage. Second, the sensitivity of ^{18}F-PSMA-1007 for LNs near the urinary bladder might be higher than that of ^{68}Ga-PSMA-11 because of the lower urinary excretion (*31*). Third, the RTOG and PIVOTAL templates were designed primarily for patients in the definitive and not in the postoperative setting, whereas the present and most of the aforementioned analyses evaluated the 3 templates in a postoperative cohort in which the lymphatic drainage might have been altered because of lymphadenectomy. Fourth, manual contouring of LNs is not completely reproducible. However, using this method, we separately assessed every LN in consideration of the respective original clinical target volume recommendation.

Despite being the gold standard in the postoperative setting of PSA persistence or recurrence and showing a good specificity of 95%, PSMA PET/CT scans have a sensitivity of only 40% in detecting LNs compared with histopathologic reports (*32*). Thus, when considering smaller radiation fields or even stereotactic body radiotherapy, one must keep in mind that the real extent of LNs might be greater than visualized on PSMA PET/CT scans. Nevertheless, the present analysis shows that PSMA PET/CT scanning before radiotherapy is a vital component for individualizing ENRT volumes for the respective patient, with a possibly higher chance for cure.

CONCLUSION

The present study analyzed the distribution of PSMA PET/CT–positive LNs in postoperative PC patients and found a distribution

similar to that of other studies. Moreover, to our knowledge, this study was the first to compare the coverage of PSMA PET–positive LNs by the RTOG, PIVOTAL, and NRG ENRT recommendations and found a significantly improved coverage by the more recent NRG template. Nevertheless, in the study population, the NRG template would have missed almost one third of all contoured LNs and would have resulted in incomplete coverage in half the patients. This result underlines the importance of advanced imaging, such as PSMA PET/CT scans, before salvage ENRT and shows the need for further individualization of ENRT fields. When ENRT volumes are enlarged, data on a possible increase in toxicity are lacking and should be prospectively collected.

DISCLOSURE

Leonie Beyer is an employee of Novartis Radiopharmaceuticals GmbH. Wolfgang Kunz has served on advisory boards for Bristol-Myers-Squibb (unrelated to the current study). No other potential conflict of interest relevant to this article was reported.

KEY POINTS

QUESTION: Which common ENRT template has the best coverage of PSMA-positive LNs in postoperative PC patients?

PERTINENT FINDINGS: LN distribution was similar to other studies. The new NRG template showed a significantly better coverage than the older RTOG and PIVOTAL templates but still resulted in incomplete coverage in half the patients in this cohort.

IMPLICATIONS FOR PATIENT CARE: The results suggest that use of the new NRG template should be recommended. The results show the importance of pretherapeutic advanced imaging, such as PSMA PET/CT scans.

REFERENCES

1. Abdollah F, Karnes RJ, Suardi N, et al. Impact of adjuvant radiotherapy on survival of patients with node-positive prostate cancer. *J Clin Oncol.* 2014;32:3939–3947.
2. Gupta M, Patel HD, Schwen ZR, Tran PT, Partin AW. Adjuvant radiation with androgen-deprivation therapy for men with lymph node metastases after radical prostatectomy: identifying men who benefit. *BJU Int.* 2019;123:252–260.
3. Jegadeesh N, Liu Y, Zhang C, et al. The role of adjuvant radiotherapy in pathologically lymph node-positive prostate cancer. *Cancer.* 2017;123:512–520.
4. Pollack A, Karrison TG, Balogh AG, et al. The addition of androgen deprivation therapy and pelvic lymph node treatment to prostate bed salvage radiotherapy (NRG Oncology/RTOG 0534 SPPORT): an international, multicentre, randomised phase 3 trial. *Lancet.* 2022;399:1886–1901.
5. Lawton CAF, Michalski J, El-Naqa I, et al. RTOG GU radiation oncology specialists reach consensus on pelvic lymph node volumes for high-risk prostate cancer. *Int J Radiat Oncol Biol Phys.* 2009;74:383–387.
6. Harris VA, Staffurth J, Naismith O, et al. Consensus guidelines and contouring atlas for pelvic node delineation in prostate and pelvic node intensity modulated radiation therapy. *Int J Radiat Oncol Biol Phys.* 2015;92:874–883.
7. Spratt DE, Vargas HA, Zumsteg ZS, et al. Patterns of lymph node failure after dose-escalated radiotherapy: implications for extended pelvic lymph node coverage. *Eur Urol.* 2017;71:37–43.
8. McClinton CM, Niroumand M, Sood S, et al. Patterns of lymph node positivity on ^{11}C-acetate PET imaging in correlation to the RTOG pelvic radiation field for prostate cancer. *Pract Radiat Oncol.* 2017;7:325–331.
9. Boreta L, Gadzinski AJ, Wu SY, et al. Location of recurrence by gallium-68 PSMA-11 PET scan in prostate cancer patients eligible for salvage radiotherapy. *Urology.* 2019;129:165–171.
10. Calais J, Czernin J, Cao M, et al. ^{68}Ga-PSMA-11 PET/CT mapping of prostate cancer biochemical recurrence after radical prostatectomy in 270 patients with a PSA level of less than 1.0 ng/mL: impact on salvage radiotherapy planning. *J Nucl Med.* 2018;59:230–237.
11. Schiller K, Stöhrer L, Düsberg M, et al. PSMA-PET/CT-based lymph node atlas for prostate cancer patients recurring after primary treatment: clinical implications for salvage radiation therapy. *Eur Urol Oncol.* 2021;4:73–83.
12. De Bruycker A, Spiessens A, Dirix P, et al. PEACE V: salvage treatment of oligorecurrent nodal prostate cancer metastases (STORM)—a study protocol for a randomized controlled phase II trial. *BMC Cancer.* 2020;20:406.
13. Hall WA, Paulson E, Davis BJ, et al. NRG Oncology updated international consensus atlas on pelvic lymph node volumes for intact and postoperative prostate cancer. *Int J Radiat Oncol Biol Phys.* 2021;109:174–185.
14. Filimonova I, Schmidt D, Mansoorian S, et al. The distribution of pelvic nodal metastases in prostate cancer reveals potential to advance and personalize pelvic radiotherapy. *Front Oncol.* 2021;10:590722.
15. De Bruycker A, de Bleser E, Decaestecker K, et al. Nodal oligorecurrent prostate cancer: anatomic pattern of possible treatment failure in relation to elective surgical and radiotherapy treatment templates. *Eur Urol.* 2019;75:826–833.
16. Fendler WP, Calais J, Eiber M, et al. Assessment of ^{68}Ga-PSMA-11 PET accuracy in localizing recurrent prostate cancer: a prospective single-arm clinical trial. *JAMA Oncol.* 2019;5:856–863.
17. Hope TA, Goodman JZ, Allen IE, Calais J, Fendler WP, Carroll PR. Metaanalysis of ^{68}Ga-PSMA-11 PET accuracy for the detection of prostate cancer validated by histopathology. *J Nucl Med.* 2019;60:786–793.
18. Ceci F, Uprimny C, Nilica B, et al. ^{68}Ga-PSMA PET/CT for restaging recurrent prostate cancer: which factors are associated with PET/CT detection rate? *Eur J Nucl Med Mol Imaging.* 2015;42:1284–1294.
19. Morigi JJ, Stricker PD, van Leeuwen PJ, et al. Prospective comparison of ^{18}F-fluoromethylcholine versus ^{68}Ga-PSMA PET/CT in prostate cancer patients who have rising PSA after curative treatment and are being considered for targeted therapy. *J Nucl Med.* 2015;56:1185–1190.
20. van Leeuwen PJ, Stricker P, Hruby G, et al. ^{68}Ga-PSMA has a high detection rate of prostate cancer recurrence outside the prostatic fossa in patients being considered for salvage radiation treatment. *BJU Int.* 2016;117:732–739.
21. World Medical Association Declaration of Helsinki. Ethical principles for medical research involving human subjects. *JAMA.* 2013;310:2191–2194.
22. Weineisen M, Simecek J, Schottelius M, Schwaiger M, Wester H-J. Synthesis and preclinical evaluation of DOTAGA-conjugated PSMA ligands for functional imaging and endoradiotherapy of prostate cancer. *EJNMMI Res.* 2014;4:63.
23. Schmidt-Hegemann N-S, Fendler WP, Ilhan H, et al. Outcome after PSMA PET/CT based radiotherapy in patients with biochemical persistence or recurrence after radical prostatectomy. *Radiat Oncol.* 2018;13:37.
24. Fendler WP, Eiber M, Beheshti M, et al. ^{68}Ga-PSMA PET/CT: joint EANM and SNMMI procedure guideline for prostate cancer imaging—version 1.0. *Eur J Nucl Med Mol Imaging.* 2017;44:1014–1024.
25. Martinez-Monge R, Fernandes PS, Gupta N, Gahbauer R. Cross-sectional nodal atlas: a tool for the definition of clinical target volumes in three-dimensional radiation therapy planning. *Radiology.* 1999;211:815–828.
26. Hegemann N-S, Wenter V, Spath S, et al. Distribution of prostate nodes: a PET/CT-derived anatomic atlas of prostate cancer patients before and after surgical treatment. *Radiat Oncol.* 2016;11:37.
27. Treglia G, Pereira Mestre R, Ferrari M, et al. Radiolabelled choline versus PSMA PET/CT in prostate cancer restaging: a meta-analysis. *Am J Nucl Med Mol Imaging.* 2019;9:127–139.
28. Supiot S, Vaugier L, Pasquier D, et al. OLIGOPELVIS GETUG P07, a multicenter phase II trial of combined high-dose salvage radiotherapy and hormone therapy in oligorecurrent pelvic node relapses in prostate cancer. *Eur Urol.* 2021;80:405–414.
29. Murthy V, Maitre P, Kannan S, et al. Prostate-only versus whole-pelvic radiation therapy in high-risk and very high-risk prostate cancer (POP-RT): outcomes from phase III randomized controlled trial. *J Clin Oncol.* 2021;39:1234–1242.
30. De Bleser E, Jereczek-Fossa BA, Pasquier D, et al. Metastasis-directed therapy in treating nodal oligorecurrent prostate cancer: a multi-institutional analysis comparing the outcome and toxicity of stereotactic body radiotherapy and elective nodal radiotherapy. *Eur Urol.* 2019;76:732–739.
31. Evangelista L, Maurer T, van der Poel H, et al. ^{68}Ga-PSMA versus ^{18}F-PSMA positron emission tomography/computed tomography in the staging of primary and recurrent prostate cancer. A systematic review of the literature. *Eur Urol Oncol.* 2022;5:273–282.
32. Hope TA, Eiber M, Armstrong WR, et al. Diagnostic accuracy of ^{68}Ga-PSMA-11 PET for pelvic nodal metastasis detection prior to radical prostatectomy and pelvic lymph node dissection: a multicenter prospective phase 3 imaging trial. *JAMA Oncol.* 2021;7:1635–1642.

Cure of Disseminated Human Lymphoma with [^{225}Ac]Ac-Ofatumumab in a Preclinical Model

Mark S. Longtine*[1], Kyuhwan Shim*[1], Mark J. Hoegger[1], Nadia Benabdallah[1], Diane S. Abou[1], Daniel L.J. Thorek[1,2], and Richard L. Wahl[1,3]

[1]*Mallinckrodt Institute of Radiology, Washington University School of Medicine, St. Louis, Missouri;* [2]*Department of Biomedical Engineering, Washington University in St. Louis, St. Louis, Missouri; and* [3]*Department of Radiation Oncology, Washington University School of Medicine, St. Louis, Missouri*

Immunotherapies that target the CD20 protein expressed on most non-Hodgkin lymphoma cells have improved clinical outcomes, but relapse is common. We prepared ^{225}Ac-labeled anti-CD20 ofatumumab and evaluated its in vitro characteristics and therapeutic efficacy in a murine model of disseminated human lymphoma. **Methods:** ^{225}Ac was chelated by DOTA-ofatumumab, and radiochemical yield, purity, immunoreactivity, stability, and chelate number were determined. In vitro cell killing of CD20-positive, human B-cell lymphoma Raji-Luc cells was assayed. Biodistribution was determined as percentage injected activity per gram (%IA/g) in mice with subcutaneous Raji-cell tumors ($n = 4$). [^{225}Ac]Ac-ofatumumab biodistribution in C57BL/6N mice was performed to estimate projected human dosimetry. Therapeutic efficacy was tested in mice with systemically disseminated Raji-Luc cells, tracking survival, bioluminescence, and animal weight for a targeted 200 d, with single-dose therapy initiated 8, 12, or 16 d after cell injection, comparing no treatment, ofatumumab, and low (3.7 kBq/mouse) and high (9.25 kBq/mouse) doses of [^{225}Ac]Ac-IgG and [^{225}Ac]Ac-ofatumumab ($n = 8$–10/cohort). **Results:** Radiochemical yield and purity were 32% ± 9% and more than 95%, respectively. Specific activity was more than 5 MBq/mg. Immunoreactivity was preserved, and more than 90% of the ^{225}Ac remained chelated after 10 d in serum. Raji-Luc cell killing in vitro was significant, specific, and dose-dependent. In tumor-bearing mice, [^{225}Ac]Ac-ofatumumab displayed low liver (7 %IA/g) and high tumor (28 %IA/g) uptake. Dosimetry estimates indicated that bone marrow is likely the dose-limiting organ. When therapy was initiated 8 d after cell injection, untreated mice and mice treated with cold ofatumumab or low- or high-dose [^{225}Ac]Ac-IgG showed indistinguishable median survivals of 20–24 d, with extensive cancer-cell burden before death. Low- and high-dose [^{225}Ac]Ac-ofatumumab profoundly ($P < 0.05$) extended median survival to 190 d and more than 200 d (median not determinable), with 5 and 9 of 10 mice, respectively, surviving at study termination with no detectable cancer cells. Surviving mice treated with high-dose [^{225}Ac]Ac-ofatumumab showed reduced weight gain versus naïve mice. When therapy was initiated 12 d, but not 16 d, after cell injection, high-dose [^{225}Ac]Ac-ofatumumab significantly extended median survival to 40 d but was not curative. **Conclusion:** In an aggressive disseminated tumor model, [^{225}Ac]Ac-ofatumumab was effective at cancer-cell killing and curative when administered 8 d after cell injection. [^{225}Ac]Ac-ofatumumab has substantial potential for clinical translation as a next-generation therapeutic for treatment of patients with non-Hodgkin lymphoma.

Key Words: CD20; lymphoma; radioimmunotherapy; ^{225}Ac

J Nucl Med 2023; 64:924–931
DOI: 10.2967/jnumed.122.265167

Non-Hodgkin lymphoma (NHL) will be diagnosed in approximately 80,000 patients and cause over 20,000 deaths in the United States in 2023 (*1*). Although chemotherapy is initially effective, many patients, even with low-grade lymphomas, relapse (*2*). This has driven development of therapeutic antibodies that target the CD20 protein expressed on the surface of mature B cells and most NHL cells, as most are of B-cell origin. Anti-CD20 immunotherapy has a highly favorable safety profile, significantly improves the outcomes of most patients, and, along with chemotherapy, is now part of the standard of care for many cases of NHL.

The chimeric mouse–human monoclonal antibody, rituximab, was the first Food and Drug Administration–approved anti-CD20 therapeutic, with others subsequently developed for improved biologic and pharmacologic properties, including fully human ofatumumab (*3*). Ofatumumab binds CD20 with high affinity, allowing targeting of cells with low CD20 expression, including those with resistance to rituximab (*4*). As a type I anti-CD20 antibody, ofatumumab is effectively internalized (*5*), which benefits imaging and therapy using residualizing radiometals, such as ^{89}Zr and ^{225}Ac.

Lymphoma is highly susceptible to ionizing radiation; however, external-beam irradiation is used sparingly in the disseminated setting. To overcome the limitations of external-beam radiotherapy, systemically administered β-particle–emitting radioimmunotherapies to anti-CD20 have been translated into 2 Food and Drug Administration–approved drugs: murine ^{131}I-tositumomab (Bexxar; GlaxoSmithKline) and ^{90}Y-ibrutumomab (Zevalin; Acrotech Biopharma LLC) (*6*). Although studies show long-term safety and effectiveness (*7*), Bexxar has been discontinued commercially in the United States, and Zevalin is used infrequently (*8,9*).

^{225}Ac has gained increased use as a therapeutic radionuclide (*10*), with its 10-d half-life matching well the pharmacokinetics of intact antibodies. In its decay pathway, ^{225}Ac yields 4 net α-particles with high linear energy transfer and short pathlengths, providing effective radiotoxicity to targeted tumor cells while relatively sparing nontargeted cells.

Received Nov. 14, 2022; revision accepted Feb. 2, 2023.
For correspondence or reprints, contact Richard Wahl (rwahl@wustl.edu).
*Contributed equally to this work.
Published online Apr. 6, 2023.

We previously demonstrated that [^{89}Zr]Zr-ofatumumab has excellent uptake into human lymphoma xenografts and enables in vivo localization using PET as well as, or better than, [^{89}Zr]Zr-rituximab (*11*). Here, we prepare [^{225}Ac]Ac-ofatumumab and demonstrate potent cytotoxicity to CD20-expressing cells in vitro and in vivo. In therapeutic studies using an aggressive, disseminated murine model of human lymphoma, [^{225}Ac]Ac-ofatumumab shows excellent, often curative, efficacy.

MATERIALS AND METHODS

Reagents and Cell Lines

Chemicals and reagents are listed in Supplemental Table 1 (supplemental materials are available at http://jnm.snmjournals.org). Water (MilliQ Integral 5 system; Millipore) was treated with a 50 g/L concentration of Chelex 100 (Bio-Rad Laboratories, Inc.). Raji and Raji-Luc cells were cultured in RPMI medium with 10% fetal bovine serum.

DOTA Conjugation, ^{225}Ac Chelation, Radiochemical Yield, Purity, and Mass Spectrometry

DOTA was dissolved in H_2O and conjugated to antibodies as previously described (*11*). For ^{225}Ac chelation, 1.85 MBq of ^{225}Ac in 0.2 M HCl was added to 2 M tetraethyl-ammonium-acetate to obtain pH 6.0. One hundred micrograms of DOTA antibody prepared at an 8:1 DOTA-to-antibody molar ratio were added, and the reaction was brought to 150 μL with 20 mM sodium acetate, 150 mM NaCl (pH 7.0), and 15 μL of a 10 mg/mL solution of sodium ascorbate. After 4 h at 37°C, diethylenetriaminepentaacetic acid (pH 7.0) was added to 5 mM final concentration for 10 min followed by size-exclusion column purification into saline with sodium ascorbate added to 10 μg/mL. All quantifications were at secular equilibrium, using a Capintec CRC 55tW dose calibrator and a Beckman 8000 γ-counter with a 250- to 480-keV energy window or by scanning of thin-layer chromatography strips. Fast protein liquid chromatography, thin-layer chromatography, and mass spectrometry were performed as previously described (*12*).

Immunoreactivity, in Vitro Stability, and Cell Killing

Immunoreactivity was assayed by Raji-cell binding as previously described (*11*), without or with cold ofatumumab blocking. To assay stability, [^{225}Ac]Ac-ofatumumab or ^{225}Ac was added to human serum, incubated at 37°C, and assayed by thin-layer chromatography as previously described (*11*).

To assay cell killing, 5×10^5 Raji-luciferase cells in 1 mL of RPMI medium with 10% heat-inactivated fetal bovine serum were added per well, followed by no antibody, native ofatumumab, [^{225}Ac]Ac-IgG, or [^{225}Ac]Ac-ofatumumab. When used, the antibody mass was 0.1 μg/well. Medium was exchanged after 24 h, and viability assays were performed 48 h later by MTS (3-(4,5-dimethylthiazol-2-yl)-5-(3-carboxymethoxyphenyl)-2-(4-sulfophenyl)-2H-tetrazolium) or bioluminescence imaging as previously described (*12*).

Biodistribution in Tumor-Bearing Mice

The Washington University in St. Louis Institutional Animal Care and Use Committee approved the animal studies. Eight- to 10-wk-old R2G2 mice (no. 021; Envigo) were inoculated subcutaneously with 5×10^6 Raji-Luc cells. When palpable tumors were present, 8–11 μg (4.07 kBq) of [^{225}Ac]Ac-ofatumumab were administered intravenously and biodistribution analyzed 7 d later. The femur was measured after marrow extraction.

Therapy and Bioluminescent Imaging

R2G2 mice were injected intravenously with 1×10^6 Raji-Luc cells. In a first study, 8 d later, the mice either were untreated or were treated with ofatumumab or 3.7 or 9.25 kBq/mouse of [^{225}Ac]Ac-IgG or [^{225}Ac]Ac-ofatumumab. In a second study, 12 or 16 d after cell injection, the mice either were untreated or were treated with 9.25 kBq of [^{225}Ac]Ac-ofatumumab. The administered antibody mass was adjusted to 20 μg/mouse of IgG or ofatumumab. Bioluminescent images were acquired and quantified as previously described (*12,13*) and normalized to the first imaging time point. The mice were humanely euthanized if they had hind-limb paralysis (HLP), more than a 20% weight loss, or morbidity or reached the scheduled study termination point.

Biodistribution and Dosimetry in Wild-Type Mice

Biodistribution and dosimetry studies were performed on 6- to 8-wk-old female C57BL/6N mice (no. 556; Charles River) injected intravenously with 3 μg (~3.7 kBq) of [^{225}Ac]Ac-ofatumumab. At selected time points after injection of [^{225}Ac]Ac-ofatumumab, the mice were euthanized and organs γ-counted at secular equilibrium to determine decay-corrected percentage injected activity per gram (%IA/g). Bone (tibia and fibula) was counted after marrow separation.

Integrated time–activity curves from the murine data and the mean absorbed dose (D) were calculated according to MIRD methodology (*14,15*) using the formula $D = A \times \Delta \times \phi$, where A is the cumulated activity, Δ is the mean α-particle energy, and ϕ is the absorbed fraction, with extrapolation to infinity, yielding a maximally conservative estimate. α particles were assumed to deposit all their energy locally ($\phi = 1$). The trapezoidal rule was used to integrate the time–activity curve of the α-particles emitted from the decay of ^{225}Ac and its α-particle–emitting daughters (^{221}Fr, ^{217}As, ^{213}Bi, and ^{213}Po) using values from International Commission on Radiological Protection publication 107 (*16*), with all daughter decays assumed to occur in the same organ as the ^{225}Ac decay, yielding a Δ of 4.42^{-12} J/(Bq·s) for ^{225}Ac and its daughters. These mouse data were extrapolated to the adult female human model using the relative organ mass scaling method. Equilibrium in the decay chain and no translocation during the decay between succeeding disintegrations were assumed. Thus, the same estimated integrated time–activity curve obtained for ^{225}Ac was applied to its daughters. The absorbed dose of [^{225}Ac]Ac-ofatumumab was summed after applying weighting factors in the 2 possible pathways, 2% for ^{209}Ti and 98% for ^{213}Po. A relative biological effectiveness of 5 for α-particles was used in the calculation of sieverts.

Statistical Methods

GraphPad Prism software, version 8.4.3, was used for statistical analyses. A P value of less than 0.05 was considered statistically significant, with statistical tests noted in the text or figure legends. Data are shown as mean ± SD.

RESULTS

[^{225}Ac]Ac-Ofatumumab Synthesis, Radiochemical Yield and Purity, Chelate Number, Immunoreactivity, and Serum Stability

[^{225}Ac]Ac-DOTA-ofatumumab was prepared using a 1-step method (*17*) and characterized (Supplemental Figs. 1A–1G). Radiochemical purity was more than 95%, and radiochemical yields were more than 30%, with more than 70% immunoreactivity and specific activities of 5.25–15.6 MBq/mg. An average of 1, 2, and 5 chelates were attached per antibody using DOTA-to-ofatumumab ratios during conjugation of 2:1, 5:1, and 8:1, respectively. Chelation was stable after 10 d in serum.

Biodistribution with Subcutaneous Raji-Cell Tumors

We used immunodeficient R2G2 mice (B6;129-*Rag2*^{tm1Fwa} *Il2rg*^{tm1Rsky}/DwlHsd) that are proficient in double-strand DNA-break repair. *Prkdc*^{scid} mice that lack double-strand DNA repair because of the *scid* mutation are known to show artifactual

radiosensitivity to DNA damage (*18*), such as that induced by α-particles. Compared with *Prkdc*^{scid} mice, we expect that the nontargeted (nontumor) cells in R2G2 mice will better reflect the response of nontargeted (nontumor) cells in humans to α-particle transit, as both tumor and nontumor cells are proficient in double-strand DNA-break repair.

The biodistribution of [^{225}Ac]Ac-ofatumumab was evaluated 7 d after injection in mice bearing subcutaneous Raji tumors (Supplemental Fig. 1H). The radioimmunotherapeutic showed a long circulatory residence time, consistent with stable chelation. This was confirmed by low liver uptake (7 ± 1 %IA/g), as free ^{225}Ac shows high liver uptake (*19*). Splenic uptake was 31 ± 6 %IA/g, similar to that of [^{89}Zr]Zr-rituximab and -ofatumumab (*11*). Marrow and femur showed 7 ± 3 and 5 ± 0.05 %IA/g, respectively. Tumor targeting was 28 ± 10 %IA/g.

[^{225}Ac]Ac-Ofatumumab–Mediated Cell Killing

To investigate in vitro cytotoxicity, Raji-Luc cells were incubated with medium only, native (cold) ofatumumab, [^{225}Ac]Ac-IgG, or [^{225}Ac]Ac-ofatumumab for 24 h, followed by medium exchange and, 48 h later, viability assays (Fig. 1). Compared with no antibody, native ofatumumab did not affect viability. A 3.7 kBq/mL dose of [^{225}Ac]Ac-IgG showed a modest (~2-fold) effect, with none at lower doses. [^{225}Ac]Ac-ofatumumab yielded significant, dose-dependent reductions in viability compared with cells without antibody or cells exposed to native ofatumumab or [^{225}Ac]Ac-IgG.

Biodistribution and Absorbed Dose of [^{225}Ac]Ac-Ofatumumab in C57BL/6N Mice

The biodistribution of [^{225}Ac]Ac-ofatumumab was evaluated using non–tumor-bearing, wild-type C57BL/6N mice (Supplemental Table 2). Blood [^{225}Ac]Ac-ofatumumab levels were high (43 ± 6 %IA/g) at 4 h after injection and slowly fell to 15 %IA/g at 12 d after injection. Uptake of ^{225}Ac-ofatumumab was 5–8 IA/g in bladder, 8–11 %IA/g in kidney, and 6–12 %IA/g in marrow, with a gradual diminution in marrow over time. Liver uptake was 10–15 %IA/g, with perhaps some contribution by dechelated ^{225}Ac, which accumulates in the liver (*20*). Fecal ^{225}Ac levels were consistent with [^{225}Ac]Ac-ofatumumab or metabolites being excreted via the gastrointestinal route.

[^{225}Ac]Ac-ofatumumab human radiation dosimetry estimates were then determined for a human female model (Table 1). As free ^{213}Bi in the kidney was not evaluated, this absorbed dose may be somewhat underestimated (*21*). Extrapolated human radiation dose estimates reveal heart wall (1,919 mSv/MBq) as the organ with the highest predicted dose, followed by liver, spleen, and red marrow at 1,833, 1,803, and 1,620 mSv/MBq, respectively. Marrow is likely the dose-limiting organ. The calculated effective dose equivalent was 1,496 mSv/MBq.

TABLE 1
Extrapolated Human Radiation Dose Estimates for [^{225}Ac]Ac-Ofatumumab

Organ	Equivalent dose (mSv/MBq)
Adrenals	400
Bladder wall	275
Brain	84
Breast	260
Gallbladder	235
Heart wall	1,919
Intestine, small	247
Intestine, large, lower	260
Intestine, large, upper	251
Kidney	1,187
Liver	1,833
Lung	1,076
Marrow, red	1,620
Muscle	313
Ovaries	943
Pancreas	507
Skin	260
Stomach wall	240
Spleen	1,803
Thymus	638
Thyroid	517
Uterus	1,446
Effective dose	883
Effective dose equivalent	1,496

Mean absorbed doses after injection of [^{225}Ac]Ac-ofatumumab into mice, extrapolated to adult human female model.

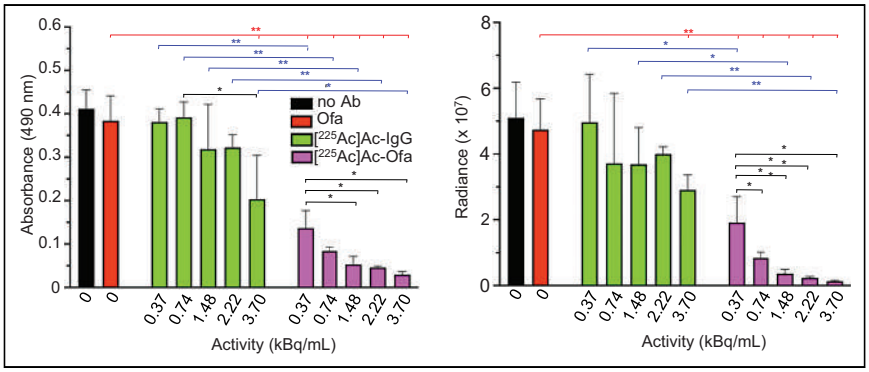

FIGURE 1. [^{225}Ac]Ac-ofatumumab in vitro cytotoxicity to Raji-Luc cells. Cell viability with no treatment control or after exposure to [^{225}Ac]Ac-IgG, or -ofatumumab was measured using MTS (left) or bioluminescence (right) assays (n = 3). Comparison was by ANOVA (red lines) or Student t test (black and blue lines). *P < 0.05. **P < 0.005. Ab = antibody; Ofa = ofatumumab.

Therapeutic Evaluation in a Disseminated Model on Day 8 After Cell Injection

The magnitude, duration, and tumor targeting of the radiopharmaceutical in the biodistribution studies, as well as the in vitro tumoricidal activity, motivated an in vivo lymphoma treatment study. Therapeutic efficacy was evaluated in R2G2 mice with intravenously injected Raji-Luc cells, which become widely disseminated (*13,22,23*). This model recapitulates many features of clinical NHL, as it invades multiple organs, including the hematopoietic compartment. HLP is a frequent cause for censoring.

First, the maximal tolerated dose of [^{225}Ac]Ac-ofatumumab in naïve R2G2 mice was identified. Eighty days after injection, 3.7, 11.1, 18.5, and 37 kBq/mouse yielded 5 of 5, 4 of 5, 3 of 5, and 0 of 5 survivors, respectively. Thus, for therapy we used single injections of the nonmyeloablative doses of 3.7 kBq/mouse (low dose) and 9.25 kBq/mouse (high dose).

In the first therapy study, 8 d after cell injection the mice were randomized to remain untreated or to be treated with native ofatumumab or low or high doses of [^{225}Ac]Ac-IgG or [^{225}Ac]Ac-ofatumumab ($n = 10$ mice per cohort). Survival, tumor burden, and weight were monitored for 200 d. In untreated mice, median survival was 21 d, with 9 of 10 mice succumbing before 29 d (Fig. 2A) and all mice showing increasing cancer-cell burden until censoring for HLP (Figs. 2B and 3). The lone surviving mouse never displayed cancer cells, suggesting an unsuccessful injection or engraftment. Native ofatumumab did not extend survival compared with untreated mice, with 10 of 10 succumbing before 29 d (Fig. 2A) and all showing increasing cancer-cell burden until censoring for HLP (Figs. 2B and 3).

Control radiolabeled nonspecific antibody, [^{225}Ac]Ac-IgG, at low and high doses yielded median survivals of 20 and 24 d, respectively (Fig. 2A), which did not differ significantly from untreated or native-ofatumumab–treated mice (Mantel–Cox, $P > 0.05$). All mice in the low-dose [^{225}Ac]Ac-IgG cohort succumbed before 31 d. Nine were censored for HLP, and 1 perished (Fig. 3). In the high-dose cohort, 6 mice were censored for HLP and 3 for weight loss, with 1 surviving mouse that likely had an unsuccessful injection or engraftment (Figs. 2 and 3). All nonsurviving mice in both cohorts showed continuous cancer-cell growth until they were euthanized (Figs. 2B and 3).

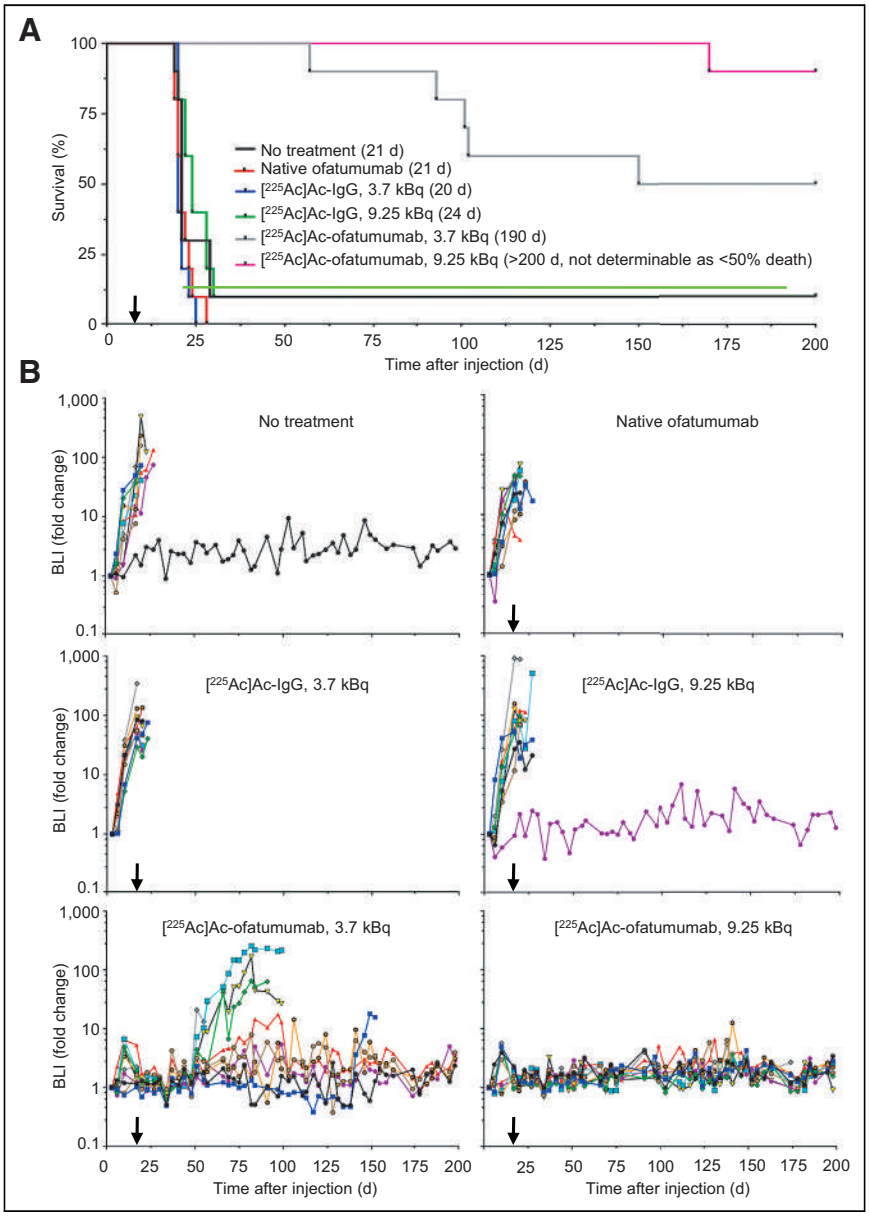

FIGURE 2. Survival and bioluminescence of mice with disseminated Raji-Luc cells untreated or receiving therapy 8 d after cell injection. (A) Kaplan–Meier graph with median survivals. Low-dose [^{225}Ac]Ac-ofatumumab was superior to all other cohorts except high-dose ofatumumab (Mantel-Cox, $P < 0.05$). High-dose [^{225}Ac]Ac-ofatumumab was superior to all other cohorts. (B) Bioluminescence. Note elimination of Raji-Luc cells in 9.25 kBq/mouse cohort. Arrow indicates initiation of therapy. n = 10/cohort. BLI = bioluminescence.

In contrast, low- or high-dose [^{225}Ac]Ac-ofatumumab treatment increased median survival to 190 d and more than 200 d (median survival was nondeterminable as there were <50% deaths), respectively (Fig. 2A), superior to survival of untreated or [^{225}Ac]Ac-IgG–treated mice (Mantel–Cox, $P < 0.05$). In the low-dose cohort, 5 of 10 mice survived. One mouse was censored for HLP, 2 for weight loss, and 1 for development of a leg tumor; 1 perished (Fig. 3). In the high-dose cohort, 9 of 10 mice survived, with 1 succumbing under anesthesia with no prior morbidity, weight loss, or detectable cancer cells (Figs. 2A and 3), indicating a death unrelated to disease or treatment. The median survival with high-dose [^{225}Ac]Ac-ofatumumab was longer than that with low-dose [^{225}Ac]Ac-ofatumumab (Mantel–Cox, $P < 0.05$), indicating a dose–response effect.

All mice treated with low- or high-dose [^{225}Ac]Ac-ofatumumab that survived had effective cancer-cell suppression with no detectable Raji-Luc cells at study termination (Figs. 2B and 3). The 5 nonsurviving mice in the low-dose cohort showed effective cancer-cell suppression for many days (~50 d for 4 mice and ~140 d for 1 mouse), followed by resumption of Raji-Luc cell proliferation, as indicated by increased bioluminescence (Figs. 2B and 3).

Because of its 10-d half-life, we wanted to determine how rapidly [^{225}Ac]Ac-ofatumumab treatment kills cancer cells. Comparison of bioluminescence from study day 3 to day 20 (5 d before and 12 d after starting therapy) revealed a continued increase in cancer-cell numbers in all cohorts except if treated with [^{225}Ac]Ac-ofatumumab (Fig. 4A). To statistically test whether [^{225}Ac]Ac-ofatumumab

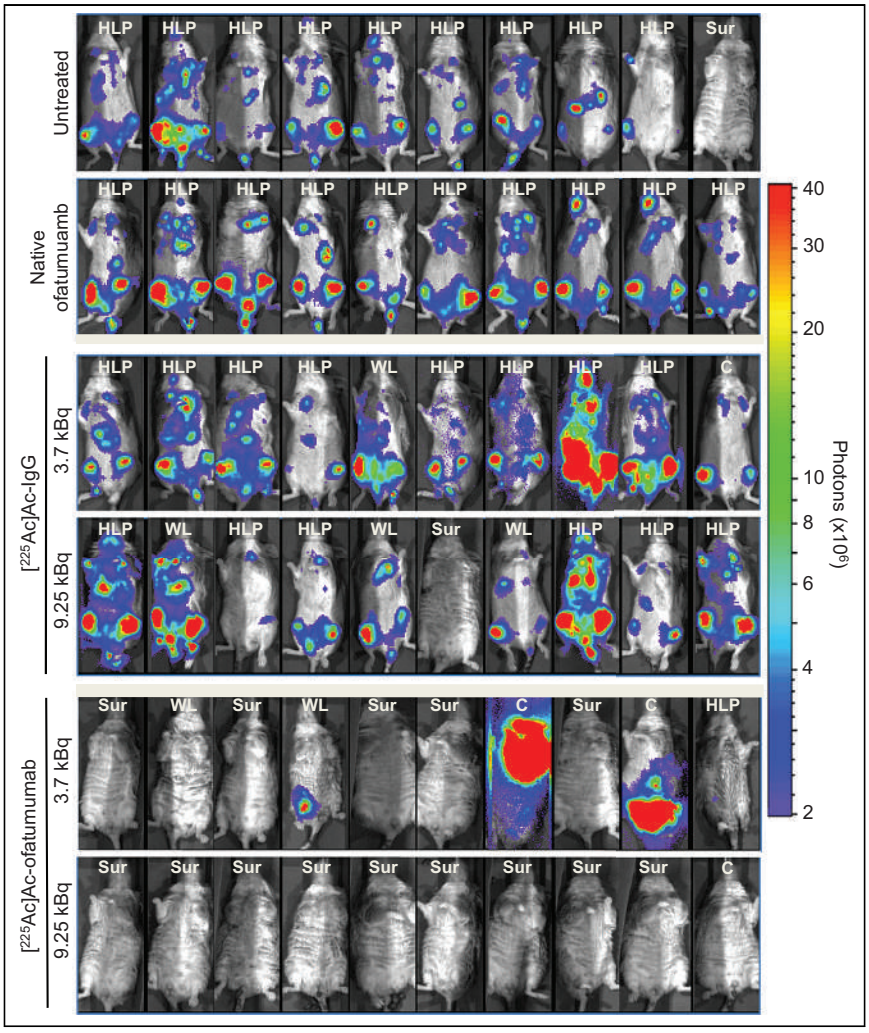

FIGURE 3. Bioluminescence of mice with disseminated Raji-Luc cells untreated or receiving therapy 8 d after cell injection. Images shown were obtained just before censoring or study termination. Median days of imaging were 20 d for no treatment and ofatumumab; 20 and 23 d for low- and high-dose [^{225}Ac]Ac-IgG, respectively; and 152 and 198 d for low- and high-dose [^{225}Ac]Ac-ofatumumab, respectively. Note elimination of bioluminescence in mice in latter 2 cohorts. Censoring was for HLP, weight loss, and other causes. C = other causes; SUR = survival; WL = weight loss.

rapidly kills cancer cells in vivo, the log of the bioluminescence values from 10 to 20 d after cell injection (2–12 d after starting therapy) was plotted. Comparison of the slopes of these lines (Fig. 4B) confirmed no effect of native ofatumumab or [^{225}Ac]Ac-IgG on cancer-cell proliferation. In contrast, both low- and high-dose [^{225}Ac]Ac-ofatumumab significantly reduced these line slopes, indicating rapid killing of cancer cells after initiation of targeted therapy.

Evaluation of Systemic Toxicity

To investigate systemic toxicity of [^{225}Ac]Ac-ofatumumab, animal weights in the therapy study initiated 8 d after cell injection were determined (Supplemental Fig. 2). Not surprisingly, most nonsurviving mice in all cohorts showed clear weight loss before they died or were euthanized for cause, consistent with the increased cancer-cell burden in these mice.

Mice in the low-dose [^{225}Ac]Ac-ofatumumab–treated cohort that survived to study termination showed a continuous gradual weight gain (Supplemental Fig. 2B, left). This was consistently slightly lower than the weight gain of control R2G2 mice that were not injected with cells or treated with therapy (Supplemental Fig. 2B), with a significant difference present only after 172 d (Supplemental Fig. 2B, right). Surviving mice in the high-dose [^{225}Ac]Ac-ofatumumab cohort showed greater systemic effects, with initial loss of weight having a nadir at 27 d, followed by recovery to initial weight at 52 d and thereafter (Supplemental Fig. 2B).

Therapeutic Evaluation in a Disseminated Model on Days 12 and 16 After Cell Injection

Next, we asked whether tumor burden at the time of therapy is a relevant parameter in treatment outcome. To answer this question, we delayed treatment from 8 d until either 12 or 16 d after cell injection (untreated mice typically die at 19–21 d after cell injection) to provide a larger pretreatment disseminated disease burden, comparing no treatment with high-dose (9.25 kBq) [^{225}Ac]Ac-ofatumumab. To assay tumor-cell burden over time, bioluminescence in untreated mice 8, 12, and 16 d after cell injection was compared (Supplemental Fig. 3) and confirmed a steadily increasing disease burden.

When therapy was initiated 16 d after cell injection, [^{225}Ac]Ac-ofatumumab provided no survival benefit versus no treatment (Fig. 5A; median survival was 19 d for both cohorts ($P > 0.05$, Mantel–Cox), with a high cancer-cell burden in both cohorts before censoring for HLP (Supplemental Figs. 4A and 4B). Because the time of survival after treatment was very short, the effect on cancer-cell burden past the initiation of treatment was not sufficient for statistical analysis, but any effect appeared minimal (Fig. 5; Supplemental Fig. 4).

In contrast, a single treatment with [^{225}Ac]Ac-ofatumumab 12 d after cell injection increased median survival to 40 d (Fig. 5A; Mantel–Cox, $P < 0.0001$), although no mice survived beyond 41 d. This treatment prevented a further increase or yielded a reduction in cancer-cell burden (Figs. 5B and 5C; Supplemental Fig. 4C). In this cohort, 5 mice were censored for HLP and 1 for weight loss; 3 perished (Supplemental Fig. 4C).

DISCUSSION

Our studies further validate the use of anti-CD20 antibodies for radioimmunotherapy of NHL. We produced [^{225}Ac]Ac-ofatumumab with high immunoreactivity, radiochemical yield, and purity and with stable chelation of ^{225}Ac in vitro and in vivo. [^{225}Ac]Ac-ofatumumab specifically killed CD20-expressing cells in vitro and showed high tumor uptake in vivo. In therapeutic studies using a murine model of disseminated human lymphoma, a single [^{225}Ac]Ac-ofatumumab treatment showed excellent efficacy, with curative ability except for very advanced disease.

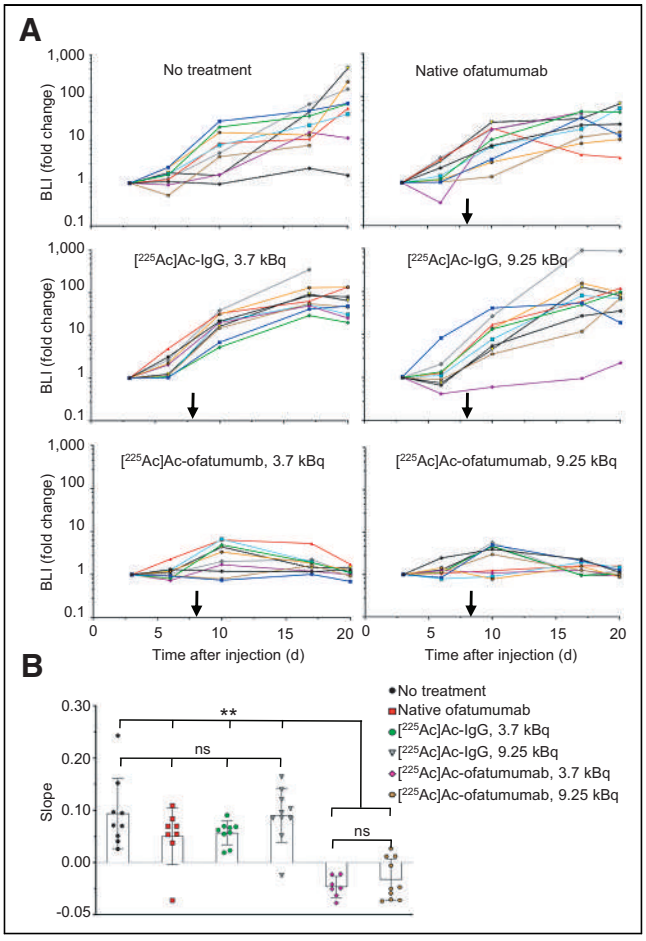

FIGURE 4. Rapidity of therapeutic effects in mice treated 8 d after cell injection. (A) Bioluminescence of mice 3–20 d after cell injection, showing profound reduction of cancer cell growth rates by [^{225}Ac]Ac-ofatumumab. (B) Comparison by ANOVA of bioluminescence from 2 to 10 d after therapy initiation (10–20 d after cell injection). n = 7–10/cohort. BLI = bioluminescence; ns = not statistically significant. $^{**}P < 0.005$.

We prepared [^{225}Ac]Ac-ofatumumab using a mild 1-step procedure in which ^{225}Ac is directly chelated to DOTA-conjugated antibody at 37°C (*17*). Other investigators also have used this approach (*24–26*). ^{225}Ac was stably chelated, and uptake of [^{225}Ac]Ac-ofatumumab uptake by CD20-expressing subcutaneous tumors (28 %IA/g) was similar to the 33 %IA/g of [^{89}Zr]Zr-DFO-ofatumumab (*11*). The approximately 5 MBq/mg specific activity obtained for [^{225}A]Ac-ofatumumab was sufficient for preclinical use and should enable scaling up for clinical use.

The major finding of the current study was the high therapeutic potency of [^{225}Ac]Ac-ofatumumab in mice with an aggressive murine model of disseminated human lymphoma, similar to micrometastatic disease in humans. When administered 8 d after cell injection, control unlabeled ofatumumab and low (3.7 kBq/mouse) or high (9.25 kBq/mouse) doses of nontargeted [^{225}Ac]Ac-IgG did not improve median survival compared with untreated mice or inhibit cancer-cell growth. In contrast, both low and high doses of [^{225}Ac]Ac-ofatumumab rapidly and significantly inhibited cancer-cell growth and increased median survivals to 190 and more than 200 d, respectively. Half the mice in the low-dose group survived, and none of the animals in the high-dose group had disease- or treatment-related mortality. All mice in these 2 cohorts that survived until study termination showed apparent complete elimination of cancer cells, as no cancer cells were detected at study completion on day 200. Also, we tested the potential for systemic anticancer effects in disease settings of further progression. Twelve days after cell injection, high-dose [^{225}Ac]Ac-ofatumumab killed cancer cells and significantly extended median survival to 40 d, showing therapeutic benefit even with a high pretreatment burden of cancer cells, although the therapy was not curative. Not surprisingly, there was a limit to therapeutic efficacy; therapy initiated 16 d after cell injection was unable to improve survival. This lack of benefit was likely because approximately 3 d before expected death was not enough time to allow for sufficient targeting and absorbance of the dose of intact radiolabeled antibody, and possibly also because of altered pharmacokinetics due to the high cancer-cell burden (*27*).

Dosimetry of organs from [^{225}Ac]Ac-ofatumumab–injected C57BL/6N mice extrapolated to an adult female human model suggests that marrow will be the dose-limiting organ, as is common with unsealed, intact antibody-based radiotherapeutics, including Bexxar and Zevalin (*6*). It is worth noting that uptake in nontumor target organs can often be significantly reduced by predosing with unlabeled antibody, which improves lesion–to–background-organ ratios, as used in the Zevalin and Bexxar therapeutic regimens and in other work (*28*). Fully human ofatumumab is unlikely to induce an immune response, increasing the potential for fractionated dosing of [^{225}Ac]Ac-ofatumumab to ameliorate myelotoxicity. In addition, autologous stem-cell transplantation after radioimmunotherapy, as used in some Zevalin and Bexxar protocols, may be useful. Development of a theranostic partner, such as [^{89}Zr]Zr-ofatumumab (*11*), for personalized image-based dosimetry is also of interest. Of course, murine models of toxicity and therapeutic benefit are useful—but imperfect—indicators for treatment of human patients, because of multiple differences including short circulation times in mice and dose–volume geometric considerations. Determination of toxicity–therapeutic trade-offs will require careful evaluation in human trials.

Notably, low-dose [^{225}Ac]Ac-ofatumumab treatment 8 d after cell injection was curative in half the mice, which displayed weight gains similar to those of control naïve mice without tumor cells or therapy. The 5 nonsurviving mice in this cohort showed effective repression of cancer-cell growth for approximately 50–140 d and gains of weight over this time of remission. Thus, fractionated cycles of this low-dose therapy may induce cancer-cell elimination, as well as curative efficacy in even more mice while maintaining reduced toxicity. Mice treated with high-dose [^{225}Ac]Ac-ofatumumab showed reduced weight gains compared with naïve mice, indicating some systemic toxicity. Some of this may result from kidney distribution of the ^{225}Ac daughter radionuclide, ^{213}Bi (*29*), although this possibility remains to be confirmed. However, if so, there are approaches that may ameliorate such toxicity (*30,31*).

We recently tested the therapeutic efficacy of β-particle–emitting [^{177}]Lu-ofatumumab using this murine disseminated Raji-Luc lymphoma model (*12*). When therapy was started 4 d after cell injection, 8.51 MBq of [^{177}Lu]Lu-ofatumumab showed remarkable therapeutic efficacy, with apparent complete elimination of tumor cells and no disease-related deaths. Our subsequent work (Mark S. Longtine, unpublished data, August 2020), however, indicates that when therapy was initiated 8 d after cell injection, [^{177}Lu]Lu-ofatumumab was ineffective, indicating potential superiority of [^{225}Ac]Ac-ofatumumab under this condition. Similar observations were noted previously using a murine disseminated multiple-myeloma model, comparing [^{177}Lu]Lu- and [^{225}Ac]Ac-daratumumab (*25*).

We recently reported the therapeutic efficacy of rituximab (an internalizing anti-CD20 antibody, like ofatumumab) radiolabeled

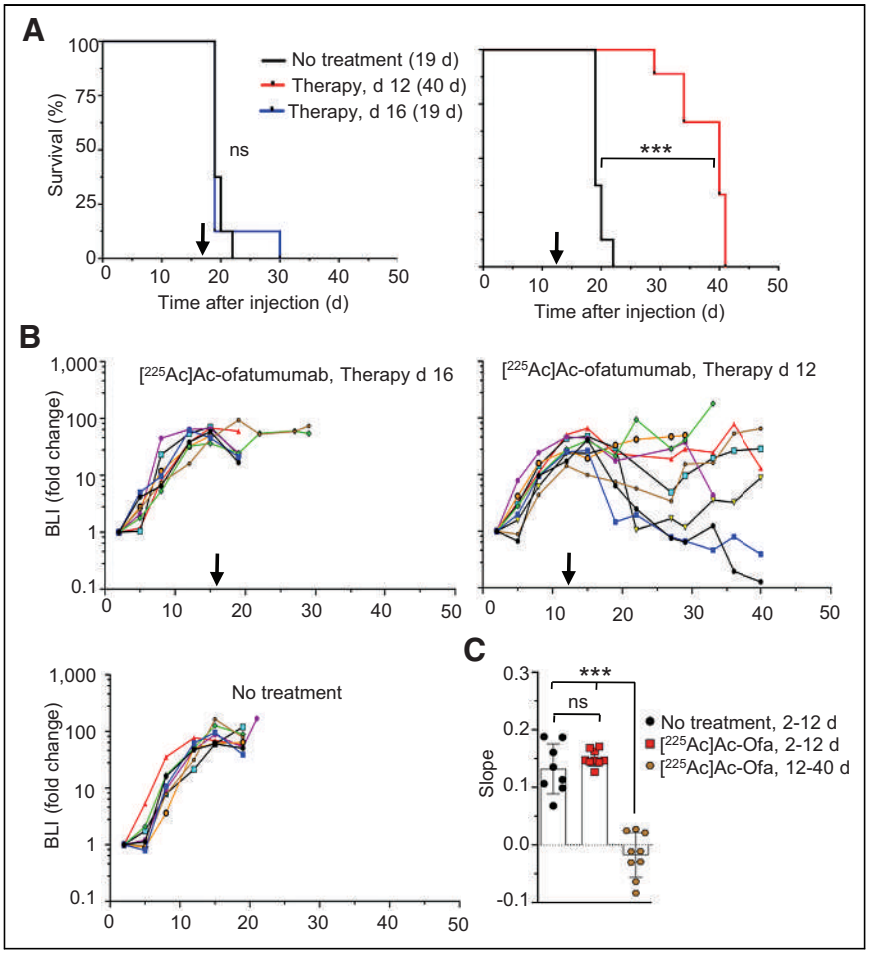

FIGURE 5. Survival and bioluminescence of mice with larger pretreatment cancer-cell burden. (A) Kaplan–Meier graph of untreated mice vs. treatment started 16 d (left) or 12 d (right) after cell injection, with median survival indicated. Significance was evaluated by Mantel–Cox test. (B) Bioluminescence, showing effect on cancer-cell numbers for cohort treated on day 12 but not day 16. (C) ANOVA comparison of cancer-cell growth of untreated mice or mice treated 12 d after cell injection. n = 7–9/cohort. BLI = bioluminescence; ns = not statistically significant. ***$P < 0.0001$.

with ^{213}Bi (half-life [$t_{1/2}$], 45.6 min; 1 net α-particle), applying a similar disseminated Raji-Luc model using *Prkdc*^{scid} mice (*23*). Cancer-cell killing was effective, and cures were common when the single-dose treatment was started 4 d after injection of 1×10^6 Raji-Luc cells. However, single-dose [^{213}Bi]Bi-rituximab treatment was much less effective when initiated 7 d after cell injection, being markedly less effective than single-dose treatment with [^{225}Ac]Ac-ofatumumab initiated 8 d after cell injection as found in the current study, although in a somewhat different animal system. These results may in part relate to the decay rates of ^{213}Bi versus ^{225}Ac and the localization times for intact antibodies to tumor. However, if targets are readily accessible, ^{213}Bi can deliver a high dose rate, but if there exist groups of cells, or even solid tumors, with reduced antibody accessibility, sufficient penetration or dose deposition may not occur before radioactive decay, rendering the therapy less effective and yielding superior results with the longer-lived ^{225}Ac. In this view, for antibody-mediated radioimmunotherapy for larger tumors, ^{225}Ac may be a more appropriate choice for α-particle–mediated therapy. Further evaluation of the comparative therapeutic and off-target effects of ^{213}Bi- versus ^{225}Ac-labeling for radioimmunotherapy with intact antibodies is of interest.

Other investigators have studied α-emitters for radioimmunotherapy of NHL using preclinical models. Park et al. (*32*) found therapeutic benefit using a pretargeted approach with a ^{213}Bi-labeled anti-CD20 1F5(ScFv)$_4$SA molecule. Similarly, [^{211}At]At-1F5 (^{211}At $t_{1/2}$, 7.2 h; 1 net α-particle) was 80% curative 6 d after intravenous cell injection with supporting stem cell transplantation but only poorly effective on subcutaneous tumors (*33*), perhaps limited by radioactive decay before tumor penetration. [^{212}Pb]Pb-rituximab (^{212}Pb $t_{1/2}$, 10.6 h; 1 net α-particle) in a disseminated model improved survival times with therapy initiated at both low- and high-tumor burdens (*34*). [^{227}Th]Th-rituximab (^{227}Th $t_{1/2}$, 18.7 d; 5 net α-particles) was often curative of small subcutaneous tumors (*35*) and was superior to [^{90}Y]Y-ibritumomab-tiuxetan, although targeting of the ^{223}Ra daughter to bone (*36*) adds complexity. Similarly, treatment with [^{149}Tb]Tb-rituximab (^{149}Tb $t_{1/2}$, 4.2 h, 1 α-particle) shortly after intravenous injection of Daudi cells significantly increased survival (*37*). Our excellent results with ^{225}Ac labeling likely reflect a very good match between antibody-specific targeting times to tumor and the half-life of this α-particle emitter. In conclusion, a single dose of [^{225}Ac]Ac-anti-CD20 ofatumumab showed excellent therapeutic efficacy in a murine model of human disseminated lymphoma and was often curative. Fractionated dosing may improve efficacy. With increasing use of targeted radiotherapies, a renewed application of radioimmunotherapy targeting CD20 for NHL seems warranted, given the exceptional therapeutic efficacy of [^{225}Ac]Ac-anti-CD20 ofatumumab and remaining unmet clinical needs in this disease.

CONCLUSION

[^{225}Ac]Ac-ofatumumab shows good in vitro characteristics and effectively targets CD20-expressing tumor xenografts. [^{225}Ac]Ac-ofatumumab showed curative efficacy in a murine model of disseminated human lymphoma.

DISCLOSURE

Richard Wahl is on the scientific advisory board of Clarity Pharmaceuticals, Voximetry, and Seno Medical; has stock in Clarity Pharmaceuticals and stock options in Voximetry; receives honoraria from Bristol Myers Squibb, Actinium Pharmaceuticals, Jubilant Draximage, Siemens, Abderra, and ITM; and receives research support from Actinium Pharmaceuticals, BMS, Bayer, Siemens, and White Rabbit AI. Diane Abou and Daniel Thorek have an advisory board role for, and own stock in, Diaprost AB and Pharma15. This study was supported in part by the Radiological Society of North America (RR1646 to Mark Hoegger), National Institutes of Health (T32EB021955 to Richard

Wahl, and R01CA240711, R01CA229893, and R01CA201035 to Daniel Thorek), the Children's Discovery Institute (MC-II-2021-961 to Diane Abou), the National Institute of General Medical Sciences (5P41GM103422 to the Washington University Biomedical Mass Spectrometry Resource). This work was performed with support of the Washington University in St. Louis Siteman Cancer Center Small Animal Imaging Core. No other potential conflict of interest relevant to this article was reported.

ACKNOWLEDGMENTS

We appreciate the assistance of the Washington University Small Animal Imaging Core and cyclotron facilities and Biomedical Mass Spectrometry Resource.

KEY POINTS

QUESTION: Can ^{225}Ac-labeled ofatumumab be produced and effectively treat human NHL in a murine model using disseminated xenograft cells?

PERTINENT FINDINGS: [^{225}Ac]Ac-ofatumumab showed stable chelation and was cytotoxic in vitro and in vivo. [^{225}Ac]Ac-ofatumumab most commonly showed dose-dependent curative therapeutic efficacy in a murine model of disseminated human lymphoma.

IMPLICATIONS FOR PATIENT CARE: [^{225}Ac]Ac-ofatumumab has excellent potential for translation into the clinic for targeted radioimmunotherapy of patients with NHL.

REFERENCES

1. Siegel RL, Miller KD, Fuchs HE, Jemal A. Cancer statistics, 2022. *CA Cancer J Clin.* 2022;72:7–33.
2. Goldsmith SJ. Radioimmunotherapy of lymphoma: Bexxar and Zevalin. *Semin Nucl Med.* 2010;40:122–135.
3. Marshall MJE, Stopforth RJ, Cragg MS. Therapeutic antibodies: what have we learnt from targeting CD20 and where are we going? *Front Immunol.* 2017;8:1245.
4. Barth MJ, Hernandez-Ilizaliturri FJ, Mavis C, et al. Ofatumumab demonstrates activity against rituximab-sensitive and -resistant cell lines, lymphoma xenografts and primary tumour cells from patients with B-cell lymphoma. *Br J Haematol.* 2012;156:490–498.
5. Herter S, Herting F, Mundigl O, et al. Preclinical activity of the type II CD20 antibody GA101 (obinutuzumab) compared with rituximab and ofatumumab in vitro and in xenograft models. *Mol Cancer Ther.* 2013;12:2031–2042.
6. Sachpekidis C, Jackson DB, Soldatos TG. Radioimmunotherapy in non-Hodgkin's lymphoma: retrospective adverse event profiling of Zevalin and Bexxar. *Pharmaceuticals (Basel).* 2019;12:141.
7. Shadman M, Li H, Rimsza L, et al. Continued excellent outcomes in previously untreated patients with follicular lymphoma after treatment with CHOP plus rituximab or CHOP plus ^{131}I-tositumomab: long-term follow-up of phase III randomized study SWOG-S0016. *J Clin Oncol.* 2018;36:697–703.
8. Rizzieri D. Zevalin® (ibritumomab tiuxetan): after more than a decade of treatment experience, what have we learned? *Crit Rev Oncol Hematol.* 2016;105:5–17.
9. Sjögreen Gleisner K, Spezi E, et al. Variations in the practice of molecular radiotherapy and implementation of dosimetry: results from a European survey. *EJNMMI Phys.* 2017;4:28.
10. Morgenstern A, Apostolidis C, Kratochwil C, Sathekge M, Krolicki L, Bruchertseifer F. An overview of targeted alpha therapy with ^{225}actinium and ^{213}bismuth. *Curr Radiopharm.* 2018;11:200–208.
11. Yoon JT, Longtine MS, Marquez-Nostra BV, Wahl RL. Evaluation of next-generation anti-CD20 antibodies labeled with ^{89}Zr in human lymphoma xenografts. *J Nucl Med.* 2018;59:1219–1224.
12. Shim K, Longtine MS, Abou DS, et al. Cure of disseminated human lymphoma with [^{177}Lu]Lu-ofatumumab in a preclinical model. *J Nucl Med.* November 10, 2022 [Epub ahead of print].
13. Hoegger MJ, Longtine MS, Shim K, Wahl RL. Bioluminescent tumor signal is mouse strain and pelt color dependent: experience in a disseminated lymphoma model. *Mol Imaging Biol.* 2021;23:697–702.
14. Bolch WE, Eckerman KF, Sgouros G, Thomas SR. MIRD pamphlet no. 21: a generalized schema for radiopharmaceutical dosimetry—standardization of nomenclature. *J Nucl Med.* 2009;50:477–484.
15. Sgouros G, Roeske JC, McDevitt MR, et al. MIRD pamphlet no. 22 (abridged): radiobiology and dosimetry of alpha-particle emitters for targeted radionuclide therapy. *J Nucl Med.* 2010;51:311–328.
16. Eckerman K, Endo A. ICRP publication 107: nuclear decay data for dosimetric calculations. *Ann ICRP.* 2008;38:7–96.
17. Maguire WF, McDevitt MR, Smith-Jones PM, Scheinberg DA. Efficient 1-step radiolabeling of monoclonal antibodies to high specific activity with ^{225}Ac for α-particle radioimmunotherapy of cancer. *J Nucl Med.* 2014;55:1492–1498.
18. Maaland AF, Saidi A, Torgue J, et al. Targeted alpha therapy for chronic lymphocytic leukaemia and non-Hodgkin's lymphoma with the anti-CD37 radioimmunoconjugate ^{212}Pb-NNV003. *PLoS One.* 2020;15:e0230526.
19. Deal KA, Davis IA, Mirzadeh S, Kennel SJ, Brechbiel MW. Improved in vivo stability of actinium-225 macrocyclic complexes. *J Med Chem.* 1999;42:2988–2992.
20. Davis IA, Glowienka KA, Boll RA, et al. Comparison of ^{225}actinium chelates: tissue distribution and radiotoxicity. *Nucl Med Biol.* 1999;26:581–589.
21. Schwartz J, Jaggi JS, O'Donoghue JA, et al. Renal uptake of bismuth-213 and its contribution to kidney radiation dose following administration of actinium-225-labeled antibody. *Phys Med Biol.* 2011;56:721–733.
22. Chao MP, Alizadeh AA, Tang C, et al. Anti-CD47 Antibody synergizes with rituximab to promote phagocytosis and eradicate non-Hodgkin lymphoma. *Cell.* 2010;142:699–713.
23. Havlena GT, Kapadia NS, Huang P et al. Cure of micrometastatic B-cell lymphoma in a SCID mouse model using ^{213}Bi anti-CD20 monoclonal antibody. *J Nucl Med.* 2023;64:109–116.
24. Cortez A, Josefsson A, McCarty G, et al. Evaluation of [^{225}Ac]Ac-DOTA-anti-VLA-4 for targeted alpha therapy of metastatic melanoma. *Nucl Med Biol.* 2020;88-89:62–72.
25. Minnix M, Adhikarla V, Caserta E, et al. Comparison of CD38-targeted α- versus β-radionuclide therapy of disseminated multiple myeloma in an animal model. *J Nucl Med.* 2021;62:795–801.
26. Sudo H, Tsuji AB, Sugyo A, et al. FZD10-targeted α-radioimmunotherapy with ^{225}Ac-labeled OTSA101 achieves complete remission in a synovial sarcoma model. *Cancer Sci.* 2022;113:721–732.
27. Daydé D, Ternant D, Ohresser M, et al. Tumor burden influences exposure and response to rituximab: pharmacokinetic-pharmacodynamic modeling using a syngeneic bioluminescent murine model expressing human CD20. *Blood.* 2009;113:3765–3772.
28. Pandit-Taskar N, O'Donoghue JA, Morris MJ, et al. Antibody mass escalation study in patients with castration-resistant prostate cancer using ^{111}In-J591: lesion detectability and dosimetric projections for ^{90}Y radioimmunotherapy. *J Nucl Med.* 2008;49:1066–1074.
29. Jaggi JS, Seshan SV, McDevitt MR, Laperle K, Sgouros G, Scheinberg DA. Renal tubulointerstitial changes after internal irradiation with alpha-particle-emitting actinium daughters. *J Am Soc Nephrol.* 2005;16:2677–2689.
30. Jaggi JS, Kappel BJ, McDevitt MR, et al. Efforts to control the errant products of a targeted in vivo generator. *Cancer Res.* 2005;65:4888–4895.
31. Pruszynski M, D'Huyvetter M, Bruchertseifer F, Morgenstern A, Lahoutte T. Evaluation of an anti-HER2 nanobody labeled with ^{225}Ac for targeted α-particle therapy of cancer. *Mol Pharm.* 2018;15:1457–1466.
32. Park SI, Shenoi J, Pagel JM, et al. Conventional and pretargeted radioimmunotherapy using bismuth-213 to target and treat non-Hodgkin lymphomas expressing CD20: a preclinical model toward optimal consolidation therapy to eradicate minimal residual disease. *Blood.* 2010;116:4231–4239.
33. Green DJ, Shadman M, Jones JC, et al. Astatine-211 conjugated to an anti-CD20 monoclonal antibody eradicates disseminated B-cell lymphoma in a mouse model. *Blood.* 2015;125:2111–2119.
34. Durand-Panteix S, Monteil J, Sage M, et al. Preclinical study of ^{212}Pb alpha-radioimmunotherapy targeting CD20 in non-Hodgkin lymphoma. *Br J Cancer.* 2021;125:1657–1665.
35. Dahle J, Borrebaek J, Jonasdottir TJ, et al. Targeted cancer therapy with a novel low-dose rate α-emitting radioimmunoconjugate. *Blood.* 2007;110:2049–2056.
36. Abou DS, Ulmert D, Doucet M, Hobbs RF, Riddle RC, Thorek DL. Whole-body and microenvironmental localization of radium-223 in naïve and mouse models of prostate cancer metastasis. *J Natl Cancer Inst.* 2015;108:djv380.
37. Beyer G-J, Miederer M, Vranješ-Đurić S, et al. Targeted alpha therapy in vivo: direct evidence for single cancer cell kill using *I*^{49}Tb-rituximab. *Eur J Nucl Med Mol Imaging.* 2004;31:547–554.

Left Ventricular Strain from Myocardial Perfusion PET Imaging: Method Development and Comparison to 2-Dimensional Echocardiography

Jingwen Huang[1], Adam J. Mitchell[2], Ernest V. Garcia[3], C. David Cooke[3], Russell Folks[3], Maria Pernetz[4], Abhinav Goyal[2], Marina Piccinelli[3], and Jonathon A. Nye[3]

[1]Department of Medicine, Emory University School of Medicine, Atlanta, Georgia; [2]Department of Medicine, Division of Cardiology, Emory University School of Medicine, Atlanta, Georgia; [3]Department of Radiology and Imaging Sciences, Emory University School of Medicine, Atlanta, Georgia; and [4]Emory Adult Congenital Heart Center, Emory University School of Medicine, Atlanta, Georgia

This study aimed to develop a measure of longitudinal, radial, and circumferential myocardial strain at rest and regadenoson during pharmacologic stress using ^{82}Rb PET electrocardiography-gated myocardial perfusion imaging (MPI). **Methods:** We retrospectively identified 80 patients who underwent rest and regadenoson-stress CT attenuation–corrected ^{82}Rb PET and had a standard resting transthoracic echocardiogram (TTE) with global longitudinal strain (GLS) analysis within 3 mo. A method was developed to compute longitudinal, radial, and circumferential strain from PET MPI at stress and rest. PET MPI–derived strain and left ventricular function were compared with resting TTE measures as the clinical reference standard. Interobserver agreement of PET MPI strain and left ventricular ejection fraction processing was reported. **Results:** Longitudinal strain assessed with resting TTE GLS showed good correlation with PET MPI at stress ($r = 0.68$, $P < 0.001$) and rest ($r = 0.58$, $P < 0.001$). Resting TTE GLS also correlated with PET MPI radial strain at stress ($r = -0.70$, $P < 0.001$) and rest ($r = -0.59$, $P < 0.001$) and circumferential strain at stress ($r = 0.67$, $P < 0.001$) and rest ($r = 0.69$, $P < 0.001$). The left ventricular ejection fraction showed good correlation between resting TTE and PET MPI at stress ($r = 0.83$, $P < 0.001$) and rest ($r = 0.80$, $P < 0.001$). Bland–Altman analysis indicated positive bias of TTE GLS compared with PET MPI longitudinal strain at stress (mean difference = 5.1%, 95% CI = [−2.5, 12.7]) and rest (mean difference = 4.2%, 95% CI = [−4.3, 12.8]). Reproducibility of PET MPI longitudinal strain showed good agreement at stress (concordance correlation coefficient = 0.73, $P < 0.001$) and rest (concordance correlation coefficient = 0.74, $P < 0.001$), with Bland–Altman analysis showing a small bias in the longitudinal direction at stress (mean difference = −0.2%) and rest (mean difference = −1.0%). **Conclusion:** Strain measured with PET MPI using an automated technique correlated well with resting GLS strain obtained by TTE, and the measure is reproducible. Strain from PET MPI should be investigated further to establish reference ranges and assess its value in routine clinical practice.

Key Words: human; strain; PET; myocardial perfusion imaging; global longitudinal strain

J Nucl Med 2023; 64:932–939
DOI: 10.2967/jnumed.122.264516

Left ventricular ejection fraction (LVEF) is a proven measure of global left ventricular (LV) function that is associated with long-term outcomes. Cardiac diseases affect individuals differently and may not conform to arbitrary ejection fraction cutoffs. Therefore, the ability to further categorize a patient's LVEF is needed, particularly in a patient with an ejection fraction of 35%–50% (*1*). Regional LV function parameters such as wall motion and thickening have been shown to contribute incrementally to assessing LV function and categorizing patients' outcomes (*2*). Although powerful, these metrics do not provide 1 global parameter of LV function that can be easily understood and applied for measuring outcomes.

Echocardiography has an extensive track record in measuring myocardial deformation (i.e., strain). Strain analysis by echocardiography is a functional imaging tool for the clinical assessment of a range of cardiac pathologies. Global longitudinal strain (GLS) is most feasibly and robustly measured by speckle-tracking echocardiography and serves as a marker of global function that contributes incrementally to LVEF in the diagnosis and prognosis of cardiac disease (*3,4*). GLS has been shown by echo to be a superior predictor of all-cause cardiac mortality compared with LVEF in patients with coronary artery disease (*5*). In addition, GLS has been shown to be a robust measure for identifying early LV myocardial dysfunction, especially in patients undergoing chemotherapy (*6*).

Myocardial perfusion imaging (MPI), including PET and SPECT, is widely used in assessment of ischemic heart disease, determination of myocardial viability, and evaluation of cardiac device–related infections (*7*). Previously, we developed an automated approach to track the LV myocardium throughout the cardiac cycle to measure LV dyssynchrony using electrocardiogram (ECG) gated MPI (*8*). Here, we expand on this approach using this tracking methodology to measure radial, circumferential, and longitudinal strain at rest and during pharmacologic stress. We compare PET MPI strain measurements with resting GLS obtained by transthoracic echocardiography (TTE), considered to be the standard of care (*9,10*).

MATERIALS AND METHODS

Patient Population and Study Protocol

In this retrospective study, we investigated patients who underwent both TTE GLS analysis and rest and regadenoson-stress ^{82}Rb PET MPI within a 3-mo period at our institute between September 1, 2019, and September 1, 2021. Patients who had both studies were excluded if they had major cardiac events (e.g., myocardial infarction, cardiac surgery,

Received Jun. 12, 2022; revision accepted Dec. 12, 2022.
For correspondence or reprints, contact Adam J. Mitchell (ajmitc3@emory.edu).
Published online Dec. 15, 2022.

revascularization, valve intervention, or start of chemotherapy) between the time the 2 studies were completed. This study was approved by the Institutional Review Board of Emory University with a waiver of informed consent based on an assessment of no more than minimal risk.

Strain Measurements

2-Dimensional (2D) Echocardiography and Strain Analysis. Patients were imaged in the left lateral decubitus position with a commercially available echocardiography system (Vivid Seven E95; GE HealthCare). Image acquisition was performed using a 3.5-MHz transducer, at a depth of 16 cm in the parasternal view, and apical, 2-chamber, and 4-chamber views. Standard 2D, color Doppler, and M mode triggered to the QRS complex were saved in cine-loop format from 3 consecutive beats. The LV volumes (end systolic and end diastolic) were calculated from the conventional apical, 2-chamber, and 4-chamber views, and LVEF was calculated with the biplane Simpson rule (*11*). All measurements were made at rest by research personnel blinded to patient history and outcomes. Resting GLS measurement was performed on apical, 2-chamber, 4-chamber, and long-axis views using speckle-tracking echocardiography analysis on raw images obtained from patients in real time, and the images were analyzed with commercially available software (GE EchoPAC PC version 204), using 2D images at a frame rate between 55 and 65 fps. This software analyzed motion by tracking frame-to-frame movement of natural acoustic markers shown on standard ultrasonic images in 2D. Myocardial motion was analyzed using automated functional imaging software within EchoPAC to determine GLS. The LV endocardial border was traced at the end-systolic frame. The LV end-systolic frame was defined by the LV outflow tract Doppler at the closure of the aortic valve. If necessary, automatic endocardial detection was manually adjusted to assure correct tracking, excluding the papillary muscles and chordae and including the LV apex. Longitudinal strain curves were displayed, and experienced echo research personnel evaluated the image quality for satisfactory tracking of the borders.

^{82}Rb PET MPI Study and Strain Analysis. ECG-gated ^{82}Rb PET MPI was performed on a Biograph 40 PET/CT (Siemens Medical Solutions) according to published guidelines (*12*). Patients were instructed to abstain from caffeine or xanthine-containing products for 12 h, as well as β-blockers and calcium channel blockers for 24 h. A low-dose CT scan was collected before the PET study for the purposes of attenuation correction. At rest, approximately 925 to 1,480 MBq of generator-produced ^{82}Rb-chloride, based on patient weight, was delivered intravenously via peripheral radial vein using an automated infusion system (Ruby-Fill; Jubilant Radiopharma). Hyperemia was induced by intravenous bolus infusion of regadenoson (0.4 mg/kg/min), followed by a second administration of ^{82}Rb-chloride at the time of peak heart rate. A total of 7 min of data were collected at rest and during hyperemia starting at the time of infusion. Static and ECG-gated images (8 temporal bins) were reconstructed with a non–time-of-flight 2D iterative ordered-subsets algorithm with attenuation and scatter correction using emission data starting at 2 min after infusion to the end of the data collection.

PET MPI strain measurements were performed using the short-axis LV endocardium detected and tracked throughout the cardiac cycle extracted from ECG-gated PET MPI studies (Fig. 1). Automatic detection of the LV endocardium was done using our standard 40 equiangular maximum count circumferential profile detection, followed by our count-based endocardial border modeling algorithm as used in the Emory Cardiac Toolbox (*8,10,13*). Strain measures were extracted on a point-by-point basis along the radial, circumferential, and longitudinal orientations on the rest and stress datasets.

Radial strain analysis uses the maximum count circumferential profiles extracted from short axis slices. The changes in these counts from each temporal frame along the cardiac cycle have been shown to be linear with myocardial thickening (*14*). The location of these samples is tracked as described earlier and then translated to the corresponding endocardial position depending on the measured thickening. The thickening for each sample in each frame is added to determine the radial strain at that temporal point. The average radial strain per frame is calculated as the sum of the strains per frame divided by the number of sample points. Global radial strain is then measured as the temporal maximum of this average strain.

Circumferential strain analysis uses the circumferential sample endocardial locations as in the radial strain described earlier. The spatial distance (L) between each pair of angular samples in each frame is calculated, and the samples' maximum separation over the cardiac cycle is assigned as L_o. For each pair of angular samples, strain is determined using the following standard equation: Strain = $100\% \times (L - L_o)/L_o$ (*15*). The average strain is then determined on a segmental basis for each temporal frame in the cardiac cycle. The average of the sum of the

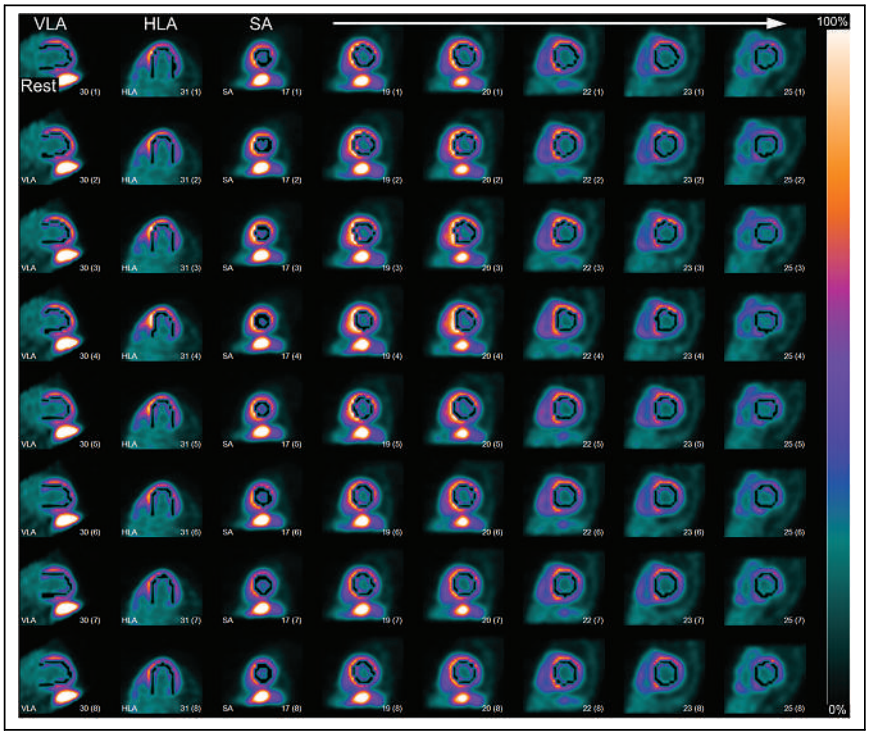

FIGURE 1. PET MPI strain autocontours. One patient example demonstrates PET MPI strain contouring methodology. Displayed images are LV endocardium detection and tracking overlay throughout cardiac cycle extracted from ECG-gated PET MPI under rest. Panels show representative vertical long axis (VLA) and horizontal long axis (HLA) slices, followed by short axis (SA) slices from apex to base along row (white arrow pointing left to right). End-diastolic frames are on top row, followed by contraction to end systole on middle rows and transitioning back to end diastole on bottom row. Color bar represents minimum to maximum normalized counts.

TABLE 1
Baseline Characteristics of Patient Population

Characteristic	Data
Age (y)	62 ± 12
Sex (men)	42 (52.5)
BSA (m^2)	2.03 ± 0.3
Days between echocardiography and PET study	14.8 ± 31.7 (0–87)
Diabetes	30 (37.5)
Systolic BP (mm Hg)	132.0 ± 25.4
Diastolic BP (mm Hg)	76.1 ± 12.3
HFrEF	20 (25)
Ischemic cardiomyopathy	−16 (80)
Chemotherapy-induced cardiomyopathy	−2 (10)
Dilated cardiomyopathy	−1 (5)
History of heart transplant	−1 (5)
HFpEF	5 (6.3)
CKD	29 (36.3)
Prior MI	15 (18.8)

Data are number and percentage or mean ± SD.
BP = blood pressure; BSA = body surface area; CKD = chronic kidney disease; HFpEF = heart failure with preserved ejection fraction; HFrEF = heart failure with reduced ejection fraction; MI = myocardial infarction.

temporal minimum strain for the nonapical segments results in the global circumferential strain. Longitudinal strain analysis starts with the same endocardial samples used for the radial and circumferential strain calculations. These samples are then translated into 40 equiangular long axis planes. Each plane is defined by equidistant endocardial samples from apex to base. The distance between samples is given by the slice thickness, with the total number of samples given by the length of the LV. This length is different for each angle depending on the distance from base to apex and is different for each time frame as the LV contracts. This length is interpolated to 20 samples for each base-to-apex length of each of the 40 long axis planes and each of the 8 frames per cardiac cycle. The spatial distance (L) between each pair of interpolated longitudinal samples in each frame is calculated, and the samples' maximum separation over the cardiac cycle is assigned as L_o. The average strain per temporal frame is calculated by summing the strains over all samples over all longitudinal planes and dividing by the total number of samples. The GLS is then determined as the minimum strain over all temporal samples. Because both longitudinal and circumferential strains are negative numbers, their minimum yields the greatest magnitude of strain measured.

Circumferential and longitudinal strains were calculated in 2D within planes (e.g., within the short axis for circumferential strain) to correlate to 2D measurements by TTE. Radial thickening as measured by the Emory Cardiac Toolbox is an inherently volumetric parameter, because it uses count changes throughout the cardiac cycle. These MPI volumetric radial strain measures were correlated to the 2D measures from TTE.

Interobserver Reproducibility

All PET MPI strain measures were computed twice by our research team (E.V.G. and R.F.), blinded to the patient condition to examine observer agreement. The Emory Cardiac Toolbox automatically determines processing parameters for the ungated study and uses these as the starting point for automatic selection of the gated parameters. Each observer had the option to adjust the apex and base slice selection and left ventricle center and radius for each of the 8 gated images. Selection of the base slice location was allowed to change by ±1 slice per gate. Stress and rest parameters, including total slices from base to apex, were matched as well as possible. Although all image parameters can affect quantitative results, in strain analysis, the most critical parameter appears to be base selection and how it is allowed to change during the cardiac cycle.

Statistical Analysis

Continuous variables are reported as mean ± SD or with 95% CI. Bland–Altman analysis, Pearson correlation, and the concordance correlation coefficient (CCC) were used to evaluate the association and agreement between resting TTE GLS and PET MPI longitudinal, radial, and circumferential strain and LVEF. CCC and Bland–Altman analysis were used to examine the interobserver agreement for all 3 PET MPI strain directions at stress and rest. In the interpretation of the CCC, a value below 0.4 is considered poor, a value between 0.4 to 0.7 is moderate, and a value greater than 0.7 is good agreement (*16*). For each CCC measure, the 95% CI is reported using the *z*-transform methods described by Lin (*17*). Evaluation of PET MPI strain differences at stress and rest for each direction were determined by examining for nonoverlapping CIs, which corresponds to a P value < 0.05.

RESULTS

Patient Population

A total of 85 patients were retrospectively identified, and 80 patients were included in our study. Three patients were excluded due to a major cardiac event (2 patients had ST-segment elevation myocardial infarction and 1 patient had coronary artery bypass surgery) between the PET MPI and the 2D TTE study. Two patients

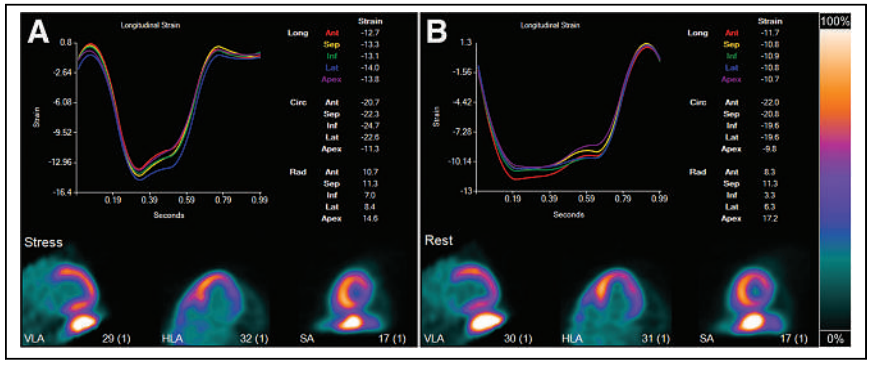

FIGURE 2. PET MPI strain. Longitudinal (Long) strain curves are from patient example in Figure 1 (stress [A] and rest [B]). Length of R-R interval has been normalized to 1 s. Strain plots over 1 cardiac cycle are color coded and reported for anterior (Ant), septal (Sep), inferior (Inf), lateral (Lat), and apical (Apex) regions. Circumferential (Circ) and Radial (Rad) strains are also displayed for corresponding myocardial walls but not plotted. Color bar represents minimum to maximum normalized counts. HLA = horizontal long axis; SA = short axis; VLA = vertical long axis.

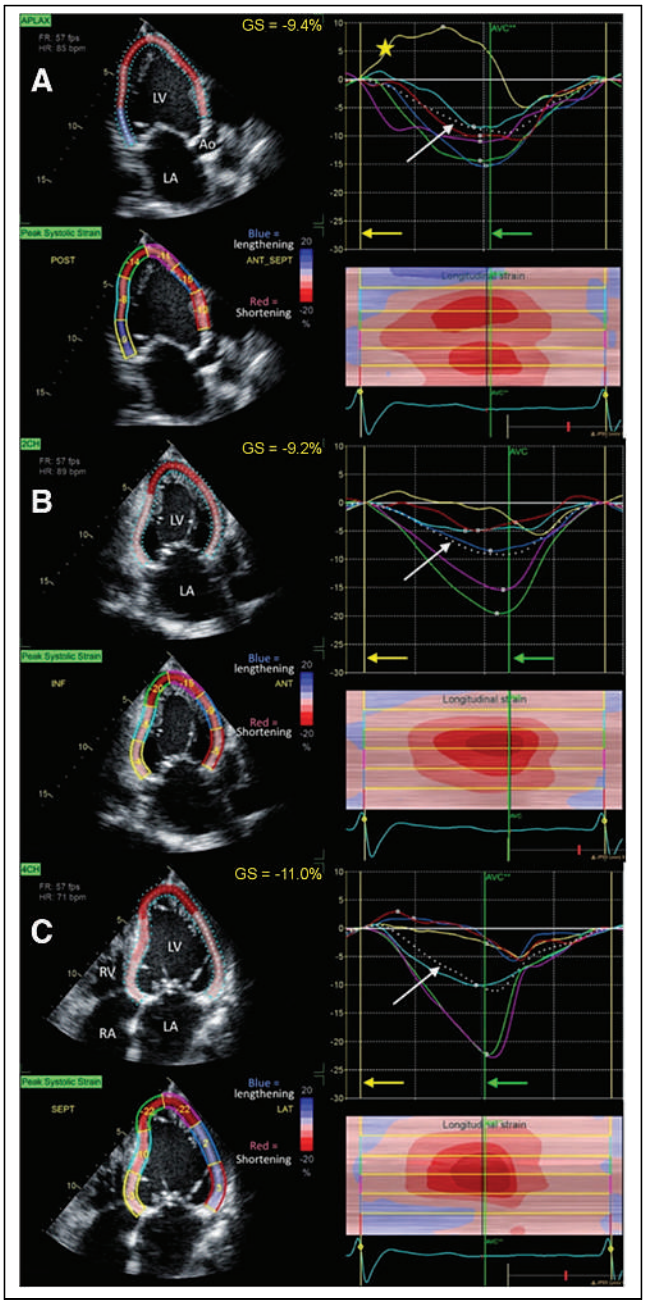

FIGURE 3. Resting TTE GLS. Rest 2D TTE strain measurements are from patient example in Figure 1. LVEF at rest was 32%, and GLS at rest was −9.9%. Three views—apical (A), 2-chamber (B), and 4-chamber (C)—are used in speckle-tracking echocardiography, and mean percentage longitudinal strain for each view is presented. Shades of red represent negative strain (contraction), whereas blue denotes positive strain (relaxation). White dotted line (white arrows) represents average strain among LV segments during cardiac cycle. Color of each trace line showing strain corresponds to anatomic color segments on 2D color image to left. Green arrows indicate aortic valve closure (AVC) line, which indicates end systole; yellow arrow shows end-diastolic (ED) line. Yellow star points out yellow curve on apical view; there is abnormal systolic lengthening of yellow segment (basal inferolateral segment). 2CH = 2-chamber; 4CH = 4-chamber; ANT = anterior; Ao = aorta; APLAX = apical long axis; FR = frame rate; GS = global strain; HR = heart rate; INF = inferior; LA = left atrium; LAT = lateral; POST = posterior; RA = right atrium; RV = right ventricle; SEPT = septal.

were excluded because PET MPI and 2D TTE were performed more than 3 mo apart. The final population (n = 80) consisted of 42 men and 38 women (mean age, 62 ± 12). The indications for PET MPI and TTE with strain analysis in these patients include chest pain (50%), preoperative evaluation or clearance (16%), dyspnea (14%), newly decreased ejection fraction (10%), abnormal ECG findings (4%), palpitations (3%), and syncope (3%). Patient characteristics and summary measures of 2D TTE and PET MPI are given in Table 1.

Strain Measurements

Figures 2 and 3 display the PET MPI strain and TTE processing at rest from a representative patient (80-y-old female with body mass index of 18.1 kg/m^2). In both techniques, strain curves are generated over the cardiac cycle, with the PET MPI including the longitudinal, radial, and circumferential directions. Table 2 summarizes the TTE GLS and PET MPI strain measurements. A greater degree of myocardial shortening is reflected by more negative longitudinal and circumferential strain values and more positive radial strain values.

Plots of resting TTE GLS compared with PET MPI strain at stress and rest in the longitudinal direction are shown in Figure 4, with the correlation and agreement summarized in Table 3. The associations of resting TTE GLS with PET MPI were good but showed low agreement, as indicated by the CCC. The low agreement can be explained by the presence of a bias between the 2 longitudinal strain measures, meaning that there is a difference in absolute scale

TABLE 2
Baseline Measures of LV Function from 2D TTE and PET MPI in Patient Population

Parameter	Mean ± SD
2D TTE parameters	
Heart rate	75.8 ± 13.9
LVEF (%)	52 ± 14
LV GLS	−15.0 ± 4.7
End-diastolic LV diameter (cm)	4.8 ± 0.7
End-systolic LV diameter (cm)	3.5 ± 0.9
Interventricular septal thickness, diastolic (cm)	1.2 ± 0.3
LV posterior wall thickness (cm)	1.1 ± 0.3
LV mass index	107 ± 35
^{82}Rb PET ECG-gated MPI parameters	
Summed stress score	5.0 ± 7.2
Summed rest score	3.2 ± 4.9
Summed difference score	1.8 ± 4.2
Stress	
LVEF (%)	60.3 ± 16.1
Longitudinal strain	−19.7 ± 5.0
Radial strain	26.6 ± 10.2
Circumferential strain	−31.5 ± 12.0
Rest	
LVEF (%)	57 ± 15
Longitudinal strain	−18.8 ± 4.9
Radial strain	21.3 ± 8.0
Circumferential strain	−28.3 ± 10.3

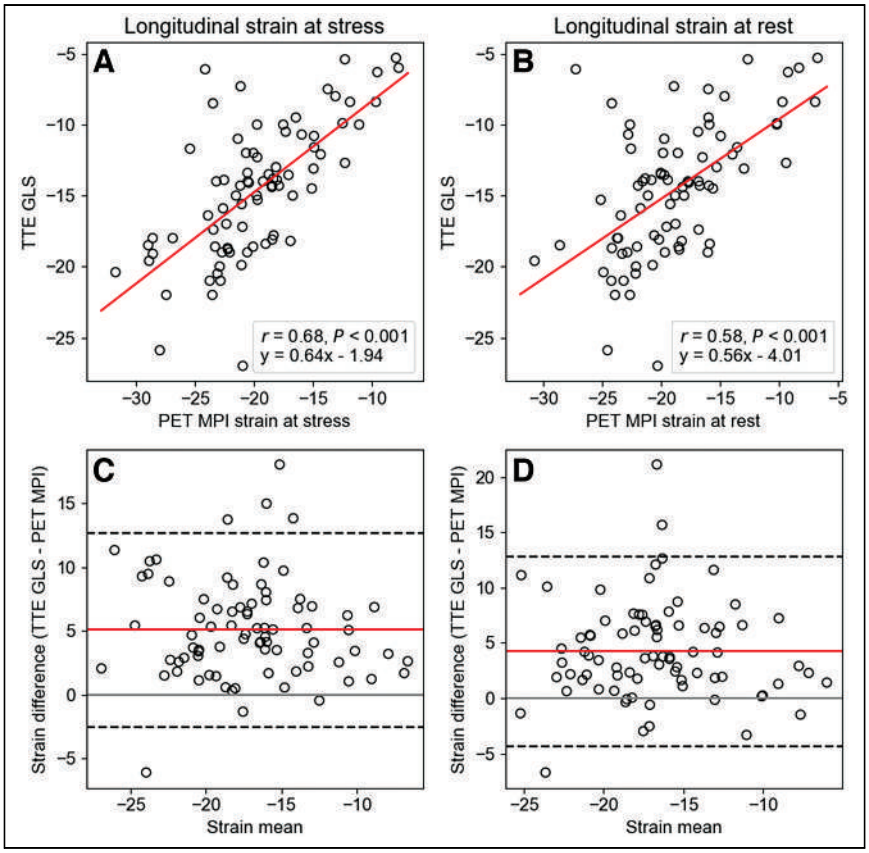

FIGURE 4. Longitudinal TTE GLS and PET MPI. (A and B) Linear regression plots showing correlation between longitudinal PET MPI and TTE GLS strain at stress (A) and rest (B), including equation of best fit. (C and D) Bland–Altman plots of longitudinal strain from resting TTE GLS and PET MPI at stress (C) (mean difference = 5.1%, 95% CI = [−2.5, 12.7]) and rest (D) (mean difference = 4.2%, 95% CI = [−4.3, 12.8]). Red line is mean measurement difference, and dashed lines are upper (mean +2 SD) and lower (mean −2 SD) limits of interval of agreement.

between the modality measures. This bias is more readily observed in Bland–Altman plots, as indicated by the nonzero mean of the measurement differences (Figs. 4A and 4B). We observed a bias in longitudinal strain between TTE GLS and PET MPI at stress (bias = 5.1%, 95% CI = [−2.5, 12.7]) and rest (bias = 4.2%, 95% CI = [−4.3, 12.8]) (Figs. 4C and 4D).

Plots of TTE GLS and PET MPI radial and circumferential strains are shown in Supplemental Figure 1, with the correlations summarized in Supplemental Table 1 (supplemental materials are available at http://jnm.snmjournals.org). There tended to be a higher correlation of resting TTE GLS with PET MPI radial and circumferential strain at stress compared with rest, but this was not significant. The negative correlation with radial PET MPI strain is due to comparison of shortening in the longitudinal direction compared with lengthening in the radial direction. No other significant differences were observed between stress and rest PET MPI strain measures.

LVEF measured by resting TTE LVEF showed very good correlation with PET MPI at stress ($r = 0.83$, $P < 0.001$) and rest ($r = 0.80$, $P < 0.001$) and good agreement at stress (CCC = 0.71, $P < 0.001$) and rest (CCC = 0.75, $P < 0.001$) (Figs. 5A and 5B). Bland–Altman plots of LVEF from TTE GLS and PET MPI revealed a small bias at stress (mean difference = −8.1%, 95% CI = [−25.6, 9.4]) and rest (mean difference = −4.7%, 95% CI = [−22.8, 13.5]) (Figs. 5C and 5D).

Interobserver Reproducibility

Interobserver agreement of PET MPI strain processing from 2 experienced authors (E.V.G. and R.F.) was good for both stress (CCC = 0.73, 95% CI = [0.56, 0.91]) and rest (CCC = 0.74, 95% CI = [0.55, 0.93]). Bland–Altman plots show a minor bias between observers at stress (mean difference = −0.2%, 95% CI = [9.0, 8.5]) and rest (mean difference = −1.0%, 95% CI = [−8.8, 6.8]), indicating good reproducibility of the proposed method (Supplemental Fig. 2). Interobserver agreement of PET MPI strain processing in the radial and circumferential directions were higher than in the longitudinal direction, but differences were not significant (Supplemental Table 2).

DISCUSSION

In this study, we used PET MPI to compute LV strain in the longitudinal, radial, and circumferential directions at stress and rest. We then compared the strain measured by PET MPI to LV strain measured by 2D TTE. It was demonstrated that PET MPI–based strain measurements strongly correlate with strain obtained by echocardiography. A small bias was observed in the

TABLE 3
Correlation Coefficients between Resting TTE GLS and Strains Measured by PET MPI

	Pearson coefficient	95% CI	*P*	CCC	95% CI	*P*
Stress						
Longitudinal strain	0.68	(0.54, 0.78)	<0.001	0.43	(0.30, 0.57)	<0.001
LVEF (%)	0.83	(0.73, 0.88)	<0.001	0.71	(0.52, 0.90)	<0.001
Rest						
Longitudinal strain	0.58	(0.41, 0.71)	<0.001	0.41	(0.27, 0.56)	<0.001
LVEF (%)	0.80	(0.70, 0.87)	<0.001	0.75	(0.55, 0.96)	<0.001

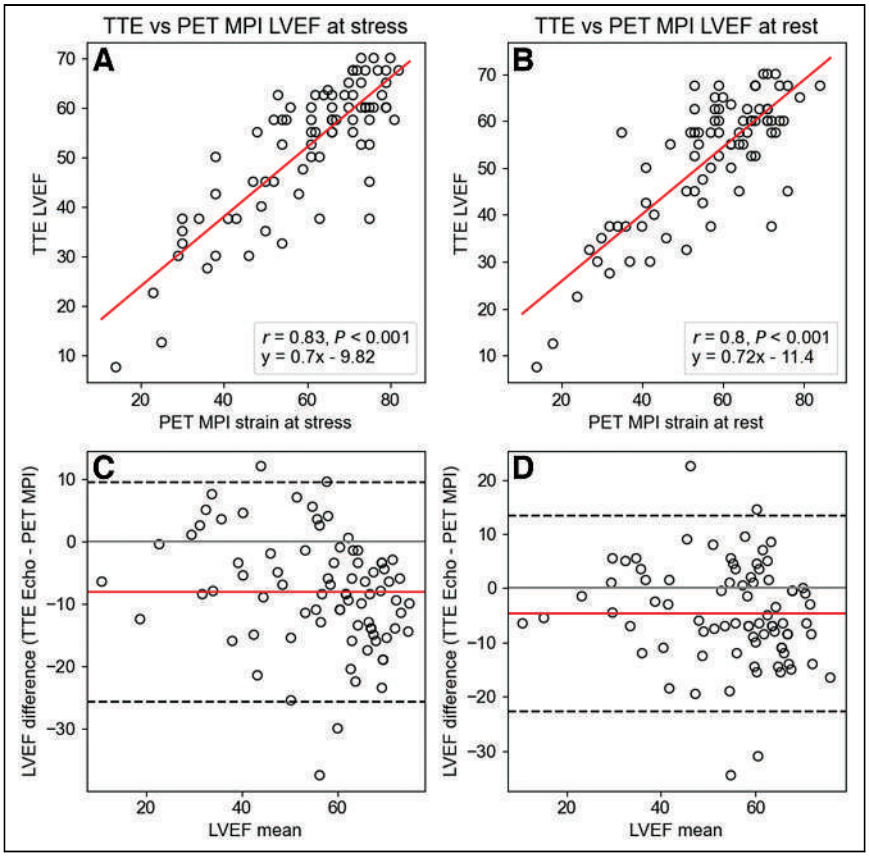

FIGURE 5. LVEF TTE and PET MPI. (A and B) Linear regression plots showing correlation between resting TTE and PET MPI LVEF at stress (A) and rest (B), including equation of best fit. (C and D) Bland–Altman plots of LVEF of resting TTE and PET MPI at stress (C) (mean difference = −8.1%, 95% CI = [−25.6, 9.4]) and rest (D) (mean difference = −4.7%, 95% CI = [−22.8, 13.5]). Red line is mean measurement difference, and dashed lines are upper (mean +2 SD) and lower (mean −2 SD) limits of interval of agreement.

longitudinal strain between the 2 modalities, indicating they were not identical on an absolute scale, but this was relatively small compared with the overall strain magnitude. Lastly, the interobserver reproducibility was lower in the longitudinal direction compared with the radial and circumferential directions, although these differences were not significant. Longitudinal strain is the most difficult of the 3 directions and is highly dependent on the operator's orientation of the valve plane, which can introduce additional error in the strain calculation, reducing the agreement. Other sources of error include differences in how the 2 datasets are measured, for example, 2D TTE vs. 3-dimensional (3D) MPI; operator preferences in positioning, particularly along the valve plane; and inherent error in the TTE GLS measure based on published test–retest data (*18*).

An important component of this study is the vendor and software package used to process strain from 2D TTE images. The algorithms used by the different echo manufacturers for measuring strain are considered intellectual property and have never been fully described. Ultrasound methods of measuring strain describe manual length measurements (*19,20*), tissue Doppler (*21*), speckle tracking (*22,23*), or a combination of techniques depending on the vendor package (*24*). This limitation may lead to significant variations among the results from the different manufacturers (*18*). Therefore, we have chosen to develop our PET MPI strain measures from basic principles. Differences in the calculation of strain may partly explain the bias observed in the longitudinal strain comparisons, but the magnitude of this contribution is unknown. These challenges likely explain our observation of a bias between TTE GLS and PET MPI, which is not unique to our SPECT methods; a bias was also observed when compared with feature tracking with cardiac MRI (CMR) (*25*).

Speckle-tracking echocardiography has been shown as a useful tool and has been widely used in clinical studies in measuring heart functions, but some practical limitations to its use exist. First, for 2D strain echocardiography, because cardiac motion is a complicated 3D process involving rotation, contraction, and shortening, the direction of the movement occurs not only in the direction of the ultrasound beam but also in the direction of the cardiac muscle fiber orientation, creating potential bias. 3D speckle-tracking strain echocardiography has been developed, but challenges remain, such as lower frame rates and lower spatial resolution (*15,26*). Second, a recent study reported a head-to-head comparison of GLS measurements using speckle-tracking echocardiographic software packages from 7 ultrasound machine vendors and showed discrepancies in measuring strain among vendors (*27*). Third, radial and circumferential strain are not typically performed using echocardiography. Circumferential strain use has little incremental information, and radial strain is the least reliable and not recommended, with one of the reasons being that the amount of myocardium used for radial strain calculation is significantly less than that use longitudinal and circumferential directions (*15*).

In comparison to 2D TTE, PET MPI has the ability to measure global radial, circumferential, and longitudinal strain at both stress and rest and requires no extra information beyond what is collected by standard PET imaging. The use of PET imaging to measure LV strain has not been well established for routine clinical practice, but some publications demonstrated PET study–derived stain in potential clinical settings. Recent publications from Kawakubo et al. (*28,29*) showed the utility of ^{13}N-ammonia PET MPI to measure LV strain. They studied endocardial strain and used it to compare blood flow and myocardial motility in ischemic patients (*28*). This method was also used to evaluate right ventricular myocardial longitudinal strain to detect reduced right ventricular myocardial motion due to ischemia in the right coronary artery territory (*29*). Separately, Kawakubo et al. evaluated the LV strain in heart transplant patients and validated ^{13}N-ammonia PET strains using CMR feature tracking strains (*29*). Compared with previous studies, our study validates PET MPI–derived strain measurements with resting 2D TTE–derived strain. The addition of strain analysis to the usual PET MPI workflow could be clinically useful to detect subclinical heart failure, evaluate and monitor patients with cardiomyopathy, and further assist characterization of ischemic heart disease.

Several limitations need to be considered in this study. First, we only had 2D strain echocardiography to assess resting GLS and LVEF and correlate with PET strain data. Comparison with 3D echocardiographic strain would be preferred to overcome limitations with 2D TTE. PET study–derived strain can be further compared with CMR tagging using PET/MRI. CMR has been widely accepted as the reference standard imaging modality for strain quantification, with the advantage that deformation is directly measured by physical properties of the tissue (*30*). In addition, if the patient's blood pressure is significantly different between PET and TTE studies, this could contribute to differences of strain measurements. PET/CMR can overcome the blood pressure issue, because the imaging for both studies is processed simultaneously.

Second, there are technologic and physiologic differences in how strain studies were acquired, processed, and compared. TTE GLS and PET MPI measurements were obtained at 2 time points up to 3 mo apart. Only the resting GLS measurements by TTE were used as the reference standard to compare with stress and rest PET MPI measures of radial, circumferential, and longitudinal strain. Although it would be better to have compared all 3 strain directions individually, resting GLS was the only strain measurement available from the echocardiographic machine used in this study. Nevertheless, resting GLS is the main measurement established to add clinical information beyond LVEF. The rationale for comparing PET MPI measurements of longitudinal, radial, and circumferential strain to TTE measurements of GLS is the mechanical relationship between the 3 strains expressed mathematically as follows: (Global Radial Strain + 1) × (Global Circumferential Strain + 1) × (GLS + 1) = 1 (*19*). The rationale for comparing PET MPI measures of rest and stress to TTE measures at rest was to determine whether the increased counts in the stress MPI studies over the rest studies improved the correlations with TTE-derived strain and to determine changes in strain between rest and stress.

There are also technical differences between TTE and MPI in how strain is measured due to inherent differences in image formation. TTE has an advantage over MPI for defining the valve plane required for GLS measurements. GLS by TTE is determined from the average of myocardial wall measurements extracted from different planes acquired at different times during the scanning session, whereas MPI global strains are measured from simultaneous acquisition of all LV myocardial walls. MPI has an advantage over TTE in measuring radial strain since MPI uses a count-based method and does not rely on border detection. These technical differences can lead to differences in strain measurements.

Because ECG-gated PET MPI studies were acquired using 8 frames per cardiac cycle, these data are perceived to have low temporal resolution. Our tracking approach, which is common with our previous phase analysis tracking of the dyssynchrony of a specific LV segment, uses continuous Fourier functions to approximate the discrete wall thickening samples. This approach has been shown to have the equivalent temporal resolution of 64 frames per cardiac cycle (*31*). Nevertheless, although our measurement of myocardial strain is mostly count density dependent, the effect of increasing the number of frames per cardiac cycle to 16 or 32 while maintaining dose and acquisition time constant is yet to be determined. Another perceived limitation is that our count-based analysis cannot be performed in myocardial regions with extremely low tracer concentration due to infarction or severe stress-induced hypoperfusion. Our simulations have shown that our tracking approach can separate normal from abnormal thickening in regions with a count density as low as 5% of the average normal myocardial uptake (*10*). Although the implication of these findings on the accuracy of strain measurements has yet to be established, the robustness of the tracking used to measure strain is well established.

CONCLUSION

We developed a methodology to measure radial, circumferential, and longitudinal strain from ECG-gated ^{82}Rb PET MPI studies. When compared with 2D TTE GLS, longitudinal PET MPI strain had good correlation and was reproducible between observers. There are currently no published reference normal strain values based on ^{82}Rb PET MPI studies, and this remains an area of needed development for clinical adoption.

DISCLOSURE

Research reported in this publication was supported by the National Heart, Lung, and Blood Institute of the National Institutes of Health under award R01HL143350. The content is solely the responsibility of the authors and does not necessarily represent the official views of the National Institutes of Health. Ernest Garcia, C. David Cooke, and Russell Folks receive royalties from the sale of the Emory Cardiac Toolbox and have equity positions with Syntermed, Inc. The terms of these arrangements have been reviewed and approved by Emory University in accordance with its conflict of interest policies. No other potential conflict of interest relevant to this article was reported.

KEY POINTS

QUESTION: How does longitudinal, radial, and circumferential strain measured from ECG-gated ^{82}Rb MPI PET compare with resting 2D TTE GLS?

PERTINENT FINDINGS: Automatic detection of the LV endocardium for the extraction of strain from ECG-gated ^{82}Rb PET MPI is strongly associated with resting 2D TTE GLS. A greater degree of myocardial shortening is reflected by more negative longitudinal and circumferential strain values and more positive radial strain values, and the interobserver agreement of ECG-gated ^{82}Rb PET MPI strain at rest and stress was good.

IMPLICATIONS FOR PATIENT CARE: Longitudinal, radial, and circumferential strain can be reliably measured from ECG-gated ^{82}Rb MPI PET and may assist with the assessment of global LV function.

REFERENCES

1. Konstam MA, Abboud FM. Ejection fraction: misunderstood and overrated (changing the paradigm in categorizing heart failure). *Circulation.* 2017;135:717–719.
2. Cheitlin MD, Armstrong WF, Aurigemma GP, et al. ACC/AHA/ASE 2003 guideline update for the clinical application of echocardiography: summary article. A report of the American College of Cardiology/American Heart Association Task Force on Practice Guidelines (ACC/AHA/ASE Committee to update the 1997 guidelines for the clinical application of echocardiography). *J Am Soc Echocardiogr.* 2003;16:1091–1110.
3. Blessberger H, Binder T. Two dimensional speckle tracking echocardiography: clinical applications. *Heart.* 2010;96:2032–2040.
4. Zhang KW, French B, May Khan A, et al. Strain improves risk prediction beyond ejection fraction in chronic systolic heart failure. *J Am Heart Assoc.* 2014;3:e000550.
5. Antoni ML, Mollema SA, Delgado V, et al. Prognostic importance of strain and strain rate after acute myocardial infarction. *Eur Heart J.* 2010;31:1640–1647.
6. Sawaya H, Sebag IA, Plana JC, et al. Early detection and prediction of cardiotoxicity in chemotherapy-treated patients. *Am J Cardiol.* 2011;107:1375–1380.

7. Slart RHJA, Glaudemans AWJM, Gheysens O, et al. Procedural recommendations of cardiac PET/CT imaging: standardization in inflammatory-, infective-, infiltrative-, and innervation- (4Is) related cardiovascular diseases—a joint collaboration of the EACVI and the EANM. Summary. *Eur Heart J Cardiovasc Imaging.* 2020;21:1320–1330.
8. Chen J, Garcia EV, Folks RD, et al. Onset of left ventricular mechanical contraction as determined by phase analysis of ECG-gated myocardial perfusion SPECT imaging: development of a diagnostic tool for assessment of cardiac mechanical dyssynchrony. *J Nucl Cardiol.* 2005;12:687–695.
9. Santana CA, Folks RD, Garcia EV, et al. Quantitative ^{82}Rb PET/CT: development and validation of myocardial perfusion database. *J Nucl Med.* 2007;48: 1122–1128.
10. Cooke CD, Garcia EV, Cullom SJ, Faber TL, Pettigrew RI. Determining the accuracy of calculating systolic wall thickening using a fast Fourier transform approximation: a simulation study based on canine and patient data. *J Nucl Med.* 1994;35: 1185–1192.
11. Schiller NB, Acquatella H, Ports TA, et al. Left ventricular volume from paired biplane two-dimensional echocardiography. *Circulation.* 1979;60:547–555.
12. Dilsizian V, Bacharach SL, Beanlands RS, et al. ASNC imaging guidelines/SNMMI procedure standard for positron emission tomography (PET) nuclear cardiology procedures. *J Nucl Cardiol.* 2016;23:1187–1226.
13. Henneman MM, Chen J, Ypenburg C, et al. Phase analysis of gated myocardial perfusion single-photon emission computed tomography compared with tissue Doppler imaging for the assessment of left ventricular dyssynchrony. *J Am Coll Cardiol.* 2007;49:1708–1714.
14. Galt JR, Garcia EV, Robbins WL. Effects of myocardial wall thickness on SPECT quantification. *IEEE Trans Med Imaging.* 1990;9:144–150.
15. Marwick TH, Kosmala W. Strain imaging applications and techniques. In: Marwick TH, Abraham TP, eds. *ASE's Comprehensive Strain Imaging.* Philadelphia, PA: Elsevier; 2022:1–19.
16. Quinn C, Haber MJ, Pan Y. Use of the concordance correlation coefficient when examining agreement in dyadic research. *Nurs Res.* 2009;58:368–373.
17. Lin LI. A concordance correlation coefficient to evaluate reproducibility. *Biometrics.* 1989;45:255–268.
18. Mirea O, Pagourelias ED, Duchenne J, et al. Variability and reproducibility of segmental longitudinal strain measurement: a report from the EACVI-ASE Strain Standardization Task Force. *JACC Cardiovasc Imaging.* 2018;11:15–24.
19. Støylen A, Mølmen HE, Dalen H. Left ventricular global strains by linear measurements in three dimensions: interrelations and relations to age, gender and body size in the Hunt study. *Open Heart.* 2019;6:e001050.
20. Aurich M, Fuchs P, Muller-Hennessen M, et al. Unidimensional longitudinal strain: a simple approach for the assessment of longitudinal myocardial deformation by echocardiography. *J Am Soc Echocardiogr.* 2018;31:733–742.
21. Kuznetsova T, Herbots L, Richart T, et al. Left ventricular strain and strain rate in a general population. *Eur Heart J.* 2008;29:2014–2023.
22. Marwick TH, Leano RL, Brown J, et al. Myocardial strain measurement with 2-dimensional speckle-tracking echocardiography: definition of normal range. *JACC Cardiovasc Imaging.* 2009;2:80–84.
23. Sun JP, Lee AP, Wu C, et al. Quantification of left ventricular regional myocardial function using two-dimensional speckle tracking echocardiography in healthy volunteers: a multi-center study. *Int J Cardiol.* 2013;167:495–501.
24. Dalen H, Thorstensen A, Aase SA, et al. Segmental and global longitudinal strain and strain rate based on echocardiography of 1266 healthy individuals: the Hunt study in Norway. *Eur J Echocardiogr.* 2010;11:176–183.
25. Onishi T, Saha SK, Delgado-Montero A, et al. Global longitudinal strain and global circumferential strain by speckle-tracking echocardiography and feature-tracking cardiac magnetic resonance imaging: comparison with left ventricular ejection fraction. *J Am Soc Echocardiogr.* 2015;28:587–596.
26. Saito K, Okura H, Watanabe N, et al. Comprehensive evaluation of left ventricular strain using speckle tracking echocardiography in normal adults: comparison of three-dimensional and two-dimensional approaches. *J Am Soc Echocardiogr.* 2009; 22:1025–1030.
27. Farsalinos KE, Daraban AM, Unlu S, Thomas JD, Badano LP, Voigt JU. Head-to-head comparison of global longitudinal strain measurements among nine different vendors: the EACVI/ASE Inter-Vendor Comparison Study. *J Am Soc Echocardiogr.* 2015;28:1171–1181.
28. Kawakubo M, Nagao M, Yamamoto A, et al. ^{13}N-ammonia positron emission tomography-derived endocardial strain for the assessment of ischemia using feature-tracking in high-resolution cine imaging. *J Nucl Cardiol.* 2022;29: 2103–2114.
29. Kawakubo M, Nagao M, Kikuchi N, et al. ^{13}N-ammonia positron emission tomography-derived left-ventricular strain in patients after heart transplantation validated using cardiovascular magnetic resonance feature tracking as reference. *Ann Nucl Med.* 2022;36:70–81.
30. Garot J, Bluemke DA, Osman NF, et al. Fast determination of regional myocardial strain fields from tagged cardiac images using harmonic phase MRI. *Circulation.* 2000;101:981–988.
31. Chen J, Faber TL, Cooke CD, Garcia EV. Temporal resolution of multiharmonic phase analysis of ECG-gated myocardial perfusion SPECT studies. *J Nucl Cardiol.* 2008;15:383–391.

Radiolabeled GPVI-Fc for PET Imaging of Multiple Extracellular Matrix Fibers: A New Look into Pulmonary Fibrosis Progression

Simon Isser[1], Andreas Maurer[1,2], Gerald Reischl[1,2], Martin Schaller[3], Irene Gonzalez-Menendez[2,4], Leticia Quintanilla-Martinez[2,4], Meinrad Gawaz[5], Bernd J. Pichler[1,2], and Nicolas Beziere[1,6]

[1]Werner Siemens Imaging Center, Department of Preclinical Imaging and Radiopharmacy, Eberhard Karls University of Tübingen, Tübingen, Germany; [2]Cluster of Excellence EXC 2180, "Image Guided and Functionally Instructed Tumor Therapies," Eberhard Karls University of Tübingen, Tübingen, Germany; [3]Department of Dermatology, University Medical Center, Eberhard Karls University of Tübingen, Tübingen, Germany; [4]Institute of Pathology and Neuropathology, Comprehensive Cancer Center, Eberhard Karls University of Tübingen, Tübingen, Germany; [5]Department of Cardiology and Angiology, University Hospital Tübingen, Eberhard Karls University of Tübingen, Tübingen, Germany; and [6]Cluster of Excellence EXC 2124, "Controlling Microbes to Fight Infections," Eberhard Karls University of Tübingen, Tübingen, Germany

Invariably fatal and with a particularly fast progression, pulmonary fibrosis (PF) is currently devoid of curative treatment options. Routine clinical diagnosis relies on breathing tests and visualizing the changes in lung structure by CT, but anatomic information is often not sufficient to identify early signs of progressive PF. For more efficient diagnosis, additional imaging techniques were investigated in combination with CT, such as ^{18}F-FDG PET, although with limited success because of lack of disease specificity. Therefore, novel molecular targets enabling specific diagnosis are investigated, in particular for molecular imaging techniques. **Methods:** In this study, we used a ^{64}Cu-radiolabeled platelet glycoprotein VI fusion protein (^{64}Cu-GPVI-Fc) targeting extracellular matrix (ECM) fibers as a PET tracer to observe longitudinal ECM remodeling in a bleomycin-induced PF mouse model. **Results:** ^{64}Cu-GPVI-Fc showed significant uptake in fibrotic lungs, matching histology results. Contrary to ^{18}F-FDG PET measurements, ^{64}Cu-GPVI-Fc uptake was linked entirely to the fibrotic activity of tissue and not was susceptible to inflammation. **Conclusion:** Our study highlights ^{64}Cu-GPVI-Fc as a specific tracer for ECM remodeling in PF, with clear therapy-monitoring and clinical translation potential.

Key Words: pulmonary fibrosis; PET; bleomycin

J Nucl Med 2023; 64:940–945
DOI: 10.2967/jnumed.122.264552

Pulmonary fibrosis (PF) is a fatal disease with a mean life expectancy of 3–5 y after diagnosis (*1,2*). It can originate from a myriad of factors such as age or exposure to chemicals and often rapidly progresses (*3*). Early identification of progressive forms of PF is crucial in populations presenting with interstitial lung diseases on CT. PF treatment outcome has been shown to significantly improve after an early treatment start (*4*), particularly since the only currently approved drugs against PF (pirfenidone and nintedanib) merely slow disease progression (*5*). Although PF is relatively easy to diagnose clinically in its advanced stage despite unspecific symptoms due to the characteristic lung honeycombing visible on CT, early stages of progressive fibrosing interstitial lung disease remain difficult to identify (*6*). High-resolution CT can provide higher sensitivity and better recognition of abnormalities in potential PF patients than can regular CT, justifying its current central role in PF diagnosis (*7,8*), but early screening of interstitial lung disease populations cannot rely on high-resolution CT alone as it provides only a snapshot of anatomic structures. Accessing early biomarkers of the disease, ideally by imaging methods, might provide early screening of patients at risk of progressive fibrosing interstitial lung disease, as well as providing monitoring of disease progression and a novel way to assess treatment efficacy. ^{18}F-FDG PET imaging has shown moderate success in PF patients (*9–11*), as this radiotracer reflects only glucose uptake; cannot distinguish between inflammation, fibrosis, and malignant cell proliferation; and can thus provide misleading results.

In PF, tissue is remodeled through increased deposition of extracellular matrix (ECM) fibers such as collagen I–III, fibronectin, and fibrinogen, which mark disease onset and early progression. As such, these fibers represent ideal biomarkers for early PF diagnosis, and radiotracers targeting individual fibers such as collagen I have been developed and have shown promising results preclinically and clinically (*12*). However, no current radiotracers can provide an overall picture of ECM remodeling during progressive PF. Interestingly, with platelet glycoprotein VI (GPVI), nature provides a molecule able to target several ECM fibers, such as collagen I–III, fibronectin, and fibrinogen (*13–15*). GPVI is naturally expressed on the surface of platelets and megakaryocytes and plays a crucial role in their aggregation during wound repair due to its high affinity after dimerization for these ECM fibers (*16,17*). To capitalize on this high affinity, an IgG1 GPVI fusion protein (GPVI-Fc) mimicking highly affine GPVI dimers has been synthesized and initially investigated as an antithrombotic agent (*18*). Imaging using fluorescent GPVI-Fc and a ^{64}Cu-radiolabeled GPVI-Fc, ^{64}Cu-NOTA-GPVI-Fc (^{64}Cu-GPVI-Fc), showed the potential of this targeting vector in thrombosis imaging (*19,20*) as well as in several models presenting a fibrotic component such as rheumatoid arthritis and cutaneous delayed-type hypersensitivity reaction (*21*). Although some of these diseases are predominantly inflammatory, with fibrosis appearing at a later stage, tracer uptake might correlate with

Received Jun. 21, 2022; revision accepted Jan. 9, 2023.
For correspondence or reprints, contact Nicolas Beziere (nicolas.beziere@med.uni-tuebingen.de).
Published online Jan. 26, 2023.

changes in the ECM and be shown on in vivo imaging experiments and ex vivo histology.

In the current study, we investigated the potential of ^{64}Cu-GPVI-Fc for early detection of PF and monitoring of its progression in a bleomycin-induced PF mouse model. Our objective was to visualize and quantify progressive PF longitudinally, noninvasively, and with high disease specificity and to study the potential of the approach in comparison to ^{18}F-FDG PET imaging of PF.

MATERIALS AND METHODS

The full version of the Materials and Methods can be found in the supplemental materials (available at http://jnm.snmjournals.org). Figure 1 shows the study workflow.

Radiotracer Synthesis

^{18}F-FDG was produced using a TRACERlab MX module (GE Healthcare) with radiochemical purity of over 95%. ^{64}Cu-GPVI-Fc was produced as described previously with a radiochemical purity of over 95% (*21*). To perform isotype experiments, NOTA-GPVI-Fc was denatured according to the procedure developed by Akazawa-Ogawa et al. (*22*) by incubation for 30 min at 70°C and subsequently radiolabeled using the same procedure as with stock NOTA-GPVI-Fc with a radiochemical purity of over 70%. Denatured ^{64}Cu-GPVI-Fc is referred to here as radiolabeled isotype.

PF Model

Animal experiments were performed in accordance with the German Animal Protection Law protocols for animal use and care, approved by the Regierungspräsidium Tübingen (NTP-ID 00034862-5-7). In short, 1 mg of bleomycin per kilogram of body weight in 50 μL of saline was deposited intratracheally in 8-wk-old C57BL/6J female mice (50 μL of saline only in control animals) on day 0, following the procedure described by Walters and Kleeberger (*23*). For ethical reasons, animals losing more than 20% of their body weight or showing signs of significant suffering were euthanized and not included in the study. The group size for each experiment can be found in the supplemental materials.

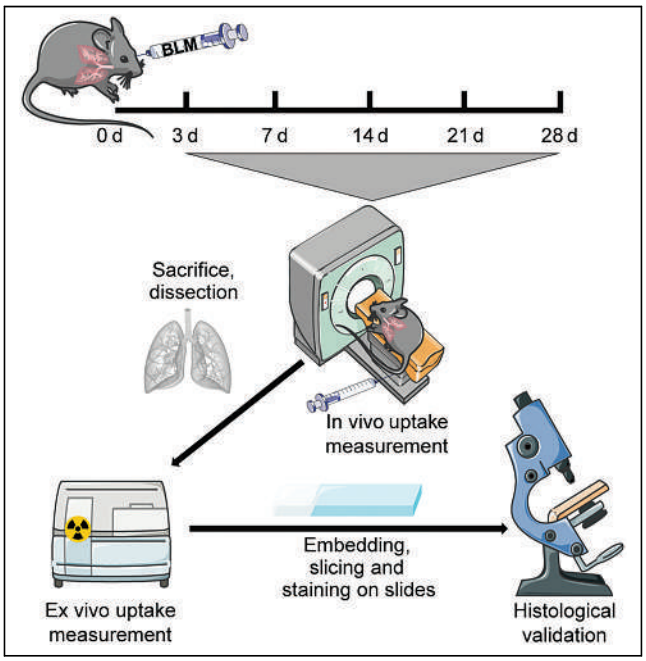

FIGURE 1. Experimental workflow for longitudinal PF imaging. Day 0: intratracheal deposition of bleomycin (BLM) or saline. Days 3, 7, 14, 21, and 28 after bleomycin deposition: PET and MRI scans after radiotracer injection. After in vivo imaging: euthanasia, biodistribution, microscopy imaging.

PET and MRI

High-resolution PET scans were performed using Inveon small-animal PET scanners (Siemens Healthcare) with Inveon Acquisition Workplace software, version 2.1.272 (Siemens Medical Solutions). Tracers (1 per animal group) were injected in the tail vein (12 ± 1.2 MBq): ^{18}F-FDG was injected 5 s after the start of a 1-h dynamic scan followed by an 827-s transmission scan; ^{64}Cu-GPVI-Fc was imaged with a 10-min static scan at 3, 24, and 48 h after injection. Each PET scan was followed by MRI sequences for anatomic reference using a 7-T small-animal scanner (ClinScan; Bruker Biospin MRI GmbH) with Paravision software, version 6.0.1 (Bruker Corp.). PET images were coregistered with MR images using fiducial markers and analyzed with Inveon Research Workplace software (Siemens Healthcare) by drawing regions of interest on the MR images and applying them to the PET images for volumetric quantification of radiotracer accumulation in the entire lung for ^{64}Cu-radiotracer–injected animals and in the right lung lobes for ^{18}F-FDG–injected animals.

Biodistribution

The mice were killed using CO_2 and perfused with 20 mL of 4°C phosphate-buffered saline through the right ventricle. Organ samples were explanted for activity measurements ex vivo using a 2480 WIZARD^2 automatic γ-counter from PerkinElmer.

Histology

For hematoxylin and eosin and Masson trichrome staining, perfused lungs were fixated in formalin, embedded in paraffin, and cut into 5-μm-thick slices using a microtome (Leica). All samples were scanned with a Nanozoomer (Hamamatsu) and processed with CaseViewer (3DHISTECH). Photomicrographic images were acquired with an Axioskop 2 Plus microscope (Zeiss) equipped with a laser optic system (ProgRes C10 Plus camera; Jenoptik) and software. The final images were prepared with Adobe Photoshop CS6. Scoring of inflammation was based on hematoxylin- and eosin-stained sections as follows: 0 (no inflammation), 1 (mild inflammation), 2 (moderate inflammation), or 3 (prominent inflammation). Fibrosis was scored following the modified Ashcroft scale (*24*).

For fluorescence microscopy, frozen lung slices were labeled with antifibronectin, antifibrinogen, anticollagen I, anticollagen II, or anticollagen III primary antibodies. For secondary antibody, antirabbit Cy3 was used to visualize ECM fibers, and antihuman IgG-Cy5 was used to visualize NOTA-GPVI-Fc. Nuclei were stained using YO-PRO-1, and images were acquired using an LSM 800 system (Zeiss) with ZEN software (version 2.3, blue edition).

Data Evaluation and Statistics

Statistical analysis was performed using ordinary 1-way ANOVA (multiple-comparison test based on Dunnett correction) in GraphPad Prism, version 9.0.1. For comparison of lungs at different time points, groups were compared with the respective controls. For ex vivo biodistribution comparison of different organs, mixed-effects analysis was used, and groups were compared with the respective controls. For comparison between uptake of ^{64}Cu-GPVI-Fc and the radiolabeled isotype control, the unpaired *t* test was used. For histologic scoring evaluation, 2-way ANOVA was used. The results show each individual data point together with the mean of each group and its SD. γ-counter results from 1 mouse in the ^{18}F-FDG study were identified as an outlier by the Grubbs test, originating from a user error during ex vivo uptake measurement, and were removed from further statistical ex vivo evaluation.

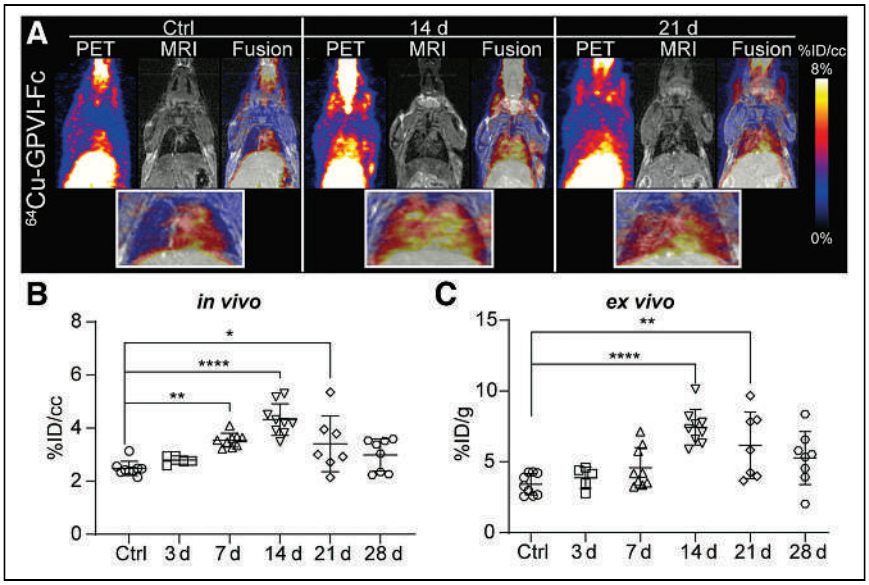

FIGURE 2. Representative images of ^{64}Cu-GPVI-Fc accumulation 48 h after radiotracer injection in animals that received intratracheal saline (control) or bleomycin 14 or 21 d after deposition. (A) Maximum-intensity-projection PET images fused with single-slice MR images (n = 4–9). (B) Corresponding quantification of in vivo tracer uptake in lungs. (C) Corresponding quantification of ex vivo tracer uptake in lungs. *$P \leq 0.05$. **$P \leq 0.01$. ****$P \leq 0.0001$. Ctrl = control.

RESULTS

^{64}Cu-GPVI-Fc Imaging of PF Progression in Bleomycin Model

Imaging measurements were performed 3, 7, 14, 21, and 28 d after deposition of bleomycin (Fig. 1). ^{64}Cu-GPVI-Fc distribution was quantified during PF progression after MRI-guided organ segmentation to investigate ECM remodeling in bleomycin-exposed mice. Preliminary experiments performed 3, 24, and 48 h after injection of ^{64}Cu-GPVI-Fc indicated that the optimal uptake ratio in diseased animals could be attained 48 h after tracer injection (Supplemental Fig. 1). Pulmonary uptake of ^{64}Cu-GPVI-Fc 48 h after injection was visibly increased in vivo 7, 14, and 21 d after deposition compared with control (Fig. 2A). Quantification of in vivo measurements (Fig. 2B) showed no significant difference in radiotracer accumulation 3 d after deposition from that in control. Afterward, lung uptake was significantly higher than in control from 7 d after deposition, peaking at 14 d with a contrast ratio of 1.74, till 21 d after deposition (3.54 ± 0.26 percentage injected dose [%ID]/cm^3, 4.32 ± 0.60 %ID/cm^3, and 3.41 ± 1.06 %ID/cm^3, respectively). At 28 d after deposition, no significantly increased uptake compared with control was observed. Ex vivo measurement of ^{64}Cu-GPVI-Fc accumulation in the lungs confirmed a significantly higher uptake 14 and 21 d after deposition than in control (7.44 ± 1.26 %ID/g, 6.17 ± 2.35 %ID/g, and 3.41 ± 0.75 %ID/g; $P \leq 0.0001$ and $P \leq 0.01$, respectively) (Fig. 2C). Analysis of ex vivo tracer biodistribution showed limited changes in other organs (Supplemental Fig. 2), with only the blood pool signal being lower 28 d after deposition than in control (2.45 ± 0.59 %ID/g to 2.91 ± 0.41 %ID/g, $P \leq 0.05$). Pathologic changes were clearly visible in hematoxylin and eosin and Masson trichrome histology sections (Fig. 3A). Mild and focal inflammatory infiltrates were seen on day 3 after deposition, followed by more intense inflammatory infiltrates and minimal fibrosis on day 7. Fibrosis peaked at 14 d after deposition, followed by a small reduction in fibrotic areas at 21 and 28 d (Supplemental Fig. 3). Scoring (Fig. 3B) highlighted a significant increase in inflammation on days 7 (2.00 ± 0) and 14 (2.00 ± 0) after deposition, followed by a decline on day 21 (1.00 ± 0). Days 3 and 28 after deposition did not display a significant increase in immune cell infiltration compared with control. Modified Ashcroft scoring

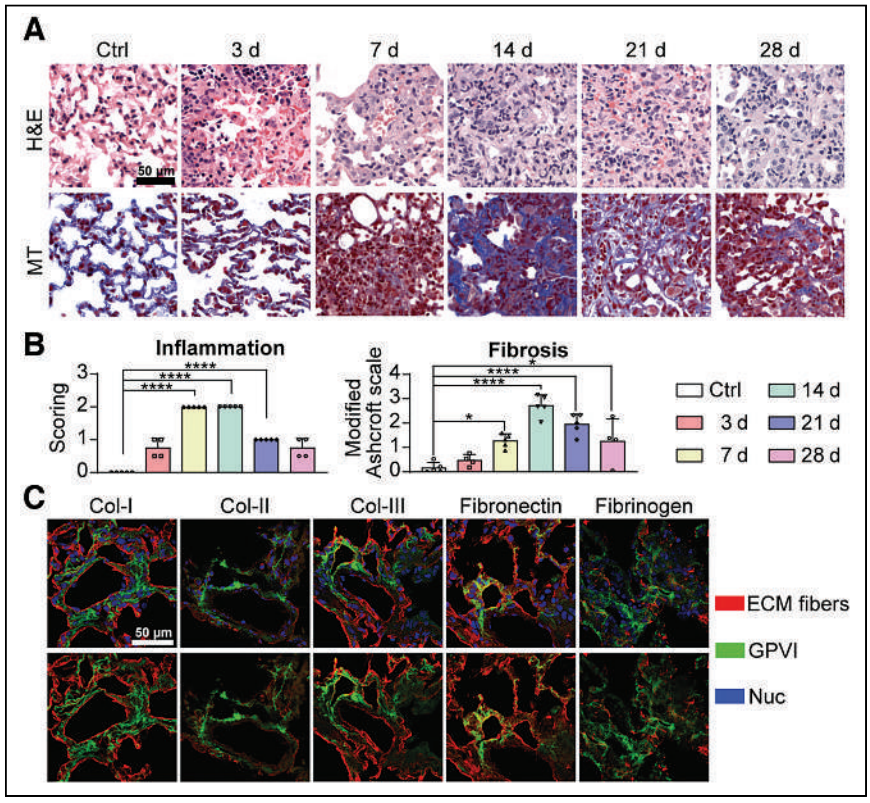

FIGURE 3. (A) Hematoxylin and eosin and Masson trichrome staining in control animals and animals on days 3, 7, 14, 21, and 28 after bleomycin deposition. (B) Histologic scoring of inflammation and modified Ashcroft score (n = 4–5) in mouse lungs compared with controls. (C) Fluorescence microscopy for colocalization of GPVI-Fc with extracellular matrix fibers of collagen I–III and with fibronectin and fibrinogen. Nuclei stain added for cell localization. *$P \leq 0.05$. ****$P \leq 0.0001$. Col = collagen; Ctrl = control; ECM = extracellular matrix; H&E = hematoxylin and eosin; MT = Masson trichrome; Nuc = nuclei.

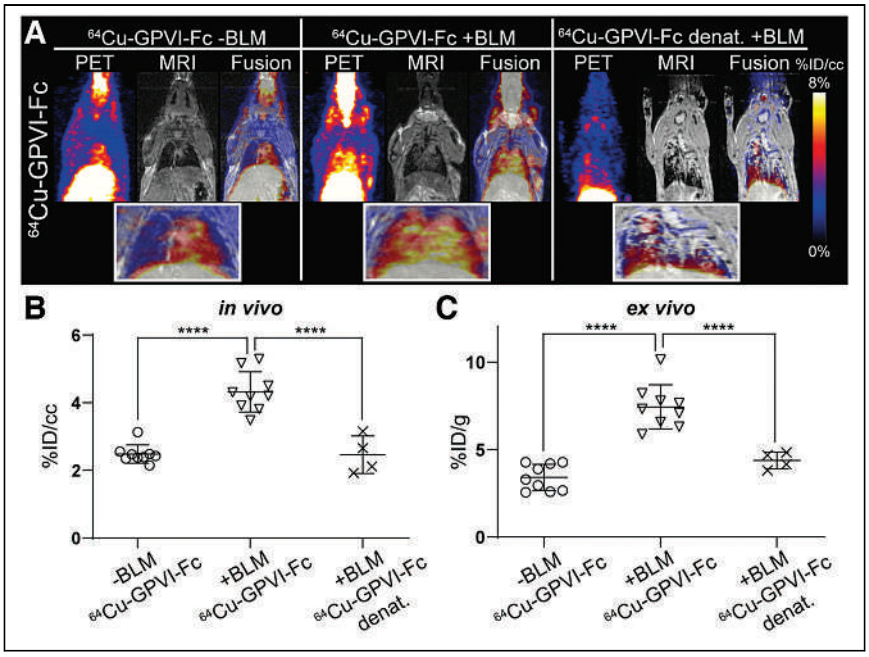

FIGURE 4. Uptake specificity of ^{64}Cu-GPVI-Fc. (A) Representative maximum-intensity-projection PET images fused with single-slice MR images 14 d after bleomycin deposition in control animals (n = 9), bleomycin-induced PF animals injected with ^{64}Cu-GPVI-Fc (n = 9), and bleomycin-induced PF animals injected with denatured ^{64}Cu-GPVI-Fc (n = 4). (B) Corresponding quantification of in vivo tracer uptake in lungs. (C) Corresponding quantification of ex vivo tracer uptake in lungs. ****$P \leq 0.0001$. -BLM = no bleomycin (control); +BLM = bleomycin-induced; denat. = denaturated.

obtained from entire lung sections, comprising both healthy parenchyma and fibrotic areas, was higher than in control on day 7 after deposition (1.27 ± 0.28) but peaked on days 14 (2.72 ± 0.44) and 21 (1.96 ± 0.42). Day 28 after deposition presented a minor increase in fibrosis compared with control (1.29 ± 0.9). Fluorescence microscopy showed colocalization of GPVI-Fc and ECM fibers, such as collagen I–III, fibronectin, and fibrinogen, 14 d after deposition, with collagen III and fibronectin showing extensive colocalization (Fig. 3C).

Specificity of ^{64}Cu-GPVI-Fc for Fibrosis

To further investigate ^{64}Cu-GPVI-Fc specificity toward fibrosis in mouse lungs after bleomycin deposition, we performed binding experiments using a heat-denatured ^{64}Cu-radiolabeled GPVI-Fc (isotype). Decreased uptake of the isotype was visible 14 d after deposition compared with intact ^{64}Cu-GPVI-Fc (Fig. 4A) 48 h after tracer injection (2.46 ± 0.56 %ID/cm^3 to 4.32 ± 0.60 %ID/cm^3, $P < 0.0001$) (Fig. 4B), confirmed by ex vivo measurement (4.37 ± 0.48 %ID/g and 7.44 ± 1.26 %ID/g, $P \leq 0.0001$) (Fig. 4C). The radiolabeled isotype showed accumulation in diseased animals close to the accumulation of ^{64}Cu-GPVI-Fc in control animals. Ex vivo biodistribution (Supplemental Fig. 4) showed a significantly decreased uptake in all measured organs compared with intact ^{64}Cu-GPVI-Fc, except in the spleen, with a significantly increased uptake of the radiolabeled isotype compared with intact ^{64}Cu-GPVI-Fc (16.55 ± 3.93 %ID/g and 9.02 ± 2.43 %ID/g, $P \leq 0.05$).

^{18}F-FDG Imaging of PF in Bleomycin-Inoculated Mice

To visualize glucose metabolism during progression of PF, we used ^{18}F-FDG PET in a distinct set of animals as it is considered the reference radiotracer even in PF imaging research (Fig. 5A) (*25*). Quantification of radiotracer accumulation in vivo (Fig. 5B) showed a significantly increased uptake at all time points, remaining stable throughout the course of the experiment (4.70 ± 0.56 %ID/cm^3 in control and 7.77 ± 0.92 %ID/cm^3 on day 3, 7.82 ± 1.14 %ID/cm^3 on day 7, 7.39 ± 1.45 %ID/cm^3 on day 14, 6.74 ± 0.41 %ID/cm^3 on day 21, and 7.21 ± 1.46 %ID/cm^3 on day 28, with $P \leq 0.001$, $P \leq 0.001$, $P \leq 0.01$, $P \leq 0.05$, and $P \leq 0.01$, respectively). This behavior was also seen ex vivo (Fig. 5C) on days 3, 7, 14, and 21 after deposition (4.65 ± 0.58 %ID/g in control and 14.10 ± 3.74 %ID/g, 12.17 ± 1.49 %ID/g, 12.20 ± 3.52 %ID/g, and 13.70 ± 2.92 %ID/g, with $P \leq 0.01$, $P \leq 0.05$, $P \leq 0.05$, and $P \leq 0.01$) but not day 28 (10.30 ± 3.91 %ID/g). A complete biodistribution analysis, however, showed no difference in uptake in other organs

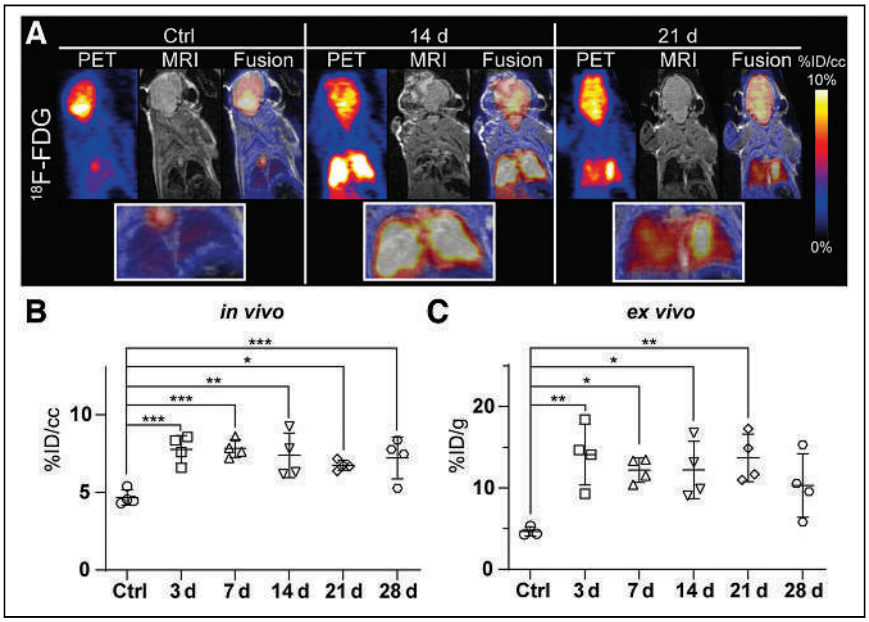

FIGURE 5. ^{18}F-FDG PET imaging of mice with bleomycin-induced PF. (A) Representative single-slice PET images fused with single-slice MR images 14 and 21 d after bleomycin deposition and in control animals (n = 4–5). (B) Mean in vivo tracer uptake in the right lung lobe. (C) Ex vivo tracer uptake in same lobe. *$P \leq 0.05$. **$P \leq 0.01$. ***$P \leq 0.001$.

(Supplemental Fig. 5). Blood glucose levels had no influence on ^{18}F-FDG uptake in this experiment (Supplemental Table 1).

DISCUSSION

In this study, we used PET imaging of the ECM fibers targeting radiotracer ^{64}Cu-GPVI-Fc to monitor fibrosis progression in a bleomycin murine model of PF, and we investigated its potential for early and specific diagnosis of the disease. We showed that the significantly increased pulmonary uptake of ^{64}Cu-GPVI-Fc found at 14 and 21 d after deposition aligned with both ex vivo biodistribution analysis and histologic validation, with Ashcroft scoring highlighting acute fibrosis during the second and third weeks of disease progression. These findings are in line with the reported PF progression in this model, with a second- and third-week peak fibrotic activity (*23,26,27*). Seven days after deposition, however, a small increase in ^{64}Cu-GPVI-Fc accumulation could be seen in vivo but not confirmed ex vivo. To dismiss the possibility of inflammation-driven ^{64}Cu-GPVI-Fc accumulation in bleomycin-deposited animals, as the bleomycin model shows early inflammation during the first 2 wk in contrast to the human presentation of the disease (*23,26,27*), we performed radiolabeled isotype experiments using heat-denatured GPVI-Fc. No specific lung accumulation of the isotype radiotracer could be seen in vivo 14 d after deposition, a time point presenting both fibrosis and inflammation. Although a signal coming from the heart could be seen in control and diseased animals using ^{64}Cu-GPVI-Fc, the isotype showed a reduction in heart signal, likely because of the overall reduced circulation time of the radiotracer due to denaturation of the Fc fragment of the protein. In addition, fluorescence microscopy highlighted colocalization of NOTA-GPVI-Fc with different ECM fibers, such as collagen I–III, fibronectin, and fibrinogen. Interestingly, radiotracer accumulation was reduced 28 d after deposition, as was Masson trichrome staining. This corresponds to the so-called resolution phase of the disease, characteristic of the bleomycin animal model (*28*). Taken together, these findings underline the specific binding potential of the tracer during progressive fibrosis and its accuracy to detect early PF progression in vivo.

As a reference point, ^{18}F-FDG experiments were performed in vivo following the same experimental plan. The increase in ^{18}F-FDG PET uptake at all time points after deposition, covering inflammatory and fibrotic stages in the mouse model, highlights the poor specificity of ^{18}F-FDG for PF, as ^{18}F-FDG merely reports glucose uptake regardless of its origin, including the inflammatory phase present during the first week of the bleomycin murine model. This finding showcases the potential of ^{64}Cu-GPVI-Fc for early and specific detection of progressive fibrosis. Achieving a good correlation between ^{18}F-FDG PET imaging and a positive PF diagnosis requires complex, expensive, and time-consuming measurements—impractical in clinical routine (*10*)—which might be avoided by the use of a specific radiotracer. Furthermore, changes in ^{18}F-FDG uptake were not detectable in a clinical study 3 mo after pirfenidone treatment (*29*), significantly limiting the use of ^{18}F-FDG in the clinic for early PF diagnosis and therapy monitoring and underlining the need for specific noninvasive detection of progressive PF.

Different tracers targeting ECM changes have been reported (*30*). In particular, collagen I–targeting PET showed a behavior similar to that of ^{64}Cu-GPVI-Fc, with similar results over time in vivo in mice (*12*). In addition, this collagen I tracer was used in rats (*31*), with results comparable to ours albeit with a shifted timeline likely due to the difference in model species. ^{68}Ga-pentixafor, targeting CXCR4, a protein upregulated in cancer as well as during progressive PF, has shown promising results in clinical trials, including a correlation between evolution of uptake and pirfenidone treatment outcome (*32*). Significant work on the fibroblast activation protein highlighted its involvement in the progression of PF and initiated the use of fibroblast activation protein–targeted radiotracers for PF imaging (*33*), which are also leading to promising results in the clinic (*34*). In contrast, ^{64}Cu-GPVI-Fc targets multiple collagen subtypes (I, II, and III) as well as fibronectin and fibrinogen (*13–15*), which are found in lung fibrotic regions with high amounts of myofibroblasts and are known to synergize to drive ECM remodeling (*35*). Thus, ^{64}Cu-GPVI-Fc may provide an alternative, more complete view of disease progression, possibly allowing for earlier detection of progressive forms of PF.

CONCLUSION

Here, we showed that ^{64}Cu-GPVI-Fc displays specific uptake during the progressive stage of PF in the bleomycin mouse model but not during the initial inflammatory phase specific to the bleomycin model. This specific uptake was confirmed ex vivo and provides a new approach by targeting multiple ECM components, giving access to a broad picture of PF progression. Therefore, ^{64}Cu-GPVI-Fc represents a new tool to image PF progression in vivo, with high clinical translation potential, able to distinguish between progressive fibrosis and inflammation effectively.

DISCLOSURE

This work was supported by the Werner Siemens Foundation, the fortüne grant (F1359053) of the Faculty of Medicine of the University of Tübingen, and the Deutsche Forschungsgemeinschaft (project 374031971–TRR 240 [molecular aspects]). No other potential conflict of interest relevant to this article was reported.

ACKNOWLEDGMENTS

We thank Linda Schramm, Miriam Owczorz, Walter Ehrlichmann, Dominik Seyfried, and Johannes Kinzler for their technical support, as well as Götz Münch from advanceCOR GmbH for supplying GPVI-Fc. The graphical abstract and Figure 1 were partly generated using Servier Medical Art, provided by Servier, licensed under a Creative Commons Attribution 3.0 unported license.

KEY POINTS

QUESTION: Can ECM disruption be applied as an early marker to depict progressive PF in a preclinical mouse model using ^{64}Cu-GPVI-Fc PET imaging?

PERTINENT FINDINGS: A preclinical bleomycin-induced PF mouse model was studied longitudinally using PET imaging of ^{64}Cu-GPVI-Fc. The radiotracer showed high specificity toward the fibrotic phase of the disease model in vivo, as shown by histology and fluorescence microscopy ex vivo.

IMPLICATIONS FOR PATIENT CARE: ^{64}Cu-GPVI-Fc PET imaging might help in early stratification of patients showing interstitial lung disease on classic high-resolution CT and in identifying early signs of progressive fibrosis without an invasive biopsy, therefore leading to an earlier treatment start.

REFERENCES

1. King TE, Pardo A, Selman M. Idiopathic pulmonary fibrosis. *Lancet.* 2011;378: 1949–1961.
2. Chen X, Guo J, Yu D, Jie B, Zhou Y. Predictors of mortality in progressive fibrosing interstitial lung diseases. *Front Pharmacol.* 2021;12:754851.
3. Raghu G. Idiopathic pulmonary fibrosis: lessons from clinical trials over the past 25 years. *Eur Respir J.* 2017;50:1701209.
4. Antoniou KM, Symvoulakis EK, Margaritopoulos GA, Lionis C, Wells AU. Early diagnosis of IPF: time for a primary-care case-finding initiative? *Lancet Respir Med.* 2014;2:e1.
5. Finnerty JP, Ponnuswamy A, Dutta P, Abdelaziz A, Kamil H. Efficacy of antifibrotic drugs, nintedanib and pirfenidone, in treatment of progressive pulmonary fibrosis in both idiopathic pulmonary fibrosis (IPF) and non-IPF: a systematic review and meta-analysis. *BMC Pulm Med.* 2021;21:411.
6. Cottin V, Hirani NA, Hotchkin DL, et al. Presentation, diagnosis and clinical course of the spectrum of progressive-fibrosing interstitial lung diseases. *Eur Respir Rev.* 2018;27:180076.
7. Walsh SLF, Devaraj A, Enghelmayer JI, et al. Role of imaging in progressive-fibrosing interstitial lung diseases. *Eur Respir Rev.* 2018;27:180073.
8. Abu Qubo A, Capaccione KM, Bernstein EJ, Padilla M, Salvatore M. The role of radiology in progressive fibrosing interstitial lung disease. *Front Med (Lausanne).* 2022;8:679051.
9. Castiaux A, Van Simaeys G, Goldman S, Bondue B. Assessment of ^{18}F-FDG uptake in idiopathic pulmonary fibrosis: influence of lung density changes. *Eur J Hybrid Imaging.* 2018;2:27.
10. Fraioli F, Lyasheva M, Porter JC, et al. Synergistic application of pulmonary ^{18}F-FDG PET/HRCT and computer-based CT analysis with conventional severity measures to refine current risk stratification in idiopathic pulmonary fibrosis (IPF). *Eur J Nucl Med Mol Imaging.* 2019;46:2023–2031.
11. Ko UW, Yoon H-y, Lee SH, et al. The value of ^{18}F-FDG PET/CT in evaluating disease severity in idiopathic pulmonary fibrosis [abstract]. *Eur Respir J.* 2017; 50(suppl 61):PA850.
12. Désogère P, Tapias LF, Hariri LP, et al. Type I collagen–targeted PET probe for pulmonary fibrosis detection and staging in preclinical models. *Sci Transl Med.* 2017;9:eaaf4696.
13. Moroi M, Jung SM. Platelet glycoprotein VI: its structure and function. *Thromb Res.* 2004;114:221–233.
14. Induruwa I, Moroi M, Bonna A, et al. Platelet collagen receptor glycoprotein VI-dimer recognizes fibrinogen and fibrin through their D-domains, contributing to platelet adhesion and activation during thrombus formation. *J Thromb Haemost.* 2018;16:389–404.
15. Mangin PH, Onselaer MB, Receveur N, et al. Immobilized fibrinogen activates human platelets through glycoprotein VI. *Haematologica.* 2018;103:898–907.
16. Chen H, Locke D, Liu Y, Liu C, Kahn ML. The platelet receptor GPVI mediates both adhesion and signaling responses to collagen in a receptor density-dependent fashion. *J Biol Chem.* 2002;277:3011–3019.
17. Jung SM, Moroi M. Platelet glycoprotein VI. *Adv Exp Med Biol.* 2008;640:53–63.
18. Ungerer M, Rosport K, Bultmann A, et al. Novel antiplatelet drug Revacept (dimeric glycoprotein VI-Fc) specifically and efficiently inhibited collagen-induced platelet aggregation without affecting general hemostasis in humans. *Circulation.* 2011;123:1891–1899.
19. Bigalke B, Lindemann S, Schonberger T, et al. Ex vivo imaging of injured arteries in rabbits using fluorescence-labelled glycoprotein VI-Fc. *Platelets.* 2012;23:1–6.
20. Bigalke B, Phinikaridou A, Andia ME, et al. Positron emission tomography/computed tomographic and magnetic resonance imaging in a murine model of progressive atherosclerosis using ^{64}Cu-labeled glycoprotein VI-Fc. *Circ Cardiovasc Imaging.* 2013;6:957–964.
21. Beziere N, Fuchs K, Maurer A, et al. Imaging fibrosis in inflammatory diseases: targeting the exposed extracellular matrix. *Theranostics.* 2019;9:2868–2881.
22. Akazawa-Ogawa Y, Nagai H, Hagihara Y. Heat denaturation of the antibody, a multi-domain protein. *Biophys Rev.* 2018;10:255–258.
23. Walters DM, Kleeberger SR. Mouse models of bleomycin-induced pulmonary fibrosis. *Curr Protoc Pharmacol.* 2008:46.
24. Hubner RH, Gitter W, El Mokhtari NE, et al. Standardized quantification of pulmonary fibrosis in histological samples. *Biotechniques.* 2008;44:507–511, 514–507.
25. Mahmutovic Persson I, von Wachenfeldt K, Waterton JC, Olsson LE; on behalf of the Tristan Consortium. Imaging biomarkers in animal models of drug-induced lung injury: a systematic review. *J Clin Med.* 2020;10:107.
26. Mouratis MA, Aidinis V. Modeling pulmonary fibrosis with bleomycin. *Curr Opin Pulm Med.* 2011;17:355–361.
27. Moore BB, Hogaboam CM. Murine models of pulmonary fibrosis. *Am J Physiol Lung Cell Mol Physiol.* 2008;294:L152–L160.
28. Tashiro J, Rubio GA, Limper AH, et al. Exploring animal models that resemble idiopathic pulmonary fibrosis. *Front Med (Lausanne).* 2017;4:118.
29. Bondue B, Castiaux A, Van Simaeys G, et al. Absence of early metabolic response assessed by ^{18}F-FDG PET/CT after initiation of antifibrotic drugs in IPF patients. *Respir Res.* 2019;20:10.
30. Désogère P, Montesi SB, Caravan PJCAEJ. Molecular probes for imaging fibrosis and fibrogenesis. *Chemistry.* 2019;25:1128–1141.
31. Mahmutovic Persson I, Fransén Pettersson N, Liu J, et al. Longitudinal imaging using PET/CT with collagen-I PET-tracer and MRI for assessment of fibrotic and inflammatory lesions in a rat lung injury model. *J Clin Med.* 2020;9:3706.
32. Derlin T, Jaeger B, Jonigk D, et al. Clinical molecular imaging of pulmonary CXCR4 expression to predict outcome of pirfenidone treatment in idiopathic pulmonary fibrosis. *Chest.* 2021;159:1094–1106.
33. Lindner T, Loktev A, Altmann A, et al. Development of quinoline-based theranostic ligands for the targeting of fibroblast activation protein. *J Nucl Med.* 2018;59: 1415–1422.
34. Röhrich M, Leitz D, Glatting FM, et al. Fibroblast activation protein–specific PET/CT imaging in fibrotic interstitial lung diseases and lung cancer: a translational exploratory study. *J Nucl Med.* 2022;63:127–133.
35. Herrera J, Henke CA, Bitterman PB. Extracellular matrix as a driver of progressive fibrosis. *J Clin Invest.* 2018;128:45–53.

Radioimmunoscintigraphy and Pretreatment Dosimetry of ^{131}I-Omburtamab for Planning Treatment of Leptomeningeal Disease

Neeta Pandit-Taskar*[1,2], Milan Grkovski*[3], Pat B. Zanzonico[3], Keith S. Pentlow[3], Shakeel Modak[4], Kim Kramer[4], and John L. Humm[3]

[1]*Department of Radiology, Memorial Sloan Kettering Cancer Center, New York, New York;* [2]*Department of Radiology, Weill Cornell Medical College, New York, New York;* [3]*Department of Medical Physics, Memorial Sloan Kettering Cancer Center, New York, New York; and* [4]*Department of Pediatrics, Memorial Sloan Kettering Cancer Center, New York, New York*

Radiolabeled antibody treatment with ^{131}I-omburtamab, administered intraventricularly into the cerebrospinal fluid (CSF) space, can deliver therapeutic absorbed doses to sites of leptomeningeal disease. Assessment of distribution and radiation dosimetry is a key element in optimizing such treatments. Using a theranostic approach, we performed pretreatment ^{131}I-omburtamab imaging and dosimetric analysis in patients before therapy. **Methods:** Whole-body planar images were acquired 3 ± 1, 23 ± 2, and 47 ± 2 h after intracranioventricular administration of 75 ± 5 MBq of ^{131}I-omburtamab via an Ommaya reservoir. Multiple blood samples were also obtained for kinetic analysis. Separate regions of interest (ROIs) were manually drawn to include the lateral ventricles, entire spinal canal CSF space, and over the whole body. Count data in the ROIs were corrected for background and physical decay, converted to activity, and subsequently fitted to an exponential clearance function. The radiation absorbed dose was estimated to the CSF, separately to the spinal column and ventricles, and to the whole body and blood. Biodistribution of the injected radiolabeled antibody was assessed for all patients. **Results:** Ninety-five patients were included in the analysis. Biodistribution showed prompt localization in the ventricles and spinal CSF space with low systemic distribution, noted primarily as hepatic, renal, and bladder activity after the first day. Using ROI analysis, the effective half-lives were 13 ± 11 h (range, 5–75 h) for CSF in the spinal column, 8 ± 3 h (range, 3–17 h) for ventricles, and 41 ± 11 (range, 23–81 h) for the whole body. Mean absorbed doses were 0.63 ± 0.38 cGy/MBq (range, 0.24–2.25 cGy/MBq) for CSF in the spinal column, 1.03 ± 0.69 cGy/MBq (range, 0.27–5.15 cGy/MBq) for the ventricular CSF, and 0.45 ± 0.32 mGy/MBq (range, 0.05–1.43 mGy/MBq) for the whole body. **Conclusion:** Pretherapeutic imaging with ^{131}I-omburtamab allows assessment of biodistribution and dosimetry before the administration of therapeutic activity. Absorbed doses to the CSF compartments and whole body derived from the widely applicable serial ^{131}I-omburtamab planar images had acceptable agreement with previously reported data determined from serial ^{124}I-omburtamab PET scans.

Key Words: antibody; radioimmunotherapy; omburtamab; leptomeningeal; neuroblastoma

J Nucl Med 2023; 64:946–950
DOI: 10.2967/jnumed.122.265131

Several pediatric and adult malignancies, such as leukemia, neuroblastoma, medulloblastoma, and other solid tumors, may metastasize to the central nervous system and present as leptomeningeal disease (*1*). Leptomeningeal disease is difficult to cure and is associated with high morbidity and mortality (*1,2*). Omburtamab is a murine monoclonal antibody that targets glycoprotein antigen B on the cell membrane (B7H3), which is expressed in several cancers, including neuroblastoma (*3*). Intrathecal or intracranioventricular administration of radiolabeled antibodies into the cerebrospinal fluid (CSF) space has been successfully applied by our group and found to be safe and effective for disease control (*4–6*). Previously, we reported on radiation dosimetry and PET imaging with ^{124}I-omburtamab for pretreatment assessment (*7*). However, given the cost and limited availability of ^{124}I, its use was restricted to only a few patients. We used ^{131}I-omburtamab imaging to evaluate the distribution and dosimetry in patients. Here, we present an analysis of pretreatment imaging, including biodistribution and γ-planar imaging-based dosimetry estimates of projected therapeutic absorbed doses for patients who underwent intraventricularly administered ^{131}I-omburtamab therapy. This paper focuses on the results of a dosimetric analysis based on the available pretreatment imaging data.

MATERIALS AND METHODS

Patient Selection

The prospective study was performed under an institutional review board–approved protocol (ClinicalTrials.gov NCT00089245). ^{131}I-omburtamab was administered under U.S. Food and Drug Administration–approved Investigational New Drug application BB-IND 9351. All patients or their legal guardians signed a written informed consent. Patients eligible for treatment under the protocol underwent pretreatment γ-imaging after administration of an ^{131}I-omburtamab dosimetry dose. The study population demographics are presented in Table 1.

^{131}I-Omburtamab Administration

The antibody omburtamab (previously 8H9) was radiolabeled with ^{131}I by Memorial Sloan Kettering Cancer Center's Radiochemistry and Molecular Imaging Probes Core Facility by the method described previously (*6*). ^{131}I-omburtamab was diluted using 1% human serum albumin and filtered using a Millipore (0.2 μm) filter. All patients were assessed for catheter patency and optimal CSF flow to rule out obstruction to CSF flow using the ^{111}In-diethylenetriaminepentaacetic acid CSF flow study. To minimize thyroid uptake, patients were premedicated with oral saturated solution of potassium iodide drops and liothyronine, which was started 5–7 d before administration of ^{131}I-omburtamab. The activity was

Received Nov. 2, 2022; revision accepted Jan. 26, 2023.
For correspondence or reprints, contact Neeta Pandit-Taskar (pandit-n@mkscc.org).
*Contributed equally to this work.
Published online Feb. 9, 2023.

TABLE 1
Subject Demographics and Clinical Characteristics (n = 95)

Characteristic	Patient number (n)
Sex	
Male	53
Female	42
Age at diagnosis (y)	
<5	34
5–10	31
>10	30
Clinical tumor type	
Neuroblastoma	61
Medulloblastoma	13
Ependymoma	5
Metastatic melanoma	2
Pineoblastoma	2
Choroid plexus carcinoma	2
Retinoblastoma	2
Embryonal neuroepithelial tumor	1
Embryonal tumor with neuropil and true rosettes	1
High-grade glioma	1
Metastatic breast carcinoma	1
Metastatic ovarian carcinoma	1
Metastatic sarcoma	1
Primitive neuroectodermal brain tumor	1
Rhabdomyosarcoma	1

administered intraventricularly via Ommaya reservoir access, with the catheter tip terminating in the lateral ventricle.

For pretherapy dosimetry imaging, patients were injected with 75 ± 5 MBq of ^{131}I-omburtamab and serial whole-body γ-camera imaging was performed, which was used to estimate the absorbed dose to the CSF and ventricles. Subsequently, patients received treatment with ^{131}I-omburtamab (activity, 370–2,960 MBq). Posttreatment dosimetric assessment was not performed.

Blood Measurements

Serial peripheral blood samples were obtained, including a baseline sample before injection of the pretherapy imaging dose of ^{131}I-omburtamab and after injection around 15 min, 30 min, 1 h, 2 h, 4–6 h, 18–24 h, and 44–48 h. Samples were weighed and counted in duplicate in the scintillation well counter (LKB Wallac) calibrated for ^{131}I (cpm/MBq), together with the appropriate standard. These data were used to determine the radiolabeled antibody kinetics and dosimetry in blood. The measured count rates were corrected for background count rate and converted to percentage of injected activity per gram, decay-corrected to the time of administration. The following biexponential function was fit to the resulting blood time–activity concentration data using Excel: $Y(t) = A\exp(-\lambda_1 t) + B\exp(-\lambda_2 t)$, where A and B are the 0 time–activity concentrations (in MBq/g), λ_1 and λ_2 are the clearance constants (in 1/h), and t is the time after administration (in h). The function Y(t) was multiplied by the exponential decay factor for ^{131}I (physical half-life, 8.04 d) to yield the decayed time–activity concentration data: $C(t) = Y(t) * \exp^{[-0.693t/(8.04*24)]}$. Integration of this function yields the ^{131}I time-integrated activity concentration; when multiplied by the average energy emitted per decay for ^{131}I β-particles (0.405 g·cGy/μCi·h), it yields the absorbed dose per unit administered activity. These absorbed-dose estimates assume complete local absorption of the ^{131}I β-particles and ignore the small ^{131}I γ-ray dose contribution.

^{131}I-Omburtamab Dosimetry

Whole-body serial planar images were acquired by γ-camera imaging on a Philips Forte (n = 78 patients), Philips/ADAC Vertex (n = 5 patients), Philips Skylight (n = 3 patients), Philips Precedence (n = 4 patients), and GE Discovery 670 (n = 5 patients). Imaging was performed at 3 time points (3 ± 1, 23 ± 2, and 47 ± 2 h) after intraventricular administration of ^{131}I-omburtamab. Planar anterior and posterior images from vertex to pelvis were obtained for all patients at a scan speed of 10 cm/min. All cameras used for imaging (Philips Forte, Vertex, and Skylight cameras and the GE Discovery 670) were equipped with 0.625-in-thick sodium iodide crystals and high-energy collimators. A calibrated ^{131}I standard of ~7.4 MBq was placed alongside the patient for all images.

Regions of interest (ROIs) were manually drawn around the spinal CSF on the posterior image acquired on day 0 and were copied to the anterior image on day 0, as well as to the anterior and posterior images acquired on days 1 and 2 after injection. A separate ROI of equal area was placed 1 to 2 cm to the right of the CSF ROI to estimate the body background activity. The difference in counts between these 2 ROIs provided the net counts within the CSF. Additional ROIs were placed over the ventricles and the whole body on both anterior and posterior images acquired at all 3 time points after injection. Background ROIs were placed adjacent to the ventricles and whole body to estimate background counts. The means were calculated from values obtained on anterior and posterior images. ROI net (background subtracted) geometric mean counts at each time point were converted to activity (in MBq) by dividing by the ^{131}I calibration factor (in counts/MBq).

CSF volume was estimated to be 140 mL, equally distributed between the spinal column and the ventricles. In addition, the CSF volume was scaled based on patient age for younger patients according to the data published by Triarico et al. (*8*). For each ROI, the time–activity data were fit to exponential functions using Excel and the respective functions. The curve was integrated; divided by the CSF, ventricle, and whole-body masses to yield the time-integrated activity concentrations; and multiplied by the equilibrium dose constant for ^{131}I β-particles to yield the respective absorbed doses. First-order attenuation corrections were performed using an ^{131}I linear attenuation coefficient of 0.11 cm^{-1}. For the ventricles, attenuation correction was based on the half-thickness of the measured anterior–posterior dimension of brain on MRI. For CSF, attenuation correction was based on the average CSF depth as measured on MRI sagittal images at the levels of C3, T1, T5, T10, and L4 vertebrae. The normal brain-surface absorbed dose was assumed to be 50% of the absorbed dose to the ventricles. The whole-body attenuation correction was based on the assumption of 10-cm average half-thickness (water equivalent) of the patient in the anterior–posterior direction.

Statistical Analysis

A Mann–Whitney U test for unpaired 2-sample data was used to investigate whether the means for various metrics among different age groups were statistically significant ($P < 0.05$).

RESULTS

Patients

A total of 95 patients (53 male and 42 female; age, 10 ± 11 y; range, 1–54 y) imaged between November 2004 and February 2020 were included in the analysis (Table 1). The average net administered activity of ^{131}I was 75 ± 5 MBq (range, 54–86 MBq). Patients had no severe adverse reactions to the administered activity. Acute side effects were minor, including headache, nausea, or vomiting, which did not vary for 1,850 vs. 2,960 MBq.

Biodistribution

Representative images of patients from different age cohorts are shown in Figure 1. Activity in the Ommaya reservoir at the injection site was not visually discernable (n = 3 patients), minimal or mild (n = 83 patients), or visibly prominent (n = 8 patients) at the first imaging time point and subsequently decreased over 24–48 h. Activity was seen in the fourth ventricle–basal cistern region and CSF canal on day 0 at 2- to 4-h imaging. Distribution along the cerebral hemisphere was noted in all patients: it was seen at 24 h in 77 patients and at 48 h in 18 patients. The uptake was symmetric for 63 patients and mildly asymmetric (differential right vs. left activity noted visually) for the remaining 32 patients. A total of 16 patients exhibited increased uptake in the left side (1 of these patients had photopenia on the right side secondary to surgery), whereas for another 16 patients, increased uptake was noted in the right side of the cerebral hemisphere.

Systemic blood-pool activity was not seen in most patients, except in 5 patients with low-level activity noted at 24–48 h. For kidneys, no discernable uptake was seen in 62 patients at initial imaging, whereas 35 patients showed mild uptake; excreted activity in kidneys and bladder was first noted at 2–4 h, with greater visualization at 24 and 48 h.

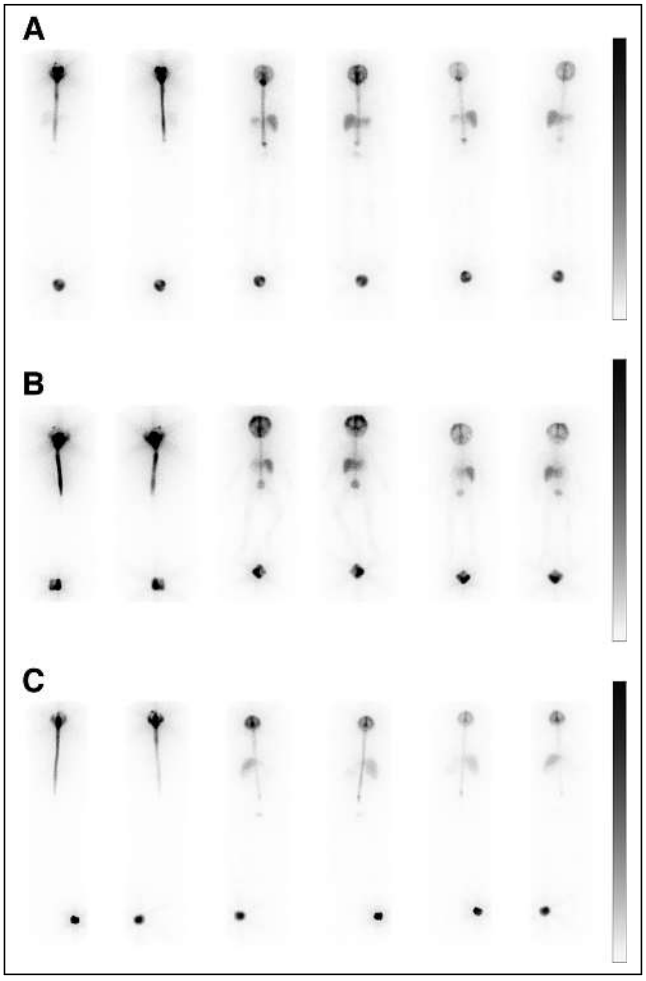

FIGURE 1. Representative planar images of patients from different age subgroups. Displayed scale is 0–100 voxel counts. (A) Anterior (left) and posterior (right) whole-body images of ^{131}I-omburtamab biodistribution at 4, 24, and 48 h. For this patient, calculated absorbed dose was 0.38 cGy/MBq for CSF and 1.36 cGy/MBq for ventricles. Initial standard activity of ^{131}I was 7.5 MBq (200 μCi). (B) Second example patient (1.8 y of age). (C) Third example patient (21 y of age).

Activity in the spinal column or CSF was uniformly noted in all patients in the initial images and decreased with time. Thyroid uptake was not visually noted in most patients (n = 91) or was visualized with mild activity at 24- or 48-h imaging in 4 patients. Liver activity was mostly seen at 24–48 h, initially increasing between 2–4 h and 24 h with later stability or slowly decreasing through 48 h. The activity in the liver was only slightly elevated above that background, and in 2 patients, it was not visually discernable. In most patients, there was no splenic uptake (n = 59), whereas mild uptake was noted in some patients (n = 36) that decreased at 48 h. Mild uptake in the stomach was noted in 18 patients at 24 h and in 3 patients at 48 h, with an overall trend of decreasing activity between 24 and 48 h. In 7 patients who had a ventriculoperitoneal shunt, mild uptake was noted in the abdomen and peritoneal region at 24–48 h (Fig. 2). Mild activity in the bones or marrow was noted in 2 patients at 24- to 48-h imaging.

Kinetics and Absorbed Doses

Clearance half-times were 13 ± 11 h (range, 5–75 h; median, 9 h) for CSF, 8 ± 3 h (range, 3–17 h; median, 8 h) for ventricles, and 41 ± 11 h (range, 23–81 h; median, 40 h) for the whole body. CSF and ventricle clearance times were significantly higher for the subcohort of patients older than 10 y compared with the subcohort of patients younger than 5 y (Table 2). For <5 y, 5–10 y and >10 y, whole-body clearance times were significantly different for each of the 3 subcohorts (<5, 5–10, and >10 y; Table 2). Whole-body retention at the 3 imaging time points was 74% ± 19%, 59% ± 16%, and 38% ± 12%, respectively (Supplemental Fig. 1) (supplemental materials are available at http://jnm.snmjournals.org). Mean absorbed doses were 0.63 ± 0.38 cGy/MBq (range, 0.24–2.25 cGy/MBq; median, 0.52 cGy/MBq) for CSF, 1.03 ± 0.69 cGy/MBq (range, 0.27–5.15 cGy/MBq; median, 0.83 cGy/MBq) for ventricles, and 0.45 ± 0.32 mGy/MBq (range, 0.05–1.43 mGy/MBq; median, 0.40 mGy/MBq) for the whole body. The CSF mean absorbed dose was higher in the subcohort of patients older than 10 y compared with the subcohort of patients younger than 5 y, whereas the blood absorbed dose was lower (Table 2). No significant differences among the subcohorts were noted for whole-body clearance times. For comparison, the median ^{131}I-omburtamab absorbed doses estimated as projected from ^{124}I-omburtamab PET imaging (*7*) were 0.52 cGy/MBq (CSF), 0.62 cGy/MBq (ventricles), and 0.45 mGy/MBq (whole body).

Effective half-lives and absorbed doses for doses CSF, ventricles, whole body, and blood are summarized in Table 2. The table also includes the corresponding results for the subgroups based on patient age (<5, 5–10, and >10 y). CSF effective half-lives and absorbed doses were significantly higher in patients older than 10 y. No significant difference in ventricle effective half-life or ventricle absorbed dose was observed among the 3 groups. However, significant differences between the oldest subgroup (>10 y) and the other 2 subgroups were observed in blood and whole-body absorbed doses (Table 2).

Blood samples were analyzed in 65 patients. The mean absorbed doses in blood were 0.05 ± 0.05 cGy/MBq (range, 0.003–0.23 cGy/MBq; median, 0.04 cGy/MBq). The mean absorbed doses in the subgroup of patients older than 10 y were significantly lower compared with those for patients in subgroup of patients younger than 5 y and in the 5- to 10-y subgroup (Table 2).

Clinical Follow-up

In phase 1 of the study (ClinicalTrials.gov NCT00089245), 1 instance of dose-limiting toxicity (transient, self-limiting hepatic transaminitis) was encountered. In patients with central nervous system

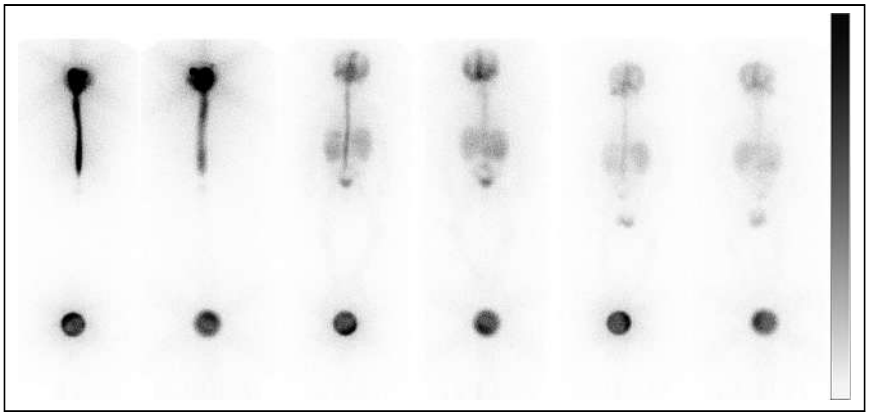

FIGURE 2. Serial anterior and posterior whole-body images of patient with ventriculoperitoneal shunt at 4, 24, and 48 h. For each image, displayed scale is 0–100 voxel counts. Mild uptake is seen in abdomen and peritoneal region at 24–48 h.

relapse of neuroblastoma ($n = 15$) treated with multimodality therapy including ^{131}I-omburtamab, median progression-free survival and overall survival were 7.5 and 11.1 y, respectively. These data are far superior to historical data for patients with central nervous system relapse of neuroblastoma, in whom reported mortality was 100% (*9*). In patients with other nonneuroblastoma diagnoses ($n = 21$), 6 patients survived more than 5 y after radioimmunotherapy, including 2 patients with ependymoma and 1 patient each with medulloblastoma, chordoma, choroid plexus carcinoma, and embryonal tumor with multilayer rosettes (*10*).

DISCUSSION

The results of the current analysis are consistent with our previously published experience with ^{124}I-omburtamab quantitative PET/CT imaging (*7*) in a patient cohort administered pretherapeutic activity of ^{131}I-omburtamab. Compared with ^{124}I-omburtamab PET imaging, ^{131}I-based planar γ-camera imaging is more widely available, more practical, and less expensive than ^{124}I-based dosimetry. However, ^{131}I planar γ-camera imaging-based dosimetry poses several technical challenges for accurate activity quantitation relative to ^{124}I-based PET imaging approaches. For the initial patients in our cohort, SPECT/CT scans could not be performed because such scanners were not available at the time (2004); therefore, only SPECT was performed. The need to anesthetize the younger pediatric patients imposed restrictions on overall scan duration. In the interest of developing a practical scan protocol for this patient population, we performed serial planar whole-body scans at the nominal times of 4, 24, and 48 h after injection and only 1 rapid (20 s/stop) SPECT scan of the head at 24 h.

The intraventricular route of administration allows the delivery of higher therapeutic absorbed-dose ratios to the CSF target volume relative to blood and the whole body. The biodistribution pattern showed good localization and retention into the CSF space, enabling dosing of leptomeningeal disease. The systemic activity distribution was low overall, as expected, with localized delivery of the radiolabeled antibody. The distribution of activity systemically in organs was visually more pronounced at later time points due to systemic absorption and dispersion over time. Activity within the CSF was clearly seen on all 3 serial images. However, the low activity levels within the major organs made our dataset unsuitable for accurate normal organ dosimetry; therefore, the study focused on the feasibility of performing dosimetry to the CSF in the ventricles of the brain and within the spinal column. Rigorous (i.e., pairwise) statistical comparison of the ^{131}I-omburtamab absorbed doses derived by ^{131}I planar imaging and ^{124}I PET imaging was not possible, because individual patients underwent either ^{131}I or ^{124}I pretherapy imaging, not both. Not surprisingly, tissue activities and the resulting absorbed doses were quite variable among patients (e.g., as indicated by the large SD of the mean absorbed doses in Table 2). On average, however, the calculated ^{131}I-omburtamab absorbed doses to the spinal CSF derived from the ^{131}I-omburtamab planar scans were similar (~10%) to the reference standard PET-based method. Larger variation and overestimation (~45%) of the dose to the ventricles only, based on planar γ-scans, was probably related to the placement of ROIs and are similar to our previously published ^{124}I-omburtamab PET data (*7*). Recognizing that quantitation of tissue activity by ^{124}I PET (with 3-dimensional images

TABLE 2
Dosimetry for CSF and Ventricles After Intracranioventricular Administration of ^{131}I-Omburtamab in 95 Patients

	CSF		Ventricles			Whole body	
Age group	Absorbed dose (cGy/MBq)	Clearance (h)	Absorbed dose (cGy/MBq)	Clearance (h)	Blood* (absorbed dose [mGy/MBq])	Absorbed dose (mGy/MBq)	Clearance (h)
<5 y, $n = 34$	0.50 ± 0.18 (0.29–1.12)	10.6 ± 11.7 (5.8–74.6)	1.13 ± 0.96 (0.30–5.15)	7.0 ± 2.3 (3.4–14.0)	0.63 ± 0.37 (0.12–1.57)	0.67 ± 0.31 (0.07–1.41)	41.2 ± 10.2 (25.2–65.0)
5–10 y, $n = 31$	0.52 ± 0.21 (0.24–1.06)	9.4 ± 2.9 (5.5–19.2)	1.01 ± 0.55 (0.38–2.47)	8.0 ± 3.0 (3.8–15.7)	0.67 ± 0.54 (0.10–2.30)	0.46 ± 0.26† (0.05–1.43)	40.6 ± 7.5 (25.8–61.0)
>10 y, $n = 30$	0.90 ± 0.52† (0.24–2.25)	19.1 ± 13.2† (7.8–57.8)	0.95 ± 0.41 (0.27–1.92)	8.3 ± 2.7† (4.3–17.2)	0.30 ± 0.40† (0.03–1.45	0.20 ± 0.16† (0.05–0.66)	42.3 ± 14.3 (22.6–80.8)
All, $n = 95$*	0.63 ± 0.38 (0.24–2.25)	13.0 ± 10.9 (5.5–74.6)	1.03 ± 0.69 (0.27–5.15)	7.7 ± 2.6 (3.4–17.2)	0.54 ± 0.46 (0.03–2.30)	0.45 ± 0.32 (0.05–1.43)	41.3 ± 10.9 (22.6–80.8)

*Blood data were available for $n = 24$, 20, and 21 patients in 3 age groups.
†Significant difference with respect to <5-y group based on Mann–Whitney *U* test for unpaired 2-sample data.
Data are median and range.

and accurate scatter and attenuation corrections) is considerably more accurate than that of ^{131}I planar scanning (with 2-dimensional images, first-order attenuation correction, and no scatter correction), the better-than-50% agreement on average between the ^{131}I- and the ^{124}I-derived absorbed-dose estimates is reasonable. The closer dosimetry agreement for the CSF within spine is likely due to its simpler geometry and greater distance from the Ommaya reservoir injection site. In addition, an important contributing factor to this discrepancy is that PET provides a direct measure of the activity per unit volume (in MBq/cc), whereas quantitative planar images can provide accurate information about the activity but not the volume of distribution in which the activity resides. These dosimetry-based estimates for administered activity were well within the designated limits of safety for normal organs. The absorbed dose to the CSF compartment was high with very low background uptake in the remainder of the body, yielding a 10-fold-higher absorbed dose to the CSF space than to the whole body (mean, 0.045 cGy/MBq). None of the patients were noted to have normal-organ toxicities involving lung, liver, kidney, or marrow. Blood estimates showed a large margin of safety as well for the activity administered in patients. Based on the absorbed-dose estimates to blood, approximately 3,700 MBq of ^{131}I-omburtamab can be administered before exceeding a maximum tolerated blood dose of 200 cGy; this administered activity threshold is well above the actual treatment activities of 1,850–2,960 MBq given intraventricularly. This reflects a high therapeutic index that can be achieved using intraventricular administration. This is supported by the finding of no significant marrow toxicity in these patients resulting from the treatment doses (*6*). There was no difference in whole-body clearance half-times (40–42 h) among age groups, yielding higher whole-body absorbed doses to younger patients as a consequence of their lower body mass (Table 2).

The limitations of the study include the use of planar imaging only and the lack of late imaging time points. Most included patients (84 of 95) were younger than 18 y, with 34 patients younger than 5 y. In principle, increasing the number of scans would have increased the accuracy of the dosimetric calculations, yet performing more than 3 scans more than 48 h after injection would have considerably increased the complexity of the acquisition and was a practical restriction in patients, especially those requiring anesthesia. An additional limitation is that only planar imaging was performed; that is, SPECT imaging was not performed in all patients. Thus, direct comparison between values obtained from planar images and those obtained from SPECT images was not possible for individual patients. Instead, populationwise dosimetric assessments as derived from planar scans were compared with those derived from fully quantitative ^{124}I-based PET.

However, this study delineates the feasibility of planar imaging using a tracer dose of ^{131}I-omburtamab. Because ^{131}I is more widely available and cheaper than ^{124}I, the use of ^{131}I-omburtamab planar imaging offers a practical alternative to theranostic dosimetry estimation. A multicenter phase 2/3 clinical trial (ClinicalTrials.gov NCT03275402) was recently completed. Further data from this completed study will help validate the use of ^{131}I-omburtamab and facilitate efforts to make this widely available for clinical use.

CONCLUSION

In this study, we demonstrate the feasibility of performing dosimetric assessments with ^{131}I-omburtamab for estimation of the absorbed dose to the CSF compartment in patients who will receive ^{131}I-omburtamab therapy. The results show acceptable agreement between dosimetry estimates performed using serial whole-body planar γ-camera imaging and those from ^{124}I-based PET imaging.

DISCLOSURE

This study was funded by a Department of Radiology Seed Grant of Memorial Sloan Kettering Cancer Center (MSK), with support from MSK's Radiochemistry & Molecular Imaging Probes Core, supported in part through NIH/NCI Cancer Center support grant P30 CA008748. Neeta Pandit-Taskar has served as a consultant or advisory board member for or received honoraria from Actinium Pharma, Progenics, Medimmune/AstraZeneca, Illumina, and ImaginAb and conducts research institutionally supported by Y-mAbs Therapeutics, ImaginAb, BMS, Bayer, Clarity Pharma, Janssen, and Regeneron. Kim Kramer received support from NIH grants K08 CA072868, R21 CA089935, and R21 CA117076, as well as grant support from Luke's Lollies and Catie Find a Cure. Pat Zanzonico serves or has served as a consultant to and received honoraria from Novartis and Radionetics and has licensed intellectual property to Y-mAbs. Milan Grkovski received support from Y-mAbs. No other potential conflict of interest relevant to this article was reported.

KEY POINTS

QUESTION: What are the dosimetry estimates for intraventricular administration of ^{131}I-omburtamab?

PERTINENT FINDINGS: Localized delivery of therapeutic antibody delivers high radiation doses to the CSF compartment with minimal systemic distribution and low doses to normal organs. The biodistribution and radiation dosimetry estimates could be reliably obtained with ^{131}I-omburtamab.

IMPLICATIONS FOR PATIENT CARE: ^{131}I-omburtamab–based dosimetry is a feasible option that allows estimation of biodistribution and radiation dose in patients before treatment. The results are comparable to those of ^{124}I-omburtamab imaging.

REFERENCES

1. Kramer K, Kushner B, Heller G, Cheung NK. Neuroblastoma metastatic to the central nervous system. The Memorial Sloan-Kettering Cancer Center experience and a literature review. *Cancer.* 2001;91:1510–1519.
2. Kramer K, Kushner BH, Cheung NK. Oral topotecan for refractory and relapsed neuroblastoma: a retrospective analysis. *J Pediatr Hematol Oncol.* 2003;25:601–605.
3. Modak S, Kramer K, Gultekin SH, Guo HF, Cheung NK. Monoclonal antibody 8H9 targets a novel cell surface antigen expressed by a wide spectrum of human solid tumors. *Cancer Res.* 2001;61:4048–4054.
4. Kramer K, Cheung NK, Humm JL, et al. Targeted radioimmunotherapy for leptomeningeal cancer using (131)I-3F8. *Med Pediatr Oncol.* 2000;35:716–718.
5. Kramer K, Humm JL, Souweidane MM, et al. Phase I study of targeted radioimmunotherapy for leptomeningeal cancers using intra-Ommaya 131-I-3F8. *J Clin Oncol.* 2007;25:5465–5470.
6. Kramer K, Kushner BH, Modak S, et al. Compartmental intrathecal radioimmunotherapy: results for treatment for metastatic CNS neuroblastoma. *J Neurooncol.* 2010;97:409–418.
7. Pandit-Taskar N, Zanzonico PB, Kramer K, et al. Biodistribution and dosimetry of intraventricularly administered (124)I-omburtamab in patients with metastatic leptomeningeal tumors. *J Nucl Med.* 2019;60:1794–1801.
8. Triarico S, Maurizi P, Mastrangelo S, Attinà G, Capozza MA, Ruggiero A. Improving the brain delivery of chemotherapeutic drugs in childhood brain tumors. *Cancers (Basel).* 2019;11:824.
9. Matthay KK, Brisse H, Couanet D, et al. Central nervous system metastases in neuroblastoma: radiologic, clinical, and biologic features in 23 patients. *Cancer.* 2003;98:155–165.
10. Kramer K, Pandit-Taskar N, Kushner BH, et al. Phase 1 study of intraventricular ^{131}I-omburtamab targeting B7H3 (CD276)-expressing CNS malignancies. *J Hematol Oncol.* 2022;15:165.

An Investigation of Lesion Detection Accuracy for Artificial Intelligence–Based Denoising of Low-Dose ^{64}Cu-DOTATATE PET Imaging in Patients with Neuroendocrine Neoplasms

Mathias Loft*[1,2], Claes N. Ladefoged*[1], Camilla B. Johnbeck[1,2], Esben A. Carlsen[1,2], Peter Oturai[1,2], Seppo W. Langer[2–4], Ulrich Knigge[2,5], Flemming L. Andersen[1], and Andreas Kjaer[1,2]

[1]*Department of Clinical Physiology and Nuclear Medicine & Cluster for Molecular Imaging, Copenhagen University Hospital–Rigshospitalet & Department of Biomedical Sciences, University of Copenhagen, Copenhagen, Denmark;* [2]*ENETS Neuroendocrine Tumor Center of Excellence, Copenhagen University Hospital–Rigshospitalet, Copenhagen, Denmark;* [3]*Department of Oncology, Copenhagen University Hospital–Rigshospitalet, Copenhagen, Denmark;* [4]*Department of Clinical Medicine, University of Copenhagen, Copenhagen, Denmark; and* [5]*Departments of Clinical Endocrinology and Surgical Gastroenterology, Copenhagen University Hospital–Rigshospitalet, Copenhagen, Denmark*

Frequent somatostatin receptor PET, for example, ^{64}Cu-DOTATATE PET, is part of the diagnostic work-up of patients with neuroendocrine neoplasms (NENs), resulting in high accumulated radiation doses. Scan-related radiation exposure should be minimized in accordance with the as-low-as-reasonably achievable principle, for example, by reducing injected radiotracer activity. Previous investigations found that reducing ^{64}Cu-DOTATATE activity to below 50 MBq results in inadequate image quality and lesion detection. We therefore investigated whether image quality and lesion detection of less than 50 MBq of ^{64}Cu-DOTATATE PET could be restored using artificial intelligence (AI). **Methods:** We implemented a parameter-transferred Wasserstein generative adversarial network for patients with NENs on simulated low-dose ^{64}Cu-DOTATATE PET images corresponding to 25% ($PET_{25\%}$), or about 48 MBq, of the injected activity of the reference full dose ($PET_{100\%}$), or about 191 MBq, to generate denoised PET images (PET_{AI}). We included 38 patients in the training sets for network optimization. We analyzed PET intensity correlation, peak signal-to-noise ratio (PSNR), structural similarity index (SSIM), and mean-square error (MSE) of $PET_{AI}/PET_{100\%}$ versus $PET_{25\%}/PET_{100\%}$. Two readers assessed Likert scale–defined image quality (1, very poor; 2, poor; 3, moderate; 4, good; 5, excellent) and identified lesion-suspicious foci on PET_{AI} and $PET_{100\%}$ in a subset of the patients with no more than 20 lesions per organ ($n = 33$) to allow comparison of all foci on a 1:1 basis. Detected foci were scored (C_1, definite lesion; C_0, lesion-suspicious focus) and matched with $PET_{100\%}$ as the reference. True-positive (TP), false-positive (FP), and false-negative (FN) lesions were assessed. **Results:** For $PET_{AI}/PET_{100\%}$ versus $PET_{25\%}/PET_{100\%}$, PET intensity correlation had a goodness-of-fit value of 0.94 versus 0.81, PSNR was 58.1 versus 53.0, SSIM was 0.908 versus 0.899, and MSE was 2.6 versus 4.7. Likert scale–defined image quality was rated good or excellent in 33 of 33 and 32 of 33 patients on $PET_{100\%}$ and PET_{AI}, respectively. Total number of detected lesions was 118 on $PET_{100\%}$ and 115 on PET_{AI}. Only 78 PET_{AI} lesions were TP, 40 were FN, and 37 were FP, yielding detection sensitivity (TP/(TP+FN)) and a false discovery rate (FP/(TP+FP)) of 66% (78/118) and 32% (37/115), respectively. In 62% (23/37) of cases, the FP lesion was scored C_1, suggesting a definite lesion. **Conclusion:** PET_{AI} improved visual similarity with $PET_{100\%}$ compared with $PET_{25\%}$, and PET_{AI} and $PET_{100\%}$ had similar Likert scale–defined image quality. However, lesion detection analysis performed by physicians showed high proportions of FP and FN lesions on PET_{AI}, highlighting the need for clinical validation of AI algorithms.

Key Words: ^{64}Cu-DOTATATE; somatostatin receptor imaging; PET/CT; neuroendocrine neoplasms; artificial intelligence

J Nucl Med 2023; 64:951–959
DOI: 10.2967/jnumed.122.264826

Neuroendocrine neoplasms (NENs) are rare diseases that originate from the diffuse neuroendocrine system. PET based on radiotracers targeting the somatostatin receptor (SSR), overexpressed in most NENs, plays a fundamental role in the clinical management of diagnosis, staging, treatment guidance, and follow-up of patients with NENs (*1–4*). Patients may undergo lifelong annual or biannual follow-up with inclusion of SSR-based PET/CT imaging (*3*), resulting in relatively high accumulated radiation exposure that underscores the importance of adhering to the as-low-as-reasonably achievable principle (*5*).

The U.S. Food and Drug Administration–approved activity dose of the SSR PET radiotracer ^{64}Cu-DOTATATE is 148 MBq, with an effective radiation dose of 4.7 mSv (*6*). One way to reduce the PET-related radiation burden is by reducing the radiotracer activity dose. By analyzing simulated dose-reduced PET images, we previously demonstrated that the injected ^{64}Cu-DOTATATE activity could be reduced to approximately 100 MBq without loss of clinically relevant information (*7*). With activity dose reduction to less than 50 MBq, image quality was suboptimal and lesion detection sensitivity was low.

Deep learning (DL), a subtype of artificial intelligence (AI), has recently been proposed as a tool for low-count PET image noise reduction (*8*), because it has been shown to outperform conventional denoising methods while retaining lesion detectability and quantitative accuracy in oncologic PET (*9,10*). However, limited contrast recovery has been observed for smaller lesions (<1 cm^3), which challenges the use of DL methods when lesion detectability is important for clinical diagnosis.

When evaluating the performance of AI methods in medical imaging, discrepancies may arise between conventional fidelity-based metrics, for example, structural similarity index (SSIM) and mean-square error (MSE), and objective clinical task–based metrics. For example, the application of a denoising DL algorithm on simulated low-dose SPECT

Received Aug. 24, 2022; revision accepted Jan. 31, 2023.
For correspondence or reprints, contact Andreas Kjaer (akjaer@sund.ku.dk).
*Contributed equally to the work.
Published online May 11, 2023.

images in a phantom study by Yu et al. (*11*) did not improve the signal detection task despite showing improvements in fidelity-based metrics. Similarly, using a denoising DL algorithm to augment low-dose SPECT myocardial perfusion scintigraphy images, Yu et al. (*12*) found poor performance in the detection of myocardial defects, whereas the fidelity-based metrics were improved. Discrepancies are not limited to denoising algorithms. Yang et al. (*13*) found that implementation of a DL algorithm for CT-less attenuation correction of ^{18}F-FDG PET/CT images from oncologic patients resulted in false-negative (FN) lesions and the appearance of false-positive (FP) lesions when the DL PET images were reviewed by radiologists, even though convincing fidelity-based metrics were found. As highlighted in the recently published Recommendations for Evaluation of Artificial Intelligence for Nuclear Medicine (RELAINCE) guidelines (*14*), it is therefore essential to include evaluation of relevant clinical tasks early in the development of the algorithms and to not rely solely on fidelity-based metrics.

In the current study, we evaluated to what extent application of a DL-based model could assist in reducing the image noise of suboptimal, low-dose ^{64}Cu-DOTATATE PET images while retaining finer image structures such as tumor lesions. The clinical goal of SSR PET imaging is to ensure correct lesion detection, disease classification, and staging of patients with NENs. In accordance with the RELAINCE guidelines (*14*), we therefore evaluated the clinical task of detecting tumor lesions on denoised, low-dose PET images from patients with NENs, in addition to evaluation of the Likert scale–defined image quality and conventional fidelity-based metrics.

MATERIALS AND METHODS

Patient Population

The study is a continuation of our previously reported activity dose reduction PET investigation performed in patients with NENs (*7*). We retrospectively included the same 38 patients with NENs referred to a

TABLE 1
Patient Characteristics

Characteristic	Data (n = 38)	Subset for clinical image analysis (n = 33)*
Sex		
Female	21 (55)	19 (58)
Male	17 (45)	14 (42)
Age (y)		
Median	64	64
Range	37–84	37–84
Site of primary tumor		
Small intestine	21 (55)	16 (49)
Pancreas	11 (29)	11 (33)
Lung	3 (8)	3 (9)
Other	3 (8)	3 (9)
Previous treatment†		
Surgery	29 (76)	27 (82)
Somatostatin analogs	23 (61)	18 (55)
Peptide receptor radionuclide therapy	12 (32)	8 (24)
Chemotherapy	10 (26)	7 (21)
Radiofrequency ablation (liver metastases)	2 (5)	2 (6)
Ki-67 proliferation index		
<3%	9 (24)	8 (24)
3%–20%	26 (68)	22 (67)
>20%	3 (8)	3 (9)
Dose (MBq)‡		
$PET_{100\%}$	191 (169–209)	191 (172–209)
$PET_{25\%}$/PET_{AI}	48 (42–52)	48 (43–52)

*Patients with >20 lesions per organ (n = 5) were excluded for clinical image analysis. Patients used for clinical image analysis (n = 33) thus represent subset of all 38 patients included in training sets.

†Some patients received multiple treatments. Therefore, total number of treatments exceeds number of patients.

‡Dose at $PET_{100\%}$ is ^{64}Cu-DOTATATE activity dose given to patient for PET/CT. $PET_{25\%}$ and PET_{AI} dose is derived from simulated equivalent dose at 25% of $PET_{100\%}$ dose.

Data are number followed by percentage in parentheses, except for age and dose (median and range).

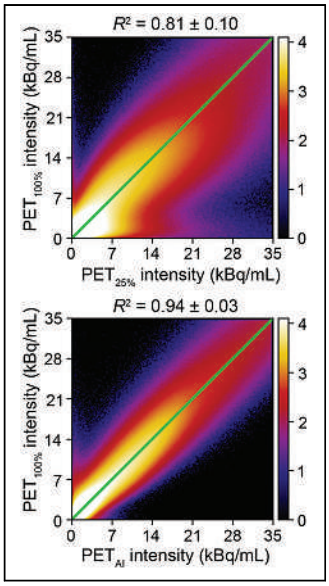

FIGURE 1. Joint histogram of PET intensity values for $PET_{25\%}$ (top) and PET_{AI} (bottom) versus reference $PET_{100\%}$. Green line is identity line, and R^2 is shown above each image. Analysis was performed on training sets (n = 38).

routine ^{64}Cu-DOTATATE PET/CT at the Department of Clinical Physiology and Nuclear Medicine, Copenhagen University Hospital–Rigshospitalet, between April and September 2019 with PET list-mode data available. The study was approved by the Danish Patient Safety Authority (reference 31–1521–453) according to Danish regulations, and the requirement to obtain written informed consent was waived.

PET/CT Acquisition and Image Reconstruction

PET/CT acquisition, PET reconstruction, and generation of reduced-dose PET equivalents were performed as previously described (*7*). Patients were injected with approximately 200 MBq of ^{64}Cu-DOTATATE based on our clinical studies (*15–18*). PET acquisition was performed approximately 1 h later with a Siemens Biograph 128 mCT PET/CT scanner with an axial field of view of 221 mm and a 4 min/bed position acquisition time. A standard routine whole-body diagnostic CT imaging series was performed. Simulated low-dose ^{64}Cu-DOTATATE PET images corresponding to 25% ($PET_{25\%}$) of the injected activity of the reference full dose ($PET_{100\%}$) were generated by randomly deleting events in the PET list-mode file using LMChopper (e7-tools; Siemens Healthineers). We created 5 realizations of the $PET_{25\%}$ images. This was done to increase the number of training samples and perform data augmentation because of noise variation among the realizations. Reconstruction of both $PET_{100\%}$ and $PET_{25\%}$ was performed using 3-dimensional (3D) ordinary Poisson ordered-subset expectation maximization with 2 iterations and 21 subsets, including time of flight at 540 ps and modeling of the point spread function, followed by smoothing by a gaussian postprocessing filter at 2 mm full width at half-maximum. The reconstructed image size was 400 × 400 × 426 voxels with a voxel size of 2.04 × 2.04 × 2.00 mm^3.

PET Image Preprocessing

$PET_{25\%}$ images were first cropped to 256 × 256 × 426 voxels to minimize the effect of voxels outside of the body. We extracted patches of 64 × 64 × 9 voxels with a stride of 9 voxels in each direction, excluding patches with maximum PET or CT values that were less than empirically selected thresholds (<10 Bq/mL or <−200 HU, respectively) to limit empty patches. A total of 762,338 patches were extracted for each of the 5 noise realizations across the 38 patients.

Network Setup and Training

To generate the denoised PET images (PET_{AI}), we implemented a parameter-transferred Wasserstein generative adversarial network (PT-WGAN) for low-dose PET noise reduction inspired by Gong et al. (*19*). The network type was chosen because the authors demonstrated it had better performance than a pure 2-dimensional (2D) or 3D convolutional neural network on the same dataset. Supplemental Appendix A gives a more detailed overview (supplemental materials are available at http://jnm.snmjournals.org). In short, the PT-WGAN consists of 2 parts, a generator and a discriminator, where the generator is a hybrid 2D and 3D U-netlike network pretrained without the discriminator to improve stability and convergence during training. The hybrid combination was introduced by Gong et al. (*19*) to limit computational resources. The model training and evaluation were done using 5-fold cross-validation. In each fold, we first reserved a test set consisting of one fifth of the 38 patients for evaluation that was not part of model training for that fold. Next, we reserved 10% of the remaining four fifths of the data for validation during training (used to detect overfitting) and trained the model on the remaining patients. After the 5 repetitions, all 38 patients had at one point been in a test set, and a PET_{AI} image was therefore created. We did not vary any hyperparameters among the folds.

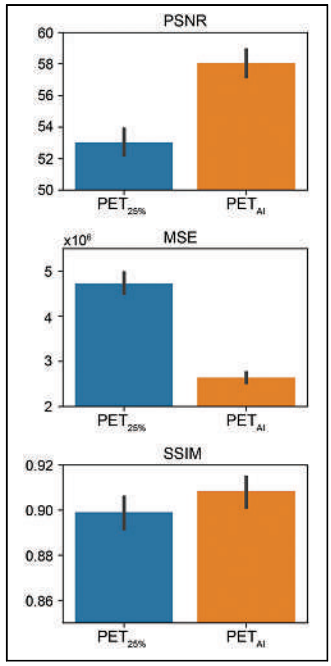

FIGURE 2. Image similarity metrics: PSNR (top), MSE (middle), and SSIM (bottom). Error bars mark 95% CI. Analysis was performed on training sets (n = 38).

Objective Visual Similarity Analysis

We evaluated the quantitative accuracy of $PET_{25\%}$ and PET_{AI} by computing a joint histogram of the PET activity relative to $PET_{100\%}$, and we compared the image fidelity using the following standard similarity comparison metrics: peak signal-to-noise ratio (PSNR), SSIM, and MSE. We restricted the comparison to voxels inside the patient volume defined using the CT image (more than −900 HU).

Clinical Image Analysis

Two readers placed side by side collectively analyzed all PET/CT scans: a board-certified nuclear medicine physician with 10 y and a nuclear medicine physician in training with 4 y of experience in reading SSR-based PET/CT scans from patients with NENs. To analyze all patients' lesions on a 1:1 basis, only PET images from a subset of patients with no more than 20 lesions in each organ system (n = 33), of the initially included 38 patients used for training, were used for the clinical image analysis. The readers were blinded to the PET image ($PET_{100\%}$ or PET_{AI}) and analyzed the images in 2 clusters, each containing either $PET_{100\%}$/CT or PET_{AI}/CT from 1 of the 33 patients, presented to the readers in random order. After 12 wk of quarantine, the second cluster was analyzed by the same readers. Mirada DBx 1.2.0 was used for the clinical analysis.

Likert Scale–Defined Image Quality

The image quality of the PET images was rated on a 5-point Likert scale: 1 (very poor), 2 (poor), 3 (moderate), 4 (good), and 5 (excellent). Scores 4 and 5 were accepted as diagnostic image quality.

Number and Certainty of Detected Lesions

On each PET image, any focus considered lesion-suspicious was annotated. The CT was used mainly to confirm the anatomic location of the PET focus. Each focus was given a certainty score for a definite lesion (C_1) and for a focus indicative of a lesion or a suspicious area (C_0), in which the presence of a lesion could not be ruled out. The images were then unblinded and the identified foci were matched on $PET_{100\%}$ and PET_{AI}. $PET_{100\%}$ was considered the standard of truth. Concordant, true-positive (TP) lesions identified on both $PET_{100\%}$ and PET_{AI} and

discordant lesions—FN lesions visible on $PET_{100\%}$ but not PET_{AI} and FP lesions visible on PET_{AI} but not $PET_{100\%}$—were grouped according to organs and regions. Organ- or region-specific and overall sensitivities and false discovery rates (FDRs) for detected lesions on PET_{AI} were calculated as TP/(TP+FN) and FP/(TP+FP), respectively, on a per-lesion basis. We evaluated the distribution of TP, FP, and FN lesions according to the number of lesions detected on $PET_{100\%}$ in the following groups: no lesions, 1 lesion, 2–5 lesions, 6–10 lesions, and more than 10 lesions. We also analyzed the per-patient sensitivities and specificities for the detection of organ- or region-specific and overall disease based on matched lesions on a per-patient basis, with $PET_{100\%}$ as the reference.

Patient Characteristics Based on Lesion Types

To analyze whether patient-specific characteristics contributed to the occurrence of FN and FP lesions, we compared patients with FN or FP lesions and patients with either TP-only or no lesions with the following variables: injected activity dose, weight, activity dose per weight, and liver background (SUV_{mean} measured in a 3-cm-diameter sphere in the right lobe of the liver in an area free of blood vessels and lesions).

Statistics

$PET_{100\%}$ was considered the standard of truth. For the clinical analysis, the proportion of PET images with Likert scale–defined image quality scores of good or excellent (considered diagnostic image quality) were analyzed with the McNemar test for paired proportions for PET_{AI} versus $PET_{100\%}$. The McNemar test was also used for analysis of the distribution of C_1 and C_0 lesion scores among TP lesions on PET_{AI} versus $PET_{100\%}$. For sensitivities, specificities, and FDR, 95% CI was calculated with the Clopper-Pearson exact method. For comparison of the patient-specific characteristics, we used Mann–Whitney *U* tests. Reference groups were patients with only TP lesions or no lesions for the patient-specific comparisons. R version 3.6.1 was used for the clinical statistical analysis. For comparison of the PET intensity correlations of $PET_{25\%}$ and $PET_{100\%}$ versus PET_{AI} and $PET_{100\%}$, we computed a goodness-of-fit value (R^2) to the identity line for each of the patients. Image fidelity metrics of $PET_{25\%}$ and $PET_{100\%}$ versus PET_{AI} and $PET_{100\%}$ were calculated with NumPy version 1.22.4 and scikit-image version 0.18.2 (*20*) in Python version 3.8.

RESULTS

Patient Characteristics

Characteristics of the patients are shown in Table 1.

Objective Visual Similarity Analysis

The AI algorithm was able to reduce the noise while improving the quantitative accuracy in the images (Fig. 1), resulting in better correlation with $PET_{100\%}$ for PET_{AI} (R^2 = 0.94) compared with $PET_{25\%}$ (R^2 = 0.81). The model increased PSNR and SSIM while decreasing MSE compared with $PET_{25\%}$ (Fig. 2).

Likert Scale–Defined Image Quality

Likert scale–defined image quality scores are shown in Figure 3. All $PET_{100\%}$ (33/33) and all but 1 PET_{AI} (32/33) had a Likert scale–defined image quality score of 4 (good) or 5 (excellent) and were thus considered diagnostic image quality. No statistically significant difference in the proportions of patients with diagnostic image quality PET was observed (P = 1.0). Figure 4 shows a representative example of the AI algorithm's ability to reduce noise and apparently restore the Likert scale–defined image quality of low-dose $PET_{25\%}$.

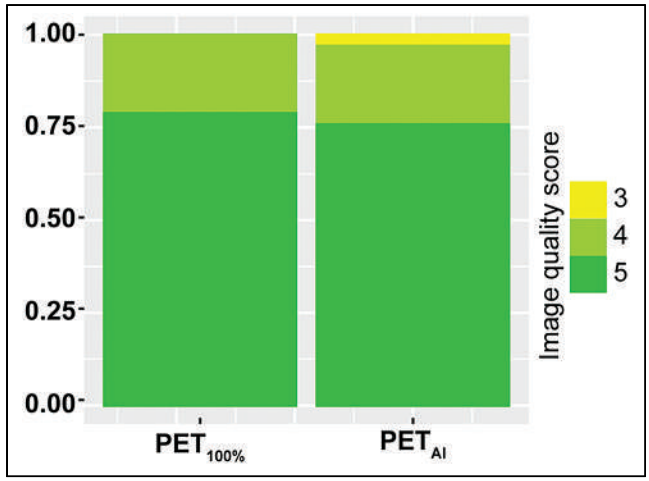

FIGURE 3. Distribution of Likert scale–defined image quality scores—3, moderate; 4, good; and 5, excellent (Likert scale–defined image quality scores 4 and 5 are considered diagnostic image quality)—on $PET_{100\%}$ and PET_{AI}. No patient had Likert scale–defined image quality score below 3. Analysis was performed on patient subset for clinical image analysis consisting of patients with ≤20 lesions per organ (n = 33).

Number of Detected Lesions

Table 2 shows the number of lesions detected on $PET_{100\%}$ and PET_{AI} grouped by organs and regions. The total number of lesions was similar on $PET_{100\%}$ and PET_{AI}, with 118 and 115 lesions detected, respectively. However, only 78 lesions were TP on PET_{AI}, yielding lesion detection sensitivity of 66% (78/118). In addition, 37 FP lesions were detected on PET_{AI}, corresponding to FDR of 32% (37/115). The same trend, with high rates of FP and

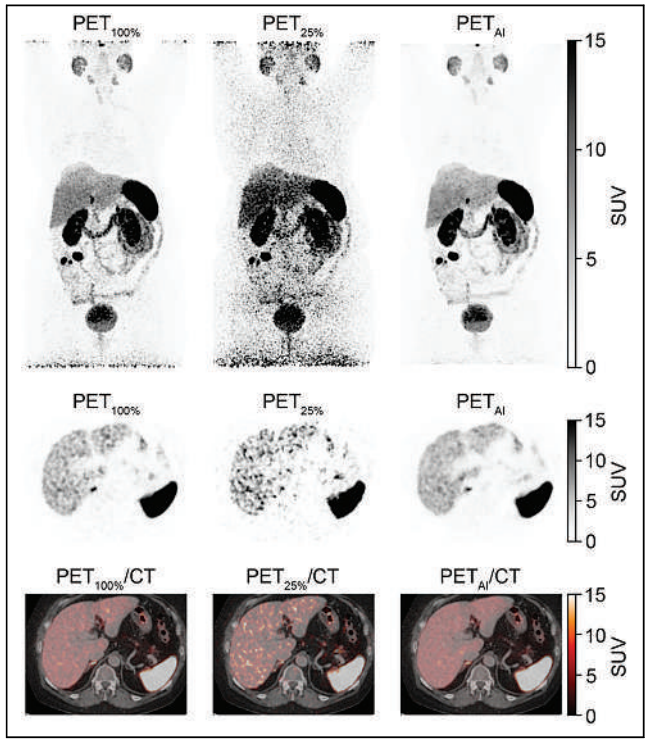

FIGURE 4. Examples of full-dose $PET_{100\%}$, low-dose $PET_{25\%}$, and denoised PET_{AI}.

TABLE 2
Number of Lesions Grouped by Organs and Regions in 33 Patients with NENs

Organ or region	No. of lesions $PET_{100\%}$	No. lesions PET_{AI}	TP	FP	FN	Sensitivity*	FDR*
Liver	36	38	17	21	19	47 (30–65)	55 (38–71)
Pancreas	6	7	6	1	0	100 (54–100)	14 (0–58)
Abdominal	49	47	36	11	13	73 (59–85)	23 (12–38)
Extraabdominal LNs	5	6	5	1	0	100 (48–100)	17 (0–64)
Bone	17	12	10	2	7	59 (33–82)	17 (2–48)
Other	5	5	4	1	1	80 (28–99)	20 (1–72)
Overall	118	115	78	37	40	66 (57–75)	32 (24–42)

*Data for sensitivity and FDR are percentages followed by 95% CI in parentheses.

Abdominal = intestines, intraabdominal carcinosis, and intraabdominal lymph nodes (LNs); other = brain (1), ovary (1), thyroid or parathyroid (1), and skin (2). Analysis is performed on patient subset for clinical image analysis consisting of patients with ≤20 lesions per organ (n = 33).

FN lesions yielding low lesion detection sensitivity and high FDR, was observed for the abdomen and liver. A representative example of a patient with a FN liver lesion is shown in Figure 5. This patient had additional TP liver lesions. Figure 6 shows a representative example of a patient with a FP lesion detected only on PET_{AI}. This was the only lesion detected on either of the scans, that is, no TP lesions. Figure 7 shows the distribution of TP, FP, and FN lesions according to the number of detected lesions on $PET_{100\%}$. Per-patient sensitivity and specificity for the detection of NEN disease across organs and regions are shown in Supplemental Table 1.

Certainty in Detected Lesions

The distributions of lesion certainty scores (C_1 and C_0) across organs and regions are shown in Table 3. Most TP lesions were given C_1 scores, suggesting that the readers were certain of the presence of a lesion on both $PET_{100\%}$ and PET_{AI}. For the FN lesions, larger fractions of C_0 lesions were observed on $PET_{100\%}$, suggesting that the readers were uncertain whether a suspicious focus indeed was a lesion in these cases. Of the 37 FP lesions detected only on PET_{AI}, 23 (62%) were given a score of C_1, suggesting that the readers were certain of the presence of a lesion.

Patient Characteristics Based on Lesion Types

Patient-specific characteristics are shown in Table 4. There was a trend of a lower weight-adjusted activity dose in the groups of patients with FP compared with the groups of patients with no lesions or only TP lesions, although this was not statistically significant.

DISCUSSION

Using randomly undersampled list-mode ^{64}Cu-DOTATATE PET data, we simulated low-dose PET images and implemented a state-of-the-art denoising PT-WGAN-based AI algorithm to test whether the image quality and lesion detection rate could be restored. Our main finding was that only 78 of 118 lesions could be detected on PET_{AI} (TP), and of 115 lesions detected on PET_{AI}, 37 were FP, corresponding to lesion detection sensitivity and FDR of 66% (78/118) and 32% (37/115), respectively. Despite the improvements of the fidelity-based metrics and the Likert scale–defined image quality performed by the AI algorithm, the discrepancies between $PET_{100\%}$ and PET_{AI} for the detection of correct lesions highlight the need for clinical validation when assessing the performance of AI algorithms.

According to the fidelity-based metrics, perceived Likert scale–defined image quality, and total number of detected lesions, the algorithm appeared successful in denoising low-dose $PET_{25\%}$. However, low lesion detection sensitivity on PET_{AI} shows that a large fraction of the lesions was not captured by the AI algorithm. Even more alarming was the high proportion of FP lesions observed only on PET_{AI}, yielding high FDR. For most of the 37 FP lesions, the readers assigned a C_1 certainty score, suggesting high certainty that the focus was indeed a lesion. Because the readers generally considered PET_{AI} to be of diagnostic image quality (Likert scale–defined image quality score of good or excellent), they may have been prone to accepting an apparent lesion-suspicious focus as a lesion without raising concern that

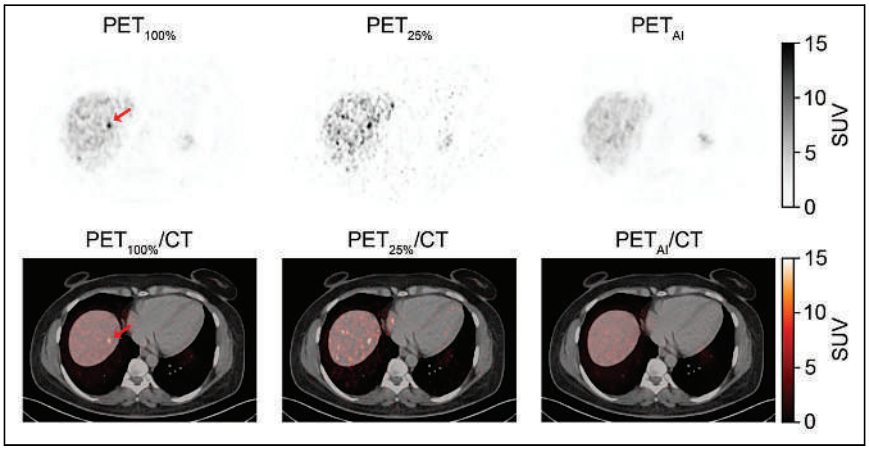

FIGURE 5. Patient with FN liver lesion. Patient had additional concordant TP liver lesions. Arrows mark lesion location on $PET_{100\%}$ and $PET_{100\%}$/CT. $PET_{25\%}$ shown for reference.

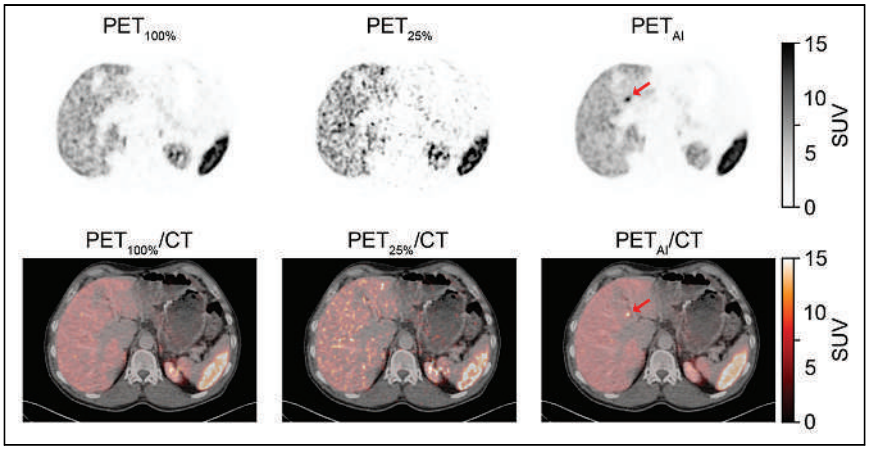

FIGURE 6. Patient with FP liver lesion on PET_{AI}. Patient had no lesions detected on $PET_{100\%}$. Arrows mark lesion location on PET_{AI} and PET_{AI}/CT. $PET_{25\%}$ shown for reference.

its appearance may result from the algorithm. Importantly, FP and FN lesions were not restricted to patients with multiple lesions on $PET_{100\%}$, in which case a single or a few FN or FP findings would have limited clinical consequences. FP and FN lesions were also found in patients with none or only 1 lesion detected on $PET_{100\%}$, in which case a single misclassified lesion could alter the patient's status from healthy to diseased, or vice versa. This was supported by low per-patient sensitivity and specificity for the presence or absence of disease across organs and regions based on matched lesions. These findings highlight the importance of focusing on the correct clinically relevant task when assessing AI algorithms, as recommended in the RELAINCE guidelines (*14*).

Compared with other advanced DL-based denoising studies on low-dose or fast-acquisition ^{18}F-FDG PET in oncologic patients who showed detection sensitivity of up to 97% (*21,22*), the detection sensitivity of our study was low. Without a comparative study, it is difficult to assess potential causes of this difference. However, the larger training cohorts, 313 patients in a study by Xing et al. (*21*) and 60 patients in a study by Sanaat et al. (*22*), could have an impact. Differences in the patients' tumor phenotypes, the physical properties of ^{18}F versus ^{64}Cu, or the biodistribution of the radiotracer may also contribute. Patients with NENs frequently have metastatic disease with multiple lesions scattered throughout the body. Metastases are often small (≤1 cm), which may impact the performance of the denoising algorithms. In line with this, Yu et al. (*11*) showed poor performance of a DL-based denoising algorithm for signal detection of small signal sizes of denoised low-dose SPECT images. In addition, the liver and the intestines are particularly lesion-prone in patients with NENs, and these organs have relatively high background uptakes of SSR-based radiotracers, making it difficult to distinguish potential lesions from surrounding tissue on low-dose PET. However, we did not find any difference in uptake of ^{64}Cu-DOTATATE in the normal liver of patients with FN or FP lesions compared with patients with no or TP-only lesions. In contrast, a trend of a lower weight-adjusted dose in the group with FP lesions was observed, which could contribute to the FP lesions because of increased image noise.

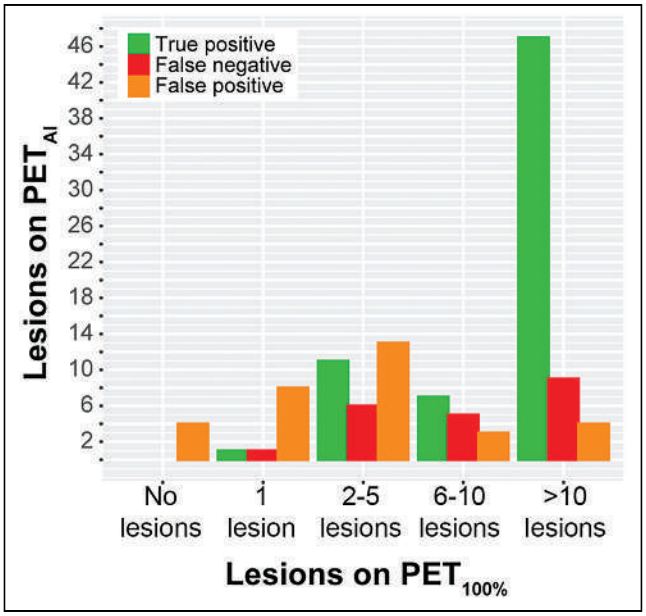

FIGURE 7. Distribution of TP, FP, and FN on PET_{AI} corresponding to number of lesions detected on $PET_{100\%}$. Analysis was performed on patient subset for clinical image analysis consisting of patients with ≤20 lesions per organ (n = 33).

If denoising AI algorithms of low-dose, whole-body SSR PET images are to be implemented clinically, the challenges of FP and FN lesions must be solved. Variations in DL training strategies, including choice of network architecture, loss function, and hyperparameters, might improve performance. We compared the effect of the network architecture by comparing PT-WGAN against traditional 3D U-netlike, residual 3D U-netlike, and adversarial network architectures and found the best performance with PT-WGAN (Supplemental Appendix B). Furthermore, we evaluated the influence of sampling patches over areas with high activity, and although this improved PSNR and MSE, there was no improvement on image structure measured with SSIM (Supplemental Appendix A). We speculate that further improvement might be achieved by incorporating a lesion-based loss term; however, this would require total tumor segmentation of the training patients and was not pursued in this work.

A limitation of the method is the low number of included patients, despite being comparable to other recently published studies of 9–31 patients (*10,19,23*). We chose to use a k-fold cross-validation training strategy to achieve a sufficient number of patients for evaluation, which is a frequently used technique to overcome a low number of patients. This is a significant limitation because clinical AI methods must be evaluated using an independent test set to show robustness and avoid potential data leakage. However, we would not expect lesion detection sensitivity and FDR to improve if tested on an independent test set. Rather, we speculate that the FP or FN findings may be even more pronounced. Although the 38 patients each contribute many data points during training because of the large, whole-body PET data files, these in turn are highly correlated with those extracted from neighboring areas. Inclusion of additional patients in the training sets may assist the AI algorithm in detecting the lesion patterns and may improve the performance. In addition, optimization

TABLE 3
Certainty of Detected Lesions in 33 Patients with NENs

Organ or region	All lesions			TP				FN			FP		
	Total	C_1	C_0	Total	C_1	C_0	*P**	Total	C_1	C_0	Total	C_1	C_0
Liver													
$PET_{100\%}$	36	31	5	17	17	0	1.0	19	14	5	N/A	N/A	N/A
PET_{AI}	38	29	9	17	17	0	N/A	N/A	N/A	N/A	21	12	9
Pancreas													
$PET_{100\%}$	6	6	0	6	6	0	1.0	0	0	0	N/A	N/A	N/A
PET_{AI}	7	7	0	6	6	0	N/A	N/A	N/A	N/A	1	1	0
Abdominal													
$PET_{100\%}$	49	45	4	36	35	1	1.0	13	10	3	N/A	N/A	N/A
PET_{AI}	47	43	4	36	36	0	N/A	N/A	N/A	N/A	11	7	4
Extraabdominal LNs													
$PET_{100\%}$	5	5	0	5	5	0	1.0	0	0	0	N/A	N/A	N/A
PET_{AI}	6	5	1	5	5	0	N/A	N/A	N/A	N/A	1	0	1
Bone													
$PET_{100\%}$	17	16	1	10	10	0	1.0	7	6	1	N/A	N/A	N/A
PET_{AI}	12	11	1	10	9	1	N/A	N/A	N/A	N/A	2	2	0
Other													
$PET_{100\%}$	5	5	0	4	4	0	1.0	1	1	0	N/A	N/A	N/A
PET_{AI}	5	5	0	4	4	0	N/A	N/A	N/A	N/A	1	1	0
Overall													
$PET_{100\%}$	118	108	10	78	77	1	0.5	40	31	9	N/A	N/A	N/A
PET_{AI}	115	100	15	78	77	1	N/A	N/A	N/A	N/A	37	23	14

*P values calculated using McNemar test for paired proportions of distribution of C_1 and C_0 lesion scores in TP lesions on $PET_{100\%}$ vs. PET_{AI}.

Abdominal = intestines, intraabdominal carcinosis, and intraabdominal lymph nodes (LNs); N/A = not applicable; other = brain (1), ovary (1), thyroid or parathyroid (1), and skin (2). Analysis is performed on patient subset for clinical image analysis consisting of patients with ≤20 lesions per organ (n = 33).

of the low-dose PET acquisition or reconstruction regime before running the AI algorithm may improve the performance.

It could be argued that a more comprehensive evaluation of the performance of the denoising algorithm, in terms of restoring lesion detection, could be obtained with a receiver-operating-characteristic analysis (*24*). For example, the detection of regional or organwise and overall ^{64}Cu-DOTATATE avid disease (yes or no), on a per-patient basis, could be performed with 5-point confidence scores (e.g., definitely normal, probably normal, unsure, probably malignant, or definitely malignant) for both $PET_{100\%}$ and PET_{AI}, using an external standard of truth for presence of disease, to compare disease detection performance as the areas under the receiver-operating-characteristic

TABLE 4
Characteristics of 33 Patients with NENs Based on Lesion Type

Parameter	TP-only or no lesions (n = 11)	FN (n = 16)	*P**	FP (n = 15)	*P**
Injected dose (MBq)	188 (181.5–201.5)	190.5 (184–198.9)	0.94	192.0 (184.0–195.6)	0.94
Weight (kg)	76.0 (67–81.5)	73.0 (64.3)	0.87	86.7 (74.0–97.5)	0.09
Dose/weight (MBq/kg)	2.5 (2.4–2.9)	2.6 (2.0–3.1)	0.82	2.3 (2.0–2.6)	0.07
Liver SUV_{mean}	5.0 (4.7–6.6)	5.0 (4.7–6.1)	0.79	6.1 (5.0–6.9)	0.22

*Mann–Whitney *U* test for comparison with reference (TP-only or no lesions group).

Data are shown as medians with interquartile range in parentheses. Analysis is performed on patient subset for clinical image analysis consisting of patients with ≤20 lesions per organ (n = 33). n refers to number of patients in each group. Patients may appear in both FN and FP groups if they have both FP and FN lesions. Accordingly, total number of patients exceeds 33.

curves (*25*). For comparison of performance for the detection of multiple lesions per patients, the areas under the free-response operating characteristic curves, which take into account detection confidence and the location of lesions, could be compared for $PET_{100\%}$ and PET_{AI} using an external standard of truth (*26*). However, we consider $PET_{100\%}$ as the standard of truth to be the most relevant reference in our case, because PET_{AI} is directly derived from the corresponding full-dose images through low-dose simulation and denoising through the AI algorithm. We find the 2-point confidence score (C_1 or C_0) to be representative of the clinical reading situation: the reader either is confident that a lesion is present (C_1) or has some uncertainty and raises a flag (C_0) such that special attention can be drawn to the suspicious area on prior or subsequent scans. Furthermore, we find that the 2-point confidence score sufficiently underscores concerns about using PET_{AI} for lesion detection, because 23 of the 37 FP cases were considered definite lesions (and thus given a C_1 score). Thus, selecting C_1 as the threshold for lesions still provides alarmingly high lesion detection FDR of 23% (23/100) and low lesion detection sensitivity of 71% (77/108).

The Likert scale–defined image quality used in this paper represents the readers' overall subjective assessment of how the images compare to standard ^{64}Cu-DOTATATE PET images seen in the clinical setting. Other definitions of image quality for assessment of AI imaging methods include objective task-based evaluations of the image quality, e.g., lesion detection like in our study, for objective assessment of image quality (*27*). The distinction between the subjective image quality and the objective lesion detection task is important, because the PET_{AI} Likert scale-defined image quality generally were rated as good or excellent; that is, to the reader, the PET_{AI} images overall appear similar to high-quality ^{64}Cu-DOTATATE PET images seen in a clinical setting, whereas the objective lesion detection task demonstrated that the PET_{AI} images were inadequate.

CONCLUSION

We implemented a state-of-the-art PT-WGAN denoising AI algorithm on simulated low-dose ^{64}Cu-DOTATATE PET images from patients with NENs of a suboptimal standard to test whether the image quality and lesion detection rate could be restored. The algorithm improved the image similarity metrics, and the perceived Likert scale–defined image quality of PET_{AI} was equivalent to the full-dose PET images. However, application of the denoising algorithm resulted in FN lesions and FP lesions when compared with full-dose PET in a clinical analysis. The discrepancies highlight the need for relevant clinical validation of AI algorithms.

DISCLOSURE

This project received funding from the European Union's Horizon 2020 research and innovation program under grant agreements 670261 (ERC Advanced Grant) and 668532 (Click-It), the Lundbeck Foundation, the Novo Nordisk Foundation, the Innovation Fund Denmark, the Neuroendocrine Tumor Research Foundation, the Danish Cancer Society, Sygeforsikringen "Danmark," the Arvid Nilsson Foundation, the Neye Foundation, the Research Foundation of Rigshospitalet, PERSIMUNE through the Danish National Research Foundation (grant 126), the Research Council of the Capital Region of Denmark, the Danish Health Authority, the John and Birthe Meyer Foundation, the Danish Agency for Digitization (20196164), and the Research Council for Independent Research. Andreas Kjaer is a Lundbeck Foundation Professor. Ulrich Knigge and Andreas Kjaer are inventors of or hold intellectual property rights on a patent covering ^{64}Cu-DOTATATE. No other potential conflict of interest relevant to this article was reported.

KEY POINTS

QUESTION: Can the image quality and lesion detection rate of low-dose (<50 MBq) ^{64}Cu-DOTATATE PET scans from patients with NENs be restored using state-of-the-art AI for image denoising?

PERTINENT FINDINGS: The denoising AI algorithm performed well on standard image fidelity-based comparison metrics, and the perceived Likert scale–defined image quality was restored. However, clinical assessment showed that more than half of the lesions found on the denoised low-dose ^{64}Cu-DOTATATE PET were FP or FN compared with the full-dose scans.

IMPLICATIONS FOR PATIENT CARE: The study highlights the importance of assessing clinically relevant endpoints when evaluating AI algorithms in nuclear medicine in accordance with the RELAINCE guidelines.

REFERENCES

1. Bozkurt MF, Virgolini I, Balogova S, et al. Guideline for PET/CT imaging of neuroendocrine neoplasms with ^{68}Ga-DOTA-conjugated somatostatin receptor targeting peptides and ^{18}F-DOPA. *Eur J Nucl Med Mol Imaging.* 2017;44:1588–1601.
2. Janson ET, Knigge U, Dam G, et al. Nordic guidelines 2021 for diagnosis and treatment of gastroenteropancreatic neuroendocrine neoplasms. *Acta Oncol.* 2021; 60:931–941.
3. Knigge U, Capdevila J, Bartsch DK, et al. ENETS consensus recommendations for the standards of care in neuroendocrine neoplasms: follow-up and documentation. *Neuroendocrinology.* 2017;105:310–319.
4. Strosberg JR, Halfdanarson TR, Bellizzi AM, et al. The North American Neuroendocrine Tumor Society consensus guidelines for surveillance and medical management of midgut neuroendocrine tumors. *Pancreas.* 2017;46:707–714.
5. International Commission on Radiological Protection. The 2007 Recommendations of the International Commission on Radiological Protection. ICRP publication 103. *Ann ICRP.* 2007;37:1–332.
6. Detectnet label. U.S. Food and Drug Administration website. https://www.accessdata.fda.gov/drugsatfda_docs/label/2020/213227s000lbl.pdf. Updated December 2021. Accessed August 5, 2022.
7. Loft M, Carlsen EA, Johnbeck CB, et al. Activity dose reduction in ^{64}Cu-DOTATATE PET in patients with neuroendocrine neoplasms: impact on image quality and lesion detection ability. *Mol Imaging Biol.* 2022;24:600–611.
8. Wang T, Lei Y, Fu Y, et al. Machine learning in quantitative PET: a review of attenuation correction and low-count image reconstruction methods. *Phys Med.* 2020;76:294–306.
9. Lu W, Onofrey JA, Lu Y, et al. An investigation of quantitative accuracy for deep learning based denoising in oncological PET. *Phys Med Biol.* 2019;64:165019.
10. Schaefferkoetter J, Yan J, Ortega C, et al. Convolutional neural networks for improving image quality with noisy PET data. *EJNMMI Res.* 2020;10:105.
11. Yu Z, Rahman MA, Jha AK. Investigating the limited performance of a deep-learning-based SPECT denoising approach: an observer-study-based characterization. *Proc SPIE Int Soc Opt Eng.* 2022;12035.
12. Yu Z, Rahman MA, Schindler T, et al. AI-based methods for nuclear-medicine imaging: need for objective task-specific evaluation. *J Nucl Med.* 2020;61(suppl 1):575.
13. Yang J, Sohn JH, Behr SC, Gullberg GT, Seo Y. CT-less direct correction of attenuation and scatter in the image space using deep learning for whole-body FDG PET: potential benefits and pitfalls. *Radiol Artif Intell.* 2020;3:e200137.
14. Jha AK, Bradshaw TJ, Buvat I, et al. Nuclear medicine and artificial intelligence: best practices for evaluation (the RELAINCE guidelines). *J Nucl Med.* 2022;63:1288–1299.
15. Pfeifer A, Knigge U, Mortensen J, et al. Clinical PET of neuroendocrine tumors using ^{64}Cu-DOTATATE: first-in-humans study. *J Nucl Med.* 2012;53:1207–1215.
16. Pfeifer A, Knigge U, Binderup T, et al. ^{64}Cu-DOTATATE PET for neuroendocrine tumors: a prospective head-to-head comparison with ^{111}In-DTPA-octreotide in 112 patients. *J Nucl Med.* 2015;56:847–854.
17. Loft M, Carlsen EA, Johnbeck CB, et al. ^{64}Cu-DOTATATE PET in patients with neuroendocrine neoplasms: prospective, head-to-head comparison of imaging at 1 hour and 3 hours after injection. *J Nucl Med.* 2021;62:73–80.

18. Johnbeck CB, Knigge U, Loft A, et al. Head-to-head comparison of ^{64}Cu-DOTATATE and ^{68}Ga-DOTATOC PET/CT: a prospective study of 59 patients with neuroendocrine tumors. *J Nucl Med.* 2017;58:451–457.
19. Gong Y, Shan H, Teng Y, et al. Parameter-transferred Wasserstein generative adversarial network (PT-WGAN) for low-dose PET image denoising. *IEEE Trans Radiat Plasma Med Sci.* 2021;5:213–223.
20. van der Walt S, Schonberger JL, Nunez-Iglesias J, et al. scikit-image: image processing in Python. *PeerJ.* 2014;2:e453.
21. Xing Y, Qiao W, Wang T, et al. Deep learning-assisted PET imaging achieves fast scan/low-dose examination. *EJNMMI Phys.* 2022;9:7.
22. Sanaat A, Shiri I, Arabi H, Mainta I, Nkoulou R, Zaidi H. Deep learning-assisted ultra-fast/low-dose whole-body PET/CT imaging. *Eur J Nucl Med Mol Imaging.* 2021;48:2405–2415.
23. Zhou B, Tsai YJ, Chen X, Duncan JS, Liu C. MDPET: a unified motion correction and denoising adversarial network for low-dose gated PET. *IEEE Trans Med Imaging.* 2021;40:3154–3164.
24. Metz CE. Receiver operating characteristic analysis: a tool for the quantitative evaluation of observer performance and imaging systems. *J Am Coll Radiol.* 2006;3:413–422.
25. Mandrekar JN. Receiver operating characteristic curve in diagnostic test assessment. *J Thorac Oncol.* 2010;5:1315–1316.
26. Thompson JD, Manning DJ, Hogg P. The value of observer performance studies in dose optimization: a focus on free-response receiver operating characteristic methods. *J Nucl Med Technol.* 2013;41:57–64.
27. Jha AK, Myers KJ, Obuchowski NA, et al. Objective task-based evaluation of artificial intelligence-based medical imaging methods: framework, strategies, and role of the physician. *PET Clin.* 2021;16:493–511.

First Total-Body Kinetic Modeling and Parametric Imaging of Dynamic ^{68}Ga-FAPI-04 PET in Pancreatic and Gastric Cancer

Ruohua Chen*[1,2,3], Xinlan Yang*[4], Yee Ling Ng[4], Xiaofeng Yu[1,2,3], Yanmiao Huo[5], Xiuying Xiao[6], Chenpeng Zhang[1,2,3], Yumei Chen[1,2,3], Chaojie Zheng[4], Lianghua Li[1,2,3], Gang Huang[1,2,3], Yun Zhou[4], and Jianjun Liu[1,2,3]

[1]Department of Nuclear Medicine, Ren Ji Hospital, School of Medicine, Shanghai Jiao Tong University, Shanghai, China; [2]Institute of Clinical Nuclear Medicine, School of Medicine, Shanghai Jiao Tong University, Shanghai, China; [3]Shanghai Key Laboratory of Molecular Imaging, Shanghai University of Medicine and Health Sciences, Shanghai, China; [4]Central Research Institute, United Imaging Healthcare Group Co., Ltd, Shanghai, China; [5]Department of Biliary-Pancreatic Surgery, Ren Ji Hospital, School of Medicine, Shanghai Jiao Tong University, Shanghai, China; and [6]Department of Oncology, Ren Ji Hospital, School of Medicine, Shanghai Jiao Tong University, Shanghai, China

Fibroblast activation protein inhibitor (FAPI) is an ideal diagnostic and therapeutic target in malignant tumors. However, the knowledge of kinetic modeling and parametric imaging of ^{68}Ga-FAPI is limited. **Purpose:** The purpose of this study was to explore the pharmacokinetics of ^{68}Ga-FAPI-04 PET/CT in pancreatic cancer and gastric cancer and to conduct parametric imaging of dynamic total-body data compared with SUV imaging. **Methods:** Dynamic total-body ^{68}Ga-FAPI-04 PET/CT was performed on 13 patients. The lesion time–activity curves were fitted by 3-compartment models and multigraphical models. The kinetics parameters derived from the 2-tissue reversible compartment model (2T4K) and multigraphical models were analyzed. Parametric V_T imaging was generated using the 2T4K and Logan models, and their performances were evaluated compared with SUV images. **Results:** 2T4K had the lowest Akaike information criterion value, and its fitting curves matched excellently with the origin time–activity curves. Visual assessment revealed that the V_T(2T4K) images and V_T(Logan with spatial constraint [SC]) images both showed less image noise and higher lesion conspicuity compared with SUV images. Objective image quality assessment demonstrated that parametric V_T(2T4K) images and parametric V_T(Logan with SC) images had a 5.0-fold and 5.0-fold higher average signal-to-noise ratio and 3.6-fold and 4.1-fold higher average contrast-to-noise ratio compared with conventional SUV images, respectively. In addition, no significant differences in signal-to-noise ratio and contrast-to-noise of pathologic lesions were observed between parametric V_T(2T4K) images and parametric V_T(Logan with SC) images (all $P > 0.05$). **Conclusions:** The 2T4K model was the preferred compartment model. Total-body parametric imaging of ^{68}Ga-FAPI-04 PET yielded superior quantification beyond SUV with enhanced lesion contrast, which may serve as a promising imaging method to make an early diagnosis, to better reflect tumor characterization, or to allow evaluation of treatment response. V_T(2T4K) images are comparable in image quality and consistent to V_T(Logan with SC) images in lesions conspicuity; however, V_T(Logan with SC) images presented an appealing alternative to V_T(2T4K) images because of their simplicity.

Key Words: pancreatic cancer; ^{68}Ga-FAPI-04; parametric imaging; kinetic modeling; total-body dynamic PET imaging

J Nucl Med 2023; 64:960–967
DOI: 10.2967/jnumed.122.264988

Fibroblast activation protein (FAP), specifically binding on cancer-associated fibroblasts, is overexpressed on stromal fibroblasts in more than 90% of epithelial cancers, which makes the FAP inhibitor (FAPI) an excellent molecular probe for tumor diagnosis (*1*). ^{68}Ga-FAPI PET/CT significantly improved the imaging sensitivity compared with ^{18}F-FDG PET/CT in many malignant tumors including pancreatic cancer (*2*) and gastric cancer (*3*). Although FAPI plays an important role in clinical diagnosis, its therapeutic value in clinical work is more concerning. In the study of Lindner et al., 2 patients with metastasized breast cancer were treated with ^{90}Y-FAPI-04, which improved clinical symptoms without side effects (*1*). Baum et al. reported that ^{177}Lu-FAP-2286 was performed in 11 patients with diverse advanced adenocarcinomas and showed high uptake and long retention in lesions with no observed side effects (*4*).

To achieve optimal oncologic diagnostics and satisfactory therapy assessment, we need to explore more about the biologic characteristic of the receptor-binding agents in the human body. Dynamic PET with kinetic modeling was reported to potentially provide superior information compared with static PET acquisitions (*5*). However, the knowledge of kinetic modeling in ^{68}Ga-FAPI-04 is limited. Geist et al. evaluated the kinetic parameters of ^{68}Ga-FAPI for hepatocellular carcinoma using a reversible 2-tissue compartment model in traditional PET/CT (*6*). However, the kinetic analysis was restricted to the liver region, and whether this kinetic model was also suitable for other pathologic lesions and normal organs entirely was still unknown.

SUV is commonly used in PET quantification analysis. SUV reflects the total activity concentration including the uptake of specific and nonspecific signals and can be easily affected by many factors (*7*). In contrast, multiparametric dynamic PET analysis via pharmacokinetic modeling and parametric imaging is a powerful absolute quantitation approach offering excess data, which is the more elaborate

Received Oct. 4, 2022; revision accepted Dec. 27, 2022.
For correspondence or reprints, contact Jianjun Liu (nuclearj@163.com) and Yun Zhou (yun.zhou@united-imaging.com).
*Contributed equally to this work.
Published online Jan. 5, 2023.

and robust method for quantification of tracer uptake (*5*). Early work regarding kinetic modeling and parametric imaging have made great achievements in enhancing parametric image quality (*8–10*). However, because of limited temporal resolution, sensitivity, and axial field of view coverage in the traditional PET scan, parametric imaging was not feasible, and the pharmacokinetic analysis was restricted to only 1 or 2 regions (*8*). Uniquely different from the traditional PET scan, the total-body PET/CT scanner provides an opportunity to simultaneously assess the radiotracer distribution in the entire human body with high sensitivity (*11*), thus tempo-spatially synchronizing the metabolic process of the radiotracer, which would have great prospect in the field of radiotheranostics (*5*). Recently, the kinetic metrics and parametric imaging has been acquired by ^{18}F-FDG total-body PET (*12*). However, parametric imaging has not been conducted in ^{68}Ga-FAPI thus far.

Thus, this study has 2 major goals: to investigate the kinetics of ^{68}Ga-FAPI-04 by PET in normal organs and lesions and to evaluate the feasibility and superiority of parametric imaging compared with conventional SUV imaging in pancreatic cancer and gastric cancer by dynamic total-body ^{68}Ga-FAPI-04 PET. This study performed total-body kinetic modeling and evaluated the clinical significance of parametric imaging in ^{68}Ga-FAPI-04 PET.

MATERIALS AND METHODS

Participants

A total of 13 patients (9 pancreatic cancer patients and 4 gastric cancer patients) who were referred to Renji Hospital for ^{68}Ga-FAPI-04 PET/CT from October 2020 to December 2021 were included. The institutional review board of Renji Hospital approved this study, and all subjects signed written informed consent.

Imaging Data Acquisition and Reconstruction

^{68}Ga-FAPI-04 was synthesized by the Renji Nuclear Medicine Laboratory using a procedure as previously described (*1*). The injected dose was 96.2–163.5 MBq. A low-dose CT scan was conducted for attenuation correction. Patients then underwent a 60-min dynamic PET scanning on a total-body PET/CT (uEXPLORER; United Imaging Health Care) with a bolus injection of ^{68}Ga-FAPI-04 into a vein near the ankle simultaneously as recommended in the expert consensus (*13*).

The images were corrected for radioactive decay, scatter, attenuation, and random and were reconstructed with an image matrix of 360 × 360 pixels, 4 iterations, and 20 subsets by list-mode ordered-subset expectation maximization algorithm incorporating time-of-flight and point-spread function modeling. The PET data were reconstructed into a total of 92 dynamic frames: 30 × 2 s, 12 × 5 s, 6 × 10 s, 4 × 30 s, 25 × 60 s, and 15 × 120 s (Fig. 1A). The representative maximum intensity projection of the reconstructed PET images is shown in Figure 1B.

Image Postprocessing

The postprocessing of the dynamic PET images was analyzed using PMOD 4.2 software (version 4.206; PMOD Technologies Ltd.). Two experts (J.L. and R.C.) in PET/CT interpretation assessed the pathologic lesions. Differences of opinion between them were resolved by reaching a consensus. The volume of interest was drawn manually over normal organs and pathologic lesions. Pathologic lesions were classified as primary tumors (PT), lymph node metastases (LNM), and other metastases (OM). The volumes of interest were drawn on at least 7 consecutive slices of dynamic PET images, and the time–activity curves were extracted at each frame. Because the previous study showed that patients could achieve perfect image quality when the acquisition time on the uEXPLORER scanner was 2 or 3 min (*11*), in our study, 5-min acquisition time (55–60 min after injection) was used to evaluate the image quality of SUV images.

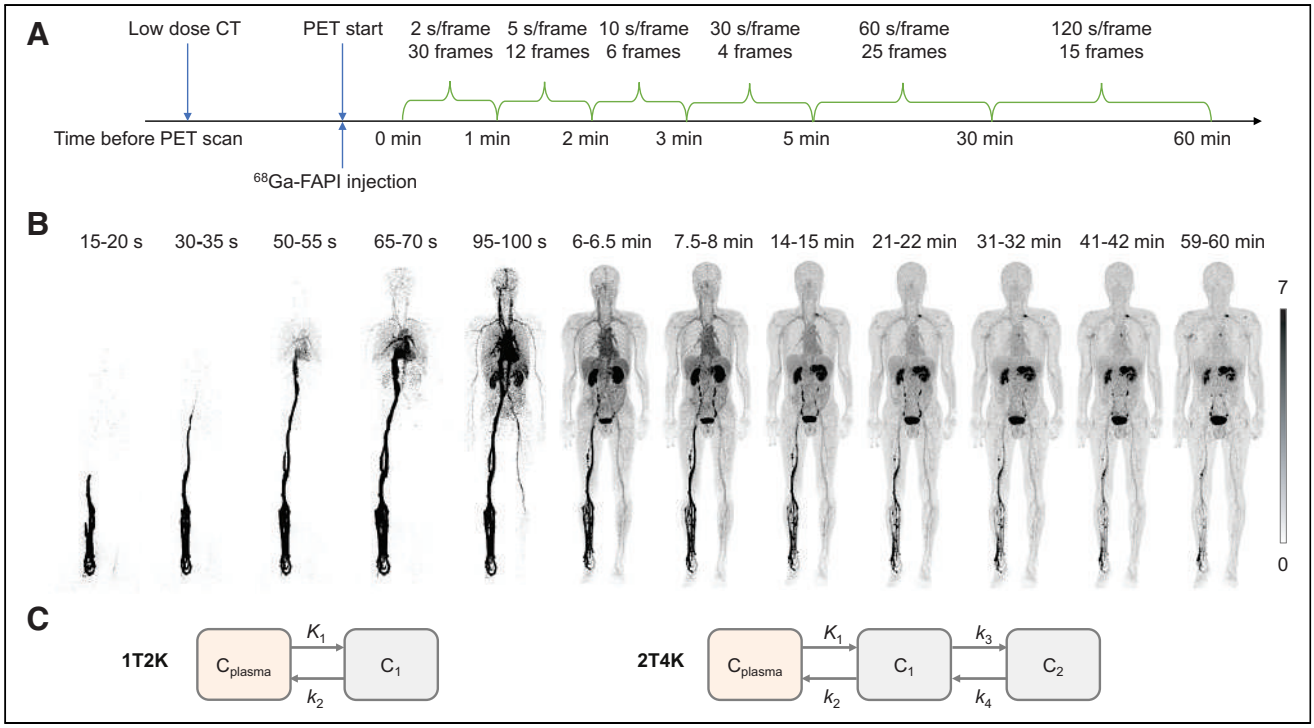

FIGURE 1. Dynamic PET/CT acquisition protocol and schematic representation of compartmental model for ^{68}Ga-FAPI-04. (A) Total-body dynamic ^{68}Ga-FAPI-04 PET/CT acquisition protocol. (B) Reconstructed dynamic total-body PET/CT maximum intensity projection images of ^{68}Ga-FAPI-04 (12 frames). (C) Schematic representation of compartmental model for ^{68}Ga-FAPI-04.

The volume of interest was drawn manually over 4 blood pools using an averaged early PET image (0–2 min), including descending aorta (DA), ascending aorta, left ventricle, and right ventricle. Previous study showed that the FAPI-04 is stable for up to 24 h in the blood (*1,14,15*), exemplifying that metabolic correction can be neglected. Hence, we did not perform metabolic correction in the present study. DA time–activity curve was used as the image-derived input function (IDIF) for kinetic modeling and parametric imaging because it contains a large blood pool (*16*), and the partial-volume effect on the IDIF is further minimized by ordered-subset expectation maximization with a point-spread function imaging reconstruction algorithm used in the total-body uEXPLORER of high spatial resolution (*17–19*).

Kinetic Compartmental Model

Three compartment models were fitted to the time–activity curves: a reversible 1-tissue compartment model (Supplemental Data; supplemental materials are available at http://jnm.snmjournals.org), an irreversible 2-tissue compartment model, and 2-tissue reversible compartment model (2T4K). In the 2-tissue compartment model, the tracer in tissue is attributed to 2 different compartments: C_1 represents unspecific bound and free tracer components in tissue, and C_2 represents the specifically bound tracer components (Fig. 1C). K_1, k_2, k_3, and k_4 were derived from compartment models. The meaning of K_1, k_2, k_3, and k_4 is provided in the Supplemental Data. The fractional blood volume v_B was fitted along with the rate constants. The total distribution volume $V_T = \frac{K_1}{k_2}\left(1 + \frac{k_3}{k_4}\right)$ and the net influx rate $K_i = \frac{K_1 k_3}{k_2 + k_3}$ were also calculated.

The Akaike information criterion (AIC) was used as an assessment of the goodness-of-fit; the more appropriate model is the one with the smaller AIC value.

Multigraphical Analysis

In addition to compartment modeling, time–activity curves were analyzed using multigraphical analysis (*20*). Generally, a Logan plot (*21*) is applied to reversible tracer kinetics, and a Patlak plot is applied to irreversible tracer kinetics (*22*). Zhou et al. proposed the relative-equilibrium (RE) plot (*23*) and the RE plot with the Patlak plot (*20*) to reduce the bias. The graphic analysis will approach a straight line after sufficient equilibration time; the slope represents the net influx rate K_i for the Patlak plot and represents the total distribution volume V_T for the Logan plot, RE plot, and RE plot with the Patlak plot. Time–activity curves were applied to multigraphical analysis, and K_i, V_T was derived over all normal organs and lesions. The linear phase t^* was fixed at 15 min.

Parametric Imaging

Total-body parametric images of ^{68}Ga-FAPI-04 were generated by 2T4K and the Logan plot using linear regression with the spatial constraint (SC) algorithm with 3-dimensional gaussian filters, with 6- and 9-mm full width at half maximum, respectively. The modified linear least square fitting method incorporated with clustering-based SC was applied (*24*). DA is used as the input function. The volumes of interest of the liver, muscle, and pathologic lesions were masked over parametric images, and then the voxel-based mean values and SD values were extracted. Those values were used to calculate the signal-to-noise ratio (SNR) and contrast-to-noise ratio (CNR).

The SNR was calculated as

$$SNR = \frac{VOI_{\text{mean,lesion}}}{VOI_{\text{SD,liver}}}.$$

The CNR was calculated as

$$CNR = \frac{VOI_{\text{mean,lesion}} - VOI_{\text{mean,muscle}}}{VOI_{\text{SD,muscle}}}.$$

Statistical Analysis

The statistical evaluation was performed using software R (version 4.2.0; R Core Team 2021). Descriptive data are presented as mean (SD). A Wilcoxon signed-rank test was used to compare the difference between SUV images and parametric images among SNR and CNR. $P < 0.05$ was considered statistically significant.

RESULTS

Patients' Characteristics

Thirteen patients were included in this study. A total of 46 lesions (10 PT, 26 LNM, and 10 OM) were included in this study. The PT and LNM were verified by histology and enhanced CT, and OM was confirmed by enhanced CT, MRI, or ^{18}F-FDG PET/CT. The detailed characteristics are shown in Table 1.

Compartment Model Selection

Figure 2 shows representative IDIFs derived from the DA, ascending aorta, left ventricle, and right ventricle. Generally, the IDIF curves are analogous to each other. The right ventricle has a slightly earlier peak than the others; apart from this, it shows good agreement between the trends of the IDIFs.

The results for evaluating compartment model fitting quality based on the AIC are displayed in Table 2. 2T4K has the lowest mean AIC in most normal organs, except the lung (1-tissue compartment model is the lowest). For pathologic lesions, 2T4K was preferred with the lowest mean AIC. In general, 2T4K provided the best fitting of time–activity curves among the 3-compartment models, and it was the most appropriate model. An example of fitting curves was displayed in Figure 3. The fitted curves generated by 2T4K matched excellently with the origin time–activity curves.

TABLE 1
Patient Characteristics (n = 13)

Characteristic	Data
Pancreatic cancer	9
Gastric cancer	4
Age (y)	Mean, 51 (range, 36–63)
Sex	
Males (*n*)	7 (53.8%)
Females (*n*)	6 (46.2%)
Injected dose (MBq)	Mean, 115.1 (range, 96.2–163.5)
Number of primary pancreatic lesions	9
Number of primary gastric lesions	1
Number of lymph node metastases	26
Pancreatic cancer	22
Gastric cancer	4
Number of bone metastases	2
Pancreatic cancer	1
Gastric cancer	1
Number of lung metastases	6
Pancreatic cancer	6
Gastric cancer	0
Number of peritoneal metastases	2
Pancreatic cancer	2
Gastric cancer	0

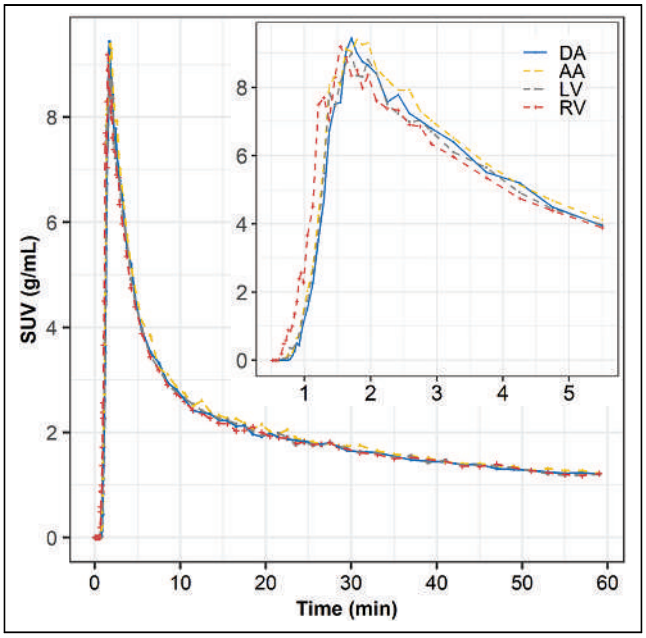

FIGURE 2. IDIFs derived from 4 different blood pools. Full IDIFs and peaks of curves are displayed separately. AA = ascending aorta; LV = left ventricle; RV = right ventricle.

Pharmacokinetics Analyses in Normal Organs and Pathologic Lesions

The kinetic parameters K_1, k_2, k_3, k_4, and V_T from 2T4K, the parameter K_i from the Patlak plot, and parameter V_T from the Logan plot and RE plot are presented in Table 3. Supplemental Figure 1 is the Logan plot, Patlak plot, and RE plot fitting of ^{68}Ga-FAPI-04 concentrations in the lesions of patients with pancreatic cancer.

The kinetic parameters varied among organs and lesions. All 3 types of pathologic lesions showed comparable mean K_1 values, with the highest in LNM (0.328 mL/cm^3/min), followed by PT (0.285 mL/cm^3/min) and OM (0.203 mL/cm^3/min). The highest K_1 values for normal organs were observed in the spleen (1.488 mL/cm^3/min). Among all pathologic lesions, LNM had the greatest k_2 values (0.900/min) followed by PT (0.325/min), and OM (0.252/min). The kidney demonstrated the highest k_2 value (3.242/min) among all organs. For k_3, PT has the greatest k_3 value of 0.377/min among all lesions, followed by LNM (0.299/min) and OM (0.133/min). The kidney demonstrated the highest k_3 value (0.588/min) among all organs. For k_4, PT had the greatest k_4 value of 0.039/min among all lesions, followed by LNM (0.028/min) and OM (0.020/min). The kidney demonstrated the highest k_4 value (0.280/min) among all organs.

Noticeably, for 2T4K, the V_T values was significantly higher in pathologic lesions than in all healthy organs, with the highest in PT (10.502 mL/cm^3), followed by OM (7.275 mL/cm^3) and LNM (6.181 mL/cm^3). The highest V_T values for normal organs were observed in the normal pancreas (2.282 mL/cm^3). Similar results were also observed in V_T derived from the Logan plot, RE plot with the Patlak plot, and RE plot.

For parameter K_i from the Patlak plot, PT had the greatest K_i value of 0.0661 mL/cm^3/min among all lesions, followed by OM (0.0351 mL/cm^3/min) and LNM (0.0310 mL/cm^3/min). Muscle demonstrated the highest K_i value (0.0038 mL/cm^3/min) among all organs.

TABLE 2
Model Validation Among 3 Compartmental Models Based on AIC for Different ROIs

Model	Heart	Lung	Liver	Spleen	Kidney	Pancreas	Thyroid	Parotid gland	Submandibular gland	Muscle	Bone	PT	LNM	OM
2T4K	200.14 (45.11)	363.22 (62.10)	218.03 (80.76)	57.14 (73.46)	154.84 (68.11)	180.30 (122.49)	159.20 (58.34)	104.24 (44.56)	48.89 (44.73)	159.62 (95.33)	249.25 (123.48)	−68.57 (82.82)	211.95 (126.82)	225.37 (161.71)
Irreversible 2-tissue compartment model	203.79 (46.39)	354.22 (71.63)	255.19 (56.81)	120.89 (47.19)	197.57 (75.15)	228.68 (83.31)	183.05 (59.47)	148.00 (48.08)	112.87 (32.84)	183.67 (84.87)	274.47 (148.32)	−0.76 (86.49)	229.74 (109.12)	233.09 (158.63)
One-tissue compartment model	216.64 (49.05)	352.32 (71.62)	310.83 (41.15)	241.75 (69.81)	236.64 (57.07)	279.22 (99.15)	273.52 (52.97)	226.40 (79.17)	208.13 (60.55)	201.30 (87.36)	275.62 (143.57)	53.27 (89.06)	248.55 (103.90)	248.46 (149.12)

AIC values are mean (SD).
ROI = region of interest.

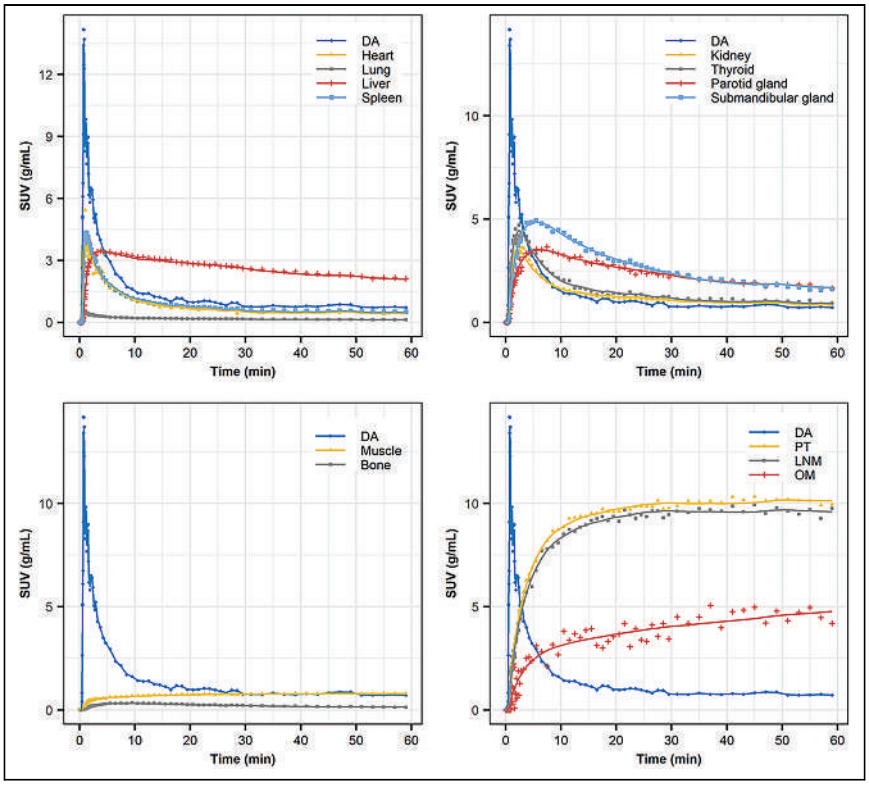

FIGURE 3. Time courses and 2-tissue compartmental model fitting of ^{68}Ga-FAPI-04 concentrations in a patient with pancreatic cancer. Lines represent fitted curves, and dots represent origin time–activity curves.

Parametric Imaging

Figure 4 shows parametric images of the V_T obtained using 2T4K (2T4K image), the Logan plot with SC (Logan with SC image), and the Logan plot (Logan image), together with the corresponding SUV image (55–60 min) of a representative patient with pancreatic cancer. For visual assessment, the 2T4K images and the Logan plot with SC images showed less image noise and higher lesion conspicuity compared with SUV images. Compared with SUV images and Logan images, 2T4K images and the Logan plot with SC images showed less nonspecific signal in typical background regions, such as the blood pool, liver, and kidney. Furthermore, no significant difference in image noise and lesion conspicuity was observed between 2T4K images and the Logan plot with SC images in visual assessment.

To evaluate the objective image quality, the comparisons of SNR and CNR among SUV images, 2T4K images, and the Logan plot with SC images (labeled as Logan) are displayed in Figure 5. Consistent with the visual assessment, no significant differences in SNR and CNR of pathologic lesions were observed (all $P > 0.05$) between the 2T4K images and Logan images.

The SNR_{2T4K} from PT showed a significant 5.0-fold higher value compared with the SNR_{SUV} from PT (90.20 vs. 18.11, $P < 0.001$), and the SNR_{Logan} from PT showed a significant 5.0-fold higher value than SNR_{SUV} (90.91 vs. 18.11, $P < 0.001$). The SNR_{2T4K} and SNR_{Logan} from LNM were significantly 4.1-fold (41.52 vs. 10.07, $P < 0.001$) and 4.4-fold (44.57 vs. 10.07, $P < 0.001$) higher than SNR_{SUV}, respectively. The SNR_{2T4K} and SNR_{Logan} from OM were significantly 5.1-fold (78.96 vs. 15.54, $P < 0.001$) and 5.1-fold (78.56 vs. 15.54, $P = 0.001$) higher than SNR_{SUV} (Fig. 5A).

The CNR_{2T4K} and CNR_{Logan} from PT were significantly 3.6-fold (149.29 vs. 40.94, $P = 0.007$) and 4.1-fold (169.89 vs. 40.94, $P = 0.001$) higher than CNR_{SUV}, respectively. The CNR_{2T4K} and CNR_{Logan} from LNM were significantly 3.2-fold (62.28 vs. 19.33, $P = 0.008$) and 3.9-fold (74.81 vs. 19.33, $P < 0.001$) higher than CNR_{SUV}. The CNR_{2T4K} and CNR_{Logan} from OM were significantly 3.4-fold (100.03 vs. 29.24, $P = 0.004$) and 3.7-fold (109.54 vs. 29.24, $P = 0.003$) higher than CNR_{SUV} (Fig. 5B).

DISCUSSION

This work describes our initial findings with kinetic modeling and parametric imaging of total-body ^{68}Ga-FAPI-04 images using the uEXPLORER scanner. The long-axial PET systems enable capturing rapid kinetics of all normal organs and pathologic lesions with high temporal resolution. Thus, we were able to evaluate the kinetic parameters both in the 2T4K and Logan models and to find the potential clinical applications of parametric imaging in pancreatic cancer and gastric cancer. This study evaluated total-body kinetic modeling and provided clinical significance for parametric imaging in ^{68}Ga-FAPI-04 PET.

Kinetic modeling in ^{68}Ga-FAPI has been evaluated by Geist et al. in traditional PET/CT (*6*). They suggested that a reversible 2-tissue compartment model was the preferred model to describe the kinetics of ^{68}Ga-FAPI-04 in liver lesions (*6*). However, whether this kinetic model was also suitable for other pathologic lesions and normal organs was unknown. In this study, we investigated the kinetic metrics using 3 compartmental models on total-body PET/CT. We found that the 2T4K model showed the best model-fitting curves, and the fitted curves generated by 2T4K matched well with the origin time–activity curves. Furthermore, $k_3, k_4 > 0.02$/min in both healthy organs and lesions also provided evidence to strengthen the selection of 2T4K. To summarize, the 2T4K could be considered the most appropriate model of the kinetics of ^{68}Ga-FAPI-04 in whole-body normal organs and pathologic lesions. Logan plot is a linear method to estimate the V_T. The fitting curve of Logan shows better results than Patlak, which is more evidence to support reversible modeling. Therefore, we further compared the image quality and lesion conspicuity between the 2T4K images, the Logan plot, and the SUV image.

Our study demonstrated that the 2T4K V_T value was significantly higher in all pathologic lesions compared with normal organs. In addition, PT had the highest k_3 and V_T among all pathologic lesions, indicating the high receptor binding and internalization rate, as well as total distribution volume. The normal pancreas showed the highest V_T compared with other all normal organs, but the K_1 and k_3 values for the normal pancreas were lower than many other normal organs, indicating that the transfer rate of FAP ligand binding to the receptor and the internalization rate in the normal pancreas were lower compared with many other normal organs. The kidney showed the highest k_2, k_3, and k_4 compared with other all normal organs; the K_1 value of kidney is second only to that of the spleen; and the V_T value

TABLE 3
Kinetic Parameters of ^{68}Ga-FAPI-04 Using 2T4K and Multigraphical Analysis Based on 60-Minute Acquisition

ROI	2T4K					Logan (V_t [mL/cm^3])	Patlak (K_i [mL/cm^3/min])	RE plot with the Patlak plot (V_t [mL/cm^3])	RE (V_t [mL/cm^3])
	K_1 (mL/cm^3/min)	k_2 (1/min)	k_3 (1/min)	k_4 (1/min)	V_t (mL/cm^3)				
Heart	0.427 (0.139)	1.403 (0.387)	0.050 (0.044)	0.088 (0.065)	0.442 (0.078)	0.540 (0.095)	0.0001 (0.0007)	0.542 (0.095)	0.540 (0.090)
Lung	0.048 (0.085)	0.392 (0.579)	0.071 (0.093)	0.060 (0.051)	0.138 (0.029)	0.205 (0.061)	−0.0005 (0.0006)	0.205 (0.061)	0.208 (0.065)
Liver	0.446 (0.140)	1.019 (0.467)	0.038 (0.045)	0.022 (0.015)	1.151 (0.622)	1.012 (0.583)	0.0032 (0.0024)	1.019 (0.584)	0.951 (0.542)
Spleen	1.488 (0.581)	2.978 (1.364)	0.043 (0.019)	0.071 (0.057)	0.991 (0.373)	0.995 (0.369)	0.0029 (0.0024)	0.999 (0.372)	0.948 (0.320)
Kidney	1.235 (0.694)	3.243 (2.585)	0.588 (0.835)	0.280 (0.256)	1.215 (0.396)	1.188 (0.274)	0.0006 (0.0024)	1.190 (0.275)	1.176 (0.272)
Pancreas	0.863 (0.569)	1.349 (0.830)	0.151 (0.097)	0.065 (0.045)	2.282 (1.331)	2.253 (1.354)	−0.0004 (0.0115)	2.294 (1.342)	2.226 (1.495)
Thyroid	1.196 (0.430)	2.510 (1.566)	0.060 (0.061)	0.047 (0.026)	1.281 (0.642)	1.223 (0.553)	0.0030 (0.0019)	1.232 (0.555)	1.185 (0.540)
Parotid gland	0.185 (0.067)	0.481 (0.303)	0.167 (0.260)	0.060 (0.039)	1.402 (0.393)	1.329 (0.403)	0.0023 (0.0050)	1.345 (0.402)	1.267 (0.392)
Submandibular gland	0.395 (0.099)	0.520 (0.197)	0.074 (0.067)	0.072 (0.056)	1.684 (0.559)	1.612 (0.573)	−0.0019 (0.0072)	1.616 (0.573)	1.624 (0.630)
Bone	0.008 (0.004)	0.083 (0.046)	0.041 (0.080)	0.139 (0.215)	0.152 (0.079)	0.126 (0.055)	0.0001 (0.0008)	0.132 (0.064)	0.118 (0.036)
Muscle	0.038 (0.072)	0.259 (0.260)	0.199 (0.190)	0.088 (0.184)	0.603 (0.510)	0.640 (0.545)	0.0038 (0.0033)	0.659 (0.541)	0.464 (0.391)
PT	0.285 (0.118)	0.325 (0.360)	0.377 (0.394)	0.039 (0.031)	10.502 (2.972)	10.042 (2.849)	0.0661 (0.0180)	10.351 (2.740)	6.098 (1.941)
LNM	0.328 (0.290)	0.900 (1.174)	0.299 (0.330)	0.028 (0.019)	6.181 (3.556)	4.236 (3.170)	0.0310 (0.0208)	4.963 (3.435)	3.248 (2.085)
OM	0.203 (0.130)	0.252 (0.313)	0.133 (0.125)	0.020 (0.009)	7.275 (2.947)	5.457 (2.296)	0.0351 (0.0306)	6.564 (2.757)	3.711 (1.103)

ROI = region of interest.

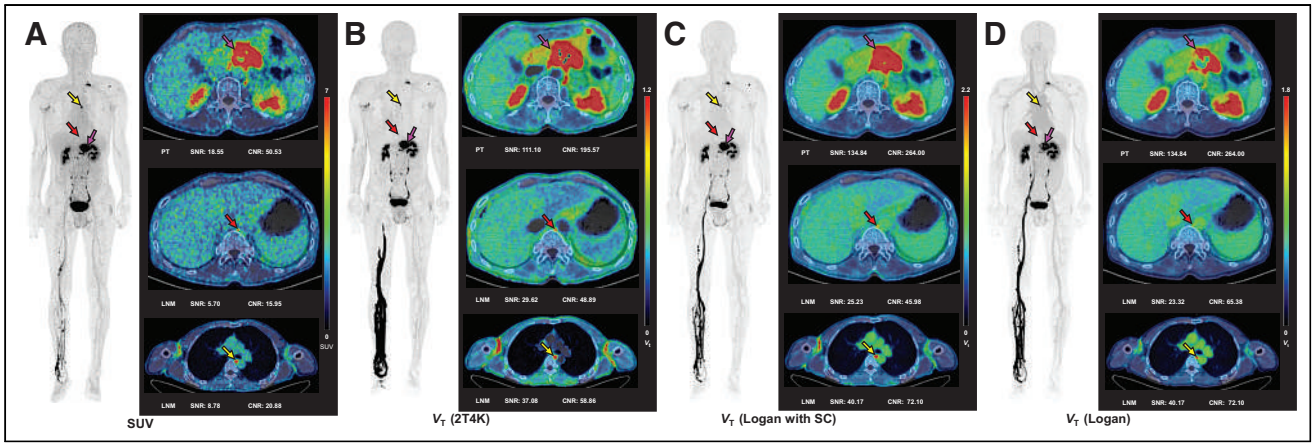

FIGURE 4. Representative SUV images, V_T(2T4K) images, V_T(Logan plot with SC) images, and V_T(Logan plot) images of 58-y-old man with pancreatic cancer. (A) Maximum-intensity projection images of SUV and axial fusion diagram combining V_T images and CT. (B) V_T(2T4K) images. (C) V_T(Logan plot with SC) images. (D) V_T(Logan plot) images. SNR and CNR of lesions are illustrated below corresponding image.

of kidney is in the middle of all normal organs. This meant that the kidney not only had a high transfer rate from plasma to the reversible compartment and a high transfer rate of FAP ligand binding to the receptor and internalization rate, but it also had a high reverse transfer rate.

Parametric imaging of ^{68}Ga-FAPI PET/CT has not been performed in previous studies because of limited temporal resolution and low SNR in traditional PET/CT. In this study, we investigated whether parametric imaging could be used as one of the diagnostic methods in clinical routine practice. For visual assessment, the V_T(2T4K) images and V_T(Logan plot with SC) images both showed less image noise and higher lesion conspicuity compared with SUV images. Although some lesions were equivocal in SUV images, the lesion conspicuity and detectability were obviously higher on V_T(2T4K) images. The V_T(2T4K) images and V_T(Logan plot with SC) images both showed less nonspecific signals in typical background regions. The liver, spleen, blood pool, and muscle were typical backgrounds that may interfere with the lesion visualization in SUV images. The V_T(2T4K) images and V_T(Logan plot with SC) images had greatly weakened the influence of background reference. This is the main reason why the V_T(2T4K) images and V_T(Logan plot with SC) images both showed less image noise and lesion conspicuity compared with SUV images. Overall, the Logan plot with SC images have somehow higher SNR and CNR values, but no significant differences were detected. The V_T(Logan plot with SC) images are vastly superior to the V_T(Logan plot) image because of the low noise levels of the spatially smoothed dynamic PET images (*24*), which illuminates the importance and necessity of spatial constraint in the parametric image. In line with the results of the visual assessment, 2T4K images and Logan plot images had higher SNR and CNR compared with conventional SUV images in pathologic lesions, thus confirming the visual impression that 2T4K images and Logan plot images were both superior to SUV images. No significant differences were observed in visual assessment and objective quality evaluation between 2T4K images and Logan plot images; thus, 2T4K images and Logan plot images were comparable in image quality and lesion conspicuity. Taken together, our results demonstrate that parametric imaging by total-body ^{68}Ga-FAPI PET/CT yielded a substantial increase in sensitivity that makes whole-body parametric imaging feasible and meets the requirements of reading imaging systems in clinical practice. Considering the computational burden of compartmental models, the Logan plot presented an appealing alternative to 2T4K because of its simplicity (*21*), making it appropriate for parametric imaging.

This study has several limitations. First, DA was used as an input function in our study, which was not equally applicable for all tissue types. For example, in the case of the liver, kinetic analysis best entails the use of both hepatic artery and portal vein input (*6*). We acknowledge that the total-body motion correction and partial volume correction for small tissue or lesions are still challenging; the accuracy of the estimated model parameters might be reduced by partial volume and motion effects on our measured dynamic PET data, and it is also fully recognized and discussed in a previous FAPI PET study (*6*). In addition, the sample was small, and it was a retrospective study. Although all primary lesions were confirmed by pathology, several metastases could not be confirmed by pathology because they were difficult to reach

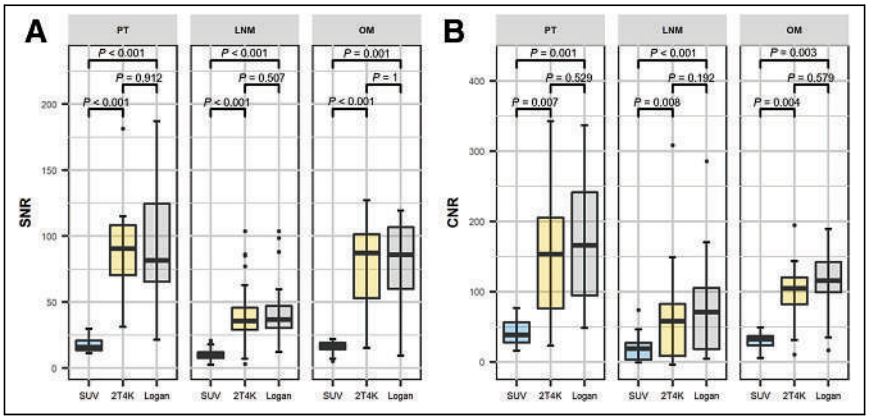

FIGURE 5. Comparison of objective image quality between SUV and parametric V_T images from 2T4K and Logan methods. Comparison of SNR (A) and CNR (B) between SUV images and parametric V_T images in PT, LNM, and OM, respectively.

anatomically. These lesions may also be combined with inflammation and whether inflammation affects kinetic modeling remain unclear. A prospective study with more samples and histopathologic investigations is needed to confirm our results. Furthermore, although parametric images showed enhanced lesion contrast over SUV images, their influence on patients' clinical diagnosis and treatment decisions should be further elaborated in the future.

CONCLUSION

The 2T4K model is the most appropriate model to describe the dynamic kinetics of ^{68}Ga-FAPI-04 PET. Total-body parametric imaging of ^{68}Ga-FAPI-04 PET yielded superior quantification beyond SUV with enhanced lesion contrast, which may serve as a more accurate imaging method for early diagnosis to better reflect tumor characterization or to allow evaluation of treatment response. V_T(2T4K) images are comparable to V_T(Logan plot with SC) images in image quality; however, V_T(Logan plot with SC) images presented an appealing alternative to V_T(2T4K) images because of their simplicity.

DISCLOSURE

No potential conflict of interest relevant to this article was reported.

ACKNOWLEDGMENTS

This study was supported by the National Key R&D Program of China (Grant 2021YFA0910004), National Natural Science Foundation of China (Grant 82171972), Clinical Research Project of Health Industry of Shanghai Municipal Health Commission (Grant 20214Y0438), and nurture projects for the Youth Medical Talents-Medical Imaging Practitioners Program (Grant SHWRS(2021)_099).

KEY POINTS

QUESTION: Should parametric imaging of dynamic ^{68}Ga-FAPI-04 datasets from total-body PET/CT in pancreatic cancer and gastric cancer be used?

PERTINENT FINDINGS: The 2T4K was the preferred compartment model for ^{68}Ga-FAPI-04. V_T images (2T4K) of ^{68}Ga-FAPI-04 showed enhanced lesion contrast and less image noise compared with conventional SUV images in visual assessment and objective quantitative analysis.

IMPLICATIONS FOR PATIENT CARE: Total-body parametric imaging of ^{68}Ga-FAPI-04 PET yielded superior quantification beyond SUV with enhanced lesion contrast, which may serve as a promising imaging method for early diagnosis to better reflect tumor characterization or to allow evaluation of treatment response.

REFERENCES

1. Lindner T, Loktev A, Altmann A, et al. Development of quinoline-based theranostic ligands for the targeting of fibroblast activation protein. *J Nucl Med.* 2018;59:1415–1422.
2. Dendl K, Finck R, Giesel FL, et al. FAP imaging in rare cancer entities-first clinical experience in a broad spectrum of malignancies. *Eur J Nucl Med Mol Imaging.* 2022;49:721–731.
3. Kuten J, Levine C, Shamni O, et al. Head-to-head comparison of [(68)Ga]Ga-FAPI-04 and [(18)F]-FDG PET/CT in evaluating the extent of disease in gastric adenocarcinoma. *Eur J Nucl Med Mol Imaging.* 2022;49:743–750.
4. Baum RP, Schuchardt C, Singh A, et al. Feasibility, biodistribution, and preliminary dosimetry in peptide-targeted radionuclide therapy of diverse adenocarcinomas using (177)Lu-FAP-2286: first-in-humans results. *J Nucl Med.* 2022;63:415–423.
5. Dimitrakopoulou-Strauss A, Pan L, Sachpekidis C. Kinetic modeling and parametric imaging with dynamic PET for oncological applications: general considerations, current clinical applications, and future perspectives. *Eur J Nucl Med Mol Imaging.* 2021;48:21–39.
6. Geist BK, Xing H, Wang J, et al. A methodological investigation of healthy tissue, hepatocellular carcinoma, and other lesions with dynamic (68)Ga-FAPI-04 PET/CT imaging. *EJNMMI Phys.* 2021;8:8.
7. Adams MC, Turkington TG, Wilson JM, Wong TZ. A systematic review of the factors affecting accuracy of SUV measurements. *AJR.* 2010;195:310–320.
8. Rahmim A, Lodge MA, Karakatsanis NA, et al. Dynamic whole-body PET imaging: principles, potentials and applications. *Eur J Nucl Med Mol Imaging.* 2019;46:501–518.
9. Zhou Y, Huang SC, Bergsneider M, Wong DF. Improved parametric image generation using spatial-temporal analysis of dynamic PET studies. *Neuroimage.* 2002;15:697–707.
10. Zhou Y, Endres CJ, Brasic JR, Huang SC, Wong DF. Linear regression with spatial constraint to generate parametric images of ligand-receptor dynamic PET studies with a simplified reference tissue model. *Neuroimage.* 2003;18:975–989.
11. Zhang YQ, Hu PC, Wu RZ, et al. The image quality, lesion detectability, and acquisition time of (18)F-FDG total-body PET/CT in oncological patients. *Eur J Nucl Med Mol Imaging.* 2020;47:2507–2515.
12. Wang G, Nardo L, Parikh M, et al. Total-body PET multiparametric imaging of cancer using a voxel-wise strategy of compartmental modeling. *J Nucl Med.* 2022;63:1274–1281.
13. Yu H, Gu Y, Fan W, et al. Expert consensus on oncological [(18)F]FDG total-body PET/CT imaging (version 1). *Eur Radiol.* 2023;33:615–626.
14. Xing H, Shi X, Dong C, et al. Preclinical and clinical translation research of (68)Ga-labeled fibroblast activation protein inhibitor for PET imaging. *Chin J Nucl Med Mol Imaging.* 2020;40:480–485.
15. Xiang Y, Zhong X, Fu J, et al. The glioma model micro-PET imaging and biodistribution of (68)Ga labeled fibroblast activation protein inhibitor. *J Isotopes.* 2022;35:368–375.
16. Wang Y, Li E, Cherry SR, Wang G. Total-body PET kinetic modeling and potential opportunities using deep learning. *PET Clin.* 2021;16:613–625.
17. Yang J, Hu C, Guo N, et al. Partial volume correction for PET quantification and its impact on brain network in Alzheimer's disease. *Sci Rep.* 2017;7:13035.
18. Ibaraki M, Matsubara K, Shinohara Y, et al. Brain partial volume correction with point spreading function reconstruction in high-resolution digital PET: comparison with an MR-based method in FDG imaging. *Ann Nucl Med.* 2022;36:717–727.
19. Zhang X, Xie Z, Berg E, et al. Total-body dynamic reconstruction and parametric imaging on the uEXPLORER. *J Nucl Med.* 2020;61:285–291.
20. Zhou Y, Ye W, Brasic JR, Wong DF. Multi-graphical analysis of dynamic PET. *Neuroimage.* 2010;49:2947–2957.
21. Logan J, Fowler JS, Volkow ND, et al. Graphical analysis of reversible radioligand binding from time-activity measurements applied to [N-^{11}C-methyl]-(-)-cocaine PET studies in human subjects. *J Cereb Blood Flow Metab.* 1990;10:740–747.
22. Logan J. A review of graphical methods for tracer studies and strategies to reduce bias. *Nucl Med Biol.* 2003;30:833–844.
23. Zhou Y, Ye W, Brasic JR, Crabb AH, Hilton J, Wong DF. A consistent and efficient graphical analysis method to improve the quantification of reversible tracer binding in radioligand receptor dynamic PET studies. *Neuroimage.* 2009;44:661–670.
24. Huang X, Zhou Y, Bao S, Huang SC. Clustering-based linear least square fitting method for generation of parametric images in dynamic FDG PET studies. *Int J Biomed Imaging.* 2007;2007:65641.

Measurement of Cerebral Perfusion Indices from the Early Phase of [^{18}F]MK6240 Dynamic Tau PET Imaging

Nicolas J. Guehl[1], Maeva Dhaynaut[1], Bernard J. Hanseeuw[1,2], Sung-Hyun Moon[1], Cristina Lois[1], Emma Thibault[1], Jessie Fanglu Fu[3], Julie C. Price[3], Keith A. Johnson[1], Georges El Fakhri*[1], and Marc D. Normandin*[1]

[1]Gordon Center for Medical Imaging, Department of Radiology, Massachusetts General Hospital, Harvard Medical School, Boston, Massachusetts; [2]Department of Neurology, Cliniques Universitaires Saint-Luc, Université Catholique de Louvain, Brussels, Belgium; and [3]Athinoula A. Martinos Center for Biomedical Imaging, Department of Radiology, Massachusetts General Hospital, Harvard Medical School, Boston, Massachusetts

6-(fluoro-^{18}F)-3-(1H-pyrrolo[2,3-c]pyridin-1-yl)isoquinolin-5-amine ([^{18}F]MK6240) has high affinity and selectivity for hyperphosphorylated tau and readily crosses the blood–brain barrier. This study investigated whether the early phase of [^{18}F]MK6240 can be used to provide a surrogate index of cerebral perfusion. **Methods:** Forty-nine subjects who were cognitively normal (CN), had mild cognitive impairment (MCI), or had Alzheimer's disease (AD) underwent paired dynamic [^{18}F]MK6240 and [^{11}C]Pittsburgh compound B (PiB) PET, as well as structural MRI to obtain anatomic information. Arterial blood samples were collected in a subset of 24 subjects for [^{18}F]MK6240 scans to derive metabolite-corrected arterial input functions. Regional time–activity curves were extracted using atlases available in the Montreal Neurologic Institute template space and using FreeSurfer. The early phase of brain time–activity curves was analyzed using a 1-tissue-compartment model to obtain a robust estimate of the rate of transfer from plasma to brain tissue, K_1 (mL·cm^{-3}·min^{-1}), and the simplified reference tissue model 2 was investigated for noninvasive estimation of the relative delivery rate, R_1 (unitless). A head-to-head comparison with R_1 derived from [^{11}C]PiB scans was performed. Grouped differences in R_1 were evaluated among CN, MCI, and AD subjects. **Results:** Regional K_1 values suggested a relatively high extraction fraction. R_1 estimated noninvasively from simplified reference tissue model 2 agreed well with R_1 calculated indirectly from the blood-based compartment modeling (r = 0.99; mean difference, 0.024 ± 0.027), suggesting that robust estimates were obtained. R_1 measurements obtained with [^{18}F]MK6240 correlated strongly and overall agreed well with those obtained from [^{11}C]PiB (r = 0.93; mean difference, −0.001 ± 0.068). Statistically significant differences were observed in regional R_1 measurements among CN, MCI, and AD subjects, notably in the temporal and parietal cortices. **Conclusion:** Our results provide evidence that the early phase of [^{18}F]MK6240 images may be used to derive a useful index of cerebral perfusion. The early and late phases of a [^{18}F]MK6240 dynamic acquisition may thus offer complementary information about the pathophysiologic mechanisms of the disease.

Key Words: [^{18}F]MK6240; PET imaging; cerebral perfusion; Alzheimer's disease

J Nucl Med 2023; 64:968–975
DOI: 10.2967/jnumed.122.265072

Developed as a second-generation tau tracer, 6-(fluoro-^{18}F)-3-(1H-pyrrolo[2,3-c]pyridin-1-yl)isoquinolin-5-amine ([^{18}F]MK6240) possesses high affinity and selectivity toward hyperphosphorylated tau (*1–4*), one of the hallmark neuropathologies in Alzheimer's disease (AD). Initial pharmacokinetic studies with arterial blood sampling also indicated a relatively fast brain penetration, as evidenced by moderately high rates of transfer from plasma to brain tissue (K_1) (*2,3,5*)—the K_1 from plasma to brain tissue that is related to cerebral blood flow (CBF) as the product of CBF and extraction (E), such that $K_1 = \text{CBF} \times \text{E} = \text{CBF} \times [1 - e^{-\text{PS/CBF}}]$, where PS is the vascular permeability–surface area product. The dynamic range of K_1 estimates across brain regions previously reported (*2,3,5*) suggests that the early phase of dynamic [^{18}F]MK6240 PET measurements might be used to provide valuable information on cerebral perfusion.

A deficit in cerebral perfusion has been well documented in AD, with a reduction in CBF reported for several cortical regions, such as the frontal, parietal, and temporal cortices (*6–10*). Decreased CBF has also been reported in other tauopathies, as well as in healthy elderly subjects when compared with young adults (*11–14*). Although it is not clear whether hypoperfusion plays a primary or secondary role in AD and related dementia, hypoperfusion is an important component to understanding the pathogenesis of these neurodegenerative diseases and may also be an important prognostic biomarker or treatment target.

Several imaging modalities have been used for in vivo measurements of CBF, including MR-based methods such as arterial spin labeling, but the gold standard technique remains [^{15}O]H_2O PET analyzed by tracer kinetic modeling. [^{15}O]H_2O possesses attractive properties for measuring blood flow, with a high extraction fraction for a wide range of flow values (*15,16*). However, its short half-life (~2 min) requires an on-site cyclotron, and performing an additional scan to obtain CBF measurements may be cumbersome, particularly in a clinical setting, potentially leading to logistic complications. Alternatively, measuring CBF using arterial spin labeling techniques would require either a simultaneous PET/MRI scanner or a separate MRI scan including additional sequences. These reasons have led several investigators to study whether the early phase of the PET acquisition of amyloid or other tau tracers (*17–22*) can be used to provide surrogate measurements of cerebral perfusion or relative delivery rate (R_1), such that $R_1 = K_1$ (target)/K_1 (reference region). Since CBF is generally tightly coupled to brain metabolism, several investigators have also performed head-to-head comparisons with [^{18}F]FDG, proposing that this early

Received Oct. 21, 2022; revision accepted Jan. 26, 2023.
For correspondence or reprints, contact Nicolas J. Guehl (nguehl@mgh.harvard.edu).
*Contributed equally to this work.
Published online Mar. 30, 2023.

phase might be used to provide a surrogate biomarker of neuronal injury (*23–29*), thus providing information on "N" (neurodegeneration) in addition to "A" (amyloid) or "T" (tau) in the A/T/N classification scheme (*30,31*).

In this article, we seek to present the first supporting evidence that the early phase of [^{18}F]MK6240 can be used to provide a surrogate index of cerebral perfusion. Our hypothesis is that the early phase of [^{18}F]MK6240 images can be used to provide quantitative information on cerebral perfusion in addition to a measure of tau load—typically obtained by a full kinetic analysis or derived from a late acquisition after tracer injection—thus augmenting the utility of this tracer. Since other investigators have shown that dynamic [^{11}C]Pittsburgh compound B (PiB) scanning may be used to measure changes in perfusion and that R_1 obtained with [^{11}C]PiB correlates well with R_1 obtained from [^{15}O]H_2O scans (*17,18*), and in the absence of [^{15}O]H_2O measurements, we also performed a direct comparison between R_1 obtained with [^{18}F]MK6240 and R_1 obtained from corresponding [^{11}C]PiB scans.

MATERIALS AND METHODS

A full version of the Materials and Methods section is provided in the supplemental materials (available at http://jnm.snmjournals.org).

Participants

In total, 49 subjects, consisting of 25 who were cognitively normal (CN), 17 who had mild cognitive impairment (MCI), and 7 who had AD, were included in this work. All subjects were identified by physicians at Massachusetts General Hospital and underwent at least one comprehensive medical and neurologic evaluation using tests that included the Mini-Mental State Examination. Clinical status (MCI, AD, or CN) was determined clinically by established criteria (*32*). All subjects signed an informed-consent form, and the study was approved by the institutional review board at Massachusetts General Hospital.

Data Acquisition

Each subject underwent a dynamic [^{18}F]MK6240 PET scan for up to 135 min, a dynamic [^{11}C]PiB PET scan for 60 min, and MRI for anatomic reference. A subset of 24 [^{18}F]MK6240 scans included arterial blood sampling (14 CNs, 8 MCIs, and 2 ADs). [^{18}F]MK6240 and [^{11}C]PiB were synthesized as previously described (*33,34*). Acquisition of [^{18}F]MK6240, [^{11}C]PiB, and MRI data was also previously described (*2,35*).

Image Processing

Dynamic PET images were motion-corrected using validated tools (*36–38*), and regional time–activity curves were extracted using the Montreal Neurologic Institute (MNI) template space (*2,39*) and FreeSurfer (*40,41*). Time–activity curves extracted using the MNI atlases were used primarily for comparisons between outcome measures while grouping all regions of interest and subjects on the same graphs. Time–activity curves resulting from the FreeSurfer parcellation were used primarily for detailed regional comparisons. PiB scores were calculated using the method of Johnson et al. (*42*)

Quantitative Analysis

Blood-Based Compartmental Analysis. The early phase of [^{18}F]MK6240 regional time–activity curves was analyzed using a simple 1-tissue-compartment model with 2 rate constants k (K_1 and k_2) and including the vascular fraction (v) as an additional model parameter (1T2kv). The time stability of K_1 and R_1 estimates was evaluated by comparing values obtained using 5 and 10 min of data. In this work, we followed the consensus nomenclature for imaging of reversibly binding radioligands described by Innis et al. (*43*)

Simulation Study. Simulations were performed with different levels of specific binding to assess the effect of neglecting the binding component on K_1 and R_1 estimates obtained from the 1T2kv model. Regional 120-min time–activity curves were simulated for the gray cerebellum (reference region) and target regions using a 2-tissue-compartment model applying arterial measurements and kinetic parameters derived from human studies. Simulated time–activity curves were truncated, and the first 5 or 10 min of data were analyzed with the 1T2kv model. K_1 and R_1 estimates were then compared with simulated ground truth values.

Reference Region–Based Analysis. Noninvasive measurements of R_1 were investigated using the simplified reference tissue model 2 (SRTM2) (*44*) and compared with those obtained indirectly from the blood-based compartmental analysis. The effect of using different strategies for fixing the reference region clearance constant, k_2', on the estimation of R_1 was investigated.

Head-to-Head Comparison with [^{11}C]PiB. A direct comparison between R_1 obtained with [^{18}F]MK6240 and R_1 obtained from corresponding [^{11}C]PiB scans was performed with SRTM2 using the first 5 min of data.

Regional Analysis of R_1 *Between Groups.* Differences in R_1 were evaluated among CN, MCI, and AD subjects. The same analysis was also repeated while grouping MCI and AD subjects.

Statistical Analysis

The Pearson correlation coefficient r was used to assess the strength of the linear correlations between outcome measures. All data were expressed as mean ± SD unless otherwise specified. A P value of 0.05 or less was considered statistically significant. Bonferroni adjustment was applied for multiple comparisons on the same datasets when appropriate. More details on statistical analysis are provided in the supplemental materials.

RESULTS

Participants

Subject demographics are summarized in Table 1. All CN subjects ($n = 25$) had a Mini-Mental State Examination result of at least 25. Other participants met the National Institute of Aging research criteria for MCI or for AD dementia. Twenty-five subjects (8 CNs, 10 MCIs, and all 7 ADs) were amyloid-β–positive as defined by a distribution volume ratio of more than 1.2 calculated in a large cortical ROI that included the frontal, lateral temporal, and retrosplenial cortices (*45*). The CN and MCI/AD groups were well matched in age (68.7 ± 12.5 y vs. 69.8 ± 11.0 y, $P = 0.7513$; unpaired 2-sample t test). The time between [^{18}F]MK6240 and [^{11}C]PiB scans was variable between subjects: 29 subjects had their [^{11}C]PiB and [^{18}F]MK6240 scans performed within 2 wk of each other (18 of which had them on the same day), and for the remaining subjects the 2 scans were separated by up to several months. Thirty-five subjects had their [^{11}C]PiB scan performed before their [^{18}F]MK6240 scan, and the remaining subjects had their [^{18}F]MK6240 scan performed first.

Blood-Based Compartmental Analysis

The K_1 estimates obtained from the 1T2kv model were stable while using 5 or 10 min of data, indicating the robustness of these measurements and thus demonstrating that the estimation of K_1 is sufficiently decoupled from the estimation of the parameter k_2. The total-least-square regression and Bland–Altman plots demonstrated a good correlation and agreement, respectively ($y = 1.02x - 0.01$, $r = 0.99$, $P < 0.0001$; mean difference, 0.000 ± 0.009 mL·cm^{-3}·min^{-1}; $P = 0.9521$) and also highlight the relatively broad range of K_1 values measured across subjects and brain regions (Supplemental Fig. 1). Similar levels of correlation and agreement were observed when comparing

TABLE 1
Participant Demographics and Clinical Characteristics

Characteristic	All	CN	MCI	AD
Total patients (*n*)	49	25	17	7
HR+	18	8	8	2
DMI	31	17	9	5
Arterial blood sampling (*n*)	24	14	8	2
HR+	10	4	5	1
DMI	14	10	3	1
Age (y)	69.3 (11.8)	68.7 (12.5)	71.5 (11.3)	65.6 (9.9)
Weight (kg)	80.5 (18.0)	79.5 (19.3)	82.0 (17.0)	80.0 (16.4)
Sex (*n*)				
Male	29	10	13	6
Female	20	15	4	1
MMSE	26.7 (3.9)	28.8 (1.3)	26.4 (2.7)	19.9 (4.5)
MMSE range	13–30	25–30	20–30	13–24
Education (y)	16.4 (2.8); 13*	16.5 (3.14); 5*	16.0 (2.7); 7*	17.0 (2.4); 1*
PiB status (*n*)				
Positive	25	8	10	7
Negative	24	17	7	0
Time between [^{11}C]PiB and [^{18}F]MK6240 scans (d)	0–392	0–95	0–392	0–200

*Number of participants for which information was not available.
HR+ = number of participants scanned on ECAT EXACT HR+ scanner; DMI = number of participants scanned on Discovery MI scanner; MMSE = Mini-Mental State Examination.
Data in parentheses are SD.

corresponding R_1 estimates ($y = 1.01x - 0.01$, $r = 0.99$, $P < 0.0001$; mean difference, -0.004 ± 0.019; $P = 0.8026$). On average, cerebellar K_1 values were lower in the MCI/AD group than in the CN group (0.326 ± 0.066 mL·cm^{-3}·min^{-1} vs. 0.391 ± 0.094 mL·cm^{-3}·min^{-1}); however, these differences were not statistically significant as assessed by a 2-tailed unpaired *t* test ($P = 0.0767$).

Simulations at Different Levels of Specific Binding

Supplemental Table 1 shows the results of the simulation study performed for 3 different R_1 values (0.4, 0.85, and 1.3) at increasing levels of specific binding in the target region as indicated by the simulated range of distribution volume ratios. When only the first 5 min of simulated time–activity curves were fitted, the bias in the estimated K_1 and corresponding R_1 in the target region was well below 2% for all levels of specific binding. When the first 10 min of time–activity curves were fitted, the bias in K_1 and R_1 estimates in the target region increased with the level of specific binding and was higher for larger simulated values of R_1 (−7.06% and −6.12%, respectively, at $R_1 = 1.3$). The measured bias on estimated K_1 in the reference region was 0.04% and 1% when using 5 min and 10 min of data, respectively.

Reference Region Model-Based Analysis

Direct estimates of R_1 obtained from SRTM2 showed a strong correlation and good agreement ($y = 0.95x + 0.07$, $r = 0.99$, $P < 0.0001$; mean difference, 0.024 ± 0.027; $P = 0.1261$) with those obtained indirectly from the blood-based compartmental analysis using the first

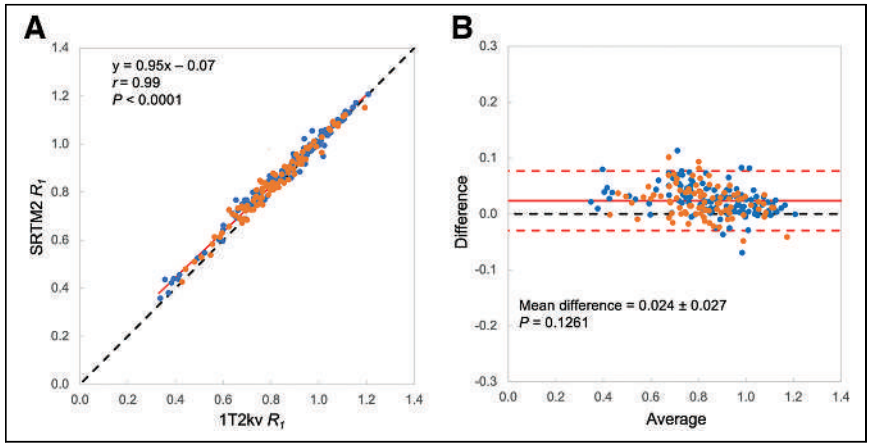

FIGURE 1. Comparison of direct R_1 estimates obtained from SRTM2 and indirect blood-based R_1 estimates obtained from 1T2kv model with [^{18}F]MK6240. (A) Correlation plot. Red line represents total-least-square regression, and black line is line of identity. (B) Corresponding Bland–Altman plot showing agreement in R_1 estimates between 2 methods. Solid red line represents mean difference, dashed red lines show mean difference ± 1.96 SD, and black line is zero line for reference. Blue dots represent CN subjects, and orange dots represents MCI/AD subjects. Data points are for all subjects, and brain time–activity curves were surveyed using atlases in MNI template space.

5 min of PET data for each method (Fig. 1). The mean subject-specific median k_2' value across subjects was $0.084 \pm 0.049\,min^{-1}$ (range, 0.022–0.270 min^{-1}). Fixing k_2' to a population-based value determined from SRTM ($\bar{k_2'}$) had a negligible effect on R_1 estimates in comparison to using subject-specific median k_2' values (mean difference across all subjects and brain regions, $-0.06\% \pm 0.40\%$). Likewise, fixing k_2' to $\bar{k_2'}_{\text{blood-based}}$ (the average cerebellar blood-based k_2' estimates, with $\bar{k_2'}_{\text{blood-based}} = 0.062 \pm 0.014\,min^{-1}$ and range = 0.040–0.088 min^{-1}) led to similar R_1 estimates in comparison to using subject-specific median k_2' values (mean difference across all subjects and brain regions, $-0.08\% \pm 0.33\%$). Therefore, for all SRTM2 analyses performed with [^{18}F]MK6240 in this work, we used $\bar{k_2'}$. The SRTM2 R_1 estimates were also stable when using 10 min of data compared with using only 5 min ($y = 1.00x - 0.02$, $r = 0.99$, $P < 0.0001$; mean difference, -0.013 ± 0.019; $P = 0.2522$).

Head-to-Head Comparison Between R_1 Estimates Obtained from [^{18}F]MK6240 and [^{11}C]PiB

Figure 2 shows a direct comparison between R_1 estimates obtained from [^{18}F]MK6240 and [^{11}C]PiB scans. When all 49 paired scans were included in the analysis, the overall correlation and agreement were good despite some variability (Figs. 2A and 2B: $y = 0.97x + 0.03$, $r = 0.93$, $P < 0.0001$; mean difference, -0.001 ± 0.068; $P = 0.9242$). When the analysis was restricted to pairs of [^{18}F]MK6240 and [^{11}C]PiB scans acquired within 2 wk, the correlation and agreement were slightly better (Figs. 2C and 2D: $y = 0.99x + 0.00$, $r = 0.95$, $P < 0.0001$; mean difference, -0.003 ± 0.059; $P = 0.8623$), possibly reflecting daily variations in CBF. Restricting the analysis to pairs of scans acquired the same day further reduced the variability (Figs. 2E and 2F: $y = 0.99x + 0.00$, $r = 0.97$, $P < 0.0001$; mean difference, -0.010 ± 0.043; $P = 0.6273$).

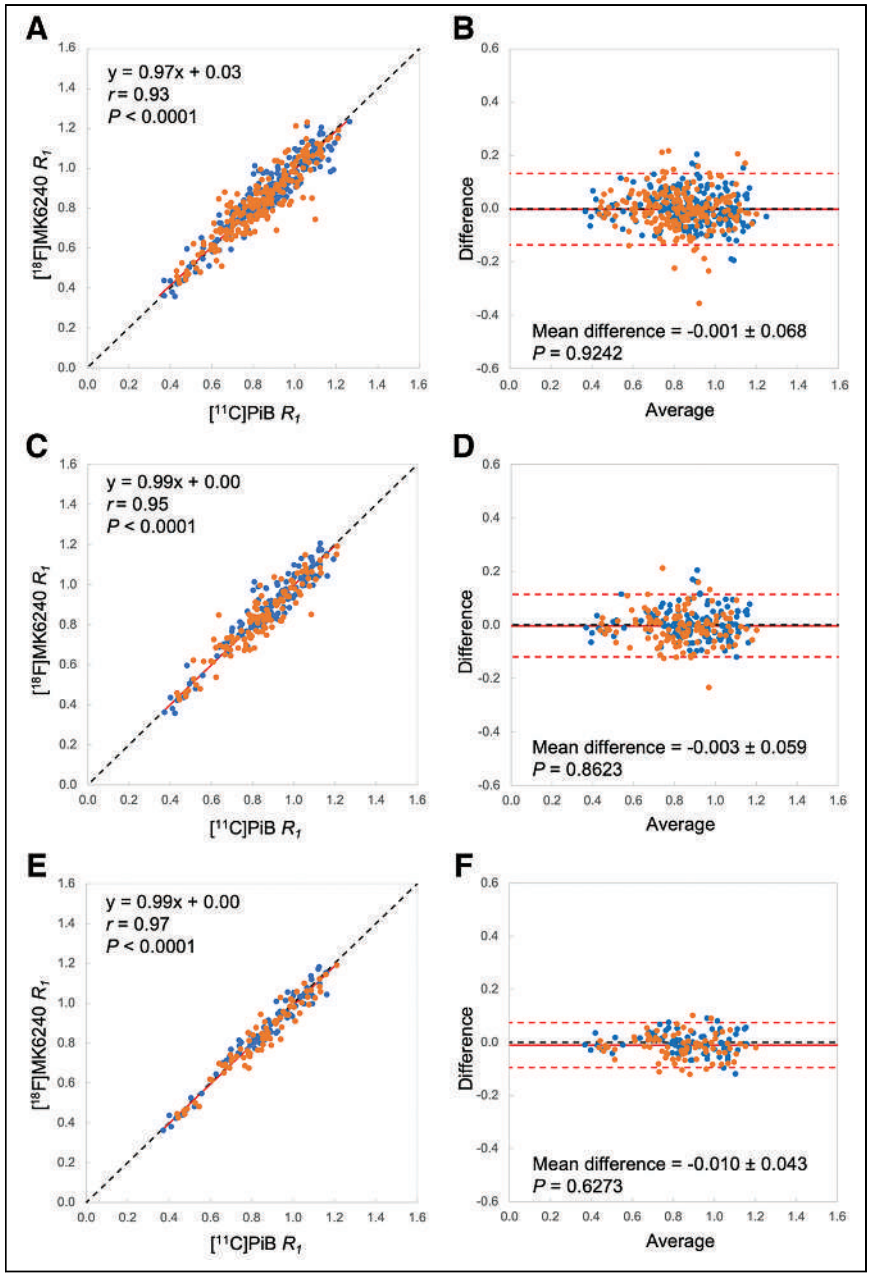

FIGURE 2. Comparison of SRTM2 R_1 estimates obtained from [^{18}F]MK6240 and [^{11}C]PiB paired scans. (A and B) Correlation and Bland–Altman plots of R_1 estimates for all paired [^{18}F]MK6240 and [^{11}C]PiB scans (49 pairs). (C and D) Correlation and Bland–Altman plots of R_1 estimates for paired scans acquired within 15 d (29 pairs). (E and F) Correlation and Bland–Altman plots of R_1 estimates for paired scans acquired on same day (18 pairs). In correlation plots (A, C, and E), solid red lines represent total-least-square regressions and black lines are lines of identity. In Bland–Altman plots (B, D, and F), solid red lines represent mean difference, dashed red lines show mean difference ± 1.96 SD, and black lines are zero lines for references. Blue and orange dots represent brain regions corresponding to CN subjects and MCI/AD subjects, respectively. Data points are for all subjects, and brain time–activity curves were surveyed using atlases in MNI template space.

Regional differences in R_1 estimates obtained from [^{18}F]MK6240 and [^{11}C]PiB scans for the FreeSurfer analysis are presented in Supplemental Table 2. After Bonferroni adjustment for multiple comparisons, none of the observed differences were statistically significant when grouping all subjects together or when considering CN subjects only. In the MCI/AD group, only differences in the inferior temporal cortex survived the Bonferroni adjustment. Overall, these results demonstrate that similar R_1 estimates were obtained from [^{18}F]MK6240 and [^{11}C]PiB scans.

Regional Analysis of R_1 Among Groups

Figure 3 shows the average regional R_1 values measured in each group for regions of interest derived from the FreeSurfer parcellation. All P values for regional comparisons can be found in Supplemental Table 3. Figure 3A shows bar plots with CN, MCI, and AD groups presented separately. When MCI and CN

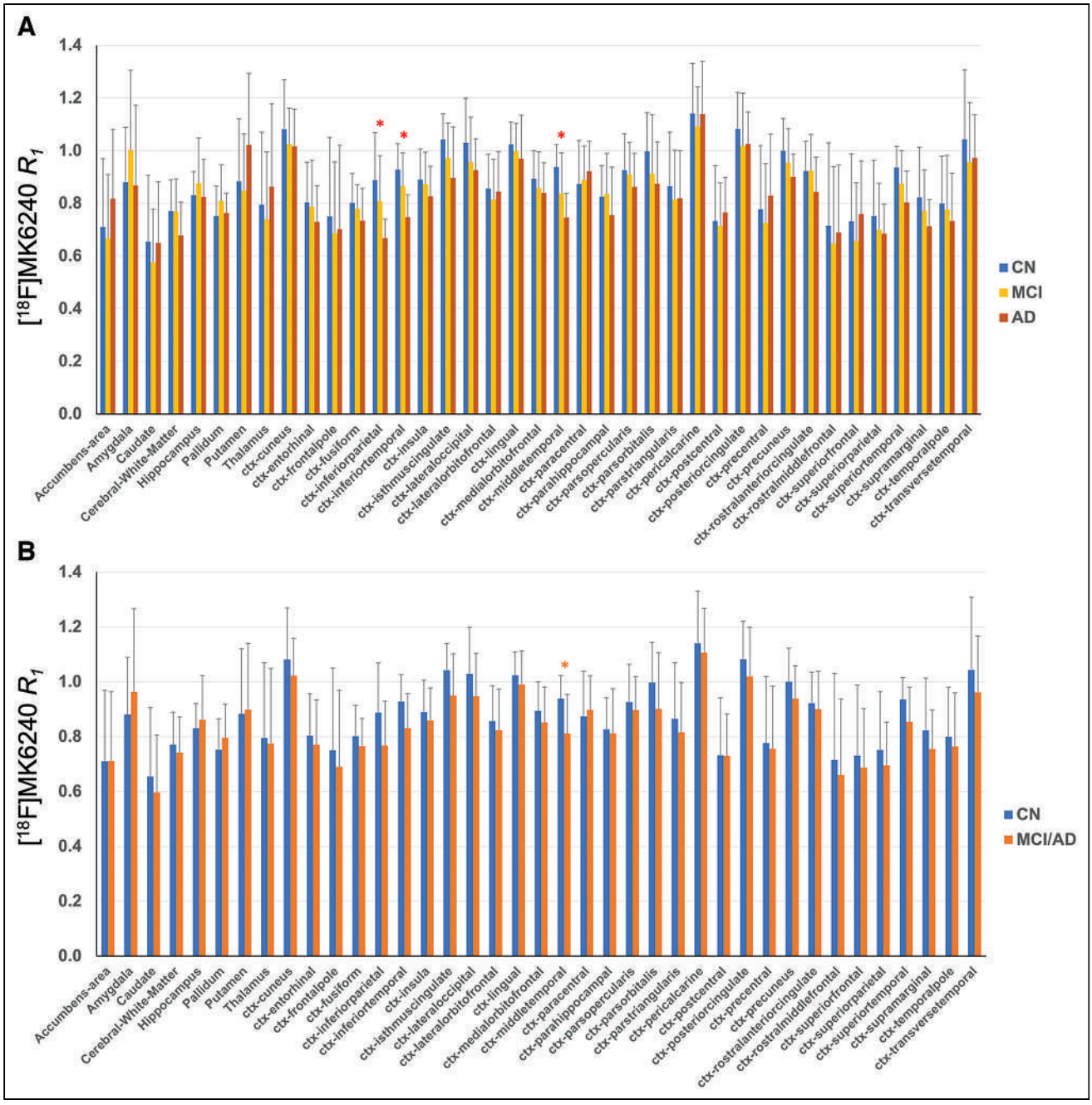

FIGURE 3. Bar plots showing differences in regional R_1 measurements among CN, MCI, and AD groups for analysis performed using FreeSurfer parcellation. (A) Plots with CN, MCI, and AD groups presented separately. (B) Plots presented while grouping MCI and AD groups. Asterisks indicate differences that were statistically significant between groups as assessed from unpaired 2-tailed *t* test assuming unequal variance and after Bonferroni adjustment ($P < 0.0013$). Asterisks in A resulted from comparison between CN and AD groups. Asterisk in B resulted from comparison between CN and MCI/AD groups. Error bars represent SD measured within each group.

subjects or MCI and AD subjects were compared, none of the measured differences that were below a *P* value of 0.05 survived Bonferroni adjustment. When AD and CN subjects were compared, only the inferior-temporal cortex, middle-temporal cortex, and inferior-parietal cortex were still statistically significant after Bonferroni adjustment. Finally, when MCI and AD subjects were grouped and compared with CN subjects, only differences in the middle-temporal cortex survived Bonferroni adjustment (Fig. 3B).

Parametric Imaging

Figure 4 shows parametric images of R_1 computed with SRTM2 using 10 min of dynamic data, along with the structural MRI for anatomic reference, the [^{11}C]PiB distribution volume ratio images showing amyloid burden, and the late [^{18}F]MK6240 SUV ratio for images from 90 to 120 min showing tau pathology. The figure shows a side-by-side comparison between a CN subject and a subject with AD of similar age. Although the CN subject showed relatively homogeneous perfusion in the cortical and subcortical areas, the AD subject showed

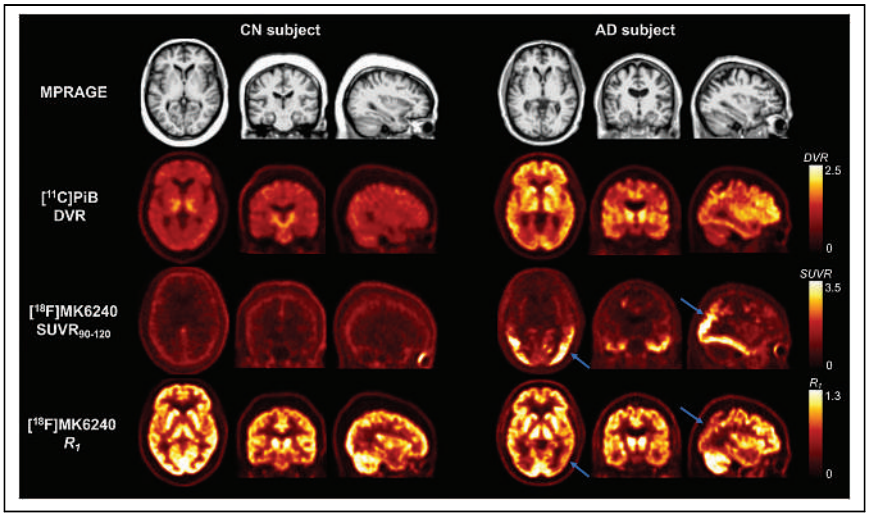

FIGURE 4. Parametric maps and corresponding MR structural images in CN subject and AD subject. First row shows magnetization-prepared rapid gradient echo as anatomic reference. Second row shows parametric [^{11}C]PiB DVR images as measure of amyloid burden. Third row shows late [^{18}F]MK6240 SUV ratio for images from 90 to 120 min as measure of tau load. Fourth row shows parametric images of R_1 computed from [^{18}F]MK6240 dynamic data. Arrows indicate areas of reduced cerebral perfusion and corresponding to high tau load. MPRAGE = magnetization-prepared rapid gradient echo; DVR = distribution volume ratio; SUVR = SUV ratio; $SUVR_{90–120}$ = SUV ratio for images from 90 to 120 min.

marked hypoperfusion in the temporal and parietal cortices, which were also areas showing tau pathology. Group-average images of [^{18}F]MK6240 R_1 are shown in Figure 5. Visually, a reduction in R_1 was apparent on the AD-average images as compared with CN and MCI subjects.

DISCUSSION

In this work, we investigated the use of early-phase [^{18}F]MK6240 dynamic images to derive an index of relative perfusion by tracer kinetic modeling. We chose to fit only the first few minutes of PET measurements since this early phase after tracer injection is the most sensitive part of the scan to changes in perfusion. Mathematically, this can be demonstrated by plotting the sensitivity curves of the model parameters (Supplemental Fig. 2). Our simulation results demonstrated that fitting the first 5 min of PET data with a simple 1-tissue-compartment model provided K_1 and R_1 estimates within 2% of ground truth, suggesting that neglecting specific binding does not introduce noticeable bias or variability. Using 10 min of data, however, resulted in a slightly higher bias that increased with increasing level of specific binding (i.e., increasing distribution volume ratios) and with simulated R_1 values. Nevertheless, we generated R_1 parametric images using 10 min of data because the quality of the parametric maps was higher than when using only 5 min after tracer injection (Supplemental Fig. 3), thus accepting a tradeoff between bias and image quality. Overall, our findings from simulations and experimental data suggest that [^{18}F]MK6240 can provide robust surrogate measurements of relative perfusion. We found good agreement between direct estimates of R_1 obtained by SRTM2 and indirect R_1 estimates from blood-based compartment modeling, as well as good agreement between [^{18}F]MK6240 and [^{11}C]PiB R_1 estimates.

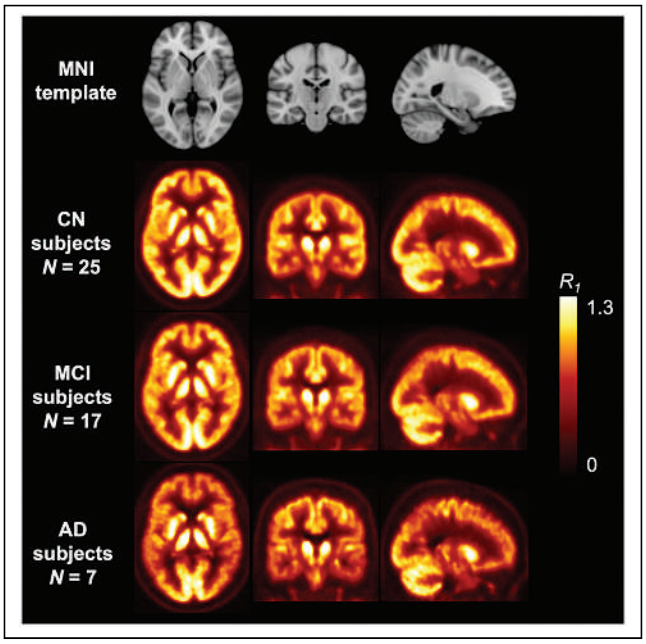

FIGURE 5. Group-average images of [^{18}F]MK6240 R_1 in CN, MCI, and AD subjects. Images are presented in MNI template space. Corresponding slices of MNI template are shown for anatomic reference.

Quantitative measurements of perfusion derived from the early phase of [^{11}C]PiB have previously been compared with the gold standard, [^{15}O]H_2O, by several investigators who reported relatively high values of the K_1 rate constant and subsequently proposed that [^{11}C]PiB might also be used to deduce changes in blood flow (*17,18,46*). Gjedde et al. previously presented evidence that the early phase of [^{11}C]PiB is not completely flow-limited, with significant but not unlimited permeability, and reported an average extraction fraction of 0.53 by comparing K_1 with CBF as measured by [^{15}O]H_2O in different brain regions of AD and CN subjects (*17*). Subsequent work by Chen et al. reported that R_1 derived from SRTM2 correlated strongly with regional relative [^{15}O]H_2O CBF measurements (*18*), and more recently, Heeman et al. demonstrated excellent test–retest reproducibility of R_1 measurement with [^{11}C]PiB, suggesting suitability for cross-sectional and longitudinal studies (*47*). Of note, the regional K_1 estimates and dynamic range of values measured in CN subjects in the present work with [^{18}F]MK6240 were about 20%–25% higher than those previously reported for [^{11}C]PiB in healthy volunteers of comparable age (*18*), suggesting that [^{18}F]MK6240 may possess a higher extraction fraction and therefore may be more sensitive to changes in CBF—although data were acquired on different scanners, using different reconstruction algorithms and different brain atlases for time–activity curve extraction, thus precluding a definitive conclusion. When we normalized by the gray cerebellum, R_1 values derived by [^{18}F]MK6240 and [^{11}C]PiB scans were similar, suggesting comparability of R_1 measurements between these 2 tracers for cross-sectional or longitudinal studies. In light of these findings and previous work with [^{11}C]PiB, future studies including head-to-head comparisons between [^{18}F]MK6240 and [^{15}O]H_2O

with arterial blood sampling would be necessary to determine the extraction fraction of [^{18}F]MK6240 and to evaluate its actual sensitivity to small changes in CBF by direct comparison of regional K_1 values between the 2 tracers and across CN, MCI, and AD subjects.

In the present work, we performed a group comparison of R_1 among CN, MCI, and AD subjects using regions of interest derived from the parcellation provided by FreeSurfer. The differences between groups were generally consistent with perfusion deficits generally reported by previous work using reference techniques (*6*), although some discrepancies exist in the literature possibly due to differences in methodology and cohorts across studies.

Although a full 120-min dynamic PET acquisition is ideal for providing fully quantitative measurements of tau pathology and indices of cerebral perfusion by tracer kinetic modeling, such a long dynamic scanning protocol is impractical in a clinical setting and typically results in patient discomfort and reduced scanning efficiency compared with shorter static scans. To address this limitation, and similarly to what was previously proposed for amyloid imaging (*48*), Kolinger et al. recently proposed a dual-time-window acquisition protocol for accurate quantitative measurements of longitudinal changes in tau load for [^{18}F]MK6240 studies (*49*). Such a protocol would be particularly suited to allow for both quantification of tau pathology—either using kinetic analysis to derive a quantitative distribution volume ratio or using a semiquantitative late SUV ratio—and derivation of an index of cerebral perfusion such as proposed in the current study.

One of the limitations of the present work is the relatively small sample size for the AD group. For this reason, in our group analyses we also presented results grouping MCI and AD subjects and comparing them with CN subjects. Our data were also acquired on 2 different systems. Although both scanners possess a similar intrinsic spatial resolution (*2*) and were calibrated and validated for absolute quantification, no further efforts were made to specifically harmonize the 2 scanners to each other. However, for each participant, paired [^{18}F]MK6240 and [^{11}C]PiB scans were performed on the same scanner and reconstructed with the same reconstruction algorithm; therefore, our results comparing the R_1 for [^{18}F]MK6240 and [^{11}C]PiB should be largely unaffected by the type of scanner. Another limitation relates to the use of a reference tissue model for deriving R_1. Although reference region techniques present the advantage of being noninvasive, that is, not requiring arterial cannulation and blood sampling, they provide a measure of only relative perfusion and cannot capture global changes in perfusion. In the present work, we used the gray cerebellum as a reference region, and although we did not find statistically significant differences in cerebellar K_1 at the group level among CN, MCI, and AD subjects, there were nonetheless some differences among subjects. Consequently, after normalization by cerebellar K_1, some group differences between the CN and MCI/AD groups that were due to global changes in perfusion (as observed in Supplemental Figs. 1A and 1B) were not apparent in R_1 estimates (Supplemental Figs. 1C and 1D). This is, however, consistent with the observation from previous studies that AD is associated with both global and regional cerebral hypoperfusion (*6*).

CONCLUSION

Our results support use of the early phase of [^{18}F]MK6240 images to derive a quantitative index of cerebral perfusion. The early and late phases of [^{18}F]MK6240 dynamic acquisitions may thus offer complementary information on cerebral perfusion and tau load, respectively. Further work including a direct comparison with the gold standard, [^{15}O]H_2O, will be needed to determine the extraction fraction of [^{18}F]MK6240 and sensitivity to small changes in CBF at different flow values.

DISCLOSURE

This study was funded by the Massachusetts General Hospital Thrall Innovation award (Nicolas Guehl); grant R21AG070714 (Nicolas Guehl); grants S10OD018035, R01AG076153, and P41EB022544 (Georges El Fakhri); and grant R01AG046396 (Keith Johnson). No other potential conflict of interest relevant to this article was reported.

ACKNOWLEDGMENTS

We thank Julia Scotton and Nicole DaSilva for preparing the subjects, scanning, and monitoring, and we thank Steven Weise and Marina MacDonald-Soccorso for helping with data management.

KEY POINTS

QUESTION: Can the early phase of [^{18}F]MK6240 dynamic imaging be used to derive a surrogate index of relative cerebral perfusion?

PERTINENT FINDINGS: Robust estimates of R_1 were obtained. The head-to-head comparison of [^{18}F]MK6240 and [^{11}C]PiB showed similar measurements of R_1, suggesting that they provide similar information on relative cerebral perfusion. Direct comparison with [^{15}O]H_2O is needed to characterize the extraction fraction of [^{18}F]MK6240 and its sensitivity to small changes in CBF.

IMPLICATIONS FOR PATIENT CARE: The early and late phases of [^{18}F]MK6240 dynamic scanning may offer complementary pathophysiologic information in AD, thus providing indices of relative cerebral perfusion and tau load, respectively.

REFERENCES

1. Hostetler ED, Walji AM, Zeng Z, et al. Preclinical characterization of ^{18}F-MK-6240, a promising PET tracer for in vivo quantification of human neurofibrillary tangles. *J Nucl Med.* 2016;57:1599–1606.
2. Guehl NJ, Wooten DW, Yokell DL, et al. Evaluation of pharmacokinetic modeling strategies for in-vivo quantification of tau with the radiotracer [^{18}F]MK6240 in human subjects. *Eur J Nucl Med Mol Imaging.* 2019;46:2099–2111.
3. Pascoal TA, Shin M, Kang MS, et al. In vivo quantification of neurofibrillary tangles with [^{18}F]MK-6240. *Alzheimers Res Ther.* 2018;10:74.
4. Betthauser TJ, Cody KA, Zammit MD, et al. In vivo characterization and quantification of neurofibrillary tau PET radioligand ^{18}F-MK-6240 in humans from Alzheimer disease dementia to young controls. *J Nucl Med.* 2019;60:93–99.
5. Lohith TG, Bennacef I, Vandenberghe R, et al. Brain imaging of Alzheimer dementia patients and elderly controls with ^{18}F-MK-6240, a PET tracer targeting neurofibrillary tangles. *J Nucl Med.* 2019;60:107–114.
6. Austin BP, Nair VA, Meier TB, et al. Effects of hypoperfusion in Alzheimer's disease. *J Alzheimers Dis.* 2011;26(suppl 3):123–133.
7. Benedictus MR, Leeuwis AE, Binnewijzend MA, et al. Lower cerebral blood flow is associated with faster cognitive decline in Alzheimer's disease. *Eur Radiol.* 2017;27:1169–1175.
8. Binnewijzend MA, Benedictus MR, Kuijer JP, et al. Cerebral perfusion in the predementia stages of Alzheimer's disease. *Eur Radiol.* 2016;26:506–514.
9. Johnson KA, Albert MS. Perfusion abnormalities in prodromal AD. *Neurobiol Aging.* 2000;21:289–292.
10. Mazza M, Marano G, Traversi G, Bria P, Mazza S. Primary cerebral blood flow deficiency and Alzheimer's disease: shadows and lights. *J Alzheimers Dis.* 2011; 23:375–389.
11. Hu WT, Wang Z, Lee VM, Trojanowski JQ, Detre JA, Grossman M. Distinct cerebral perfusion patterns in FTLD and AD. *Neurology.* 2010;75:881–888.

12. Celsis P, Agniel A, Cardebat D, Demonet JF, Ousset PJ, Puel M. Age related cognitive decline: a clinical entity? A longitudinal study of cerebral blood flow and memory performance. *J Neurol Neurosurg Psychiatry.* 1997;62:601–608.
13. Leenders KL, Perani D, Lammertsma AA, et al. Cerebral blood flow, blood volume and oxygen utilization: normal values and effect of age. *Brain.* 1990;113:27–47.
14. Lu H, Xu F, Rodrigue KM, et al. Alterations in cerebral metabolic rate and blood supply across the adult lifespan. *Cereb Cortex.* 2011;21:1426–1434.
15. Herscovitch P, Markham J, Raichle ME. Brain blood flow measured with intravenous $H_2^{15}O$. I. Theory and error analysis. *J Nucl Med.* 1983;24:782–789.
16. Raichle ME, Martin WR, Herscovitch P, Mintun MA, Markham J. Brain blood flow measured with intravenous $H_2^{15}O$. II. Implementation and validation. *J Nucl Med.* 1983;24:790–798.
17. Gjedde A, Aanerud J, Braendgaard H, Rodell AB. Blood-brain transfer of Pittsburgh compound B in humans. *Front Aging Neurosci.* 2013;5:70.
18. Chen YJ, Rosario BL, Mowrey W, et al. Relative ^{11}C-PiB delivery as a proxy of relative CBF: quantitative evaluation using single-session ^{15}O-water and ^{11}C-PiB PET. *J Nucl Med.* 2015;56:1199–1205.
19. Ottoy J, Verhaeghe J, Niemantsverdriet E, et al. ^{18}F-FDG PET, the early phases and the delivery rate of ^{18}F-AV45 PET as proxies of cerebral blood flow in Alzheimer's disease: validation against ^{15}O-H_2O PET. *Alzheimers Dement.* 2019;15:1172–1182.
20. Rodriguez-Vieitez E, Carter SF, Chiotis K, et al. Comparison of early-phase ^{11}C-deuterium-l-deprenyl and ^{11}C-Pittsburgh compound B PET for assessing brain perfusion in Alzheimer disease. *J Nucl Med.* 2016;57:1071–1077.
21. Bilgel M, Beason-Held L, An Y, Zhou Y, Wong DF, Resnick SM. Longitudinal evaluation of surrogates of regional cerebral blood flow computed from dynamic amyloid PET imaging. *J Cereb Blood Flow Metab.* 2020;40:288–297.
22. Visser D, Wolters EE, Verfaillie SCJ, et al. Tau pathology and relative cerebral blood flow are independently associated with cognition in Alzheimer's disease. *Eur J Nucl Med Mol Imaging.* 2020;47:3165–3175.
23. Meyer PT, Hellwig S, Amtage F, et al. Dual-biomarker imaging of regional cerebral amyloid load and neuronal activity in dementia with PET and ^{11}C-labeled Pittsburgh compound B. *J Nucl Med.* 2011;52:393–400.
24. Peretti DE, Vallez Garcia D, Reesink FE, et al. Diagnostic performance of regional cerebral blood flow images derived from dynamic PIB scans in Alzheimer's disease. *EJNMMI Res.* 2019;9:59.
25. Peretti DE, Vallez Garcia D, Reesink FE, et al. Relative cerebral flow from dynamic PIB scans as an alternative for FDG scans in Alzheimer's disease PET studies. *PLoS One.* 2019;14:e0211000.
26. Rodriguez-Vieitez E, Leuzy A, Chiotis K, Saint-Aubert L, Wall A, Nordberg A. Comparability of [^{18}F]THK5317 and [^{11}C]PIB blood flow proxy images with [^{18}F]FDG positron emission tomography in Alzheimer's disease. *J Cereb Blood Flow Metab.* 2017;37:740–749.
27. Beyer L, Nitschmann A, Barthel H, et al. Early-phase [^{18}F]PI-2620 tau-PET imaging as a surrogate marker of neuronal injury. *Eur J Nucl Med Mol Imaging.* 2020;47:2911–2922.
28. Brendel M, Wagner L, Levin J, et al. Perfusion-phase [^{18}F]THK5351 tau-PET imaging as a surrogate marker for neurodegeneration. *J Alzheimers Dis Rep.* 2017;1:109–113.
29. Hammes J, Leuwer I, Bischof GN, Drzezga A, van Eimeren T. Multimodal correlation of dynamic [^{18}F]-AV-1451 perfusion PET and neuronal hypometabolism in [^{18}F]-FDG PET. *Eur J Nucl Med Mol Imaging.* 2017;44:2249–2256.
30. Jack CR Jr, Bennett DA, Blennow K, et al. A/T/N: an unbiased descriptive classification scheme for Alzheimer disease biomarkers. *Neurology.* 2016;87:539–547.
31. Jack CR Jr, Bennett DA, Blennow K, et al. NIA-AA research framework: toward a biological definition of Alzheimer's disease. *Alzheimers Dement.* 2018;14:535–562.
32. Albert MS, DeKosky ST, Dickson D, et al. The diagnosis of mild cognitive impairment due to Alzheimer's disease: recommendations from the National Institute on Aging-Alzheimer's Association workgroups on diagnostic guidelines for Alzheimer's disease. *Alzheimers Dement.* 2011;7:270–279.
33. Collier TL, Yokell DL, Livni E, et al. cGMP production of the radiopharmaceutical [^{18}F]MK-6240 for PET imaging of human neurofibrillary tangles. *J Labelled Comp Radiopharm.* 2017;60:263–269.
34. Wilson AA, Garcia A, Chestakova A, Kung H, Houle S. A rapid one-step radiosynthesis of the β-amyloid imaging radiotracer N-methyl-[^{11}C]2-(4′-methylaminophenyl)-6-hydroxybenzothiazole ([^{11}C]-6-OH-BTA-1). *J Labelled Comp Radiopharm.* 2004;47:679–682.
35. Becker JA, Hedden T, Carmasin J, et al. Amyloid-beta associated cortical thinning in clinically normal elderly. *Ann Neurol.* 2011;69:1032–1042.
36. Alpert NM, Berdichevsky D, Levin Z, Morris ED, Fischman AJ. Improved methods for image registration. *Neuroimage.* 1996;3:10–18.
37. Jenkinson M, Bannister P, Brady M, Smith S. Improved optimization for the robust and accurate linear registration and motion correction of brain images. *Neuroimage.* 2002;17:825–841.
38. Jenkinson M, Beckmann CF, Behrens TE, Woolrich MW, Smith SM. FSL. *Neuroimage.* 2012;62:782–790.
39. Wooten DW, Guehl NJ, Verwer EE, et al. Pharmacokinetic evaluation of the tau PET radiotracer ^{18}F-T807 (^{18}F-AV-1451) in human subjects. *J Nucl Med.* 2017;58:484–491.
40. Fischl B, Salat DH, Busa E, et al. Whole brain segmentation: automated labeling of neuroanatomical structures in the human brain. *Neuron.* 2002;33:341–355.
41. Fischl B, van der Kouwe A, Destrieux C, et al. Automatically parcellating the human cerebral cortex. *Cereb Cortex.* 2004;14:11–22.
42. Johnson KA, Schultz A, Betensky RA, et al. Tau positron emission tomographic imaging in aging and early Alzheimer disease. *Ann Neurol.* 2016;79:110–119.
43. Innis RB, Cunningham VJ, Delforge J, et al. Consensus nomenclature for in vivo imaging of reversibly binding radioligands. *J Cereb Blood Flow Metab.* 2007;27:1533–1539.
44. Wu Y, Carson RE. Noise reduction in the simplified reference tissue model for neuroreceptor functional imaging. *J Cereb Blood Flow Metab.* 2002;22:1440–1452.
45. Mormino EC, Papp KV, Rentz DM, et al. Heterogeneity in suspected non-Alzheimer disease pathophysiology among clinically normal older individuals. *JAMA Neurol.* 2016;73:1185–1191.
46. Blomquist G, Engler H, Nordberg A, et al. Unidirectional influx and net accumulation of PIB. *Open Neuroimag J.* 2008;2:114–125.
47. Heeman F, Hendriks J, Lopes Alves I, et al. Test-retest variability of relative tracer delivery rate as measured by [^{11}C]PiB. *Mol Imaging Biol.* 2021;23:335–339.
48. Heeman F, Yaqub M, Lopes Alves I, et al. Optimized dual-time-window protocols for quantitative [^{18}F]flutemetamol and [^{18}F]florbetaben PET studies. *EJNMMI Res.* 2019;9:32.
49. Kolinger GD, Vallez Garcia D, Lohith TG, et al. A dual-time-window protocol to reduce acquisition time of dynamic tau PET imaging using [^{18}F]MK-6240. *EJNMMI Res.* 2021;11:49.

Artificial Intelligence Algorithms Need to Be Explainable—or Do They?

Tyler J. Bradshaw[1], Melissa D. McCradden[2], Abhinav K. Jha[3], Joyita Dutta[4], Babak Saboury[5], Eliot L. Siegel[6], and Arman Rahmim[7]

[1]*University of Wisconsin–Madison, Madison, Wisconsin;* [2]*Hospital for Sick Children, University of Toronto, Toronto, Ontario, Canada;* [3]*Washington University in St. Louis, St. Louis, Missouri;* [4]*University of Massachusetts Amherst, Amherst, Massachusetts;* [5]*National Institutes of Health, Bethesda, Maryland;* [6]*University of Maryland School of Medicine, Baltimore, Maryland; and* [7]*University of British Columbia, Vancouver, British Columbia, Canada*

With the growing role of artificial intelligence (AI) in radiology, there is concern over the black-box nature of modern AI algorithms. Users of AI often have no way of knowing how or why an algorithm arrived at a prediction, which makes it difficult for a user to appraise or critique the quality of the prediction. The group of methods collectively known as explainable AI (XAI) aims to overcome this limitation by providing human-understandable explanations of the causal relationships between an algorithm's inputs and outputs. XAI's motivations include promoting trust between clinicians and AI systems, enabling detection of errors, and facilitating informed consent. However, it has been argued that XAI may not in fact address the needs of clinicians and may also introduce unintended consequences, potentially compromising the purported value of XAI (*1*). At the 2022 Society of Nuclear Medicine and Molecular Imaging annual meeting, we held a debate over the clinical need for XAI. We summarize that debate here by discussing 5 key arguments. For each argument, we present the case for and against the use of XAI from the perspectives of data science, clinical practice, and bioethics.

First, it should be recognized that the term *XAI* refers to a variety of approaches, most of which were originally developed for uses outside of medicine (*2*). XAI includes interpretable methods in which AI algorithms are designed to be inherently explainable, as well as post hoc methods that are applied to already-trained algorithms. The way that explanations are presented can also vary (*3*). In radiology, XAI is often presented through saliency maps, which highlight the parts of an image that have the most impact on the model's predictions. For example, Miller et al. showed how saliency mapping can highlight the most influential regions of the myocardium for AI-based diagnosis of coronary artery disease in SPECT images (*4*).

IDENTIFICATION OF CONFOUNDING FACTORS

A potential benefit of XAI is that it might help uncover AI biases caused by confounding factors. The tendency for AI to rely on shortcuts—spurious correlations unrelated to biomedical pathology—is well documented. DeGrave et al. demonstrated how an AI system learned to mistakenly rely on laterality markings in radiographs for diagnostic predictions (*5*). XAI could be used as a quality control method, potentially helping users identify these confounding factors. Conversely, correlations uncovered by XAI might turn out to be real but previously unknown biomedical relationships, in which case XAI could be used as a tool for scientific discovery. The counterargument is that the task of identifying confounding factors should not be the responsibility of the users. The workflow of a user, which consists of looking at individual AI predictions during clinical reads, is not well matched to the workflow required to identify confounding factors, which requires inspecting XAI explanations across many samples to discern spurious relationships. In this context, XAI might be better suited as a quality control tool for developers rather than for users. Additionally, biases caused by confounding factors will be better uncovered by comprehensive clinical evaluation of AI algorithms, including learning which patient populations would benefit from the use of an algorithm.

DETECTION OF ALGORITHMIC ERRORS

Another argument in favor of XAI is that it can help users know when an AI algorithm errs. XAI can help users know when to follow and when to reject AI predictions based on the plausibility of the explanation. Also, the additional information provided by XAI explanations could lead to better failure-mode profiling of a system. This could result in a better understanding of the functional dependencies of a system and its vulnerabilities. On the other hand, recent evidence suggests that XAI can actually have the opposite effect and could potentially lead some users to make more judgment errors (*1*). The presence of explanations alongside predictions may further persuade users to follow incorrect outputs by appearing to corroborate erroneous AI predictions (*6*).

RELIABILITY OF EXPLANATIONS

Although XAI is in its early stages, it has already provided meaningful contributions to guiding AI development (*5*). As the field matures, the quality of explanations will continue to improve. Future methods will include more sophisticated explanations beyond just saliency mapping. However, a major criticism of current XAI approaches is that their explanations are too unreliable to be

Received Sep. 23, 2022; revision accepted Mar. 17, 2023.
For correspondence or reprints, contact Tyler Bradshaw (tbradshaw@wisc.edu).
Published online Apr. 28, 2023.

DOI: 10.2967/jnumed.122.264949

clinically beneficial. Studies have found inconsistencies in the explanations provided by different XAI techniques and have demonstrated their sensitivity to clinically inconsequential changes in input images (*7*). With different XAI methods providing different explanations, how can users know which one is correct? And if both the predictions and the explanations can be wrong, this adds another avenue for an AI system to err. A more fundamental challenge is that explanations from current XAI methods superficially represent the computational complexity that underlies a prediction (*3*). Additionally, the best approach for evaluating the quality of an explanation is uncertain. Different approaches have been used to evaluate XAI, including user feedback studies, simulation studies, and studies measuring XAI impact on diagnostic accuracy, but each has potential shortcomings, such as subjectivity, lack of reality, and high costs. Although the current challenges facing XAI should not dissuade us from pursuing explainability as a goal, there is no guarantee that XAI will become sufficiently reliable, especially as AI complexity continues to increase.

TRANSPARENCY AND TRUSTWORTHINESS

Another potential benefit of XAI is that it could enhance the transparency and trustworthiness of AI systems. XAI provides users with a better understanding of an AI system's reasoning, which can lead to trust between user and algorithm. Furthermore, clinicians generally prefer AI systems with XAI over systems without it (*8*), and providing them with XAI could lead to broader adoption of beneficial AI tools. A rebuttal to this argument is that a mechanistic understanding of how an intervention works is not necessary for either trust or transparency. Many drugs have unknown mechanisms of action, yet we learn the conditions under which they should and should not be used. Furthermore, given the questionable reliability of XAI, the transparency offered by XAI may not be the kind of transparency that is valuable and could be worse than no information at all. As long as developers provide detailed information on the development and validation of their AI system, including its expected benefits and risks, the additional transparency provided by XAI may not be necessary.

PATIENT-CENTERED CARE

Lastly, it can be argued that XAI empowers clinicians to provide more patient-centered care. Without explainability, clinicians lack power to adequately critique an AI decision on behalf of their patient. XAI gives an opportunity for providers and patients to understand AI decisions, giving both of them greater control over clinical decisions. Additionally, clinicians are accountable for obtaining informed consent from patients, which may not be well served by black-box algorithms. The counterargument is that XAI may lead to less emphasis on patient input and testimony in decision-making, particularly given the possibility of overreliance on AI systems (*9*). Currently, neither AI nor XAI considers patient preferences or values (*10*), and XAI may shift clinicians further into a decision-making mode that assumes that the AI system holds all the knowledge to guide clinical decisions. Additionally, informed consent has never required a mechanistic understanding of an intervention, only its risks and benefits.

CONCLUSION

XAI may play an essential role in the era of collaborative AI–human intelligence systems within medicine. But the potential benefits of XAI need to be carefully weighed against potential risks. A cautious approach to the clinical adoption of XAI is warranted. Future directions for research should include improved robustness of XAI with more standardized methods of objectively measuring explanation quality. Furthermore, an understanding of the multifaceted impact that XAI will have on clinical decision-making is needed, which will require a concerted multidisciplinary effort.

DISCLOSURE

No potential conflict of interest relevant to this article was reported.

REFERENCES

1. Jacobs M, Pradier MF, McCoy TH, Perlis RH, Doshi-Velez F, Gajos KZ. How machine-learning recommendations influence clinician treatment selections: the example of antidepressant selection. *Transl Psychiatry.* 2021;11:108.
2. Linardatos P, Papastefanopoulos V, Kotsiantis S. Explainable AI: a review of machine learning interpretability methods. *Entropy (Basel).* 2021;23:18.
3. Evans T, Retzlaff CO, Geißler C, et al. The explainability paradox: challenges for xAI in digital pathology. *Future Gener Comput Syst.* 2022;133:281–296.
4. Miller RJH, Kuronuma K, Singh A, et al. Explainable deep learning improves physician interpretation of myocardial perfusion imaging. *J Nucl Med.* 2022;63:1768–1774.
5. DeGrave AJ, Janizek JD, Lee S-I. AI for radiographic COVID-19 detection selects shortcuts over signal. *Nat Mach Intell.* 2021;3:610–619.
6. Gaube S, Suresh H, Raue M, et al. Do as AI say: susceptibility in deployment of clinical decision-aids. *NPJ Digit Med.* 2021;4:31.
7. Arun N, Gaw N, Singh P, et al. Assessing the trustworthiness of saliency maps for localizing abnormalities in medical imaging. *Radiol Artif Intell.* 2021;3:e200267.
8. Diprose WK, Buist N, Hua N, Thurier Q, Shand G, Robinson R. Physician understanding, explainability, and trust in a hypothetical machine learning risk calculator. *J Am Med Inform Assoc.* 2020;27:592–600.
9. McCradden M, Hui K, Buchman DZ. Evidence, ethics and the promise of artificial intelligence in psychiatry. *J Med Ethics.* December 29, 2022 [Epub ahead of print].
10. Birch J, Creel KA, Jha AK, Plutynski A. Clinical decisions using AI must consider patient values. *Nat Med.* 2022;28:229–232.

Submillimeter-Resolution PET for High-Sensitivity Mouse Brain Imaging

Han Gyu Kang[1], Hideaki Tashima[1], Hidekatsu Wakizaka[1], Fumihiko Nishikido[1], Makoto Higuchi[2], Miwako Takahashi[1], and Taiga Yamaya[1]

[1]*Department of Advanced Nuclear Science, National Institutes for Quantum Science and Technology, Chiba, Japan; and* [2]*Department of Functional Brain Imaging, National Institutes for Quantum Science and Technology, Chiba, Japan*

PET is a powerful molecular imaging technique that can provide functional information on living objects. However, the spatial resolution of PET imaging has been limited to around 1 mm, which makes it difficult to visualize mouse brain function in detail. Here, we report an ultrahigh-resolution small-animal PET scanner we developed that can provide a resolution approaching 0.6 mm to visualize mouse brain function with unprecedented detail. **Methods:** The ultrahigh-resolution small-animal PET scanner has an inner diameter of 52.5 mm and axial coverage of 51.5 mm. The scanner consists of 4 rings, each of which has 16 depth-of-interaction detectors. Each depth-of-interaction detector consists of a 3-layer staggered lutetium yttrium orthosilicate crystal array with a pitch of 1 mm and a 4 × 4 silicon photomultiplier array. The physical performance was evaluated in accordance with the National Electrical Manufacturers Association NU4 protocol. Spatial resolution was evaluated with phantoms of various resolutions. In vivo glucose metabolism imaging of the mouse brain was performed. **Results:** Peak absolute sensitivity was 2.84% with an energy window of 400–600 keV. The 0.55-mm rod structure of a resolution phantom was resolved using an iterative algorithm. In vivo mouse brain imaging with ^{18}F-FDG clearly identified the cortex, thalamus, and hypothalamus, which were barely distinguishable in a commercial preclinical PET scanner that we used for comparison. **Conclusion:** The ultrahigh-resolution small-animal PET scanner is a promising molecular imaging tool for neuroscience research using rodent models.

Key Words: submillimeter resolution; preclinical PET; depth of interaction; in vivo mouse brain imaging

J Nucl Med 2023; 64:978–985
DOI: 10.2967/jnumed.122.264433

In vivo imaging of rodent models is crucial to understand the underlying mechanisms of various human diseases such as cancer (*1,2*) and neurodegenerative diseases (*3,4*); in turn, this understanding can lead to the discovery of new drugs for human diseases. PET has been playing a distinctive role in preclinical research as a molecular imaging tool that provides spatiotemporal information on biochemical processes in living animals (*5*). Small-animal PET imaging is particularly useful to discover and assess specific biomarkers of cancer and neurodegenerative diseases at a measurable picomolar level.

However, the spatial resolution of commercial PET scanners (*6–9*) has been limited to around 1.0–1.3 mm, which cannot distinguish the components of small objects such as the mouse brain, whose substructural organs (e.g., cortex and thalamus) are located near one another on the order of a few hundred micrometers. Even for the state-of-the art small-animal PET scanners developed since late 2020 by laboratories (*10–14*) and companies (*15–18*), the spatial resolutions are still around 0.8–1.2 mm and not good enough to identify small mouse-brain structures in detail, making it difficult to assess subtle alterations of mouse brain activity in neurodegenerative disease models.

One major factor limiting the spatial resolution of small-animal PET scanners is the crystal pitch, which typically ranges from 1.2 to 1.6 mm (*19*). A second factor is depth-of-interaction (DOI) information, which can preserve the spatial resolution in a small-ring-diameter geometry in which resolution blurring by the photon noncollinearity effect is relatively small (*20*). Intercrystal scattering (ICS) is a third factor that degrades spatial resolution by assigning the line of response to the wrong crystal positions, especially in finely pixelated crystal arrays (*21*).

In this study, we developed an ultrahigh-resolution small-animal PET scanner that addresses these technical issues to provide submillimeter resolution in a 51.5-mm-long axial coverage. A silicon photomultiplier (SiPM)–based staggered 3-layer DOI detector (*22*) was used to build a PET scanner for in vivo submillimeter imaging of the rodent brain.

MATERIALS AND METHODS

Submillimeter-Resolution Small-Animal PET Scanner

The submillimeter-resolution small-animal PET scanner (referred to here as the SR-PET) has 4 rings of 16 DOI detectors each, resulting in a 52.5-mm inner diameter and a 51.5-mm axial field of view (FOV) (Fig. 1A). Each DOI detector (*22*) consists of a 3-layer lutetium yttrium orthosilicate (LYSO) crystal array (EPIC Crystal), a 1-mm-thick acrylic light guide, and an SiPM 4 × 4 array (S14161-3050HS-04; Hamamatsu Photonics K.K.) (Fig. 1B; Supplemental Video 1; supplemental materials are available at http://jnm.snmjournals.org). The 3-layer LYSO crystal array consists of a first (10 × 9), second (10 × 10), and third (11 × 11) layer stacked in a staggered configuration with an offset of crystal half pitch in the radial and axial directions to encode the DOI information in the crystal map (Supplemental Fig. 1). The crystal thicknesses of the first, second, and third layers are 4, 4, and 7 mm, respectively. The LYSO crystals (0.9 × 0.9 mm cross section) are optically isolated using a 0.1-mm-thick $BaSO_4$ powder layer, resulting in a

Received Aug. 15, 2022; revision accepted Dec. 22, 2022.
For correspondence or reprints, contact Han Gyu Kang (kang.hangyu@qst.go.jp).
Published online Dec. 29, 2022.

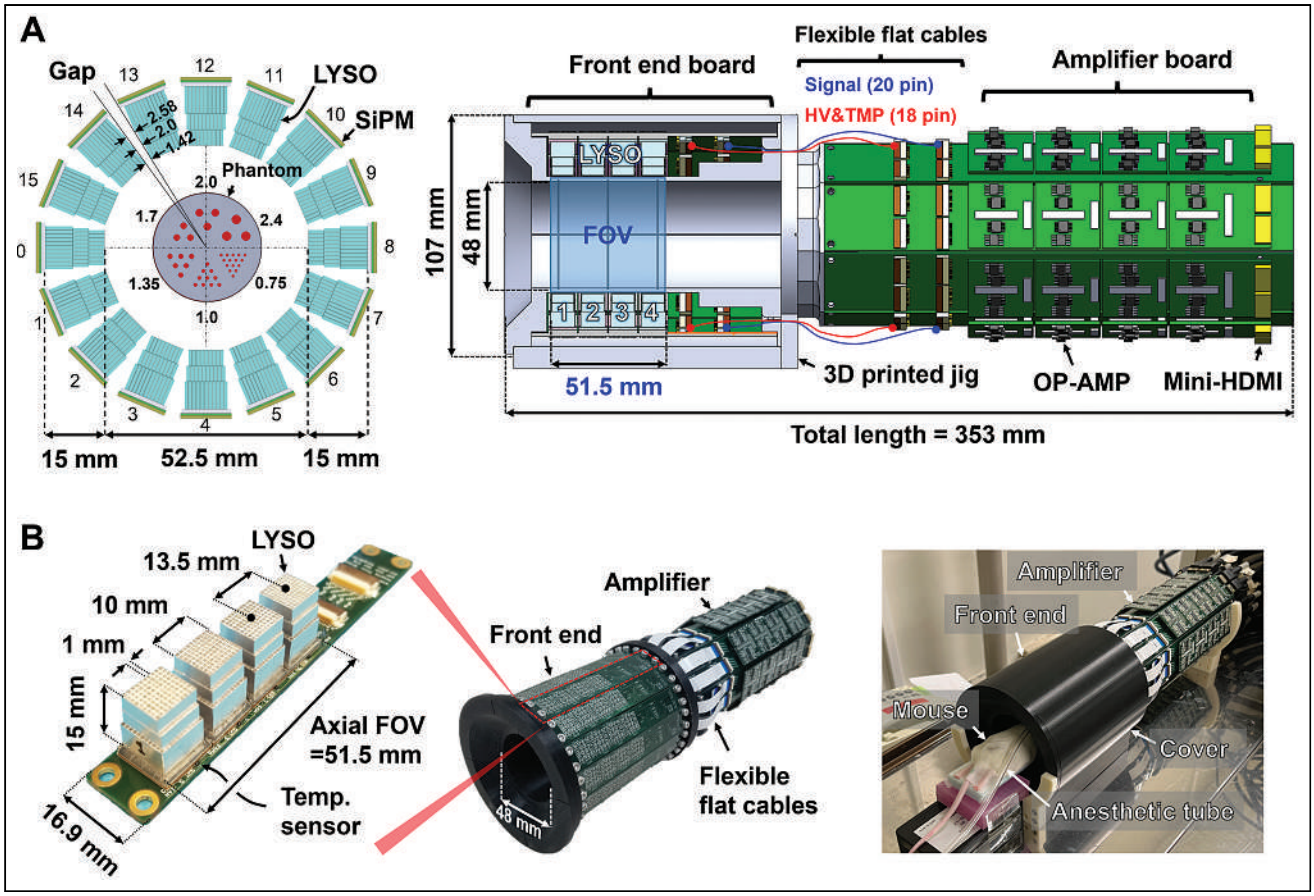

FIGURE 1. (A) Schematic drawings of SR-PET scanner in front and side views. (B) Photographs of SR-PET scanner with one front-end board, and in vivo mouse imaging setup with PET scanner. HDMI = high-definition multimedia interface cables; HV = high-voltage; OP-AMP = operational amplifier; TMP = temperature.

1-mm crystal pitch. Each crystal layer is optically coupled using epoxy glue (refractive index, 1.52; EPO-TEK 301-1 [Epoxy Technology]). The 3-layer LYSO crystal array, light guide, and SiPM are optically coupled using room temperature vulcanizing silicon rubber (refractive index, 1.45; KE420 [Shin-Etsu Chemical Co., Ltd.]). The top surface of the first crystal layer is covered by 2 layers of Teflon (Nichias) tape with a total thickness of 0.2 mm. The radial gap distances between the detector blocks are 1.42, 2.0, and 2.58 mm, for the first, second, and third layers, respectively (Fig. 1A). Four LYSO crystal arrays are mounted on the SiPM with a spacing of 13.5 mm in the axial direction (Fig. 1B). A cylindric lighttight cover is used to block external light.

For the SiPM signal readout and amplifications, custom-made front-end and amplifier boards are used (Supplemental Fig. 2A). A front-end board has 4 SiPMs, which are mounted with a central pitch of 13.5 mm in the axial direction (Supplemental Fig. 2B). An SiPM bias voltage of +41.0 V (overvoltage, 3.2 V) is applied to the common cathode (Supplemental Fig. 2C). Sixteen anode signals of each SiPM are reduced into 4 positional signals using a resistive network (Supplemental Fig. 2D). The positional signals from the front-end board are transferred to the amplifier boards through 10-cm-long flat, flexible cables. A timing signal that also carries the energy information is generated by summing the 4 positional signals. Each amplifier board consists of 4 add-on amplifier boards, and each add-on board can process 10 analog signals from 2 DOI detectors (Supplemental Fig. 2E).

The positional signals are amplified using a low-power quad-channel amplifier (OPA4684IPWT; Analog Device). The timing signal is fed to a fast amplifier (AD8000; Analog Device), and then a pole-zero-cancellation circuit is used to obtain fast pulse rise (26 ns) and decay (144 ns) times (Supplemental Fig. 2F). The temperature of each SiPM is monitored by a sensor (LM94023; Texas Instruments) attached near the SiPM. The SiPM ambient temperature is maintained at 26°C ± 0.4°C by an air conditioner in the experimental room to minimize the SiPM gain drift because of the temperature change. No temperature compensation technique was used for the SiPM since the maximum variation of the ambient temperature was within only ±0.4°C. The amplified SiPM analog signals from each amplifier board are transferred to a custom-made interface board via four 3-m-long high-definition multimedia interface cables (Supplemental Fig. 3). Subsequently, the SiPM signals are sent to a custom-made data acquisition system (*23*) via four 1.8-m-long radiofrequency shielded cables (Hewtech). The 320-channel 8-bit data acquisition system is used to digitize the SiPM analog signals with a sampling rate of 50 MSPS and an integration time of 250 ns.

The list-mode PET data are acquired in the singles mode and then stored on the hard disk of a desktop personal computer. Subsequently, the prompt coincidence events are identified using coincidence processing software with a coincidence window of 10 ns. The random coincidence events are recorded by a delayed coincidence window with a time offset of 260 ns.

The normalization data are obtained for 72 h by rotating a 0.16-MBq ^{68}Ge–^{68}Ga line source (diameter, 2 mm; length, 260 mm) using a motor stage (SGSP-80YAW; Sigmakoki) with a rotating radius of 22.5 mm.

Image Reconstruction

For image reconstruction, analytic and iterative algorithms are used—namely the 2-dimensional (2D) filtered-backprojection (FBP) and list-mode 3-dimensional (3D) ordered-subset expectation-maximization (OSEM) algorithms. A voxel size of $0.25 \times 0.25 \times 0.25$ mm^3 and a matrix size of $200 \times 200 \times 206$ are used for image reconstruction. For the 2D FBP algorithm, oblique sinograms are rebinned into direct sinograms using a single-slice rebinning algorithm (*24*) and then are reconstructed with a gap-filling method (*22*) that does not degrade the spatial resolution (Supplemental Fig. 4).

For the list-mode 3D OSEM algorithm, the detector response function modeling and normalization factors are incorporated into the system matrix. The system matrix is computed using the Siddon ray tracing algorithm with 5 subdivided crystal positions for each crystal layer (*22*). Eight subsets and 10 iterations are used unless otherwise specified. 3D gaussian image domain blurring (IDB) is incorporated during the image reconstruction to smooth the reconstructed images. The iteration number and IDB kernel size (i.e., full width at half maximum) are determined by a visual check, depending on the imaging object (Supplemental Table. 1). For PET data correction, normalization and random correction are performed. Scatter and attenuation corrections are not used. For all reconstructed PET images, contrast is adjusted only for the maximum level whereas the minimum level is set to zero, without any adjustment.

Physical Performance Evaluation

Evaluation of the physical performance of the SR-PET scanner was based on the National Electrical Manufacturers Association (NEMA) protocol. To evaluate the spatial resolution and sensitivity, a NEMA ^{22}Na point source (Eckert and Ziegler Isotope Products) with a diameter of 0.25 mm and an activity of 0.26 MBq was used.

The energy resolution and coincidence timing resolution were evaluated with the ^{68}Ge line source positioned at the center of the FOV. A Voronoi diagram was applied to a crystal map to extract the energy information on individual crystals (*22,25*). Subsequently, a global energy spectrum was generated by summing all energy spectra of 64 DOI detectors after photopeak alignment for individual crystals. Then, system energy resolution was calculated by the ratio of full width at half maximum to the photopeak position without applying SiPM saturation correction (*22*). A global timing spectrum was obtained from the time stamp information of the 64 DOI detectors with an energy window of 400–600 keV after time skew correction (*23*).

The axial sensitivity profile was obtained by translating the ^{22}Na point source with a step distance of 0.5 mm (crystal half pitch) from −26.5 to 26.5 mm. PET data were taken for 1 min for each axial position. ^{176}Lu intrinsic radioactivity and the positron branching ratio of the ^{22}Na source (i.e., 0.91) were considered for the sensitivity calculation.

Spatial resolution was measured using the ^{22}Na point source from the center to the 15-mm radial offset position with a step distance of 2.5 mm (Supplemental Fig. 5A). In addition, spatial resolution was measured at different axial offset positions of 6.25, 13.5, and 19.75 mm, with an interval of 6.25 mm corresponding to the half pitch of the ring (Supplemental Fig. 5B). List-mode PET data were reconstructed using a 2D FBP algorithm without any gap-filling method. Iterative algorithms can artificially enhance spatial resolution for a point source in air, especially with extremely high iterations (*26*). Therefore, we chose 10 iterations for OSEM, where the radial full-width-at-tenth-maximum improvement plateaued and the radial full-width-at-half-maximum improvement had not yet plateaued (Supplemental Fig. 6). A line profile was extracted from the reconstructed PET image, and the full widths at half maximum and tenth maximum were then evaluated. An energy window of 440–560 keV was used, and the ^{22}Na point source diameter, 0.25 mm, was not subtracted from the spatial resolution.

Count rate performance was evaluated with a 70-mm-long cylindric NEMA mouselike phantom (diameter, 25 mm). A 60-mm-long tubing source containing ^{18}F solution (initial activity, 18.2 MBq) was inserted into the 3.2-mm-diameter hole of the phantom. PET data were acquired for 1 min every 30 min, until the activity decreased to 0.02 MBq. The true, scatter, random, and noise-equivalent count rates were calculated with energy windows of 250–750, 350–650, 400–600, and 440–560 keV, respectively (*22*).

To evaluate the recovery coefficient, spillover ratios, and uniformity, a NEMA NU4 image-quality phantom was filled with ^{18}F-FDG of 1.7 MBq and then scanned for 180 min. An energy window of 400–600 keV was used. For the OSEM algorithm, an IDB kernel size of 1.25 mm was used without applying any postprocessing filter. For the FBP algorithm, the gap-filling method was applied, followed by 3D gaussian postprocessing filtering with a kernel size of 1 mm. The recovery coefficient, spillover ratios, and uniformity were calculated from the axially summed images with a 10-mm slice thickness.

Resolution Phantom Imaging

The spatial resolution of the PET scanner was evaluated with 3 resolution phantoms in which the center-to-center distance of each rod was twice the rod diameter (Supplemental Fig. 7). First, a modified Ultra-Micro Hot Spot Phantom (Japan Radioisotope Association) (*22*) containing ^{22}Na gel (0.77 MBq) was scanned for 60 min at the center of the PET FOV. The modified Ultra-Micro Hot Spot Phantom had 6 rod sectors (rod diameters of 0.75, 1.0, 1.35, 1.7, 2.0, and 2.4 mm) and an axial length of 8 mm (Supplemental Fig. 7A). The number of coincidence events was about 22 million. Image reconstruction used 10 iterations, a 0.5-mm IDB kernel size, and a 440- to 560-keV energy window. The reconstructed transverse PET images were projected in the axial direction with an 8-mm thickness, thereby producing an axially summed image. In addition, the effect of the energy window on spatial resolution was also investigated with various energy windows (250–750, 350–650, 400–600, and 440–560 keV), as ICS events can be discriminated on the basis of pulse height information with the 3-layer DOI detector (*22,25*).

The same-resolution phantom was also scanned using a commercial preclinical PET scanner (Inveon D-PET; Siemens) (*8*) for 10 min with an energy window of 350–650 keV to obtain 24 million true coincidence events. PET images were reconstructed using 2 different algorithms: 2D FBP and 2D OSEM. For 2D OSEM, 16 subsets and 4 iterations were used. A voxel size of $0.194 \times 0.194 \times 0.796$ mm and a matrix size of $256 \times 256 \times 159$ were used for Inveon PET image reconstruction.

Second, a SPECT rat phantom (*22*) having 6 different rod sectors (rod diameters of 0.7, 0.8, 0.9, 1.0, 1.2, and 1.5 mm) and a 12-mm axial length was filled with ^{18}F of 2.1 MBq (Supplemental Fig. 7B). The SPECT rat phantom was placed at the center of the PET FOV and scanned for 60 min. PET images were reconstructed using OSEM with 10 iterations, a 0.5-mm IDB kernel size, and a 440- to 560-keV energy window. The transverse PET images were projected in the axial direction with a 12-mm thickness to generate a summed image.

Lastly, a PET mouse phantom having 6 rod sections (rod diameters of 0.45, 0.5, 0.55, 0.75, 0.8, and 0.85 mm) and a 10-mm axial length was filled with ^{18}F of 1.1 MBq (Supplemental Fig. 7C). The PET mouse phantom was placed at the center of the PET FOV and then scanned for 60 min. For OSEM image reconstruction, 50 iterations and a 440- to 560-keV energy window were used. The reconstructed transverse PET images were axially projected with a thickness of 10 mm (i.e., 40 slices) to generate a summed image.

For quantitative evaluation of the spatial resolution, the valley-to-peak ratio (VPR) was calculated from the line profiles of each rod sector. Subsequently, resolvability (*22,27*) was calculated for each rod sector as follows:

$$\text{Resolvability} = \frac{N_{Rayleigh}}{N_{Total}} \times 100\%,$$

where $N_{Rayleigh}$ is the number of line profiles with VPR below the Rayleigh criterion (i.e., a VPR of 0.735) (*22,27*) and N_{Total} is the total number of line profiles for each rod sector. The effects of IDB kernel sizes on SPECT rat and PET mouse phantom images were also investigated.

In Vivo Animal Imaging

For metabotropic glutamate receptor imaging of a mouse brain, a 7-MBq dose of ^{18}F-FITM (*28*)—a radioligand for metabotropic glutamate receptor 1—was administered to a conscious 9-wk-old, 20-g male nude BALB/cSlc-nu-mouse via the tail vein. Forty minutes after the injection, the mouse was anesthetized with 1.5%–2.0% isoflurane and underwent PET for 30 min. The 3D OSEM image reconstruction used 20 iterations, a 1.25-mm IDB kernel, and a 440- to 560-keV energy window.

For glucose metabolism imaging of a mouse brain, ^{18}F-FDG with a radioactivity dose of 7 MBq was administered to a conscious 7-wk-old, 30.5-g male Slc:ddY mouse via the tail vein. The mouse was then allowed to move freely inside a cage for 30 min without any anesthesia so as to induce metabolic trapping of the radiotracer, reflecting cerebral glucose metabolism in an awake condition (*29*). Next, the mouse was anesthetized using isoflurane to minimize motion artifacts during the PET scan, and a 30-min PET data acquisition was done 34 min after injection. After this imaging session, an additional scan of the same mouse using the Inveon PET scanner was initiated 70 min after radiotracer injection and lasted 30 min. The Inveon PET data were reconstructed using 3D OSEM followed by maximum a posteriori estimation with 16 subsets, 2 iterations, a 350- to 650-keV energy window, and a matrix size of 256 × 256 × 159. The numbers of prompt coincidence events were 20 million for the Inveon PET scanner and 24 million for the SR-PET scanner. After the series of 2 PET scans, the mouse was imaged in a preclinical CT scanner (CosmoScan GX; Rigaku) using a 70-kV tube voltage and an 80-μA tube current to obtain anatomic information. The CT images had a voxel size of 0.24 × 0.24 × 0.24 mm^3 and a matrix size of 256 × 256 × 512. To register the PET and CT images, PMOD software (version 3.4) was used. For all mouse brain PET images, the central 25 × 25 mm^2 square was cropped and displayed.

For glucose metabolism imaging of a rat brain, ^{18}F-FDG with a radioactivity dose of 12.3 MBq was administered to a conscious 8-wk-old, 283-g male Sprague–Dawley rat via the tail vein. The rat was anesthetized with isoflurane, and a 50-min brain scan with the SR-PET was done 140 min after ^{18}F-FDG injection. Ten iterations, a 1.25-mm IDB kernel size, and an energy window of 440–560 keV were used for OSEM image reconstruction.

All animal experiments were conducted in accordance with the animal experiment guidelines of the National Institutes for Quantum Science and Technology after being approved by the local ethical committee of the institute.

RESULTS

Physical Performance

The system coincidence timing resolution was 9.5 ns, and the system energy resolution was 24.3% (Fig. 2A). The axial sensitivity profiles had symmetric distributions, with peak axial sensitivities of 8.66%, 4.39%, 2.84%, and 1.56% for energy windows of 250–750, 350–650, 400–600, and 440–560 keV, respectively (Fig. 2B). The peak noise-equivalent count rate decreased from 46.9 to 5.14 kcps as the energy window was narrowed from 250–750 to 440–560 keV (Supplemental Fig. 8; Supplemental Table 2).

The average radial resolutions from center to the 10-mm radial offset position for the axial offset positions of center and 6.25, 13.5, and 19.75 mm were 1.00 ± 0.16, 0.91 ± 0.05, 0.98 ± 0.12, and 0.91 ± 0.04 mm with FBP (Supplemental Table 3) and 0.58 ± 0.12, 0.61 ± 0.19, 0.58 ± 0.19, and 0.56 ± 0.19 mm with OSEM (Supplemental Table 4).

Spatial resolution was dependent not only on radial position but also axial position (Fig. 3). The axial resolution with FBP was degraded at an axial offset of 0 and 13.5 mm, where there were no direct lines of response. Resolution degradations in the axial and tangential directions were effectively reduced using the OSEM algorithm, which accounted for the geometric factors. However, axial resolution was degraded for positions near the axial center because of parallax error in the axial direction. Even with high iterations of over 10 (Supplemental Fig. 9), the radial resolution improvement for the radial offset of 10 and 15 mm was less dramatic than the radial offsets of within 5 mm because of parallax error.

The NEMA NU4 phantom images (Supplemental Fig. 10) and analysis results (Supplemental Table 5) indicate good image quality in terms of recovery coefficient, uniformity, and spillover ratios.

Resolution Phantom Images

The 0.75-mm rod structures of the modified Ultra-Micro Hot Spot Phantom were resolved with an average VPR of 0.543 ± 0.065 and 100% resolvability (Fig. 4A). The 0.75-mm rod structure could also be resolved using the 2D FBP algorithm with an average

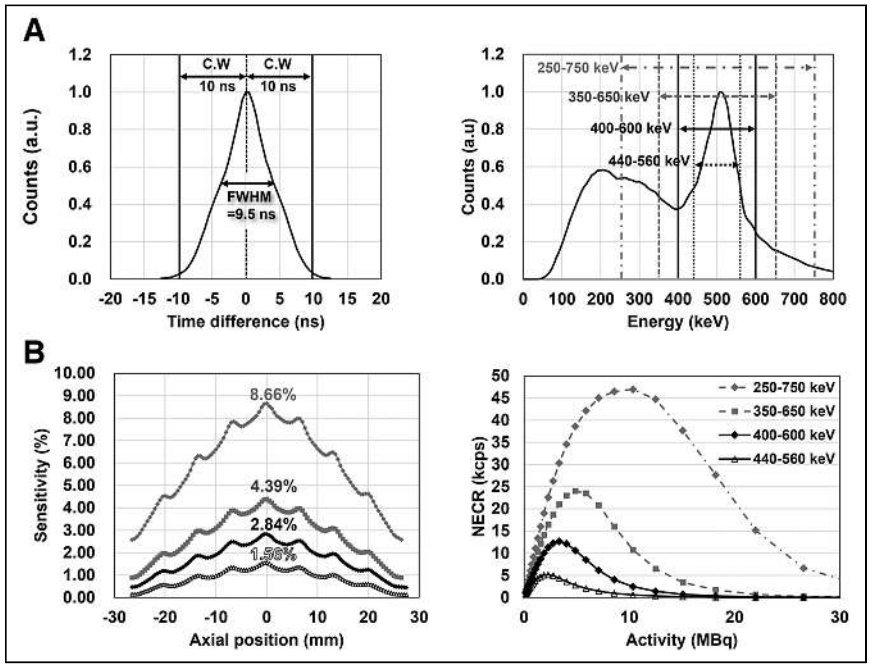

FIGURE 2. (A) Global timing and energy spectra. (B) Axial sensitivity profiles, and noise-equivalent count rate curves with energy windows of 250–750, 350–650, 400–600, and 440–560 keV. a.u. = arbitrary units; C.W = coincidence window; NECR = noise-equivalent count rate; ns = not statistically significant.

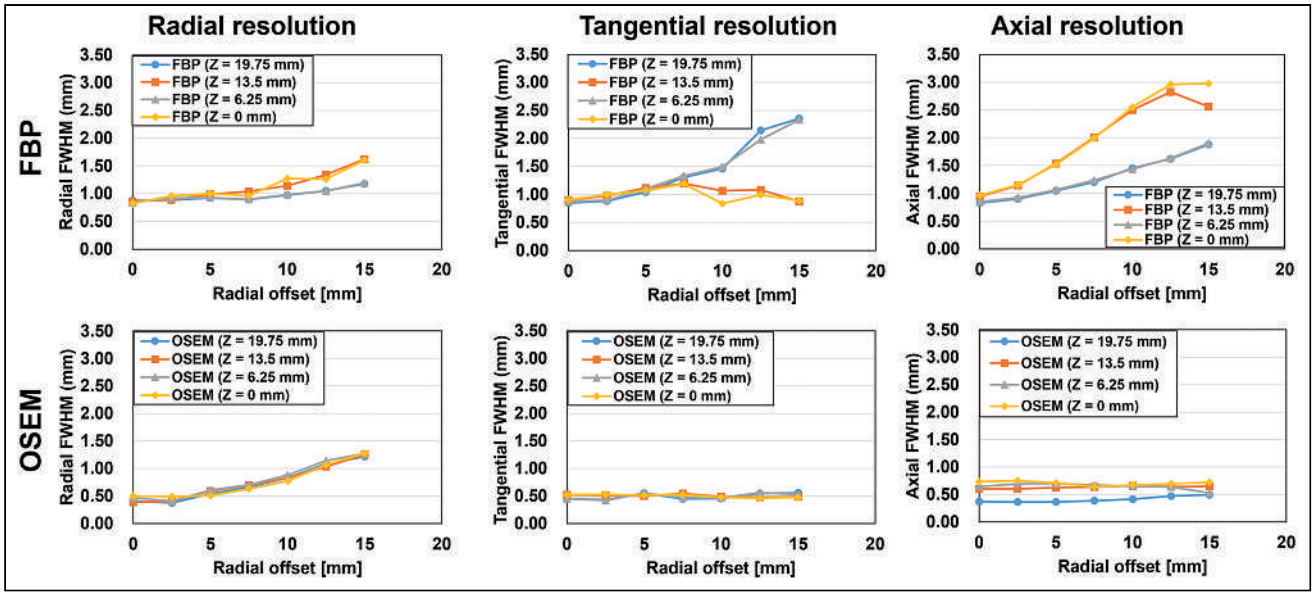

FIGURE 3. Spatial resolution measurements with ^{22}Na point source at different radial and axial offset positions using energy window of 440–560 keV. Radial, tangential, and axial resolutions are shown with FBP (top) and OSEM using 10 iterations (bottom).

VPR of 0.775 ± 0.079 with a resolvability of 33.3% (Fig. 4B). In contrast, the Inveon PET could not resolve the 0.75-mm rod structure of the same phantom with FBP (Fig. 4C) and OSEM (Fig. 4D) because of the limited spatial resolution of 1.0–1.3 mm. For the SR-PET scanner, spatial resolution improved as the energy window was narrowed from 250–750 keV to 440–560 keV (Supplemental Figs. 11 and 12) because of decreased ICS events at the expense of sensitivity (Supplemental Table 6).

For the reconstructed OSEM image of the SPECT rat phantom, all rod patterns from 0.7 to 1.5 mm were resolved 100% (Supplemental Table 7).

To resolve structures smaller than 0.6 mm, 50 iterations were used for the PET mouse phantom (Supplemental Fig. 12), thereby resolving the 0.55-mm rod pattern with an average VPR of 0.527 (resolvability, 100%) (Fig. 5). However, the resolvability for the 0.5- and 0.45-mm rod patterns was only 55%, and 8%, respectively (Supplemental Table 7).

In Vivo Rodent Brain Images

For rodent brain imaging, an IDB kernel size of 1.25 mm was used to smooth the images while maintaining submillimeter resolution (Supplemental Figs. 14 and 15). Representative coronal mouse brain PET images at 4 different planes 1 mm apart were selected for visual display (Fig. 6). High accumulations of ^{18}F-FITM in the thalamus and cerebellum of the nude mouse could be observed in the PET images (Fig. 6A; Supplemental Video 2). The cortex, thalamus, hypothalamus, and amygdala of the nude mouse were also well delineated. In the sagittal image, the olfactory bulb and prefrontal cortex were well identified.

^{18}F-FDG images of the mouse brain allowed clear identification of the cortex, thalamus, and hypothalamus, which were located close to one another, with only 0.5- to 0.75-mm separations (Fig. 6B). In addition, the amygdala, whose position was near the cortex, could be identified. In contrast to the SR-PET, the Inveon PET could barely resolve brain structures in the same mouse because of the low spatial resolution (Fig. 6C).

^{18}F-FDG SR-PET images of the mouse brain coregistered well with CT images in the coronal, sagittal, and transverse planes (Fig. 7). Details of brain structures within

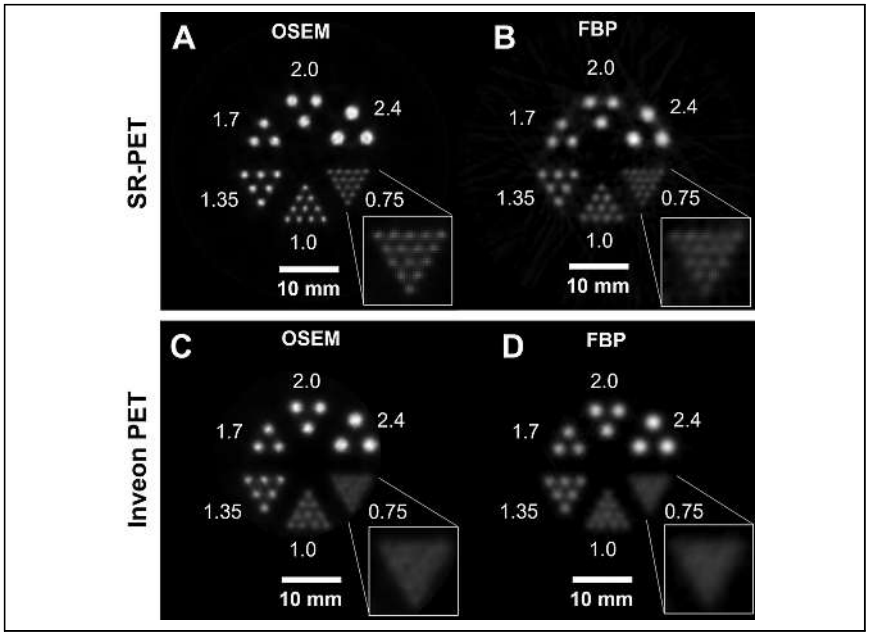

FIGURE 4. (A and B) Reconstructed PET images of modified Ultra-Micro Hot Spot Phantom with SR-PET using OSEM (A) and FBP (B). (C and D) Reconstructed PET images of same phantom with Inveon PET using OSEM (C) and FBP (D). Rod diameters are 0.75, 1.0, 1.35, 1.7, 2.0, and 2.0 mm. Inset represents 0.75-mm rod sector.

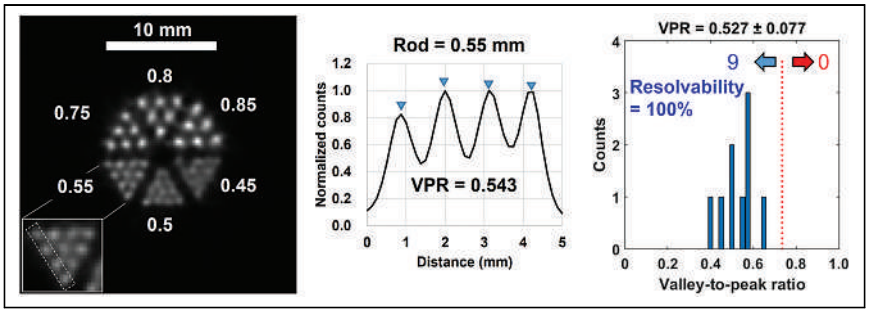

FIGURE 5. (Left) Reconstructed image of mouse phantom obtained with SR-PET for 60 min after cropping 25 × 25 mm central square. (Center) Line profiles of 0.55-mm rod sectors obtained as marked by white dotted boxes of insets. (Right) VPR histogram for diameter of 0.55 mm. Numbers of line profiles with VPRs under and over 0.735 are shown at left and right arrows, respectively.

the cranial bone were delineated well. In addition, glucose metabolism in the rat brain was clearly visualized with SR-PET (Supplemental Fig. 16).

DISCUSSION

We developed the SR-PET using 3-layer DOI detectors that can achieve submillimeter spatial resolution in a 51.5-mm-long axial coverage (Fig. 1). Several factors limit the spatial resolution of a small-animal PET scanner (*20,30*), including crystal pitch, crystal decoding error, sampling error, parallax error, photon noncollinearity, positron range (*20*), and ICS events (*21*). The fine crystal pitch (1 mm) combined with the staggered 3-layer DOI configuration can substantially minimize sampling error (*31,32*) and parallax error (*30*). The staggered 3-layer DOI detector allowed us to construct the PET scanner with small gaps between detector blocks, thereby minimizing loss of projection information because of detector gaps (*32*). The crystal decoding error (*30*) was substantially reduced using a diffusive reflector material ($BaSO_4$ powder) (*25*). The small ring diameter (52.5 mm) of the PET scanner minimized spatial resolution degradation caused by photon noncollinearity (*20*). Furthermore, parallax error caused by the small ring diameter was effectively reduced by the 3-layer DOI information. Finally, ICS events could be rejected with the narrow energy window of 440–560 keV (Supplemental Figs. 11 and 12) since ICS events have relatively lower or higher pulse height than photoelectric events because of the light collection efficiency difference, which depends on the crystal layer (*22,25,33*). As a result, the SR-PET resolved the 0.55-mm rod structure with resolvability of 100% (Fig. 5). Previously, a spatial resolution of 0.55 mm was reported by a research group at UC Davis (*34*). However, the axial FOV (7 mm) was too short to cover the entire brain of a mouse, which is typically about 15 mm in length from the olfactory bulb to the cerebellum. A SPECT scanner using a clustered pinhole collimator dedicated to high-energy

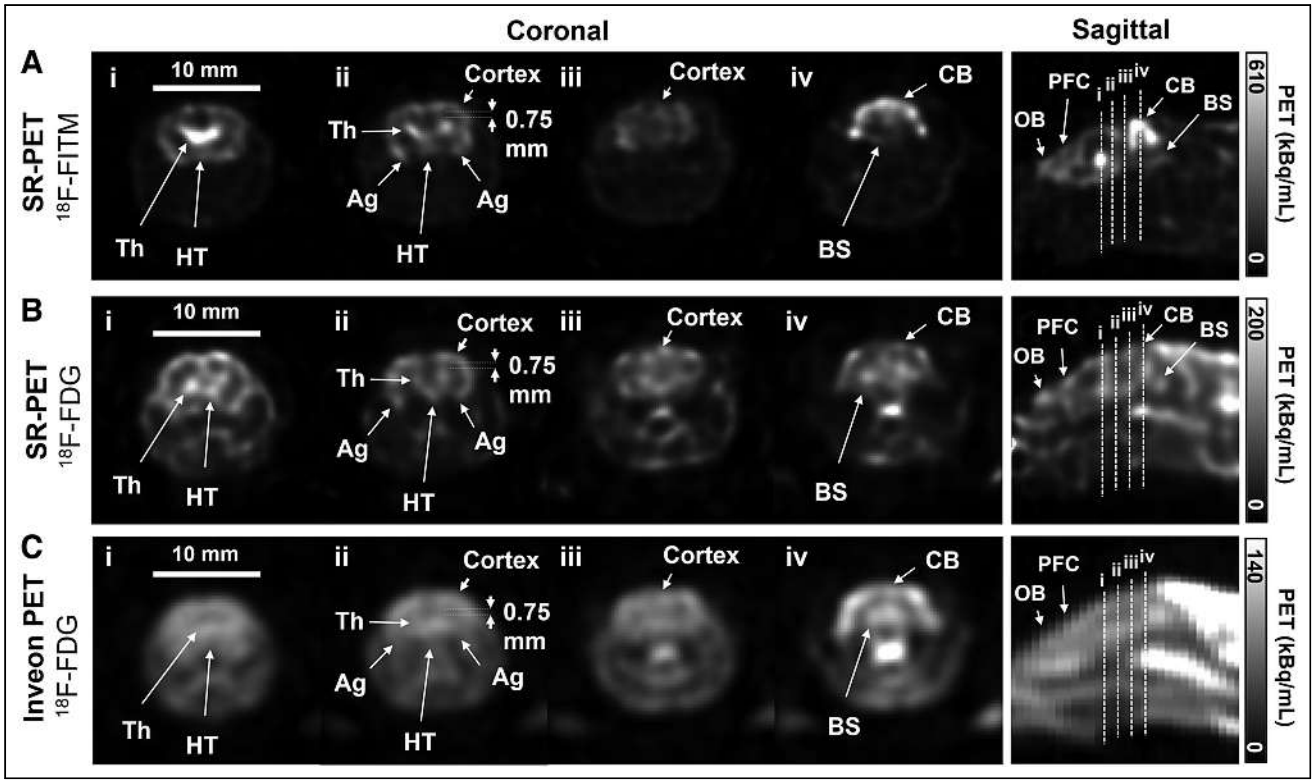

FIGURE 6. (A) Mouse brain images of ^{18}F-FITM (7 MBq) obtained for 30 min with SR-PET 40 min after injection. (B) Mouse brain images of ^{18}F-FDG (7 MBq) obtained for 30 min with SR-PET 34 min after injection. (C) Mouse brain images of ^{18}F-FDG (7 MBq) obtained for 30 min with Inveon D-PET 70 min after injection. For all images, 25 × 25 mm central square was cropped and displayed. Coronal images were selected from 4 different slices as indicated in sagittal images by dotted lines (i–iv). Ag = amygdala; BS = brain stem; CB = cerebellum; HT = hypothalamus; OB = olfactory bulb; Th = thalamus; PFC = prefrontal cortex.

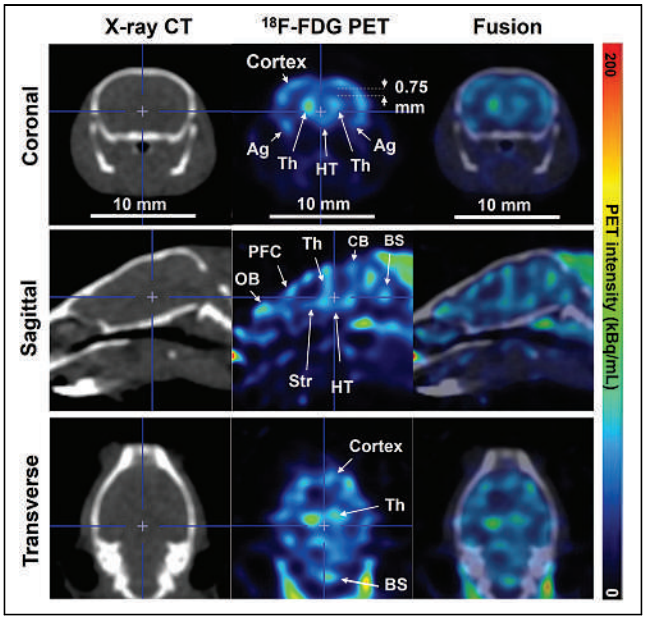

FIGURE 7. Mouse brain images obtained with ^{18}F-FDG PET, CT, and their fusion in coronal (top), sagittal (middle), and transverse (bottom) planes. For all images, 17 × 17 mm central square was cropped for image display. Ag = amygdala; BS = brain stem; CB = cerebellum; HT = hypothalamus; OB; olfactory bulb; Str = striatum; Th = thalamus; PFC = prefrontal cortex.

radiation (e.g., 511 keV) can resolve the 0.65-mm rod structure (*35*). However, the physical collimation technique demands an extremely high activity of over 20 MBq because of the poor sensitivity, 0.25%, whereas our small-animal PET scanner provides peak sensitivity of 1.56% even with a narrow energy window of 440–560 keV.

The closely adjacent cortex, thalamus, and hypothalamus were separately identified on in vivo mouse brain images with the SR-PET, whereas the Inveon PET scanner could not distinguish these structures, whose ^{18}F-FDG distributions may show little change from those of the SR-PET scan because of washout (Fig. 6).

Although the SR-PET resolved the 0.55-mm rods in the resolution phantom, the resolution for in vivo mouse brain imaging was degraded to around 0.85 mm because of the reduced iteration number (from 50 to 20) (Supplemental Fig. 13) and increased IDB kernel size (from 0.5 to 1.25 mm) (Supplemental Fig. 14). Thus, we plan to optimize the in vivo imaging protocol (e.g., injection dose and scan time) to obtain more coincidence events so as to minimize resolution loss, especially by IDB kernel size. In addition, our next study will focus on integration of the PET scanner inside an ultrahigh-field MRI scanner to simultaneously obtain high-resolution morphologic information (*10,11,17,36*) while pushing the PET resolution limit using a high magnetic field (*37,38*). Finally, we plan to use the SR-PET scanner to detect subtle changes in cortical brain activity in mouse models of Alzheimer disease (*39,40*).

CONCLUSION

We developed the SR-PET, a scanner that can provide a spatial resolution approaching 0.55 mm in a 51.5-mm-long axial coverage. The SR-PET can serve as a useful molecular imaging tool for translational neuroscience research using rodent models.

DISCLOSURE

This work was supported by KAKENHI grants (20H05667 and 21K19936) and by grants from the Nakatani Foundation, the QST Future Laboratory Program, and the Directorate's Fund Project given by Dr. Takashi Nakano. No other potential conflict of interest relevant to this article was reported.

ACKNOWLEDGMENTS

We thank Drs. Tometeru Yamasaki, Atsushi B Tsuji, and Ming-Rong Zhang for their support with the small-animal imaging experiments.

KEY POINTS

QUESTION: Can we explore mouse brain function with submillimeter resolution using a highly sensitive small-animal PET scanner for neuroscience research?

PERTINENT FINDINGS: The SR-PET provides a spatial resolution approaching 0.55 mm in a 51.5-mm-long axial coverage. Glucose metabolism in a mouse brain can be visualized in detail by resolving the cortex, thalamus, hypothalamus, and amygdala, which were barely distinguishable with a commercial preclinical PET scanner.

IMPLICATIONS FOR PATIENT CARE: The SR-PET can serve as a useful molecular imaging tool for translational neuroscience research and discovery of new drugs for neurodegenerative diseases in rodent models.

REFERENCES

1. Massoud TF, Gambhir SS. Molecular imaging in living subjects: seeing fundamental biological processes in a new light. *Genes Dev.* 2003;17:545–580.
2. Weissleder R, Pittet MJ. Imaging in the era of molecular oncology. *Nature.* 2008; 452:580–589.
3. Misgeld T, Kerschensteiner M. In vivo imaging of the diseased nervous system. *Nat Rev Neurosci.* 2006;7:449–463.
4. Herfert K, Mannheim JG, Kuebler L, et al. Quantitative rodent brain receptor imaging. *Mol Imaging Biol.* 2020;22:223–244.
5. Phelps ME. PET: the merging of biology and imaging into molecular imaging. *J Nucl Med.* 2000;41:661–681.
6. Tai Y-C, Chatziioannou AF, Yang Y, et al. MicroPET II: design, development and initial performance of an improved microPET scanner for small-animal imaging. *Phys Med Biol.* 2003;48:1519–1537.
7. Tai Y-C, Ruangma A, Rowland D, et al. Performance evaluation of the microPET Focus: a third-generation microPET scanner dedicated to animal imaging. *J Nucl Med.* 2005;46:455–463.
8. Bao Q, Newport D, Chen M, Stout DB, Chatziioannou AF. Performance evaluation of the Inveon dedicated PET preclinical tomograph based on the NEMA NU-4 standards. *J Nucl Med.* 2009;50:401–408.
9. Goertzen AL, Bao Q, Bergeron M, et al. NEMA NU 4-2008 comparison of preclinical PET imaging systems. *J Nucl Med.* 2012;53:1300–1309.
10. Ko GB, Yoon HS, Kim KY, et al. Simultaneous multiparametric PET/MRI with silicon photomultiplier PET and ultra-high-field MRI for small-animal imaging. *J Nucl Med.* 2016;57:1309–1315.
11. Stortz G, Thiessen JD, Bishop D, et al. Performance of a PET insert for high-resolution small-animal PET/MRI at 7 Tesla. *J Nucl Med.* 2018;59:536–542.
12. Gaudin É, Thibaudeau C, Arpin L, et al. Performance evaluation of the mouse version of the LabPET II PET scanner. *Phys Med Biol.* 2021;66:065019.
13. Kuang Z, Wang X, Ren N, et al. Physical and imaging performance of SIAT aPET under different energy windows and timing windows. *Med Phys.* 2022;49:1432–1444.
14. Gu Z, Taschereau R, Vu NT, Prout DL, Lee J, Chatziioannou AF. Performance evaluation of HiPET, a high sensitivity and high resolution preclinical PET tomograph. *Phys Med Biol.* 2020;65:045009.
15. Vrigneaud JM, McGrath J, Courteau A, et al. Initial performance evaluation of a preclinical PET scanner available as a clip-on assembly in a sequential PET/MRI system. *Phys Med Biol.* 2018;63:125007.

16. Krishnamoorthy S, Blankemeyer E, Mollet P, Surti S, Van Holen R, Karp JS. Performance evaluation of the MOLECUBES β-CUBE: a high spatial resolution and high sensitivity small animal PET scanner utilizing monolithic LYSO scintillation detectors. *Phys Med Biol.* 2018;63:155013.
17. Gsell W, Molinos C, Correcher C, et al. Characterization of a preclinical PET insert in a 7 tesla MRI scanner: beyond NEMA testing. *Phys Med Biol.* 2020;65:245016.
18. Kim KY, Son JW, Kim K, et al. Performance evaluation of SimPET-X, a PET insert for simultaneous mouse total-body PET/MR imaging. *Mol Imaging Biol.* 2021;23:703–713.
19. Miyaoka RS, Lehnert AL. Small animal PET: a review of what we have done and where we are going. *Phys Med Biol.* 2020;65:24TR04.
20. Levin CS, Hoffman EJ. Calculation of positron range and its effect on the fundamental limit of positron emission tomography system spatial resolution. *Phys Med Biol.* 1999;44:781–799.
21. Lee S, Lee JS. Inter-crystal scattering recovery of light-sharing PET detectors using convolutional neural networks. *Phys Med Biol.* 2021;66:185004.
22. Kang HG, Tashima H, Nishikido F, et al. Initial results of a mouse brain PET insert with a staggered 3-layer DOI detector. *Phys Med Biol.* 2021;66:215015.
23. Yoshida E, Tashima H, Shinaji T, et al. Development of a whole-body dual ring OpenPET for in-beam PET. *IEEE Trans Radiat Plasma Med Sci.* 2017;1:293–300.
24. Daube-Witherspoon ME, Muehllehner G. Treatment of axial data in three-dimensional PET. *J Nucl Med.* 1987;28:1717–1724.
25. Kang HG, Nishikido F, Yamaya T. A staggered 3-layer DOI PET detector using $BaSO_4$ reflector for enhanced crystal identification and inter-crystal scattering event discrimination capability. *Biomed Phys Eng Express.* 2021;7:035018.
26. Gong K, Cherry SR, Qi J. On the assessment of spatial resolution of PET systems with iterative image reconstruction. *Phys Med Biol.* 2016;61:N193–N202.
27. Hallen P, Schug D, Schulz V. Comments on the NEMA NU 4-2008 standard on performance measurement of small animal positron emission tomographs. *EJNMMI Phys.* 2020;7:12.
28. Yamasaki T, Fujinaga M, Kawamura K, et al. In vivo measurement of the affinity and density of metabotropic glutamate receptor subtype 1 in rat brain using ^{18}F-FITM in small-animal PET. *J Nucl Med.* 2012;53:1601–1607.
29. Mizuma H, Shukuri M, Hayashi T, Watanabe Y, Onoe H. Establishment of in vivo brain imaging method in conscious mice. *J Nucl Med.* 2010;51:1068–1075.
30. Moses WW. Fundamental limits of spatial resolution in PET. *Nucl Instrum Methods Phys Res A.* 2011;648(suppl 1):S236–S240.
31. Derenzo SE, Budinger TF, Huesman RH, Cahoon JL, Vuletich T. Imaging properties of a positron tomograph with 280 BGO crystals. *IEEE Trans Nucl Sci.* 1981; 28:81–89.
32. Zhang X, Stortz G, Sossi V, et al. Development and evaluation of a LOR-based image reconstruction with 3D system response modeling for a PET insert with dual-layer offset crystal design. *Phys Med Biol.* 2013;58:8379–8399.
33. Binder T, Kang HG, Nitta M, et al. Performance evaluation of a staggered three-layer DOI PET detector using a 1 mm LYSO pitch with PETsys TOFPET2 ASIC: comparison of HAMAMATSU and KETEK SiPMs. *Phys Med Biol.* 2021; 66:125016.
34. Yang Y, Bec J, Zhou J, et al. A prototype high-resolution small-animal PET scanner dedicated to mouse brain imaging. *J Nucl Med.* 2016;57:1130–1135.
35. Goorden MC, Beekman FJ. High-resolution tomography of positron emitters with clustered pinhole SPECT. *Phys Med Biol.* 2010;55:1265–1277.
36. Judenhofer MS, Wehrl HF, Newport DF, et al. Simultaneous PET-MRI: a new approach for functional and morphological imaging. *Nat Med.* 2008;14:459–465.
37. Iida H, Kanno I, Miura S, Murakami M, Takahashi K, Uemura K. A simulation study of a method to reduce positron annihilation spread distributions using a strong magnetic field in positron emission tomography. *IEEE Trans Nucl Sci.* 1986;33:597–600.
38. Christensen NL, Hammer BE, Heil BG, Fetterly K. Positron emission tomography within a magnetic field using photomultiplier tubes and lightguides. *Phys Med Biol.* 1995;40:691–697.
39. Deleye S, Waldron AM, Verhaeghe J, et al. Evaluation of small-snimal PET outcome measures to detect disease modification induced by BACE inhibition in a transgenic mouse model of Alzheimer disease. *J Nucl Med.* 2017;58:1977–1983.
40. Kimura T, Ono M, Seki C, et al. A quantitative in vivo imaging platform for tracking pathological tau depositions and resultant neuronal death in a mouse model. *Eur J Nucl Med Mol Imaging.* 2022;49:4298–4311.

Theranostic Radiopharmaceuticals: A Universal Challenging Educational Paradigm in Nuclear Medicine

Jean-Luc Urbain[1], Andrew M. Scott[2], Sze Ting Lee[3], John Buscombe[4], Charlotte Weston[4], Jun Hatazawa[5], Seigo Kinuya[6], Baljinder Singh[7], Mohamad Haidar[8], Andrew Ross[9], Francois Lamoureux[9], Jolanta Kunikowska[10], Wolfgang Wadsak[10], Rudi Dierckx[10], Diana Paez[11], Francesco Giammarile[11], Kyung-Han Lee[12], Joo Hyun O[12], Modiselle Moshe[13], Lizette Louw[13], Stuart More[13], Helen Nadel[1], Daniel Lee[1], and Richard Wahl[1]

[1]Society of Nuclear Medicine and Molecular Imaging, Reston, Virginia; [2]Australian and New Zealand Society of Nuclear Medicine, Vermont South, Victoria, Australia; [3]Australasian Association of Nuclear Medicine Specialists, Balmain, New South Wales, Australia; [4]British Society for Nanomedicine, Liverpool, United Kingdom; [5]Asia Oceania Federation of Nuclear Medicine and Biology, Osaka, Japan; [6]Japanese Society of Nuclear Medicine, Tokyo, Japan; [7]Society of Nuclear Medicine, India, Mumbai, India; [8]Arab Society of Nuclear Medicine, Beirut, Lebanon; [9]Canadian Association of Nuclear Medicine, Rosemère, Quebec, Canada; [10]European Association of Nuclear Medicine, Vienna, Austria; [11]International Atomic Energy Agency, Vienna, Austria; [12]Korean Society of Nuclear Medicine, Seoul, Korea; and [13]South African Society of Nuclear Medicine, Cape Town, South Africa

The field of nuclear medicine traces its origin to the accidental discovery and naming of radioactivity by Henri Becquerel and Marie Curie in 1896 and 1905. In March 1936, Hamilton and Stone in California used "radiosodium," the first artificially produced radioisotope, to treat 3 patients with leukemia and allied diseases. The same year, J.H. Lawrence at Berkeley initiated the therapeutic use of ^{32}P for the treatment of leukemia and polycythemia vera. Saul Hertz's success with radioiodine ablation of hyperthyroid patients between 1937 and 1942 paved the way for a seamless transition to Samuel Seidlin's investigations with radioactive iodine (^{131}I) in thyroid cancer. Nuclear medicine first became recognized as a potential medical specialty in 1946 when Seidlin reported on the success of radioactive iodine in treating a patient with advanced thyroid cancer.

By the 1950s, the clinical use of radioactive isotopes in medicine had become widespread as researchers increased their understanding of detecting radioactivity and using radionuclides and the rectilinear scanner to monitor biochemical processes. By 1960, the use of radioiodine in the examination of thyroid disease had become a prominent subject (*1,2*).

More than a half century ago (1971), the American Medical Association acknowledged nuclear medicine as an official medical specialty (*3*). Many countries around the globe followed suit and recognized nuclear medicine as a full-blown specialty through their health-care system regulatory agencies and by forming nuclear medicine societies and associations.

The educational requirements, organization, and practice of nuclear medicine vary from one country to another and are largely dictated by the regulatory framework in place in each country. Nuclear medicine is an advanced diagnostic and therapeutic medical and scientific field and a combination and convergence of many different disciplines. As such, it must be handled by well-educated and trained professionals such as radiochemists, nuclear physicists, radiopharmacists, engineers, technologists, physicians, and other health-care professionals.

THERANOSTIC RADIOPHARMACEUTICALS

The concept of theranostics refers to the integration of therapeutics and diagnostics in a single management approach allowing image-guided therapy and defining of treatment outcome at an early stage. The word *theranostics,* the new buzzword in medicine, was first coined in 1998 by John Funkhouser (a U.S. consultant), in a press release from the company Cardiovascular Diagnostics, to describe a material that combines the modalities of therapy and diagnostic imaging and was used in the early 2000s by the same John Funkhouser (then chief executive officer of PharmaNetics) to define the vision for his company as a blend of therapeutics and diagnostics.

Over the past 2 decades, one of the most significant outcomes of the human genome project in nuclear medicine has been the development of new theranostic radiopharmaceuticals that are based on patients' disease genotypes and phenotypes and that are labeled with radionuclide pairs. Through their exquisite sensitivity and specificity, these nuclear theranostics, in combination with sophisticated high-performance digital hybrid imagers (SPECT/CT, PET/CT, and PET/MRI), have started to play a major role in precision medicine by significantly improving patient disease management, particularly in oncology (*4*).

As exciting as it sounds, the clinical implementation of theranostic radiopharmaceuticals in nuclear medicine faces significant challenges. The practice of a fully integrated diagnostic and therapeutic nuclear medicine specialty requires an in-depth knowledge of many different fields of medicine, radiochemistry, radiopharmacy, dosimetry, radiopharmacology, and complex imaging equipment, along with an in-depth understanding of diseases and their management, health-care systems, and health-care economics. This type of complex knowledge, experience, and expertise represents both unique

Received Feb. 14, 2023; accepted Feb. 14, 2023.
For correspondence or reprints, contact Jean-Luc Urbain through Teresa Ellmer at the Society of Nuclear Medicine and Molecular Imaging (tellmer@snmmi.org).
Published online May 4, 2023.

DOI: 10.2967/jnumed.123.265603

opportunities and significant challenges for medical schools, imaging centers, and nuclear medicine centers across the globe.

EDUCATIONAL CHALLENGES AND OPPORTUNITIES

Over the past 2 decades, numerous clinical trials with theranostic radiopharmaceuticals have been performed, confirming their potential in the management of certain types of cancer. The documented success of these trials conducted first in Europe and Australia and more recently in the United States and the rest of the world has driven significant interest by health-care professionals, particularly in oncology, and by patients, who are requesting access to these unique and specific precision medicine therapies.

The significant increased demand for these types of therapy across the globe and their medical use have been and remain quite challenging in many aspects. Their manufacturing, transportation, distribution, availability, and medical use are still in their infancy and require stringent regulatory frameworks. Fundamental to their appropriate and safe medical applications are the education-and-training, experience, and expertise requirements of the health-care professionals who will be interpreting the images and the administration of these theranostic radiopharmaceuticals.

THERANOSTIC EDUCATION ACROSS THE GLOBE

At the 2018 completion of a project on access to and availability of radiopharmaceuticals, the global initiative committee of the Society of Nuclear Medicine and Molecular Imaging (SNMMI) launched an initiative aimed at assessing the educational and training resources available on theranostics.

Similarly to the explosion and lack of preparedness of the imaging community vis-à-vis the Internet revolution of the 1990s and early 21st century, nuclear medicine communities around the globe are witnessing the explosion of theranostic radiopharmaceuticals and scrambling to provide their health-care professionals with appropriate education, training, and expertise. There is an urgent need to develop the knowledge and expertise to practice theranostics.

The aim of this white paper is to summarize current educational and training initiatives for theranostic physicians by the nuclear medicine communities that were part of the global initiative committee of the SNMMI on theranostics between 2018 and 2022.

Australian and New Zealand Society of Nuclear Medicine

For more than a decade, Australia and New Zealand have been at the forefront of clinical trials in theranostics.

All nuclear medicine specialists in Australia are qualified physicians or radiologists. Trainees have to complete basic physician training and examinations before entry into the nuclear medicine advanced training program, which consists of 2 core years and 1 elective or fellowship year. Radiology trainees also have to pass radiology examinations before entering the nuclear medicine advanced training program, which consists of 2 core years. During advanced training in nuclear medicine, the minimum required exposure to concepts on radionuclide therapy is the use of radioiodine therapy in benign and malignant thyroid conditions. Because novel radionuclide therapies such as peptide receptor radionuclide therapy and peptide receptor radioligand therapy are not approved in Australia, there are only a limited number of sites that perform these in a compassionate-access scheme or via clinical trials, to which advanced trainees have limited exposure during their core training years. The requirements for advanced training in nuclear medicine are overseen by the committee for joint college training, which has representatives from the Royal Australasian College of Physicians and the Royal Australian and New Zealand College of Radiologists. Theranostic recommendations will be specifically included in the curriculum update for nuclear medicine.

In 2020, the Australasian Association of Nuclear Medicine Specialists published a position statement on the practice of theranostics in Australia (*5*). This statement represents a consensus of recommendations regarding the provision of safe, high-quality delivery and administration of nuclear theranostic therapies. The rapidly evolving field of theranostics, the need for an in-depth understanding of the medical and scientific aspects of these new diagnostic and therapeutic radiopharmaceuticals, patients' disease genotype and phenotype, and the goals of and the need for a medical multidisciplinary approach to treat patients served as the main parameters to establish the guidelines.

Asia Oceania Federation of Nuclear Medicine and Biology

With a population of more than 5 billion people and nearly 40 countries under its umbrella, the nuclear medicine communities in Asia have probably the biggest challenge of all in delivering high-quality basic and specialized nuclear medicine education, training, and practice to professionals. In addition to physician training, the federation acknowledges that there is a clear need for education and theranostic training of radiochemists, physicists, technologists, and nursing staff.

The federation endeavors to establish centers of excellence in theranostics and to educate and train nuclear medicine staff in collaboration with regional associations and societies and the International Atomic Energy Agency (IAEA), particularly in underserved countries.

The Asia Oceania School of Nuclear Medicine, the *Asia Oceania Journal of Nuclear Medicine and Biology,* and the congresses and events of the federation bridge the gap between clinical practice and formal education and create networking and learning opportunities through exchanges within Asia and Oceania.

Arab Society of Nuclear Medicine and Molecular Imaging

The Arab Society of Nuclear Medicine is a young organization. It was inaugurated during a meeting of the project called ARASIA (Cooperative Agreement for Arab States in Asia for Research, Development and Training Related to Nuclear Science and Technology). The meeting, which was held in Vienna in 2014, was titled "Strengthening Nuclear Medicine Applications through Education and Training to Help Fighting Noncommunicable Diseases in the Arab Asian Member States." The main objective of the society is to educate health-care and medical professionals about the remarkable growth of nuclear medicine in diagnostic imaging and therapeutics. It also aims to strengthen regional and international cooperation between nuclear medicine and molecular imaging professionals, groups, and societies active in the field.

British Nuclear Medicine Society

The British Nuclear Medicine Society is concerned with clinical practice, education, and research and development in nuclear medicine within the United Kingdom. Except for some endocrinologists treating benign thyroid disease and rheumatologists using radionuclide synovectomy, the only 2 specialties that can receive a nuclear medicine license in Great Britain are clinical oncologists and nuclear medicine physicians. Clinical oncologists normally limit themselves to just 1–2 cancer types; also, they have no training in the diagnostics of theranostics. The only practitioners who can acquire licenses for all radionuclide therapies and understand

the relevant molecular imaging are nuclear medicine physicians. Training for nuclear medicine physicians and clinical oncologists is 6 y after general internal medical training (itself 3 y after intern training). Because the number of training posts in the United Kingdom is limited, the number of trained people in the United Kingdom who are giving radionuclide therapy beyond ^{131}I for thyroid cancer is low (probably less than 100 for a country of 60 million).

A new initiative starting in 2021 increased the number of training posts, which enables a trainee radiologist with internal medicine boards and 1 year of nuclear medicine training to take a further 1-y course to gain experience in diagnostic and therapeutic aspects of theranostics.

Canadian Association of Nuclear Medicine

The Canadian Association of Nuclear Medicine strives for excellence in the practice of diagnostic and therapeutic nuclear medicine by promoting the continued professional competence of nuclear medicine specialists, establishing guidelines for clinical practice, and encouraging biomedical research. In Canada, the Royal College of Physicians and Surgeons of Canada provides education and certification of competency through Royal College accreditation and examination of nuclear medicine residencies. Because of the provincial bases of health-care delivery, there are regional differences in practice. The Royal College provides the underlying continuity and standards. Radioisotope therapy has been an objective of training in this process. The rapid evolution of the field of theranostics has challenged this objective, as there are regional differences in access for patients and therefore in the training required. The needs for education, training, experience, and expertise in diagnostic and therapeutic theranostics are currently under assessment by the Royal College specialty committee for nuclear medicine. The process has been somewhat further complicated by the fact that the Royal College system of training and assessment is undergoing a relatively radical evolution to a competency-based system. The first residents in this new model have just entered training.

European Association of Nuclear Medicine

The European Association of Nuclear Medicine is promoting the theranostic idea in education by its European School of Multimodality Imaging and Therapy and has initiated official events during its annual congress or dedicated focus meetings (*6*).

As the national countries and their health-care and accreditation programs are responsible for adequate education and training of residents, harmonization of the legal basis and curricula for education toward radionuclide therapeutic applications is a big challenge in Europe. The activities of the European School of Multimodality Imaging and Therapy endeavor to provide a common basis with goals and state-of-the-art educational content.

The European Association of Nuclear Medicine certifies experts in radiopharmaceutical sciences, including both diagnostic and therapeutic applications, after completion of a postgraduate diploma course and many years of hands-on training within nuclear medicine institutions.

The European Union of Medical Specialists supports the free movement of European medical specialists while ensuring the highest quality of medical care for European citizens, and standardization of training is therefore a prerequisite. The European Union of Medical Specialists program covers the many aspects involved in the use and safe administration of nuclear theranostics (*7*).

IAEA

In October 2019, the IAEA published a training curriculum for nuclear medicine physicians (*8*). The IAEA recognizes that theranostic radiopharmaceuticals for the diagnosis and treatment of disease are an important but not exclusive part of the large family of theranostic concepts and compounds. The diagnostic and therapeutic use of radioactive iodine is the most common theranostic application globally in nuclear medicine, both in hyperthyroidism and in well-differentiated thyroid cancer. For the purpose of the training discussed in this publication, it is better to limit the scope of the theranostic radiopharmaceuticals to nuclear diagnostic and therapeutic oncology applications, particularly in view of their complexity. The major barriers to the development of theranostic programs in low- and middle-income countries are related to the complexity of the procedures, including logistic, financial, and regulatory aspects.

Without a doubt, innovation in research and development is a driving force of theranostics. New radiopharmaceuticals, applications, and medical evidence are produced at a fast pace and need to be propagated. New standards of best practice should not be emphasized only as a part of training programs but also in an effort to keep the medical community abreast of developments to optimize patient care and professional growth. We are facing major educational gaps, essentially in the therapeutic field. Professionals involved in theranostics should acquire additional hard and soft skills to properly manage patients and deal with complex theranostic applications. There is a need to include not only radioiodine therapies but also more complex theranostic applications as part of the curriculum and to harmonize the training requirements globally.

In addition, the establishment of a clear legal framework and policies should be emphasized and differentiated from those of external-beam radiotherapy. The IAEA's recommendation is to add, as a minimum, 1 full year of theranostic education and training to the curriculum for nuclear medicine physicians (*8*).

The global initiative committee should reach an agreement recommending and promoting a harmonized approach to the education and training of professionals who use and administer theranostic radiopharmaceuticals. The committee should also consider facilitating the establishment of accreditation and regulatory frameworks for the use of nuclear theranostics.

Japanese Society of Nuclear Medicine

In Japan, nuclear medicine is a subspecialty of radiology, radiation oncology, or internal medicine. The Japanese Society of Nuclear Medicine certifies physicians to practice nuclear medicine through a board examination. To be eligible, applicants must have 5 y of education, training, and experience in nuclear medicine that follows the Japanese Society of Nuclear Medicine–prescribed curriculum in a training program certified by the Japanese Society of Nuclear Medicine. The nuclear medicine certificate is renewed every 5 y on the basis of a mandated educational and training maintenance of certification.

There is currently no specific educational or training program in theranostics. Radionuclide therapy is practiced by institutions without a standardized framework. This is related in part to the diverse background of nuclear medicine specialists and in part to the absence of designated radionuclide therapy beds in hospitals.

Korean Society of Nuclear Medicine

In South Korea, a physician board-certified in nuclear medicine and licensed as a radiation worker by the regulating agency may practice

theranostics. The 4-y nuclear medicine residency program requires trainees to participate in a specific number of radionuclide therapies. Radioiodine therapy has been widely used in Korea since its first administration in 1959, and there are no perceivable gaps in training for conventional radionuclide therapy. However, training does not adequately cover novel theranostics, largely because of limited clinical applications to date. Currently, ^{223}Ra-dichloride and ^{177}Lu-DOTATATE are approved for use, and ^{177}Lu-PSMA radiopharmaceuticals are available through expanded-access programs. Anticipating a substantial increase in the number of theranostic procedures, the Korean Society of Nuclear Medicine is currently updating and increasing its educational programs.

South African Society of Nuclear Medicine

In South Africa, nuclear medicine is an independent specialty. Resident training requires a skill set that includes a broad range of knowledge and experience in radiobiology and physics, as well as dosimetry and radiation protection knowledge. Training program requirements include successful participation in and performance of radionuclide therapies.

The training programs are coordinated by the various academic institutions in the country, and summative examinations are administered by the College of Nuclear Physicians (part of the College of Medicine of South Africa). There is a minimum number of therapy cases that need to be performed and observed by residents (at least 180 cases).

The South African Society of Nuclear Medicine provides training opportunities in terms of master classes and webinars with local and international experts to enhance the training and application of theranostics in southern Africa. With the rapidly evolving field of theranostics, nuclear medicine training in South Africa will need to be optimized for these new oncologic therapies.

Society of Nuclear Medicine, India

The Society of Nuclear Medicine, India, aims to promote, encourage, and assist the development and advancement of nuclear medicine as a specialty. In India, nuclear medicine theranostics (*9*) are being practiced primarily in the public-sector hospitals that are affiliated with academic institutions and in only a few private-sector hospitals. Although formal guidelines do not exist for the development and regulation of theranostic programs in India, individual centers have developed their own sets of protocols for the use of theranostic radiopharmaceuticals.

The present training for nuclear medicine physicians in India requires a 3-y period of residency after completion of medical school. This period includes rigorous, cross-over training in both diagnostic and therapeutic nuclear medicine and in allied specialties such as radiology and radiation oncology. Similarly, nuclear medicine physicists and technologists also receive training in diagnostic and therapeutic nuclear medicine. The current challenges include limited exposure to and practice of dosimetry, despite extensive permeation of the radionuclide therapies. This limitation results primarily from the lack of skilled and dedicated specialists in performing radionuclide dosimetry. Adopting an integrative and all-inclusive approach can help build a comprehensive and uniform theranostic program that will be beneficial not only to the Indian populace but also to the global nuclear medicine fraternity.

SNMMI

The requirements of the accreditation council for graduate medical education for graduate medical trainees in nuclear medicine, published in July 2022, include several statements on procedural competencies involving radiopharmaceutical therapies, including the following statement, "When appropriate, thyroid studies must include measurements of iodine uptake and dosimetry calculations for radio-iodine therapy" (*10*). Although no other specific radiopharmaceutical therapies are directly mentioned in this document, probably because of the rapidly evolving state of radiopharmaceutical therapy availability and practices, the document does state that there should be an understanding of the "therapeutic administration of other unsealed radiopharmaceuticals for malignant and benign diseases … [as well as] scheduling and performing post-therapy follow-up" among the many other tasks involved in patient care. The document also states that faculty members must have appropriate qualifications in their field—that is, be certified by a governing board or possess qualifications that are acceptable to the review committee—but it does not state what those qualifications must be.

The SNMMI has been actively involved in radiopharmaceutical therapies and theranostics. Through committees and task forces, its therapy center of excellence is dedicated to all aspects of the development and use of radiopharmaceutical therapy as an alternative to other treatments. A resourceful trove and prime collection of educational and clinical information, the therapy.snmmi.org web portal of the SNMMI now has therapy guidelines available for nuclear medicine professionals and patients. In addition, the SNMMI has benchmarked criteria for designating radiopharmaceutical therapy centers of excellence where patients and trainees can obtain state-of-the-art radiopharmaceutical treatment and education.

UNIVERSAL FRAMEWORK FOR POSTGRADUATE EDUCATION AND TRAINING OF NUCLEAR MEDICINE PHYSICIANS FOR PROFICIENCY IN NUCLEAR THERANOSTICS

Across the globe, physicians involved in the administration of radionuclide therapies include, for the most part, nuclear medicine, internal medicine, and radiologist and radiation oncology specialists.

Given the diversity in the backgrounds of providers and to ensure appropriate and safe use of nuclear theranostics, a curriculum template with minimum requirements is desirable to provide proper education, training, and expertise for the use of theranostic radiopharmaceuticals.

This paper offers generic guidelines for training and practice based on international recommendations, expert consensus, and relevant medical publications when available in relation to the practice of theranostics and molecular targeted radionuclide therapies.

Besides experts in the radiopharmaceutical and equipment manufacturer industry, also critical to the practice of nuclear medicine are radiochemists, radiopharmacists, nuclear physicists, technologists, nurses, nurse practitioners, allied health professionals, support staff, and physicians. Elaborating a generic educational and training framework addressing the needs of all these professions would be quite challenging and definitely outside the scope of this paper. We therefore focus on the training of nuclear medicine physicians, particularly those who treat adults. Pediatric radiopharmaceutical therapies require further specialized education and training and will be addressed in a separate publication.

Educational and training requisites for physicians using theranostic radiopharmaceuticals should include basic and specific aspects.

Basic entry requirements and pathways include a formal medical degree with appropriate certification by the accrediting body; 1 y of clinical experience that can be completed in a clinical medicine specialty, preferably in a field relevant to theranostics (e.g.,

sports medicine, ophthalmology, and dermatology would not be satisfactory); and a board certification in nuclear medicine as a specialty or subspecialty of, for example, internal medicine, radiology, and radiation oncology after a minimum of 3 y of a residency or fellowship in nuclear medicine.

The additional minimum curriculum requisites or the education, training, experience, and expertise for theranostic proficiency and accreditation should entail an additional residency or fellowship year in an accredited nuclear medicine or nuclear radiology center or program.

The accredited program should operate in a multidisciplinary setting, ideally a hospital or medical center with a comprehensive oncology practice. The program should have proper and adequate infrastructure, personnel, and equipment to practice standard-of-care and preferably state-of-the-art diagnostic and therapeutic nuclear medicine procedures, including a systemic dosimetry program.

Theranostic radiopharmaceutical physicians are expected to have sufficient knowledge and understanding of basic aspects of the practice of nuclear medicine such as mathematics and statistics applied to diagnostic and therapeutic nuclear medicine; natural, medical, and professional radiation exposure and radiation biology; radiopharmacy and radiochemistry; all equipment and instrumentation used in nuclear medicine; principles of radionuclide therapy; principles of quality management systems; and quality control and regulatory issues.

Theranostic nuclear medicine physicians should also have, as part of their education and training, a detailed understanding of the physiology and anatomy of the specific organ or region being studied or targeted; an in-depth knowledge of the anatomy, pathophysiology, anatomic pathology, and histopathology and of the genomics, proteinomics, and other omics of the disease being assessed, treated, and followed; a clear undersanding of the current diagnostic and therapeutic algorithms used by the oncology providers to diagnose, stage, treat, and follow up their patients; an in-depth knowledge of the chemical, biochemical, pharmacokinetics, and biodistribution of the diagnostic and therapeutic theranostics and their associated radionuclides; an in-depth understanding of the appropriateness, administration, and side effects of the theranostics used in their practice; a minimum number of diagnostic and therapeutic theranostic procedures defined by their national accreditation and regulatory bodies based on guidelines recommended by experienced theranostic specialist physicians via their national and international associations; a clear understanding of local, regional, and national legal and regulatory requirements; quality management applied to nuclear medicine; departmental, interdepartmental, medical center, and hospital operations and policies; and sufficient knowledge of the cost, reimbursement, and financial aspects of the diagnostic and therapeutic theranostic radiopharmaceuticals.

Complementary additional and important, if not critical, aspects for theranostic physicians that should be acquired through their education and training include mandatory participation in multidisciplinary tumor boards and meetings relevant to their local theranostic practice; continuing scientific and medical education related to the field of theranostics; attendance at and active participation in medical and scientific meetings that are directly or indirectly related to theranostics; and participation in patient support and advocacy groups.

FRAMEWORK FOR EDUCATION AND TRAINING OF CURRENT NUCLEAR MEDICINE PHYSICIANS FOR PROFICIENCY IN NUCLEAR THERANOSTICS

In most parts of the world, physicians who are board-certified in nuclear medicine should have received education and training in thyroid disease therapy with radioiodine. Education, training, and clinical experience and expertise with most recently available theranostic radiopharmaceuticals is variable across the globe and is directly and indirectly related to availability, access, and regulatory approval. For those board-certified practicing nuclear medicine physicians who want to be actively involved in theranostic radiopharmaceuticals and treat patients but might not have had an adequate educational or training opportunity during their residency or fellowship, there is now ample information, educational material, and opportunity available through nuclear medicine societies and association web portals and specialized theranostic radiopharmaceutical centers to obtain proper education and possibly training experience in theranostic radiopharmaceuticals.

Like the other fields in medicine, the science and practice of theranostic radiopharmaceuticals are rapidly evolving. Continuing medical education will be critical to maintain sufficient up-to-date knowledge and expertise to perform diagnostic and therapeutic nuclear medicine procedures.

CONCLUSION

Today's medical use of unsealed radioactive compounds is driven by an unprecedented level of diagnostic and therapeutic molecular targeting opportunities that the human genome project and the omics of diseases, particularly in oncology, have unraveled and continue to discover. As an intimate part of the patient management team, nuclear medicine physicians across the globe are now challenged by the need to understand and eventually master a vast amount of specialized and sophisticated knowledge on various type of cancers and their cognate diagnostic and therapeutic radiopharmaceutical probes that have been or are actively being developed. Becoming proficient in this new field requires significant dedication to education and training as well as an additional level of experience and expertise.

This review has outlined the world's currently available offerings in education and accreditation for theranostics. It also frames the educational and proficiency challenges that countries across the globe face in developing educational and training curricula, and it offers generic guidelines toward providing physicians with sufficient knowledge and experience to confidently and safely perform nuclear theranostic procedures.

DISCLOSURE

No potential conflict of interest relevant to this article was reported.

ACKNOWLEDGMENTS

The writing of this white paper would not have been possible without the extraordinary administrative support of Teresa Elmer and the SNMMI staff and the contributions of the many dedicated members of the imaging and nuclear medicine community from across the globe.

REFERENCES

1. Fahey FH, Grant FD, Thrall JH. Saul Hertz, MD, and the birth of radionuclide therapy. *EJNMMI Phys.* 2017;4:15.
2. Ehrhardt JD Jr, Güleç S. A review of the history of radioactive iodine theranostics: the origin of nuclear ontology. *Mol Imaging Radionucl Ther.* 2020;29:88–97.

3. ACGME program requirements for graduate medical education in nuclear medicine. ACGME website. https://www.acgme.org/globalassets/pfassets/programrequirements/200_nuclearmedicine_2022v2.pdf. Published July 1, 2022. Accessed March 10, 2023.
4. Idée JM, Louguet S, Ballet S, Corot C. Theranostics and contrast-agents for medical imaging: a pharmaceutical company viewpoint. *Quant Imaging Med Surg.* 2013;3:292–297.
5. Lee ST, Emmett LM, Pattison DA, et al. The importance of training, accreditation and guidelines for the practice of theranostics: the Australian perspective. *J Nucl Med.* 2022;63:819–822.
6. Dierckx R, Ke Herrmann K, Hustinx R, et al. European Association of Nuclear Medicine response to the proposed ASTRO's framework for radiopharmaceutical therapy curriculum development for trainees. *Eur J Nucl Med Mol Imaging.* 2022; 50:1–3.
7. Training requirements for the specialty of nuclear medicine. European Union of Medical Specialists website. https://www.uems.eu/__data/assets/pdf_file/0017/43523/UEMS-European-Training-Requirements-NUCMED-final.pdf. Accessed March 10, 2023.
8. Training curriculum for nuclear medicine physicians. IAEA website. https://www-pub.iaea.org/MTCD/Publications/PDF/TE-1883web.pdf. Published 2019. Accessed March 10. 2023.
9. Kumar R, Singh B, Singh H, Watts A, Kamaldeep. Radiotheranostics practice in India: advancing to precision oncology [editorial]. *Indian J Nucl Med.* 2023; 37(suppl 1):S13–S14.
10. Accreditation Council for Graduate Medical Education (ACGME). ACGME Program Requirements for Graduate Medical Education in Nuclear Medicine. ACGME website. https://www.acgme.org/globalassets/pfassets/programrequirements/200_nuclearmedicine_2022v2.pdf. Accessed April 23, 2003.

Incidental Focal ^{68}Ga-FAPI-46 Uptake in a Urachal Remnant: A Potential Pitfall Mimicking a Malignant Peritoneal Lesion

Peter George Maliha, Mahbod Jafarvard, Johannes Czernin, Jeremie Calais, and Masatoshi Hotta

Ahmanson Translational Theranostics Division, Department of Molecular and Medical Pharmacology, David Geffen School of Medicine at UCLA, University of California Los Angeles, Los Angeles, California

A 75-y-old man who was scheduled for resection of a lipomatous lesion of the left upper back underwent preoperative PET/CT with ^{68}Ga-fibroblast activation protein inhibitor-46 (^{68}Ga-FAPI-46) as part of a prospective study (NCT04147494). The images revealed an incidental small focus of uptake (SUV_{max}, 4.1) in a 0.8 × 0.7 × 1.2 cm cystic structure in the inferior third of a urachus remnant (Fig. 1). There was no ^{68}Ga-FAPI-46 uptake in the remainder of the urachus remnant. A prior ^{18}F-FDG PET/CT study with intravenous CT contrast medium that had been performed 4 y 1 mo previously was retrospectively reviewed. It showed incomplete obliteration of the urachus with a cystic structure in its inferior third, consistent with a urachus remnant, all with no ^{18}F-FDG uptake. The urachal remnant and cystic structure on ^{68}Ga-FAPI-46 PET/CT were anatomically the same as seen on the reviewed ^{18}F-FDG PET/CT and on a subsequent follow-up CT scan obtained 1 y 3 mo later, suggesting a benign etiology. Differential diagnosis included a ^{68}Ga-FAPI-46–positive and ^{18}F-FDG–negative urachal cyst due to fibrosis and a urachal diverticulum, intermittently accumulating urine-excreted radiotracer.

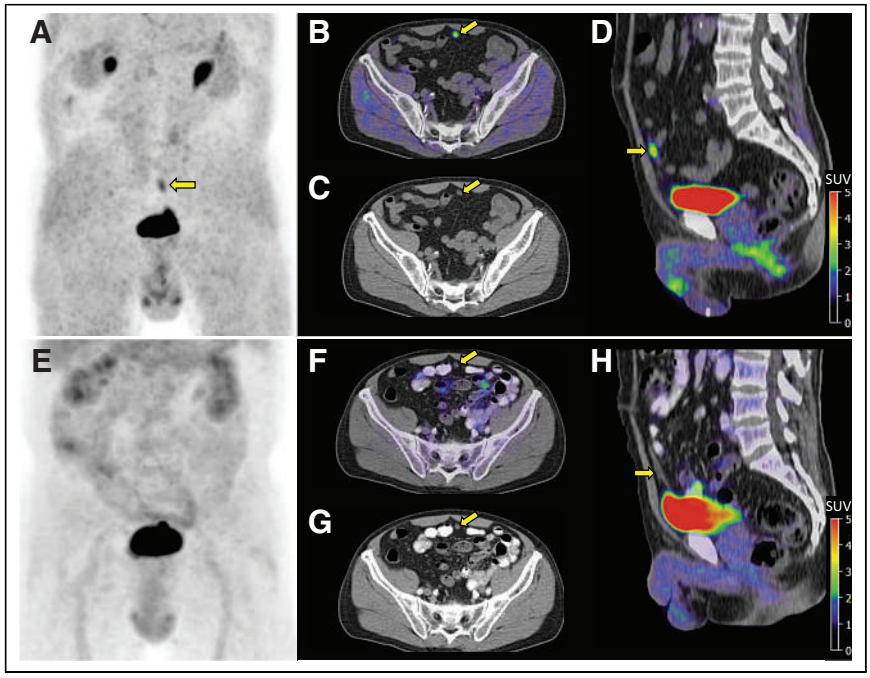

FIGURE 1. Maximum-intensity projections (A and E), fused PET/CT axial images (B and F), CT axial images (C and G), and fused sagittal PET/CT images (D and H) demonstrating mild ^{68}Ga-FAPI-46 uptake (SUV_{max}, 4.1; A–D) and no ^{18}F-FDG uptake (E–H) in a cystic structure of a urachal remnant (arrows).

The urachus is an embryologic structure connecting the umbilicus to the bladder. Normally, it obliterates to become the medial umbilical ligament. Very rarely, it does not obliterate, and remnant urachal anomalies persist to adulthood (*1*). Of these anomalies, a cystic structure can remain between the umbilicus and the bladder.

Several studies have suggested that ^{68}Ga-FAPI-46 PET/CT has a promising role in the detection of peritoneal metastases in various malignancies, notably because of low physiologic bowel uptake (*2–4*). The above-described ^{68}Ga-FAPI-46 PET signal in the urachal remnant should be a known potential false-positive pitfall in that region.

DISCLOSURE

No potential conflict of interest relevant to this article was reported.

REFERENCES

1. Wilson AL, Gandhi J, Seyam O, et al. Urachal anomalies: a review of pathological conditions, diagnosis, and management. *Transl Res Anat.* 2019;16:100041.
2. Veldhuijzen van Zanten SEM, Pieterman KJ, Wijnhoven BPL, et al. FAPI PET versus FDG PET, CT or MRI for staging pancreatic-, gastric- and cholangiocarcinoma: systematic review and head-to-head comparisons of diagnostic performances. *Diagnostics (Basel).* 2022;12:1958.
3. Guo W, Chen H. ^{68}Ga FAPI PET/CT imaging in peritoneal carcinomatosis. *Radiology.* 2020;297:521.
4. Meyer C, Dahlbom M, Lindner T, et al. Radiation dosimetry and biodistribution of ^{68}Ga-FAPI-46 PET imaging in cancer patients. *J Nucl Med.* 2020;61:1171–1177.

Received Oct. 14, 2022; revision accepted Dec. 20, 2022.
For correspondence or reprints, contact Peter George Maliha (peter.maliha@mail.mcgill.ca).
Guest Editor: Barry A. Siegel, Mallinckrodt Institute of Radiology.
Published online Jan. 12, 2023.

DOI: 10.2967/jnumed.122.265029

Incidental Airway Findings on PET/CT with ^{18}F-PSMA

Jason Orciuolo[1], Akash Sharma[2], Ephraim E. Parent[2], Joseph M. Accurso[2], Manoj K. Jain[2], and Jason R. Young[2]

[1]Liberty University College of Osteopathic Medicine, Lynchburg, Virginia; and [2]Department of Radiology, Mayo Clinic, Jacksonville, Florida

A 76-y-old man presented with a history of difficulty with urination, frequent awakening at night due to nocturia, and an elevated level of prostate-specific antigen (27.4 ng/mL). The past medical history included chronic obstructive pulmonary disease with prior emergency room visits due to exacerbation. Prostate MRI discovered a very high-risk 2.3-cm prostate lesion invading the seminal vesicles and prostate capsule, with suggestive left external and internal iliac lymph nodes. Prostate biopsy showed prostate adenocarcinoma with a Gleason score of 4 + 3 = 7. To complete the staging, a prostate-specific membrane antigen (PSMA) PET/CT examination was performed using 370 MBq (10 mCi) of ^{18}F-piflufolastat, which demonstrated intense activity within the prostate lesion, many lymph nodes (bilateral iliac, bilateral paraaortic, and right retrocrural), and diffuse bronchial uptake (Fig. 1).

^{18}F-piflufolastat was approved by the Food and Drug Administration on May 27, 2021, to identify prostate cancer metastasis or recurrence. Although PSMA usually localizes to prostate cancer, this antigen is expressed on a variety of cells. Afshar-Oromieh et al. showed ^{68}Ga-PSMA-11 uptake in benign inflamed lymph nodes, with high PSMA expression in nodes undergoing follicular hyperplasia (*1*). Gordon et al. found high PSMA expression in neovascularization and inflammatory cell using formalin-fixed tissues (*2*).

^{68}Ga-PSMA-11 has been reported to localize in small peripheral airways in the setting of bronchiectasis, with follow-up bronchoscopy and lavage demonstrating inflammatory cells (*3*). However, to the best of our knowledge, ours is the first clinical report of large-airway PSMA localization. The patient had poorly controlled chronic obstructive pulmonary disease, with likely chronic inflammation of the airways resulting in PSMA localization, a potential false-positive finding that is important to highlight.

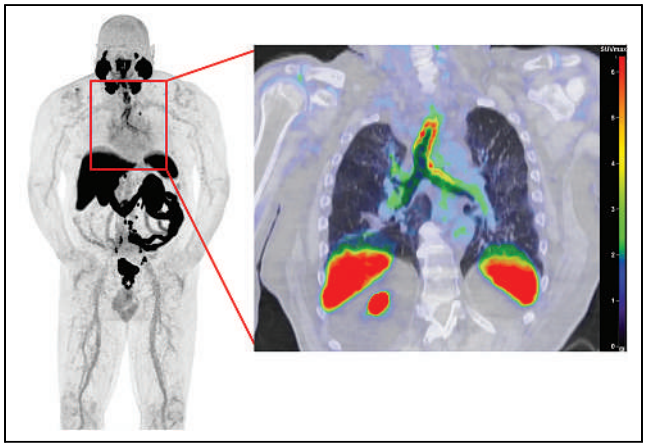

FIGURE 1. ^{18}F-piflufolastat PSMA PET/CT highlighting increased uptake throughout large airways.

DISCLOSURE

No potential conflict of interest relevant to this article was reported.

REFERENCES

1. Afshar-Oromieh A, Sattler LP, Steiger K, et al. Tracer uptake in mediastinal and paraaortal thoracic lymph nodes as a potential pitfall in image interpretation of PSMA ligand PET/CT. *Eur J Nucl Med Mol Imaging.* 2018;45:1179–1187.
2. Gordon IO, Tretiakova MS, Noffsinger AE, Hart J, Reuter VE, Al-Ahmadie HA. Prostate-specific membrane antigen expression in regeneration and repair. *Mod Pathol.* 2008;21:1421–1427.
3. Bouchelouche K, Vendelbo MH. Pulmonary opacities and bronchiectasis avid on ^{68}Ga-PSMA PET. *Clin Nucl Med.* 2017;42:e216–e217.

Received Nov. 29, 2022; revision accepted Dec. 21, 2022.
For correspondence or reprints, contact Jason R. Young (young.jason@mayo.edu).
Published online Jan. 5, 2023.

DOI: 10.2967/jnumed.122.265270

Molecular Imaging of Pulmonary Inflammation: Claiming That Vaping Is More Harmful Than Smoking Is Unsupported

TO THE EDITOR: We read with interest the recent pilot study by Wetherill et al. (*1*). The authors used ^{18}F-6-(1/2)(2-fluoropropyl)-4-methylpyridin-2-amine (^{18}F-NOS) PET imaging to quantify inducible nitric oxide synthase expression to characterize oxidative stress and inflammation in the lungs of 5 electronic cigarette (EC) users, 5 tobacco cigarette (TC) smokers, and 5 controls who had never smoked or vaped. PET imaging showed much greater ^{18}F-NOS nondisplaceable binding potential in the lungs of EC users than in TC smokers, but contrary to expectations, no difference between TC smokers and controls was found.

The reported absence of difference in ^{18}F-NOS nondisplaceable binding potential between TC smokers and controls is inconsistent with the suggestion given by enhanced nondisplaceable binding potential on ^{18}F-NOS imaging that there is oxidative stress and inflammation in the lungs, given that smoking causes both inflammatory responses and oxidative stress. This issue renders interpretation of the study's findings invalid. In consideration of the very small sample size and low reproducibility of ^{18}F-NOS PET imaging, the likelihood of chance findings is very high. There would have been more confidence in the interpretation if former smokers had been included in the study design; however, this was not done. Important confounders, such as allergies of the upper respiratory tract with inducible nitric oxide synthase upregulation and high levels of exhaled nitric oxide (*2*) and prior and present exposure to tobacco smoking among EC users (*3*)—who are typically either former smokers or dual users—were not taken into consideration. As it is impossible to decouple the lung health impact of EC aerosol emissions from prior tobacco smoke exposure, only long-term follow-up of exclusive EC users who have never smoked TCs in their life would have been a better-suited study design to verify potential harm caused by EC use. In a 3.5-y prospective clinical trial, daily exclusive EC users who had never smoked TCs did not exhibit any increase in exhaled nitric oxide (*4*).

Additionally, given the cross-sectional design of the study, the observed correlation between EC use and improved ^{18}F-NOS PET imaging does not infer causation.

The results of the study are inconsistent with the evidence that cigarette smoking reduces, not increases, inducible nitric oxide synthase expression and NO production from lung epithelial cells (*5*), as well as with the evidence that smoking is consistently linked to low levels of exhaled nitric oxide that return to normal after smoking is stopped (*6–8*).

Therefore, this pilot study does not support the argument that vaping is more harmful than smoking, and it contradicts clinical evidence showing that ECs may have some benefits in minimizing the harm caused by cigarette smoke and are unlikely to cause serious respiratory issues (*3,4,9*).

DISCLOSURE

Riccardo Polosa has received grants from U-BIOPRED, AIR-PROM, the Integral Rheumatology and Immunology Specialists Network (IRIS), the Foundation for a Smoke Free World, Pfizer, GlaxoSmithKline, CV Therapeutics, NeuroSearch A/S, Sandoz, Merck Sharp & Dohme, Boehringer Ingelheim, Novartis, Arbi Group Srl., Duska Therapeutics, Forest Laboratories, and Ministero dell'Università e della Ricerca (MUR) Bando PNRR 3277/2021 (CUP E63C22000900006) and 341/2022 (CUP E63C22002080006), funded by NextGenerationEU, the European Union (EU) economic recovery package. He is founder of the Center for Tobacco Prevention and Treatment (CPCT) at the University of Catania and of the Center of Excellence for the Acceleration of Harm Reduction at the same university. He receives consultancy fees from Pfizer, Boehringer Ingelheim, Duska Therapeutics, Forest Laboratories, CV Therapeutics, and Sermo Inc. He is being paid textbook royalties from Elsevier. He is also involved in a patent application for ECLAT Srl. He is a pro bono scientific advisor for Lega Italiana Anti Fumo (LIAF) and the International Network of Nicotine Consumers Organizations (INNCO), and he is the chair of the European Technical Committee for Standardization on "Requirements and Test Methods for Emissions of Electronic Cigarettes" (CEN/TC 437; WG4). Stefano Palmucci has received personal consulting fees or speaker fees from Boehringer Ingelheim and F. Hoffmann La Roche Ltd. outside the submitted work; is working in the scientific committee of the research project RF 2019-12371462 "Model for Optimized Implementation of Early Lung Cancer Detection: Prospective Evaluation of Preventive Lung Health," promoted by "Ministero della Salute" (Italy); has received consultancy fees from Elma Research srl (Milano, Italy); and has received support from Bracco Imaging SpA and Bayer Schering for congress registrations and congress accommodations/travels. No other potential conflict of interest relevant to this article was reported.

REFERENCES

1. Wetherill RR, Doot RK, Young AJ, et al. Molecular imaging of pulmonary inflammation in electronic and combustible cigarette users: a pilot study. *J Nucl Med.* 2023;64:797–802.
2. Abdullah Alwi AH, Zahedi FD, Husain S, Wan Hamizan AK, Abdullah B. Diagnostic value and clinical application of nasal fractional exhaled nitric oxide in subjects with allergic rhinitis. *Am J Rhinol Allergy.* 2023;37:307–312.
3. Polosa R, O'Leary R, Tashkin D, Emma R, Caruso M. The effect of e-cigarette aerosol emissions on respiratory health: a narrative review. *Expert Rev Respir Med.* 2019;13:899–915.
4. Polosa R, Cibella F, Caponnetto P, et al. Health impact of E-cigarettes: a prospective 3.5-year study of regular daily users who have never smoked. *Sci Rep.* 2017;7:13825.
5. Hoyt JC, Robbins RA, Habib M, et al. Cigarette smoke decreases inducible nitric oxide synthase in lung epithelial cells. *Exp Lung Res.* 2003;29:17–28.
6. Travers J, Marsh S, Aldington S, et al. Reference ranges for exhaled nitric oxide derived from a random community survey of adults. *Am J Respir Crit Care Med.* 2007;176:238–242.
7. Robbins RA, Millatmal T, Lassi K, Rennard S, Daughton D. Smoking cessation is associated with an increase in exhaled nitric oxide. *Chest.* 1997;112:313–318.
8. Campagna D, Cibella F, Caponnetto P, et al. Changes in breathomics from a 1-year randomized smoking cessation trial of electronic cigarettes. *Eur J Clin Invest.* 2016;46:698–706.
9. Morjaria JB, Campagna D, Caci G, O'Leary R, Polosa R. Health impact of e-cigarettes and heated tobacco products in chronic obstructive pulmonary disease: current and emerging evidence. *Expert Rev Respir Med.* 2022;16:1213–1226.

Riccardo Polosa*
Lucia Spicuzza
Stefano Palmucci
**University of Catania*
Catania, Italy
E-mail: polosa@unict.it

Published online May 11, 2023.
DOI: 10.2967/jnumed.123.265533

Reply: Molecular Imaging of Pulmonary Inflammation: Claiming That Vaping Is More Harmful Than Smoking Is Unsupported

REPLY: We thank Drs. Polosa, Spicuzza, and Palmucci for their interest and comments on our study. The team's comments highlight evidence supporting traditional combustible cigarettes as a proinflammatory phenotype and the potential of electronic cigarettes for harm reduction as a tool for smoking cessation. Harm reduction represents an important strategy in public health, because smoking combustible nicotine cigarettes remains the largest preventable cause of death worldwide (*1,2*).

In our innovative pilot study, we found increased radiotracer binding of ^{18}F-6-(1/2)(2-fluoropropyl)-4-methylpyridin-2-amine (^{18}F-NOS) in the lungs of electronic cigarette users compared with traditional combustible cigarette users (*3*). This unanticipated finding led us to conclude that electronic cigarette use leads to unique physiologic changes in the lungs, distinct from combustible cigarettes, including relatively increased inflammation in younger, otherwise healthy individuals. We neither concluded nor implied that vaping was more harmful than combustible cigarettes nor measured metrics of harm such as death or contribution to other diseases such as cancer, heart disease, or stroke.

Although there is evidence that electronic cigarettes can achieve cigarette quit rates superior to those for the nicotine patch (*4*), the long-term public health effects of electronic cigarettes, first introduced in the United States and the European Union in 2006, remain unclear (*1,5*). Given the decades of public health research documenting the various adverse outcomes that manifest after years of combustible cigarette smoking, including chronic obstructive pulmonary disease, cancer, and heart disease (*6–8*), it is important to acknowledge that electronic cigarettes are not harmless and could have long-term adverse health effects that are distinct from those associated with combustible cigarette use.

Electronic cigarettes are not unique to individuals trying to quit or who have quit smoking cigarettes. The Centers for Disease Control and Prevention report that 36.9% of individuals who vape also smoke combustible cigarettes and that 23.6% have never smoked combustible cigarettes, with the remaining 39.5% being former smokers (*9*). Electronic cigarette use among youth in the United States is alarming, with an estimated 2.14 million high school students and 380,000 middle school students reporting use (*10*). A harm reduction strategy for most of these individuals is not applicable; there is only the potential for harm. Thus, our study aimed to examine those who exclusively vape.

How electronic cigarette use alters cardiopulmonary physiology and the local pulmonary cellular milieu remains unclear. In agreement with our study, there is growing evidence that electronic cigarette use results in a proinflammatory phenotype (*11–15*). We carefully excluded subjects with asthma or allergies and those taking medications that could temper inflammation. Additionally, we did not observe a decreased PET signal in conventional smokers or suggest that combustible cigarette use results in diminished pulmonary inflammation.

With the epidemic rates of electronic cigarette use among youth continuing to rise and most adult users not using electronic cigarettes for smoking cessation, the long-term public health consequences of this relatively new behavior cannot be dismissed because of the lack of long-term data.

REFERENCES

1. *WHO Report on the Global Tobacco Epidemic 2021: Addressing New and Emerging Products.* World Health Organization; 2021. License CC BY-NC-SA 3.0 IGO.
2. *The Health Consequences of Smoking: 50 Years of Progress—A Report of the Surgeon General.* U.S. Department of Health and Human Services; 2014:1–943.
3. Wetherill RR, Doot RK, Young AJ, et al. Molecular imaging of pulmonary inflammation in electronic and combustible cigarette users: a pilot study. *J Nucl Med.* 2023;64:797–802.
4. Hajek P, Phillips-Waller A, Przulj D, et al. A randomized trial of E-cigarettes versus nicotine-replacement therapy. *N Engl J Med.* 2019;380:629–637.
5. Hajek P, Etter J-F, Benowitz N, Eissenberg T, McRobbie H. Electronic cigarettes: review of use, content, safety, effects on smokers, and potential for harm and benefit. *Addiction.* 2014;109:1801–1810.
6. Løkke A, Lange P, Scharling H, Fabricius P, Vestbo J. Developing COPD: a 25 year follow up study of the general population. *Thorax.* 2006;61:935–939.
7. Tindle HA, Stevenson Duncan M, Greevy RA, et al. Lifetime smoking history and risk of lung cancer: results from the Framingham Heart Study. *JNCI. J Natl Cancer Inst.* 2018;110:1201–1207.
8. Ding N, Shah AM, Blaha MJ, Chang PP, Rosamond WD, Matsushita K. Cigarette smoking, cessation, and risk of heart failure with preserved and reduced ejection fraction. *J Am Coll Cardiol.* 2022;79:2298–2305.
9. Cornelius ME, Loretan CG, Wang TW, Jamal A, Homa DM. Tobacco product use among adults: United States, 2020. *MMWR Morb Mortal Wkly Rep.* 2022;71:397–405.
10. Park-Lee E, Ren C, Cooper M, Cornelius M, Jamal A, Cullen KA. Tobacco product use among middle and high school students: United States, 2022. *MMWR Morb Mortal Wkly Rep.* 2022;71:1429–1435.
11. Higham A, Rattray NJ, Dewhurst JA, et al. Electronic cigarette exposure triggers neutrophil inflammatory responses. *Respir Res.* 2016;17:56.
12. Singh KP, Lawyer G, Muthumalage T, et al. Systemic biomarkers in electronic cigarette users: implications for noninvasive assessment of vaping-associated pulmonary injuries. *ERJ Open Res.* 2019;5:00182–02019.
13. Song M-A, Reisinger SA, Freudenheim JL, et al. Effects of electronic cigarette constituents on the human lung: a pilot clinical trial. *Cancer Prev Res (Phila).* 2020;13:145–152.
14. Moshensky A, Brand CS, Alhaddad H, et al. Effects of mango and mint pod-based e-cigarette aerosol inhalation on inflammatory states of the brain, lung, heart, and colon in mice. *eLife.* 2022;11:e67621.
15. Sharma A, Lee J, Fonseca AG, et al. E-cigarettes compromise the gut barrier and trigger inflammation. *iScience.* 2021;24:102035.

Reagan R. Wetherill*
Jacob Dubroff
**University of Pennsylvania*
Philadelphia, Pennsylvania
E-mail: rweth@pennmedicine.upenn.edu

Published online May 11, 2023.
DOI: 10.2967/jnumed.123.265570

PSMA PET/CT and Therapy Response Evaluation in Metastatic Prostate Cancer: Is It Time to Surpass the Old Way?

TO THE EDITOR: I have read with great interest the paper recently published in your journal entitled, "^{68}Ga-PSMA PET/CT for Response Assessment and Outcome Prediction in Metastatic Prostate Cancer Patients Treated with Taxane-based Chemotherapy" by Shagera et al. (*1*). The paper is very interesting and thought-provoking.

First, it is useful to standardize the criteria for therapy response evaluation, and although much has been accomplished in this regard through the European Organization for Research and Treatment of Cancer criteria (*2*), PERCIST (*3*), and other methods, the key to evaluating treatment response may perhaps be evaluation of the entire tumor volume expressing prostate-specific membrane antigen (PSMA), either for hormone therapies or for the taxane-based regimen. The entire tumor volume expressing PSMA can easily and reproducibly be evaluated using specific software, without focusing on a few selected lesions. Moreover, response-monitoring data similar in terms of survival outcome have already been reported for other radiopharmaceutical therapeutic agents, such as ^{223}Ra-dichloride (*4*), and data from Anton et al. (*5*) and Simsek et al. (*6*) found that total volume PSMA expression on PET is linked to the response to taxane-based therapy.

Second, careful attention should be given to disease extent at the bone level, to avoid an overestimation that can be linked to a poor prognosis rather than a better prognosis. Again, it is important to have a specific tool to detect bone metastases and monitor their changes during therapy. One such tool has already been tested (*7*) but is not yet available worldwide.

Finally, the authors concluded that PSMA PET/CT can be useful for assessing response early during therapy, but the available studies have not used this assessment until the end of therapy (*5,6*). Therefore, as correctly stated by the authors, prospective trials are needed to test the value of a PSMA-based response soon (4–8 wk) after the start of chemotherapy. I believe that PSMA PET/CT in the evaluation of therapy response will surpass the limits of morphologic imaging and is ready to move forward. Furthermore, PSMA PET/CT would also be useful in guiding the introduction of ^{177}Lu-PSMA–based therapy, which has an important role in the early phase of metastatic disease as recently demonstrated by the PSMAfore trial (*8*).

REFERENCES

1. Shagera QA, Artigas C, Karfis I, et al. ^{68}Ga-PSMA PET/CT for response assessment and outcome prediction in metastatic prostate cancer patients treated with taxane-based chemotherapy. *J Nucl Med.* 2022;63:1191–1198.
2. Young H, Baum R, Cremerius U, et al. Measurement of clinical and subclinical tumour response using [^{18}F]-fluorodeoxyglucose and positron emission tomography: review and 1999 EORTC recommendations. European Organization for Research and Treatment of Cancer (EORTC) PET Study Group. *Eur J Cancer.* 1999;35:1773–1782.
3. O JH, Lodge MA, Wahl RL. Practical PERCIST: a simplified guide to PET Response Criteria in Solid Tumors 1.0. *Radiology.* 2016;280:576–584.
4. Alongi P, Laudicella R, Lanzafame H, et al. PSMA and choline PET for the assessment of response to therapy and survival outcomes in prostate cancer patients: a systematic review from the literature. *Cancers (Basel).* 2022;14:1770.
5. Anton A, Kamel Hasan O, Ballok Z, et al. Use of prostate-specific membrane antigen positron-emission tomography/CT in response assessment following upfront chemohormonal therapy in metastatic prostate cancer. *BJU Int.* 2020;126:433–435.
6. Simsek DH, Kuyumcu S, Karadogan S, et al. Can PSMA-based tumor burden predict response to docetaxel treatment in metastatic castration-resistant prostate cancer? *Ann Nucl Med.* 2021;35:680–690.
7. Hammes J, Täger P, Drzezga A. EBONI: a tool for automated quantification of bone metastasis load in PSMA PET/CT. *J Nucl Med.* 2018;59:1070–1075.
8. Sartor AO, Morris MJ, Chi KN, et al. PSMAfore: a phase 3 study to compare ^{177}Lu-PSMA-617 treatment with a change in androgen receptor pathway inhibitor in taxane-naïve patients with metastatic castration-resistant prostate cancer [abstract]. *J Clin Oncol.* 2022;40(suppl):TPS211.

Laura Evangelista
University of Padua
Padua, Italy
E-mail: laura.evangelista@unipd.it

Published online May 11, 2023.
DOI: 10.2967/jnumed.122.265308

NOW AVAILABLE

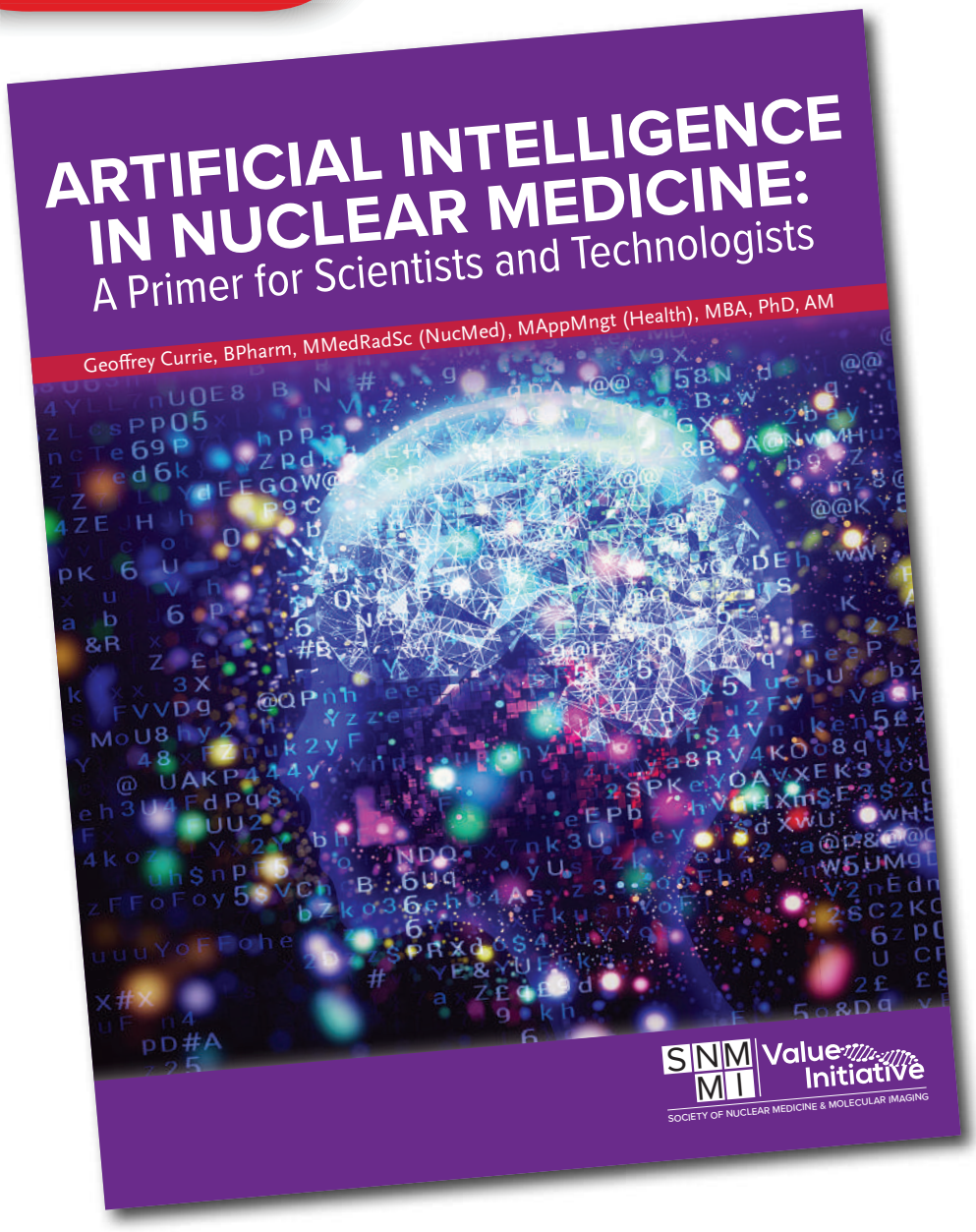

Artificial Intelligence in Nuclear Medicine: A Primer for Scientists and Technologists provides a grounding in how artificial intelligence, artificial neural networks, machine learning, and deep learning work; how their capabilities improve outcomes; how and where they should be integrated into your clinical and research practice; and the challenges and considerations involved in their implementation.

Grab your copy today!

www.snmmi.org/AIbook

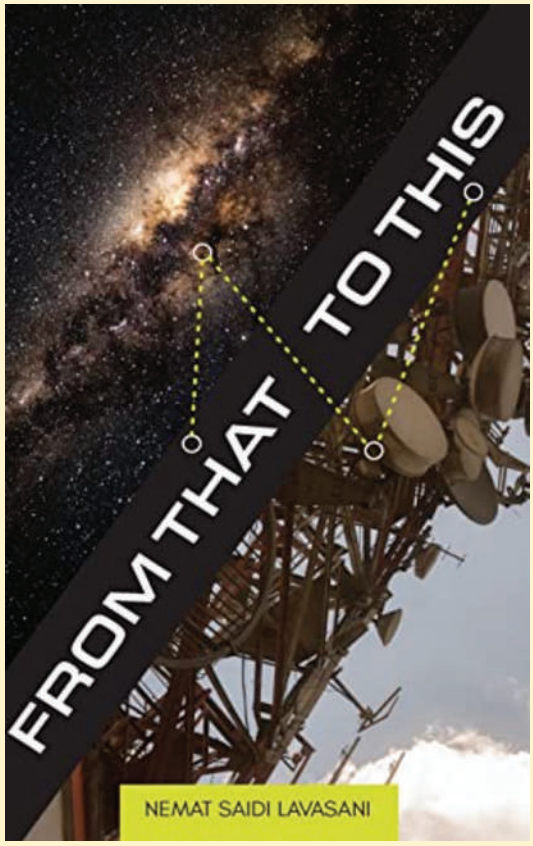

TO ALL DOCTORS AND TECHNOLOGISTS

Please have your patients read this book (from Chapter 14 on).

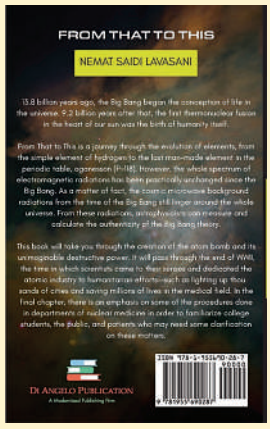

A – It saves you a bundle of time explaining the unfamiliar radiology exams, especially Nuc-Med and PET procedures.

B – It spares your patients much anxiety before their diagnostic tests (the procedures are explained in layman's terms).

C – It is a "must" read for patients taking the I-131 therapy dose.

This book will take the reader through an amazing history of the universe from the time of the Big-Bang, 13.8 billion years ago to the present time when the whole spectrum of electromagnetic radiation is being utilized in different sub-departments of radiology such as: ultrasound, MRI, CT, Nuc-Med and PET. This book is a crash course to understand radiation and how to protect oneself and others from it.

It can be purchased on Amazon.

SNMMI 2023 Therapeutics Conference

SEPTEMBER 21-23

Marriott Baltimore Waterfront
Baltimore, MD

This comprehensive two-and-a-half-day program will focus on the latest innovations and clinical applications in radiopharmaceutical therapy, including the following topic areas:

- Setting up a Theranostics Clinic
- Radiopharmaceutical Supply Chain
- Thyroid Therapies Lectures & Mock Tumor Board
- Prostate Therapies Lectures & Mock Tumor Board
- GI/Neuroendocrine Therapies Lectures & Mock Tumor Board
- Pediatric Therapies Lectures & Mock Tumor Board
- Radiopharmaceutical Dosimetry
- Updates on Clinical Trials

WWW.SNMMI.ORG/TC2023

SNMMI

VISIT SNMMI'S
"Radiopharmaceutical Therapy Central"

YOUR SOURCE FOR THE LATEST RADIOPHARMACEUTICAL THERAPY NEWS, EDUCATION, AND RESOURCES FROM SNMMI.

www.snmmi.org/Therapy

SOCIETY OF NUCLEAR MEDICINE & MOLECULAR IMAGING

BE PREPARED. GET CERTIFIED.

2023 SNMMI Nuclear Medicine Review Course – Live Virtual Meeting

This comprehensive review course is designed to help individuals prepare for their ABNM board certification, as well as providing a refresher for more experience clinicians. The program will be offered in a live virtual environment over two days, covering the following topics:

Day 1 Program – September 9, 2023

- Neurology
- Thyroid/Parathyroid/Head & Neck
- Pediatrics
- PET/CT
- Pulmonary/Thoracic
- Cardiovascular
- Infection/Inflammation
- Musculoskeletal

Day 2 Program – September 10, 2023

- Renal
- Gastrointestinal
- Male/Female-Benign/Malignant
- Therapies
- Treatment Response-Criteria/Imaging
- NRC Regulations/Radiation Safety
- Artifacts/Corrections
- Physics/Instrumentation

Register Today:
www.snmmi.org/nmrc

SNMMI | SOCIETY OF NUCLEAR MEDICINE & MOLECULAR IMAGING

ATTEND THE SNMMI 2023 ANNUAL MEETING

The **SNMMI 2023 Annual Meeting** provides you with access to 130+ scientific and CE sessions, more than 1,000 scientific posters, pre-meeting categorical seminars, industry-led satellite symposia, and great networking events. Plus, you can learn about leading products and innovations in the field from more than 185 exhibiting companies. It's the can't miss opportunity for you to elevate your skills and become your clinic's expert on the latest developments, research, and clinical applications advancing precision medicine and therapy.

Register Today

WWW.SNMMI.ORG/AM2023

SNMMI SOCIETY OF NUCLEAR MEDICINE & MOLECULAR IMAGING

Virtual registration options are also available.

REACH EVEN GREATER HEIGHTS WITH CARDIAC PET IMAGING

RUBY™ partners with you to help establish and grow your cardiac PET program today – and well into the future. Our RUBY-FILL® (Rubidium Rb 82 Generator) and RUBY Rubidium Elution System™ are supported by our comprehensive line of offerings, including financial modeling, reimbursement consultancy, education, and marketing expertise – as well as 24-hour customer assistance to ensure your growing PET practice runs smoothly and efficiently.

Isn't it time to discover how far you can soar?

Visit booth #2065 to learn more

INDICATION FOR USE:

RUBY-FILL is a closed system used to produce rubidium Rb 82 chloride injection for intravenous use. Rubidium Rb 82 chloride injection is a radioactive diagnostic agent indicated for Positron Emission Tomography (PET) imaging of the myocardium under rest or pharmacologic stress conditions to evaluate regional myocardial perfusion in adult patients with suspected or existing coronary artery disease. (1)

WARNING: HIGH LEVEL RADIATION EXPOSURE WITH USE OF INCORRECT ELUENT AND FAILURE TO FOLLOW QUALITY CONTROL TESTING PROCEDURE

Please see full prescribing information for complete boxed warning

High Level Radiation Exposure with Use of Incorrect Eluent

Using the incorrect eluent can cause high Strontium (Sr 82) and (Sr 85) breakthrough levels (5.1)

- **Use only additive-free 0.9% Sodium Chloride Injection USP to elute the generator (2.5)**
- **Immediately stop the patient infusion and discontinue the use of the affected RUBY-FILL generator if the incorrect solution is used to elute the generator (4)**
- **Evaluate the patient's radiation absorbed dose and monitor for the effects of radiation to critical organs such as bone marrow (2.9)**

Excess Radiation Exposure with Failure to Follow the Quality Control Testing Procedure

Excess radiation exposure occurs when the levels of Sr 82 or Sr 85 in the Rubidium Rb 82 Chloride injection exceed specified limits. (5.2)

- **Strictly adhere to the generator quality control testing procedure (2.6)**
- **Stop using the generator if it reaches any of its Expiration Limit. (2.7)**

The risk information provided here is not comprehensive. Please visit RUBY-FILL.com for full Prescribing Information including BOXED WARNING. You are encouraged to report negative side effects of prescription drugs to the FDA. Visit www.fda.gov/Safety/MedWatch or call 1-800-FDA-1088.

Jubilant DraxImage Inc. dba Jubilant Radiopharma™
16751 Trans-Canada Highway, Kirkland, Quebec, Canada H9H 4J4
Phone: 1.888.633.5343 / 514.630.7080
www.jubilantradiopharma.com

RUBY-FILL® RUBIDIUM Rb82 GENERATOR | JUBILANT RADIOPHARMA

6
23

The Journal of Nuclear Medicine

June 2023 ▪ Vol. 64 ▪ Pages 829–996